(NASA-CR-135730) SPACE PROGRAMS SUMMARY NO. 37-16, VOLUME 1 FOR THE PERIOD 1 MAY - 1 JULY 1962. THE LUNAR PROGRAM (Jet Propulsion Lab.) 235 p
N73-74114
Unclas
00/99 18918

Space Programs Summary No. 37-16, Volume I

for the period May 1, 1962 to July 1, 1962

The Lunar Program

(Title Unclassified)

CLASSIFICATION CHANGE
TO = UNCLASSIFIED ~~CONFIDENTIAL~~
By authority of E.O. No. 11652
Changed by A M Liebland Date 5/9/73

JET PROPULSION LABORATORY
CALIFORNIA INSTITUTE OF TECHNOLOGY
PASADENA, CALIFORNIA

July 31, 1962

This document contains information affecting the national defense of the United States, within the meaning of the Espionage Laws, Title 18, U.S.C., Sections 793 and 794, the transmission or revelation of which in any manner to an unauthorized person is prohibited by law.

CONFIDENTIAL

CONFIDENTIAL

NATIONAL AERONAUTICS AND SPACE ADMINISTRATION
CONTRACT NO. NAS 7-100

Space Programs Summary No.37-16, Volume I

for the period May 1, 1962 to July 1, 1962

The Lunar Program

(Title Unclassified)

00391

Copy No._____

JET PROPULSION LABORATORY
CALIFORNIA INSTITUTE OF TECHNOLOGY
PASADENA, CALIFORNIA

July 31, 1962

CONFIDENTIAL

Preface

The *Space Programs Summary* is a six volume, bimonthly publication designed to report on JPL space exploration programs, and related supporting research and advanced development projects. These activities are conducted under the sponsorship of the National Aeronautics and Space Administration.

All information formerly documented in the JPL *Research Summary,* together with reports on advanced development projects, is reported in Volumes IV and V. The subtitles of all volumes of the *Space Programs Summary* are:

Vol. I. The Lunar Program (Confidential)

Vol. II. The Planetary–Interplanetary Program (Confidential)

Vol. III. The Deep Space Instrumentation Facility (Unclassified)

Vol. IV. Supporting Research and Advanced Development (Unclassified)

Vol. V. Supporting Research and Advanced Development (Confidential)

Vol. VI. Space Exploration Programs and Space Sciences (Unclassified)

The *Space Programs Summary,* Volume VI is an unclassified digest of appropriate material from Volumes I through V, plus the reports of the JPL Space Sciences Division.

W. H. Pickering, *Director*
Jet Propulsion Laboratory

This document contains information affecting the national defense of the United States, within the meaning of the Espionage Laws, Title 18, U.S.C., Sections 793 and 794, the transmission or revelation of which in any manner to an unauthorized person is prohibited by law.

Space Programs Summary No. 37-16
Volume I

Copyright © 1962
Jet Propulsion Laboratory
California Institute of Technology

CONFIDENTIAL

Contents

I. Program Objectives 1

II. *Ranger* Project 3

A. Systems 3
B. Spacecraft Design 30
C. Guidance and Control 34
D. Telecommunications 41
E. Space Sciences 45
F. Propulsion 49
G. Supporting Activities and Engineering Facilities 49
Reference 55

III. *Ranger* Lunar Capsule 57

A. Introduction 57
B. Engineering and Test Effort 57

IV. *Ranger* TV Subsystem 63

A. Introduction 63
B. Structure 63
C. Electrical Integration 65
D. Environmental Testing 66
E. Electronics 67
F. Thermal Control 73
G. Ground Support Equipment 77

Reference 78

V. *Surveyor* Project 79

A. Introduction 79
B. Scientific Experiments 79

VI. *Surveyor* Spacecraft System 81

A. System Engineering Summary 83
B. Scientific Payload 91
C. System Analysis 112
D. Flight Control 128
E. Electronics 147
F. Electrical Power Supply 162
G. Thermal Control 170
H. Engineering Mechanics 185
I. Propulsion 198
J. Spacecraft Vehicle and Mechanisms for Basic Bus 202
K. Reliability and System Test 209
L. Mission Operations 221
References 237

CONFIDENTIAL

I. Program Objectives

The JPL Lunar Program consists of two major projects: *Ranger* and *Surveyor*. The *Ranger* Project has entered the flight stage; *Surveyor* is in hardware development.

The objective of the *Ranger* Project is to exploit present technology in support of the U.S. manned lunar flight program. Nine *Ranger* launchings, using *Atlas–Agena* B rockets, are now planned. Four of these flights have been made; the next is scheduled for this year.

Rangers 1 and 2 were engineering evaluation flights to test the basic system to be employed in later lunar and planetary vehicles. Several scientific experiments were carried, but on a noninterference basis. The *Ranger* 3, 4, and 5 spacecraft carries a gamma-ray instrument, a radar reflection experiment, a TV camera, and a rough-landing seismometer capsule. The 1963 flights (beginning with *Ranger* 6) will carry a high-resolution TV package and additional radiation experiments.

The objective of the *Surveyor* Project is to take the next step in advancing lunar technology, by making reconnaissance surveys from lunar orbit, and controlled soft landings on the Moon. Seven flights using *Centaur* launch vehicles are now planned. *Surveyor* spacecraft, being designed and built by the Hughes Aircraft Company under JPL subcontract, will carry a variety of instruments including TV cameras, radiation environment monitors, and geophysical equipment for determining characteristics of the lunar surface.

Page intentionally left blank

II. *Ranger* Project

A. Systems

1. Flight Performance

a. **Ranger** *3. The following paragraph supersedes the third paragraph, p. 3, SPS 37-14, Vols. I and II:*

The *Ranger* 3 launch was the first to include varying guidance parameters and the associated real-time range functions. The countdown was smooth and the vehicle lifted off early in the launch window on January 26, 1962, at 203011 GMT. Shortly after launch, an airborne guidance component in the *Atlas* failed, preventing acquisition by the radio command system. The vehicle flew on autopilot, with events generated by internal program and backup sources, with the result that the velocity was out of tolerance at vernier engine cutoff. The *Agena* functioned successfully, though it added somewhat to the injection error due to a slightly improper accelerometer setting. All other functions were normal and the spacecraft was injected on a trajectory that was soon determined to be above escape energy.

The over-all flight performance of the *Ranger* 3 spacecraft was quite successful, but there were a few failures which resulted in some modifications to the *Ranger* 4 spacecraft and supporting operations. The stations of the Deep Space Instrumentation Facility provided tracking and telemetry coverage continuously for 5 days except for periods when the RF signal was too weak to recover. The spacecraft signal was essentially lost at 1854 GMT on January 31, shortly after the supply of gas used for attitude stabilization was depleted.

b. **Ranger** *4.* Sometime between electrical disconnect from the *Agena* at 16 min, 33 sec after liftoff and acquisition by the mobile tracking station (MTS) 22 min, 51 sec after liftoff a failure occurred in the spacecraft. This failure has been described in *SPS 37-15,* Vol. I. There was an apparent loss of the 400-cps pulse train in the CC&S along with a loss of the 25-pps signal which is counted down from the 400-cps signal. The 25 pps normally drives the data encoder commutator and is required by the command decoder. Also the CC&S failed to give the programmed commands after the failure.

Since no data is received from the spacecraft between electrical separation from the *Agena* and DSIF acquisition, there is no coverage of the failure and the cause is unknown. The failure occurred before *Agena* retromotor ignition, and the mechanical separation from the *Agena* and *Agena* turnaround appear completely normal.

It is fairly certain that the spacecraft transmitter B+ had been switched up to full voltage before the failure.

Table 1. Actual *Ranger* 3 trajectory characteristics

Time of event	x R	y ϕ	z θ	$\dot{x}$ v	$\dot{y}$ γ	$\dot{z}$ σ	a e	i Ω	ω ν	Period Apogee Perigee
	Epoch			Central body			Epoch of pericenter passage			
Premid-course orbit	1-26-62	20 h 50 m	09.000 sec	Earth			1-26-62	20 h 49 m	21.311 sec	
	3394.2596 6663.2494	5710.8051 4.4275950	514.39773 341.07499	−7.7937433 10.554971	5.6169558 2.3583413	−5.3058356 120.51785	−496876.02 1.0133894	29.536534 247.12882	166.48433 4.5062043	N.A. N.A. 6652.8822
Postmid-course orbit	1-27-62	10 h 28 m	06.000 sec	Earth			1-26-62	20 h 44 m	16.427 sec	
	−129803.64 161519.94	−82370.716 −17.863269	−49545.683 289.15144	−1.6953469 11.059594	−1.5456074 12.058764	−.52111462 271.04436	−665436.51 1.0096024	31.533682 244.08175	168.34241 155.74760	N.A. N.A. 6389.7578
Closest approach to Moon (CAM)	1-28-62	23 h 48 m	06.000 sec	Earth			1-26-62	20 h 46 m	18.160 sec	
	−307446.30 410459.32	−253156.22 −14.003800	−99325.518 94.688474	−1.1617491 28.976549	−1.0990688 3.1760260	−.23703484 270.30911	−593540.53 1.0128986	56.023123 229.14449	181.19200 161.84171	N.A. N.A. 7655.8675
	1-28-62	23 h 48 m	06.000 sec	Sun			1-26-62	05 h 16 m	51.463 sec	
	−.92229629E8 .14732751E9	.10540102E9 18.076367	.45713423E8 131.18708	−24.937487 31.833300	−18.239030 .32951137	−7.6693230 104.79201	.16836094E9 .12506087	23.199543 .78818374	125.06790 2.9652321	436.08127 .18941631E9 .14730558E9
	1-28-62	23 h 48 m	06.000 sec	Moon			1-28-62	23 h 25 m	07.566 sec	
	−378.82031 36975.552	−13261.681 −44.336352	−34513.415 222.80872	−1.8240261 1.9403666	−.42016253 3.7161249	.04673394 284.11330	−1512.2482 25.393331	110.35805 193.50257	271.37399 4.0028143	N.A. N.A. 36888.773
CAM + 10 days	2-7-62	23 h 48 m	06.000 sec	Earth						
	−1008672.0 1392745.9	−942903.00 −7.5235677	−182357.50 88.433171	−.68115115 100.67328	−.66071177 .53982826	−.06024348 270.03671				
	2-7-62	23 h 48 m	06.000 sec	Sun			1-23-62	01 h 37 m	52.078 sec	
	−.11195169E9 .14772097E9	.88338078E8 15.119958	.38531658E8 141.72397	−20.812119 31.126051	−21.316626 1.2397348	−9.0160003 107.81626	.16028272E9 .08128640	23.207377 .78788150	121.87659 16.676064	405.07500 .17331152E9 .14725391E9
CAM + 100 days	5-8-62	23 h 48 m	06.000 sec	Earth						
	−9629609.0 10258232.0	−3488919.0 −3.2073603	−573945.50 336.57202	−2.3135319 746.84256	−.87224674 .19116675	−.41826427 269.97857				
	5-8-62	23 h 48 m	06.000 sec	Sun			1-18-62	17 h 23 m	18.375 sec	
	−.11089346E9 .16010609E9	−.10629198E9 −16.380033	−.45151063E8 223.78626	19.311819 28.561654	−19.291396 3.6173194	−8.4061722 106.78600	.15760513E9 .06504956	23.287619 .71393276	117.79715 107.70815	394.96711 .16785727E9 .14735298E9

CONFIDENTIAL

CONFIDENTIAL

Since the CC&S would normally have given the power-up command (its first flight command) at 22 min, 47 sec after liftoff (4 sec before first MTS data) it appears likely that the CC&S worked for 6 min, 14 sec after electrical separation, although this is not certain. The apparent position of the commutator is a position that the commutator would have been in 3.6 sec after the power-up command as well as a number of other times during the data gap. There is no known interrelationship in the spacecraft which would account for a failure in the CC&S or its power source being caused by the increase in transmitter power.

2. *Trajectory Analyses*

a. **Ranger 3.** Launch for the *Ranger* 3 mission occurred on January 26, 1962 at 203011 GMT. The launch was normal through the *Atlas* booster phase. However, a component failure in the *Atlas* booster caused a delay in booster cutoff, precluded corrective guidance during the sustainer phase and, in addition, caused a delay in the termination of the parking orbit.

Although the subsequent *Agena* B first burn, coast in parking orbit, and *Agena* B second burn occurred normally, the combined effect of the booster, sustainer and parking orbit coast time errors resulted in excessive altitude, velocity and position errors being imparted to the spacecraft at separation.

The injection conditions were in error such that the available mid-course maneuver would not have been sufficient to cause the spacecraft to impact the Moon. As an engineering experiment, the mid-course maneuver was performed during the spacecraft's first pass over the Goldstone Space Communications Stations.

The premid-course and postmid-course orbits were determined using the JPL orbit determination program (ODP). The trajectory characteristics of these orbits are tabulated in Table 1 for selected trajectory epochs. (Table 2 presents the legend for Tables 1, 3, 4 and 5.)

The energy of the postmid-course orbit (as well as the premid-course orbit) was sufficient to cause the spacecraft to escape the Earth's gravitational field and become a satellite of the Sun in a heliocentric orbit not too different from the Earth's heliocentric orbit. Figure 1 shows the relative positions of the spacecraft and Earth in their respective heliocentric orbits during 1962.

For comparison, the standard trajectory characteristics based on nominal flight conditions are presented in Table 3. The most notable difference between the actual and standard *Ranger* 3 trajectory is in the flight time from injection to lunar encounter. This difference in flight time as well as difference in other trajectory characteristics are illustrated in Fig. 2 which compares the actual and standard *Ranger* 3 trajectories.

Table 2. Legend for Tables 1, 3, 4, and 5

Parameter	Definition
x, y, z	Vernal equinox cartesian coordinates in a geocentric equatorial system. The origin is the center of the central body. The principal direction ($\vec{x}$) is the vernal equinox direction of date and the principal plane (xy) is the equatorial plane of date. $\vec{z}$ is along the direction of the Earth's spin axis of date, km
$\dot{x}, \dot{y}, \dot{z}$	First time derivatives of x, y, and z, respectively; i.e., cartesian components of the probe space-fixed velocity vector, km/sec
	Earth as central body
R	Probe radius distance, km
ϕ	Probe geocentric latitude, deg
θ	Probe east longitude, deg
v	Probe Earth-fixed velocity, km/sec
γ	Pitch angle of the probe Earth-fixed velocity vector with respect to the local horizontal, deg
σ	Azimuth angle of the probe Earth-fixed velocity vector measured east of true north, deg
	Moon as central body
R	Probe radius distance, km
ϕ	Probe selenocentric latitude, deg
θ	Probe selenocentric east longitude, deg
v	Probe selenocentric-fixed velocity, km/sec
γ	Pitch angle of the probe selenocentric-fixed velocity vector with respect to the local horizontal, deg
σ	Azimuth angle of the probe selenocentric-fixed velocity vector measured east of the Moon's mean spin axis, deg
	Sun as central body
R	Sun–probe radius distance, km
ϕ	Probe celestial declination, deg
θ	Probe celestial right ascension, deg
v	Probe space-fixed velocity, km/sec
γ	Pitch angle of the probe space-fixed velocity vector with respect to the local horizontal, deg
σ	Azimuth angle of the probe space-fixed velocity vector measured east of true north, deg
a	Semi-major axis, km
e	Eccentricity
i	Inclination of the orbit plane to the equatorial plane, deg
Ω	Longitude of the ascending node, deg
ω	Argument of pericenter, deg
ν	True anomaly, deg
	Period is measured in days, apogee and perigee in kilometers. N.A. = Not applicable.

CONFIDENTIAL

Table 3. *Ranger* 3 standard[a] trajectory characteristics

Event	x R	y ϕ	z θ	$\dot{x}$ v	$\dot{y}$ γ	$\dot{z}$ σ	a e	i Ω	ω ν	Period Apogee Perigee
	Epoch			Central body			Epoch of pericenter passage			
Injection	1-26-62 20 h 49 m 35.410 sec			Earth			1-26-62 20 h 49 m 01.028 sec			
	3513.1948 6570.4653	5508.5460 6.0805562	695.98719 339.41220	−7.6461246 10.545225	5.9024730 1.6921828	−5.1806727 119.82969	334954.07 .98039997	29.176277 248.47037	164.16177 3.2885337	22.329223 663343.02 6565.1090
Lunar impact	1-29-62 14 h 07 m 45.824 sec			Earth						
	−268651.49 390439.96	−272146.71 −11.640266	−78777.624 245.08582	−1.8709869 28.538549	−1.0741018 4.1068621	−.03860675 270.76815				
	1-29-62 14 h 07 m 45.824 sec			Moon			1-29-62 14 h 15 m 43.562 sec			N.A.
	1647.9565 1738.0898	549.44500 −6.7966494	57.500104 324.41177	−2.6326895 2.6849601	−.48331726 −79.695690	.22048056 73.480830	−3113.5410 1.0229900	39.499517 16.137576	156.62949 −153.64818	N.A. 71.580480

[a]As determined by JPL using the actual launch time and the specified lunar impact conditions.

Table 4. Actual[a] *Ranger* 4 trajectory characteristics

Time of event	x R	y ϕ	z θ	$\dot{x}$ v	$\dot{y}$ γ	$\dot{z}$ σ	a e	i Ω	ω ν	Period Apogee Perigee
	Epoch			Central body			Epoch of pericenter passage			
Postinjection orbit	4-23-62 21 h 04 m 19 sec			Earth			4-23-62 21 h 03 m 45.053 sec			
	−3893.0895 6568.8828	5026.1205 14.574054	1652.9353 320.25897	−8.6979759 10.543285	−4.8240304 1.6687774	−4.5972464 117.27733	306543.84 .97858815	29.698773 334.87970	146.22976 3.2465826	19.549453 606524.01 6563.6685
Impact conditions	4-26-62 12 h 50 m 00.38 sec			Earth						
	149460.51 378795.94	−323786.17 −19.703532	−127712.30 248.23571	−.82511277 27.417922	−1.5337943 2.2259672	−.23562437 270.27416				
				Moon			4-26-62 12 h 58 m 45.736 sec			N.A.
	1682.6893 1738.0898	−123.21191 −11.965175	−417.53132 231.45130	−1.7580050 2.6692629	−1.9757244 −33.722636	−.33305879 276.41444	3343.5162 1.3802314	156.86051 211.19802	275.21326 −57.529497	N.A. 1271.3099

[a]As determined by the JPL Orbit Determination Group.

CONFIDENTIAL

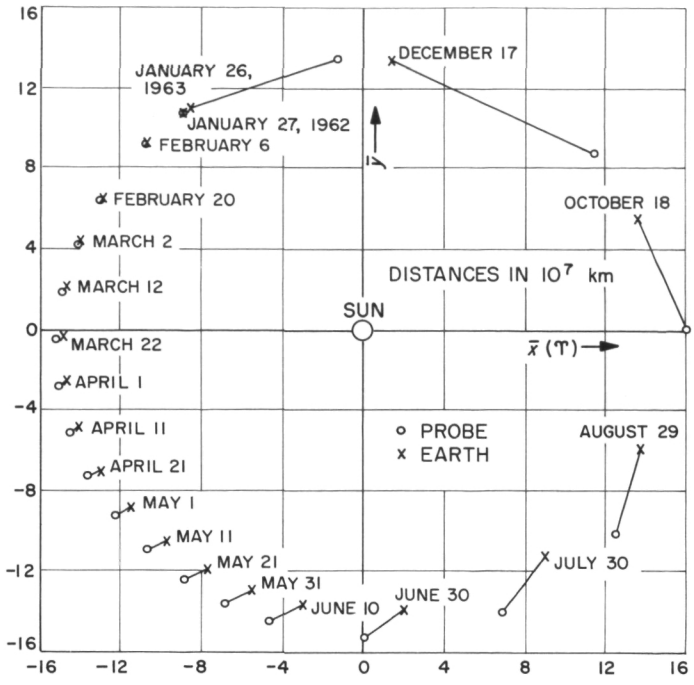

Fig. 1. Heliocentric orbits of the Earth and probe for the year ending January 26, 1963, projected in the equatorial plane

b.* Ranger *4. Launch for the *Ranger* 4 mission occurred on April 23, 1962 at 205015 GMT. The *Atlas–Agena* boost phases were normal throughout the ascent into parking orbit, the parking orbit coast, and the second *Agena* burn. The performances of the booster vehicles were well displayed in that the *Ranger* spacecraft was injected into an orbit which resulted in lunar impact without the use of a corrective mid-course maneuver.

However, following the electrical interface disconnect between the *Agena* and *Ranger* spacecraft a malfunction of the spacecraft occurred which precluded the accomplishment of spacecraft engineering and scientific experiments.

The postinjection orbit was determined using the JPL ODP. The trajectory characteristics of this orbit are tabulated in Table 4. For comparison the standard trajectory characteristics based on nominal flight conditions are presented in Table 5. A diagram of the actual *Ranger* 4 trajectory is presented in Fig. 3.

c. Trajectory characteristics for* Ranger *5. The *Ranger* launching schedule has been altered since the publication of *SPS 37-7*. The current *Ranger* 5 launch dates are presented in Table 6 for three possible launch periods. Changes in schedule affect the lunar missions because of the continuously changing positions of the celestial bodies. The result of the latest schedule change of the *Ranger* 5 mission was to shift the injection locations over the Earth's surface and to alter the flight time (and, therefore, the impact speed).

Launch period and firing window. Permissible launch dates for *Ranger* 5 have been restricted to 4 or 5 days of the month near lunar third quarter. These days were chosen since they best satisfy the constraints of the spacecraft attitude control system and scientific mission. The scheduling of launch pad facilities and scientific payloads allow launch periods to occur during the months of October, November, and December 1962. The launch azimuths for the *Ranger* 5 mission are restricted between 93 and 111 deg east of true north by range safety considerations. The firing windows provided by this azimuth range are given in Table 6. However, the firing windows for the dates noted in Table 6 may be reduced due to constraints imposed by lunar arrival conditions with respect to the Goldstone Space Communications Stations.

Trajectory description. The *Ranger* 5 standard trajectories might be classed as slow trajectories in that their flight times are of the order of 66 hr. Choice of flight time is made on the basis of visibility of impact to the Goldstone station and guidance accuracy considerations. Injections occur about 3.3 deg past perigee of the geocentric conic.

For each launch period for *Ranger* 5, the injection locations are shown in Figs. 4, 5 and 6 for trajectories of 93- through 111-deg launch azimuths, and for the successive days on which firings are permissible. Each line represents the location of injection for the launch date noted. Tables 7 and 8 give injection and lunar impact conditions for the first and last permissible launch dates of those considered for each launch period of *Ranger* 5 for 93- and 111-deg launch azimuth trajectories.

Explanation of Tables 7 and 8. Except for inertial speed, the coordinates of injection are all relative to a rotating Earth. Path angle is measured from the geocentric local horizontal plane, and azimuth angle is measured in the geocentric local horizontal plane eastward from true north. Geocentric latitude is measured positive north of the Earth's equator and geocentric longitude is measured positive east of Greenwich meridian. Except for inertial speed, the coordinates of impact are relative to a rotating Moon. Path angle is measured from the selenocentric local horizontal plane, and azimuth angle is measured in the selenocentric local horizontal plane

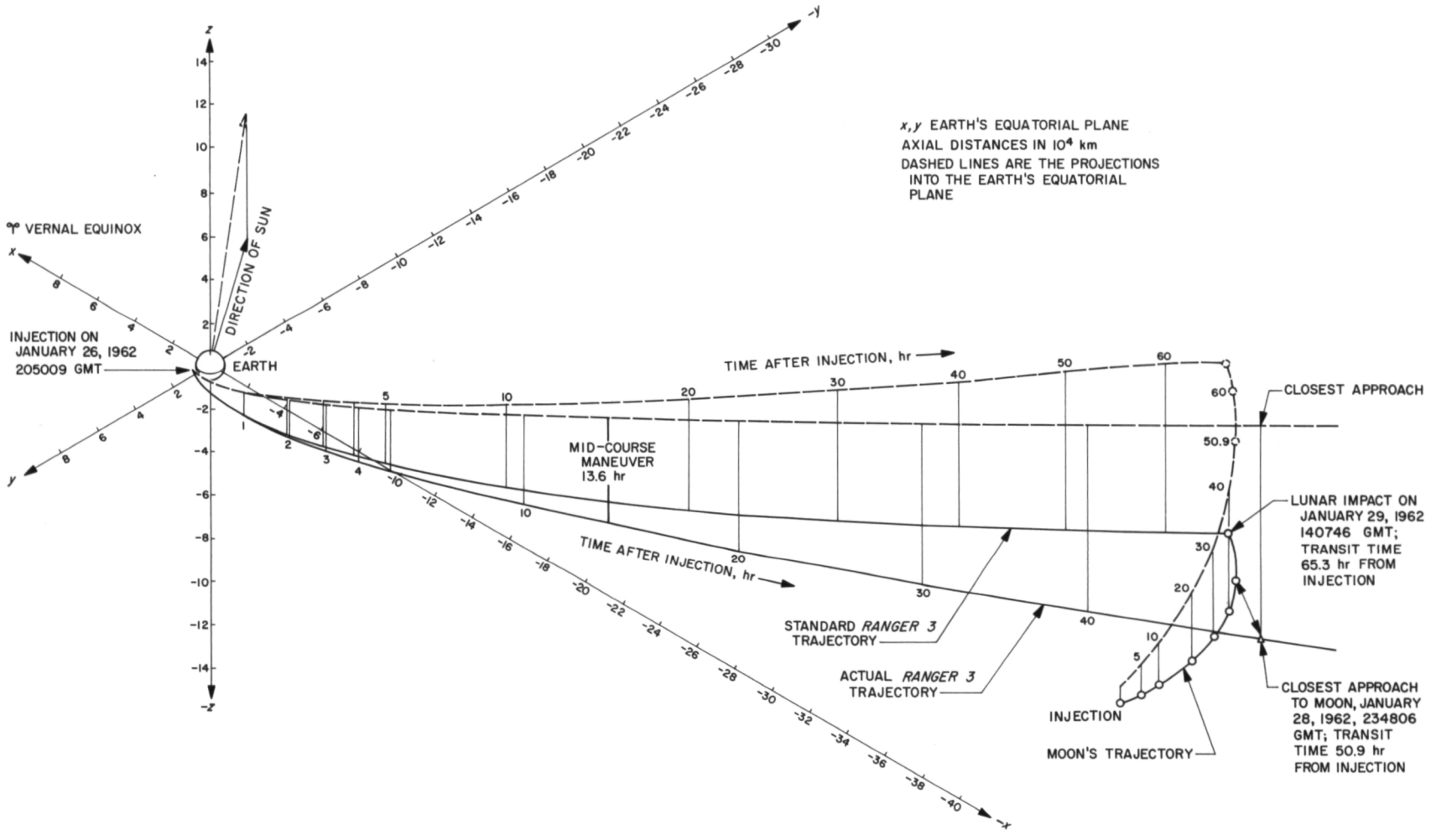

Fig. 2. Actual and standard *Ranger* 3 trajectories to lunar encounter

CONFIDENTIAL

CONFIDENTIAL

Table 5. *Ranger* 4 standard[a] trajectory characteristics

Event	x R	y ϕ	z θ	$\dot{x}$ v	$\dot{y}$ γ	$\dot{z}$ σ	a e	i Ω	ω ν	Period Apogee Perigee
	Epoch			Central body			Epoch of pericenter passage			
Injection	4-23-62 21 h 04 m			Earth			4-23-62	21 h 03 m 43.303 sec		
	−3871.2852	5038.8846	1664.0211	−8.7114591	−4.7794548	−4.6072547	283251.93	29.811932	146.18212	17.364210
	6568.5741	14.674689	320.04307	10.539157	1.6347042	117.35835	.97682782	334.73038	3.1832877	55994.029
										6563.5660
Lunar impact	4-26-62	13 h 51 m	57.219 sec	Earth						
	151507.68	−320412.21	−126281.56	.14350666	−1.9627172	−.65902836				
	376252.03	−19.610867	233.23556	26.626034	4.2007831	269.98989				
	4-26-62	13 h 51 m	57.219 sec	Moon			4-26-62	13 h 59 m	54.301 sec	N.A.
	270.22142	1591.4137	644.46848	−.78517725	−2.4136530	−.76000790	−3549.7582	37.503718	194.24174	N.A.
	1738.0897	−2.6096283	321.64118	2.6488356	−80.676393	61.299818	1.0161636	49.014448	−156.72165	57.376823

[a]As determined by Space Technology Laboratories using nominal flight conditions.

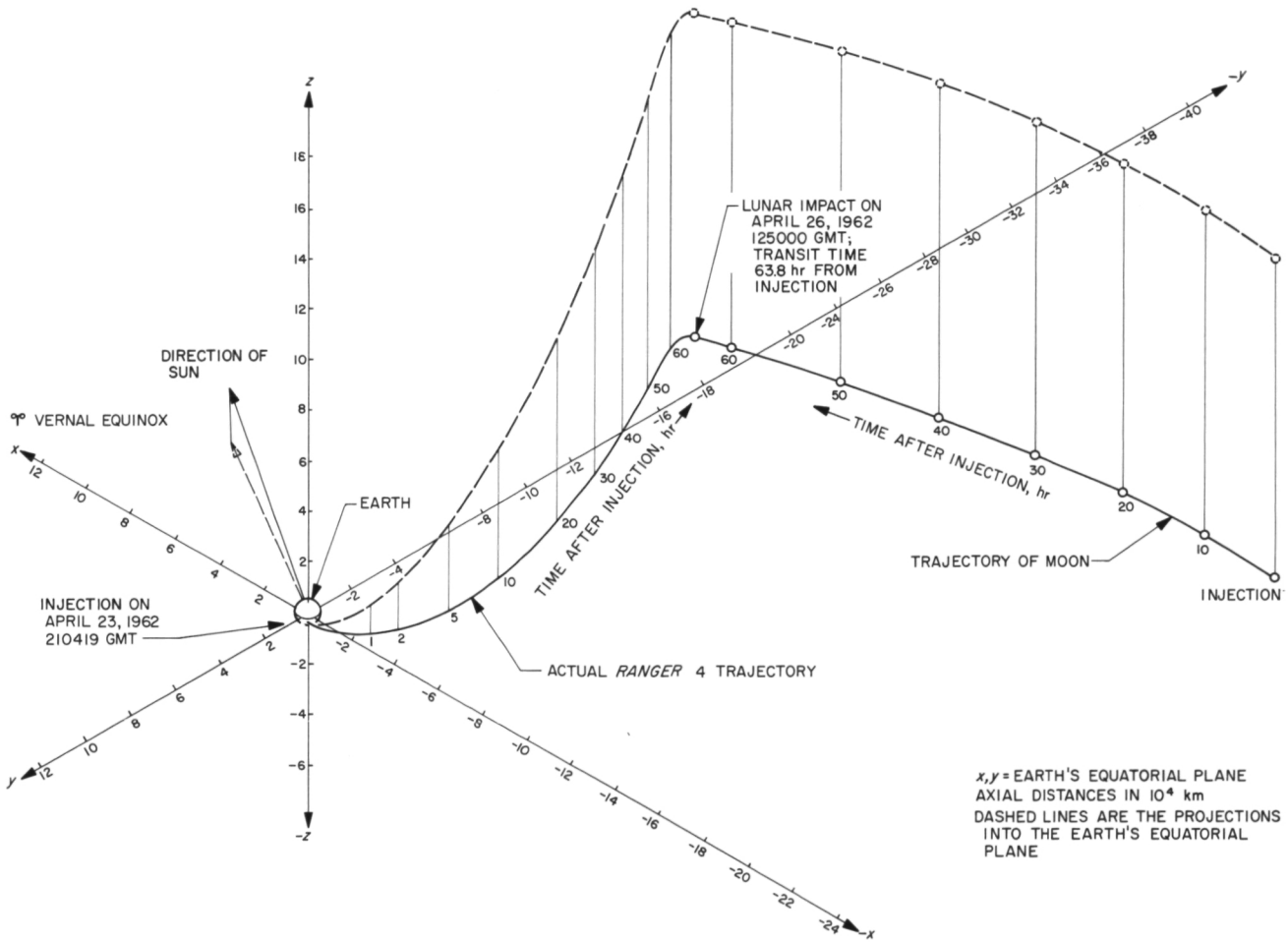

Fig. 3. Actual *Ranger* 4 trajectory to lunar impact

eastward from the selenocentric north direction. The selenocentric latitude and longitude are defined in Fig. 7. The geocentric latitude and longitude are as defined except for the probe at impact.

d. Preliminary trajectory characteristics for Rangers *6 through 9. Rangers* 6 through 9 will be launched from AMR at a launch azimuth between 90 and 114 deg east of true north. The launch vehicle is the same as those

Table 6. Launch dates and launch windows for the *Ranger* 5 mission

Mission	Launch date, 1962	Launch window for 93- to 111-deg launch azimuth range	
		hr	min
Ranger 5	October 16	2	52.1[a]
	17	2	49.1
	18	2	42.6
	19	2	34.5[a]
Ranger 5 alternate	November 14	2	48.0[a]
	15	2	39.8
	16	2	31.5
	17	2	23.4
	18	2	15.8[a]
Ranger 5 alternate	December 14	2	28.8[a]
	15	2	20.8
	16	2	13.2
	17	2	05.8
	18	1	58.7[a]

[a]This launch window may be reduced (not smaller than 1 hr) due to constraints on the arrival conditions relative to the Goldstone tracking station.

of *Rangers* 1 through 5, consisting of a General Dynamics/Astronautics *Atlas* D Mod II first stage, a Lockheed *Agena* B second stage, and the JPL *Ranger* spacecraft as the payload. The spacecraft are similar to *Rangers* 3, 4 and 5 except that the lunar capsule will be replaced by a high-resolution TV subsystem being developed by RCA. (See Section IV; *Ranger TV Subsystem.*)

The ascent trajectory for each of the *Ranger* 6 through 9 missions will be similar to those of *Rangers* 1 through 5 in that the parking orbit concept will be used. In a parking orbit trajectory (Fig. 8) the vehicle first enters a low-altitude, circular, Earth-satellite trajectory, coasts in this satellite orbit for a predetermined period, and subsequently leaves this orbit by the application of a final impulse. Such parking orbits effectively diminish the geometrical constraints such as a fixed launch site by permitting injection to occur at any point over the Earth's surface and still providing good payload capability. The parking orbit altitude for *Rangers* 6 through 9 will be 100 n m.

The launch philosophy associated with a mission which involves impacting the Moon when launching from the

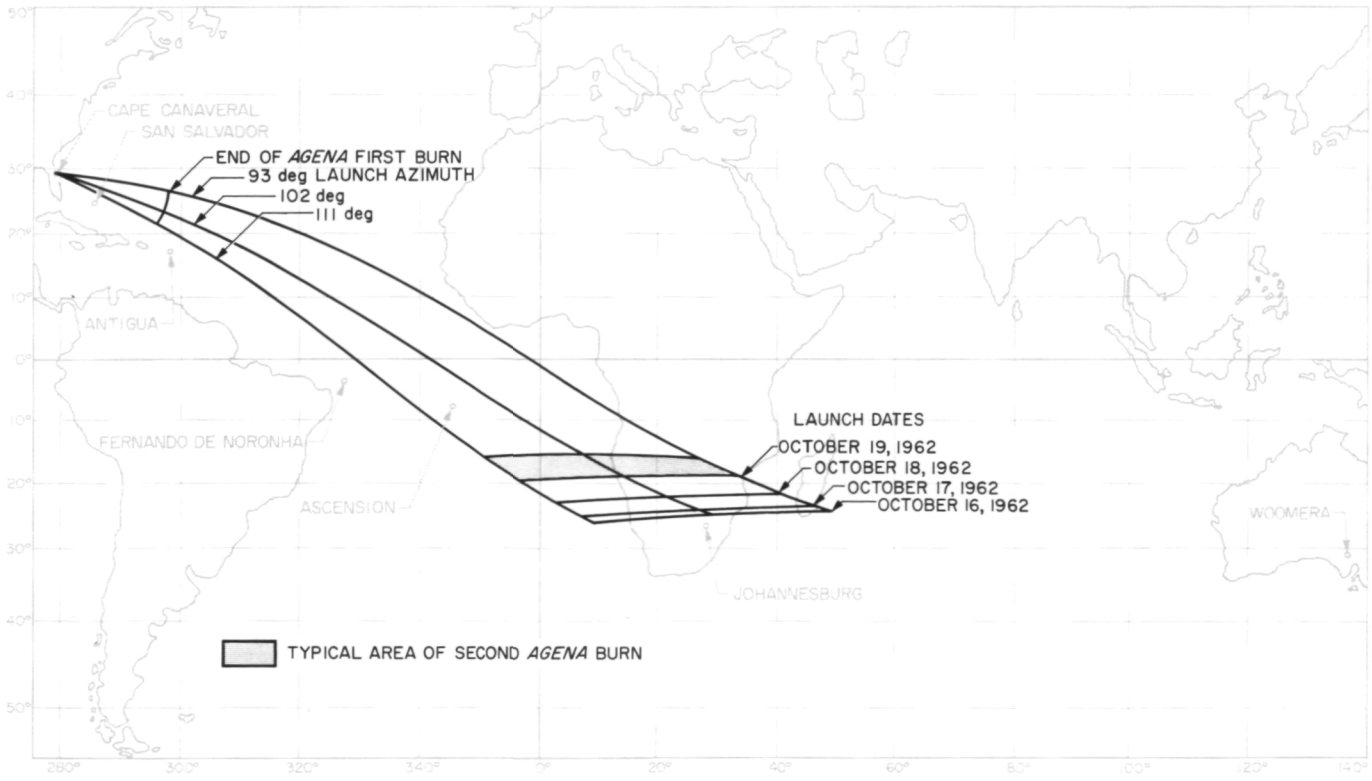

Fig. 4. Injection locations for the *Ranger* 5 mission

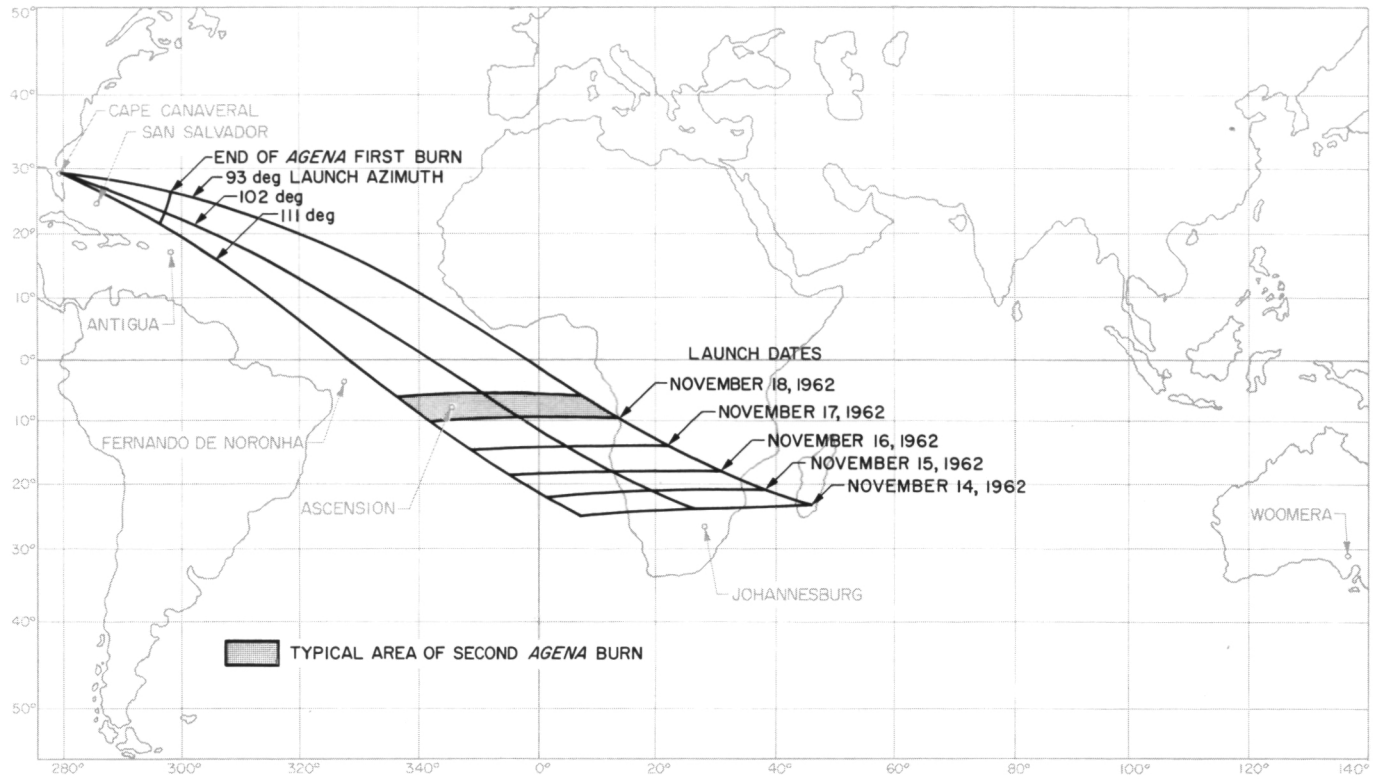

Fig. 5. Injection locations for the *Ranger* 5 mission, first alternate launch period

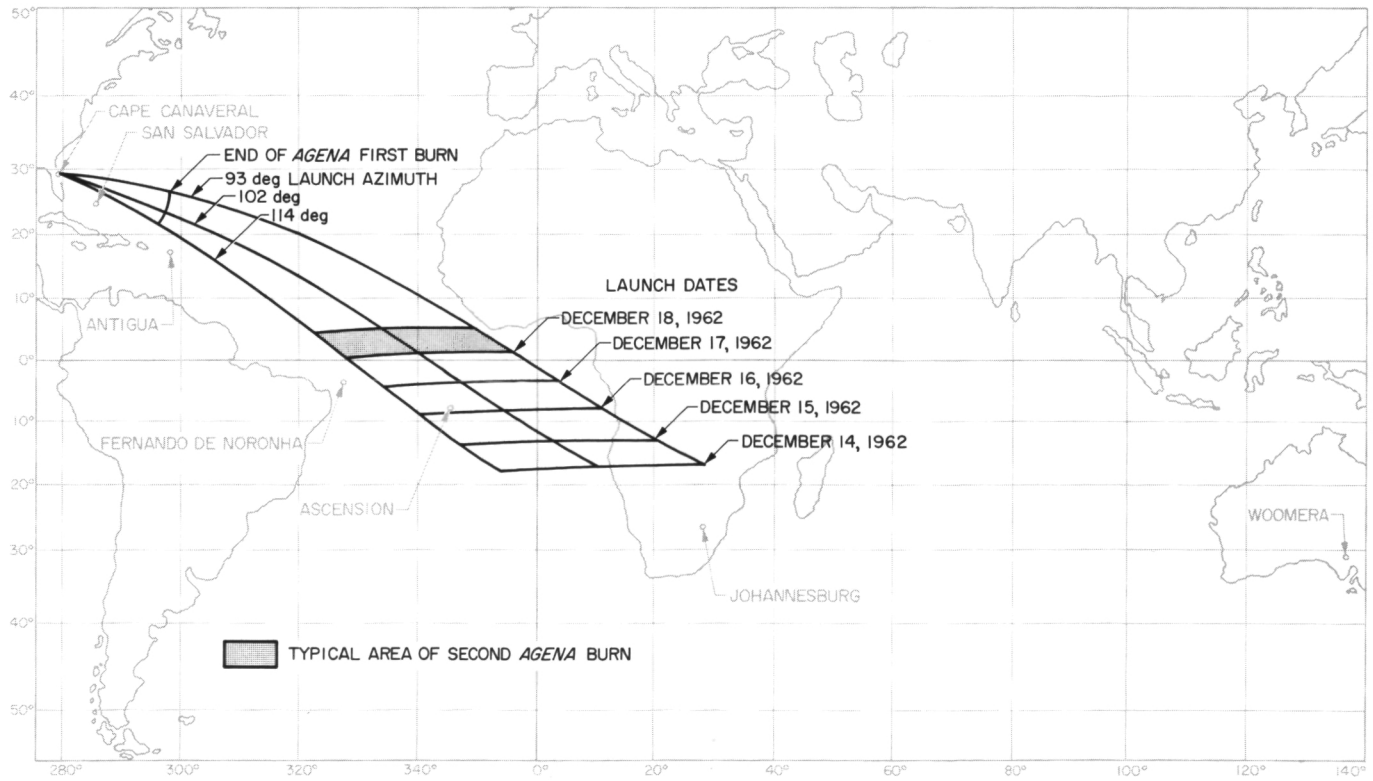

Fig. 6. Injection locations for the *Ranger 5* mission, second alternate launch

CONFIDENTIAL

Table 7. Injection and lunar impact conditions, first launch dates

Event	Launch azimuth 93 deg			Launch azimuth 111 deg		
	Ranger 5	*Ranger* 5 alternate	*Ranger* 5 alternate	*Ranger* 5	*Ranger* 5 alternate	*Ranger* 5 alternate
Launch date	10-16-62	11-14-62	12-14-62	10-16-62	11-14-62	12-14-62
Injection						
GMT, hr min sec	14 55 5	14 43 46	16 8 18	17 38 27	17 23 14	18 29 31
Time after launch, sec	2326.876	2273.378	1999.607	1804.548	1761.1760	1541.901
Radius, m	6570551.5	6570536.9	6570429.5	6570019.1	6570034.5	6570069.0
Speed, m/sec	10531.815	10537.367	10546.513	10557.955	10563.513	10572.612
Path angle, deg	1.6907604	1.6934139	1.6959752	1.6842239	1.6868006	1.6891382
Azimuth angle, deg	106.09340	107.70222	114.43109	114.36978	115.69109	121.08707
Geocentric						
Latitude, deg	−24.254388	−23.236451	−16.734635	−25.699585	−24.496325	−17.617240
Longitude, deg	49.879439	46.283842	28.818897	10.024355	7.2314619	353.93403
Speed, inertial, m/sec	10952.029	10957.428	10965.728	10952.478	10957.851	10966.031
Impact (unretarded)						
Flight time from injection, hr	66.061462	65.051877	64.946623	66.293846	65.264548	65.081288
GMT, hr min sec	8 58 46	7 46 53	9 5 6	11 56 5	10 39 6	11 34 24
Geocentric						
Latitude, deg	20.794773	19.365389	11.582388	20.749204	19.123851	11.188553
Longitude, deg	302.78208	314.15134	298.85146	260.04763	272.57441	262.64758
Selenocentric						
Latitude, deg	−16.480694	2.3749507	−8.7632154	−17.803927	1.4179421	−9.3872138
Longitude, deg	347.01069	356.13489	349.16263	346.87795	355.73298	348.72250
Speed, m/sec	2609.4246	2629.5202	2661.6660	2613.6565	2634.7627	2667.2734
Path angle, deg	−66.938775	−65.038100	−69.472915	−66.742779	−64.814653	−69.301236
Azimuth angle, deg	123.39579	86.356781	95.230663	122.86570	85.863423	94.923526
Earth–Moon–probe angle, deg	28.048872	11.268070	15.809910	28.875210	11.449301	16.267402
Lighting angle, deg	59.158473	58.702128	57.892159	60.713644	59.761982	58.768513
Miss parameters						
B • T, km	1358.1655	1686.7058	1351.1626	1358.1799	1686.3814	1350.8895
B • R, km	924.93251	−270.69154	46.877338	925.63475	−268.63122	47.630722
Speed, inertial, m/sec	2610.8810	2631.4718	2663.2647	2615.1229	2636.7306	2668.8826

Earth is complex. The continuous changes in the geometry of the celestial bodies require continuous changes in the launch parameters. The lunar impact trajectories must satisfy the celestial geometry as well as design limitations imposed from four principal areas. These areas are: (1) attitude control, (2) scientific mission, (3) telecommunications, and (4) temperature control. (The specific constraints in each area are discussed at length in Ref. 1.) Two of the launch parameters which evolve are launch day and launch time. The permissible launch days define the launch period and the permissible launch times, in any one day, define the firing window.

Launch periods for the *Ranger* 6 through 9 missions are determined primarily by the attitude control constraints and by the scientific mission constraints. Figure 9 shows a sketch of the Earth, Moon, and Sun geometry indicating the positions of the Moon at impact which do not satisfy the attitude control constraints. These positions occur near new and full Moons. As a result, the attitude control constraints dictate two permissible launch periods, referenced about first and third quarters, each having a maximum length of 8 consecutive days. Table 9 lists the launch periods for each month in 1963 which satisfy the attitude control constraints. The scientific mission constraints dictate which of the two launch periods in any one month is acceptable. In addition, these constraints restrict the length of the acceptable launch period to less than the maximum length of 8 days

CONFIDENTIAL

Table 8. Injection and lunar impact conditions, last launch dates

Event	Launch azimuth 93 deg			Launch azimuth 111 deg		
	Ranger 5	*Ranger* 5 alternate	*Ranger* 5 alternate	*Ranger* 5	*Ranger* 5 alternate	*Ranger* 5 alternate
Launch date	10-19-62	11-18-62	12-18-62	10-19-62	11-18-62	12-18-62
Injection						
GMT, hr min sec	18 39 23	20 2 59	21 14 27	21 6 0	22 11 47	23 7 0
Time after launch, sec	2071.824	1745.983	1422.912	1597.411	1326.809	1056.545
Radius, m	6570.4031	6570306.9	6570237.9	6570.0063	6570074.2	6570166.1
Speed, m/sec	10534.527	10539.009	10544.658	10560.658	10565.045	10570.592
Path angle, deg	1.6893662	1.6899407	1.6930553	1.6825582	1.6829722	1.6861688
Azimuth angle, deg	112.91463	118.26182	119.76042	119.92637	124.34062	125.71934
Geocentric						
Latitude, deg	−18.632482	−9.3122055	1.0500758	−19.465227	−9.9502622	.29678538
Longitude, deg	33.273146	13.852410	355.71789	357.17433	341.96416	327.73048
Speed, inertial, m/sec	10953.961	10957.561	10962.911	10954.295	10957.757	10962.972
Impact (unretarded)						
Flight time from injection, hr	71.418175	71.183974	68.229415	71.565710	71.252287	68.236663
GMT, hr min sec	18 4 29	19 14 1	17 28 13	20 39 56	21 26 55	19 21 12
Geocentric						
Latitude, deg	14.495843	4.3307548	−6.5363628	14.148153	3.9418362	−6.8620579
Longitude, deg	207.04024	191.80226	217.65657	169.36050	159.50779	190.21713
Selenocentric						
Latitude, deg	−7.6191083	−7.7821741	−11.087003	−8.4873423	−8.3540401	−11.574728
Longitude, deg	310.27434	315.46978	315.41001	309.50454	314.85123	314.81448
Speed, m/sec	2610.5316	2631.1514	2663.1604	2616.3964	2636.8795	2668.7766
Path angle, deg	−84.013228	−89.890077	−89.903338	−83.925110	−89.912084	−89.902582
Azimuth angle, deg	237.35312	284.97544	264.20338	237.31825	277.07711	270.75075
Earth–Moon–probe angle, deg	55.171382	46.600727	43.263649	55.824050	47.083173	43.773175
Lighting angle, deg	62.085275	72.914100	76.865634	62.714538	73.452640	77.247113
Miss parameters						
B • T, km	−331.30224	−.60979662	.22345253	−331.81046	.80070674	0
B • R, km	275.16716	−1.8819178	.72702383	277.38729	−.88383250	0
Speed, inertial, m/sec	2610.1334	2631.1473	2663.1570	2615.9933	2636.8770	2668.7730

for several of the landing sites under consideration (Fig. 10).

All the vertical or near-vertical impact trajectories for the *Ranger* 6 through 9 missions must impact on the western portion of the lunar surface and any trajectory which impacts on the eastern portion of the lunar surface must be a nonvertical impacter. Figure 9 shows that in order to satisfy the lighting constraint (Sun–Moon–probe angles at impact from 20 to 70 deg), a trajectory which impacts on the lunar west side must be launched during the third quarter period, and a nonvertical impact trajectory which impacts on the lunar east side must be launched during the first quarter period. In addition, it follows that a nonvertical impact trajectory which impacts near the Earth–Moon line, neither east nor west, must be launched within or near the full Moon period.

There are at least 4 launch days in each third quarter period on which vertical impact trajectories satisfy the lighting angle constraint. In addition, by biasing the vertical impact trajectories on additional launch days, the Sun–Moon–probe angles at impact can be shifted so that the values will be between the required 20- to 70-deg range. These biased trajectories are near-vertical impacters having impact angles of less than 20 deg. In

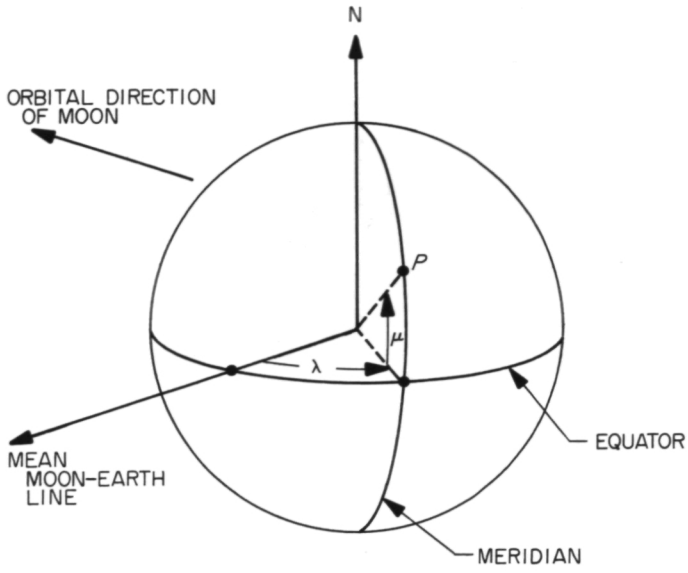

THE SELENOGRAPHIC LONGITUDE λ AND LATITUDE μ FOR THE POINT *P* ON THE MOON'S SURFACE ARE SHOWN IN THE POSITIVE DIRECTIONS

THE SELENOGRAPHIC COORDINATES OF THE TRUE MOON-EARTH LINE ARE TIME VARIANT

Fig. 7. Definition of selenographic coordinates

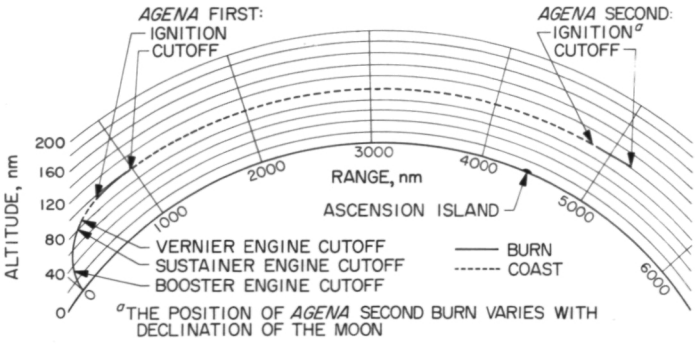

Fig. 8. Ascent trajectory profile

this manner, 8 consecutive days of third quarter launch period is obtained.

Since *Rangers* 6 and 7 are to impact vertically or near-vertically, the landing area must be on the western portion of the lunar surface and, as a result, launch must occur during the third quarter period. In the case of *Rangers* 8 and 9, the trajectory is not restricted to vertical or near-vertical impacters, and therefore the landing areas can be varied. The launch period varies as a function of the landing area chosen (Fig. 10). If the *Ranger* 3 through 7 impact area is chosen, then the launch period

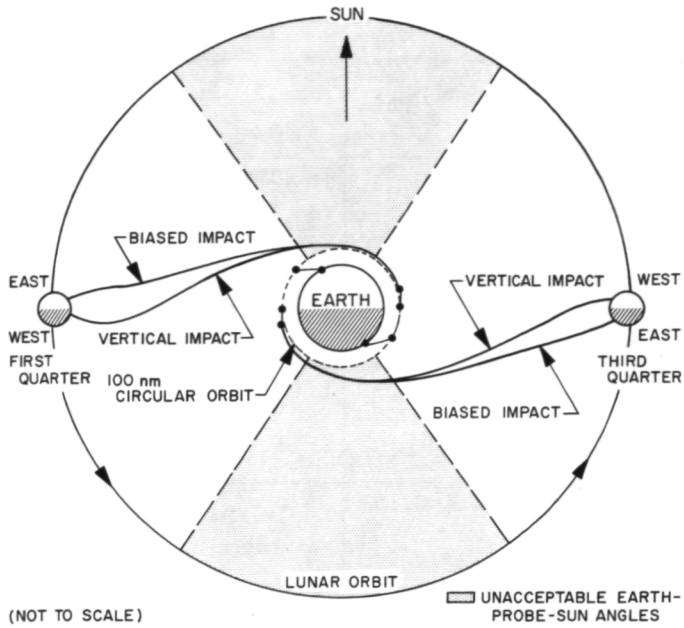

Fig. 9. Lighting angle geometry at impact

is 8 consecutive days during the third quarter similar to the *Ranger* 6 and 7 launch periods. If the landing area Mare Tranquillitatis, Mare Vaporum, or Sinus Medii is chosen, the scientific mission constraints limit the launch period to something less than 8 days (the limitation of the attitude control system).

Figure 11 presents a plot of the Sun–Moon–probe angle at impact versus launch day during the month of May 1963. According to current launch pad availability schedules, May is the first possible launch month for *Ranger* 8.

Table 9. Maximum launch periods for 1963

Month	Day of month	
	Third quarter launchings leading edge (western longitude)	First quarter launchings trailing edge (eastern longitude)
Jan	11, 12, 13, 14, 15, 16, 17, 18	
Feb	10, 11, 12, 13, 14, 15, 16, 17	
March	11, 12, 13, 14, 15, 16, 17, 18	
April	10, 11, 12, 13, 14, 15, 16, 17	
May	10, 11, 12, 13, 14, 15, 16, 17	23, 24, 25, 26, 27, 28, 29, 30
June	8, 9, 10, 11, 12, 13, 14, 15	22, 23, 24, 25, 26, 27, 28, 29
July	7, 8, 9, 10, 11, 12, 13, 14	22, 23, 24, 25, 26, 27, 28, 29
Aug	5, 6, 7, 8, 9, 10, 11, 12	20, 21, 22, 23, 24, 25, 26, 27
Sept	3, 4, 5, 6, 7, 8, 9, 10	19, 20, 21, 22, 23, 24, 25, 26
Oct	3, 4, 5, 6, 7, 8, 9, 10	19, 20, 21, 22, 23, 24, 25, 26
Nov	1, 2, 3, 4, 5, 6, 7, 8	17, 18, 19, 20, 21, 22, 23, 24
Dec	1, 2, 3, 4, 5, 6, 7, 8	17, 18, 19, 20, 21, 22, 23, 24

CONFIDENTIAL

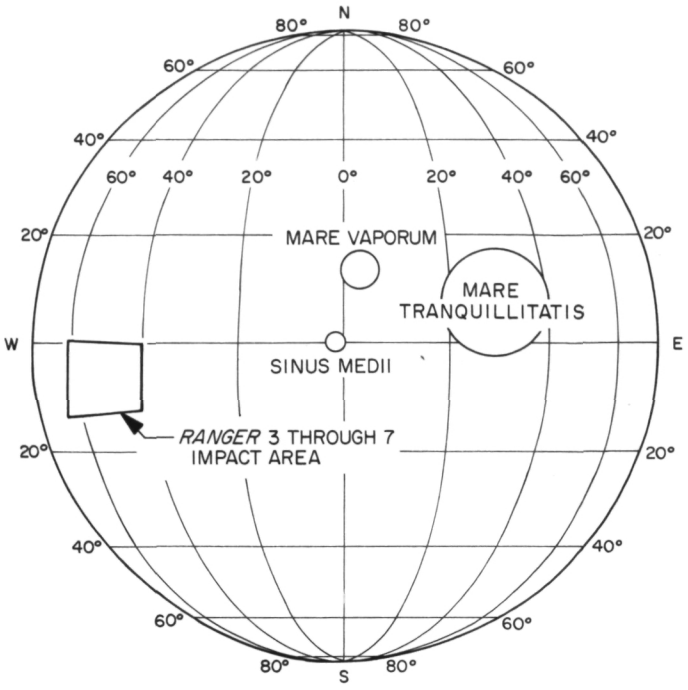

Fig. 10. Lunar landing sites

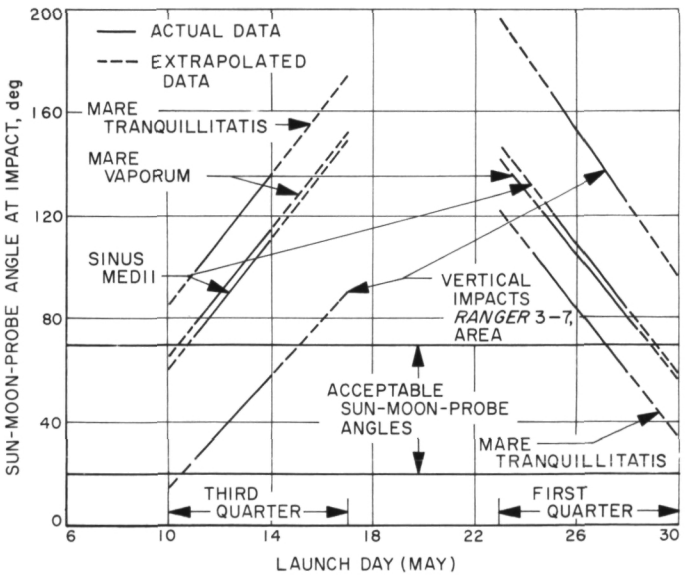

Fig. 11. Sun–Moon–probe angle at impact versus launch day, May 1963

The permissible lighting angle range is represented by the crosshatched area. The lunar west side impacters (*Ranger* 3 through 7 impact area) have acceptable lighting angles at impact for launches during the third quarter period and unacceptable lighting angles at impact for launches during the first quarter period. The lunar east side impacters (Mare Tranquillitatis area) have acceptable lighting angles at impact for launches on 4 consecutive days during the first quarter period and unacceptable lighting angles at impact for launches during the third quarter period. The impacters near the meridian of the Earth–Moon line, Mare Vaporum and Sinus Medii areas, have acceptable lighting angles at impact for 1 day at the start of the third quarter period (the end of the full Moon period) and for 2 days at the end of the first quarter period (the start of the full Moon period). Similar launch periods exist in the remaining *Ranger* 8 and 9 launch months.

The firing window is determined by the allowable launch azimuth range. As launch time varies in any one day, the launch azimuth and the parking orbit coast time must also vary in order to compensate for the motions of the Earth and Moon. In this manner, the minimum and maximum values of launch azimuth limit the length of the firing window. The launch azimuth range used in this discussion is from 90 to 114 deg. The final permissible launch azimuth range may be reduced at a later date due to tracking and range safety limitations. Figure 12 presents the launch times versus the launch day for each of the maximum launch periods in 1963 for azimuths from 90 to 114 deg at 6-deg intervals. Figure 13 presents the maximum firing window versus launch day for 1963.

The near-Earth postinjection trajectories are characterized by flight times of the order of 66 hr. The 66-hr lunar trajectory is a highly elliptical trajectory which may be described in a general manner by the conic elements at injection. These are as follows: a vis viva energy of -1.0 km^2/sec^2, an eccentricity of 0.98, a semi-major axis of 388,000 km, an inclination varying from 28 to 36 deg depending on the launch azimuth, a perigee distance of 6563 km, and a true anomaly at injection of 3.3 deg (injection occurs 3.3 deg past perigee). The injection points for this type of trajectory lie in the Atlantic Ocean area between the United States and South Africa. The exact locations of these injection points depend upon the declination of the Moon at lunar impact. Figures 14, 15, and 16 present the plots of injection loci for January third quarter, May third quarter, and May first quarter launchings. First and third quarter launchings behave in a very similar manner. The injection loci are in the same general area and move according to the motion of the Moon. Figures 17 through 23 present the Earth tracks for the months of January and May. All the Earth tracks are seen to be similar in nature.

CONFIDENTIAL

Table 10. Trajectory parameters for vertical impact trajectories

Launch day, Jan	12			13			
Launch azimuth, deg	90	102	114	90	102	114	90
Injection conditions							
GMT, hr min sec	16 06 9.4	17 38 13.4	18 53 4.1	17 18 05.8	18 47 53.7	19 59 59.4	18 29 39.6
Time after launch, sec	1745.2807	1440.4417	1202.7982	1702.3773	1428.4460	1176.1875	1569.0918
Radius, km	6570.8302	6570.3132	6569.9501	6570.7660	6568.3667	6569.9983	6570.6887
Speed, km/sec	10.542279	10.551530	10.580144	10.544965	10.555853	10.580342	10.546511
Path angle, deg	1.6940039	1.6901089	1.6850666	1.6955970	1.7251896	1.6847310	1.6967137
Azimuth angle, deg	117.95727	120.19934	125.83755	119.09442	121.23303	126.89751	119.59846
Geocentric latitude, deg	−9.7180784	−9.8351316	−11.010831	−5.5565560	−5.7060040	−6.4618626	−1.2718768
Geocentric longitude, deg	20.184187	357.61577	338.54155	12.633720	350.65331	332.44049	5.1741982
Inertial speed, km/sec	10.961501	10.961935	10.964680	10.963963	10.965984	10.964610	10.965403
Impact conditions							
Flight time from injection, hr	68.138	68.204	67.155	67.698	67.734	67.787	67.261
GMT, hr min sec	12 4 26.5	13 50 29.2	14 02 22.8	12 59 57.0	14 31 57.9	15 47 13.9	13 45 18.1
Geocentric							
Latitude, deg	4.544325	4.1694035	4.1337183	−.026775195	−.24898430	−.47589599	−4.3749820
Longitude, deg	243.29056	219.96149	217.07043	242.35716	219.99622	201.70526	241.38941
Selenocentric							
Latitude, deg	−8.1913143	−8.4259125	−8.7673409	−9.6375547	−9.8386602	−10.269043	−10.752044
Longitude, deg	316.39468	316.18327	316.69100	316.42555	316.14288	315.60831	316.22829
Speed, km/sec	2.6494849	2.6513686	2.6664425	2.6600888	2.6620388	2.6672857	2.6687639
Path angle, deg	−89.897444	−89.931470	−89.935137	−89.901334	−89.877053	−89.898162	−89.913769
Azimuth angle, deg	268.47985	280.86491	300.32858	258.90200	270.34779	264.87822	262.12610
Earth–Moon–probe angle, deg	45.206482	45.333023	44.821560	43.871706	44.069780	44.534885	42.753605
Sun–Moon–probe angle, deg	20.420024	21.056384	21.743159	32.617901	33.140311	33.352828	44.687989
Earth–probe–Sun angle, deg	65.571083	65.300779	65.389296	75.788659	76.481012	77.047888	86.935449
Inertial speed, km/sec	2.6494810	2.6513676	2.6664424	2.6600853	2.6620333	2.6672818	2.6687614

Since the trajectories are designed to allow the spacecraft to impact the Moon during the lunar day, the probe will be in direct sunlight except for brief periods during its travel in the vicinity of the Earth. The spacecraft never enters the shadow of the Moon. The time that the spacecraft spends in the Earth's shadow will vary according to launch date and launch azimuth. Third quarter launchings will be of the same order of magnitude as *Rangers* 3 through 5. First quarter launchings will be in the direct sunlight from injection to lunar impact (Fig. 9).

The trajectory parameters at lunar arrival are presented in Tables 10 through 13 for the months of January and May. The January trajectories are characteristic of the *Ranger* 6 and 7 trajectories and the May trajectories are characteristic of the *Ranger* 8 and 9 trajectories.

Tables 10 and 11 present detailed trajectory parameters for the month of January. Table 10 lists the parameters for the acceptable vertical impact trajectories at launch azimuths of 90, 102, and 114 deg for each of 5 launch days referenced about the third quarter. In addition, there are near-vertical impacters which satisfy the design constraints. Characteristics of these biased trajectories are presented in Table 11. All the near-vertical trajectories have impact angles of less than 20 deg as constrained. Impact angle is equal to path angle plus 90 deg. The lighting angles at impact for each launch day are between 20 and 70 deg as constrained. The vertical impact trajectories having launch days of January 12 through 16 resulted in acceptable lighting angles at lunar encounter. The vertical impact trajectories having launch days of January 11, 17 and 18 resulted in unacceptable lighting angles at lunar encounter. The January 11 case had a lighting angle of less than 20 deg and was therefore biased away from the selenocentric subsolar point. The January 17 and 18 cases had lighting angles greater than 70 deg and therefore were biased toward the selenocentric subsolar point.

CONFIDENTIAL

January 1963 launch azimuths of 90, 102, and 114 deg

14		15			16		
102	114	90	102	114	90	102	114
19 56 46.1	21 03 12.1	19 41 48.6	21 06 11.8	22 06 53.6	20 55 8.0	22 16 39.2	23 6 51.4
1304.1696	1069.8495	1436.7557	1181.1980	965.23015	1307.8756	1062.3499	879.04748
6568.4196	6570.0497	6570.5989	6568.4465	6570.0929	6570.5021	6568.4480	6570.1409
10.557286	10.581796	10.546792	10.557469	10.581989	10.545868	10.556465	10.584936
1.7268263	1.6855387	1.6971551	1.7279038	1.6857974	1.6968418	1.7282965	1.6878165
121.71613	127.37170	119.47098	121.62561	127.38745	118.74456	120.99993	127.06451
−1.4449495	−2.2396728	3.0073817	2.7950252	1.9378117	7.1199992	6.8511091	5.3653261
343.84018	326.98291	357.79377	337.12564	321.64680	350.54667	330.58728	317.23348
10.967315	10.965941	10.965707	10.967521	10.966134	10.964924	10.966656	10.969173
67.270	67.306	66.835	66.821	66.845	66.404	66.372	64.905
15 12 58.1	16 21 34.4	14 31 54.8	15 55 28.3	16 57 38.4	15 19 22.3	16 38 59.8	16 01 10.8
−4.6317672	−4.8340134	−8.6135275	−8.8448404	−9.0180224	−12.538181	−12.737321	−12.644178
220.08795	203.41838	240.26414	219.97551	204.88143	239.29417	219.98538	229.15220
−10.940570	−11.393795	−11.502882	−11.717469	−12.217846	−11.843503	−12.094730	−12.506157
315.99750	315.42749	315.82132	315.58576	315.03421	315.21240	315.03235	315.82562
2.6707950	2.6760242	2.6747962	2.6768964	2.6821201	2.6778873	2.6800191	2.7013667
−89.914338	−89.903086	−89.923382	−89.910157	−89.907211	−89.888091	−89.908539	−89.916360
274.19648	258.22938	274.07569	271.00044	255.43796	284.23302	272.07568	264.92354
42.908227	43.421802	41.916223	42.089840	42.604658	41.427309	41.566732	40.800138
45.214974	45.312998	56.563242	57.048465	57.089424	68.236834	68.738210	69.292757
87.593739	88.109984	98.116631	98.748344	99.219602	109.42515	110.03605	109.74319
2.6707925	2.6760208	2.6747942	2.6768935	2.6821172	2.6778829	2.6800160	2.7013643

Tables 12 and 13 present detailed trajectory parameters at one launch azimuth, 102 deg, for the month of May. Four launch days referenced about first quarter and 4 launch days referenced about third quarter are presented. The intent of these tables is to show the general trajectory characteristics of a *Ranger* 8 type mission. The differences between a first and third quarter launching and the differences resulting from varying the landing area are presented. The impact angles for the acceptable May third quarter cases (impacts in the *Ranger* 3 through 7 impact area) are all less than 20 deg as constrained. The impact angles for the acceptable May first quarter cases, impacts at Mare Tranquillitatis, Mare Vaporum, or Sinus Medii, are greater than 20 deg. A special study has shown that these large first quarter impact angles are permissible if the TV cameras are pointed along the impact velocity vector during the terminal portion of flight. The lighting angles for May are presented in Fig. 11 for each of the landing areas under consideration. In the case of the vertical impact trajectories (*Ranger* 3 through 7 impact area), 5 launch days during the May third quarter period exhibit acceptable lighting angles at impact. The 3 launch days with unacceptable lighting angles at impact will be biased with respect to the selenocentric subsolar point so as to shift the lighting angles at impact into the acceptable region.

The geocentric longitudes of the probe at arrival are approximately 220 deg for the 102-deg launch azimuths. Since the longitude of Goldstone is 243 deg, the loci of impact points as seen from the Earth are off center from the Goldstone meridian. The final trajectories will be adjusted so that the loci of impact points will be symmetrically centered about the Goldstone meridian. The remaining azimuths will lie on either side of the meridian since the injection energy in any one day must be a constant.

The flight times vary from 66 to 70 hr as a result of the changing lunar distance and declination.

CONFIDENTIAL

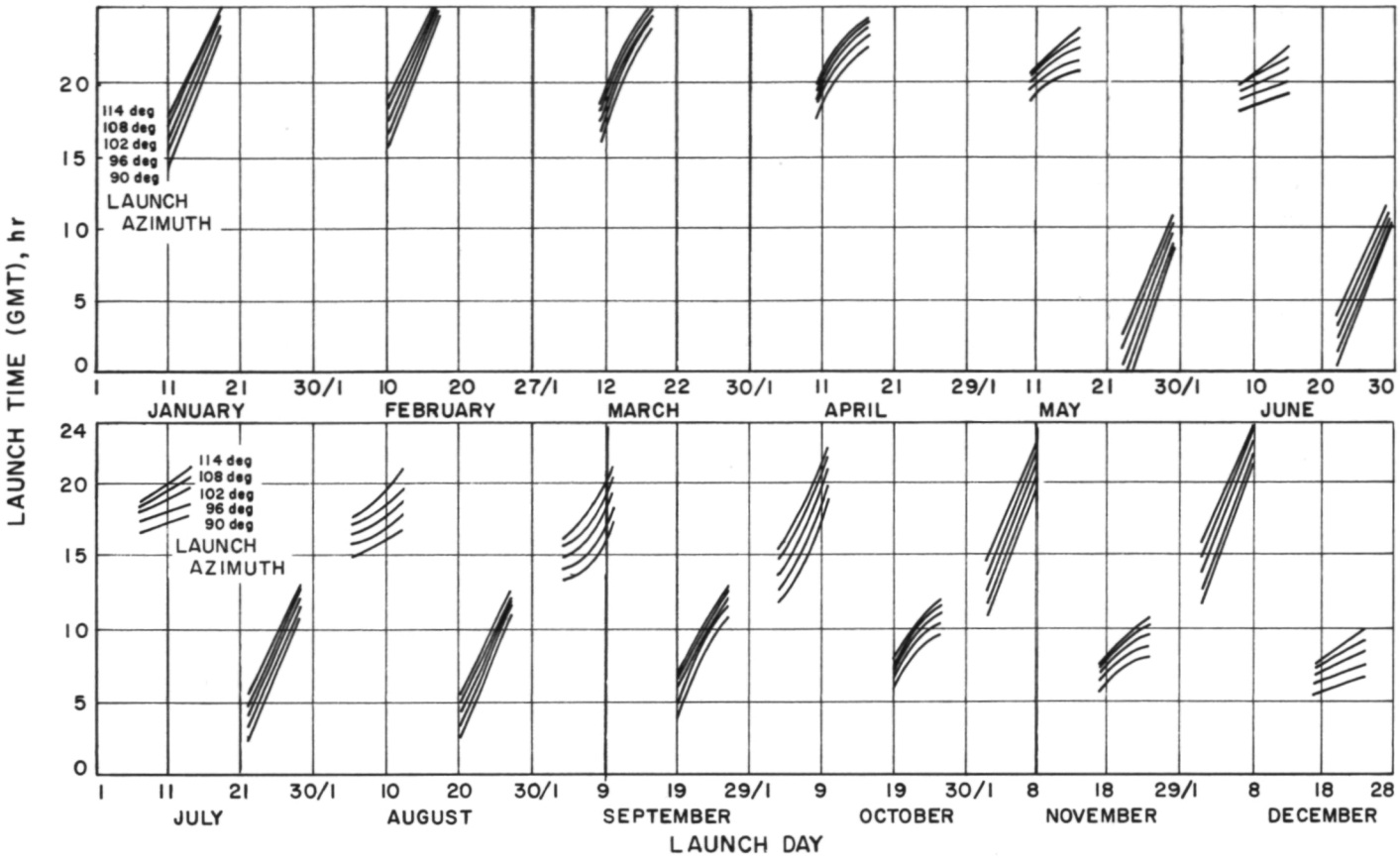

Fig. 12. Launch time versus launch day for 1963

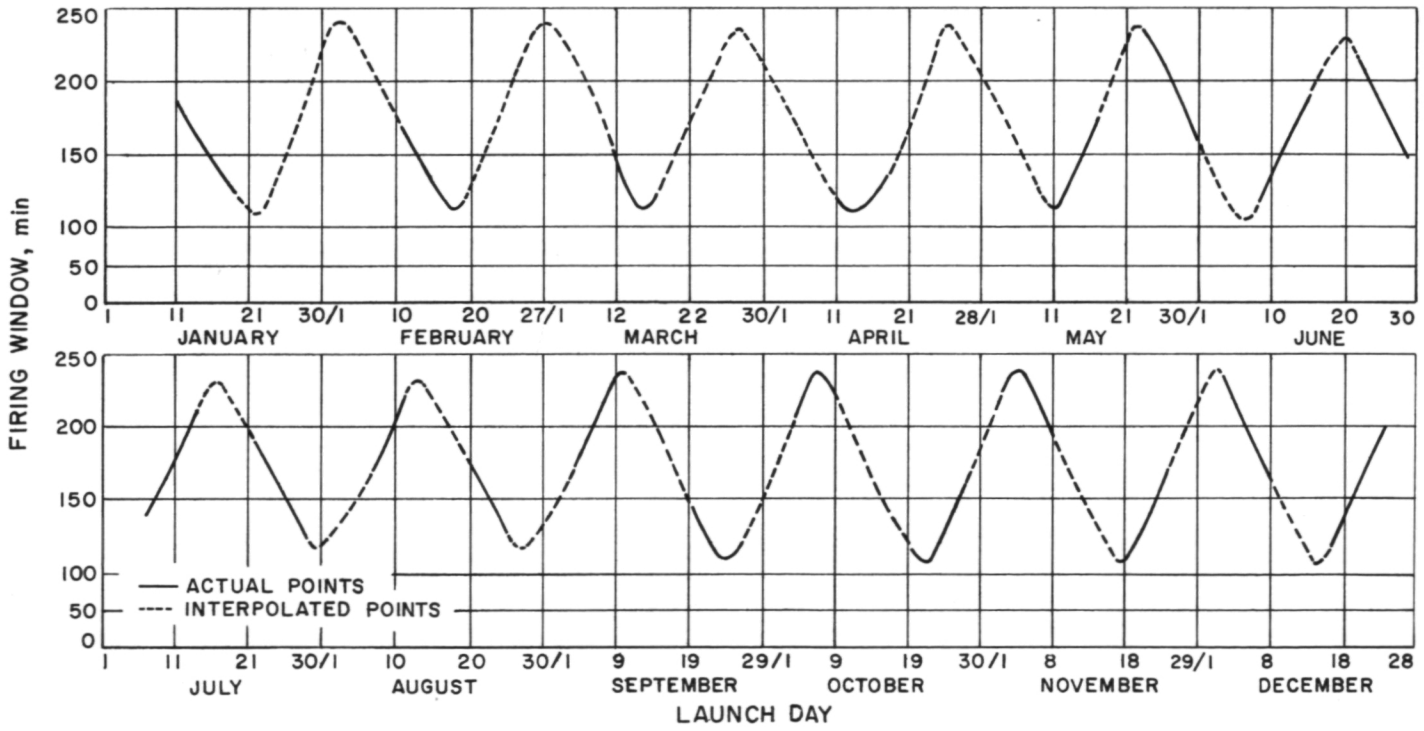

Fig. 13. Maximum firing window versus launch day for 1963

Table 11. Trajectory parameters for the biased impact trajectories, January 1963 launch azimuths of 90, 102, and 114 deg

Launch day, Jan	11			17			18		
Launch azimuth, deg	90	102	114	90	102	114	90	102	114
Injection conditions									
GMT, hr min	14 53	16 28	17 53	22 10	23 27	24 20	23 24	24 38	25 22
Time after launch, sec	1966.	1652.	1386.	1186.	930.	765.	1081.	835.	699.
Radius, km	6570.8844	6570.3072	6569.8878	6570.4068	6570.2578	6570.1418	6570.3242	6570.2359	6570.1678
Speed, km/sec	10.538710	10.548013	10.574251	10.543814	10.552762	10.576130	10.540903	10.549813	10.576047
Path angle, deg	1.6921563	1.6885747	1.6821859	1.6957046	1.6912351	1.6828621	1.6938724	1.6895258	1.6830158
Azimuth angle, deg	116.20758	118.58524	124.57472	117.51326	119.94809	126.16505	116.00265	118.66734	125.38950
Geocentric latitude, deg	−13.635421	−13.765993	−14.542190	10.873888	10.558781	9.8475036	14.000086	13.593914	12.396564
Geocentric longitude, deg	27.834619	4.5867008	343.55690	343.59498	324.48256	311.29338	337.38137	319.07250	307.76982
Inertial speed, km/sec	10.958247	10.958733	10.959086	10.963098	10.963223	10.960602	10.960448	10.960522	10.960714
Impact conditions									
Flight time from injection, hr	68.6	68.7	68.8	66.0	66.0	67.1	65.6	65.6	65.6
GMT, hr min	11 26	13 07	14 37	16 10	17 25	19 25	17 2	18 14	18 56
Geocentric									
Latitude, deg	8.7642946	8.4783068	8.2201931	−15.981765	−16.140661	−16.391982	−18.739797	−18.852030	−18.920978
Longitude, deg	244.53440	220.07799	198.18329	238.20963	219.96648	190.93136	237.34423	219.99278	209.81966
Selenocentric									
Latitude, deg	−17.049479	−14.621975	−15.192674	−11.212005	−11.457637	−12.040838	−10.566784	−10.586477	−11.307206
Longitude, deg	326.38341	323.47417	322.80558	303.86692	303.63439	303.14998	291.88314	287.85756	287.44941
Speed, km/sec	2.6378018	2.6396379	2.6449868	2.6775685	2.6796858	2.6847614	2.6740973	2.6761110	2.6815025
Path angle, deg	−79.578270	−82.2238968	−82.2392808	−82.3316358	−82.3375545	−82.3517180	−74.359135	−71.598481	−71.631030
Azimuth angle, deg	315.5527	315.3879	316.2534	94.279	94.2773	94.5043	86.117	85.3842	87.324
Earth–Moon–probe angle, deg	37.838693	39.987216	40.642628	51.633926	51.831216	52.299101	62.808151	66.745081	67.126339
Sun–Moon–probe angle, deg	23.423300	20.302100	20.772329	69.405536	69.819378	69.809391	69.978380	66.628954	66.638087
Earth–probe–Sun angle, deg	53.177001	53.956389	54.653626	120.96663	121.55805	121.95716	132.81599	133.39521	133.73620
Miss parameter B, km	722.19197	538.58023	532.97019	502.03256	500.19323	495.85993	1019.2221	1190.0409	1179.2665
Inertial speed, km/sec	2.6378022	2.6398431	2.6449881	2.6775705	2.6796907	2.6847648	2.6741009	2.6761142	2.6815058

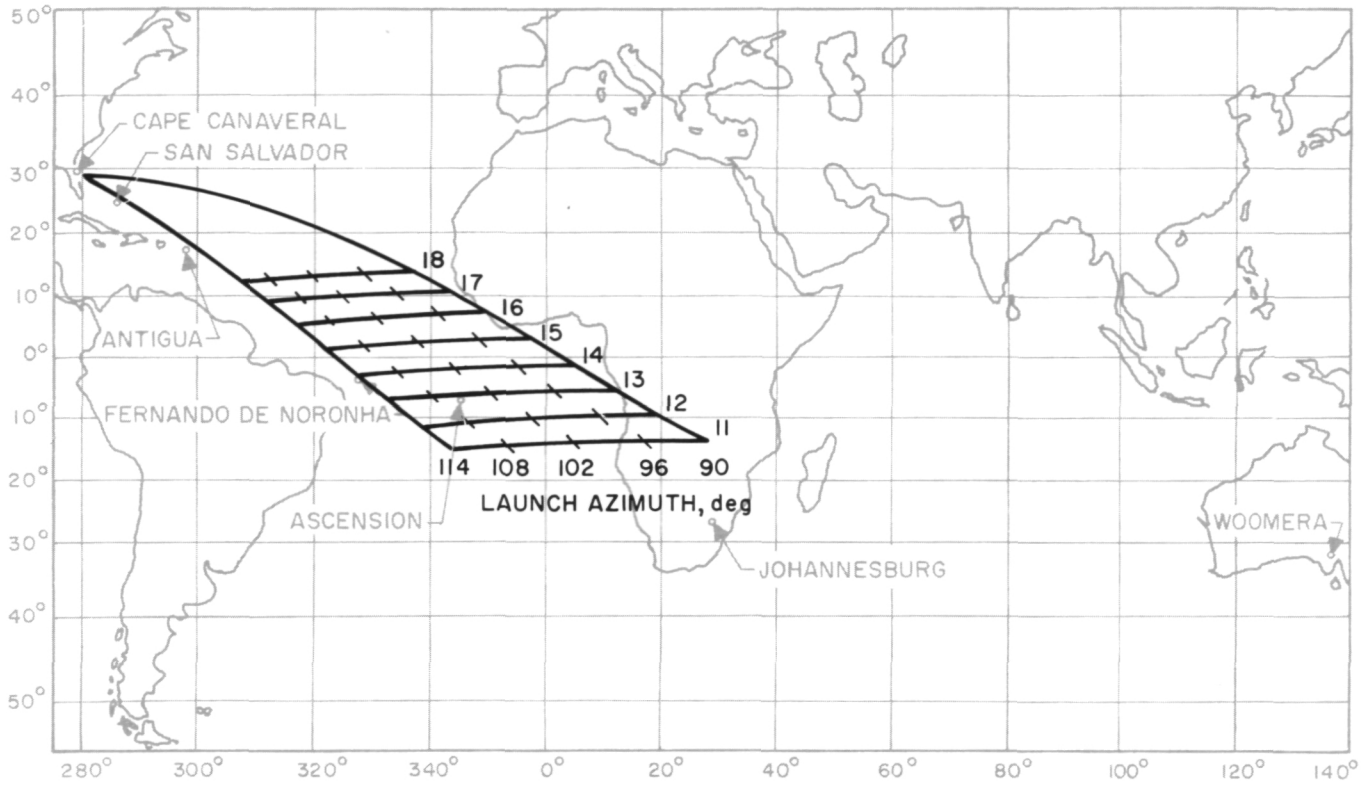

Fig. 14. Injection loci, third quarter, January 1963

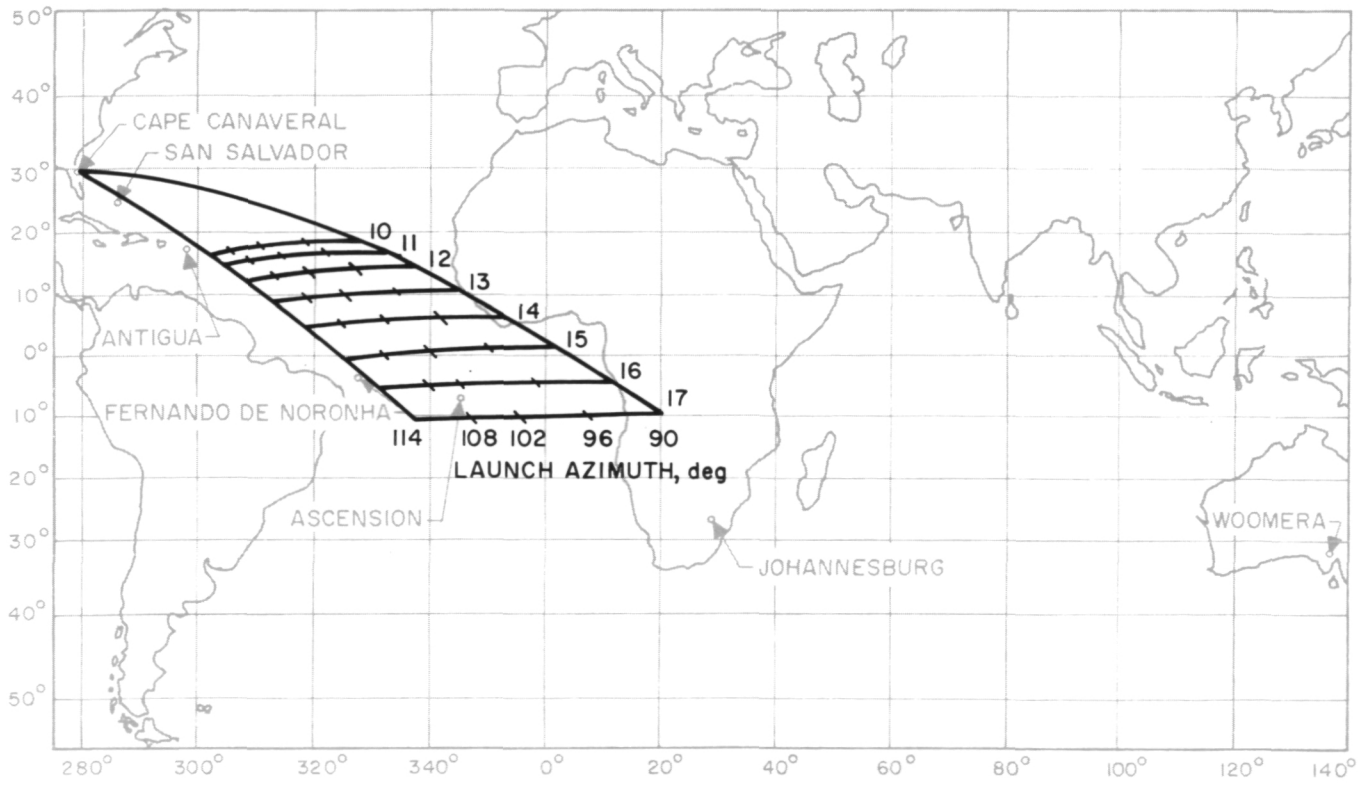

Fig. 15. Injection loci, third quarter, May 1963

Table 12. Trajectory parameters for 4 days of the May 1963 launch period, third quarter, launch azimuth of 102 deg

Launch day, May	11				12				13				14			
Type of impact	Vertical	Biased	Biased	Biased	Vertical	Biased	Biased	Biased	Vertical	Biased	Biased	Biased	Vertical	Biased	Biased	Biased
Impact point	*Rangers 3–7*	Mare Tranquillitatis	Mare Vaporum	Sinus Medii	*Rangers 3–7*	Mare Tranquillitatis	Mare Vaporum	Sinus Medii	*Rangers 3–7*	Mare Tranquillitatis	Mare Vaporum	Sinus Medii	*Rangers 3–7*	Mare Tranquillitatis	Mare Vaporum	Sinus Medii
Impact conditions																
Flight time from injection, hr	65.3	65.3	65.3	65.3	65.6	65.6	65.6	65.6	66.1	66.1	66.1	66.1	66.6	66.6	66.6	66.6
GMT, hr min	14 00	14 00	14 00	14 00	14 52	14 52	14 52	14 52	15 44	15 44	15 44	15 44	16 35	16 35	16 35	16 35
Geocentric																
Latitude, deg	−21.	−21.	−21.	−21.	−19.	−19.	−19.	−19.	−15.	−15.	−15.	−15.	−11.	−11.	−11.	−11.
Longitude, deg	220.	220.	220.	220.	220.	220.	220.	220.	220.	220.	220.	220.	220.	220.	220.	220.
Selenocentric																
Latitude, deg	−6.079	3.0	14.0	0.0	−4.490	3.0	14.0	0.0	−2.924	3.0	14.0	0.0	−1.387	3.0	14.0	0.0
Longitude, deg	311.983	25.0	4.0	0.0	310.362	25.0	4.0	0.0	308.665	25.0	4.0	0.0	307.073	25.0	4.0	0.0
Speed, km/sec	2.6629779	2.6629742	2.6629742	2.6629742	2.6524272	2.6524235	2.6524235	2.6524235	2.6408859	2.6408811	2.6408811	2.6408811	2.6290642	2.6290612	2.6290612	2.6290612
Path angle, deg	−89.901334	−37.560352	−50.172637	−55.175756	−89.901582	−36.798599	−49.704445	−57.031125	−89.888311	−36.014357	−49.174138	−53.366602	−89.909885	−35.318695	−48.693106	−52.503808
Azimuth angle, deg	269.67886	262.7518	252.2556	261.8469	270.23343	264.5335	254.7449	264.1162	269.14904	266.269	257.1809	266.2579	271.08049	267.9428	259.4865	268.2617
Earth–Moon–probe angle, deg	41.436176	32.354109	18.862706	7.1982901	42.770071	32.642761	19.013533	7.4835807	44.519987	32.551550	18.941253	7.3918966	46.559715	32.021669	18.615332	6.8647313
Sun–Moon–probe angle, deg	25.229105	97.916290	77.592095	72.863136	35.955706	110.54472	89.839951	85.507244	46.816130	123.17760	102.10805	98.155450	57.870504	135.81412	114.36000	110.80869
Earth–probe–Sun angle, deg	66.0	66.0	66.0	66.0	78.4	78.4	78.4	78.4	91.1	91.1	91.1	91.1	104.3	104.3	104.3	104.3
Miss parameter **B**, km	0	3044.6918	2459.9787	2193.3634	0	3124.2873	2523.3621	2276.9110	0	3213.3490	2597.1630	2370.4461	0	3304.9892	2673.6931	2465.5655
Inertial speed, km/sec	2.6629744	2.6629777	2.6629777	2.6629777	2.6524236	2.6524271	2.6524271	2.6524271	2.6408812	2.6408858	2.6408858	2.6408858	2.6290613	2.6290641	2.6290641	2.6290641

Table 13. Trajectory parameters for 4 days of the May 1963 launch period, first quarter, launch azimuth of 102 deg

Launch day, May	25				26				27				28			
Type of impact	Vertical	Biased	Biased	Biased	Vertical	Biased	Biased	Biased	Vertical	Biased	Biased	Biased	Vertical	Biased	Biased	Biased
Impact point	*Rangers 3–7*	Mare Tranquillitatis	Mare Vaporum	Sinus Medii	*Rangers 3–7*	Mare Tranquillitatis	Mare Vaporum	Sinus Medii	*Rangers 3–7*	Mare Tranquillitatis	Mare Vaporum	Sinus Medii	*Rangers 3–7*	Mare Tranquillitatis	Mare Vaporum	Sinus Medii
Impact conditions																
Flight time from injection, hr	69.9	69.9	69.9	69.9	69.5	69.5	69.5	69.5	69.1	69.1	69.1	69.1	68.6	68.6	68.6	68.6
GMT, hr min	1 57	1 57	1 57	1 57	2 48	2 48	2 48	2 48	3 35	3 35	3 35	3 35	4 19	4 19	4 19	4 19
Geocentric																
Latitude, deg	19.	19.	19.	19.	16.	16.	16.	16.	12.	12.	12.	12.	8.	8.	8.	8.
Longitude, deg	220.	220.	220.	220.	220.	220.	220.	220.	220.	220.	220.	220.	220.	220.	220.	220.
Selenocentric																
Latitude, deg	−2.2541186	3.0	14.0	0.0	−4.4318604	3.0	14.0	0.0	−6.4055571	3.0	14.0	0.0	−8.1734346	3.0	14.0	0.0
Longitude, deg	313.88713	25.0	4.0	0.0	315.70371	25.0	4.0	0.0	317.08165	25.0	4.0	0.0	317.96530	25.0	4.0	0.0
Speed, km/sec	2.5939608	2.594	2.594	2.594	2.6071674	2.607	2.607	2.607	2.6217671	2.622	2.622	2.622	2.6366160	2.6366135	2.6366135	2.6366135
Path angle, deg	−89.881510	−40.800572	−53.670407	−57.847390	−89.886357	−41.548980	−54.039799	−58.777713	−89.915778	−41.982011	−54.105763	−59.353719	−89.917538	−42.091749	−53.875744	−59.564630
Azimuth angle, deg	269.93440	266.5977	255.8581	266.8739	262.56518	264.1464	252.4496	263.6674	271.38941	261.9058	249.4247	260.6381	271.21783	259.9095	246.8794	257.8932
Earth–Moon–probe angle, deg	53.175824	18.349799	15.409424	7.1915344	50.976101	18.636707	15.344324	6.8972695	48.841964	19.278787	15.230726	6.2453123	46.938030	20.194779	15.120171	5.3219373
Sun–Moon–probe angle, deg	167.66779	97.064140	117.40893	122.01057	153.10610	84.427092	105.16413	109.35739	139.03756	71.823395	92.914610	96.733380	125.53830	59.261101	80.703141	84.143925
Earth–probe–Sun angle, deg	114.6	114.6	114.6	114.6	102.3	102.3	102.3	102.3	90.3	90.3	90.3	90.3	78.7	78.7	78.7	78.7
Miss parameter **B**, km	0	3269.9303	2559.0912	2298.8183	0	3151.4028	2472.7470	2182.7689	0	3048.8324	2404.6423	2090.6587	0	2968.3692	2358.2167	2026.3187
Inertial speed, km/sec	2.5939557	2.5939605	2.5939605	2.5939605	2.6071627	2.6071673	2.6071673	2.6071673	2.6217647	2.6217669	2.6217669	2.6217669	2.6366136	2.6366159	2.6366159	2.6366159

Page intentionally left blank

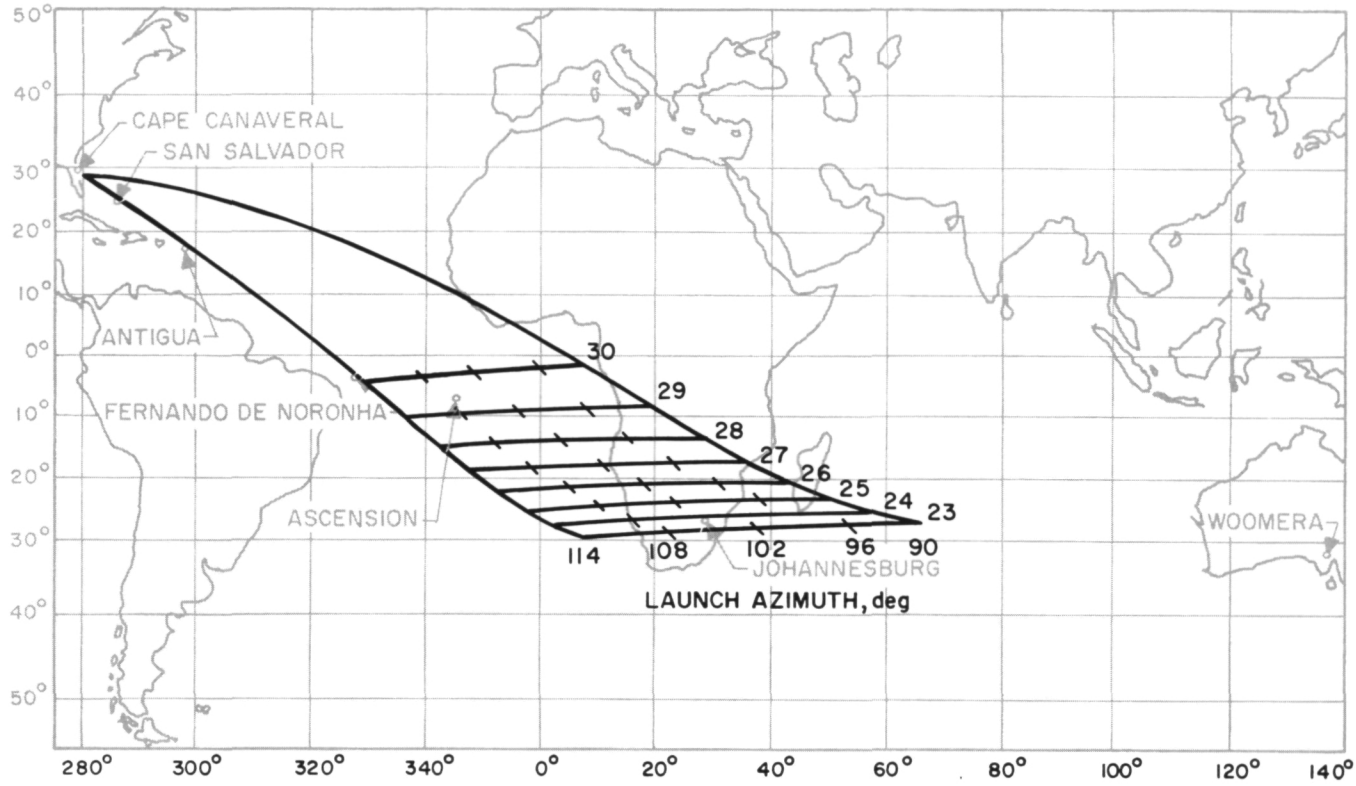

Fig. 16. Injection loci, first quarter, May 1963

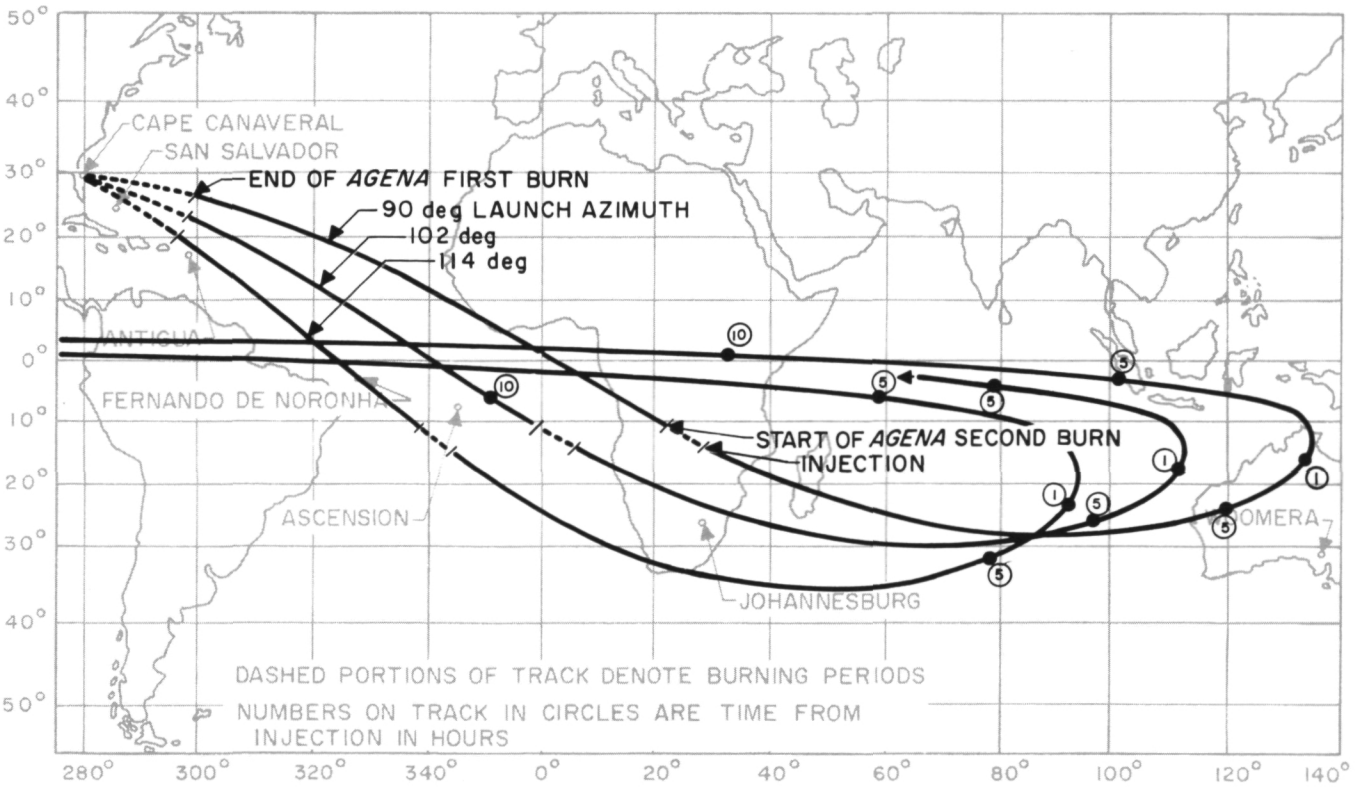

Fig. 17. Earth track, January 11, 1963

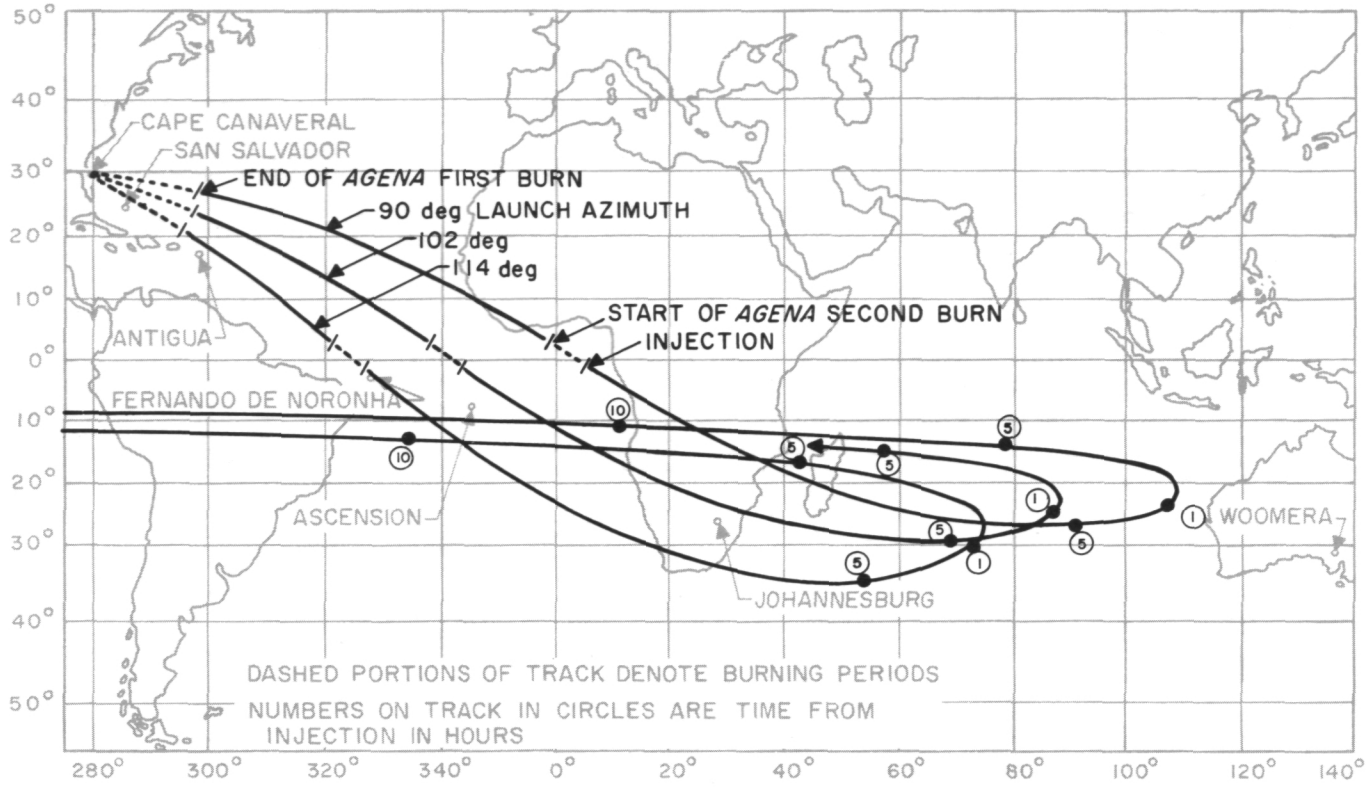

Fig. 18. Earth track, January 14, 1963

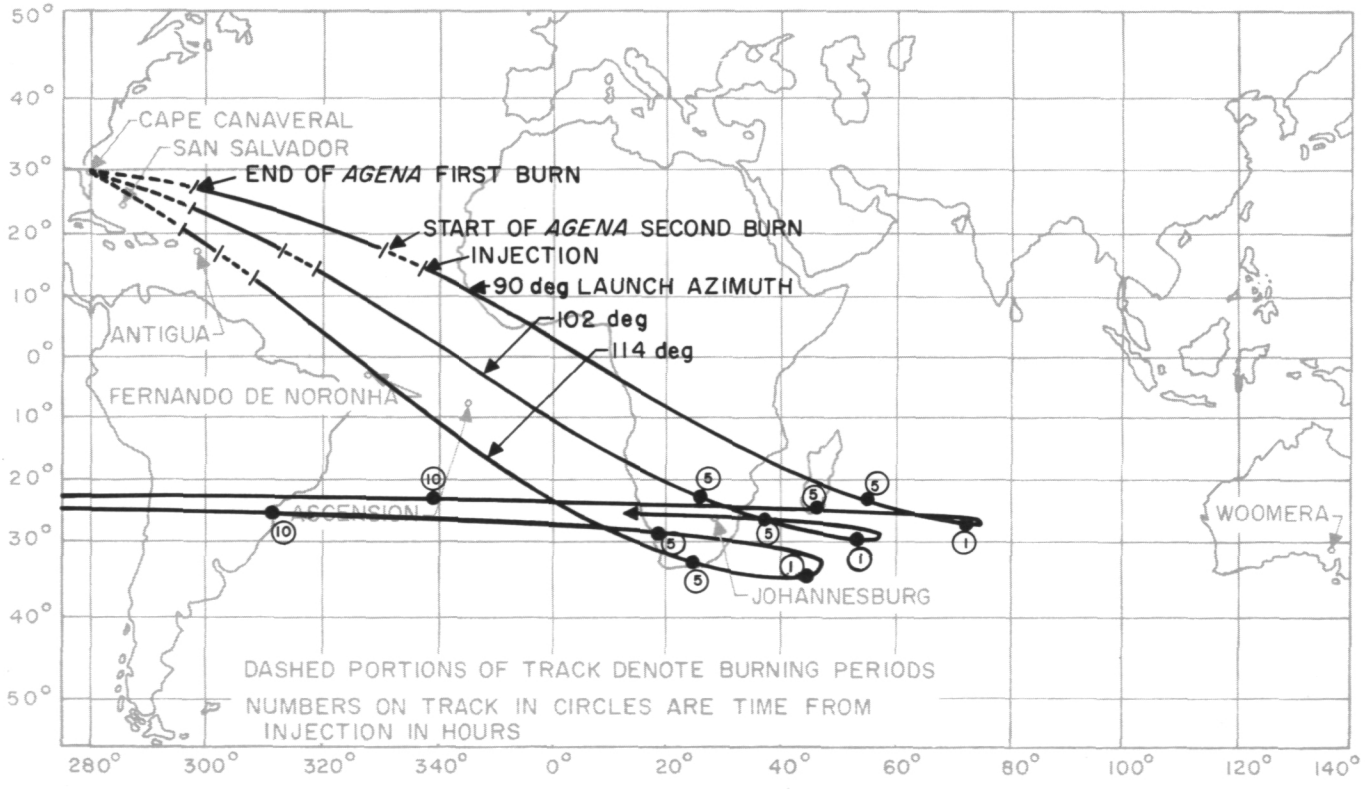

Fig. 19. Earth track, January 18, 1963

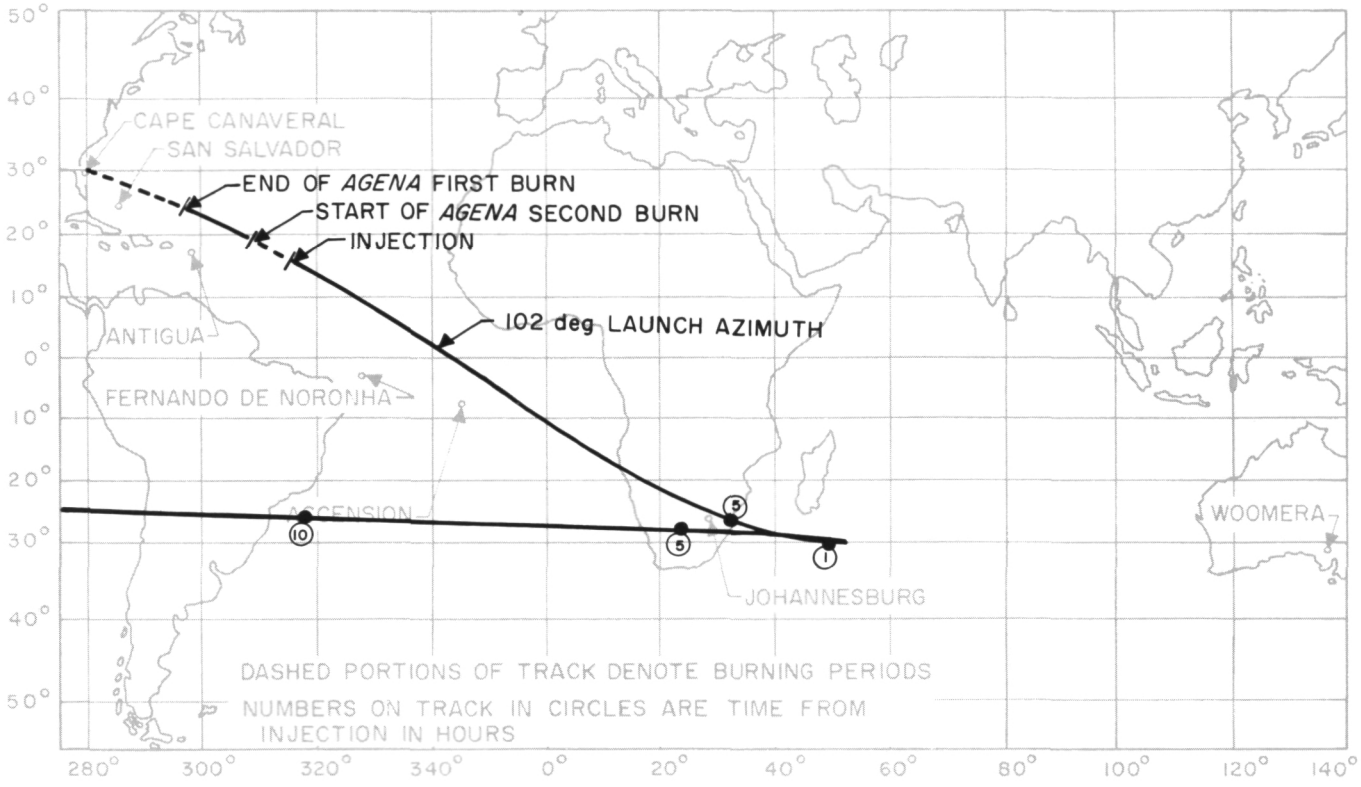

Fig. 20. Earth track, third quarter, May 11, 1963

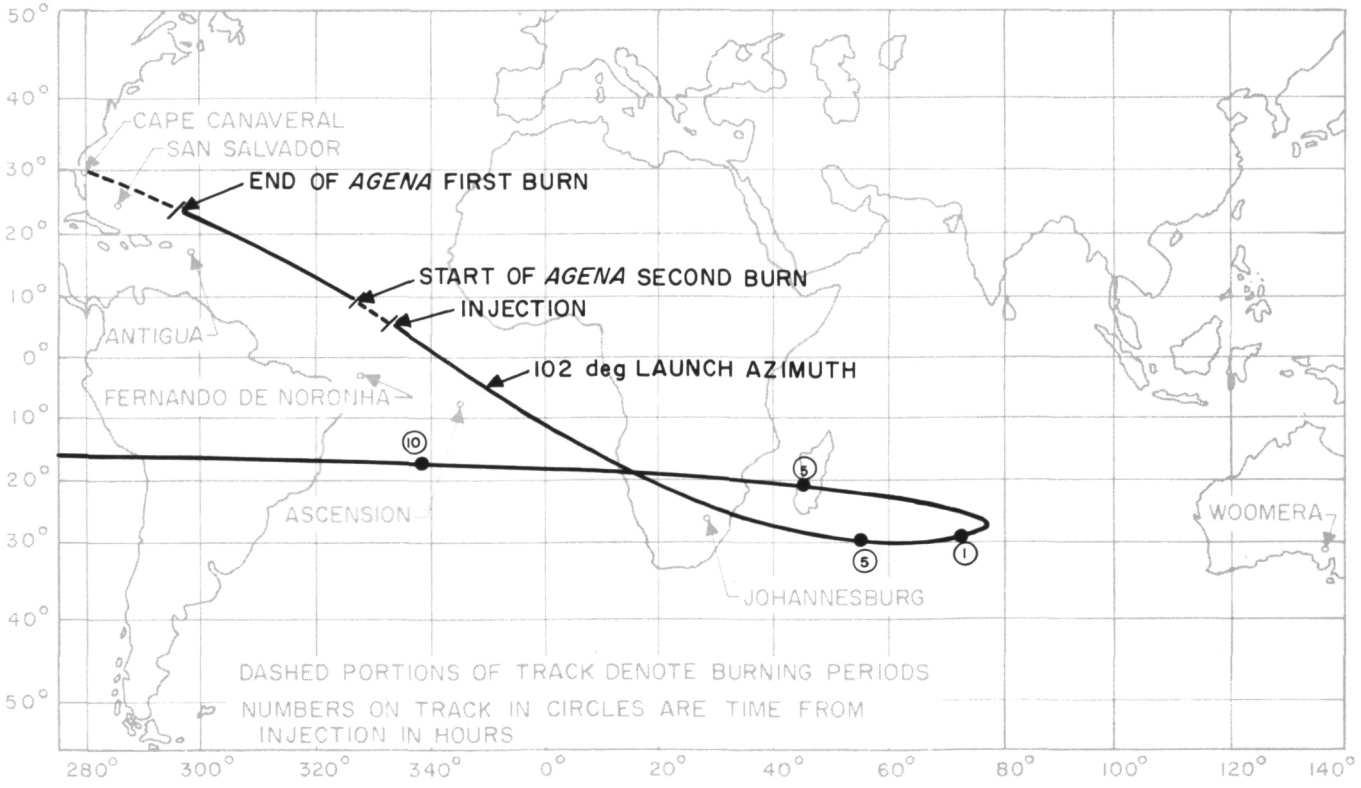

Fig. 21. Earth track, third quarter, May 14, 1963

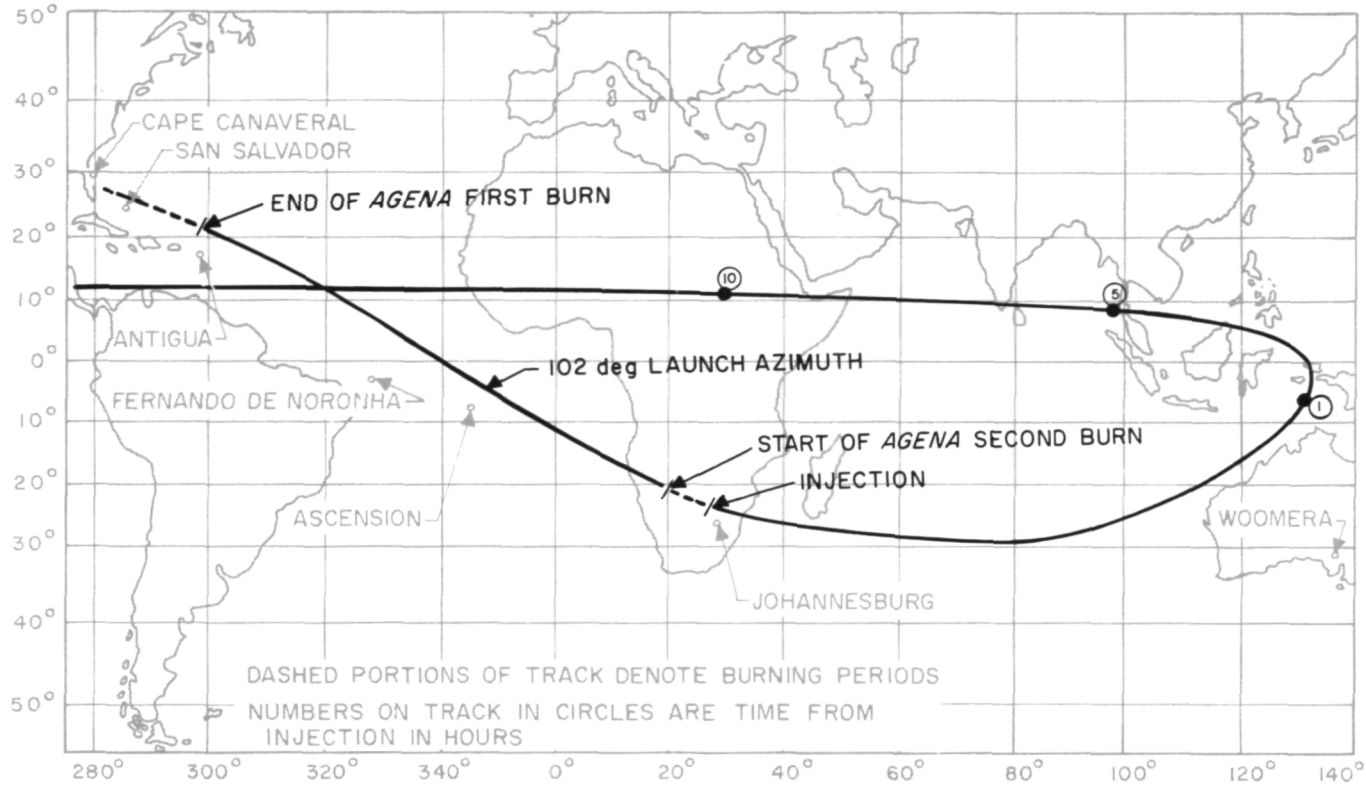

Fig. 22. Earth track, first quarter, May 25, 1963

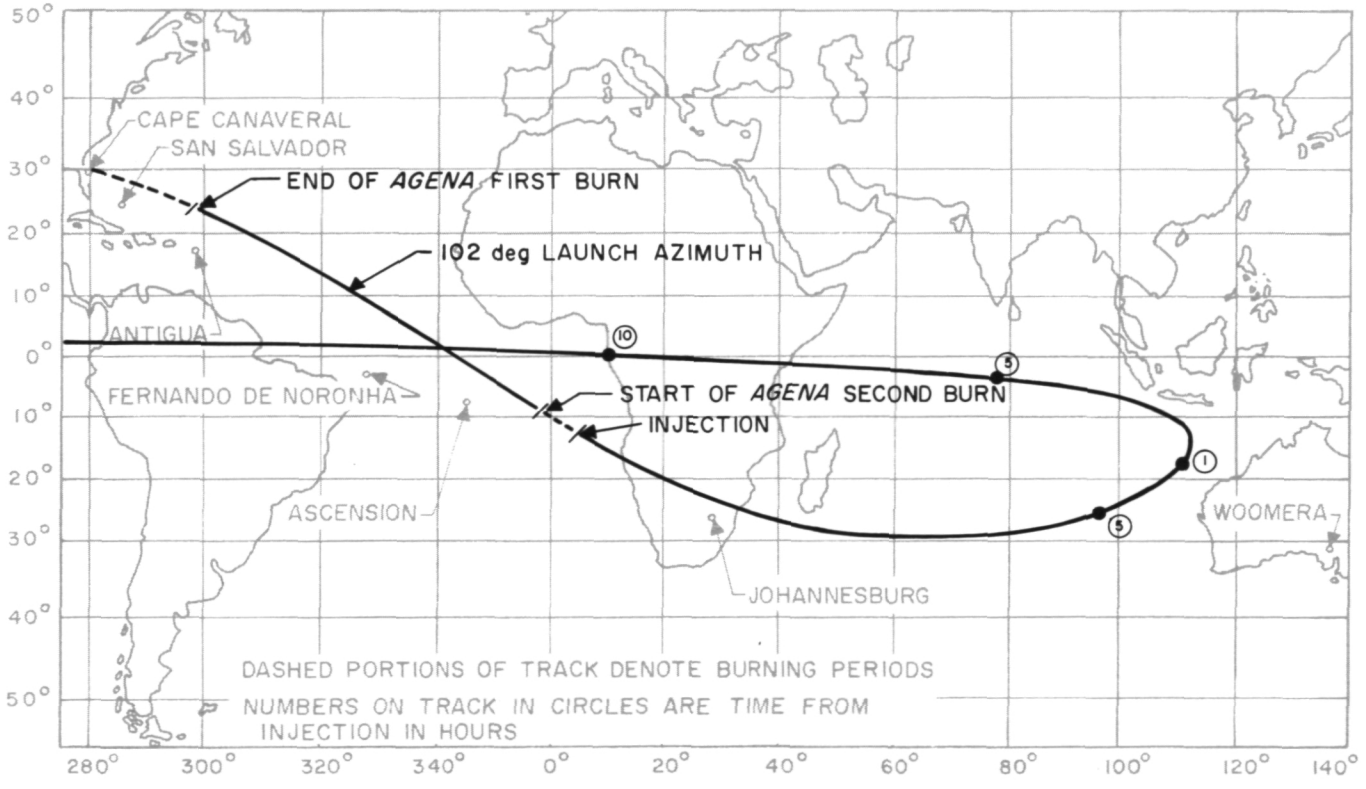

Fig. 23. Earth track, first quarter, May 28, 1963

This variation of flight time allows the spacecraft to arrive at the Moon during the Goldstone view period.

3. Spacecraft Integration

a. **Ranger *5 system design.*** Some design changes have been initiated on *Ranger* 5 as a direct result of the inflight failure of *Ranger* 4. Unfortunately, the exact cause of the *Ranger* 4 failure is unknown, in that the data encoder commutator stopped at the moment the synchronizing signals from the CC&S ceased. For this reason, a backup synchronizing clock has been installed in *Ranger* 5 and subsequent data encoders. This backup clock will be inhibited as long as the CC&S continues to furnish commutator sync signals (25 pps). If the CC&S should fail the commutator will continue to run, but at a reduced rate (24 pps; the lower stepping rate is necessary as part of the inhibiting mechanism.) Autodecommutation on the ground may be lost due to the difference in stepping rate, and methods are being studied to preserve real-time readout if the backup clock is utilized.

Based on the supposition that the *Ranger* 4 failure might have been caused by a failure of the separation connectors (connectors between the spacecraft and the *Agena* adapter) at electrical separation, the gender of the separation connectors has been reversed. Formerly, the male plug was on the spacecraft side of the interface leaving pins exposed (some with power on them,) at the pyrotechnically operated plug spin-off, which executes electrical separation 5 sec before mechanical separation.

Another change has been to put the CC&S inverter monitor on telemetry. Formerly, it was only monitored during ground testing. The data encoder converter monitor was removed from telemetry to make room for the new measurement.

During testing on *Ranger* 5, an in-line splice failed in the ring harness. A review showed that this type of splice is prone to failure, especially if it is located in a flexible portion of the harness. All case harnesses which contain splices and the ring harness for *Ranger* 5 were either reworked or replaced with new harnesses employing the butt splice, which is more reliable and can stand considerable abuse. The failure on *Ranger* 4 cannot be traced to a broken splice.

An additional attitude control nitrogen gas bottle has been added to the system, which allows for a lower pressure with the same amount of gas. This should prevent the problem noted on the flight of *Ranger* 3, as reported in *SPS 37-14.*

b. **Ranger *6 through 9 system design.*** That which was accomplished for *Ranger* 5 also applies to *Rangers* 6 through 9, with the exception of the additional gas bottle. The reason that the additional bottle is not required is that they will require less gas. Their moments of inertia are much less than that for the *Ranger* 3, 4, 5 design. For instance, the 2.64 lb of gas allotted allowed for only a 15% reserve at the Moon for *Rangers* 3 and 4, whereas for *Rangers* 6 through 9, a 52% reserve should be realized.

In addition to the backup clock for the data encoder, a backup clock for the command subsystem becomes effective with *Ranger* 6. The command system used on *Ranger* is asynchronous, requiring on-board synchronizing. Loss of the normal sync signals from the CC&S also prevents inserting a real-time command. The backup clock for the command subsystem is necessary to allow the TV subsystem to be turned on in the event of a CC&S failure. Sun and Earth acquisition procedures position the spacecraft such that the camera line-of-sight would sweep the Moon, even without a mid-course or terminal maneuver, in most trajectories. Also, an independent command subsystem may allow incorporating real-time backup commands for some of the early flight CC&S commands, such as transmitter power up, solar panels open, Sun and Earth acquisition, which *Ranger* 4 failed to execute. It is planned to incorporate, if possible, these backup commands at an early change point.

A close look at spacecraft reliability has been initiated on the over-all *Ranger* Project. A system review of the use of redundancy, where necessary (as evidenced by the previously mentioned design changes); a closer look at component reliability; and a review of test time and testing procedures, as they apply to reliable operation, are all efforts to increase spacecraft reliability.

c. GSE for **Rangers *6 through 9.*** Due to the change in the assembly and operations schedule for *Rangers* 5 and 6, a new test equipment utilization schedule has been prepared. Some of the test equipment that will be used for *Ranger* 5 at AMR will have to be up-dated before it can be used for *Ranger* 6. Present plans are to up-date the equipment by replacing obsolete subassemblies with subassemblies that have been up-dated at JPL.

Since the 25-ft space simulator will not be available for thermal–vacuum testing of *Ranger* 6, the 6-ft space simulator will be used. The 6-ft space simulator is not large enough to hold the spacecraft when the TV subsystem is in place; consequently, the TV subsystem will be placed external to the space simulator, but will be electrically

connected to the spacecraft during the thermal–vacuum tests.

Vibration testing of *Ranger* 5 has been added to the operations plan. The vibration test will be conducted in one plane only. Since only portions of the spacecraft are operating during the launch phase when vibration is experienced, only those portions are operated during the vibration test. The dummy run GSE will be used to operate the spacecraft during the vibration tests. After the vibration test has been completed, the spacecraft will be given a thorough operational test with the system test complex (STC) to verify that all subsystems are still functioning properly. When vibration tests are performed on *Ranger* 6, the STC will be used to operate the spacecraft. Testing plans for *Ranger* 6 call for vibration tests in all three planes; consequently, the STC is needed at the environmental facility to perform comprehensive tests when the direction of vibration is changed from one plane to another.

The STC for *Ranger* 6 has been assembled in the Spacecraft Assembly Facility (SAF). Since the STC must be moved to various locations during test operations, the ability to move the TV GSE without causing the camera in the film recorder cabinet to become misalined is of great concern. The TV GSE was moved to the SAF without excessive misalinement. Compatibility testing between the TV GSE and the engineering test model TV subsystem is in process.

The read–write–verify (RWV) GSE is a duplicate of the equipment used to send commands to the spacecraft during flight. In order to ensure that each spacecraft will respond to the commands from the ground station, each spacecraft is compatibility tested with the RWV GSE. Since the RWV GSE is not needed to control or monitor the spacecraft during test, the decision was made to eliminate the RWV GSE from the STC during environmental testing.

Provisions have been made to add four racks of science test equipment to the STC for *Ranger* 7. The necessary system cabling has been coordinated and released for procurement.

4. Test Operations, Ranger 5

a. Subsystems testing. Subsystems testing, which started during April 1962, was completed during the first week of May. Deficiencies and nonspecification conditions, encountered during this phase of operations, were investigated and resolved by the cognizant subsystem groups. Equipment modification and repairs, as required, were handled in an expeditious manner and the subsystems were completely checked out well in advance of the scheduled completion date.

b. System testing. System testing, started in early May 1962, has produced time consuming problems which have resulted in a 2- to 3-wk schedule slippage. A summation of the system test operations follows:

Preliminary systems test. During this test, two major problems occurred, the first was a mid-course motor turn-off command failure, and the second was spurious mode changes of the data encoder as a result of manual motor turn-off by the CC&S. These problems were thought due to a nonflight-type battery, a lead-acid cell, interconnected with the spacecraft by 30-ft cables. As normal spacecraft operations could not be achieved with this battery installation, a flight-type battery was installed on the spacecraft, and the problems appeared to have been eliminated.

Systems Test 1. The over-all system test ran exceptionally well, with only one problem arising, the mid-course motor again failed to turn off. As this problem was originally thought to have been corrected by the installation of a flight-type battery, a full problem investigation period was initiated. While attempting to resolve the turn-off problem, intermittent spikes were observed on the output of the accelerometer package. Investigation showed that an unprotected relay in the autopilot integrator, when actuated, caused an inductive spike that was then introduced into the accelerometer output signal, producing the spike that negated the CC&S motor turn-off command. In addition, these spikes had to be within 4 msec from an accelerometer pulse to cause a failure. This condition greatly reduced the probability of recurrence and extended the troubleshooting period excessively.

Systems Test 2. Systems Test 2 produced no major equipment problems.

Systems Test 3 (June 20, 1962). This systems test was conducted with a new procedural concept that appeared to work quite well. All subsystems operated properly. The only discrepancy which appeared was noise on telemetry Channels 5 and 6. This discrepancy was investigated and found to be a residual condition that was inherited from prior *Ranger* operations. This noise is mathematically expected and is due to intermodulation distortion within the transponder modulator. The *Ranger* 4 DSIF tests indicate that this noise is not considered serious.

The currently scheduled system test program was completed without any further major problem occurrence. All discrepancies or problems have been resolved and corrected, and no known discrepancies exist on the spacecraft. It is anticipated that the spacecraft schedule will be met provided all flight hardware is received in sufficient time so that calibration can be achieved with the system.

c. Space simulation test. The completed *Ranger* 5 test complex and spacecraft have been moved from the JPL SAF and transported to the space simulation area. The spacecraft was prepared with the necessary thermocouples and component paint patterns, and then installed and cabled in the space chamber. The GSE has been checked and initial power applied to the spacecraft. The chamber evacuation operations and spacecraft testing are planned for the first week of July. The objectives of this mission test will be to prove the adequacy of the spacecraft and components in a space-simulated high-temperature environment.

5. Assembly Operations, Ranger 6

The mechanical assembly of *Ranger* 6 is essentially complete. In addition the STC has been constructed and checked. The only major nondelivered flight items are: (1) Case I command harness, (2) Case 4 attitude control harness, (3) solar panels, (4) propulsion system, (5) Earth sensor light hood assembly, (6) television, (7) ion chamber, and (8) Channel IV VCO.

A microscopic inspection was performed on all modules installed in the spacecraft except for foam-potted CC&S modules; the only problem discovered was bent pins on a data encoder harness.

In two instances, cases which were delivered as flight units had to be returned for rework: (1) Communications Case II for nonsterile harnesses which were replaced, and (2) CC&S Case I for a nicked wire, probably damaged in SAF during assembly of connector hardware.

During the directional antenna alinement, it was discovered that the clutch would not hold the antenna in a l-*g* field. This was resolved to be caused by the following factors: (1) a new interpretation of the specification by a subcontractor, and (2) a directional antenna which weighs approximately 1 lb more than previous units. The problem is not completely resolved and a test will have to be performed to determine if the *Ranger* 6 antenna will not sag and possibly interfere with the LMSC adapter at separation.

No major problems have been encountered and the *Ranger* 6 spacecraft is now in the subsystem check and calibration period.

6. Launch Complex Design Improvements

The original launch complex GSE installation at Pad 12 AMR was based on the immediate and forseeable requirements of the *Ranger* Project. Since then several limitations have become evident and a noninterference improvement program has been started. To date, replacement of one each catenary, tower, and pad cable have been completed to minimize voltage drop in critical power lines.

The tower J-box for *Ranger* follow-on is being up-dated to allow all signals through the umbilical to be monitored by routing all catenary cables through the box. The box is also designed to minimize the effects of moisture and fungus and to allow circuit changes or complete wiring revisions with a minimum of rework.

(To accommodate the needs of *Mariner* R, a "hard-line" conduit installation of 400-cps power has been added with outlets at the launch control shelter and the top of the umbilical tower with control at the blockhouse. The generators are mobile units which could be made available for other applications when not required at the pad. A video-pair installation to the top of the umbilical tower has been completed to allow direct connection from the output of critical signal conditioning modules via video pair to any required location served by the AMR communications installation.)

Planned changes (on noninterference basis) include replacement of one catenary cable with low-capacity, temperature-stable type; eventual elimination or enclosure of the presently exposed signal cable interface at the bottom of the umbilical tower; and redesign of the blockhouse GSE area J-boxes to allow permanent connection of the hard lines.

Addition of a dummy run trailer for installation of launch control GSE at the lab is planned beginning with *Ranger* 6. The use of the trailer will minimize setup time and allow more flexibility to accommodate test location changes. Improved control and storage of the launch control GSE between tests will also be possible. A similar trailer will be available at the explosive safe area at AMR to allow tests in that area starting with *Ranger* 5.

B. Spacecraft Design

1. Introduction

Technical effort on the *Ranger* Project has continued to be centered primarily on *Rangers* 6 through 9 with the addition of science experiments on the bus.

Because of the apparent failure of the CC&S shortly after spacecraft separation, it was not possible to evaluate the functioning of the *Ranger* 4 spacecraft mechanical and structural components. Vibration measurements taken at the *Agena*–spacecraft interface during the powered flight phase of *Ranger* 4 indicate unusually low levels throughout the flight. Mechanical separation of spacecraft from *Agena* was apparently normal.

2. Structures

The mechanical test model (MTM) for the *Ranger* 6 mission has passed type approval shake tests *(SPS 37-15,* Vol. I) per JPL specification.

Additional requirements have been placed on *Rangers* 7, 8, and 9. These include the addition of more scientific experiments. There is a total of eight experiments on board. For most of the experiments a universal plate bracket design has been created for supporting the experiment sensors and some of the associated electronics. There are three of these brackets, each spans between the outer support tube which connects adjacent bus feet and the bottom of the hexagonal section of the bus [Figs. 24, and 25 (a), (b) and (c)].There are two reasons which made this design and location most advantageous:

(1) The tests described in *SPS 37-15,* Vol. I showed the bus to be the least rigid in the section between the bus feet and the bottom of the hexagonal section. These plate brackets are located in that section and should aid the rigidity considerably. Preliminary modal shake surveys have already indicated this to be true.

(2) The required fields of view for the various experiments are best accommodated by locating them in this area.

Five experiment units are mounted in a different manner than is described above. They are the particle flux detector, ionization chamber, magnetometer and the two cosmic dust collector plates [Figs. 25 (a) and (d), and 26].

Bay I does not contain any experiments mainly because of the presence of the K-braces.

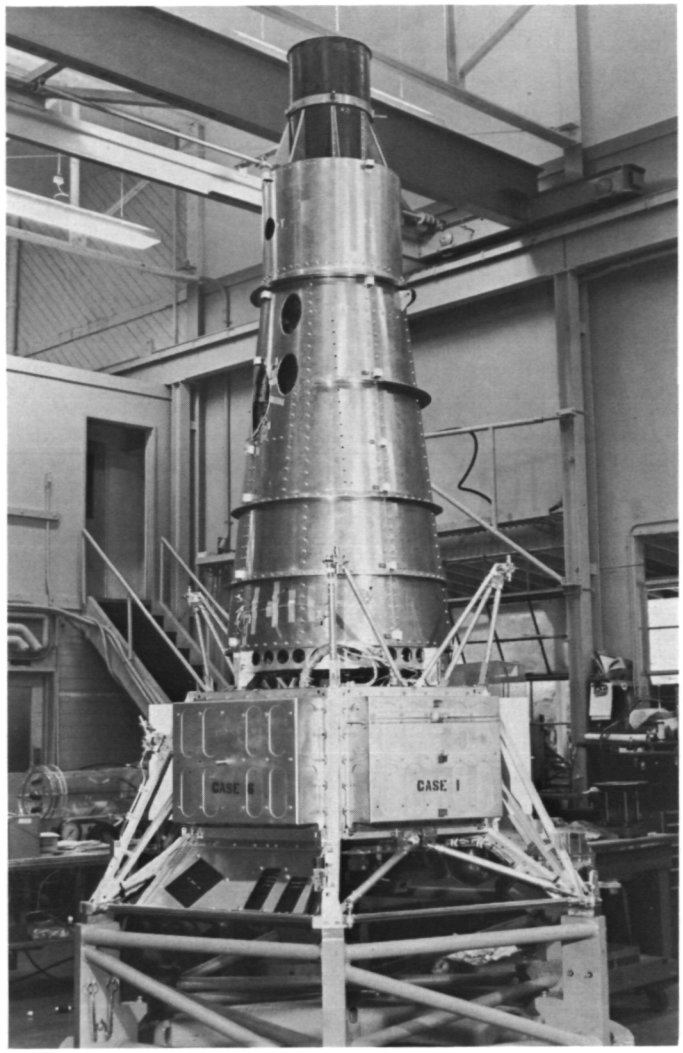

Fig. 24. MTM, *Rangers* 7, 8, and 9

Bay II contains the electron flux experiment and search coil magnetometer electronics mounted on a plate bracket.

Bay III contains the particle flux detector and the spherical ionization chamber. These are not mounted on a plate bracket.

Bay IV contains K-braces and no science experiments.

Bay V contains the low-energy plasma probe and the cosmic dust detector electronics mounted on a plate bracket.

Bay VI contains the low-energy ion experiment and the electron–proton spectrometer sensor and electronics.

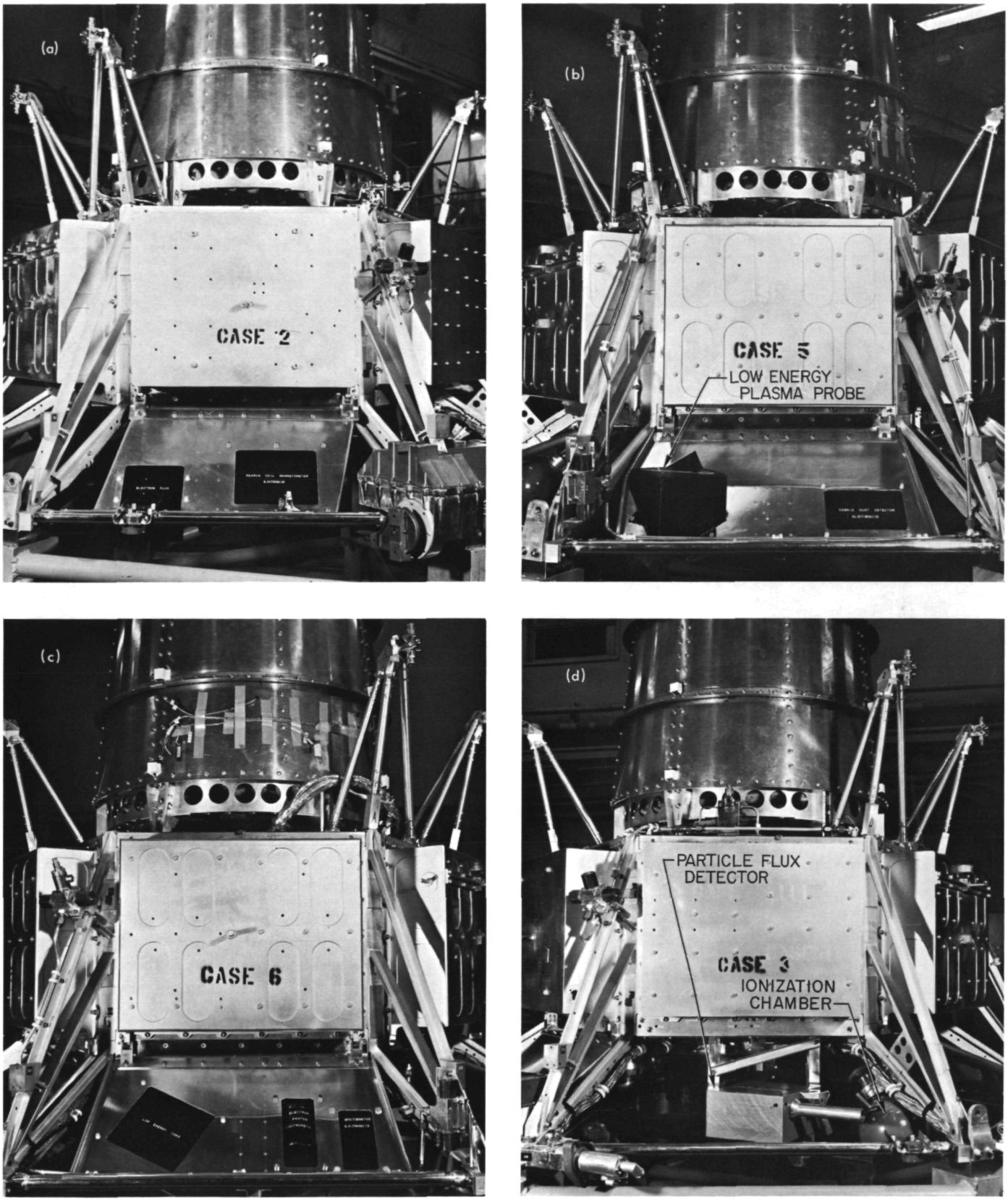

Fig. 25. MTM with additional science, *Rangers* 7, 8, and 9

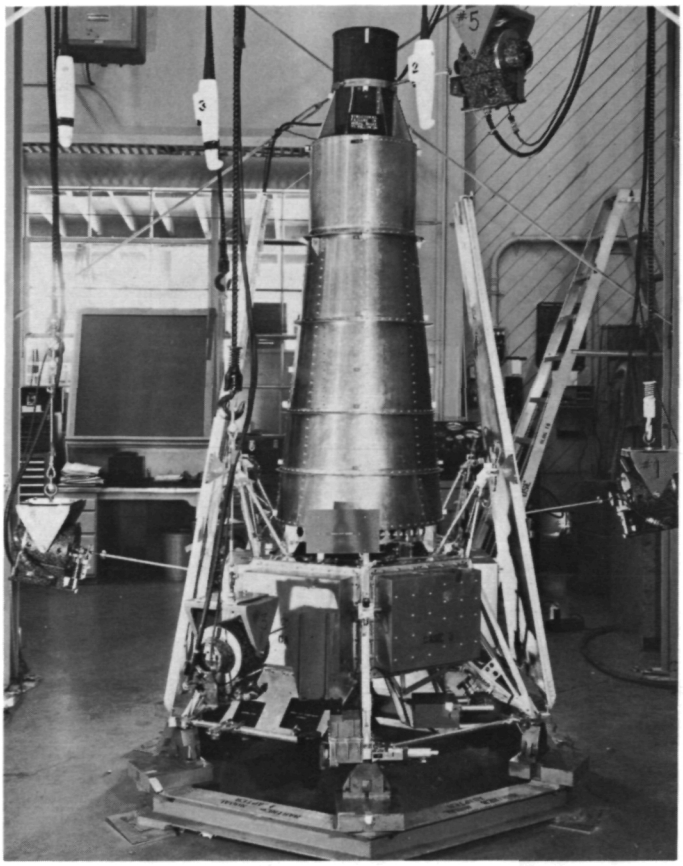

Fig. 26. MTM with cosmic dust sensor mounted above bus

The two cosmic dust detector plates are mounted on top of the bus near the RCA television package over Legs F and C.

The magnetometer is mounted on the high-gain antenna backside opposite the pivot arm to keep it as far as possible from the spacecraft and away from RF interference.

The vehicle described in *SPS 37-15*, Vol. I went through the equivalent of approximately three complete type approval shake tests. In addition, some of the accelerations imparted to the MTM vehicle were up to 2.8 times the levels specified. The last complete sequence of tests, however, was run at the specified levels by refinement of the use of the new test facility and the incorporation of an averaging circuit to control the shaker inputs.

During subsequent analytical modal shakes two failures were noted in the MTM:

(1) The ring in the RCA omni-antenna support showed fatigue cracks (Fig. 27).

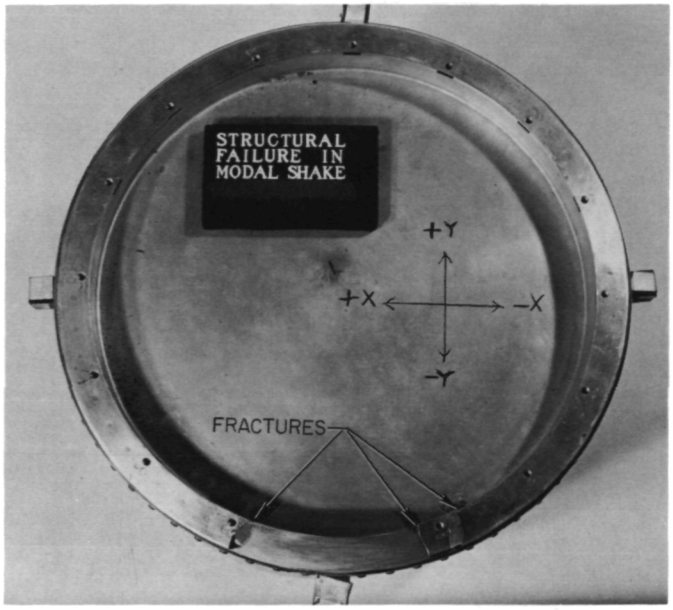

Fig. 27. Omni-antenna support showing cracks in ring

(2) A fatigue crack in the hexagonal section diagonal near the top of the Leg F (Fig. 28).

It is considered that neither of these occurrences would have affected the performance of the vehicle.

In view of the fact that the spacecraft structure had undergone a great deal more overloading and time on the shake table than is considered reasonable, it is being replaced by a new structure. The new structure is presently being incorporated into the MTM. It is expected that the MTM with the additional science on board will be subjected to more modal shakes and type approval shakes during the next reporting period.

3. Temperature Control

a. **Rangers 3, 4 and 5.** Based upon *Ranger* 3 flight data, the value used in *Ranger* 4 analysis for the emittance of white paint was reduced from 0.81 to 0.76. This, coupled with a general trend toward higher power dissipation, resulted in larger painted areas on the *Ranger* 4 bus.

The gamma ray spectrometer underwent considerable analysis and testing to explain the unacceptable high temperature before boom extension during *Ranger* 3 flight. The tests showed that a large reflected heat input could come from the retro shield and other specular spacecraft surfaces. To counteract these heat inputs, the retro shield was covered with black nylon material and the painted areas were increased on the sphere, boom,

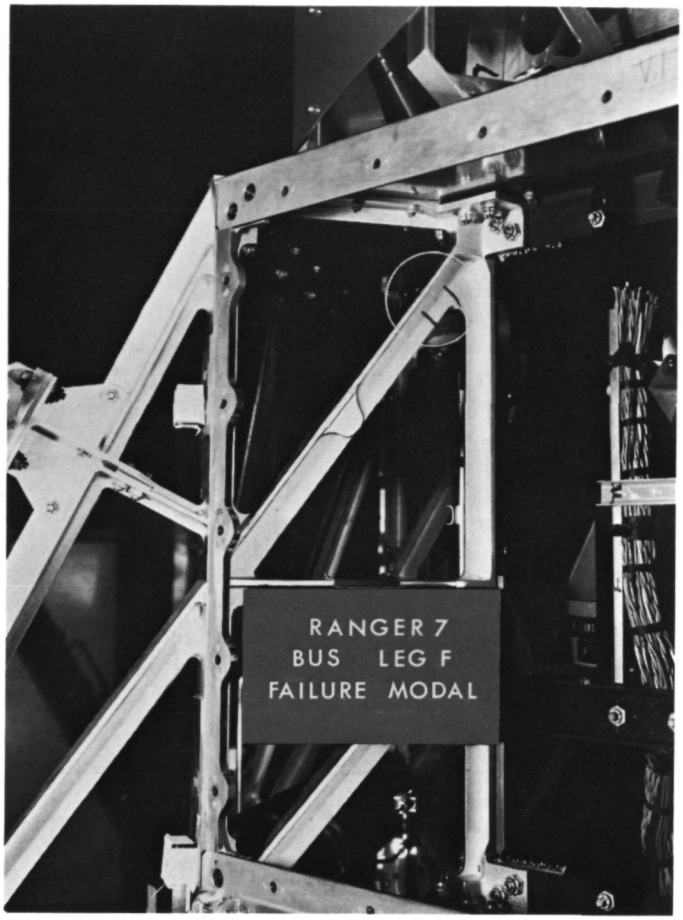

Fig. 28. MTM showing location of crack in bus after overtesting

cable dispenser, and solar panel support structure. Unfortunately, the failure of *Ranger* 4 occurred before any confirmation for the above modifications could be obtained.

Ranger 5 is presently being prepared for flight. This preparation includes a new type of power survey. Although as yet incomplete, it is expected that these new techniques will result for the first time in an internally consistent set of figures. The figures may then be given more weight in the analysis than was possible with the internally inconsistent power surveys obtained for *Rangers* 3 and 4. Any differences between the *Ranger* 4 and 5 patterns will be a result of these more accurate power figures.

b.* Rangers *6 through 9. Thermal control on the *Rangers* 6 through 9 is divided into three areas: (1) the RCA TV system (including the omni-antenna and the interface problem to the bus), (2) the bus and associated components (solar panels, high-gain antenna, gear box, Earth sensor, etc.) and (3) science experiments.

The last area has been vastly expanded by the addition of six new science experiments, making a total of eight. The original experiment was composed of the ion chamber (starting on *Ranger* 6) and the particle flux detector (starting on *Ranger* 7). The six additions will start with *Ranger* 7. Thermal control design on the ion chamber and the particle flux detector has been completed. The ion chamber design has been verified by a test with a simulated space environment. The particle flux detector will be tested in conjunction with some of the new science experiments, as discussed in the following paragraph.

Of the six additions, four will be mounted on special mounting plates located adjacent Bays II, V and VI. The mounting plates are bolted between the underside of the hex structure and the support tube attached to the legs. The plates are to be made of highly polished aluminum on the top (Sun) side in order to reflect (specularly) the Sun energy away from the cases of the bus. The underside of the plates will be adjusted between a polished surface and a white paint surface in order to yield a mounting plate temperature which is an average of the design temperatures of the experiments mounted to it. The plates will have cutouts and the experiments are to be mounted from underneath the plates so that the cutouts will allow solar energy to impinge on the experiments (both from thermal control and to meet Sun view requirements). Each experiment is being analyzed individually, but the design approach is essentially the same for all: the Sun side will be a polished surface (either gold plated or aluminum) to avoid diffuse reflections onto the bus; the sides of the experiment underneath the mounting plate will be balanced with a polished low ε surface and a white paint surface, keeping the latter wherever possible on those sides which radiate mostly to space.

The cosmic dust detector (which consists of two thin, large plates) will be mounted on top of the bus, at either side of the TV tower. Since the temperature range of these plates is substantially wide, no thermal problems are anticipated.

The search coil magnetometer, will be mounted on the high gain antenna on the side opposite to the yoke. The thermal approach here will be to insulate the experiment as well as possible from the high gain antenna (which has a very large thermal variation) and to design an internal heater which will vary in output with temperature, thereby providing an active control.

The TV subsystem has undergone chamber tests with heater simulation on a thermal test model (TTM) at RCA.

The results were very satisfactory. The only critical problem is the amplifiers, which have a very high power output and a rapid heat rise during the operation period of the terminal maneuver. Components tests and a PTM flight sequence chamber test to be performed soon at RCA will yield a better appreciation of this problem. Measurements are being made, both at JPL and UCLA, of ε and α_s to corroborate the measurements made by RCA on the surfaces which are planned for the TV system.

Interface tests have been performed on the shimming to be used between the bus and the TV system. A heat transfer of 1.5 w/leg is expected from bus to TV system. While this is not the adiabatic interface originally contemplated, this small transfer will present no problems. The PTM tests at RCA will further verify these values.

The thermal design of the bus and associated components is similar to that of *Rangers* 3, 4, and 5. In view of the unavailability of the 25-ft chamber for *Ranger* 6 (and very likely for *Ranger* 7), this spacecraft will be tested in the 6-ft chamber as was done for previous *Rangers*. The TV system will be cabled from outside to the bus within the chamber.

C. Guidance and Control

1. Secondary Power

Ranger secondary power activities are presently concerned with the flight acceptance testing of flight hardware. A study is being undertaken to increase the intrinsic reliability of the electrical conversion system for *Rangers* 6 through 9 by the substitution of high-reliability components and by the qualification and acceptance screening of parts now designated. There is a continuing evaluation of the battery handling procedures.

The capacity of any battery is highly dependent upon the method and procedure used in its preparation. For example, the *Ranger* 3 battery was received from the manufacturer in the charged sealed condition. The battery was then subjected to a single discharge/charge cycle in order to optimize its stand characteristics; this is commonly known as a mellowing cycle. Subsequent test data from the vendor showed that this single cycle was not necessary, provided care was taken in battery handling and storage. Also, the single cycle had decreased the capacity by about 5 amp-hr. Therefore, in order to utilize this added built-in capacity with no sacrifice in weight or reliability, the *Ranger* batteries are now used without the mellowing cycle. *Ranger* 4 was the first spacecraft to use a battery incorporating the new preparation procedure. The test and flight records for *Rangers* 3 and 4 show a 10% increase in amp-hr.

The analysis of the *Ranger* 4 flight brought to light a possible shorting in the separation connector. Since both charge and monitor lines from the battery go through one of these connectors, shorts may occur. Future flights will incorporate a diode and a fuse to add isolation to the charge and monitor lines, respectively.

2. Attitude Control

a. Earth sensor. The *Ranger* Earth sensor is a device which utilizes a variable aperture shadowing technique on three photomultiplier tubes so arranged that their current outputs can be resolved into 2-axis error signals. Previous *SPS* reports have traced the development of the Earth sensor in detail (*SPS 37-4, -5, -6, -7,* and 9): The following discussion is a current look at the *Ranger* Earth sensor noting in particular the test equipment, some test data, performance in *Rangers* 1 through 4, and the development of an Earth sensor light hood.

Figure 29 shows the equipment used to check out the *Ranger* Earth sensor at AMR; Fig. 30 is a block diagram of the test equipment. The short range Earth simulator simulates the Earth at its color temperature, various sizes, and light intensities of the Earth at mid-course and terminal maneuvers. The long range Earth simulator has the added feature of providing various phase angles of the Earth. The short range Earth sensor is mounted on top of a mechanical alinement fixture and a T-2 theodolite (Fig. 29). The Earth sensor can be rotated to any desired angle with respect to the Earth by means of the theodolite, and the mechanical null position of the Earth sensor with respect to the Earth can be determined with the mechanical alinement fixture. The small telescope on the mechanical alinement fixture is adjusted parallel to the mounting reference surfaces on the Earth sensor using autocollimation techniques. Voltage outputs of the Earth sensor are read out of the dynamics meters after the signal has passed through demodulators and simulated loads as would be in the attitude control subsystem. Figure 31 is the final circuit diagram of the *Ranger* Earth sensor.

Figure 32 is the actual Earth sensor plot of roll and hinge voltage outputs versus angle. Table 14 shows typical

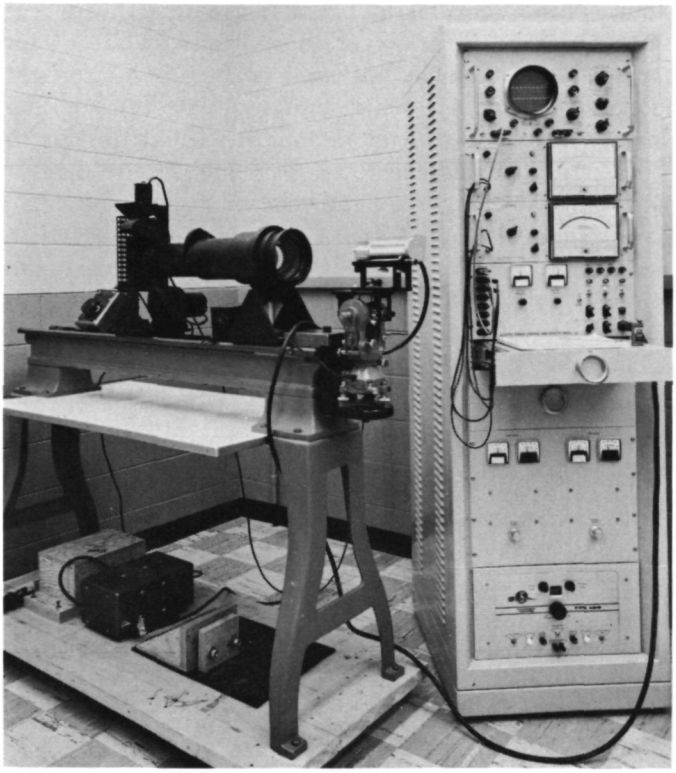

Fig. 29. *Ranger* Earth sensor test equipment

Table 14. Values for third quarter trajectories for *Rangers* 3 through 7

Maneuver	Diameter of Earth, deg	Sun–Earth–probe angles, deg
First acquisition of Earth sensor	12	90 to 140
Mid-course maneuver	4.4	80 to 130
Terminal maneuver	1.9	70 to 130

third quarter values (*Rangers* 3 through 7) of Earth diameter and Sun–Earth–probe angles when the Earth sensor is first turned on, during mid-course maneuver, and at terminal maneuver. The long range Earth simulator was used to simulate the Earth at its approximate color temperature, a Sun–Earth–probe angle of 90 deg as shown in the sketch on the plots, the corresponding light intensities during the respective maneuvers, and the approximate Earth diameters. The rounding of the curves near the saturation points is due to the finite size of the Earth. If the Earth were a point of source of light, the curves would be a straight line saturating at 1.25 deg for roll and 2.5 deg at hinge. The finite size of the Earth causes these intersecting lines to curve in a region of plus and minus the radius of the Earth from the saturation points of a point source. This is readily seen in Fig. 32(a).

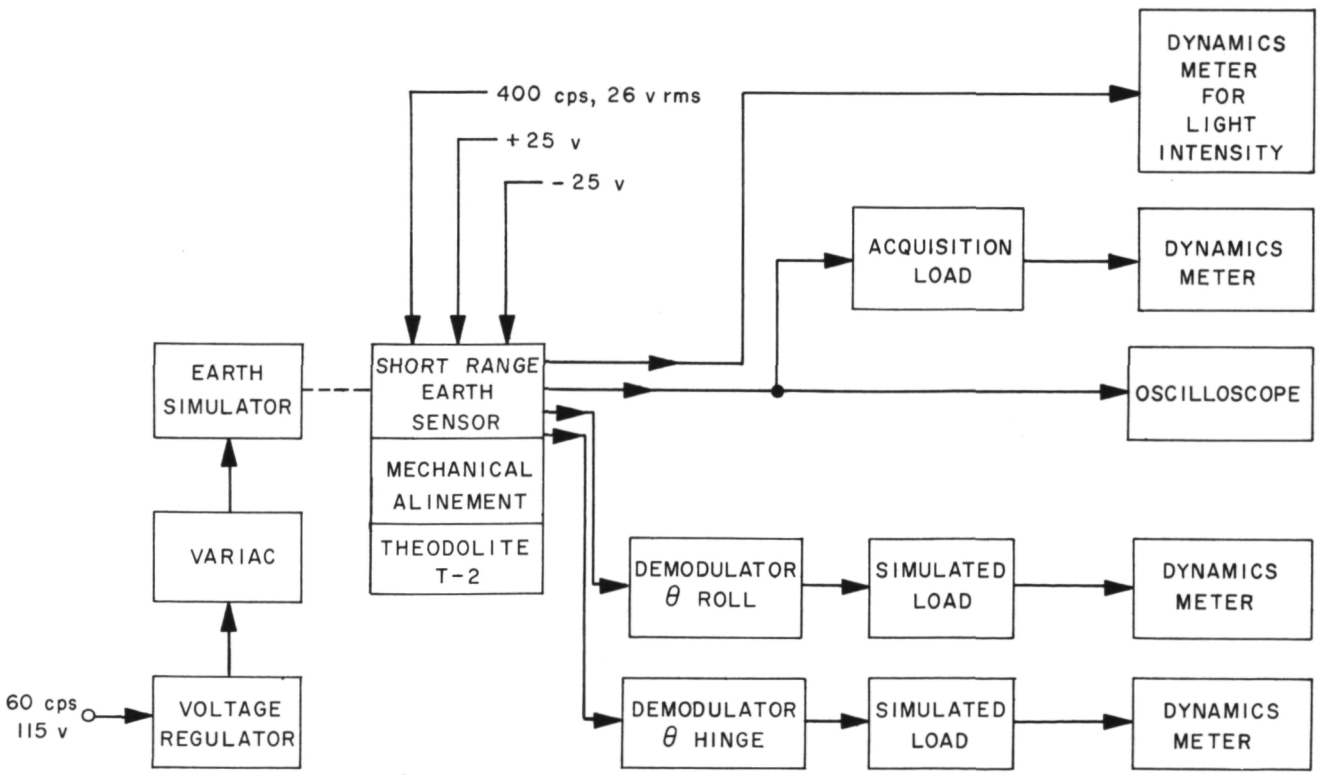

Fig. 30. Test facility for short range Earth sensor

Because there is only a half illuminated Earth in the hinge direction in Fig. 32(b), this effect is very much diminished.

The Earth sensor functioned in *Rangers* 1, 2, and 3. On *Ranger* 4 the Earth sensor was never energized. *Rangers* 1 and 2 operated in a low Earth orbit and the Earth sensors indicated acquisition on lighted objects with *Ranger* 1 giving more information, in general. The Earth sensor appeared to be operating correctly even though its temperature was close to the maximum allowable Earth sensor temperature, and the intensity of the Earth was 10 times brighter than expected on normal *Ranger* trajectories.

Ranger 3 provided the first good inflight evaluation of Earth sensor performance. This evaluation indicated that the sensor performed as intended during flight. A spurious pitch command at terminal (Moon distance) caused the spacecraft to pitch in the direction of Earth, eventually bringing the Sun shade between Earth sensor and Earth. This caused a loss of Earth acquisition. From this point on, the spacecraft performance became quite confused and further Earth sensor performance cannot be adequately stated.

Figure 33 is a plot of simulated Earth sensor light intensity data calculated for the *Ranger* 3 flight and light intensity telemetered back from the *Ranger* 3 Earth sensor during flight. The correlation between the two sets of data is good. The simulated data was calculated considering the Earth to be a perfectly diffuse (Lambert) reflector with an Earth albedo of 0.4.

Asymmetrical snow and cloud cover coupled with finite size of the Earth will cause the Earth sensor to have a roll axis error. (Hinge errors are unimportant to guidance.) An estimate of these errors indicates them to be approximately 5% (3σ) of the Earth apparent diameter (approximately 0.1 deg at terminal and 0.25 deg at midcourse.)

The *Ranger* Earth sensor needs a light hood to shade its optics during terminal maneuver for Earth–probe–Sun angles less than 93 deg. The light hood would experience the following rather wide range of temperatures: a maximum temperature needed for heat sterilization of 326°F for 2 hr to a minimum temperature during the cruise phase of flight of −300°F. The light hood must be deformed in shape to fit into the Earth sensor cavity in the *Agena* B adapter. The light hood, combined with all other factors, cannot cause a tipoff rate larger than 3 deg/sec during *Agena* B–*Ranger* separation. Figure 34 is a picture of the *Ranger* 4 light hood in the *Agena* B adapter Earth sensor cavity. Another constraint is that if a light hood is larger than the one used on *Ranger* 4, the light hood will come in contact with the Earth sensor Sun shield when the high-gain antenna is rotated 180 deg to be clear of the mid-course motor firing. Figure 35 is a picture of the *Ranger* 4 light hood at an antenna angle approaching 180 deg. A last constraint is that the Earth sensor must be able to track the Earth to a maximum antenna angle of 145 deg.

The *Ranger* 4 light hood is made out of silastic rubber with thin strips of Teflon film bonded to it at the areas that touch the walls of the Earth sensor cavity in the *Agena* B adapter. This light hood permits ±180-deg yaw angles and an Earth–probe–Sun angle of 73 deg or larger. This hood had undergone a rather thorough test evaluation prior to the *Ranger* 4 flight, and is the most logical light hood to be used on *Rangers* 5, 6, and 7. From preliminary trajectory information, the *Ranger* 4 light hood would permit firing on 17 days out of a possible 21 days.

Other light hoods which would permit more firing days have been and are being designed. A prototype model of a metallic light hood, which would permit an Earth–probe–Sun angle of 65 deg or larger and ±180-deg yaw angles, is being evaluated.

b. Gyro control electronics module and gyro module. The gyro control electronics module and the gyro module make up the inertial reference system for *Rangers* 3 through 9. The functions of the combination of these two modules are to: (1) supply rate information during acquisition and cruise modes, (2) supply both rate and position information during the commanded turn and mid-course correction autopilot modes.

The gyro control electronics module contains the majority of the circuits for the inertial system and includes: the caging electronics used to capture the gyros for use as a rate information source; precision command current regulators and pattern field regulators; and electronics damping circuits.

An intermittent failure of the roll amplifier in Package 009 (slated for *Ranger* 5), reported by the subcontractor, was traced to a Silicon Transistor Corporation transistor Type 2N1050 which is used in the output stage of the three caging electronics amplifiers. Microscopic examination revealed what appeared to be an improper emitter lead to the chip connection; in addition, corrosion was noticed on both the emitter lead and the base lead.

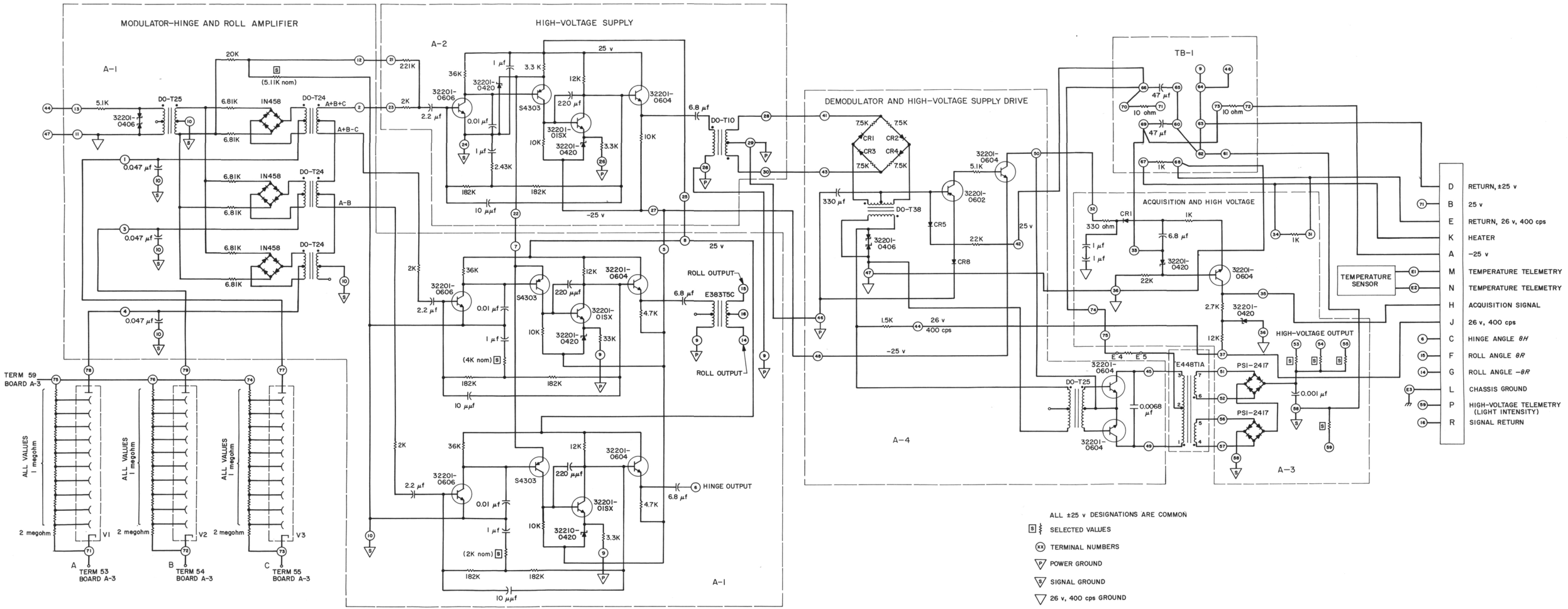

Fig. 31. Final Earth sensor circuit diagram

Page intentionally left blank

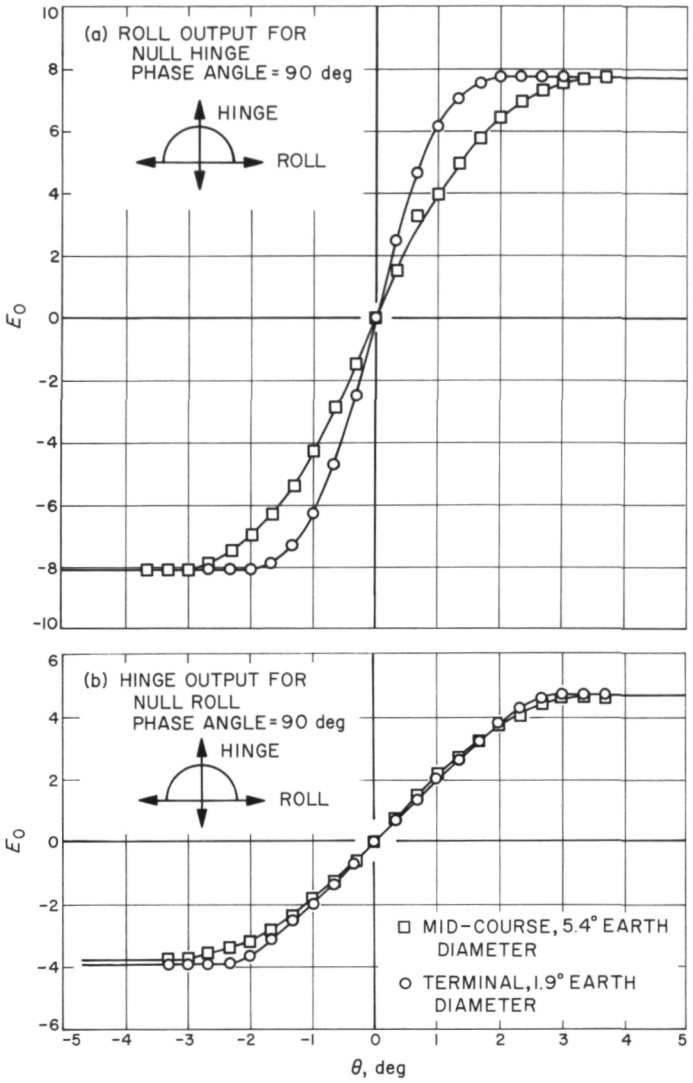

Fig. 32. Roll and hinge output versus θ for Earth sensor

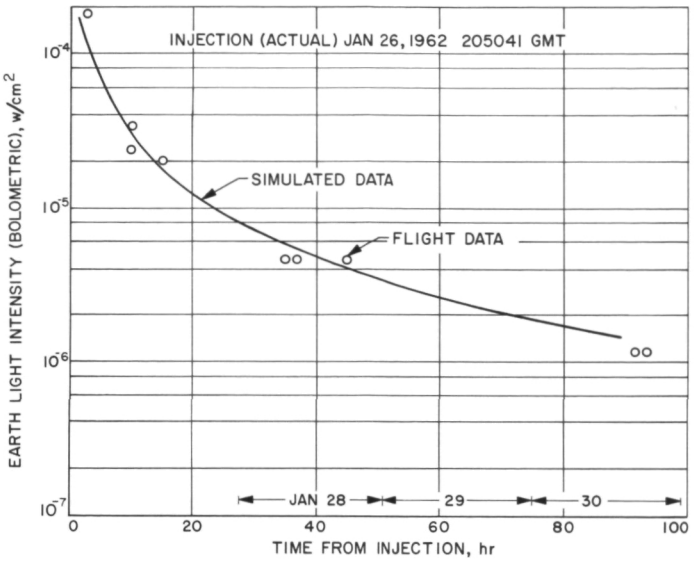

Fig. 33. Simulated and flight data of Earth-light intensity for *Ranger* 3

The remainder of the 2N1050 transistors in the flight package showed deterioration from specifications (notable V_{ce}). A total of eight transistors was examined revealing corrosion in all eight as well as large variations in geometry of base and emitter leads, and significant lack of correlation of chip sizes and placement of emitter and base connections on the chips. Representatives of the Silicon Transistor Corporation established the fact that a large batch of 2N1050 transistors had become contaminated and confirmed JPL's findings. The decision was made to switch to Texas Instrument 2N1050 transistors which have no history of this type failure. At this date, the only package with Silicon Transistor Corporation's 2N1050's is the *Ranger* 5 spare and this has been up-dated accordingly. The use of the 2N1050 in the caging electronics is well within the design capability of the 2N1050's; therefore, no further difficulty is foreseen. As an added precaution, a few samples of the Texas Instrument transistors were opened after burn-in screening and found to have no trace of corrosion.

The gyro module contains, in addition to the three Minneapolis-Honeywell Model GG49-E12, low-damped, floated rate, single axis gyros: twelve 1020-μ capacitors to generate the angular position information; a 10-sec, one-shot multivibrator for cycling the above capacitors; and the scale factor resistors for establishing the rate scale factors of the switching amplifier and autopilot.

Difficulty, involving high resistances, where direct connections between terminals exist, was observed in two modules. This was localized to the printed circuit boards which have been investigated, and the results of testing of all present packages show opens and high resistances limited to Packages 013 and 014 (*Rangers* 8 and 9). The connections between the printed circuit on the back side of the board and the terminal was at fault and since the board is glued (Epon) to an insulator, repair was impossible. The terminal boards have been redesigned and are being installed with printed circuits now located on one side only resulting in increased reliability.

c. Velocity shutoff subsystem. The magnitude of the velocity increment to be added to the spacecraft during the corrective mid-course maneuver of *Rangers* 3 through 9 will be measured by an accelerometer and integrator combination. Since a digital computer is carried in the CC&S unit and the size of the corrective velocity incre-

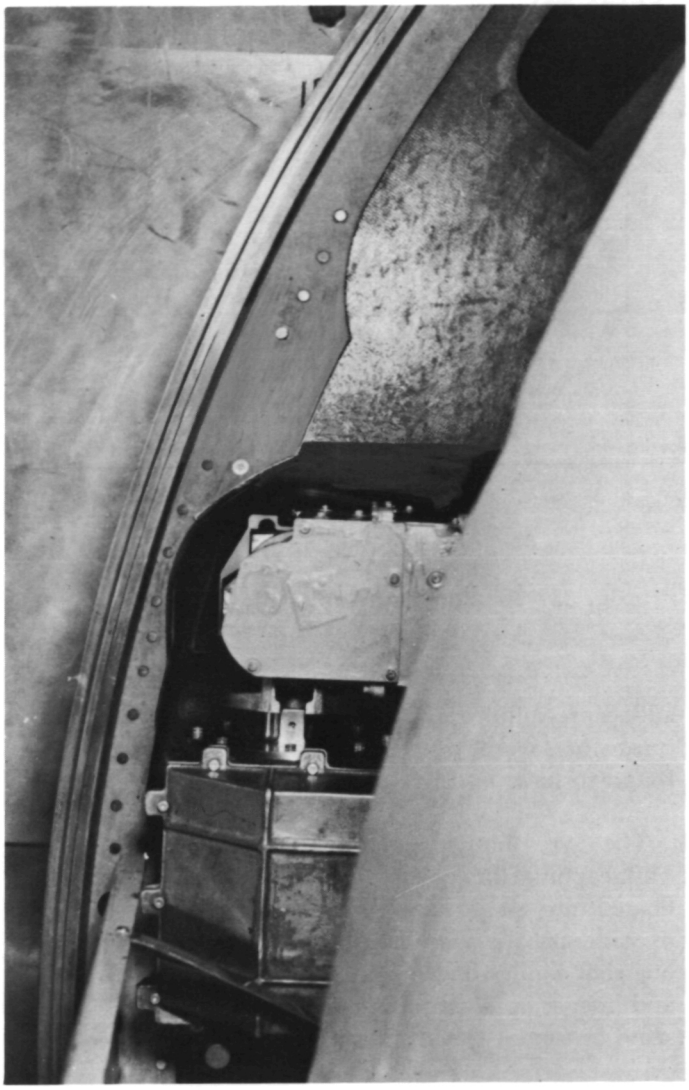

Fig. 34. *Ranger* 4 light hood in the *Agena* B adapter Earth sensor cavity

ment is transmitted digitally from Earth, a digital accelerometer is required. This system has been developed at JPL and is operated in conjunction with the digital CC&S for the purpose of controlling the mid-course motor shutoff.

This digital accelerometer system consists of a force balance accelerometer with a pulse torqued rebalance loop to provide capture current to the proof mass. In this mode of operation, the pulsing rate is directly proportional to the applied acceleration and each pulse produced represents a constant value of velocity increase (or decrease, depending on the direction of the applied acceleration). In the *Ranger* system application, this value or scale factor is $\frac{1}{10}$ ft/sec of velocity increase.

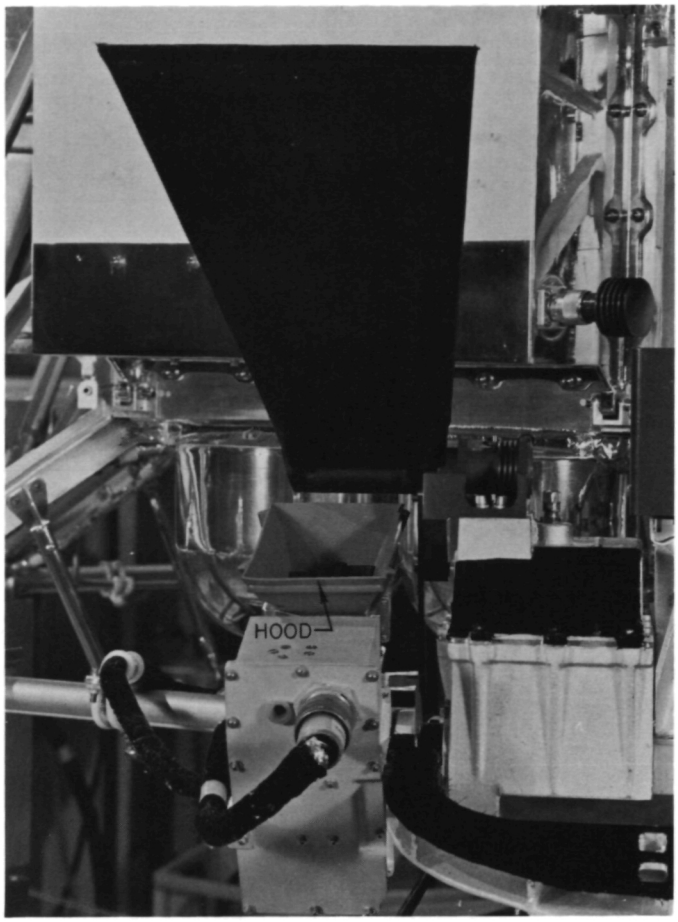

Fig. 35. *Ranger* 4 light hood at an antenna angle approaching 180 deg

Units up to and including *Ranger* 7 have been environmentally tested and delivered. All units have been well within the required $\pm 0.25\%$ accuracy tolerance over the entire 0 to 70°C temperature span.

One spare *Ranger* unit has been placed on a life test operation at 0.5-*g* input, which is over 7 times the actual operating level in flight. At this input, the unit produces 161 pps, 24 hr a day. Normal accuracy tests are performed at approximately 500-hr intervals. The unit has accumulated 2265 hr without failure or serious shift of calibration.

One unexpected area of difficulty was encountered during the last reporting period. Early in the evaluation of the accelerometer transducer, it was discovered that the seismic proof mass within the instrument was subject to random static charge effects. These static charges would produce error torques of large and variable magnitudes. To eliminate these errors, a fix consisting of a radioactive static discharger was installed at the vendor's

facility. No system design constraints existed with regard to small radioactive sources on board the spacecraft at this time. During the final testing of *Ranger* 4 at AMR, a radioactivity mapping operation, using the gamma ray experiment from the spacecraft, disclosed that enough gamma radiation was coming from the accelerometer to create a detrimental effect in the gamma ray measurement system. Due to the fact that insufficient time remained prior to launch of *Ranger* 4, no reduction of this spurious radiation was possible.

Testing at JPL disclosed that it was possible to change from the existing radium isotope source to a polonium source without impairing the accelerometer's performance. The advantage of the polonium static discharger is that it emits mostly alpha particles and that the gamma radiation present was below the interference level with respect to the gamma ray experiment. The alpha particles do not pass through the accelerometer case at all.

All available accelerometer modules for *Rangers* 5, 6, and 7 and spares were converted to the polonium source. Retesting of these modules proved that no degrading of performance or accuracy was produced by the change. Accelerometers for *Rangers* 8 and 9 have not yet been assembled and will, therefore, contain the polonium source.

Future applications of this instrument will contain a mechanical redesign which will allow the proof mass to be grounded to eliminate any static charge buildup; the radioactive source will then be completely unnecessary.

d. Celestial simulation. Engineering studies regarding the celestial simulation facilities are given in Section G, *Supporting Activities and Engineering Facilities.*

D. Telecommunications

1. Antennas and RF Components

a.* Ranger *5. Radiation patterns of the omnidirectional antenna on the *Ranger* 5 mockup, both with and without the RF shielding described in *SPS 37-15*, Vol. I have been completed. Comparison of these patterns shows some performance degradation caused by the RF shield. This degradation is primarily for extreme nose and tail aspects not likely to be encountered in flight. The degradation is not considered sufficient grounds to preclude the use of the RF shield, if the shield is useful in solving the ADF capsule transmitter–JPL transponder RF interference problem.

b.* Rangers *6 through 9. Because of the RF interference problem between the capsule transmitter and the transponder, possible similar problems with the RCA TV subsystem were investigated. Tests were made at the JPL Mesa facility antenna range of the coupling at 890 Mc between the *Ranger* high-gain antenna and the *Ranger* omnidirectional antenna. The high-gain antenna will be carrying the RCA TV signal, while the omni-antenna serves as the transponder receiving antenna. The results of the test are shown in Fig. 36. The coupling varied from −45 to −75 db depending on high-gain antenna position.

Presently available information indicates that the RCA TV subsystem radiates sufficient power at 890 Mc, the transponder receiver frequency, so that it appears that the transponder may see spurious signal levels of −139 dbm for high-gain antenna look angles near 180 deg. This level may be sufficient to interfere with proper transponder operation. However, during normal missions, the look angles will not approach 180 deg.

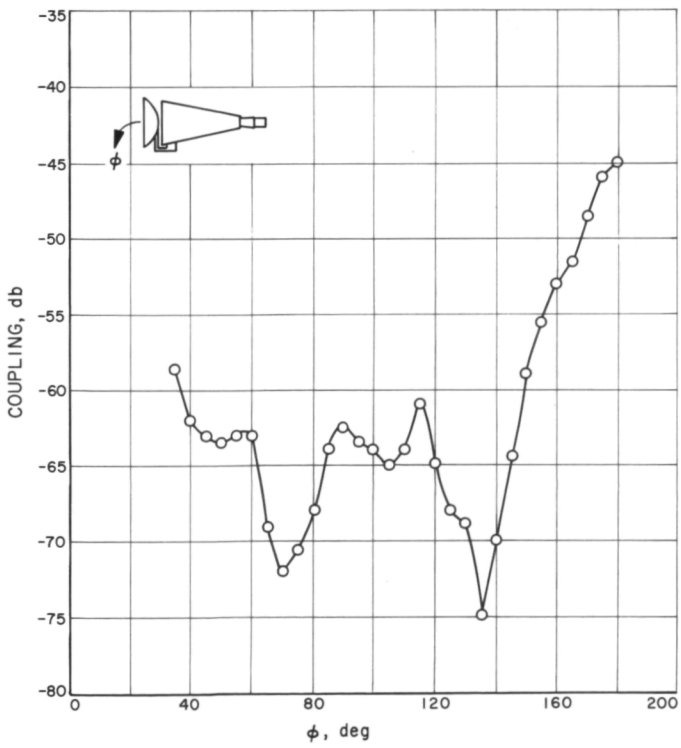

Fig. 36. Coupling between *Ranger* 6 high-gain antenna and the omni-antenna, as a function of high-gain antenna look angle ϕ, at 890 Mc

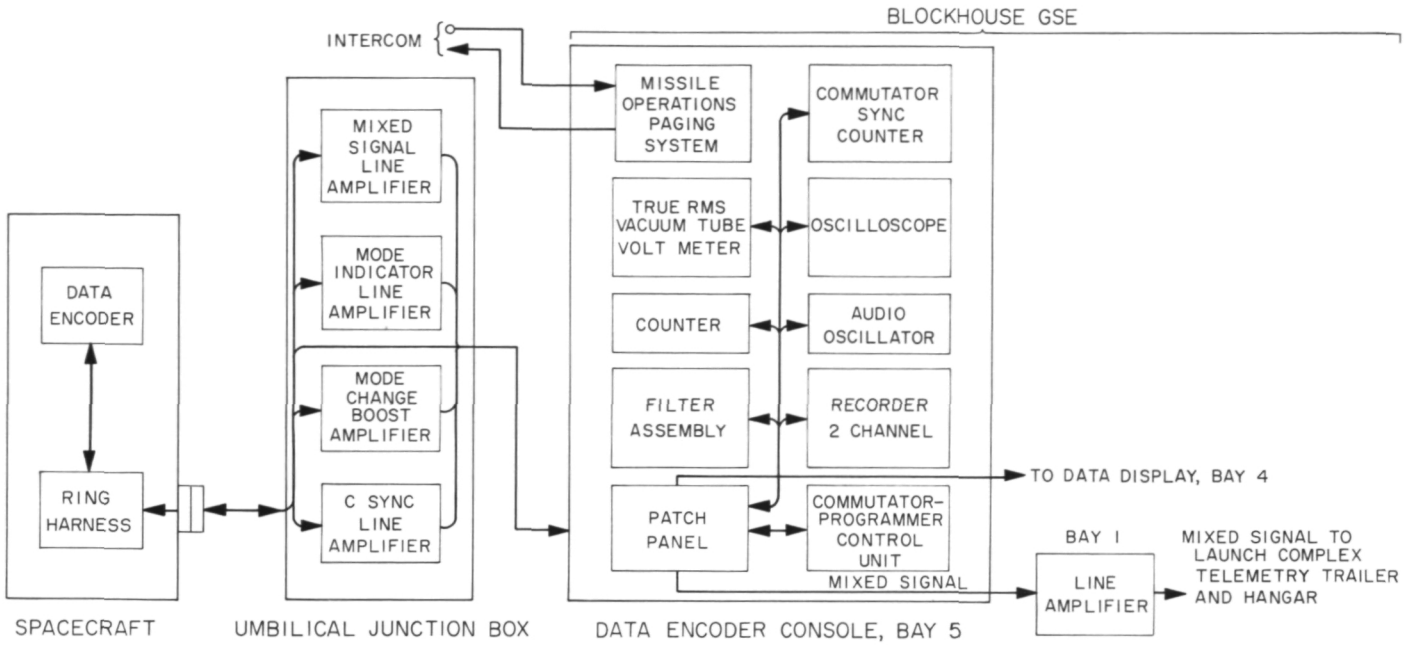

Fig. 37. Data encoder launch complex GSE

2. Ranger *Data Encoder*

The basic system for encoding telemetry data in a form suitable for modulation of the RF carrier for *Ranger* spacecraft is a PAM/FM or time division multiplex/FM subcarrier method. In this system many data points are periodically sampled, and the sampled data then frequency modulates an oscillator. The outputs of several FM oscillators, each being modulated with sampled data, are linearly mixed and the composite signal then modulates the transponder.

The last encoder report (*SPS 37-14*, Vol. II) described the equipment used by the data encoder in the system test complex. This issue will cover the launch complex ground support equipment and two special items: the encoder spacecraft simulator and the calibration console.

a. Launch complex. The data encoder ground support equipment used in the *Ranger* launch complex is shown in Fig. 37. This equipment provides capability to control and monitor the data encoder when the spacecraft is on the launch pad.

Interconnection from the encoder to the blockhouse is made through the umbilical connector and umbilical junction box. The inputs and outputs of the data encoder are the same as in the system test configuration. They are:

(1) Signals from the encoder—
Hardline mixed signal.
Mode I indication (6.8 v).
Mode II indication (6.8 v).
Mode III indication (6.8 v).
Mode IV indication (6.8 v).
H sync output (−6 v).
C sync output (−6 v).

(2) Signals to the encoder—
Mode change pulses.
Mode relay set pulses.
External inhibit command (28 v).
External clock pulses.

The mixed signal output is analyzed at the blockhouse by both data encoder and data display. This same signal is amplified at the blockhouse and transmitted via video cable first to the launch complex telemetry trailer (LCTT) for tape recording, and then to the hangar for reduction by data display which provides a digital readout of channel frequencies for the spacecraft evaluation group.

Four isolation amplifiers (Fig. 37) are used by the data encoder group in the launch complex. All these amplifiers are used to overcome the loading effects of the relatively long lines used in the launch complex. The mixed signal line amplifier provides several additional features. It isolates the blockhouse ground from spacecraft common. It also has a constant gain figure over the encoder output frequency range so that encoder VCO output amplitudes can be measured accurately at the blockhouse console.

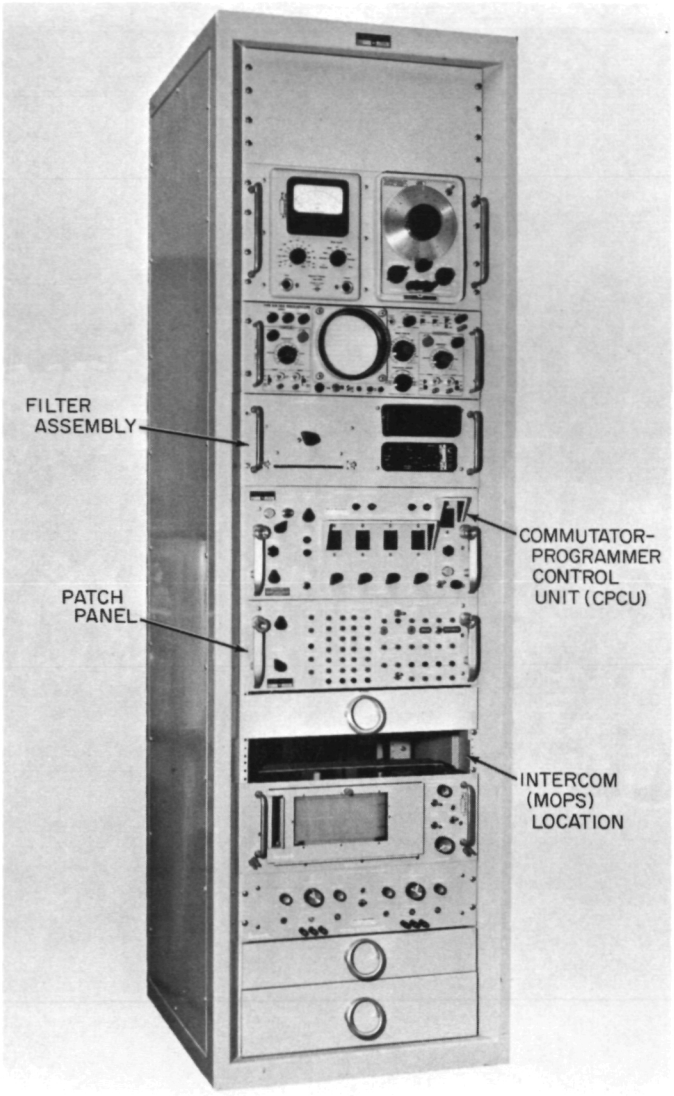

Fig. 38. Data encoder blockhouse console

The data encoder blockhouse console (Fig. 38) is essentially a slightly simplified version of the system test console. The only important item missing in the blockhouse console is the discriminator rack. Subcarrier analysis which requires the use of discriminators is provided by the data display group, whose console is directly adjacent to the data encoder in the launch complex GSE.

The patch panel provides interconnection of test equipment and access to the outputs of data display discriminators. Access to the *Agena* telemetry mixed signal from the *Agena* receiver in the LCTT is also provided at the patch panel.

The commutator programmer control unit (CPCU; Fig. 39) provides capability for external control of the encoder commutators and programmer (data mode selector). The CPCU indicates the encoder commutator and programmer positions on the small projection type windows.

The commutator sync pulse counter (Fig. 40) counts the H sync pulses from the spacecraft. These pulses are derived from the slowest rate commutator deck of the encoder, and reception of a pulse indicates a complete cycle or frame of commutation. This H sync count provides a record of operation which will be used in arriving at a life estimate for the relay commutators.

All other equipment in the encoder blockhouse console is used for mixed signal analysis.

b. Spacecraft simulator. The encoder spacecraft simulator (Fig. 41) is a device which provides operating characteristics similar to that of an actual encoder. It is used for checkout of the launch complex. Two important functions are thus performed:

(1) Damage to the encoder due to faulty wiring in the complex is prevented.

(2) No time is lost in troubleshooting the complex once the spacecraft arrives at the pad ready for tests and subsequent launch.

A block diagram of the simulator is shown in Fig. 42. In several cases, the simulator provides an output which simply checks a line from encoder to blockhouse. Where a critical pulse is delivered either from the blockhouse GSE to the simulator or vice-versa, the circuitry in the simulator is almost identical to that of the actual encoder. Thus, a satisfactory checkout of the complex using the simulator provides confidence that the complex will not adversely affect operation of the encoder.

c. Calibration console. The calibration console (Fig. 43) is a special test equipment used with the encoder in the system test configuration. The console can provide all the functions to the encoder which are not provided by the encoder system test console. The calibrator functions are:

(1) Simulation of any binary inputs to the encoder, such as B2 events, B20 events, or Channel 8 midcourse acceleration input is provided.

(2) Provision is made for simulated calibration of the encoder on either a voltage or resistance input channel.

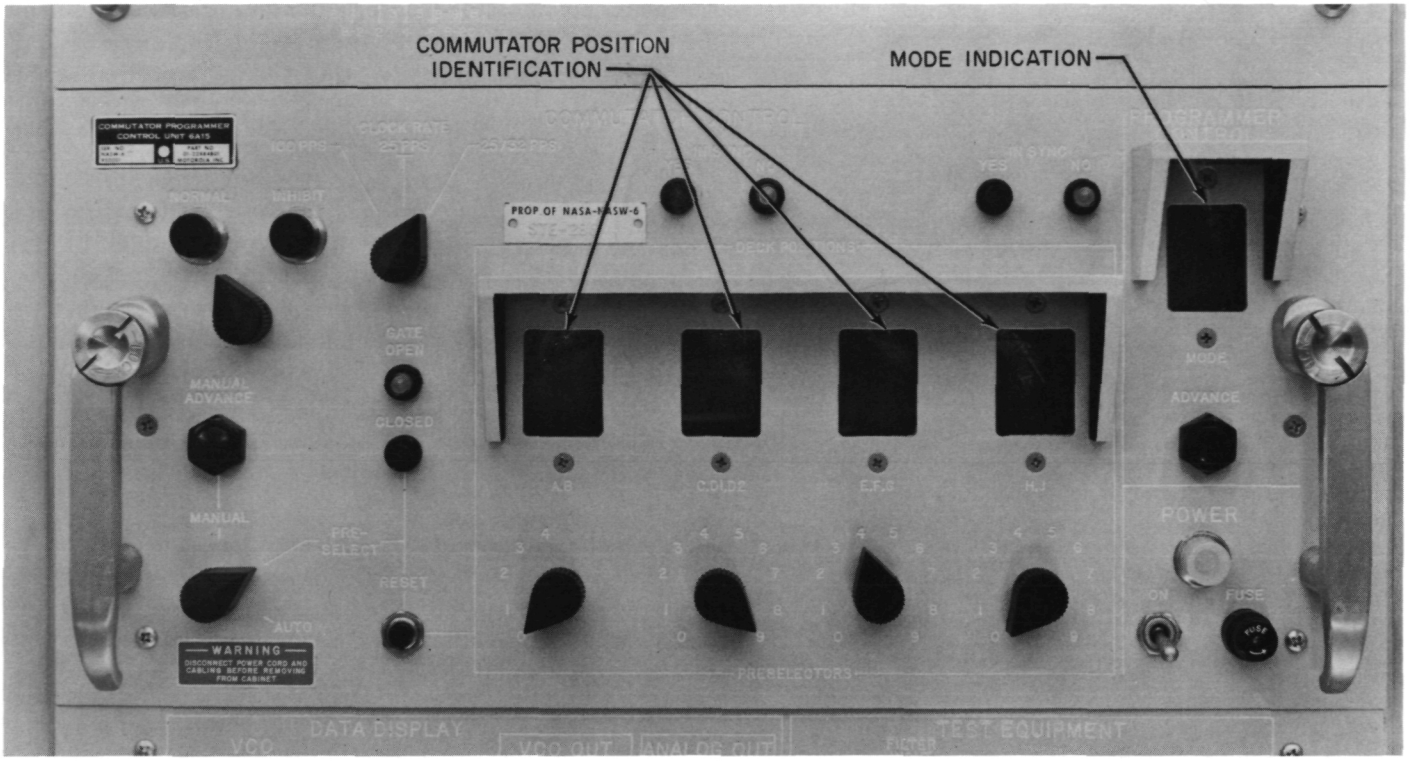

Fig. 39. Commutator–programmer control unit

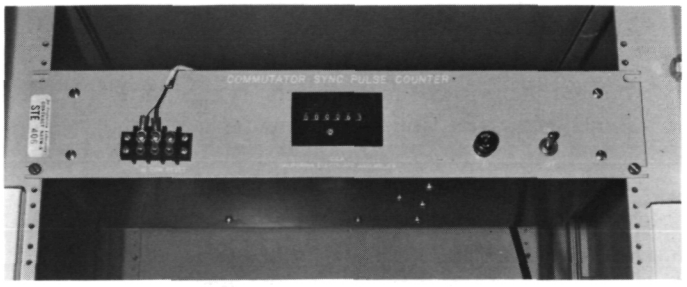

Fig. 40. Commutator sync pulse counter, *Ranger* data encoder

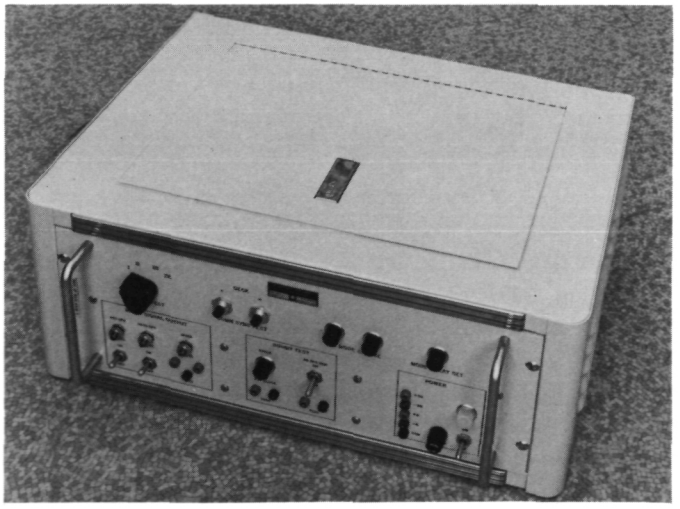

Fig. 41. Data encoder spacecraft simulator

(3) The calibrator can measure the transducer output of any channel before application of this output to the encoder; this prevents damage to the encoder due to any out of tolerance inputs.

(4) During real calibrations, the calibration console is used to monitor the input voltage to the encoder and thus ascertain proper operation of the encoder during the calibration.

(5) Capability for monitoring or simulating the Channel 1, vidicon, or gamma ray inputs is provided.

(6) Access to both the transponder and *Agena* mixed signal lines is provided; using the spectrum analyzer provided, analysis of these mixed signal lines can be performed.

The primary unit in the calibration console is the data calibrator and is shown alone in Fig. 44. The relay and switching circuits which control the operation of the calibration console are located in this unit. The plastic cards shown on the front of the calibrator provide the

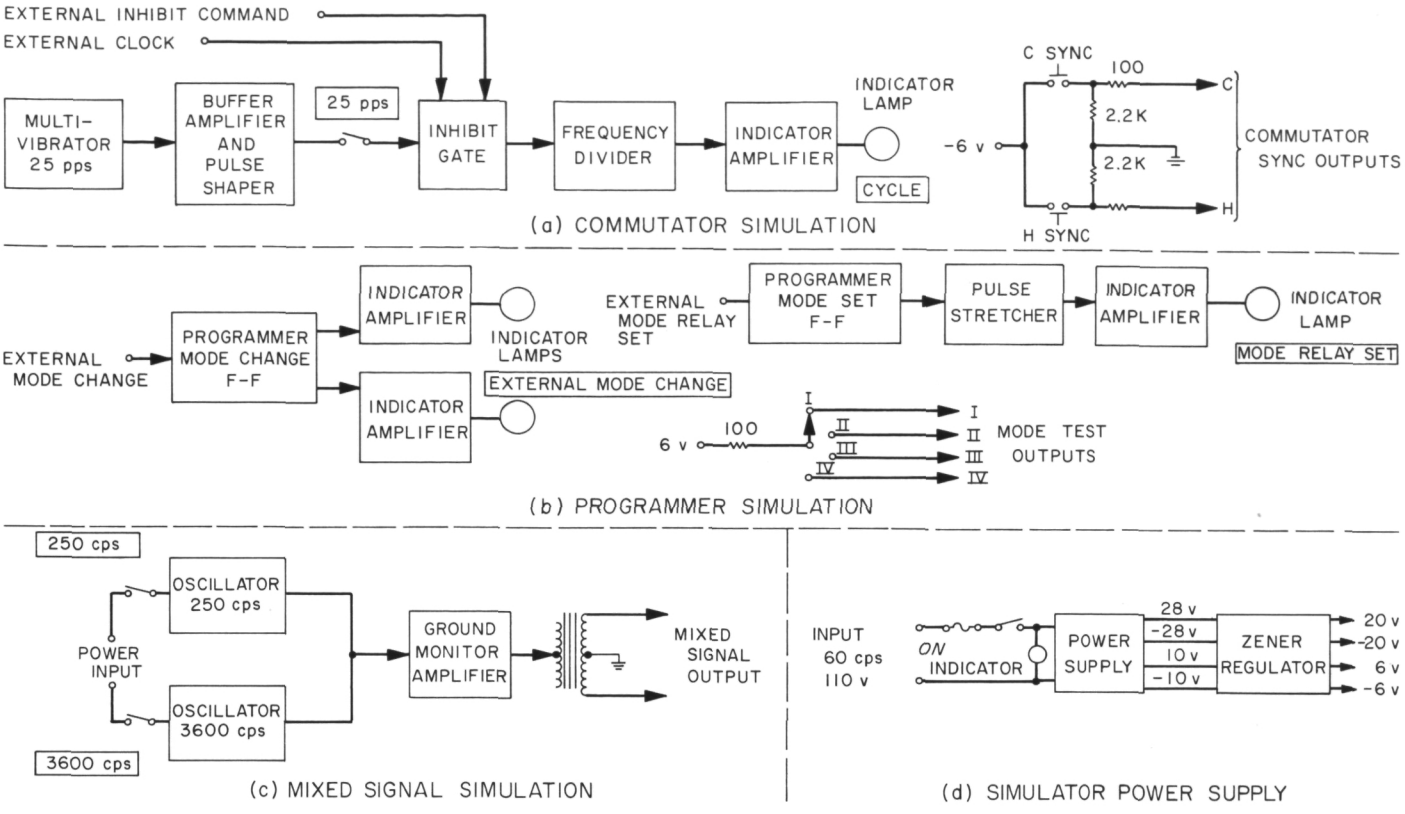

Fig. 42. Data encoder simulator simplified block diagram

information on transducer source inpedances, output voltages, etc., necessary for performing simulated calibrations. (The circuit configuration of the calibrator is quite complex and will not be described in this issue.)

Installation of the calibration console into the system is made by connecting the unit between the data encoder harness and the ring harness. Since this configuration is definitely nonstandard the console must be removed for system tests.

E. Space Sciences

1. Ranger 6 through 9 Scientific Experiments

a. Scientific objectives. The primary scientific objective of the *Ranger* 6 through 9 mission is acquisition of knowledge of lunar topography sufficient for determination of its gross effects on lunar landing vehicles. This objective will be achieved by means of relatively high-resolution photography of a portion of the lunar surface from the impacting *Ranger* vehicle, and subsequent quantitative analyses of these photographs. This mission will be performed within the constraints of a *Ranger* standard impact trajectory with a velocity at time of impact of approximately 2700 m/sec.

Achievement of this objective requires that the system provide a resolution in the photographs as received on Earth at least 10, and preferably 50, times better than the present *Ranger* 3, 4, 5 camera system is expected to obtain. Photography must be started at a time before impact or a distance from the Moon such that the initial photographs are comparable in resolution with the best now available from Earth-based astronomical observatories, and this photography must be continued at a regular rate until impact.

The desired quality of the photographs is directly linked to their usefulness in planning the design of unmanned vehicles and the initial manned lunar exploration program. To be of value, the pictures should indicate the suitability of the lunar terrain for landing and launch and the problems of surface mobility. On consideration of these objectives and the ultimate scientific use of the *Ranger* 6–9 photographs, resolution of the final image as received on Earth must be at least 0.5 m, and preferably 0.1 m.

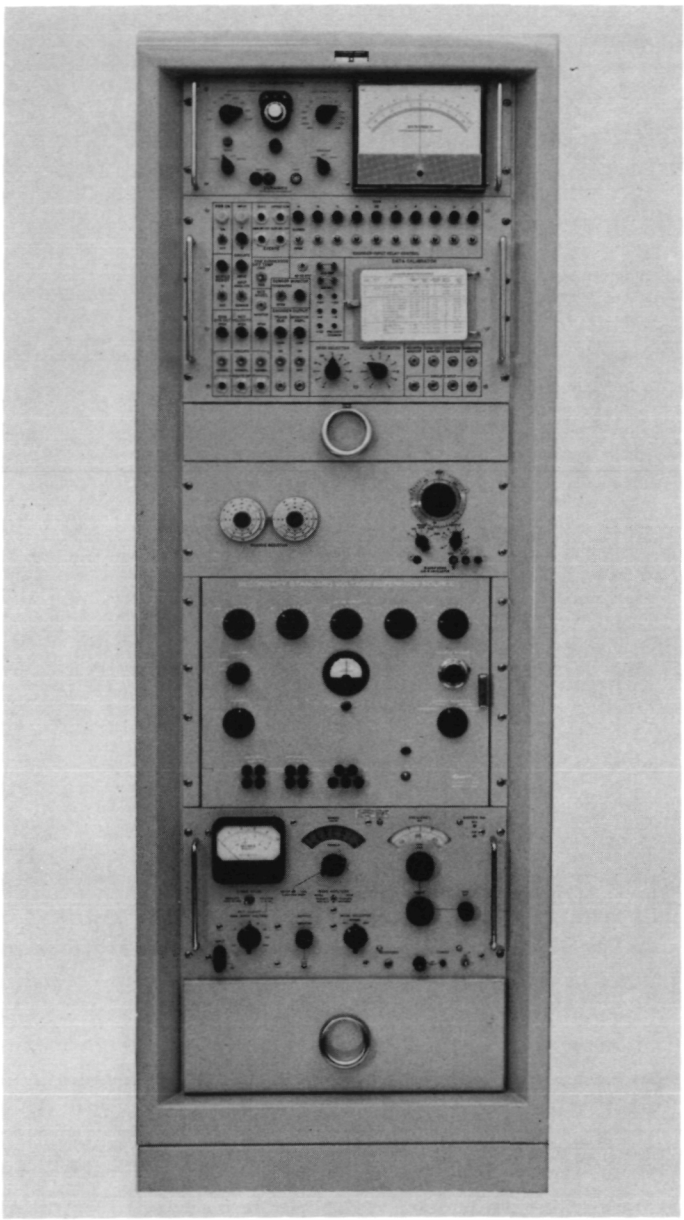

Fig. 43. Data encoder calibration console

A secondary scientific objective of the mission is acquisition of knowledge of the fields and particles environment of cislunar and lunar space which may be of importance to manned lunar flights, or which may yield data pertinent to the origin of these environments. Specifically, the several fields and particles experiments to be carried on the *Ranger* spacecraft will provide data on magnetic fields, micrometeoroids, and particle radiation.

b. Experiments. In consideration of the above scientific objectives, the following scientific experiments are planned for the *Ranger* 6 through 9 mission:

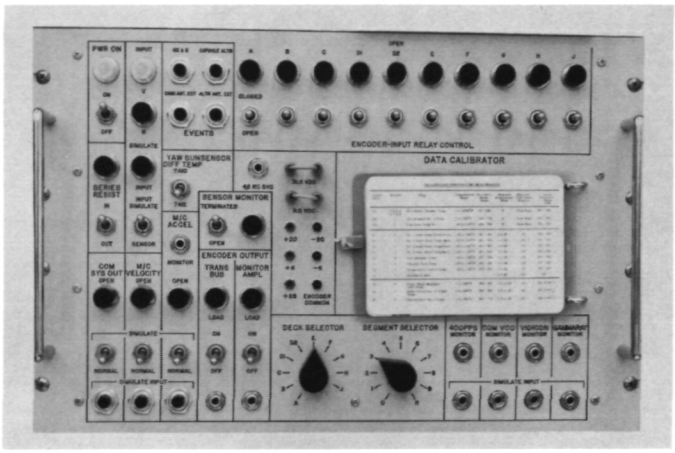

Fig. 44. Data calibrator, *Ranger* data encoder

High-resolution photography experiment. The television experiment consists of six 1-in. vidicon cameras. These are arranged as two wide-angle cameras, designated Cameras A and B, and four narrow-angle high-resolution cameras designated as Cameras 1, 2, 3, and 4.

Cameras A and B are fully scanned producing 800 TV resolution lines over the tube format of 0.44 by 0.44 in. with a side field coverage of 8.4 deg. The four clustered cameras utilize a reduced raster, scanning a 0.11- by 0.11-in. central portion of the tube at the same line density, thus giving a tube format of 200 TV resolution lines. The angular resolution of each camera is then the same; however, the reduced format of the partially scanned system enables a much faster picture cycle; thus pictures may be taken at lower altitudes than with the fully scanned system.

This leads to a natural nomenclature of Type F cameras for fully scanned and Type P for partially scanned. The Type F and Type P cameras use the same imaging transducers and optical equipments and differ only in the detail of their electronic circuitry. The image transducer is an electro-magnetically focused and deflected 1-in. vidicon with an ASOS photoconductor with a resolving capability in excess of 800 lines/picture height.

The Type F utilizes 1152 active horizontal scan lines over the 0.44- by 0.44-in. faceplate area. The horizontal scan rate is 450 cps with 0.22 msec appropriated to horizontal blanking. The time required to cover the active scan lines plus 46.6 msec for vertical blanking add up to a 2.56-sec frame period. At the end of its active scan the Type F camera enters an erase phase which occupies an equal amount of time. In the *Ranger* TV subsystem two Type F cameras are alternately scanned and erased in

such a manner that one is being scanned while the other is being erased.

The Type P camera utilizes 300 active horizontal scan lines over a 0.11- by 0.11-in. faceplate area. The horizontal line rate is 1500 cps with 111.1 μsec allocated for horizontal blanking. The vertical scan plus a 6.6-msec blanking period occupies 0.2 sec. At the end of the vertical scan an erase procedure is initiated which occupies 0.64 sec. The four Type P cameras are sequentially scanned; while one is being scanned the remaining three are in various portions of their erase cycles. A 40-msec pulse is used to separate each sequence of four Type P camera exposures. The total period per sequence is then 0.84 sec.

Fields and particles experiments. There will be eight fields and particles experiments performed on *Ranger* 7 through 9 missions.

(1) *Integrating ionization chamber.* The detector for the integrating ionization chamber experiment is a quartz fiber instrument of the Neher type. It consists of a thin spherical metal shell filled with gas at a pressure of several atmospheres. The wall thickness is such that protons above 10 Mev in energy and electrons above 0.4 Mev can pass through into the gas. A voltage is maintained between a cylindrical collecting electrode inside the chamber and the external spherical wall. This voltage is high enough to cause the collection of all of the charged particles created in the gas by the incident ionizing radiations. When a precalibrated amount of charge is collected, the quartz fiber system activates a recharging pulse from the high voltage power supply. The time interval between recharging pulses is inversely proportional to the radiation dose rate. The recharging pulse is amplified and shaped by the chamber amplifier and electronics system into a form suitable for processing by the data conditioning system prior to transmission by telemetry.

(2) *Particle flux experiment.* The instrumentation for this experiment consists of three Geiger-Müeller counters and associated electronics. Two of these counters are Type RCL 10311 and each is shielded such that protons above 10 Mev in energy and electrons above about 0.4 Mev in energy can penetrate into the gas volume and be detected. One of these counters is shielded with material that is essentially identical in composition and thickness to that of the wall of the integrating ionization chamber. Since they will each be detecting the same types of particles, and since the ion chamber measures the total ionization, the combined data from this counter and the ion chamber will give a fairly complete picture of the charged particle flux. The other 10311 tube is shielded with beryllium. This provides some discrimination between protons and electrons. The two RCL 10311 tubes will also be operated in coincidence to give directional information. The other Geiger-Müeller counter is an Anton 213 with a thin end window which allows lower energy particles (protons above 0.5 Mev and electrons above 35 Kev) to be counted.

(3) *Dust particle.* The primary purpose of the dust particle experiment is to provide information on the density, direction of motion, and distribution in terrestrial–lunar space of micrometeoroid particles.

The instrument consists of two detector plates with attached preamplifiers and one electronics power supply package. The detector plates serve to detect particle impact; the generated signal is conditioned and amplified by the attached preamplifier. The electronics power supply package generates the required internal dc voltages and senses the detector preamplifier output. The count rate is not expected to exceed 1/min.

Location of the sensors on the spacecraft will be 180 deg from one another in the plane of the ecliptic and in the direction of the velocity vector. Under these conditions, one plate will look in the general direction of the Moon while the other plate will look at low inclination particles in the ecliptic plane.

(4) *Search coil magnetometer.* The primary purpose of the search coil magnetometer is to provide a survey of lunar electrodynamics in the frequency range of 1 to 1000 cps. The instrument consists of a single-axis search coil magnetometer and associated electronics, divided into two packages. The main electronics package contains a spectrometer, power supply, and associated circuitry. The spectrometer will consist of tuned bandpass amplifiers, with center frequencies of 3, 10, 30, 100, and 300 cps, which will analyze signals with frequency components in this range. This instrument will have inflight calibration capability as well as automatic scale switching.

The instrument is to be mounted on the spacecraft so as to provide a remote location of the detecting coil–preamplifier package, and to mini-

mize spacecraft generated magnetic noise. The orientation of the detecting coil is not critical.

(5) *Low-energy ion detector.* This instrument will detect the number-density and energy of positively charged particles with energies from 0.1 to 30 ev using a retarding potential technique. The experiment will be effective in detecting low energy ions in the transition regions of the Earth's upper ionosphere, in the cislunar plasma, and in any lunar ionosphere.

The instrument consists of a planar ion trap sensor made up of a collector and two grids. The outermost grid will be energized by a variable or staircase potential source. The innermost grid will be biased negatively to suppress photoemission from the collector plate.

Positively charged particles, up to mass 32, with sufficient energy to overcome the retarding potential on the outermost or aperture grid will be recorded by the collector plate. By varying the aperture grid potential, the particle energy spectrum may be resolved. An analog output of the collector current will provide the spectral data.

(6) *Electron flux detector.* The electron flux instrument consists of three solid state detectors to identify electrons in the 0.250 to 3 Mev energy range. The detectors are silicon solid state of the lithium drifted variety. Two of these detectors have a depletion layer 1.0mm thick. One is shielded by an aluminum absorber which allows only minimum ionizing protons to be counted, and sets the upper electron energy limit for the system. The other, with a heavier aluminum shield, is the active detector, the output of which is a composite of electrons of minimum ionizing energy and protons of approximately 2-Mev energy level.

The third detector has a depletion layer of approximately 5μ. This detector, shielded in the same manner as the active detector, is insensitive to electrons, due to the thin depletion layer; it thus serves to count only the 2-Mev protons. By subtracting the count of the two detectors from the count of the active detector, the electron flux is obtained.

Each detector is followed by a preamplifier–amplifier combination. The output of the amplifier serves as an input to a pulse height analyzer.

(7) *Electron–proton spectrometer.* This instrument is designed to unambiguously separate electrons from protons and measure the fluxes and energies of each in the range of 50 to 800 kv for electrons and 500 to 1500 kv for protons. The instrument will consist of a plastic scintillator and a cesium iodide crystal, both mounted on the face of a single photomultiplier tube. The separation of electron and proton pulses will be accomplished by means of pulse shape discrimination circuits. The pulses will be energy discriminated by means of an eight channel differential pulse height analyzer, and the counts in each channel will be stored in analog form as charge on a capacitor. Two temperature sensors are provided to indicate temperatures of the photomultiplier tube and the amplifier assembly. Thus, there are ten channels of data, consisting of analog voltages to be read out cyclically in response to sequence pulses from the data conditioning system which converts the analog voltages to seven bit digital words for transmission by the telemetry system.

(8) *Low-energy solar protons.* The instrument for this experiment is designed to detect the magnitude and direction of the proton flux in the solar plasma in the energy range of 500 to 20,000 ev.

The unit consists of four separate, curved plate, electrostatic analyzers. Charged particles entering the analyzers are deflected by an electric field which is approximately transverse to the particle velocity. Those particles with positive charge, within a certain range of energy per unit charge and a certain range of angle of incidence, are deflected onto a charge collector. Particles which enter with a negative charge, wrong energy per unit charge, or wrong angle of incidence, strike the analyzer walls and are not recorded. The energy distributions are determined by varying the magnitude of the deflection voltage. By varying the voltage on another set of plates, in front of the analyzer, different look angles can be sampled.

c. Data automation system. The eight fields and particles experiments are accommodated on the spacecraft by means of a science data automation system (DAS), which forms the interface between the instruments and the spacecraft data encoder. All experiment data, including temperatures and calibrations, are essentially of two types, namely pulse rate or analog. Pulse rate data is counted for various predetermined intervals, providing the capability of monitoring rates from 0 to 65 kc. Analog

data is converted to digital data in the form of seven binary digit (bit) words. The conversions to digital data of both pulse rate and analog data are performed with 1% accuracy. Appropriate logic and timing functions effect a channeling of the multiple input data into a serial train of bits which, while conforming closely to the basic format structure of the *Mariner* R DAS, is transmitted at the rate of 25 bits/sec to telemetry. The format also provides for frame identification and synchronization.

A more detailed description of each scientific experiment and the data automation system will be presented in subsequent *Space Program Summaries*.

F. Propulsion

Accomplishment of the missions of *Rangers* 5 through 9 will require the spacecraft to undergo a single mid-course propulsion maneuver to remove or reduce *Agena* injection dispersion errors. This maneuver will be accomplished through the use of a small, monopropellant-hydrazine-fueled propulsion system of 50-lb vacuum thrust and capable of delivering a variable total impulse in conjunction with an integrating accelerometer system. A more detailed description of the propulsion system, the operational design philosophy, and a system schematic are contained in *SPS 37-3*. Developmental progress is reported in *SPS 37-3* through *-15*.

During this report period, flight acceptance testing of the *Ranger* 6 and 6 spare mid-course propulsion system was completed, and the *Ranger* 6 propulsion system was delivered to the Spacecraft Assembly Facility to be installed in the spacecraft for systems testing. Flight acceptance testing and assembly of the *Ranger* 7 mid-course propulsion system is proceeding on schedule.

Fabrication of the enlarged propellant tank and propellant tank bladder to be used on the *Ranger* 6 through 9 mid-course propulsion systems is progressing on schedule. To date, three propellant tanks and two bladders have been received. The three propellant tanks will be subjected to type approval testing and burst testing to ensure the adequacy of the tank design. Both fuel tank bladders have successfully passed flight acceptance level tests. Eight propellant tanks and bladders are yet to be delivered.

G. Supporting Activities and Engineering Facilities

1. Space Simulation Testing

***a.* Rangers *6 through 9*.** The *Ranger* 6 through 9 ion chamber was tested in the 6-ft space simulator to check its temperature control pattern. The environment was: vacuum, 10^{-5} mm Hg; wall temperature, −300°F; spectrum, carbon arc. The test lasted 12 hr; test objectives were met.

Tests were also conducted in the 6-ft space simulator on the Aeronutronic *Ranger* 6 through 9 radio altimeter to determine the temperature control pattern (Fig. 45).

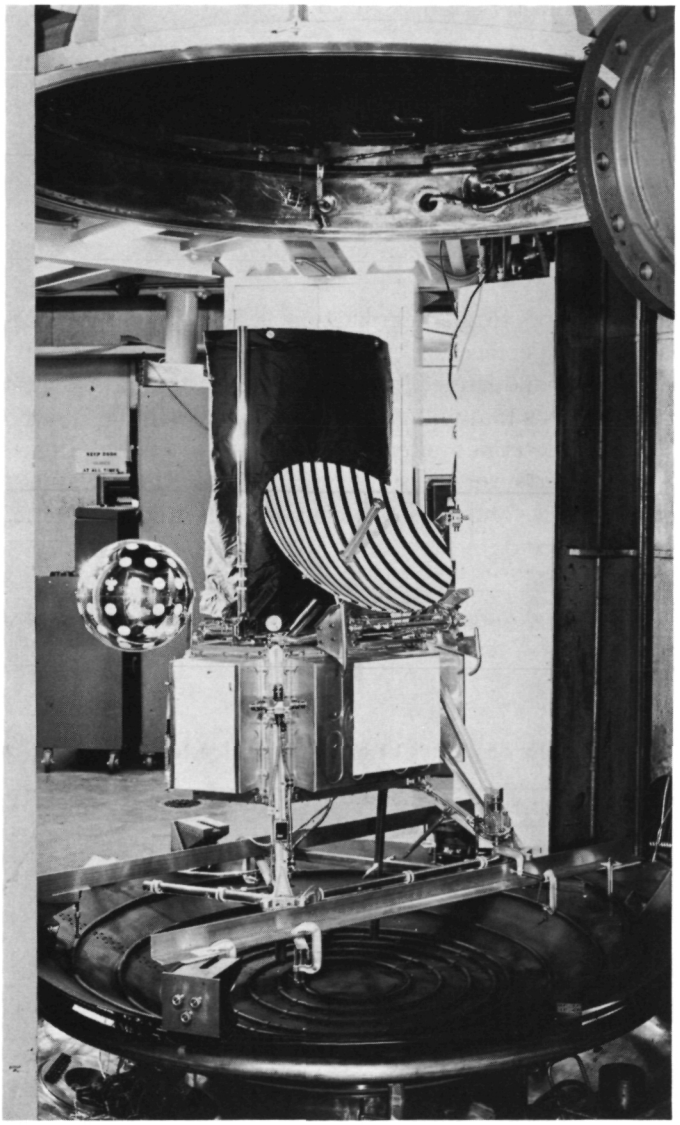

Fig. 45. *Ranger* 6 through 9 radio altimeter in 6-ft space simulator

A series of five tests was conducted, each with a different test item orientation. The total test time was 15 hr. The environment was: vacuum, 10^{-5} mm Hg; shroud temperature, −300°F; spectrum, carbon arc; heater pads were used. The test objectives were met.

b. Sterilization procedure testing. The committee on contamination by extra-terrestrial exploration (CETEX), representing the international scientific unions, has recommended the sterilization of space probes, but has not recommended sterilization procedures. JPL has established sterilization procedures based on the following anticipated recommendations:

(1) Components of heat-sensitive assemblies should be sterilized before assembly.

(2) Sterilization of parts should be "built-in", particularly in areas where moisture would occur.

(3) Terminal sterilization procedures should be used.

(4) Sterilization should be maintained after completion of sterilization operations.

In addition to gas sterilization testing in accordance with JPL specifications, gas sterilization research tests have been conducted. These tests are an attempt to determine methods that will give maximum sterilization results *without deleterious effects to the test specimen.* Items tested include rocket fuels and binders, dirt samples, seismometers, and miscellaneous organic and inorganic materials.

c.* Ranger *environmental testing. A summary of *Ranger* environmental testing during May and June is given in Table 15.

Table 15. *Ranger* environmental testing

Type of test	No. of tests
6-ft space simulator	4
Vacuum	8
Vacuum–temperature	34
Vibration	58
Low frequency vibration	9
Centrifuge	32
Shock	8
Temperature	40
Temperature–humidity	7
Gas sterilization	3
Total	203

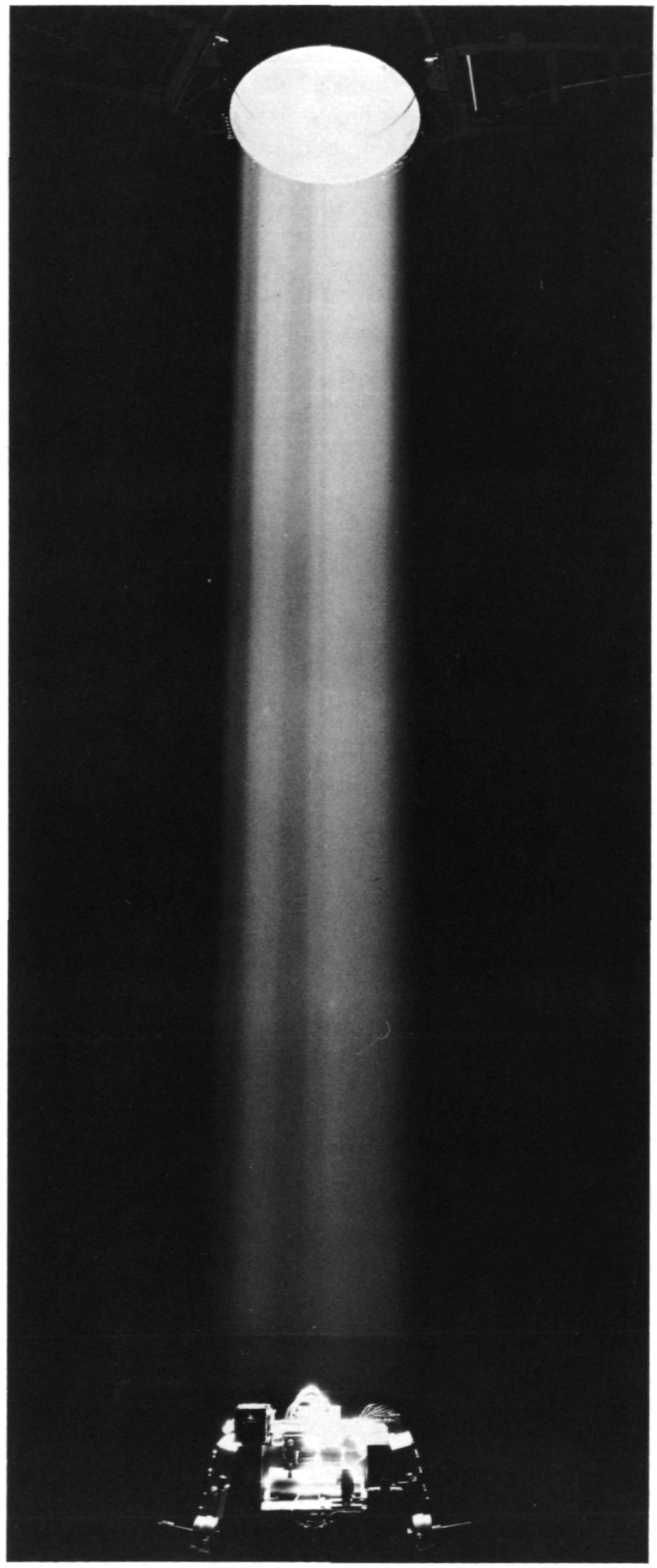

Fig. 46. Illuminated dust particle shaft, celestial simulator building

2. Celestial Simulator Laboratory Test Facility

The celestial simulator building (*SPS 37-5*) has a very high dust particle count. The 24-in. D beam of sunlight, when directed down through the air, results in a bright shaft of illuminated particles (Fig. 46). This particle illumination has interfered with certain critical sensor tests when the sensor is being checked for stray light sensitivity. An indication of the brightness of these particles is given in Table 16.

This level of brightness even at the 0-deg elevation is sufficient to cause the *Ranger* short-range Earth sensor to deliver an acquisition signal. Calculations show that if sensor viewing path lengths are to be held down to 10 cm (sensor within the light beam and looking out), and dust particle background illumination is to contribute only 10% of the Earth sensor threshold level, the brightness must be reduced to 0.03 ft-lamberts (looking through the 24-in. beam). This reduction should be possible through several modifications currently being planned. The modifications are:

(1) Installation of a 3000-ft^3/min blower (10-min air change) to create a positive pressure in the dome, drawing air out at the bottom of the dome, passing it through a bank of 99% efficient filters (at 0.3μ) and returning it to the dome near the top.

(2) Removal of black carpet and installation of black tile floor; since little or no air is introduced into the dome at present, it is felt the carpet is the major cause of the dust problem.

A slight positive pressure seems to exist at present in the dome room since dust particles rise up through the Sun opening in the top. As these particles strike the 45-deg front surfaced mirror, many of them adhere to it, contaminating the surface. Reducing the dust level should reduce the amount of cleaning required for the mirror.

Table 16. Brightness levels as a function of view elevation[a]

View elevation, deg	Early morning brightness, ft-lamberts	Mid-afternoon brightness, ft-lamberts
0	0.10	0.18
30	0.20	0.30
45	0.48	0.62

[a]Solar flux input level = 3500 ft-candles.

This is important since the mirror is not over coated, and its surface is easily scarred by cleaning.

3. Sun Sources

a. Heliostat system. Although no spectral distribution curve has been taken as yet, for either the real Sun (heliostat system) or the artificial carbon arc Sun source, foot-candle levels have been measured at the cement pad on the floor in the dome room. Atmospheric contamination determines how accurately the heliostat servosystem will follow the Sun across the sky. The tracking error has been observed to vary from 6 sec of arc on a smog free day to from 30 to 60 sec of arc on a heavy smog day. On days of heavy air pollution, the edge of the Sun's image is not sharply defined, thus the servosystem hunts in seeking the zero error. The flux level using the heliostat system is approximately 3500 ft-candles, or 27.8% of the free space solar constant in ft-candles. This is significantly better than can be produced by the carbon arc simulator at the correct Sun diameter.

Figures 47 and 48 show that the heliostat mirror and the 45-deg mirror are extremely dirty. The heliostat mirror is not pitted to any significant extent, thus cleaning should return it to its original condition. The 45-deg mirror, however, seems to be pitted in spots, and may have to be resurfaced.

b. Carbon arc artificial Sun source. This artificial Sun source was installed to allow tests to be run in the build-

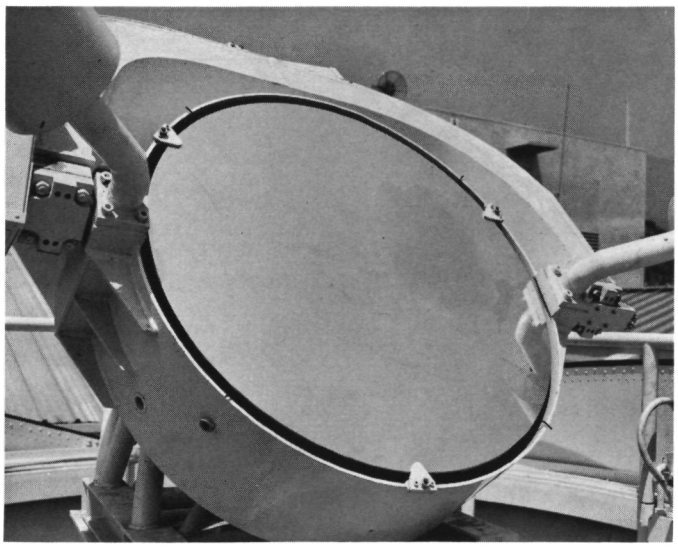

Fig. 47. Heliostat mirror

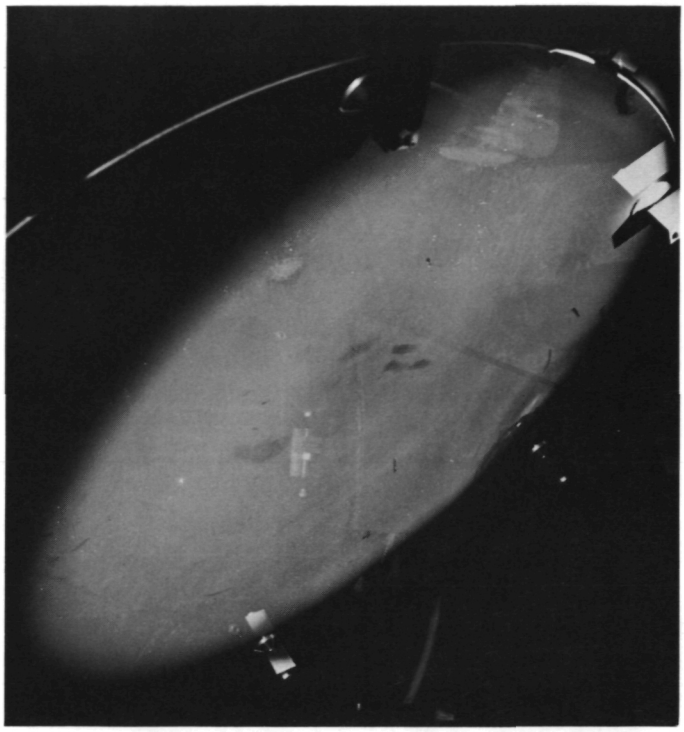

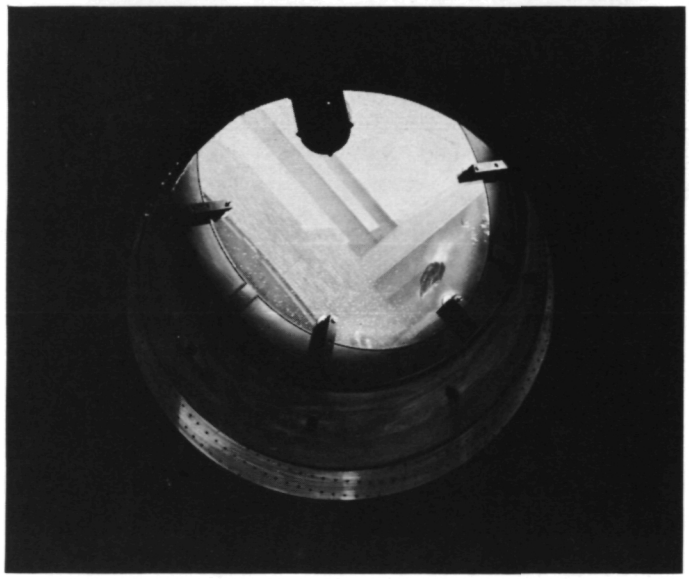

Fig. 48. Mirror (45 deg)

ing when the sky is overcast, and when higher levels of ultraviolet are needed than can be obtained from the Sun through the Earth's atmosphere.

The lamp housings are equipped with removable water cooled apertures; the water cooling is to keep the apertures near room temperature during lamp operation so they do not appear as bright infrared sources.

At present, there are three different apertures available, which simulate the Sun's diameter at Venus, Earth, and at Mars. The highest intensity level is obtained with no aperture on the lamp housing. Intensity levels are:

Aperture	Measured intensity, ft-candles	Percent of desired
None	5500	–
Sun–Venus	3500	12.0
Sun–Earth	2300	18.6
Sun–Mars	1100	16.7

The arc crater is at the primary focus of an elliptical reflector inside the lamp housing, and the aperture is at its secondary focal point. The aperture is also at the focal point of an off-axis parabola, which is 24 in. in diameter. The crater image is then reflected to the front surfaced 45-deg mirror and down to the cement pad in the dome. Figures 48 and 49 show the 45 deg and the parabolic

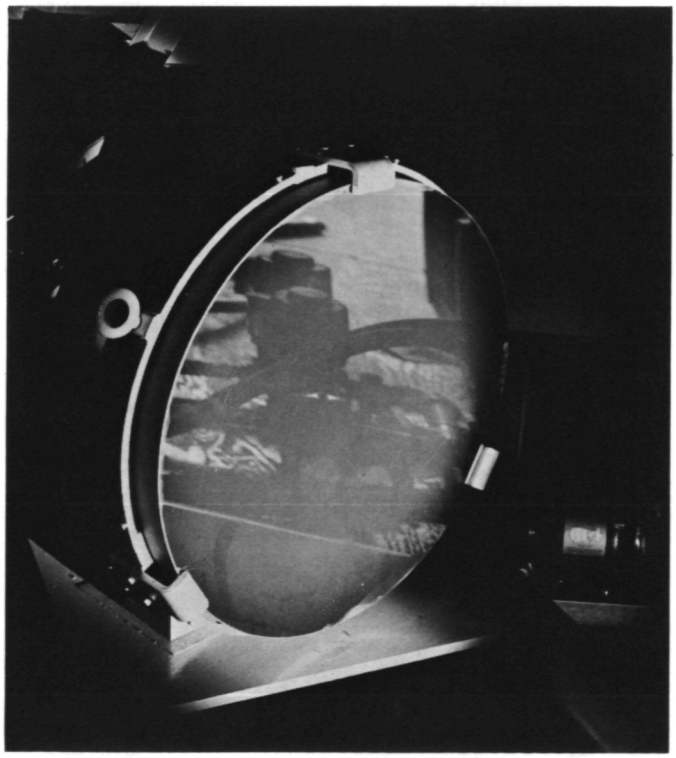

Fig. 49. Off-axis parabolic mirror

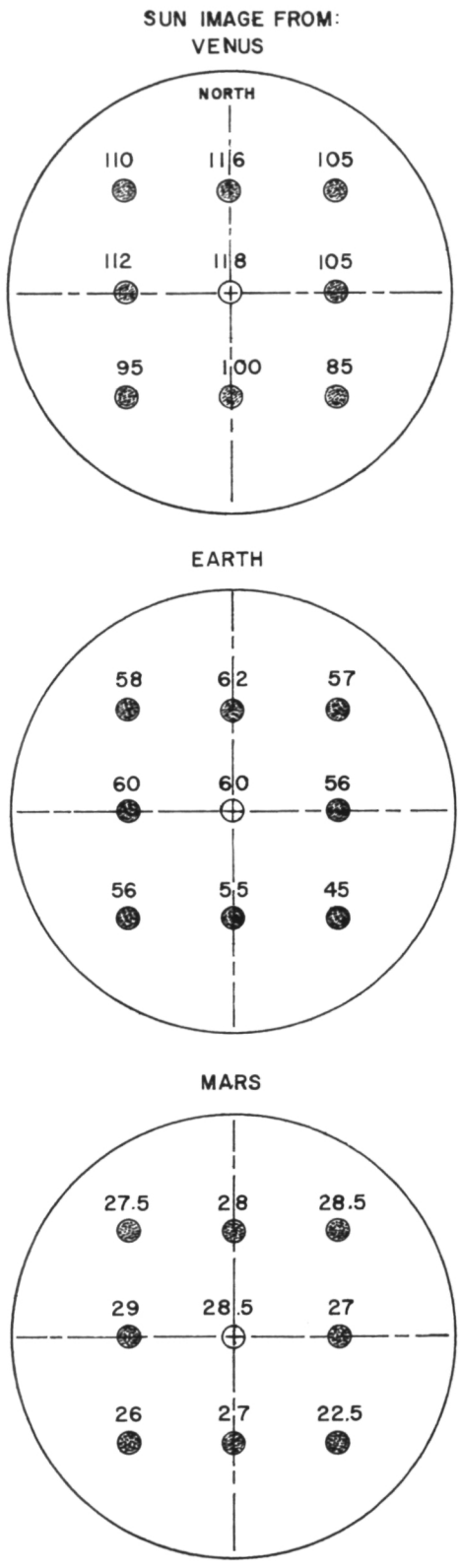

Fig. 50. Variations in flux across simulated Sun source beam

mirror being used with the arc lamps. It is interesting to note that these mirrors, which have not been specially coated to increase reflectance at any particular wavelength, are only 75 to 85% efficient (per mirror) in the silicon solar cell region.

Figure 50 shows relative variation in flux across the simulated Sun source beam. These measurements were taken using the carbon arc Sun simulator and three apertures were used to obtain the size of the Sun as seen from Venus, Earth, and Mars. Readings were taken from a 10-ohm load across the output of a Hoffman silicon solar cell Type 200A. The image was focused on the cell through a 10-in. telephoto lens with an aperture setting of *f*22. For comparison, the same cell and lens setting was used to measure Sun intensity at JPL on July 26, 1961:

Test condition	Intensity readings, mv
Full Sun (outside)	242
Through heliostat (1 mirror)	196
Through heliostat (2 mirrors)	147

4. Celestial Sensor Lab Dark Room Facilities

Dark rooms have been constructed for conducting tests on various sensors and optical breadboarding; these dark rooms had three essential requirements:

(1) Convenience of access between dark rooms and electronic breadboarding technician areas.

(2) Versatility such that varying phases of sensor development could all be handled by the dark rooms.

(3) Several light-tight compartment so that testing could be conducted on many items simultaneously.

These requirements led to the construction of a long dark tunnel divided by four plastic folding curtains. The folding curtains allow each small room to be sealed for individual experimentation. When requirements arise for a long optical shot the four curtains are all pulled aside as shown in Fig. 51.

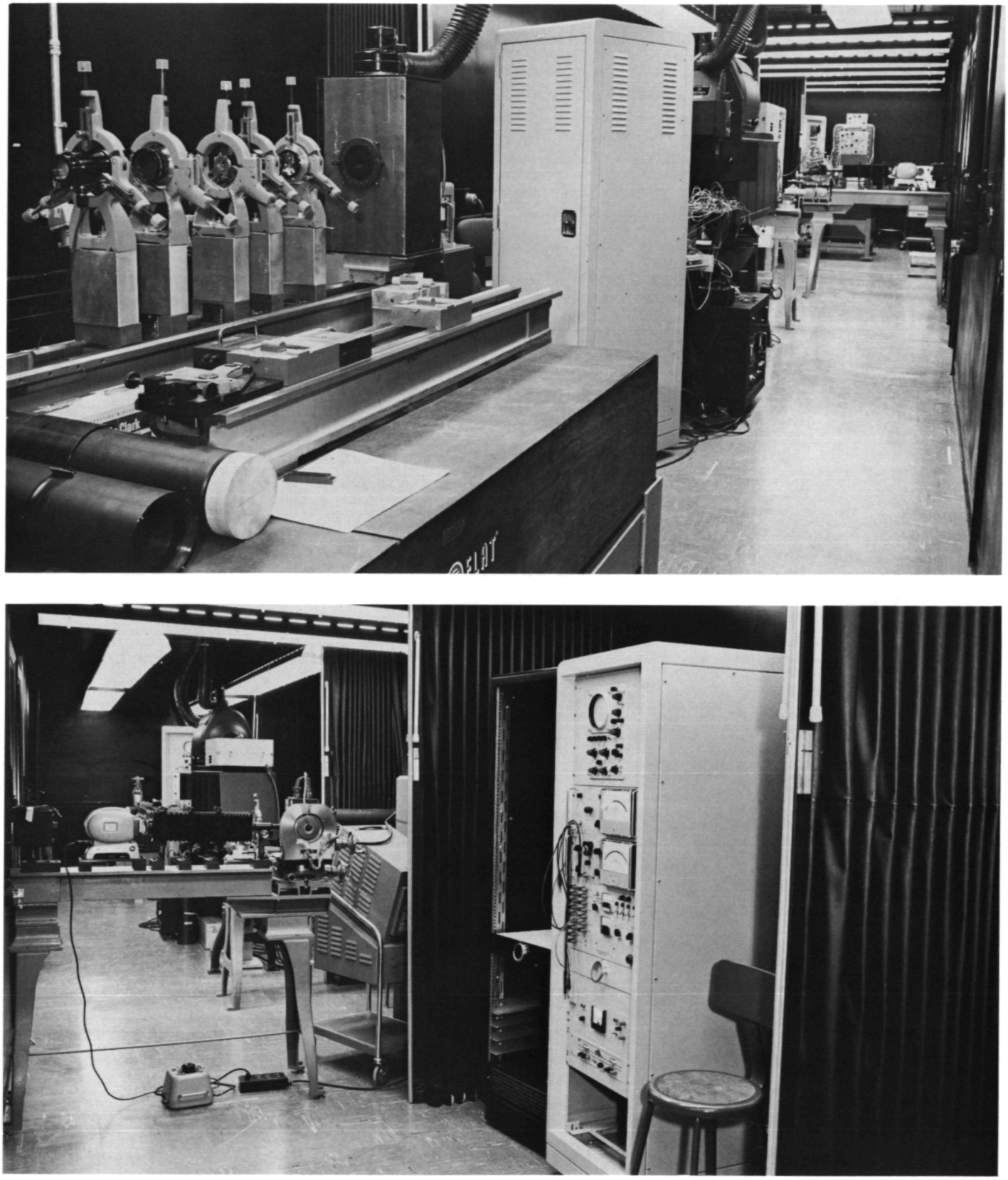

Fig. 51. Dark room facilities across rear section of the celestial simulator building

Reference

1. Dallas, S. S., "Preliminary Trajectory Characteristics for RA-6 Through 9," *Engineering Planning Document No. 80*, Jet Propulsion Laboratory, Pasadena, May 11, 1962.

Page intentionally left blank

III. *Ranger* Lunar Capsule

A. Introduction

Aeronutronic Division of Ford Motor Company, under a JPL subcontract, has developed a complete lunar capsule subsystem for *Rangers* 3, 4, and 5. Capsules have been supplied for *Rangers* 3 and 4 on schedule and with no significant deviations from specifications.

The major in-plant effort subsequent to the *Ranger* 4 launching has been engineering, design, and test work required to develop and incorporate authorized changes in the design for *Ranger* 5. Primary emphasis has been on repackaging of capsule electronics and the power and sequencing assembly. In some cases minor circuit changes have been made to improve particular performance parameters.

Additional work included testing and analysis of spare capsules from *Rangers* 3 and 4. These tests indicated the desirability of several changes to improve performance and increase reliability.

Considerable work has been done in planning the effort required to support *Ranger* 5. The residual materials from the previous units were inventoried, and the additional hardware requirements determined. Detailed design release, procurement, and fabrication schedules were established. Component and subassembly schedules are closely coordinated to provide delivery of *Ranger* 5 flight and spare capsules by September 15, 1962.

Material handling and component qualification procedures have been reviewed and up-graded to provide additional assurance of quality flight hardware.

B. Engineering and Test Effort

1. Landing Sphere Assembly

a. Capsule transmitter. The redesign effort on the transmitter includes minor changes in components, circuits, and board layout:

(1) Layout of buffer amplifier and power amplifier to minimize ground loop problems.

(2) Addition of a trimpot in the 560-cps postamplifier output to replace a capacitive divider used to adjust modulation index.

(3) Installation of Teflon bushings to protect cables in bulkhead holes.

(4) Redesign of cavity: (a) investigate the effect of raising the cavity floor, thereby providing a lower

input impedance (this should increase power output due to an improved impedance match) and increase load Q, reducing the possibility of 890-Mc interference; (b) provide a silver bushing at the cavity bottom to allow a press-fit of the cavity post without risking the removal of plating and possible exposure of bare magnesium; and (c) replace the ¾-in. threaded plug in the cavity feed with a flat plate to preclude misalinement and breakage of the tuning capacitor or the varactor diode.

(5) Replacement of all JFD glass tuning capacitors with Johanson air dielectric units; these units are more rugged because the aluminum body of the Johanson capacitor is less subject to breakage than the glass of the JFD capacitor body.

(6) Provision of a bulkhead terminal connection for cabled wires presently connecting the RF section of the transmitter with power input and VCO compartments, which will allow working within the VCO compartment without disturbing RF wiring.

(7) Provision of additional clearance between the VCO header and the postamplifier board and the four trimpots; reroute VCO leads and improve lead dress.

(8) Layout of postamplifier board to facilitate assembly.

(9) Relocation of certain bottom cover holes interfering with capacitor mounting holes.

A test cavity was fabricated to permit evaluation of various varactor matching impedances for the last doubler stage. Using this special cavity, the input impedance was optimized, and its effect on RF interference and transmitter efficiency was investigated. Due to unavailability of a sensitive receiver, measurement of any possible changes in 890-Mc output at significant power levels could not be made. The results of the power level and efficiency tests did not show conclusive evidence of significant improvement. Rather than make major design changes to obtain potentially minor improvement, the basic cavity design was left unchanged. All of the other changes considered were incorporated in the *Ranger* 5 design.

A test transmitter is presently being fabricated. The housing for this transmitter was obtained by reworking a surplus housing of the previous design. This transmitter will be used for performance tests and impact qualification tests. After sled tests, it will be included in the design proof test lunar capsule sphere No. 6 (DPT-6) capsule.

b. Sequencer timer. The sequence timer is used to sequence the following events after impact: (1) capsule recage, (2) sphere venting, and (3) turn-on of seismometer centering motor.

The electrical design of the timer for *Ranger* 5 remains the same as that of *Ranger* 4; however, a major redesign of the physical package has been completed. The new design incorporates a completely welded package. This design results in improved fabrication techniques, ensures a higher quality product and, consequently, improved reliability.

c. Squib switch assembly. Major redesign of the squib switch assembly is underway. The assembly in *Rangers* 3 and 4 incorporated point-to-point wired terminal boards with the associated complex wire runs. The new design uses printed circuit boards between which the squibs are mounted, thereby minimizing the wiring complexity and simplifying the assembly procedures.

The M-7 squibs are being replaced by the *Atlas* squibs. These squibs can be heat-sterilized, allowing the complete assembly to be built up prior to baking. In addition, these squibs have the higher no-fire current required to meet the AMR specifications.

2. Payload Testing

a. Sphere 010. Sphere 010 has undergone extensive testing as reported in *SPS 37-15*, Vol. I. Subsequent to that period, post-morten testing and analysis had been completed. The final report is being prepared and will be published soon.

Important data in relation to storage and life were obtained in the Sphere 010 tests. The sphere was operable after 3 months of storage and 1 of testing. The battery survived for 760 hr of operation and failed finally at a temperature of −20°F during the vacuum–thermal test.

Seismometer. There was no evidence that the seismometer functioned during the test. Post-mortem examination revealed two disconnected wires on the bottom side of the header; one wire was broken and the other was disconnected from its solder connection.

Close examination of the RTV-11 potting compound encapsulation of the wire bundle revealed several voids. Movement of the RTV mass into these voids during impact apparently caused the wire breakage. For the

Ranger 5 units, the RTV will be bonded to the header to reduce the load on the wires, and the assembly will be X-rayed to show any significant voids.

Transmitter. Six days after the Hyge impact test, the transmitter failed. The primary cause of failure was an open circuit in the wiper arm of the trim pot supplying bias to the first varactor tripler. Removal of bias caused detuning of the circuit and subsequent overload of Q3, resulting in burnout. Replacement of the trim pot and Q3 restored the transmitter to normal operation.

b. Sphere 014. Sphere 014 was subjected to electrical and environmental testing.

The capsule was vibrated with both sine and noise inputs at the component proof test levels. The vibration level between 20 and 40 cps was about 10 *g* as compared to 6 *g* for previous capsules. Post-vibration X-ray showed the sphere to be uncaged. From the X-rays it was determined that the preimpact caging foot had broken off, and the planned test cycle was continued. During postmortem of the capsule, the previous conclusion was confirmed; the No. 2-56 screw that holds the caging foot and shims had failed. A design change has been made in which the caging loads are carried through a shoulder on the foot, rather than through the attaching threads; this change will be tested on DPT-6.

To arm the sequence timer prior to Hyge impact, the capsule was accelerated to 40 *g* for 15 sec. The capsule was thrown at 193 ft/sec against the 45-deg double impact fixtures 8 min after arming. Impact occurred at 45 deg from the retromotor mounting flange. At 14 min, 43 sec after arming, both penetrators fired and the flotation fluid drained, apparently in a normal manner. The capsule transmitter was being monitored during the test; at impact the capsule signal was lost. It was determined that the transmitter was operating at a very low signal level.

A preimpact spectrum check of Sphere 014 was made using an Empire Device NF-105 receiver; the results of this check are shown in Fig. 1. Subsequent to the impact test another check was made of the transmitter output spectrum. The levels of signals observed at the carrier frequency were approximately 60 db down from the level measured prior to the test. Examination of the transmitter revealed that the first tripler bias choke had broken loose at the bond joint to the housing, thereby breaking a lead wire. When a repair to the choke was made, a direct measurement indicated a normal 122.5-db

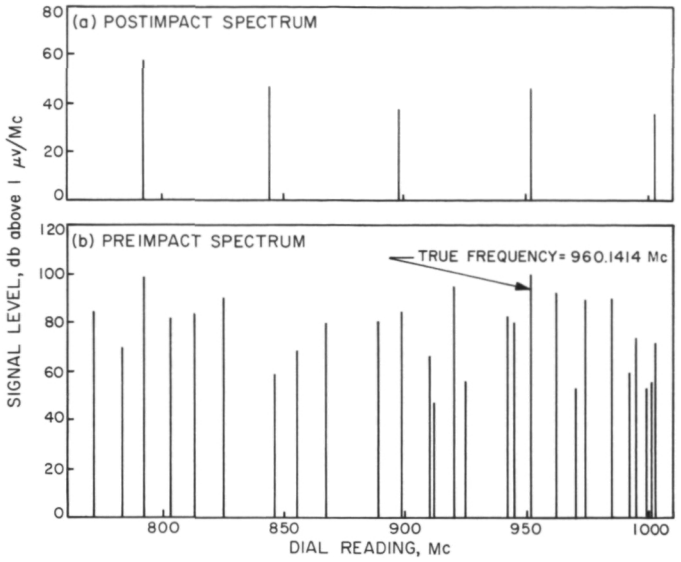

Fig. 1. Hyge test data for Sphere 014

level of output at the carrier frequency; retuning of the first tripler tank coil was required.

Further analyses of the transmitter will be required to determine the amount of detuning which was caused by the impact test and its effect on transmitter operation.

c. Sphere 015. The test sequence will start in simulated lunar night within a liquid N_2 cold wall and without solar illumination. The cold exposure will continue for 14 days or until the capsule temperature reaches the minimum safe level, whichever is sooner. The environment will then be changed to lunar day and lunar night in 14-day cycles until the test is completed.

d. DPT-6. The *Ranger* 5 lunar capsule assembly will incorporate several changes which require proof test requalification. The changes occur in the capsule and on external components. The changes to be tested include the transmitter, sequence timer, squib switch assembly and the mercury switch assembly within the capsule, and the external wiring, altimeter structure, and power and sequencing assembly external to the capsule.

Proof test plan B-35 was written to define the tests to be conducted. The capsule internal components will first be subjected to sled impact tests. DPT-6 will include the previously sled-tested transmitter, a new sequence timer, a new squib switch assembly, and a new mercury switch assembly.

A system vibration and flight shock test will be run, including the DPT sphere, power and sequencing assem-

bly, and modified external hardware of a complete dynamic test model. The DPT sphere will then be impacted in the Hyge to complete the requalification.

e. RF interference tests. An interference problem between the capsule transmitter and the bus transponder receiver was discovered at AMR in January. Since that time there has been a limited investigation into segments of the system.

The problem was still evidenced during the *Ranger* 4 checkout at AMR. During system tests it was found that Sphere 013 was compatible with the spacecraft system, but Sphere 014 was found to be incompatible. Sphere 014 was sent to JPL, Pasadena, for testing. After a series of tests on the proof test model (PTM) spacecraft, it was determined that Sphere 014 was satisfactory for flight provided it was clocked to an optimum position in azimuth on the spacecraft. While at JPL, a spectrum check was made on the unit which confirmed previous suspicions that a spectrum change had occurred between the final check at ADF Newport Beach and its arrival at AMR. No explanation for this has been determined. The sphere was returned to AMR for use as a flight spare.

A series of tests was conducted to develop a suitable decoupling material to be installed between the sphere and the spacecraft omnidirectional antenna. An aluminum baffle plate was installed in the omni-adapter ring and tested for effect on the antenna patterns and attenuation between the antennas. The antenna pattern for the sphere antenna was found to be slightly improved in the forward direction and the omni-antenna was not adversely affected. Measurement of the VSWR showed a slight improvement in the omni-antenna and no adverse effect on the sphere antenna.

A retest of Sphere 014 was conducted on the PTM spacecraft in an attempt to confirm the reduction in RF interference through the use of the baffle plate. Numerous tests were conducted in various configurations, and it was found that there was no difference in the amount of interference with or without the baffle plate installed, emphasizing that an over-all system approach to the problem is necessary. Tests on individual components of the system (the capsule transmitter and the omni-capsule antenna coupling) are to continue.

3. Ancillary Equipment

a. Power and sequencing assembly. Redesign effort on the power and sequencing assembly is in two major areas:

(1) Major repackaging to incorporate welded modular construction of the various elements.

(2) Minor electrical modification to improve timer circuit performance.

The packaging redesign is presently about 50% complete. The new design will facilitate the fabrication of the unit and will permit easier, more thorough, and positive inspection of the subassemblies. The new design incorporates completely modular construction. Each of the timing circuits and the squib switch module can be installed or replaced individually. The squib switch module will be a plug-in type, which will eliminate resoldering wires when the module is replaced after acceptance test of the unit.

The electrical design modification has been made on the various timers to improve their performance over a wider variation of battery voltage. This change has been thoroughly tested, and the results indicate that improved accuracy and reliability are obtained with this design change.

b. External wiring. Work has been started on the redesign of the external wiring. The major changes, all aimed at improving reliability, will be:

(1) Modification of contact fingers on the lower separation joint clamp.

(2) Simplification of the terminal board in the J-box with provision for wiring it before installation in the box.

(3) Relocation of the connector on the inboard side of the J-box to a more accessible location.

(4) Elimination of the low-torque connector at the altimeter erection hinge joint.

(5) Elimination of the contact pads in the area of the altimeter restraining bolts.

c. Altimeter battery. The original specification for the lunar capsule altimeter battery has been revised and released. The new revision is compatible with the Wiley flight model altimeters and requires a higher voltage, more current capability, and a longer operating life than originally specified. These improvements are made possible by allowing approximately twice the previous battery volume. However, a battery meeting the new

requirements will still fit within the same size battery mounting box as was used for *Rangers* 3 and 4.

d. Altimeter thermal test. The altimeter thermal test was conducted to determine the temperature extremes encountered by the altimeter during transit and to verify that adequate thermal protection is provided to ensure proper operation. The bus geometry and thermal control surfaces were simulated over a 120-deg sector. This assembly was installed in the JPL 6-ft space simulation chamber, and temperatures were measured.

The mean cruise equilibrium temperature of the electronic components was found to be approximately 104°F, at a solar flux of 1.2 solar constants. It is predicted that a temperature of 80°F would be experienced at 1 solar constant.

The experimentally derived temperatures of the altimeter electronics under the expected turn-on conditions were in the range 10 to 150°F. The test conditions were conservative; thus the temperature limits of the design proof test (20 to 140°F) are felt to be sufficient to ensure satisfactory operation of the altimeter.

The temperature of the altimeter battery did not deviate from the cruise equilibrium more than 4°F during the mid-course, terminal, and deployed test conditions.

Page intentionally left blank

IV. *Ranger* TV Subsystem

A. Introduction

A TV subsystem is being developed for *Rangers* 6, 7, 8, and 9 by RCA under contract to JPL. The primary objective of *Rangers* 6, 7, 8, and 9 will be to produce high-resolution TV pictures of the lunar surface.

The *Ranger* 6, 7, 8, and 9 spacecraft is composed of two basic units: the RCA TV subsystem and the JPL-produced bus. The TV subsystem will mate with the bus as does the lunar capsule of the *Ranger* 3, 4, and 5 series. Two significant differences are that the subsystem structure will not separate from the bus, and there will be no retrorocket to reduce the impact velocity, which will be approximately 6500 mph.

The subsystem structure consists of three major assemblies: (1) the central box which houses the main electronic components, (2) the camera subassembly with associated bracketry and equipment, and (3) the thermal shield. Camera view apertures are provided in the thermal shield.

The following material relating to the subsystem development is abstracted from the RCA report, *Ranger TV Subsystem, Fifth Bimonthly Progress Report,* June 15, 1962:

Qualification testing of the subsystem assemblies has progressed during this reporting period. The results of the environmental testing pointed up design deficiencies in the communications and camera areas which were corrected. Acceptance testing of assemblies was completed for the proof test model which has been assembled and prepared for RF interference testing.

Assembly integration and testing of the engineering test model have continued. Satisfactory operation of both the engineering and proof test models with the GSE were confirmed. Modifications to the flight model structures were made to accommodate the new camera bracket and revised cable harness design; fabrication of assemblies has been initiated.

B. Structure

The qualification test specification for the new camera mounting cast bracket (Fig. 1) was completed and released for publication. This specification includes magnification factors, based on vibration testing the mechanical test model (MTM) at AED and JPL, and is to be used to verify the structural integrity of the camera mount assembly. A detailed stress analysis of the mounting bracket was completed and the results incorporated into the bracket design. Resulting safety margins were found to be satisfactory. Qualification testing of the redesigned

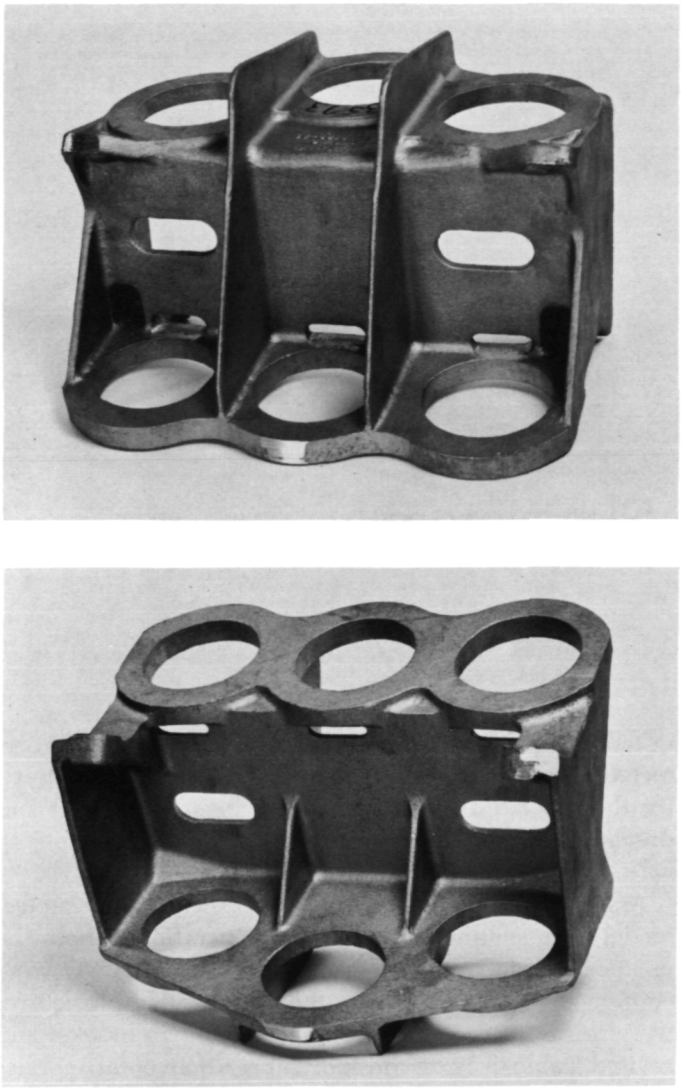

Fig. 1. Revised camera mounting bracket

camera bracket (casting versus weldment) has been started, and completion is expected by June 13, 1962.

Structural changes required for the new camera alinement have been completed and all affected drawings revised. An interference layout study disclosed the critical areas affected by the new camera requirements. The shroud assembly (Fig. 2) was modified to include the new camera cutouts and the addition of two vertical stiffeners in the cutout region.

The proof test model (PTM) and engineering test model (ETM) were modified to incorporate the new camera mounting bracket and associated changes. The structure for the flight model has been returned to Lavelle Aircraft for necessary modifications.

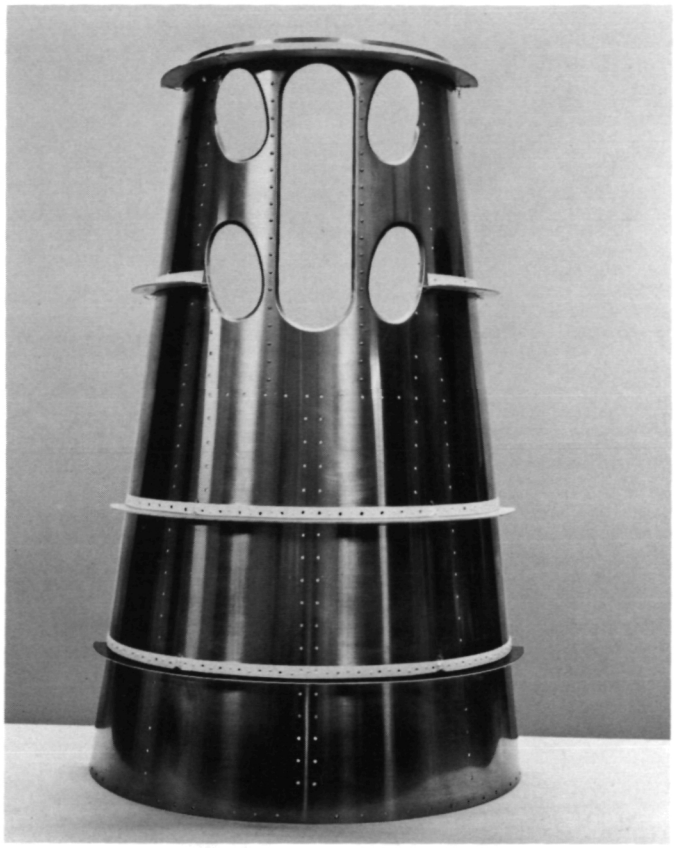

Fig. 2. New thermal shroud

A new battery mounting bracket was completed for the new lightweight battery configuration. The bracket replaces the former ⅛-in. thick aluminum cover plate. To provide a method for removing the batteries without disassembling the shroud, four ½-in. diameter access holes are required.

To provide for electrical harness and omni-antenna cable routing, a removable deck panel section (Fig. 3) and several 1-in. diameter holes were added to the deck sections.

The latest weight schedule is shown in Table 1. The center of gravity, and moments have been calculated to be as follows:

Center of gravity

$\bar{x} = 0.015$
$\bar{y} = 0.053$
$\bar{z} = 457.461$

Moments, slug-ft^2

$I_{xx} = 18.4$
$I_{yy} = 18.9$
$I_{zz} = 3.1$

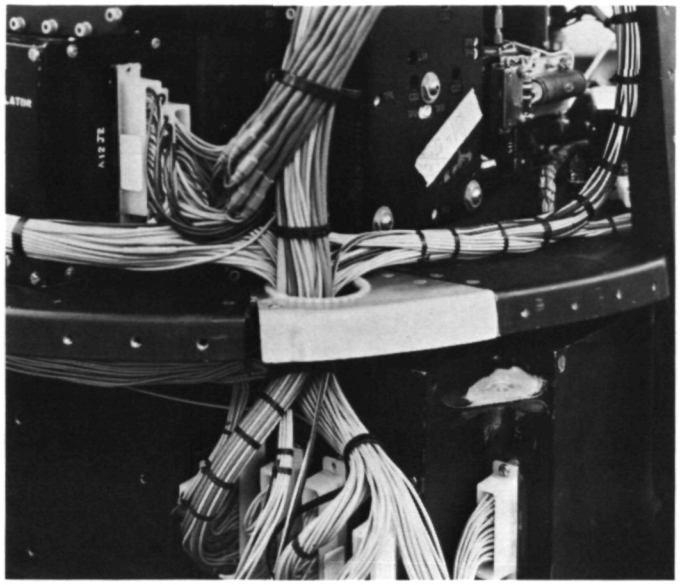

Fig. 3. Removable deck panel section

C. Electrical Integration

1. Test Models

The ETM was checked out using available engineering model components and was prepared for shipment to JPL in June.

The PTM was completely assembled and checked out as a complete system, using the Serial 2 GSE for the first time. The complete *Ranger* TV subsystem test procedure, in preliminary form, was utilized for the initial checkout of the PTM TV subsystem.

The PTM cable harness has been completed and breadboarded. A photograph of the harness on the breadboard is shown in Fig. 4. A second ETM harness was completed during this reporting period and mounted on a breadboard for evaluation. The ETM harness was made available to minimize down time of the ETM in event any problems occur.

All harnesses continue to be refined through experience gained in testing and to optimize cable harness density. The second ETM harness included lengthened cables for the transmitters and transmitter power supply to accommodate the slightly different ETM configuration. Extension cables were made for the telemetry on the camera electronics box where connector locations were changed.

Table 1. Weight schedule

Designation	Item	Weight, lb
A-1	Camera A and color wheel	7.26
	Camera B	6.68
	Camera 1	6.02
	Camera 2	5.99
	Camera 3	5.98
	Camera 4	5.93
A-2 through -7	Camera electronics	47.82
A-8	Video combiner	2.60
A-9	Sequencer with external harness	13.37
A-10 and -11	Batteries (new design)	85.40
A-12	Terminal mode regulator	2.37
A-13	Command switch	1.28
A-14 and -19	Transmitter modulator	8.00
A-15 and -20	60-w amplifier	6.92
A-16 and -21	Power supply	23.84
A-17	Cruise mode regulator	0.75
A-18 and -23	Signal sampler	0.20
A-24	4-port hybrid	1.25
A-25	Dummy load	1.08
A-26	Telemetry	10.68
A-27	Temperature sensor	0.36
A-28	Sequencer power supply	3.44
A-29 and -30	Telemetry processor	0.82
A-31 and-32	IPA 1 and 2	2.14
	Harness and filters	22.00
	Structure	70.56
	Camera bracket	6.63
	Miscellaneous brackets and hardware	3.50
	Fin heaters	1.00
	Camera harness bracket	0.40
	Total	354.27

Of the 134 connectors and 22 cables now in the harness system, the main interconnection cable has 68 connectors and 425 wires. While the PTM components were placed on the structure, this main cable was laid out on a full-scale plastic model of the TV subsystem. The cable was then removed and laid out to make a cable board, and then put in the structure.

With the decrease in cable length, thus reducing the weight to about 8 lb, a direct path between the camera sequencer and camera electronics was used. A detachable structural cutout was required to permit easy installation and removal of the cable; this cutout has been designed.

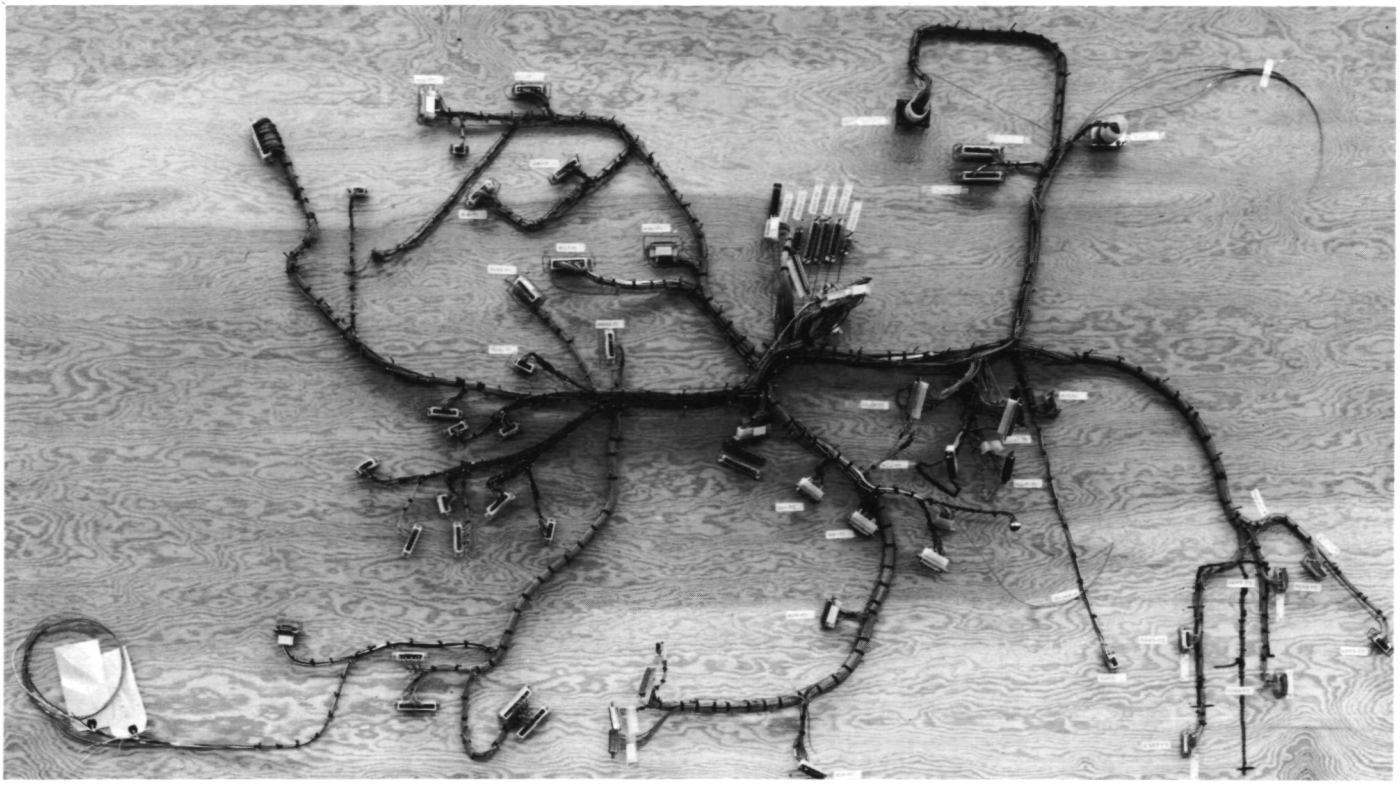

Fig. 4. PTM cable harness

In the evolution of the camera design, a vidicon mesh, bypass capacitor was found necessary. The capacitors are mounted, directly behind the vidicon socket, on a nylon post and connect between the vidicon socket and the nearby poke socket. Since the new camera bracket imposes some rigid dimensional requirements, a physical mockup was made using three camera housings and a plastic model of the bracket. The mockup verified the compatibility of the bracket design and the capacitor requirements. The design of a socket–capacitor mount, suitable for this configuration and for the environmental requirements, has been initiated.

2. Command Switch

Explosive atmosphere tests have been conducted to determine if a potential problem area might exist in the command switch operation. Verification was needed as to the possible arcing of the K1 relay (battery heater and low-current circuits) when the RTC-7 rotary switch opened the K1 coil circuit. A redesign of the command switch was made to reduce wiring harness density.

D. Environmental Testing

Acceptance testing of the assemblies for the PTM have been completed. The signal sampler and dummy load will definitely be tested before the end of June.

Units which have successfully met all qualification test requirements are:

(1) New lightweight battery.

(2) Sequencer.

(3) Sequencer power supply.

(4) Video combiner.

As a result of the difficulties experienced during thermal–vacuum testing with the cameras, the upper temperature limit was reduced from 55 to 40°C. Thermal–vacuum and thermal–humidity testing of the qualification cameras were both conducted at a reduced upper temperature limit of 45°C.

All processed data recorded during the operations of the MTM indicated that the accelerations obtained were within the limits anticipated prior to testing.

E. Electronics

1. Cameras

The integration of cameras for the PTM has revealed areas where modifications are required. These modifications are designed primarily to increase reliability and to reduce noise feedback from the dc-to-dc converter to the main vehicle power supply. Changes are being incorporated into units starting with Unit 006.

One change in system concept was incorporated in the camera electronics. The amplitude of the video signal during the *erase* portion of the cycle is sufficient to override the video gates in the video combiner. This problem was solved by using existing clamping circuits in the camera electronics to clamp the video output to "black," except during the active portions of the *read* cycle; this modification was also incorporated into units starting with Unit 006.

Two cameras, one each Type P and F, are currently undergoing qualification testing and are scheduled for completion during June. The two life test units are being electrically tested. The partial-scan unit is scheduled for completion of testing in early June and is to be included in the ETM. The Type F unit, upon completion of electrical testing, will be subjected to the prescribed acceptance tests and will then be placed on life test.

The problem of vidicon procurement still exists. The primary area of difficulty continues to be the evaporation of suitable targets for the tubes and is related to the presence of a gold mask used to establish a reference black level. In a great majority of the tubes currently available, the mask is leaky; that is, the signal resulting from scanning the mask with the electron beam is not as black as the signal obtained from scanning the remaining active area of the vidicon faceplate with the lens capped. This means that the black reference is not a true black. Furthermore, past experience indicates that this departure from black varies with faceplate temperature. As a result, the reference is not only in error but the amount of error varies with temperature. This situation could result in the clipping of low-light video information.

For the Type F vidicons, a possible solution to this problem is to reduce the thickness of the vidicon faceplate from 0.100 to 0.050 in. and to apply the mask on the outside of the faceplate. Initial tests on a 0.100-in. faceplate tube indicate satisfactory operation from a circuit standpoint. However, there is a loss of picture information (approximately 7 to 8% in each horizontal line). Since the edge of the mark is no longer sharply defined on the photoconductor and a gradual transition from black up to picture level results, reduction of faceplate thickness to 0.050-in. should reduce the loss by 50%.

Theoretically, if the partial-scan vidicon problem is approached in the same manner, a loss of about 15% of the total format along each horizontal line will result. Tests will be made to verify the theory, and to supply actual data for evaluation.

Twenty collimators have been received from Farrand Optical Company and will be modified to correct the color temperature. An optical filter will be used to correct the spectral distribution of radiation from a tungsten lamp operating at 2878°K so that the collimator illuminance on the vidicon has a spectral distribution approximating sunlight. The filters proposed by Farrand are the Corning 1-61 and -62. Either filter will approximate sunlight in the range 450 to 620 mμ.

A comparison was made of the illuminance from the filters luminous transmittance.

$$T_L = \frac{\int W_\lambda S_e T_f d\lambda}{\int W_\lambda S_e d\lambda}$$

where

W_λ = spectral distribution of tungsten lamp

T_f = filter transmittance

S_e = eye luminosity function

The luminous transmittances of filters were found to be 23 and 16% for the Corning 1-61 and -62, respectively. Figure 5 shows that:

(1) The light from Filter 1-62 matches the spectral distribution over a greater range than Filter 1-61.

(2) Filter 1-61 gives a better spectral match below 440 mμ.

(3) Either filter gives a better match than the unmodified tungsten illumination.

(4) Filter 1-61 has a higher luminous transmittance.

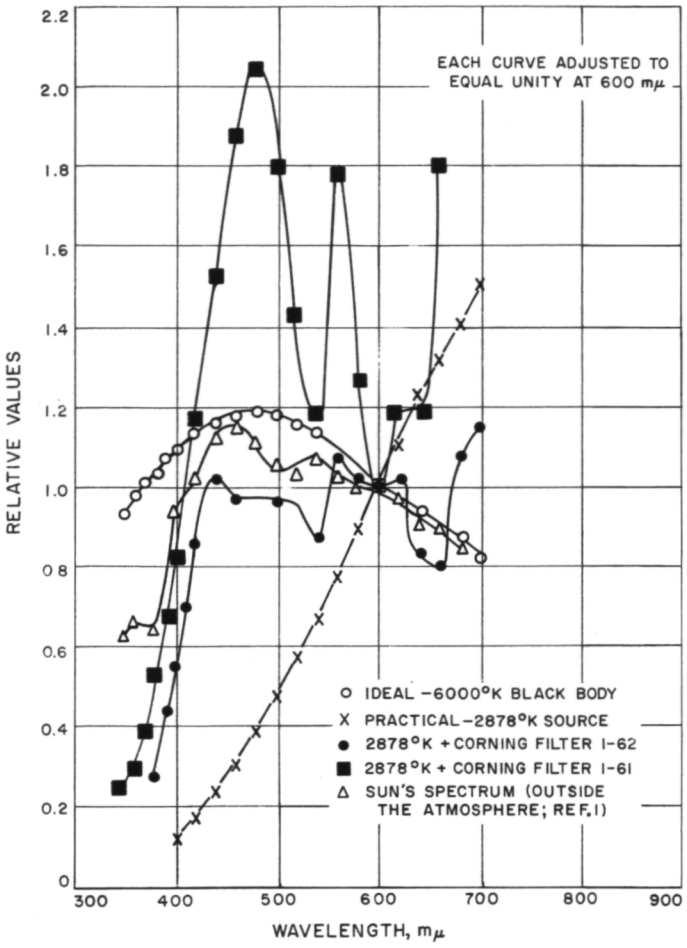

Fig. 5. Results of optical filters evaluation

Filter 1-62 has been chosen because it gives the best approximation to the spectral distribution of direct sunlight. Even though Filter 1-61 gives a better match below 440 mμ, it will not be used because the excess energy above 640 mμ may cause improper settings of the dark currents of the vidicons. This error arises because the vidicon is more sensitive to the radiation above 640 mμ than the instrument used to measure the brightness of the source. This fact is important, and it should be considered not only in this application, but also in applications using unmodified tungsten illumination.

2. Control Programmer and Camera Sequencer

A significant modification in sequencer logic has been devised as a result of integration problems. It is possible, when operating with a video combiner, to have sync pulse tips clamped to different dc levels because of combiner gate variations. This problem was solved by using a horizontal blanking pulse to close all combiner gates at the end of each line, thus setting all sync tips at the same dc level.

A minor modification, to lower the impedance of the horizontal output pulse to the four Type P cameras, has also been incorporated. The mission concept requires that the output of the four cameras feed both transmitters during the concluding minutes of the mission. The original design of the system specified that these cameras would feed two identical sets of combiner circuits which, in turn, would feed the transmitters. The loading of the combiners and the dc offsets in the combiner gates serve to upset the proper operation of the camera electronics video output stage. A tentative solution would be to use one combiner circuit on the Type P cameras in the original fashion. The output of this device would then feed one transmitter and one gate in the second combiner circuit. The gate in the second circuit would then open on command and the second transmitter would be fed the same video signal as the first unit. A feasibility model has been constructed and this modification is currently undergoing tests.

The qualification test model (QTM) has operated satisfactorily under all prescribed tests, and the PTM and the life test model (LTM) have satisfactorily met the acceptance test requirements.

3. Telecommunications

Vacuum testing of the PTM revealed that certain RF units (the power amplifier, the 4-port hybrid, and the dummy load) failed under vacuum conditions. The necessary modifications have been made, and will be incorporated into the units for the QTM, PTM, LTM, and flight models. The modified units have successfully met the requirements for acceptance vibration and thermal–vacuum tests.

Qualification tests are now being made on the modified transmitter power supply, the telemetry processor, the pressurized power amplifier, the signal sampler, the 4-port hybrid, and the dummy load.

a. Transmitter power supply. Several changes in the transmitter power supply were required as the result of recent failures. An autotransformer was added within the power supply for the purpose of supplying additional filament voltage to the two intermediate power amplifier units. The power transformer was redesigned to provide greater reliability. This redesign included the use of a larger core and of larger wire for each winding. In addition, the toroid will be potted in silicon rubber plus an outer coating of a new type epoxy which is a good heat conductor.

Relay failures have recently been experienced as the result of capacitive loading which has produced large surge currents at the time of power being turned on. To correct this situation, a 200-ohm current-limiting resistor has been added to the positive 1000-v and negative 750-v lines. All units have been modified to include this current-limiting resistor.

A slave relay has been added to all units for the purpose of decreasing the negative 27.5-v dc regulated current drain below a value of 100 ma.

b. Telemetry processor. A constant-current regulator has been added to all units for the purpose of controlling the power amplifier cathode current, and thus stabilizing the time–temperature power output profile. Units incorporating this change have satisfactorily met the thermal–vacuum requirements of the PTM. The power amplifier output now reaches a value of 60 w within a period of 1 min and remains constant for a minimum time of 20 min.

c. Power amplifier. As outlined in Fig. 6, the temperature of the 60-w amplifier after 5 min of warmup and 10 min of operation will be about 80°C; 10 min later the temperature would be 100°C. Since these measurements were made, the unit has been pressurized because of arc-over problems encountered when vacuum–thermal testing the unit. The power amplifier and pressurized housing are shown in Fig. 7. The pressurized container provides a heat sink for the amplifier. Qualification tests of the 60-w amplifier and pressurized housing will be rerun and the temperature closely monitored to determine the heat sink characteristics of the housing.

d. Pressurization effects. The possible effects of unequalized pressure on each of the power amplifiers, signal samplers, 4-port hybrids, and dummy loads were

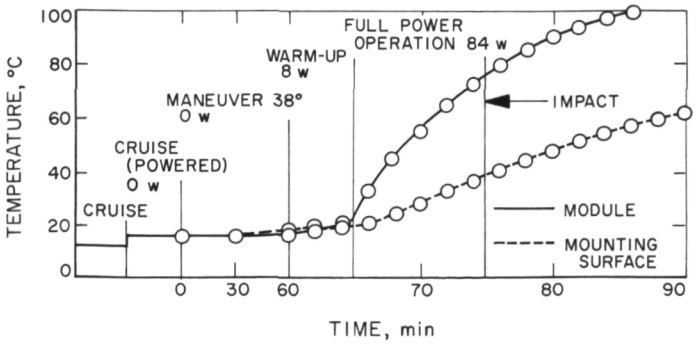

Fig. 6. Temperature–time history for TTM 60-w amplifier (A-15)

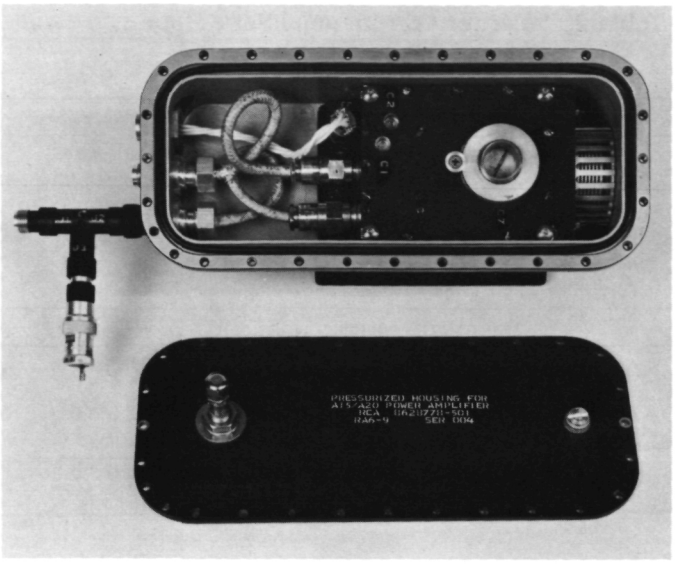

Fig. 7. Power amplifier and pressurized housing

studied during this reporting period. Each of these units is partially sealed to ambient conditions. It is known that this partial sealing retards (and in some cases even prevents) pressure equalization between the inside and the outside of the unit. Under this condition, ambient vacuum conditions could result in an inside critical pressure condition (rarefied atmosphere) at which electrical breakdowns would occur. This electrical breakdown condition is a function of: gases present, pressure, electrode contour and spacing, and temperature.

Various equalizing techniques were evaluated. The technique of drilling holes in the unit, thereby improving the outgassing capability of the unit, and hence the pressure equalization capabilities, was successful when applied to the 4-port hybrid and the signal sampler (as a precautionary measure). However, because of the high operating temperature to which they are subjected, this technique could not be applied to the power amplifier and the dummy load. The power amplifier has been sealed in a pressurized housing and pressurized to 15 psig with dry nitrogen. The dummy load has been hermetically sealed. All units, except those for mounting on the ETM, have been modified to include these new techniques.

e. Recomputed performance analysis of the RCA–DSIF communications system. As a result of a review at JPL, the performance analysis of the RCA–DSIF communications system has been recomputed. Table 2 presents the information which is a result of the latest evaluation and forms the basis for the RCA preamplifier design. The

Table 2. Basis for RCA preamplifier design as a result of re-evaluation

Receiving system parameters	Value, db
Antenna gain	45.7 ±0.8
Axial ratio	0.5 ±0.1
Diplexer loss	0.25±0.03
Line loss	0.2 ±0.1
Maser gain (2-Mc bandwidth)	9.6 ±0.5
Parametric amplifier gain (10-Mc bandwidth)	20
System noise temperature	**Value, °K**
Antenna	33 +2.0 −5.0
Maser/parametric amplifier	38 ±5.0
Moon	32
Total	103 +7.0 −10.0

Table 3. Summary of recomputed performance analysis of the RCA–DSIF communications system

Parameter	Value
Transmitter power (60 w), db	17.8 ±1.0
Losses, db	
RCA circuit	3.5 ±0.4
JPL circuit (*Rangers* 8, 9)	1.7 +0.5 −0.7
Spacecraft antenna (*Rangers* 8, 9)	−18.1 ±0.5
Antenna painting	0.3 +0.1 −0.3
Polarization	0.14 ±0.1
Path loss	204.5
DSIF antenna	−45.7 ±0.8
Receiving circuit	0.45 ±0.13
Total losses	146.8 +2.53 −2.93
Total power received (input to maser), dbw	−129.0+3.93 −3.53
System noise temperature, °K	103+7.0 −10.0
Noise bandwidth, kc	800 ±100
Receiver noise power, dbw	−149.5+0.7 −0.8
Received carrier-to-noise ratio	20.5+4.73 −4.23

change in maser gain should be noted; the previous JPL value was about 20 db. Table 3 presents a summary of the recomputed performance analysis of the RCA–DSIF communications system, and Fig. 8 is a block diagram showing the recomputed signal levels for the RCA–DSIF communications system. As shown in Fig. 8, the recomputed net gain from the input to the maser to the input to the RCA preamplifier is 32.6 db. The 4.2-db margin is still the worst case above a 12-db threshold.

4. Power Supplies

a. Voltage regulator. High-amplitude noise spikes were observed at the regulated output of the high-current voltage regulator. The spikes were caused by the chopper power supplies connected to the regulator and may appear in the camera outputs. In order to reduce the amplitude of these spikes, the engineering model of the regulator was modified by connecting a brass strip across the terminals on the output connector and running short wires directly to the 1000-nf capacitor across the output

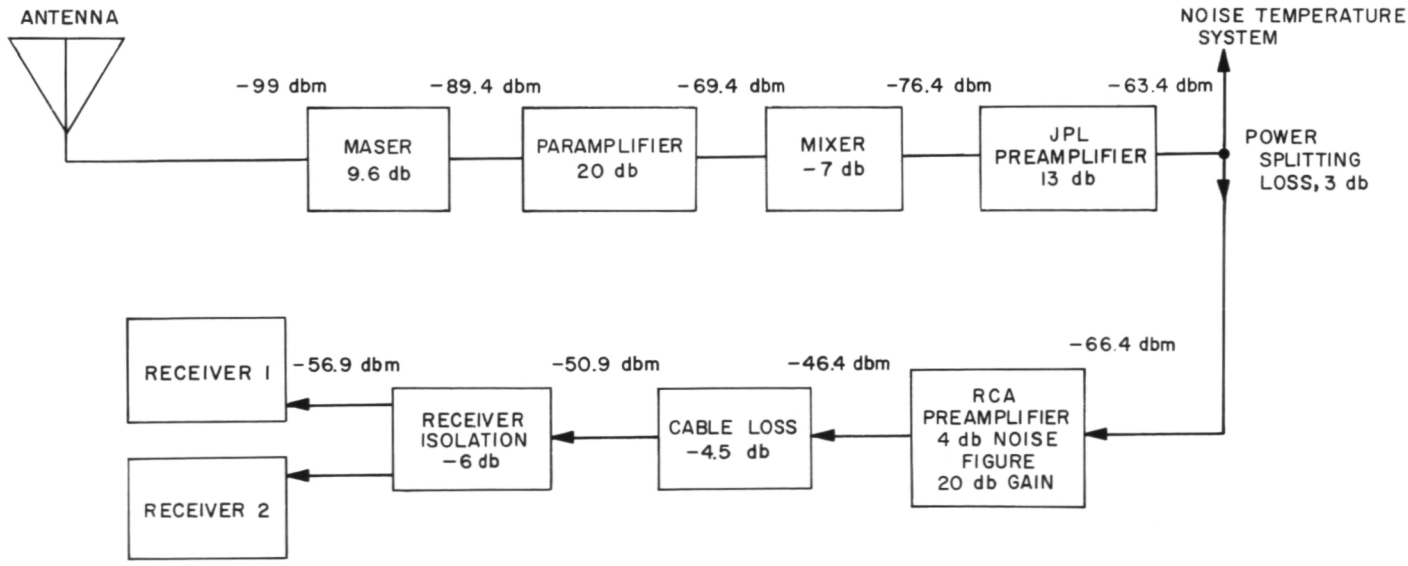

Fig. 8. RCA–DSIF communications system showing recomputed signal levels

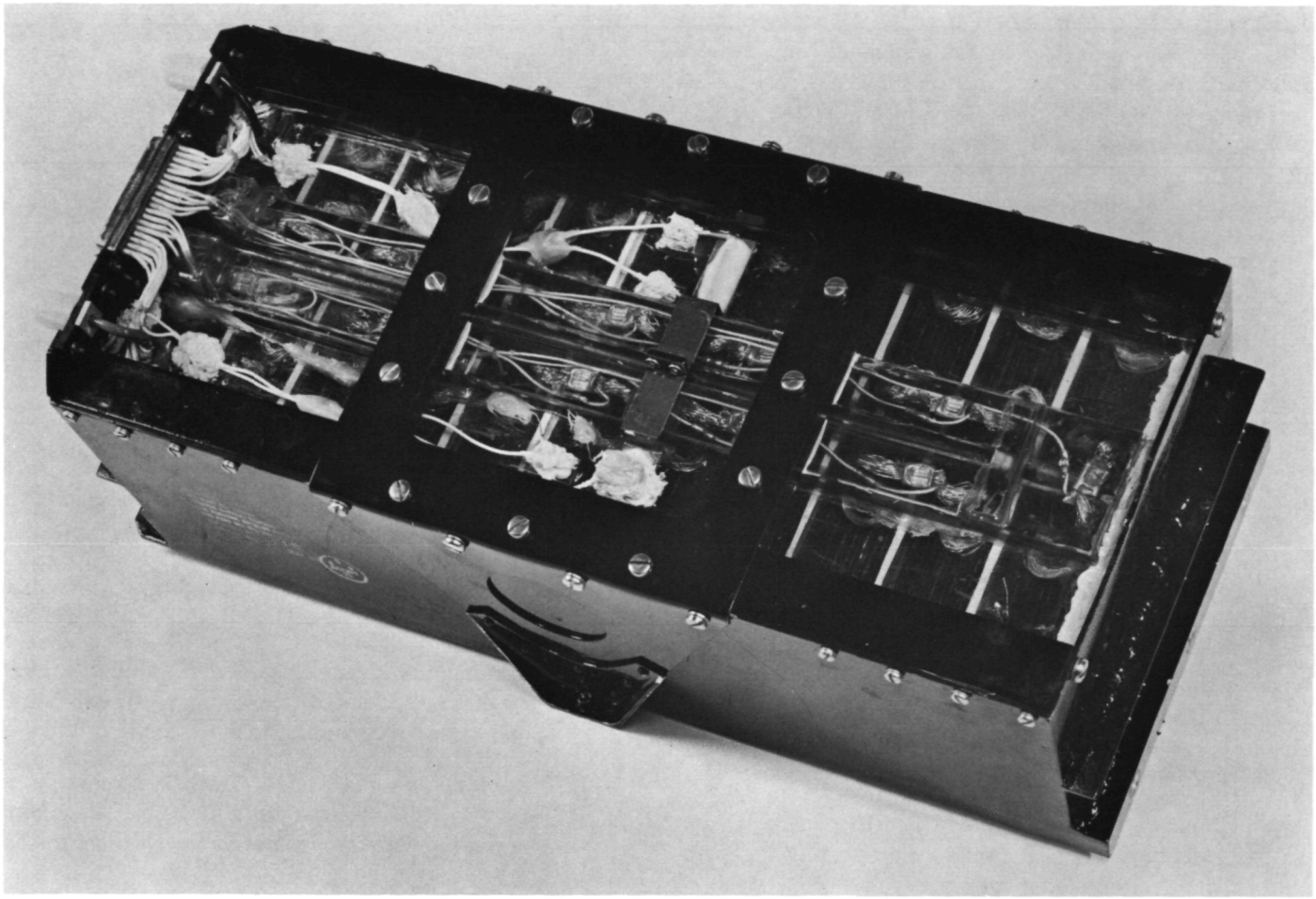

Fig. 9. New lightweight qualification battery

of the regulator. A direct comparison between the modified regulator and the unmodified regulator showed that the amplitude of the spikes was reduced by a factor of three in the modified regulator. The change in the design of the regulator to reduce the spikes has not been incorporated because the unit has already passed qualification tests, and a further test to see if this modification reduces spikes in the output of the cameras has not yet been made.

The LTM of both the low- and high-current voltage regulators were intended for life testing but have been used instead in the PTM. The production of replacement units for life testing are nearly complete.

b. Battery. Qualification Battery 15 (QTM), constructed with Cycolac T-2502 white molded cell jars, has successfully qualified in all phases of the battery environmental test program. Qualification Batteries 16 and 17W both failed, Battery 16 in thermal storage and 17W in vibration. Battery 15, originally scheduled to be used for life testing, was modified to correct design deficiencies uncovered during the tests on Batteries 16 and 17W. This battery passed all qualification tests. After qualification, Battery 15 was modified structurally to reduce weight and then requalified. A new qualification battery, 18, which is still lighter, has been designed and built and is shown in Fig. 9. This lightweight battery is now undergoing qualification testing.

Qualification Battery 16 failed because it had a low insulation resistance (3 megohms) after thermal storage. An examination of the battery after failure showed that this condition was caused by the leakage of electrolyte through a crack in the potting channel. The crack was caused by the nonuniform expansion of the large epoxy mass used for encapsulation on the top side of the battery. This condition was remedied in Battery 15 by reinforcing the epoxy with glass cloth.

The failure in qualification Battery 17W after vibration also appeared as a low insulation resistance, indicating a fracture through which electrolyte leakage occurred. This was remedied in Battery 15 by reinforcing the battery structure with a ⅛-in. aluminum top plate. After incorporating these two modifications, Battery 15 was subjected to the qualification test program and qualified.

The weight of the qualified battery with the aluminum plate is approximately 46.5 lb. In order to save approximately 0.75 lb per battery or 1.5 lb per payload, the cover plate was removed and the battery held rigid with a center strap. This modified battery was again subjected to all the mechanical qualification tests. In order to reduce the weight of the battery still further (to approximately 43 lb), Battery 18 was constructed. This battery differs from the latest modification of Battery 15 only in that the top glass-reinforced epoxy encapsulation was omitted completely.

The modifications will be:

(1) Eliminate two small magnesium heat transfer plates by providing a single thermostat and transducer mounting tab on the large magnesium heat transfer plate, an integral unit of the battery chassis.

(2) Eliminate the nine layers of EM 65 glass cloth and the final epoxy seal currently used to fill and reinforce the top of the battery.

(3) Add two small sheet copper brackets to anchor the thermostat and transducer to the single tab on the long magnesium heat transfer plate.

(4) Securely bolt the battery support bracket to the battery chassis assembly.

Batteries 18, 19, 20, and 21 will have the battery support bracket attached at assembly by ESB. ESB will also drill and ream the battery chassis mounting holes used to anchor the battery in the spacecraft. RCA has supplied the drill and reaming jig to ESB on a loan basis.

The battery chassis will be supported with the battery support bracket firmly attached to the chassis to ensure high reliability. The bracket will be attached to the chassis during all phases of the environmental testing schedule.

The existing battery cell design utilizes Type M-40 KOH electrolyte solution in combination with ESB-Philadelphia grey Synpor separator material. The monobloc unit cell-assemblies are of similar construction with these exceptions:

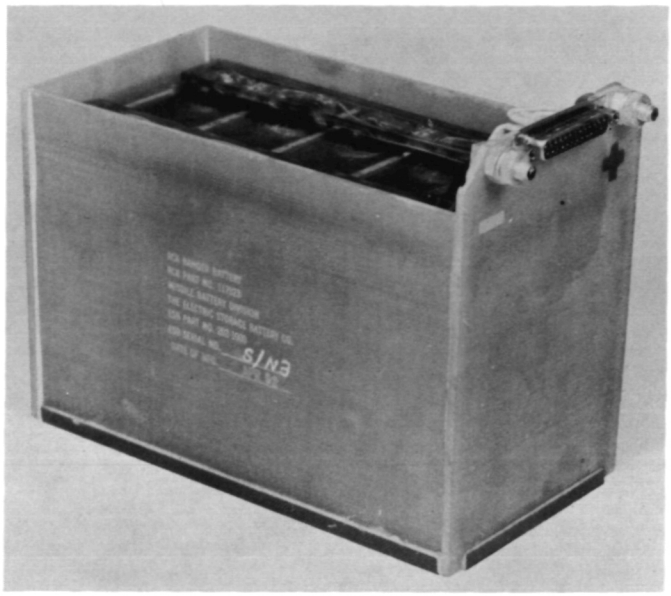

Fig. 10. Monobloc test assembly

(1) Two monobloc assemblies, Units 1 and 2, contain Type 40% KOH electrolyte and ESB-Reeves white Synpor separator material to insulate the cell plates.

(2) Two monobloc assemblies, Units 3 and 4, contain Type 40% KOH electrolyte and ESB-Philadelphia grey Synpor separator material as cell plate insulation.

All cells have three layers of 0.009-in. cellophane and one layer of Synpor separator material as used in the battery construction.

c. Monobloc test objectives and results. The objective of the discharge tests performed on the monobloc assemblies (Fig. 10) was to determine the relative voltage output levels of the 5-mil white Synpor and 8-mil grey Synpor in 40% KOH electrolyte. Table 4 gives the relative physical properties of the white and the grey Synpor

Table 4. Synpor separator material physical properties

Physical properties	ESB-Reeves white Synpor	ESB-Philadelphia grey Synpor
Thickness, in.:		
Dry	0.004	0.008
Wet 40% KOH	0.004	0.008
Wet weight increase, mg/in.^{2}	54	107
Electrolyte retention (40% KOH), cm^3/in.^{2}/mil	0.0096	0.0100
Void, %	59	61
Mean pore diameter, Å	888	780
Ac impedance milli-ohm/in.^{2}/mil	1.12	2.85

obtained from ESB tests. Minor differences exist in pore diameter and ac impedance in Type 40% KOH.

In tests of four monoblocs discharged at 50°F on the RCA qualification test profile, the mean cell voltage of cells having the 5-mil white Synpor was 0.02 v higher than cells with 8-mil grey Synpor during the 35.0-amp pulse. At discharge rates twice the RCA test profile, one cell of test monobloc having grey Synpor reversed under a 70.0-amp drain. Cells with white Synpor gave voltages 0.10 v higher at 70.0 amp than the cells having grey Synpor. Cell voltages of the test monoblocs when pulsed at the 35-amp rate for 10 min and the 18-amp rate for 5 min immediately after full charge were almost identical.

Figure 11 shows a plot of cell voltage versus discharge current density at 50°F. Note that differences between cells using the grey and white Synpor do not become significant until the discharge rate exceeds 35 amp/in.^{2}. During the 67-hr low-rate pulse, the monobloc voltage output of the cells constructed with ESB-Reeves white Synpor separator material was approximately 0.22 v/cell higher than the grey Synpor separator material during 33 hr continuous discharge. The comparative results between the two distinct types of plate separators tested produce the conclusion that significant voltage increases cannot be expected by changing the construction of the ESB Model 202 battery cells from grey Synpor to white Synpor separator material.

The original ESB Model 202 battery design included a total battery weight of 43.50 lb maximum. This weight was increased to 44.25 lb by the addition of extra Epon 815 epoxy and nine layers of EM 65 glass cloth to further reinforce the battery chassis during vibration, shock testing, and thermal shock testing. The battery weight was further increased by attaching an aluminum hold-down bracket, at ESB request, to the battery chassis to add additional support to the battery when mounted in the spacecraft. The weight increase was 2.8 lb per battery, or 5.6 lb added to the spacecraft.

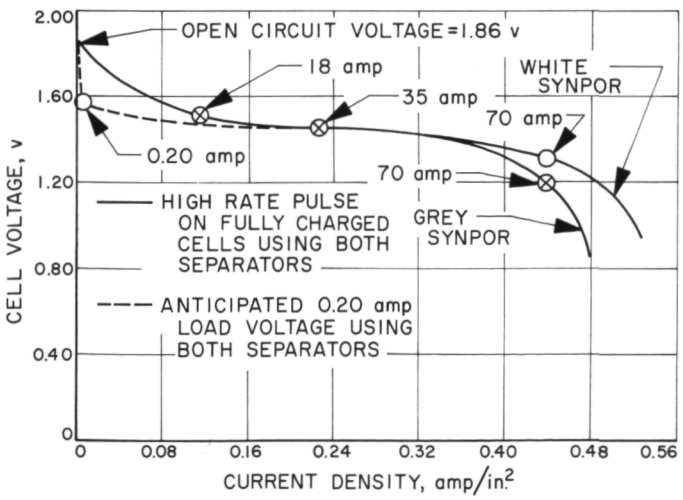

Fig. 11. Cell voltage versus discharge current density for the monobloc assemblies at 50°F

F. Thermal Control

An intensive surface-finish measurement program is being conducted to increase the reliability of the passive thermal design. Permissible variations in the thermal properties of surface finishes were established, and steps were taken to meet these requirements.

All temperature-sensor units, with the exception of flight units, have successfully undergone acceptance testing. The life test unit has successfully completed approximately 200 hr.

1. Surface-Finish Verification

The effectiveness of a passive temperature-control design is dependent upon the thermal properties (primarily the emissivity and solar absorptivity) of exposed surfaces. The combination of surface finishes that will produce the desired temperature distribution are determined, and then the finishes that are reliable and controllable within appropriate design margins may be obtained.

In *SPS 37-15*, Vol. I, the first phase of the design was established from the results of thermal test model testing; the tentative values of emissivity ε and solar absorptivity α for all surfaces on the TV subsystem were resolved. During the current reporting period, primary effort has been placed upon obtaining the required finishes. This surface-finish evaluation program was given even more emphasis since the possibility of solar-simulation testing of the subsystem is uncertain.

In order to determine the accuracy required for the values of thermal properties, a simple analytical model

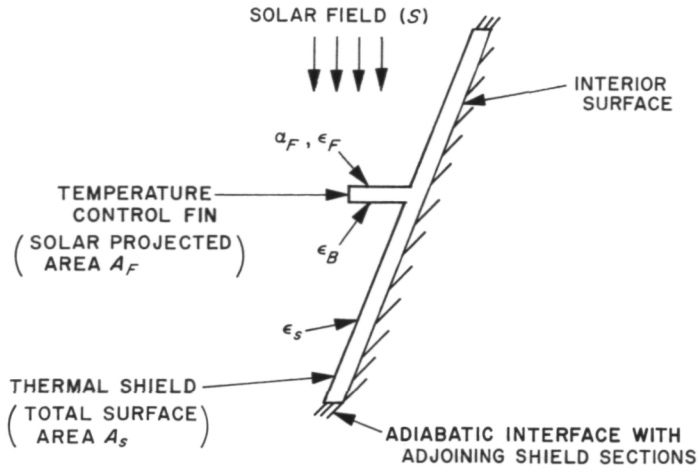

Fig. 12. Analytical model for the determination of temperature change due to small changes in the thermal properties of the surface

(Fig. 12) was used. This model represents a section of the thermal shield which can be considered as isothermal. A thermal energy balance of the analytical model during Sun-oriented flight can be written as:

$$\sigma T_s^4 = \frac{\alpha_F S}{\varepsilon_F + \varepsilon_B + \left(\frac{A_s}{A_F}\right)\varepsilon_s} \tag{1}$$

where

σ = the Stefan-Boltzmann constant

T = absolute temperature

α_F = absorptivity of the solar-projected area

S = the solar constant

ε_F = emissivity of the solar-projected area

ε_B = emissivity of the underside of the temperature control fin

ε_s = emissivity of the total surface area of the analytical model

A_s = total surface area of the analytical model

A_F = solar-projected area

To determine the influence of each of the thermal properties of the surfaces on the temperature of the section, partial differentials have been taken of Equation (1):

$$\frac{\partial(\sigma T_s^4)}{\partial \alpha_F} = \left\{\frac{S}{\varepsilon_F + \varepsilon_B + \left(\frac{A_s}{A_F}\right)\varepsilon_s}\right\} \tag{2}$$

$$\frac{\partial(\sigma T_s^4)}{\partial \alpha_F} = -\left\{\frac{S\alpha_F\left(\frac{A_s}{A_F}\right)}{\left[\varepsilon_F + \varepsilon_B + \frac{A_s}{A_F}\varepsilon_s\right]^2}\right\} \tag{3}$$

$$\frac{\partial(\sigma T_s^4)}{\partial \varepsilon_F} = \frac{\partial(\sigma T^4)}{\partial \varepsilon_B} = -\left\{\frac{S\alpha_F}{\left[\varepsilon_F + \varepsilon_B + \frac{A_s}{A_F}\varepsilon_s\right]^2}\right\} \tag{4}$$

For small changes in the thermal properties, the following relationships may be obtained from Equations (2), (3), and (4):

$$\Delta(\sigma T_s^4)_\alpha = \left[\frac{S}{\varepsilon_F + \varepsilon_B + \left(\frac{A_s}{A_F}\right)\varepsilon_s}\right](\Delta\alpha_F) \tag{5}$$

$$\Delta(\sigma T_s^4)_{\varepsilon_s} = -\left[\frac{S\alpha_F\left(\frac{A_s}{A_F}\right)}{\left(\varepsilon_F + \varepsilon_B + \frac{A_s}{A_F}\varepsilon_s\right)^2}\right]\Delta\varepsilon_s \tag{6}$$

$$\Delta(\sigma T_s^4)_{\varepsilon_B\varepsilon_F} = -\left[\frac{S\alpha_F}{\left(\varepsilon_F + \varepsilon_B + \frac{A_s}{A_F}\varepsilon_s\right)^2}\right][\Delta\varepsilon_F + \Delta\varepsilon_B] \tag{7}$$

A total maximum allowable temperature change of ± 6°C from the nominal cruise temperature of 10°C due to surface-finish error was assumed. If the temperature error is equally divided among the three variables and assuming that all errors lie in the same direction toward higher temperature (which is highly improbable), the following tolerance on the finishes can be calculated from representative finish information:

(1) Variation of solar absorptivity for 2°C error is 0.03 based upon a solar absorptance of 0.64. (This value is required to obtain a 10°C temperature for the model initially.)

(2) Variation of skin emissivity (irridite) for 2°C error is -0.009 based on the nominal emissivity value of 0.08 for the skin.

(3) Variation of fin emissivity (both sides varying an equal amount) for 2°C error is -0.04 based on a nominal emissivity value of 0.90 for the fin.

These values represent the worst conditions and are based on the assumption that all errors are cumulative.

2. Spectral and Thermal Measurements

Having established an acceptable margin of error on the values of α and ε from the analytical model, a development program for the finishes was initiated. Two techniques of measurement are utilized to check the values obtained:

a. Spectral measurements. The spectral coefficient of absorptivity of the samples is determined by reflectivity measurements (1 minus the reflectivity equals the absorptivity at each wavelength) using the test setup shown in Fig. 13. A Coblentz-type integrating hemisphere is utilized to integrate over-all angles of incidence at each wavelength. This device is an aluminum hemisphere having 96 lamps distributed uniformly over its inner surface. The illuminated target-surface specimen is positioned at the center of the hemisphere basal plane. The reflected flux which passes through an arbitrary aperture in the side of the hemisphere wall is a measure of the total reflectivity of the target. This flux is then channeled through the entrance slit of the monochromator, and the relative spectral total reflectivity is measured. By use of a standard target, the relative distribution is converted into an absolute measurement. The present range of measurement extends from 0.34 to 2.4 μ, which is the most significant portion of the solar spectrum for this use.

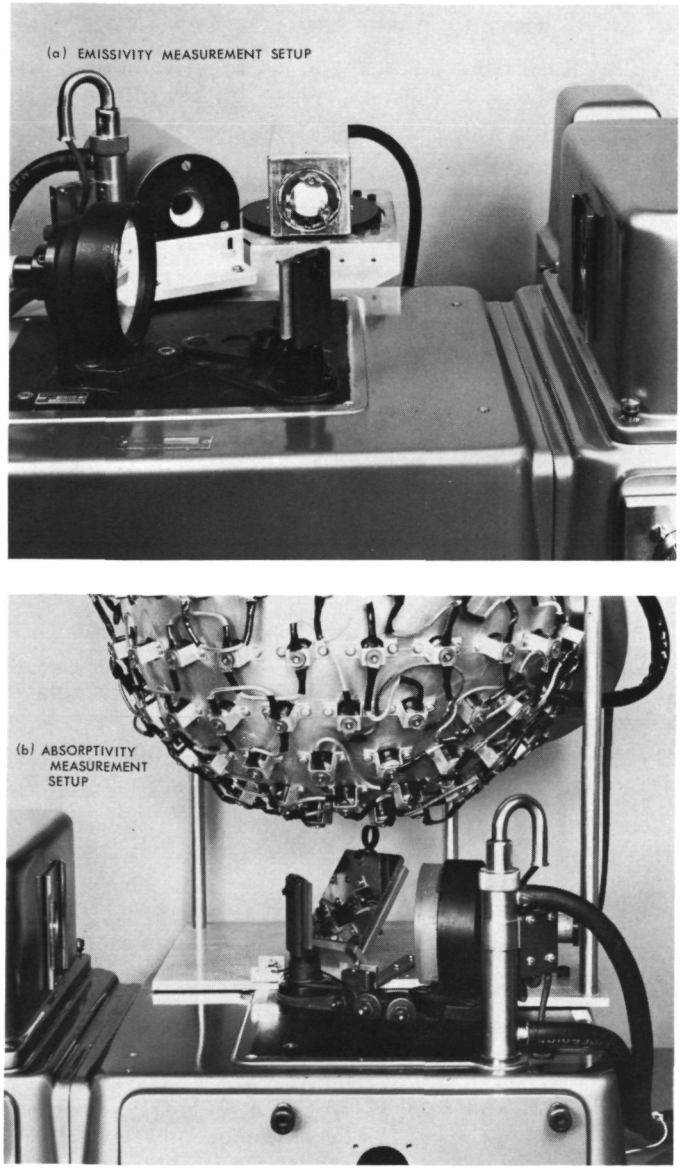

Fig. 13. Test setup for measurement of absorptivity and emissivity of finishes for the *Ranger* thermal design

Normal spectral emittance of materials is made with the monochromator operating in a single-beam comparison manner. Instrumentation is utilized, whereby the radiance from a black body at a temperature range between 80 to 230°C can be alternately replaced in the entrance slit of the monochromator with the radiance from the sample specimen at an identical temperature, and again with the radiance of a black body at room temperature. A thermocouple detector gives a signal that is proportional to the flux received from each source. Thus, the deflections of the recorded output of the spectrometer are proportional to the radiation signals. The entrance slit of the monochromator is optically projected to lie within the surface boundaries of the sources; thus, the signals derived are proportional to the slit projection area. The slit, as projected onto the various sources, is precisely controlled to contain identical surface areas.

The integrated value of α is obtained by multiplying the absorptance value obtained at each wavelength of measurement by the corresponding energy of the solar spectrum (Johnson curve) at that wavelength. An "absorbed" solar-energy curve is thus produced over the range of 0.34 to 2.4 μ for each specimen. The ratio of the area of this curve to the area of the solar spectrum curve is the solar absorptivity α.

A similar technique is used to evaluate the emissivity with the exception that a 25°C black body curve is used in place of the Johnson curve. Measurements of emissivity are made at closely spaced wavelengths over the range of 3.2 to 24 μ by the monochromator.

b. Gross thermal measurements. The values of α and ε are obtained directly by use of a small solar-simulation facility. A carbon-arc lamp provides simulation of the solar field. The specimen is suspended by a small thermo-

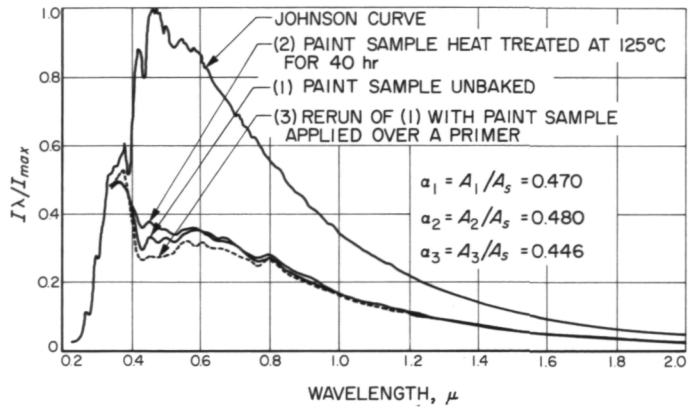

Fig. 14. Absorptivity comparison between the paint sample and the solar spectrum

couple in a black body cavity having a liquid-nitrogen wall temperature. The cavity is positioned inside a vacuum chamber which has the capabilities of 10^{-6} mm Hg. A small hole in the cavity permits the solar flux to strike the specimen at normal incidence after entering the vacuum chamber through a quartz window. Gross values of α and ε can be obtained directly from the recorded temperature history of the specimen. Recent modifications were incorporated into the test apparatus to reduce error in the measurements.

3. Materials Investigated

Measurements have been made upon black epoxy paint, irridite (chromate film) on clad aluminum, and silicone alkyd paints.

The black epoxy paint is used on the interior of the thermal shield and on all components and the structure. All that is thermally required of this paint is a high emissivity to provide a black body environment for the electrical components.

The outer surface of the aluminum skin which constitutes the largest exposed surface area of the TV subsystem will receive irridite treatment. During the Sun-oriented cruise mode, only the emissivity of the surface is of interest. However, the terminal maneuver exposes the skin to the solar field so the correct absorptivity is also required.

The thermal fins are painted with mixtures of black and white silicone alkyd paint to obtain the required value of solar absorptivity. Extensive measurements have been made to determine the relationship of the absorptivity to the mixture proportion of black and white paint.

Problems were encountered in obtaining measurements on samples of the grey paints, since the resulting values of α and ε are dependent on: (1) the thickness of the paint applied to the sample, and (2) the heat treatment of the sample. Nine paint mixtures were selected for initial analysis. Each mixture was applied to an aluminum disk sample in each of the three sets of samples. Each set consists of nine samples (total of 27 samples), and the sets were prepared as follows:

Set	Procedure
1	Each paint mixture applied to an aluminum disk without a primer coat
2	Each paint mixture applied to an aluminum disk without a primer coat, and heat treated at 125°C for 36 hr (equivalent to the sterilization requirement)
3	Each paint mixture applied to an aluminum disk over a primer coat

A representative result of these measurements for absorption and emission is shown in Figs. 14 and 15. Significant variations in the spectral properties of the paint samples (although they are of the same paint material) are indicated in the curves. These variations are apparently due to insufficient application (or coat thickness) of paint.

A comparison between the curves for Sets 1 and 2 in Fig. 14 revealed that there is a window in the paint coating between the 0.4 and 0.6 μ. The aluminum sublayer for Set 1 resulted in a higher measured reflection through the window than that for the primer material sublayer for Set 3. Heat treating the samples seems to alter the measured values slightly, regardless of the thickness of the applied paint coat.

These discrepancies resulted in the establishment of the following preparation procedures for the measurement program:

(1) Prepare specimens with a known thickness of primer and top coat, the top coat varying from 1 to 10 mil in thickness. Measurements on these samples determine the minimum thickness of paint required to assure an opaque surface. All painting done on flight models shall conform to this specification.

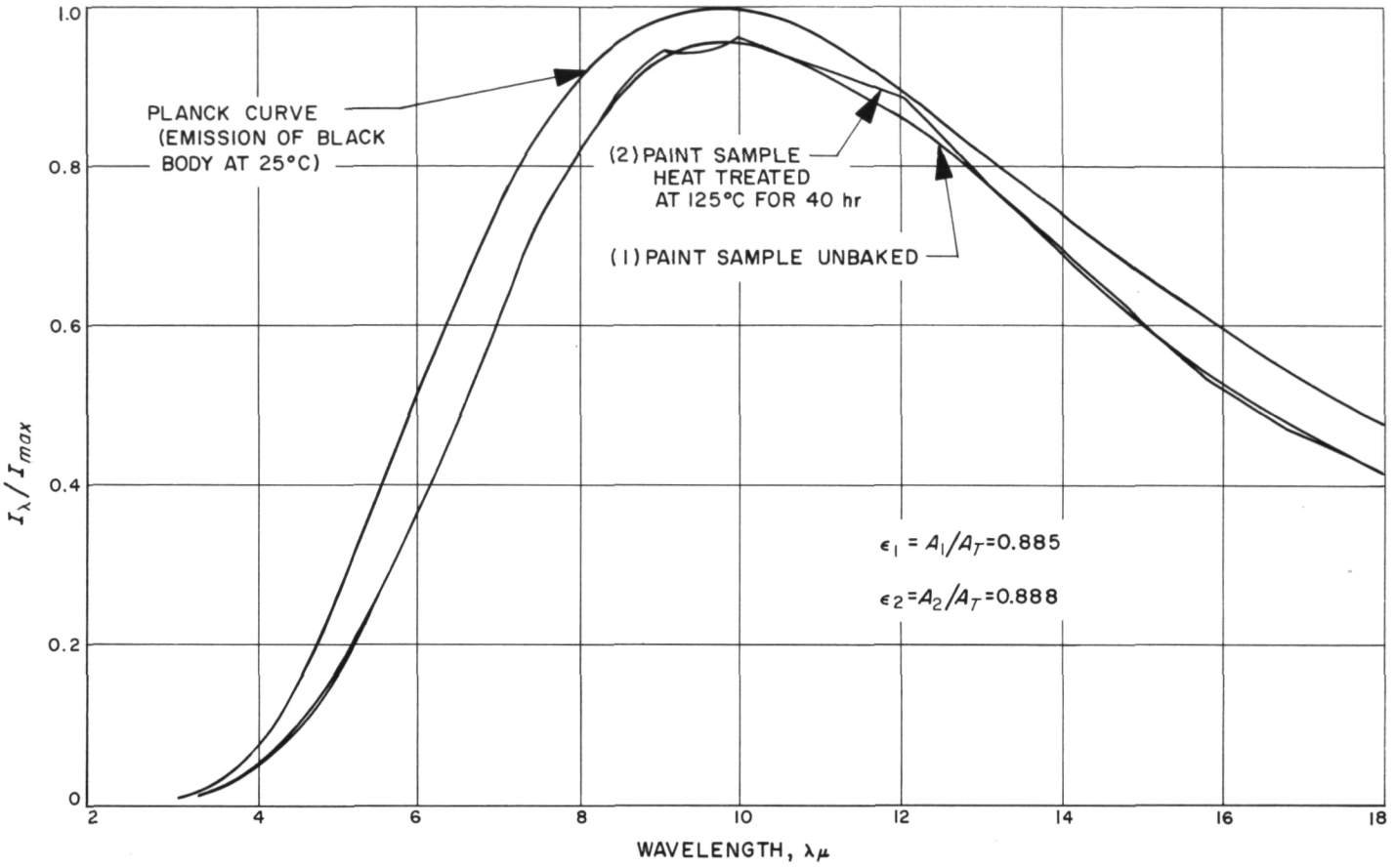

Fig. 15. Emissivity comparison between the paint sample and the solar spectrum

(2) Mix an adequate quantity of paint for each surface application for all models and determine the values of α and ε for each batch by extensive measurements. Thus, uncertainties arising from using different batches of materials can be eliminated. Prior to performing measurements on the specimens, the specimens will be heat treated in accordance with the sterilization requirement to assure compatibility with completed flight models.

(3) Minor alterations in the values of α and ε are anticipated since each model may require a unique combination of finishes to produce the desired temperature field. The alteration requirements will be revealed primarily from the thermal-vacuum testing of each model. A master curve of solar absorptivity as a function of paint mixture will be established for the batches of standard paints. A required change in the thermal property will be accomplished by taking a sufficient amount from the standard batch, remixing it to the new thermal value, and measuring samples of the mix to validate this value.

(4) Specimens of finishes used on the flight model will be supplied to JPL for measurement, providing a cross-check on the accuracy of AED measurement.

4. Temperature Sensors

All temperature sensor units with the exception of flight units and spares have successfully undergone acceptance testing. The life test unit has completed approximately 200 hr of operation with no difficulties.

G. Ground Support Equipment

1. TV Recording and Display

An improved CRT, together with the video amplifier modifications required, has been installed into Unit 1. It is now possible to attain a height of 1200 lines. Coincident with these modifications, improved shielding materials for the tube and various components in the film-recorder chassis were also installed. The ac hum problem which

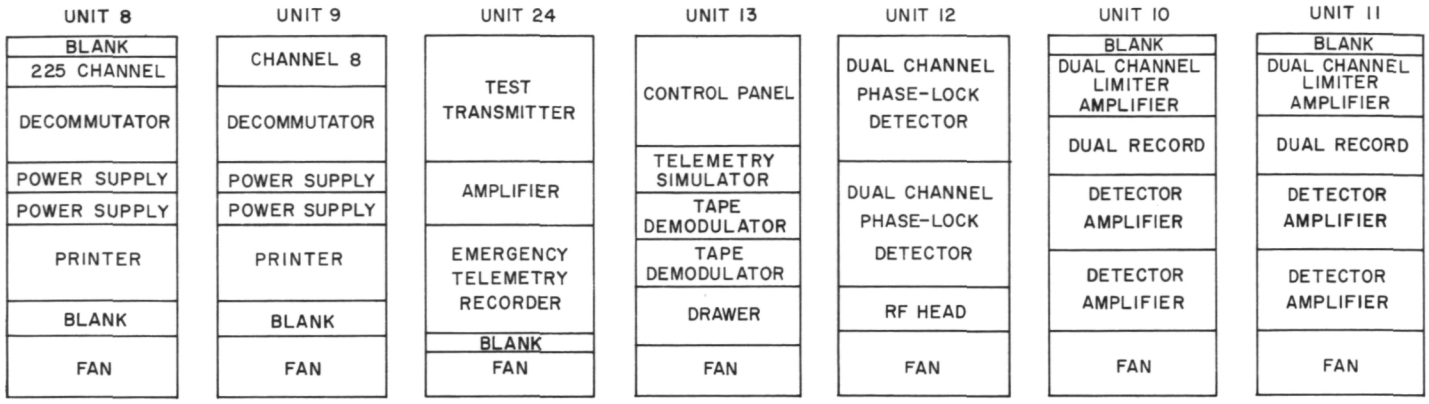

Fig. 16. Revised ground communications equipment layout for DSIF at the Goldstone station

had been prevalent since the initial setup of Unit 1 has now been virtually eliminated.

To improve the quality of the 35-mm film record, changes in both Units 1 and 2 have been initiated. Modification of the circuitry in the deflection-amplifier chassis was required to eliminate chopper amplifier interference that was reducing final picture quality. State-of-the-art advances in circuitry and wiring in the sync and tone processing chassis have greatly reduced cross-channel interference and have increased the reduced-amplitude tone signal handling capabilities. It should be possible to reduce even further the mechanical vibrations which are detrimental to the quality of the 35-mm pictures.

2. Communications

Unit 3 has been delivered to JPL and contains two band-pass filters in series with the two receiving channels. The use of these filters has successfully reduced the interchannel interference to a level of 35 db below the 1-v peak-to-peak signal. In addition, AGC has been incorporated in the Dytronics record IF amplifier to ensure proper level input to the tape recorder under all conditions.

The subsystem control panel for the ground communications equipment controls, essentially, the mode of operation of the communications subsystem and presents equipment status in the form of indicator lights. The controls will permit full subsystem test of the communications equipment. It will also permit testing of the entire RCA *Ranger* data recovery system at the DSIF stations.

The revised ground communication equipment layout for the Goldstone station is shown in Fig. 16. The test transmitter is now located with the equipment rather than at the collimator tower.

Reference

1. *Handbook of Geophysics*, U.S. Air Force, Cambridge Research Directorate, Rev. ed., The Macmillan Co., New York, 1960.

V. *Surveyor* Project

A. Introduction

Surveyor is a lunar-surface-investigation project which includes seven missions for soft landing modest scientific payloads on the lunar surface in 1963, 1964, and 1965. The project is managed by the Jet Propulsion Laboratory for the National Aeronautics and Space Administration. Hughes Aircraft Company is under contract to JPL to develop and operate the spacecraft.

The launch vehicle system will be the *Atlas–Centaur* involving the cooperation of Marshall Space Flight Center at Huntsville and its Launch Operations Directorate at Atlantic Missile Range. Tracking and spacecraft control will involve the cooperative use of the JPL Deep Space Instrumentation Facility and the Space Flight Operations Facility.

The performance objectives of the *Atlas–Centaur* launch vehicle system have been under study for the past several months by the NASA Headquarters and the Marshall Space Flight Center. Such studies have led to the reprogramming of the seven soft-lander *Surveyor* missions calling for a first launch in October, 1963, four in 1964, and two in early 1965. The first five missions are planned to use the 2100-lb gross-separated-weight spacecraft (*SPS 37-14*, Vol. II, pp. 207–229).

Hughes Aircraft Company (HAC), under JPL Contract is responsible for design, development, manufacture, and operation of the *Surveyor* spacecraft system. The HAC effort has been reprogrammed from concentration on the 2500-lb (A-25) spacecraft to the 2100-lb (A-21) configuration (see Section VI, of this report).

A group of approximately a dozen scientists is participating in the scientific activities of *Surveyor*.

B. Scientific Experiments

1. Seismograph System

Delivery of the first flight prototype of the *Surveyor* seismograph system (Figs. 1 and 2) was made to the Lamont Geological Observatory of Columbia University in May 1962 by the International Telephone and Telegraph Company Federal Laboratory.

Acceptance testing was performed by JPL and was concerned primarily with determining if the prototype was an operational seismograph. Since the *Surveyor* seismograph was designed for operation in the lunar gravitational field, testing of operational performance required compensation for the increased gravitational field of the Earth.

Compensation for the long-period seismometers is accomplished by removing five-sixths of the seismic masses.

Fig. 1. *Surveyor* seismometer system with outer cover attached

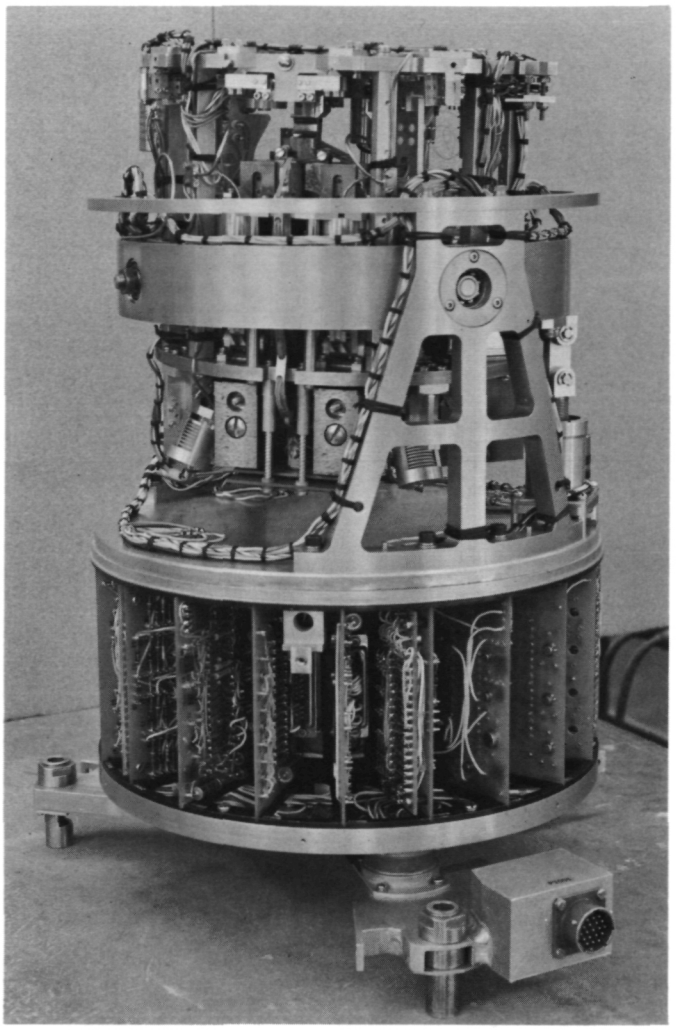

Fig. 2. Interior view of seismometer system

The effects of this mass reduction on the behavior of the instrument are:

(1) Equilibrium position of booms: instruments centered with lunar springs in place.

(2) Feedback required: same as for lunar operation.

(3) Tilt sensitivity: same as for lunar operation.

(4) Natural period: 6.1 sec, a factor of 1/6½ less than the natural period for lunar operation (15 sec).

(5) Fraction of critical damping: 1.73, a factor of 6½ greater than that intended for lunar operation (0.7).

For the short-period seismometer, compensation is effected by using an auxiliary spring device to balance five-sixths of the seismic mass. This fixture allows the seismometer to be operated on Earth with the lunar springs in place.

Operational tests showed that the instrument operated satisfactorily as a seismograph system. Figure 3 is a seismogram obtained at Palisades, New York, by one long-period horizontal seismometer of the system showing a

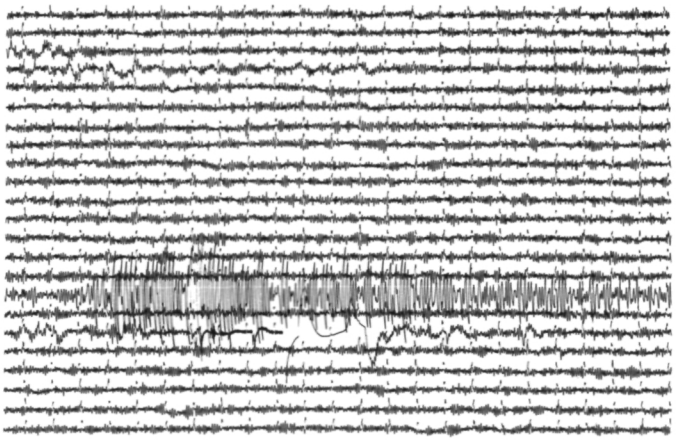

Fig. 3. Seismogram written by one long-period horizontal seismometer

Rayleigh wave train from an earthquake in British Columbia.

VI. *Surveyor* Spacecraft System

The following material relating to the Surveyor *Spacecraft System was prepared by the Hughes Aircraft Company:*

System engineering summary. The configuration of the reduced weight (2100-lb) A-21 version of the spacecraft has been determined and the drawings placed under formal change control.

Scientific payload. Effort has concentrated on system integration of the payload selected for the A-21 spacecraft: (1) television (two topside cameras with color), (2) subsurface sampler, (3) subsurface geophysical instruments, and (4) surface temperature instrument. A payload compatibility laboratory is being set up for combined tests of sensors, electronic auxiliaries, and data processing systems.

System analysis. Beamwidth requirements for the DSIF have been analyzed to determine a suitable search technique for initial acquisition of the spacecraft. A detailed procedure for star-mapping as a check of Canopus sensor lockon has been worked out. An operations sequence has been defined for determination of spacecraft attitude after landing. The design mission sequence has been formulated for the first A-21 mission.

Flight control. Design verification testing of the coast phase attitude control system resulted in some circuit parameter changes. Successful demonstrations on the single-axis air bearing table were made of the rate stabilization, inertial, and Sun modes of operation. A developmental model of the Canopus sensor was received and capture of a simulated star achieved. Flight control system modifications required for the change to the A-21 version of the spacecraft were defined. The three-axis flight control circuit breadboards for electrical compatibility tests were completed. Drawings are being released for the prototype flight control sensor group. Three engineering models of the roll actuator are being tested.

Electronics. Preliminary measurements of a developmental planar antenna with an etched aluminum-clad fiberglass panel for the aperture plate gave satisfactory patterns. Development of a slotted-cone omnidirectional antenna is nearly completed. All transmitter circuitry, except the high-power mode RF power monitor and the solid-state RF Module No. 2, has been developed. Emphasis on the altitude marking radar has been on fabricating breadboard AMR test equipment for the STEA, product design, and subcontracting of the modulator and RF assembly. Release of drawings and fabrication of components for the radar altimeter and doppler velocity sensor for use on the T-2 vehicle is well advanced.

Electrical power supply. Vibration testing is underway on the solar panel support structure, modified as a result of a deficiency disclosed in previous vibration tests. Solar cell test data indicate that panel output will be higher than that calculated. Tests of the initial eight experimental batteries show that modification is necessary for operation at the temperature extremes of 0°F and 125°F. Manufacturing drawings are being made and parts procured for the central power control system for the T-2 and T-21 spacecraft.

Thermal control. Thermal testing of the first MT-1 full-scale spacecraft sector has started. View factors from critical radiating surfaces of the spacecraft have been determined for the A-21 spacecraft. Thermal characteristics of various subsystems including the radar altimeter and doppler velocity sensor, vernier propulsion system, and several payload items have been analyzed.

Engineering mechanics. Landing gear shock absorber parameters have been determined for the A-21 spacecraft. Tests of landing characteristics using the full-scale T-1 test spacecraft have included drops under 16 different velocity conditions on a 15-deg slope, and the results have generally confirmed the expected performance. Several means of improving footpad characteristics are being tested. Testing on 25-deg slopes is underway, and cross-hill drops are among those to be performed soon. Preparations are being made to start vibration tests using S-2, an A-21 type vehicle with components more nearly representative of the flight spacecraft than those on the earlier S-1 vibration test vehicle. Static tests of the landing gear lock strut will result in minor redesign to improve the structure.

Propulsion. Contract negotiations with Thiokol, Elkton Division, for a revised retro-engine program to include the A-21 engine have been completed. Initial tests of the retro-engine in the high-altitude facility at AEDC have been made. Acceleration testing of the vernier propulsion system has been successfully completed.

Spacecraft vehicle and mechanisms for basic bus. Preliminary tests of landing gear deployment are providing valuable design evaluation. A full-scale engineering mockup of the A-21 spacecraft and Vehicles S-6 and S-7 for vernier propulsion system testing are nearing completion. Thermal–vacuum testing of the planar array/solar panel positioners has started. Following modifications, stepping motors for mechanism drives have operated up to 3 hr at 275°F and a vacuum of 10^{-6} mm Hg.

Reliability and system test. New reliability estimates indicate increased success probability for all major mission phases, due largely to clearer definition of mission phases and reassessment of component failure rates. The recovery system for the T-2 flight control test vehicle has been designed, and a series of tests has been made on the air-bag system for impact absorption. Fabrication of components for the system test equipment assembly is underway. Design of the telecommunications RF test rack was completed.

Mission operations. The prototype command and data handling has been assembled and system test is in progress. A system design study has resulted in a simpler *Surveyor* spacecraft simulator which has essentially all the important operational features of the previous design. A detailed plan has been developed for testing in conjunction wtih General Dynamics, Astronautics Div., of the air-conditioning provisions for the spacecraft within the *Centaur* shroud. A preliminary definition of spacecraft handling equipment and procedures has been completed.

A. System Engineering Summary

1. Configuration

The configuration for the 2100-lb A-21 spacecraft has been determined and the drawings placed under formal change control. The general arrangement is shown in Figure 1; the spacecraft is shown pictorially in Figure 2.

Steps taken to reduce weight of the A-21, as mentioned in Reference 1, were: 1) deletion of the 5-lb auxiliary battery, 2) elimination of multiplexing provisions for the tape recorder, 3) removal of certain engineering – information accelerometers, and 4) elimination of Equipment Compartment D. An additional step was to eliminate a separate preseparation arming device for the omnidirectional antenna and spacecraft leg squib circuitry. A contingency allowance of 10 lb of vernier propulsion propellants was originally planned. This allowance has been reduced to 4 lb, at slightly increased risk, as a further weight reduction. The risk associated with reduction of vernier propellant is compensated by reduced retro-engine burnout dispersion resulting from improved control of engine temperature.

2. Weight Summary

The current weight summary for the A-21 design is shown in Table 1. A more detailed weight breakdown of the spacecraft weights is shown in Table 2.

Table 1. A-21 spacecraft weight summary

Item	Maximum allowable weight, lb	Current design weight, lb	Anticipated weight lb
Total separated weight	2100.00	2100.36	2105.66
Basic bus	653.82	654.33	659.63
Usable propellant	1331.69	1331.69	1331.69
Scientific payload	114.49	114.34	114.34

3. RTG Study

In accordance with JPL instructions, the SNAP-11 radioisotope thermo-electric generator (RTG) will be carried on launches P-47 and P-48. The estimated RTG total system weight is 41.3 lb, including the necessary dc to dc converter, as shown in Table 3. The use of the RTG results in a net weight saving of 30.7 lb, as shown in Table 4.

In order to define the RTG-spacecraft requirements, an interface specification is being prepared in close coordination with Martin Nuclear Division.

4. Electrical Energy

The A-21 series spacecraft utilize a single 46-lb battery with a rated capacity of 2650 w-hr based on a nighttime thermal history developed on the basis that compartment temperatures should be maintained at 0°F or higher. In general, scientific experimentation will be conducted during the first lunar day and the data will be transmitted back during that same period. During the lunar night, thermal test information on Compartments A and B, along with certain engineering data, will be transmitted back to Earth approximately once per hour. The night tests require that heating power be supplied to the surface temperature instrument and result in depletion of electrical energy prior to lunar morning. The spacecraft is expected to survive for approximately 240 hr after the day-night terminator.

As a part of an analysis and preliminary design of an A-21 type vehicle in which lunar night survival can be assured, the tradeoff between increase in battery capacity as it is affected by increase in temperature versus the increase in thermal losses from the basic bus equipment compartments was studied. The results, which are included in Reference 2, have shown that operation of Compartment A, in which the battery is housed, at a nominal 40°F temperature throughout the lunar night instead of 0°F, results in a net increase in the total time that the battery can maintain the basic bus at these temperatures. The study showed, in fact, that the single 46-lb battery is capable of providing approximately 3200 w-hr of energy, compared to a total of 3010 w-hr required for a minimum operation basic bus survival for the lunar night. The improvement in system operation achieved by operating Compartment A at 40°F is not unique to the night survivability demonstration vehicles (SC-5 and SC-6) and is being implemented in the spacecraft intended for the first three launches. The operational utilization of the vehicle will be modified to take advantage of this additional battery capacity.

5. Commands

A summary of the commands required for the A-21 spacecraft is shown in Table 5. There are now a total of

Table 2. A-21 spacecraft weight breakdown

Item	Maximum allowable weight, lb	Current design weight, lb	Item	Maximum allowable weight, lb	Current design weight, lb
1.0 Basic bus (total)	653.82	654.33	Electrical wiring		
1.1 Flight control	51.77	51.77	Pneumatic lines, attitude control		
Sensor group			Release mechanism, retro-rocket		
Secondary solar sensor			Engineering measurement sensors		
Attitude control system			Latch, spacecraft-to-*Centaur*		
1.2 Electronics	95.18	95.18	1.6 Spacecraft propulsion (not including usable propellant)	223.40	224.82[a]
Data link (antennas, RF switches, transmitter-diplexer, command receiver, and transponder)			Rocket engine, main retro		
Central command decoder			Vernier propulsion system		
Central signal processor			Unusable vernier propellant		
Altitude marking radar			Helium		
Doppler velocity sensor and altimeter			Insulation, main retro-engine		
Power control system			2.0 Usable propellant (total)	1331.69	1331.69
TV camera 4			2.1 Retro-rocket propellant		1186.40
Engineering data processing			2.2 Vernier propellant		144.69
Mechanisms auxiliaries			2.3 Pyrogen propellant (igniter)		0.60
Heater control			3.0 Scientific payload (total)	114.49	114.34
1.3 Electrical power	54.50	54.50	3.1 TV Cameras 2 and 3 and mirrors		34.40
Solar panel			3.2 Geophysical thermal and TV auxiliaries		4.80
Battery			3.3 Subsurface sampler		27.85
1.4 Mechanisms	31.20	30.50	3.4 Spacecraft anchoring device		10.14
Positioner, antenna-solar panel			3.5 Surface temperature instrument		.70
Antenna mechanism, omni-directional			3.6 Interferometer spectrometer		2.00
Separation sensing and arming provisions			3.7 Subsurface geophysical probe		2.70
1.5 Spacecraft vehicle	197.77	197.56	3.8 Tape recorder and auxiliaries		11.80
Spacecraft basic structure			3.9 Engineering instrumentation		5.00
Equipment attaching hardware			3.10 Electrical wiring		9.70
Landing gear installation			3.11 Subsurface sampler and geophysical auxiliaries		5.25
Paint					
Equipment Compartments A and B					

[a] Anticipated weight changes to main retro-engine are (1) destruct system (+3.30 lb), (2) safety and arming device (+2.00 lb).

Table 3. RTG/dc-to-dc converter system weight

Item	Estimated weight, lb
RTG	33.0
DC-to-DC converter	1.0
Shunt regulator	0.3
Attach brackets	3.0
Shielding on mechanisms	3.0
Wiring (additional)	1.0
Total	41.3

Table 4. Weight comparison

Battery-solar panel system		100.5 lb
Battery	92.0	
Solar panel	8.5	
RTG-battery-solar panel system		69.8 lb
Battery	20.0	
Solar panel	8.5	
RTG	41.3	
Weight difference		30.7 lb

seven subsystem decoders on the basic bus, five located in the central command decoder, and two located in the engineering mechanisms auxiliary and the flight control electronics unit respectively. This provides a total command capacity of 224 command channels for the basic bus. A total of 146 command outputs are presently in use.

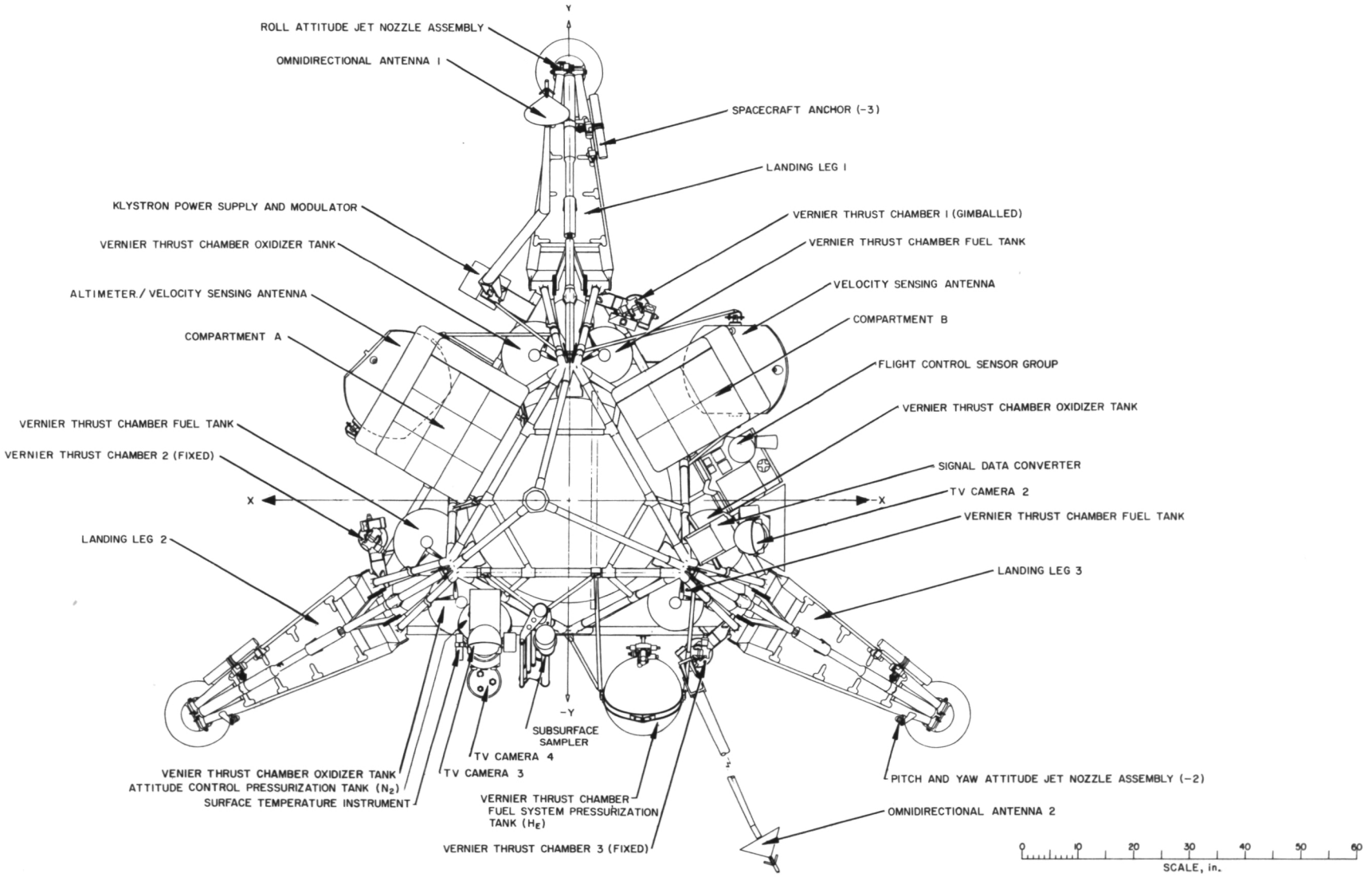

Fig. 1. Spacecraft general arrangement

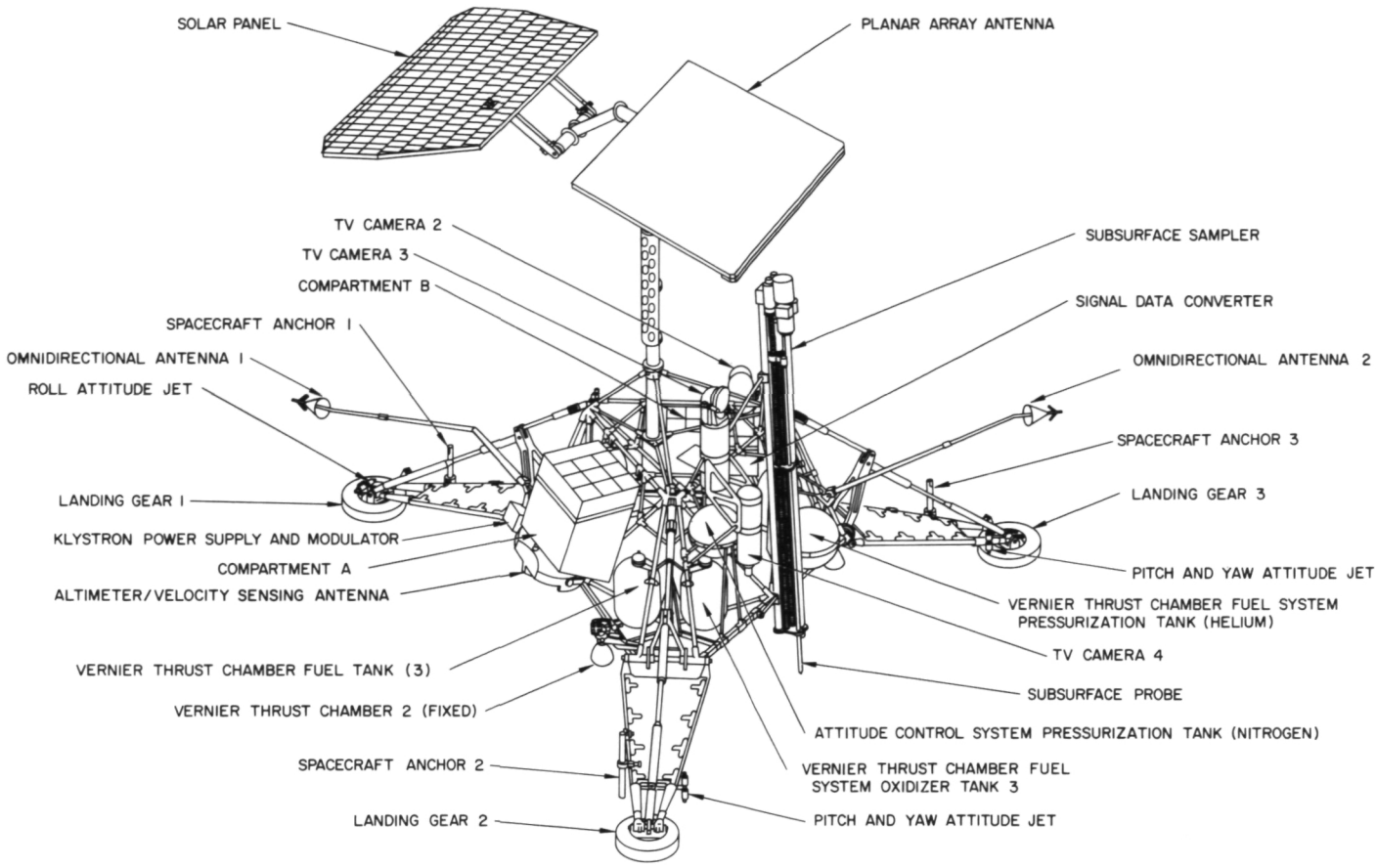

Fig. 2. A-21 spacecraft

The scientific payload commands are supplied by subsystem decoders packaged within the auxiliaries associated with each scientific instrument or experiment. These decoders will have a command capacity of 8, 20, or 32 commands. The choice of decoder size is determined by the existing command requirements plus a reasonable number of spares. The A-21 spacecraft will not contain any "8-command" subsystem decoders but will contain three "20-command" decoders.

6. *Data Channels*

A summary of the data to be telemetered on the A-21 spacecraft is shown in Tables 6 and 7. The data listed in Table 6 are processed via the engineering signal processor on one of four engineering commutators or on one of six separate subcarrier oscillators. These data include all basic bus engineering instrumentation with the exception of the seven channels of engineering data on the tape recorder. The engineering commutators also contain several channels of scientific payload data which do not require special processing.

The data listed in Table 7 are processed via commutators or subcarrier oscillators contained in the indicated payload auxiliaries. All data listed in this table are sent on analog channels even though some are digital in nature, in order to minimize the amount of hardware required.

There are a total of nine commutators in the A-21 spacecraft. These commutators and some of their characteristics are listed in Table 8. The magnetic susceptibility and interferometer spectrometer commutators are tentative and may change when the signal processing requirements are more fully defined.

All commutated data are converted to an 11-bit format and transmitted via pulse code modulation (PCM) at one of three bit rates: 550, 1100, or 4400 bit/sec. The resulting PCM data (except for TV) is sent on one of three subcarrier oscillators: 3.9, 7.35, or 33 kc. The commutated data for TV Cameras 2 and 3 are transmitted directly on the main carrier immediately following the video.

Table 5. Spacecraft command channels

Subsystem command decoder	Number of commands presently assigned	Number of available commands
Basic bus		
Central Decoder 1 (data link and TV Camera 4)	30	32
Central Decoder 2 (signal processing)	29	32
Central Decoder 3 (electrical power)	12	32
Central Decoder 4 (mechanisms and vehicle)	14	32
Central Decoder 5	0	32
Engineering mechanisms auxiliaries	31	32
Flight control electronics unit	30	32
	146	224
Scientific payload		
Tape recorder auxiliary	13	20
Subsurface sampler auxiliary	11	32
Subsurface geophysical auxiliary	8	20
Geophysical thermal auxiliary	18	20
TV auxiliary	30	32
	80	124
Total	226	348

The bit rates and subcarrier frequencies listed in Table 8 will normally be used at the times indicated under *Principal use*. Subcarrier oscillator selection is independent of the bit rate, however, and both are independent of the selected commutator. Therefore, the only limitation on the use of higher bit rates is bandwidth. The hourly engineering interrogations during transit will consist of reading out Engineering Commutators 1, 2, and 4 at a bit rate consistent with available bandwidth.

7. Surveyor Spacecraft for Lunar Orbital Reconnaissance

Study of application of the *Surveyor* basic bus to lunar orbital missions has continued. New designations have been given to the two configurations under study:

	Old Designation	Injected weight, lb
Surveyor Orbiter	*Surveyor* B Mark I	800
Advanced *Surveyor* Orbiter	*Surveyor* B Mark II	1600 to 2000

The payload-spacecraft interface document for the first version of *Surveyor* Orbiter was delivered to JPL on April 19, 1962. This spacecraft design resulted in the following payload characteristics:

Weight	40 lb
Power, continuous	10 w
Power, sunlit only	30 w
Sampled data channels	15
Command channels	32
Video bandwidth	200 kc

After reviewing this design, which was based on using the *Surveyor* soft-landing spaceframe mounted in either an *Agena* bulbous shroud or a *Centaur* shroud, JPL requested a revision to the design to permit increased payload capability. The revised design is to be mountable to an *Agena B* booster with *Mariner* interconnect structure and shroud, and the spaceframe is to be redesigned as necessary to the *Surveyor* Orbiter requirement. The payload-spacecraft interface document for this design will be delivered to JPL on June 19, 1962, and will delineate the following payload characteristics:

Weight	60 lb
Power, continuous	10 w
Power, sunlit only	50 w
Sampled data channels	15
Command channels	32
Video bandwidth	350 kc

The most significant differences between the two designs are in the areas of spaceframe and thermal control. The *Surveyor* Orbiter design calls for a nearly closed thermal design (nearly all components requiring thermal control are located within one thermally controlled system) and a spaceframe fabricated from sheet metal, rather than the tubular structure of the initial design.

Payload objectives for the Advanced *Surveyor* Orbiter have been established during this period as follows:

Weight	200 lb
Power, continuous	70 w
Power, sunlit only	165 w
Sampled data channels	25
Command channels	32 or 64
Video bandwidth	~ 1 mc

Table 6. Spacecraft data channels via engineering signal processor

Item	Commutated data (PCM) Digital	Commutated data (PCM) Analog	Subcarrier oscillators
Basic bus data			
Data link			
Transmitter filaments on	2		
Transponders phase locked	2		
Message enable-reject	2		1 (2.3 kc)
Central decoder state	1		
Transmitter power outputs		2	
Static phase errors		2	
Receiver AGC		2	
Receiver AFC		2	
Transmitter temperatures		2	
	7	10	
TV Camera 4			
Power on	1		
Vidicon thermal control on	1		
Vidicon faceplate temperature		1	
Camera electronics temperature		1	
	2	2	
Signal processing			
Potentiometer reference voltage		2	
		2	
Mechanisms			
Omnidirectional antennas extended	2		
Antenna-solar panel mast extended	1		
Vehicle separation	1		
Antenna-solar panel position		4	
Planar array temperature		1	
Antenna-solar panel positioner temperatures		2	
	4	7	
Propulsion			
Helium and manifold pressures		2	
Retro case temperature		2	
Vernier lines temperatures		3	
Vernier fuel tank temperatures		3	
Vernier oxidizer tank temperatures		3	
Vernier engine temperatures		3	
Helium tank temperature		1	
		17	
Vehicle			
Landing gears extended	3		
Retro ejected	1		
Vehicle accelerometers (high gain outputs)			4 (52.5, 70, 90, 110 kc)
Landing gear deflections		3	
Compartment A temperatures		7	
Compartment B temperatures		5	
Thermal tunnel temperature		1	
Spaceframe temperatures		4	
Shock absorber temperatures		3	
Retro attach point temperatures		3	
Spaceframe temperatures		4	
Landing gear temperature		1	
Antenna-solar panel mast temperature		1	
	4	28	

Item	Commutated data (PCM) Digital	Commutated data (PCM) Analog	Subcarrier oscillators
Electrical power			
Compartment thermostats	2		
Voltage measurements		4	
Current measurements		7	
Current calibration		3	
Battery temperature		1	
Central power control temperature		1	
Solar panel temperature		1	
	2	17	
Radar			
Altitude marking radar (AMR) on	1		
AMR enabled	1		
Radar altimeter and doppler velocity sensor beam reliable signals	4		
Radar altimeter and doppler velocity sensor lunar reflectivity measurement	8	4	
AMR power output		1	
AMR AGC		1	
AMR temperatures		2	
Radar altimeter and doppler velocity sensor temperatures		4	
	14	12	
Flight control			
Sun and star lockon	2		
Magnitude readout	10		
Gyro precession signals	6		
Retro sequence timing signals	11		
Programmer states	12		
Gyro speeds			1 (5.4 kc)
Nitrogen pressure		1	
Primary Sun sensor errors		2	
Secondary Sun sensor signal		5	
Canopus error		1	
Star intensity signal		1	
Gyro errors		3	
Thrust commands to vernier engines		3	
Retro accelerometer		1	
Radar altimeter range		1	
Doppler velocity signals		3	
Roll actuator signal		1	
Precession commands		3	
Gyro temperatures		3	
Electronics unit temperatures		2	
Canopus sensor temperature		1	
Nitrogen tank temperature		1	
	41	32	
Scientific payload data			
Subsurface sampler			
Limit switches	5		
Drill position		2	
Logging sonde position		2	
Drill motor current		1	
Drill motor temperature		1	
	5	6	

CONFIDENTIAL

Table 6 (Continued). Spacecraft data channels via engineering signal processor

Item	Commutated data (PCM) Digital	Commutated data (PCM) Analog	Subcarrier oscillators	Item	Commutated data (PCM) Digital	Commutated data (PCM) Analog	Subcarrier oscillators
Subsurface geophysical				Geophysical thermal			
Caliper reading		1		Temperatures		4	
Magnetic susceptibility temperature reference		1			0	4	
		2		Total	79	139	

Table 7. Spacecraft data channels via scientific payload auxiliaries

Auxiliary	Commutated data (PCM)	Subcarrier oscillators	Auxiliary	Commutated data (PCM)	Subcarrier oscillators
Tape recorder			Subsurface interferometer spectrometer radiometer	1	
Engineering data			Subsurface thermal diffusivity	1	
Shock absorber strain gauges		3 (33,52.5, 70 kc)		3	
Vehicle accelerometers (low gain outputs)		4 (90, 110, 130, 150 kc)	Television (Cameras 2 and 3)		
			Camera number	1	
Scientific data			Mirror position	2	
Spares		[a](33,52.5, 70, 90)	Lens settings	3	
			Filter wheel position	1	
Analog-to-digital converter output		1 (185 kc)	Calibration voltage	1	
Subsurface geophysical			Lens iris servo on	1	
			Shutter open	1	
Subsurface density		1 (70 kc)	Multiple step focus mode on	1	
Subsurface magnetic susceptibility	8		Vidicon faceplate temperature	1	
			Camera electronics	1	
	8			13	
Geophysical thermal					
Surface interferometer spectrometer radiometer	1		Total	24	9

[a]These channels use the same subcarrier oscillators listed under *Engineering data* above.

Table 8. Spacecraft commutator characteristics

Commutator	Principal use	Bit rate, bits/sec	Subcarrier frequency, kc	Commutator frame size, words	Number of sync words	Number of analog channels	Number of digital channels
Engineering Commutator 1	Midcourse correction	1100	7.35	100	2	10 at 5/frame 8 at 2/frame 23 at 1/frame	10 at 5/frame 40 at 1/frame
Engineering Commutator 2	Terminal descent (with high gain antenna)	4400	33	100	2	11 at 2/frame 67 at 1/frame	10 at 3/frame 60 at 1/frame
Engineering Commutator 3	Terminal descent (with omnidirectional antennas)	550	3.9	50	2	5 at 4/frame 4 at 2/frame 8 at 1/frame	10 at 9/frame 30 at 1/frame

CONFIDENTIAL

Table 8 (Continued). Spacecraft commutator characteristics

Commutator	Principal use	Bit rate, bits/sec	Subcarrier frequency, kc	Commutator frame size, words	Number of sync words	Number of analog channels	Number of digital channels
Engineering Commutator 4	Acquisition and lunar operation	all	all	100	2	4 at 5/frame 75 at 1/frame	30 at 1/frame
Subsurface magnetic susceptibility commutator		550	3.9	16	1	15 at 1/frame	None
Surface interferometer spectrometer commutator		4400	33	16	1	1 at 15/frame	None
Subsurface interferometer spectrometer commutator		4400	33	16	1	1 at 15/frame	None
Subsurface thermal diffusivity commutator		550	3.9	16	1	1 at 15/frame	None
Television commutator (Camera 2 or 3)		4400	Main carrier	16	1	2 at 2/frame 11 at 1/frame	None

B. Scientific Payload

1. Summary

Although special systems integration studies on alpha scattering and the petrographic microscope have continued during this report period, work on instruments not applicable to the A-21 spacecraft has been limited principally to technical assistance to JPL. The effort has been concentrated on the selected A-21 payload, which is as follows:

(1) Television (two topside cameras with filters and one downward-looking camera for use during lunar approach)

(2) Subsurface sampler

(3) Subsurface geophysical instruments (logging sonde)

(4) Surface temperature instrument (interferometer spectrometer)

Work is continuing on these items, to assure not only the adequacy of a particular unit in its application but also proper over-all system operation of the payload and spacecraft. A key item has been to establish the payload compatibility laboratory. The purpose of this laboratory is to verify experimentally compatibility of the experiment sensor, its associated Hughes electronics, and the spacecraft data processing system. Much of the test equipment required to perform its functions is available for use. The remaining effort is expected to be completed by July 1 in order to enable compatibility verification tests to be completed prior to delivery of lightweight payload subsystems to the T-21 systems test spacecraft.

2. Television

The television system for the A-21 spacecraft employs two cameras for visual surveillance of the lunar surface and a third camera for obtaining approach pictures of the Moon during the descent phase. The lunar surface surveillance cameras employ variable focal length lenses for wide or narrow angle capability. Scanning is accomplished by means of moving mirror assemblies mounted on each of the two cameras. Both surveillance cameras include a filter wheel with clear, red, blue, and green color segments. The third or approach camera utilizes a fixed focal-length lens. The A-25 spacecraft will employ an additional lunar surface surveillance camera, as well as a fifth camera utilizing a telescopic lens to obtain high-resolution pictures of selected areas.

Each camera contains the electronic circuitry necessary to process the image formed on a vidicon tube. The modes of operation – normal and emergency – are provided in each camera except the downward-looking approach camera, which has normal mode only. Under normal operation, single-frame pictures can be produced at a maximum rate of one every 3.6 sec. The sweep circuits in the camera free-run continuously. Shutter operation and picture readout, including identification code, are initiated by command from Earth at the proper time in the sweep cycle and synchronized by video logic circuitry in each camera. Prior to a succeeding shutter and readout cycle, time is allotted for vidicon erasure, effected by the continuous sweeping of the tube, and for operation of mirror and lens mechanisms by Earth commands. Control circuitry for the mechanisms also is included in each camera.

Emergency mode operation is similar to normal mode except for a reduction in sweep rate and open-shutter operation. In this mode, the picture rate is reduced to one in about 62 sec. The emergency mode will be used if a failure in the communications link severely reduces the available transmission bandwidth.

a. Camera packaging. Design of the electronics modules, their mounting chassis, and the housings for the electronics, vidicon and optics is proceeding. Detail drafting has been completed for the 25 cordwood modules contained within a camera. Detail drafting has been completed on the lens control chassis (Chassis 1 and 2) and is expected to be completed by late June on the remaining four electronic chassis (normal and emergency mode sweep, sync, and blanking circuits; video amplifier and logic; and temperature sensing and flashing light circuits for vidicon erasure) and the electronic conversion unit. The detail mechanical design of the camera housing, vidicon housing, vidicon heater, and flashing light system is progressing.

Hardware is being fabricated for a flight configuration breadboard camera. The flight configuration breadboard will be identical in configuration and operation to the

flight cameras except for the use of nonqualified components and material. This breadboard camera will be used to eliminate anomalies in performance resulting from the required high-density packaging. It is expected that camera fabrication will be completed and ready for test by late July. A structural model of the TV camera is being fabricated and will be subjected to environmental and structural testing prior to fabrication of T-21 hardware.

b. Variable focal length lens assembly. Final outline and mounting assembly drawings of the lens, filter wheel, and shutter subassemblies were received from Bell and Howell in this report period, and final negotiations of the lens/camera interface were successfully completed. Lens, filter wheel, and shutter detail designs have been completed. Detail fabrication and assembly drawings, together with indentured parts lists of these subassemblies, were received from Bell and Howell and are currently being reviewed by Hughes.

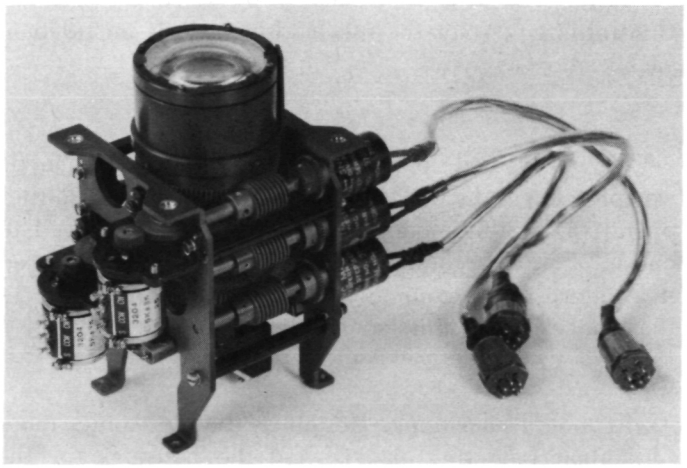

Fig. 3. Variable focal length lens assembly

The first prototype lens assembly was received by Hughes on schedule on June 4, 1962 (Fig. 3). This assembly is now being integrated with the lens drive circuits and iris servo of the breadboard camera. A beam splitter redesign has been incorporated in this prototype, changing the light sample to the iris servo photodiode from 6% of the total light passing through the lens to 12.5%, in order to match the response of the iris servo circuit to the dynamic response of the vidicon tube.

The photodiode has been moved farther away from the main lens axis so that the photosensitive area of the photodiode lies beyond the light ray crossover point of the condensing lens, defocusing the light sample sufficiently to utilize the entire photosensitive area of the diode. The addition of a copper strap, equivalent in cross-sectional area to a No. 20 AWG wire, placed around the photodiode near the photosensitive end and connected to the vidicon tube heat radiator strap will provide thermal control of the photodiode, maintaining its temperature near that of the vidicon tube.

Fabrication of lens assemblies for type approval tests and the T-21 spacecraft are proceeding on schedule. Operational tests of the complete lens assembly under high vacuum conditions are scheduled for completion in August of this year. Type approval and flight acceptance test procedures were received from Bell and Howell in late May. Changes to these test procedures are now being negotiated with this vendor.

A sample iris assembly consisting of photo-etched stainless steel blades coated with molybdenum disulphide dry lubricant was subjected to humidity and cycling tests. After 170,000 cycles of operation under laboratory ambient conditions, the iris was still functioning properly.

The shutter base plate has been enlarged to encompass much of the cross-sectional area of the camera housing as practical to prevent any possible outgassed particles from the lower camera housing and electronics from depositing on the lens optical surfaces and lens adjustment gears.

A teflon felt bumper will be used to prevent shutter blade bounce during the shutter opening cycle. Solenoid-actuated, spring-loaded mechanical latches have been added to the shutter to further reduce the possibility of blade bounce. The blades will be latched in both the "at rest" and "energized" positions, preventing movement of the shutter blades until the latching solenoids are energized by the shutter drive circuitry. The latching solenoids are series-connected to the main shutter drive solenoids. Because they have less inductance than the main drive solenoids, unlatching occurs prior to actuation without separate sequence logic elements. Figures 4 and 5 show prototypical shutter and filter wheel assemblies from Bell and Howell.

c. Thermal studies. A thermal analysis of the television cameras on the A-21 spacecraft (Cameras 2, 3 and 4) has been initiated. Less lunar and solar shading of the cameras by surrounding elements of the A-21 spacecraft, compared to the A-25, is extpected to extend the time intervals during which camera temperature will not restrict TV operation. Radiosity techniques will be used in an IBM 7090 computer analysis. View factors will be determined by photographic methods on the A-21 space-

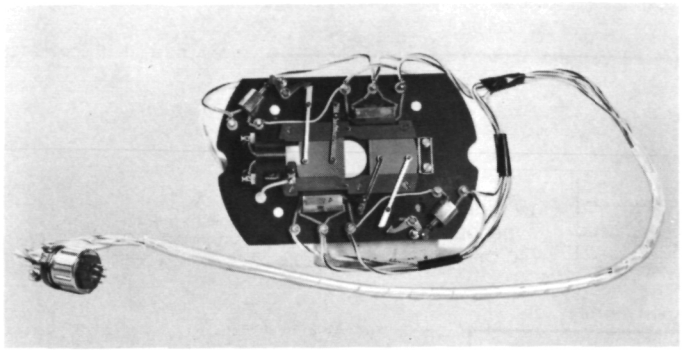

Fig. 4. Variable focal length lens shutter assembly

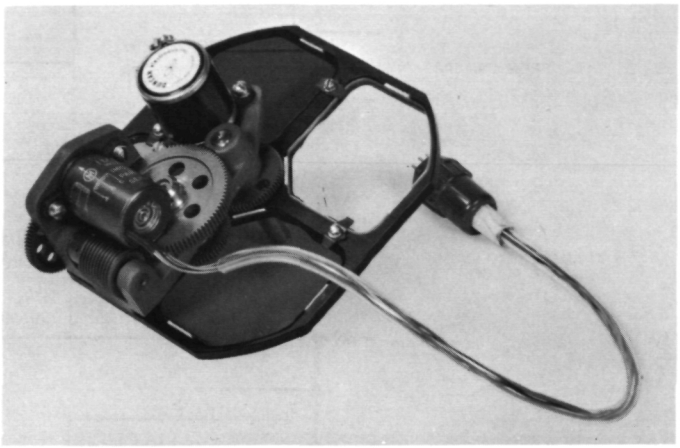

Fig. 5. Variable focal length lens filter wheel assembly

craft mockup. It is expected that the thermal analysis will be completed in late July.

d. Circuit development. Final circuit releases have been made for all portions of the spacecraft television system. A complete breadboard camera system has been put into operation. The system includes the prototype variable focal-length lens with variable focus and iris control, breadboard shutter, light flash vidicon erasure unit, and all the television camera electronics including the electronic conversion units. The system is sequenced through its various modes by means of a command generator simulator which provides all the necessary commands.

e. Vidicon evaluation. The television camera system uses a 1 in. diameter vidicon tube employing electro static focusing and magnetic deflection. An extensive evaluation program has been conducted to obtain an adequate photoconductive surface for the vidicon. Many standard and special vidicons from the General Electrodynamics Corporation, RCA, and Westinghouse have been tested. An RCA vidicon using a selected Sb_2S_3 photoconductor has given the best over-all performance and has been selected for use on the T-21 spacecraft. Testing and evaluation of advanced tubes from RCA, Westinghouse, and General Electrodynamics Corporation will continue with the objective of finding an even better vidicon for use in flight spacecraft.

The general vidicon requirements and the performance of the selected RCA vidicon (in parenthesis at the end of each item) are as follows:

(1) After picture readout, the image must erase in the normal picture sequence to such a point that at reexposure no noticeable trace of the previous image exists. (The stored image on the RCA tube is erased to less than 7%.)

(2) The vidicon image storage must be adequate to provide operation in the emergency mode, 20-sec frame readout, and in the shuttered normal mode, 1-sec frame readout. High sensitivity is desired to allow large lens f-numbers to be used with low light levels. (In the selected tube, the sensitivity in emergency mode is reduce by a factor of approximately 40 from the sensitivity in normal mode. This difference is overcome by increasing the video amplifier gain and by operating with the shutter open. The sensitivity in normal mode is lower than desired by approximately a factor of three.)

f. TV auxiliary. The television auxiliary (Fig. 6) is required to combine the outputs of the various TV cameras such that the data may be transmitted to Earth. The main functions in the auxiliary are video summing amplifiers, frame identification commutator, command decoding, electrical power conversion, and camera heater power switches.

The video outputs from each camera are combined in a pair of summing amplifiers. Separate video outputs are provided for each transmitter for redundancy. This also eliminates impedance matching problems caused by the OFF transmitter. No more than one camera is energized at a time, so that no switching circuits are required in the video circuits. A sixth channel is included in each summing amplifier to allow transmission of the frame identification data which has been digitized by the analog-digital converter in the central signal processor. A frame identification enable gate passes the analog-to-digital output signal at the appropriate times in the TV

CONFIDENTIAL

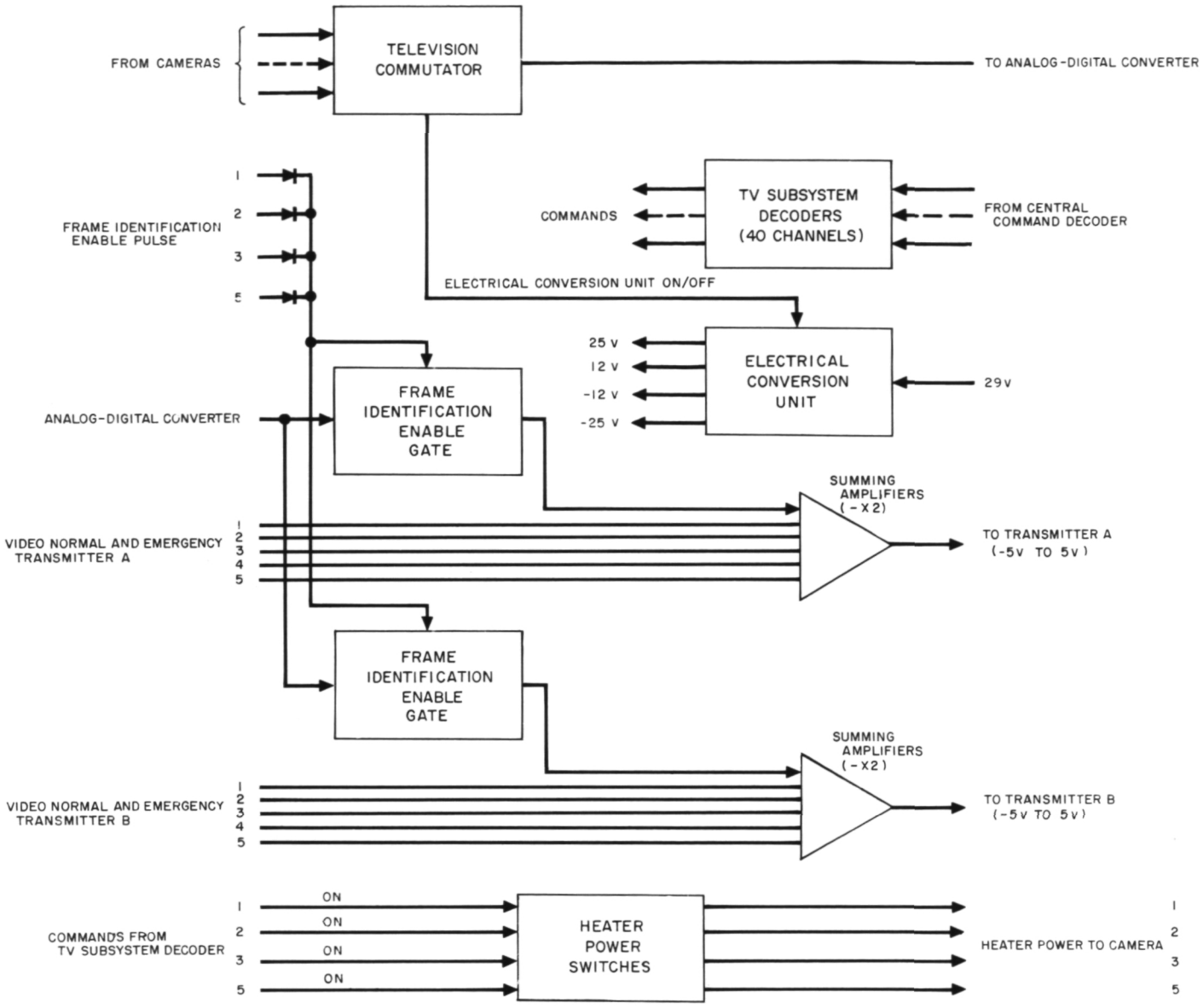

Fig. 6. Television auxiliary

frame sequence. Synchronizing pulses for this gate are derived from the camera sweep circuits.

The commutator is used to multiplex the frame identification data for conversion to a digital form. The commutator is designed such that it automatically selects only the data received from the ON camera. Circuitry for this commutator is basically the same as that used in the engineering signal processor commutator. Different logic is used to accommodate the particular format used for frame identification.

The command decoder is composed of two regular subsystem decoders. A 40-channel command capability is provided for the television system. Some commands are fed to all cameras simultaneously. The system is designed such that only the ON camera responds to these commands. A considerable saving of command channels is achieved in this manner.

The auxiliary contains one electrical conversion unit which provides the various voltages to the circuits in the auxiliary. The unit is of the regular switching type and is turned on when power is applied to any camera.

Power switches for the camera heaters are located in the auxiliary. These provide heating power to the cameras

CONFIDENTIAL

if the pictures are to be taken early in the lunar day when the cameras are too cold for unassisted operation.

g. Video amplifier. The video amplifier for the television cameras has been modified from the design described previously. Noise characteristics and stability have been improved. The keyed clamping circuits have been designed to provide a more stable clamping level.

In the modified video amplifier (Fig. 7), the input stage, Transistors Q_1 and Q_2, consists of a common collector/common emitter configuration using low noise 2N930 transistors. This replaces a feedback pair which used an alloy transistor with a higher noise figure. An amplifier gain change between normal and emergency modes of operation has been incorporated in Amplifier Q_3. Attenuation in the collector circuit of Q_3 is caused to be higher in the normal mode (less amplifier gain) than in the emergency mode by application of the normal mode 25 v to the diode network CR_1, CR_2, and CR_3. Transistors Q_4, Q_5 and Q_6 form a feedback amplifier. A lag network at the output of Q_6, consisting of R_1 and C_1, is used to reduce noise at frequencies beyond the required video bandwidth. This prevents excessive noise in the following stages, which results from the equalization that is applied to the signal in the next stage, Q_7. The high frequency response of Q_7 is increased by the network composed of R_2, R_3, and C_2 in order to equalize the roll-off in frequency response caused by the input capacity of the first stage and vidicon capacity.

The output of Amplifier Q_7 is coupled to the keyed clamp circuit through Emitter Follower Q_8. Transistor Q_9 operates as the keyed clamp which restores the dc level of the video signal such that the video may be combined with the sync-blank pulses. It is normally cut off by a positive voltage fed from either the normal or emergency keyed clamp drive lines through Diodes CR_4 and CR_6. When the negative keyed clamp pulse occurs, Q_9 is saturated and charges Coupling Capacitor C_3 to a voltage determined by the voltage across Resistor R_4 and the saturation voltage of Q_9. This restores the video level to a fixed point during each keyed clamp pulse. Diode CR_8 serves to prevent the video signal from exceeding the black level and disturbing the synchronizing action in the ground receiver. Transistors Q_{10} and Q_{11} comprise a summing circuit which combines the clamped video signal and the sync-blank pulses to form the composite video signal.

The output from the summing circuit is coupled through Diode CR_{11} to Emitter Follower Q_{13}. Diode CR_{11} and Transistor Q_{12} serve as a video gate to disable the video signal during frame identification and during the non-active frames in the video sequence when transmission is stopped. A positive voltage from the video gate circuit normally keeps Q_{12} cut off. When the video is to be gated off, the video gate voltage goes negative and causes Q_{12} to saturate. This opens Diode CR_{11} and clamps the video signal at the black level. Diode CR_{12} serves to prevent the video signal from exceeding the maximum voltage corresponding to the white level.

The output of the video gate circuit is capacitively coupled to the output emitter follower, Q_{15} and Q_{16}. The video signal is dc restored to a level determined by Resistors R_8 and R_9 in a second keyed clamp circuit. The negative keyed clamp pulse causes Q_{14} to be saturated, clamping the bases of Q_{15} and Q_{16} to essentially the voltage at the emitter of Q_{14}. Separate outputs from Q_{15} and Q_{16} feed the summing amplifiers in the television auxiliary. The circuits are direct-coupled from this point through the transmitter modulator. Two keyed clamps are used in the system because of conflicting requirements as to output video level and the level at which the signal could be combined with the sync-blank pulses.

h. Power supply. In the television camera power supply (Fig. 8), a switching type dc-to-dc converter transforms the main regulated bus voltage (29 v) to various levels. On some voltage forms, further regulation is provided to meet the power requirements of the camera circuitry. Power on-off switching of the regulated and unregulated buses is also provided to supply regular bus voltages to some of the circuits. A separately controllable power switch supplies power to the vidicon faceplate heater to allow independent heater operation.

The basic circuit of the dc-to-dc converter (Fig. 9) consists of two switching transistors, Q_1 and Q_2, and a saturable core transformer, T_1. The circuit is designed such that oscillations do not occur normally. Both Q_1 and Q_2 are cut off and no power is supplied to the camera. A "camera on" command pulse is fed into the transistor bases, initiating the switching action. A negative voltage is generated in Secondary N_6, which saturates the PNP transistor, Q_3, to provide a return path for the base current of the switching transistors and maintain the oscillations. Power turnoff is achieved by applying a positive command pulse to the base of Q_3 to cut it off and stop the oscillations. The various voltages are obtained by secondary windings and full wave rectifiers. These voltages feed regulator circuits, camera circuits, and Power Switches Q_4 and Q_5, which turn on power directly from the 29 v and 22 v bus, respectively.

Two types of regulators are used in the television power supply. The first type (common) feeds power to

CONFIDENTIAL

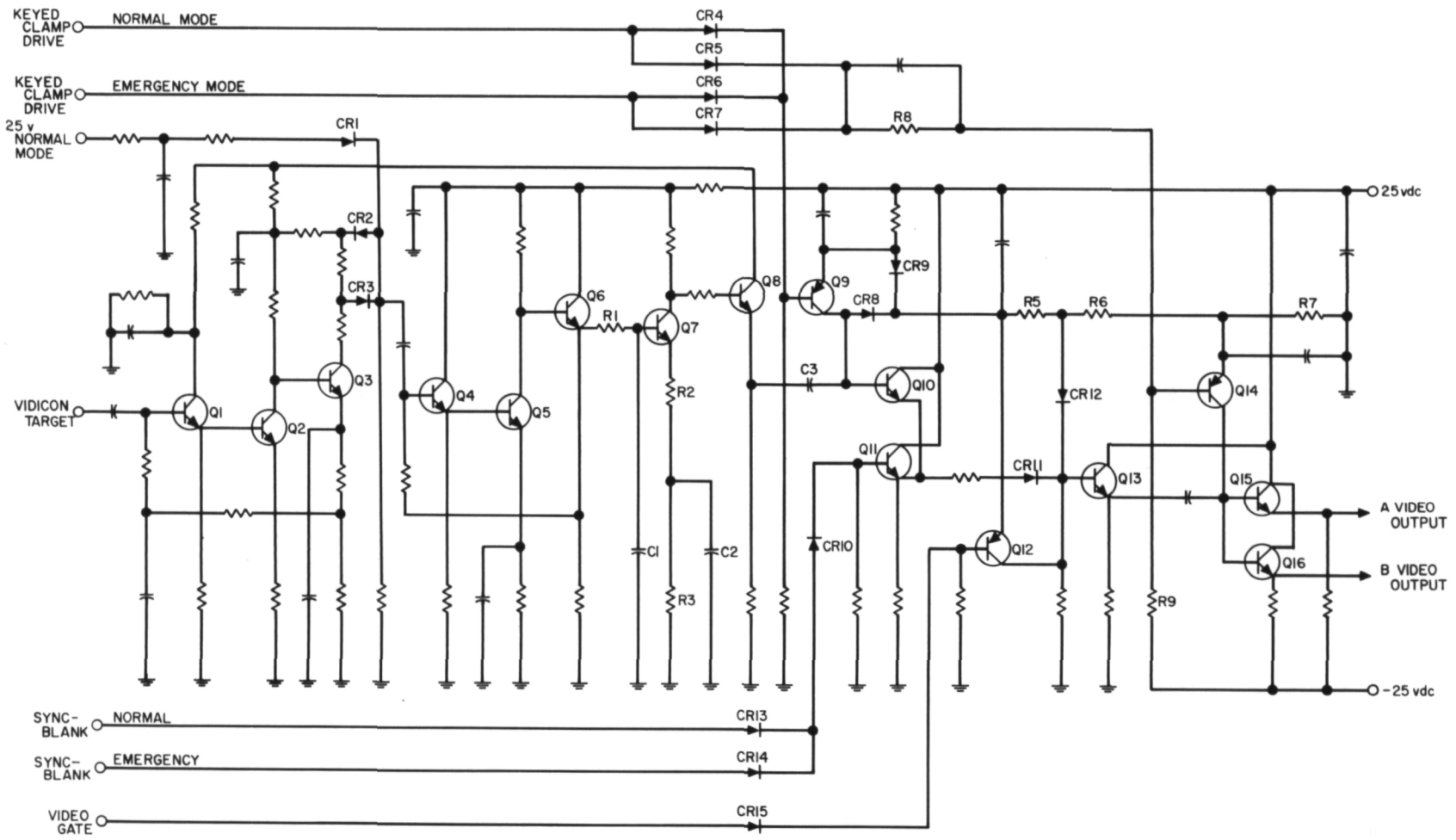

Fig. 7. Video amplifier

CONFIDENTIAL

CONFIDENTIAL

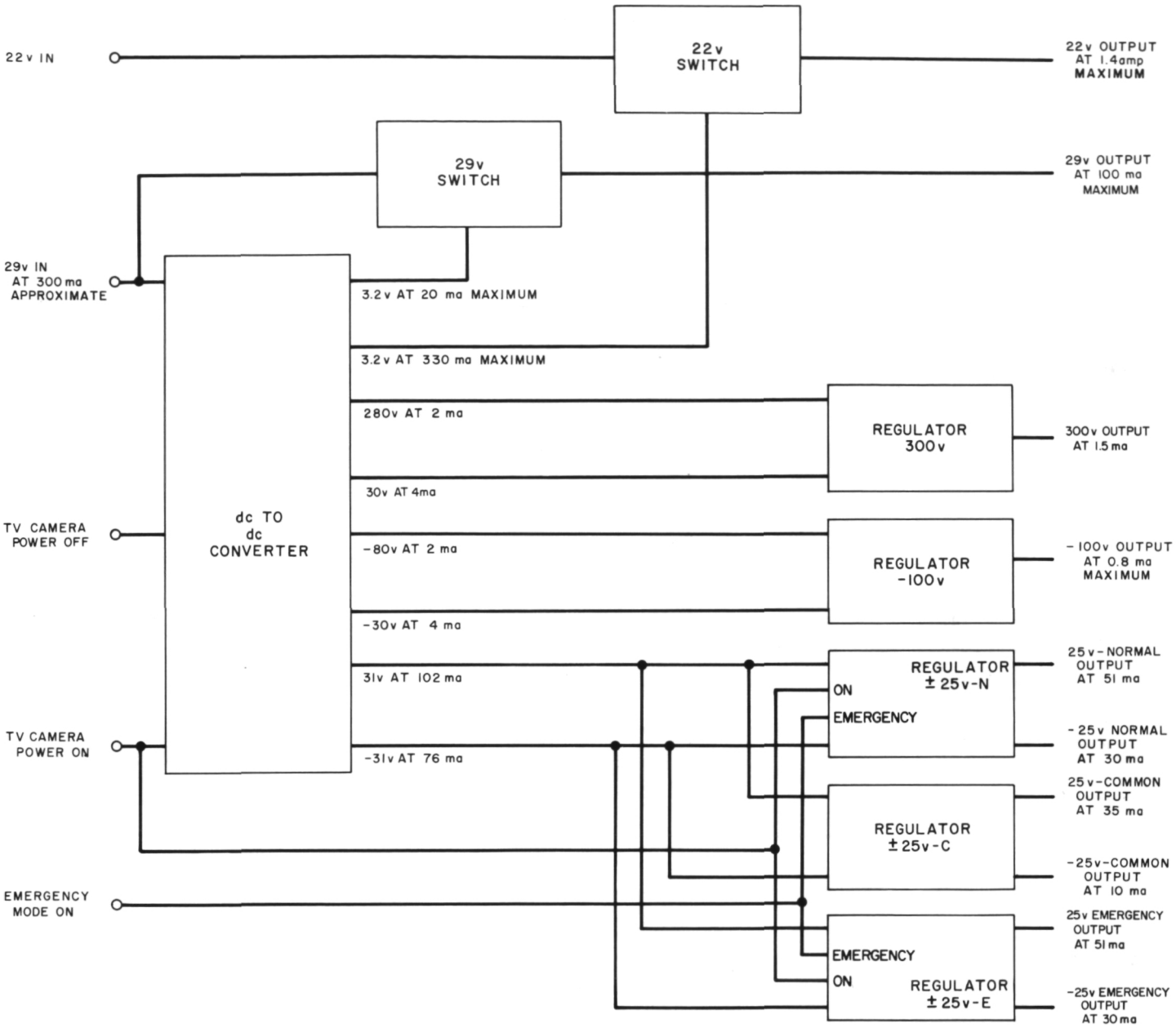

Fig. 8. Camera power supply

the circuits in the camera that operate in both camera modes and are standard series type regulators. Figure 10 shows the regulator circuit for the ±25 v common supply. A high voltage regulator is shown in Figure 11. This configuration, used in the 300 v and −100 v supplies, is fed from two secondaries, a high voltage and a 30 v output. Series regulation is applied to the 30 v output to allow the use of low voltage components.

The power to the circuits peculiar to either the normal or emergency mode of camera operation is supplied through regulators with on-off capability. Figure 12 shows the circuit of the ±25 v regulator for the normal mode. The emergency mode regulator is identical except for a reversal in the connections for the input command pulses. When camera power is turned on, transistors Q_6 and Q_7 remain cut off, and no current is fed to the bases of Q_8 and Q_9 unless the camera-on pulse also is applied to the base of Q_8, as is done in the normal mode regulator through Resistors R_{15} and CR_{25}. The pulse is sufficient to cause the series transistor, Q_6, to turn on and supply output voltage. The circuit is latched by current

CONFIDENTIAL

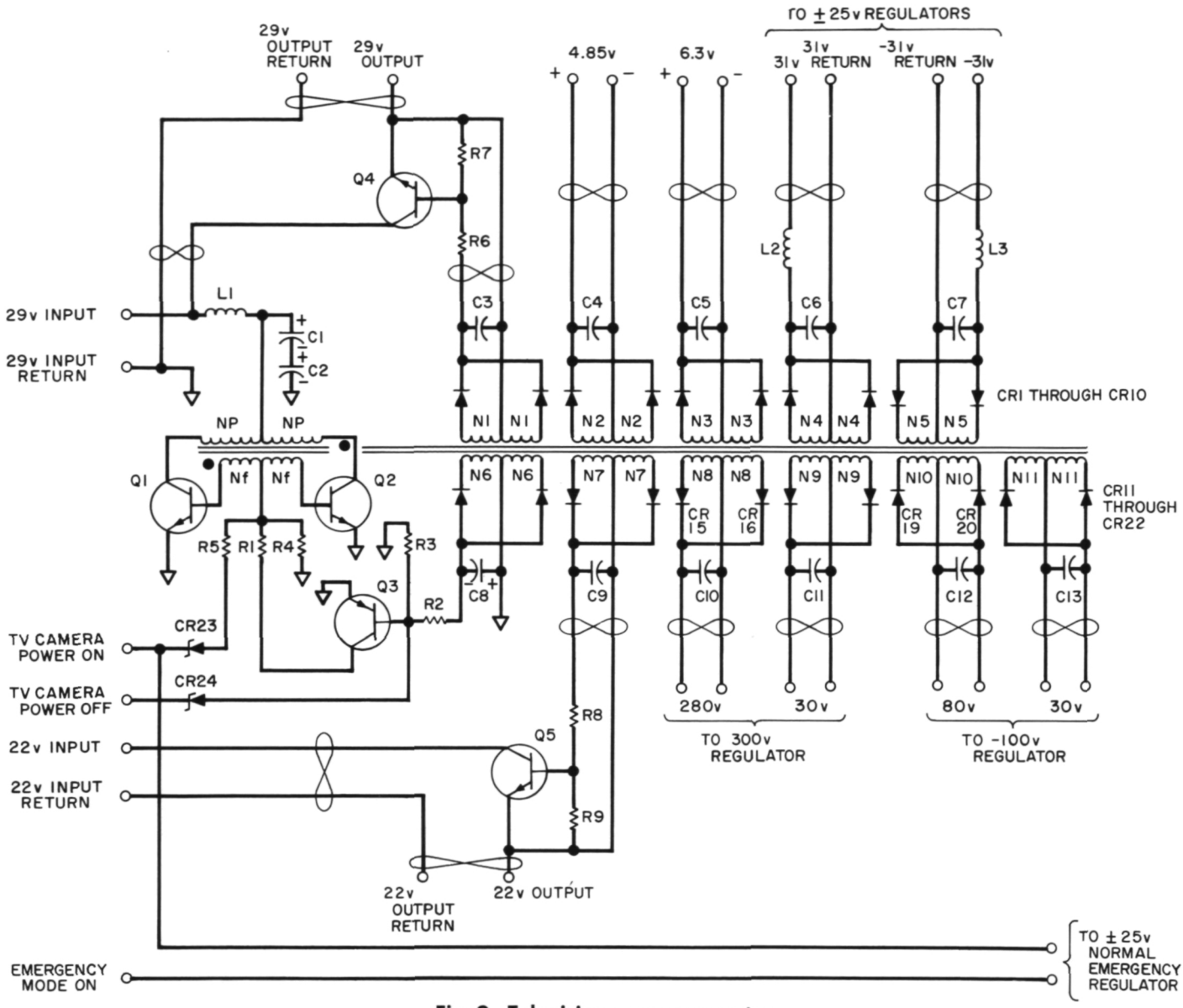

Fig. 9. Television power converter

supplied through R_{11} and R_{14} from the output and operates as a normal series regulator. Thus the camera-on command turns on the camera in the normal mode. When emergency mode is desired, a command pulse is fed through R_{17} and CR_{26} to saturate Transistor Q_{10}. This cuts off Q_8, Q_7 and Q_6 and causes the regulator to latch in the OFF state. The opposite occurs in the emergency mode regulator. It stays in the OFF state when camera power is turned on and switches to the ON state when the emergency mode ON pulse occurs.

3. *Tape Recorder*

Development and manufacture of the tape recorder is under subcontract to the Data Recorders Division of Consolidated Electrodynamics Corporation (CEC). The tape recorder is to be capable of recording and reproducing data, on command, during two operational phases of the spaceraft. During the boost and landing phases, engineering data will be recorded on seven analog channels (5 to 1000 cps); both record and reproduce will be at 20 in/sec. For lunar surface operation, up to 18 hr recording time is provided at 1/3 in/sec. Playback is at 20 in/sec. Three analog channels covering the range 1/60 to 5 cps and one analog channel for the range 1/20 to 20 cps are provided for recording the high frequency output of the seismograph instrument. Two digital channels (NRZ) are provided for recording time-shared data

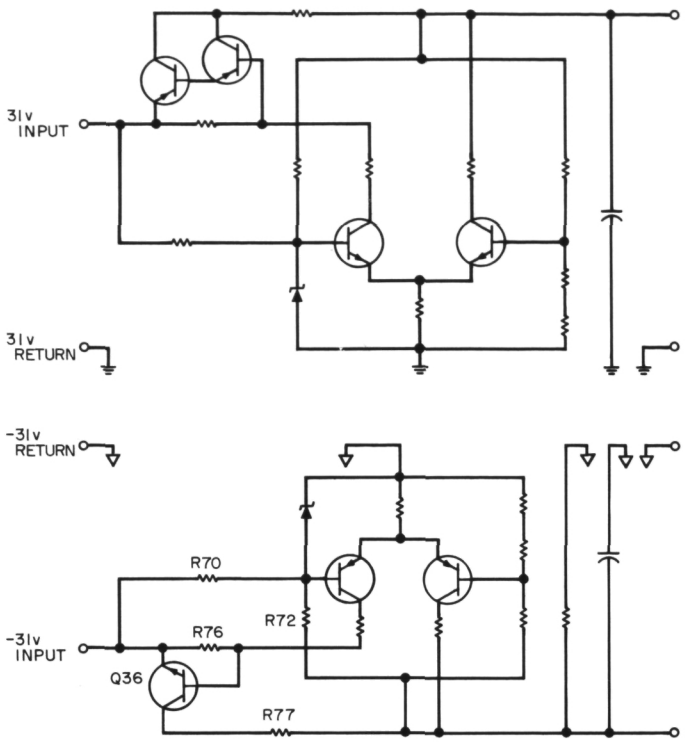

Fig. 10. ±25 volt common regulator

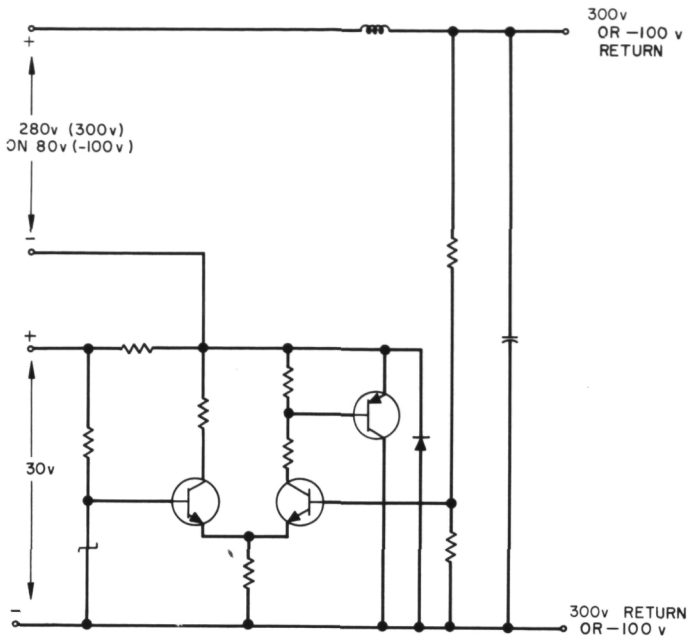

Fig. 11. High voltage regulator

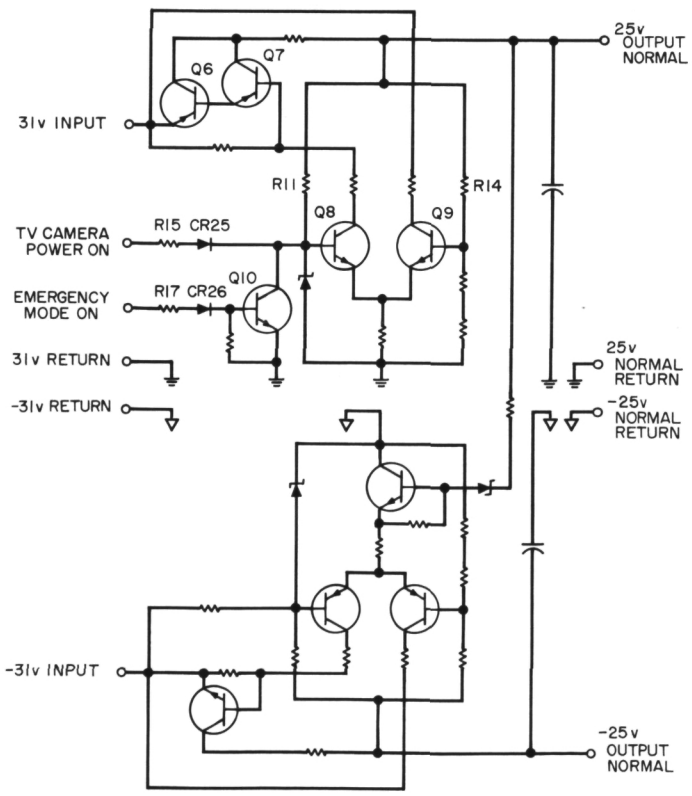

Fig. 12. Normal mode ±25 volt regulator

from the plasma probe, the very low frequency seismometer (tide) date, and the magnetometer.

The level of CEC effort has been reduced during this period, in accordance with rescheduling of delivery of prototype hardware for the A-21 spacecraft and funding limitations. Effort has been limited to tasks required to complete basic development and prepare the manufacturing drawings which later will be used for fabrication of prototype and flight hardware.

a. Electronic development. Development of circuitry for the tape recorder is essentially complete. Thus packaging effort can proceed in parallel with system testing, particularly tests of performance over the expected temperature range.

Redesign of the capstan motor servo amplifier to achieve the desired low power dissipation of 15 mw has been completed. This improvement, together with improvements in the control circuitry for commanding the various modes of operation, has resulted in reducing the power required during lunar record to less than 600 mw.

The major effort has been in the completion of circuit layouts in "stick" (Fig. 13) and module forms for the record amplifier, reproduce amplifier, control circuits, and capstan motor servo amplifier. Each of these circuits has been built in typical prototype form. In final packaging, the sticks are assembled into larger modules corre-

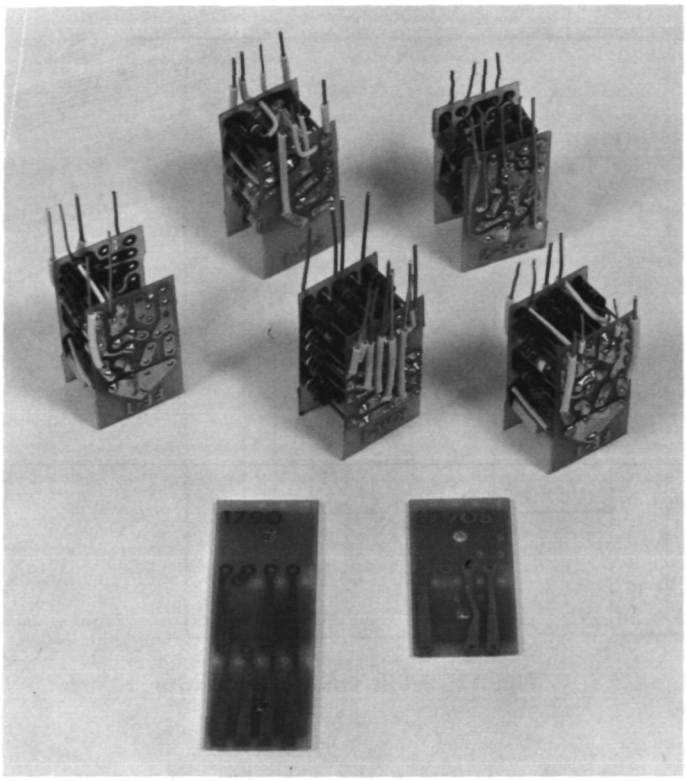

Fig. 13. Control circuit stick modules

sponding to the seven channels of the tape recorder. Building and testing of these circuits in stock form has provided a check of art work and drawings which will be used for etched circuitry fabrication and assembly. One module of each typical circuit has been completed, and these modules are being subjected to bench and temperature testing.

A special test fixture has been built for testing the stick circuits of the record amplifiers, reproduce amplifiers, and control circuits as complete channels (Fig. 14). This fixture allows plugging in portions of the circuit (sticks). Similar fixtures will be used in quality control for testing of prototype and flight hardware assemblies prior to assembly into module form.

Temperature tests to date indicate that there will be no problem in obtaining satisfactory operation over the temperature range of 0 to 130°F (ambient) which will be experienced in the thermally controlled compartment of the spacecraft. For verification of design margin, circuit performance is being checked to 160°F.

Electrical tests have been completed on magnetic recording heads which had been subjected to temperature cycling simulating heat sterilization. These tests verify that heat sterilization will not damage the heads. All components in the recorder, except the tape, are now expected to survive heat sterilization.

b. Electromechanical development. A second breadboard of the electromechanical assembly (tape transport) has been built, more nearly resembling the final design configuration. The new breadboard incorporates an improved clutch and machined parts simulating castings. This assembly has been tested, together with the electronics of the first breadboard, and the problem of excessive flutter which was experienced with the first breadboard appears to have been considerably reduced. The result has been improvement in signal-to-noise ratio; a ratio of 52 db (peak-to-peak signal to rms noise) was obtained for the lunar mode seismometer analog channels.

Mechanical design and drawing of the tape transport have been completed. Casting and machine drawings for the base casting, transmission housing, reel hub, and transport deck have also been completed and sample (check) castings have been obtained and machined (Fig. 15). Work has begun on assembly drawings of the tape transport.

Design of the "mother board," which will accommodate the various electronic modules, is essentially complete. A multilayer etched circuit laminated board (epoxy resin impregnated glass) will be used for the "mother board." The container and proposed seal designs have been completed and leak checked. The proposed seal, an epoxy adhesive, has yet to be checked in a thermal-vacuum environment. All mechanical drawings are now ready for checking. A preliminary release has been made

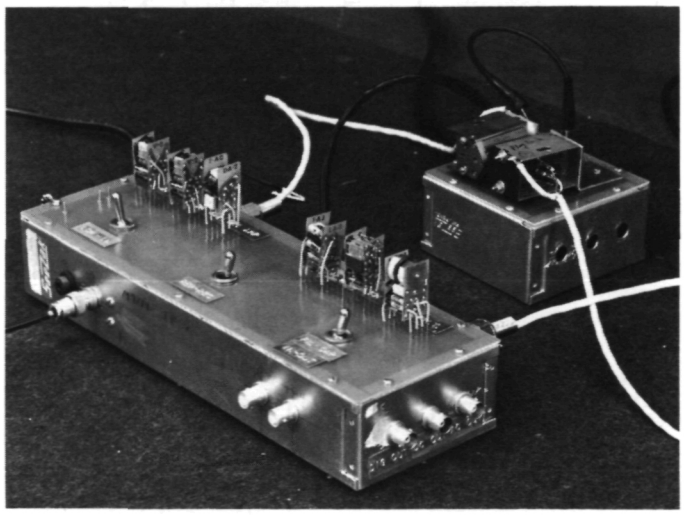

Fig. 14. Stick module test fixture

for planning purposes, particularly for fabrication tooling planning.

c. Reliability. A reliability estimation based on the final circuit design has been completed. This report gives the following predictions of reliability:

(1) The probability that the recorder will complete two cycles of boost and landing operation and 28 cycles of lunar operation has been computed to be 98.29%.

(2) The probability that the recorder will complete two cycles of boost and landing operation and 84 cycles of lunar operation has been computed to be 92.31%.

Qualification of all critical components has been completed with the exception of the motor, clutch, and magnetic recording heads.

d. Tape recorder auxiliary. The tape recorder auxiliary is used to couple the tape recorder to the rest of the telecommunication system. The circuits in the auxiliary can be classified in four major functions: (1) command decoding, (2) processing, (3) electrical conversion, and (4) engineering data timing system. A block diagram of the auxiliary is shown in Figure 16.

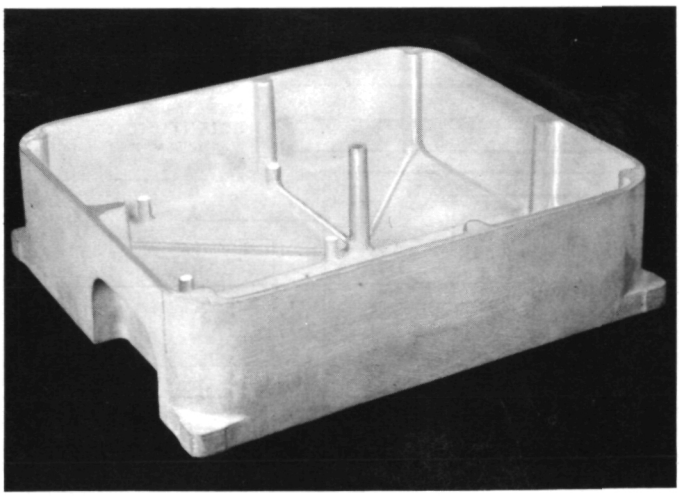

(a) Container base casting

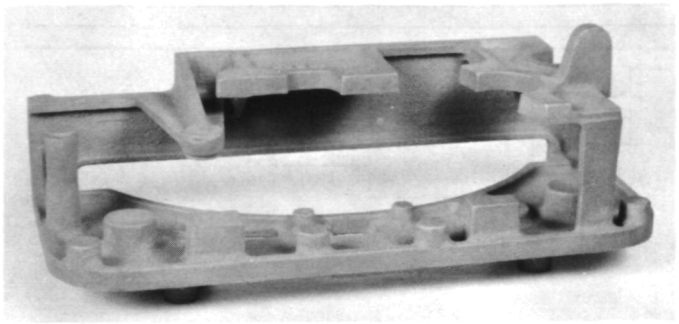

(b) Transmission housing casting

Fig. 15. Sample tape recorder castings

The command decoder is the standard subsystem decoder used throughout the spacecraft system. Thirteen channels are provided. Some commands are used internally in the auxiliary to turn on and off power switches and electrical conversion units. Several commands feed directly to the tape recorder to switch it to the proper mode of operation.

The signal processing circuits process the outputs of the reproduce amplifiers in the tape recorder during playback of recorded data. These output signals are fed to subcarrier oscillators whose outputs are then summed and fed to the central signal processor. During the transit phase of the mission, seven channels of analog data are recorded. The data are played back through seven of the subcarrier oscillators, which are turned on by Power Switches 2 and 3. The center frequencies of these channels are 33, 52.5, 70, 90, 110, 130, and 150 kc. The outputs of the seven subcarrier oscillators are combined in the engineering data summing amplifier and fed to the phase modulation summing amplifiers in the central signal processor.

For lunar operation of the tape recorder, four channels of analog and two channels of digital data are recorded. During playback, the analog data are transmitted through the same subcarrier oscillator as the first four used for the transit analog data (33, 52.5, 70, and 90 kc). Power Switch 3 again turns these four oscillators on. Two different subcarrier oscillators, turned on by Power Switch 1, are used to handle the digital data. These operate at center frequencies of 185 and 130 kc. The six lunar mode subcarrier signals are combined in the scientific data summing amplifier and fed to the frequency modulation summing amplifiers in the central signal processor. The electrical conversion portion of the auxiliary provides the proper voltage forms to the tape recorder and to the timing system in the auxiliary. The electrical conversion units are of the general basic configuration used throughout the spacecraft.

The timing system (Fig. 17) is used to control the recording of engineering data when the DSIF stations are not available for transmission of commands to the spacecraft. The data are recorded only periodically since the engineering signal processor requires a significant amount of operating power.

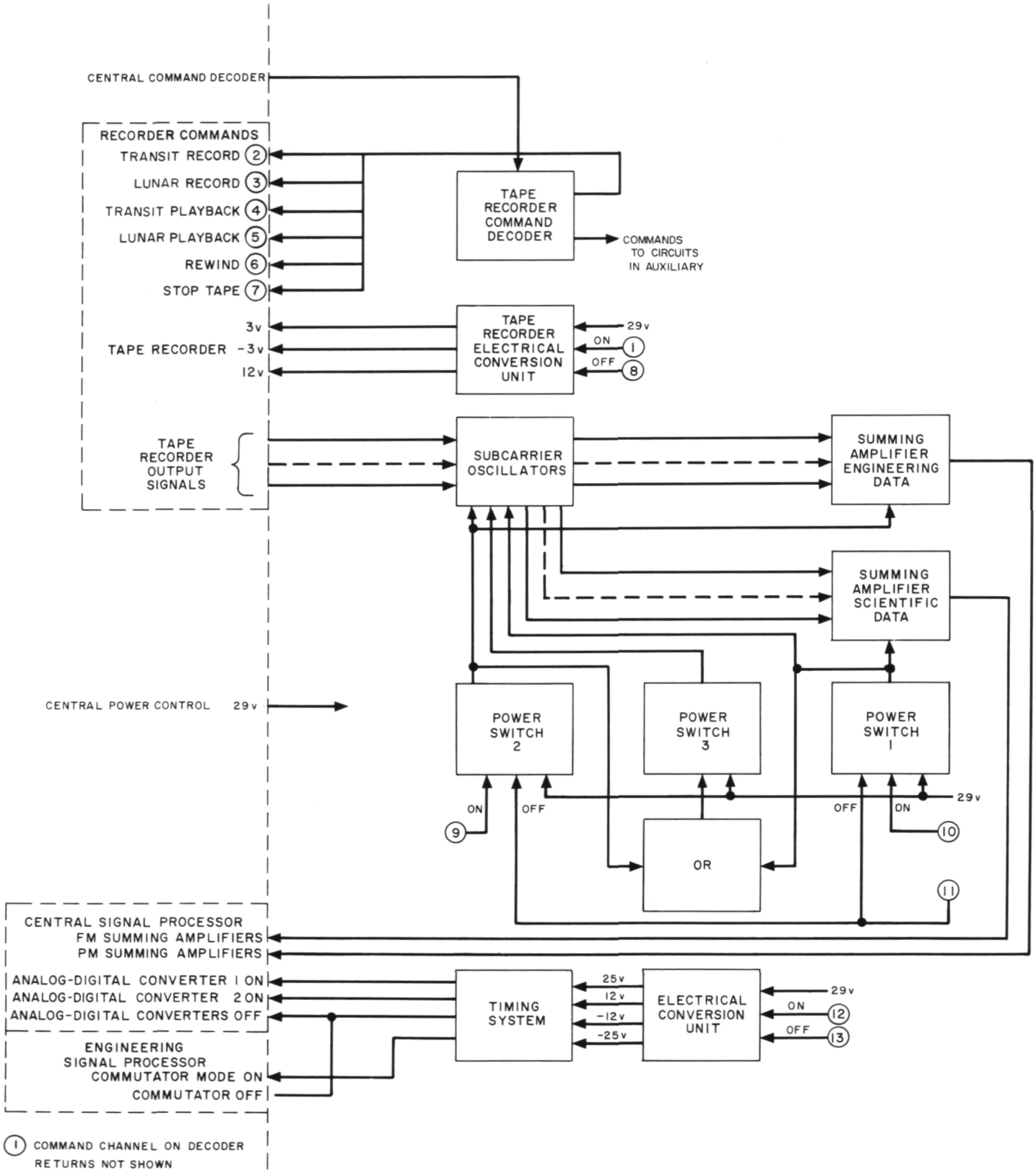

Fig. 16. Tape recorder auxiliary

At the start of the sequence, Pulse 1 turns on Analog-to-Digital Converter 1 in the central signal processor; ½ min later Pulse 2 is fed to the engineering signal processor to turn on the engineering commutator and set it in Mode 1. At 1-min intervals, Pulses 3, 4, and 5 sequence the commutator through its three other modes. Pulse 6 finally turns off the engineering commutator and the analog-to-digital converter. The next series of events occurs 59.5 min later. Operation is identical to the previous sequence except that Pulse 7 turns on Analog-to-Digital Converter 2. Thus the recording of engineering data occurs every 64 min. A different analog-to-digital converter is used on alternate recordings, so that a failure of one converter causes only a reduction of the amount of data.

The timing system and summing amplifier breadboards are currently undergoing temperature environmental testing. When these tests are completed, the breadboards will be used for subsystem integration with the remainder of the telecommunication system. Subcarrier oscillators are being developed by a subcontractor and have not yet been delivered. The tape recorder auxiliary circuitry has been released for layout and fabrication.

4. Subsurface Density

The signal processing circuitry for the subsurface density is shown in Figure 18. The circuits process the signals received from the density sensor, a Geiger-Mueller (G-M) tube, located in the subsurface geophysical probe. An operation type amplifier, Q_1 and Q_2, receives the discharge pulses from the G-M tube. This type of amplifier is used to minimize the effect of the capacitance in the long cable between the G-M tube and the processing circuits. The output pulses from the operational amplifier feed a trigger amplifier, Q_3, which provides trigger pulses to a bistable multivibrator consisting of Transistors Q_4 and Q_5. The multivibrator output is fed through a low-pass filter and modulates a subcarrier

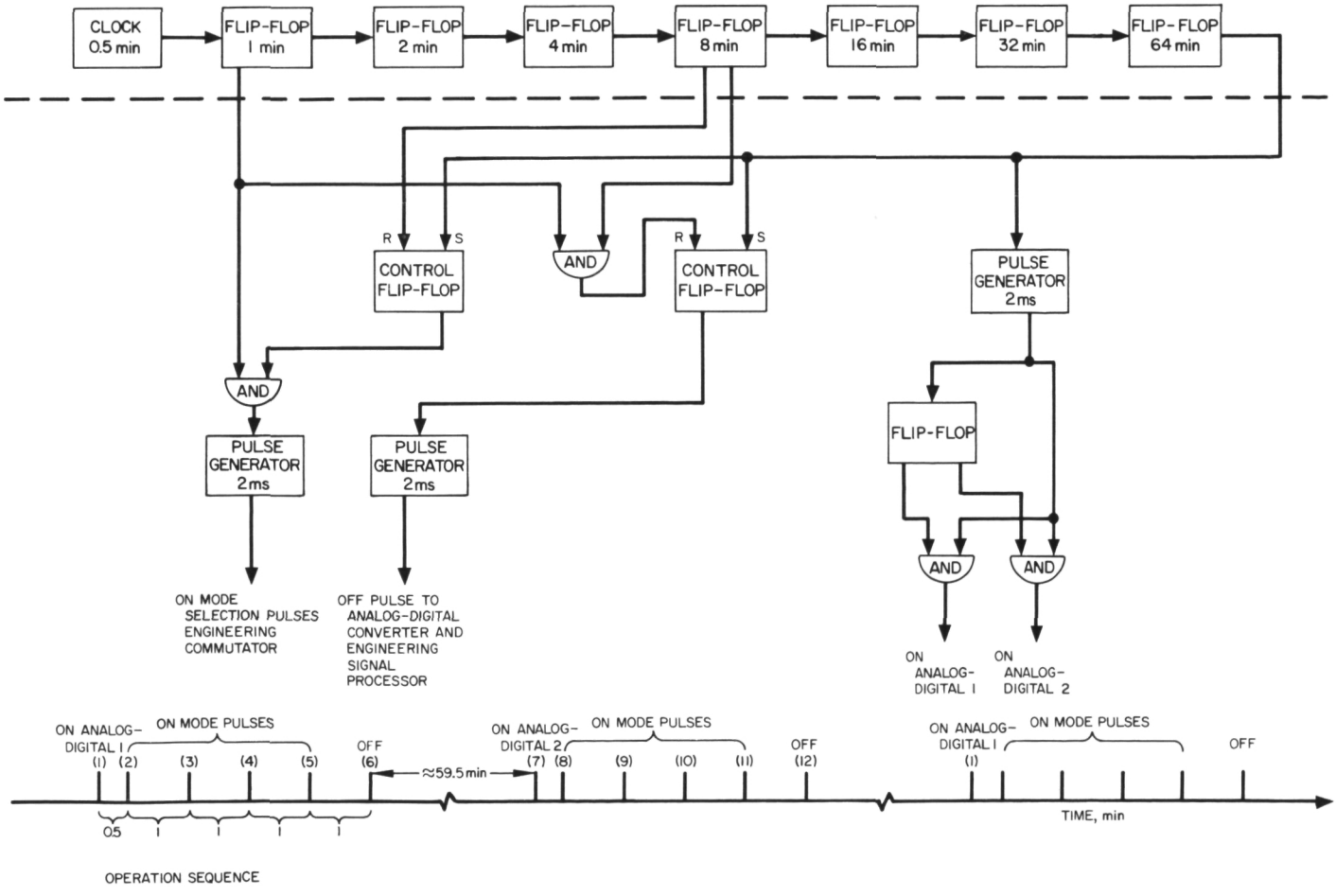

Fig. 17. Timing system and operation sequence

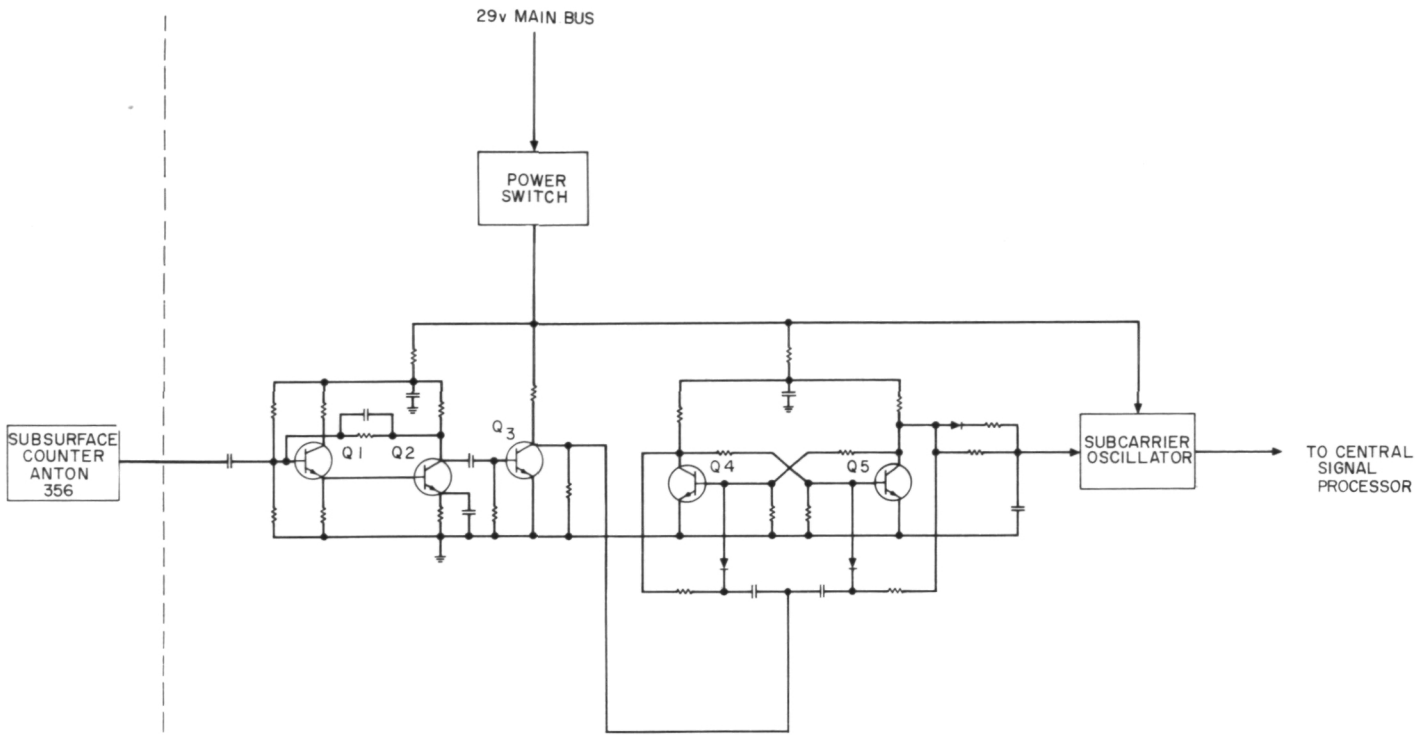

Fig. 18. Subsurface density signal processing

oscillator. The subcarrier signal is routed to the central signal processor for combination with other subcarriers in the spacecraft system.

The density signal processing circuits have been released for layout and fabrication. Tests have been conducted of the breadboard circuits with a sample Anton 356 Geiger-Mueller tube provided by JPL. These tests have indicated satisfactory performance. The breadboard was capable of responding to counting rates over three times the maximum required for the experiment.

5. Subsurface Thermal Diffusivity

The signals from the subsurface thermal diffusivity experiment are derived from a differential thermocouple. In order to process the extremely low level signals, a dc amplifier has been designed which uses a low noise mechanical chopper (Fig. 19). The range of input signal level is 0 to 5 mv. Drift requirements are ± 25 μv referred to the input. The breadboard model of the amplifier has been tested over the environmental temperature range and exhibits less than 5 μv drift. A preliminary release of the circuit has been made for product engineering.

6. X-Ray Diffractometer

The vendor, Philips Space Development, recently delivered the first operating prototype of the X-ray diffractometer (Fig. 20) to JPL. Hughes has also recently assisted JPL and Philips in planning modifications to the X-ray diffractometer. Some of the planned modifications are as follows:

(1) Redesign of X-ray tube

(2) Replacement of the geiger counter with a side window proportional counter

(3) Redesign of the internal wiring

(4) Reduction in the size of the X-ray diffractometer head

(5) Redesign of the sample holder

(6) Redesign of the dust cover door

(7) Redesign of the goniometer assembly

(8) Repackaging of the Compartment B electronics

(9) Redesign of the 25 kv high voltage power supply

7. X-Ray Spectrometer

The primary effort in this reporting period has been technical assistance to JPL in defining requirements for

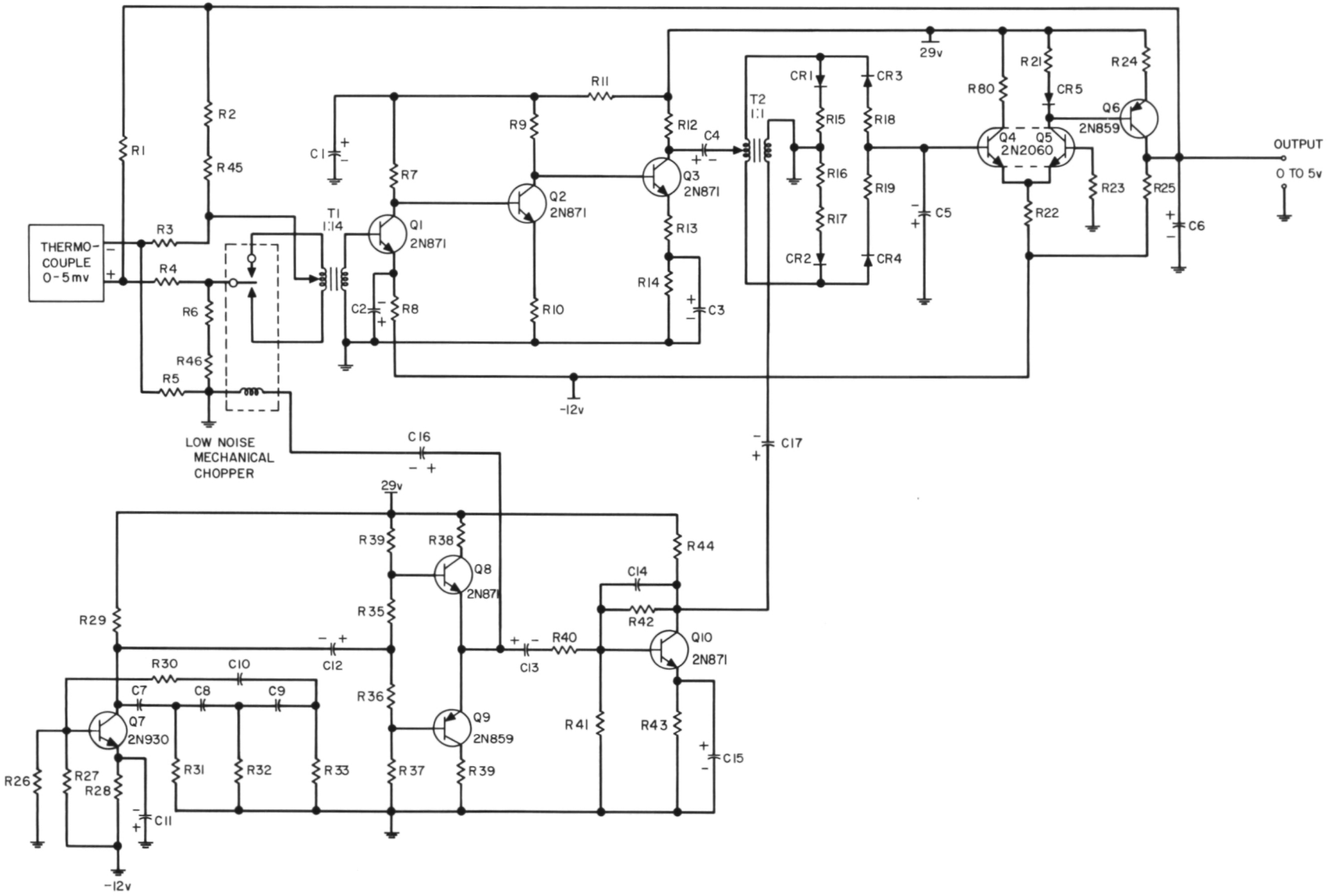

Fig. 19. DC amplifier for subsurface thermal diffusivity experiment

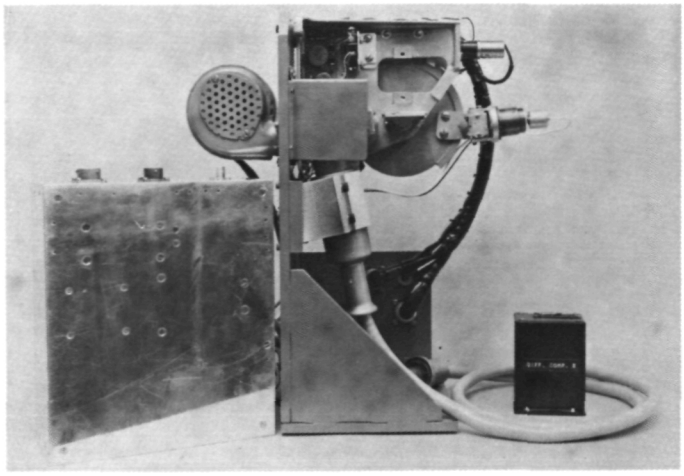

Fig. 20. X-ray diffractometer

the instrument modification programs to be conducted by Philips Space Development. Typical among the modifications definitized as a result of the joint Hughes/JPL/Philips effort are the following:

(1) Redesign of the proportional counter amplifier circuits

(2) Repackaging of the electronics

(3) Addition of three temperature sensors

(4) Addition of high voltage adjustment for the geiger counter tubes

(5) Redesign of the internal wiring

(6) Provision of capability for electrical-optical plug-in assembly in the spectrometer head

(7) Redesign of the electron gun

(8) Formation of Compartment B spectrometer package containing the instrument electronics and pulse-height analyzer

(9) Redesign of the 25 kv high voltage power supply

It is expected that these modifications, when completed, will result in a reduction in weight and volume and an improvement in reliability.

8. Gas Chromatograph

Preliminary negotiations have been completed to establish current mounting requirements for the gas chromatograph and X-ray instruments. The redesign, which will be compatible with the new instrument configurations, is expected to result in the following system improvements:

(1) Reduction in weight

(2) Improvement in the ease of instrument removal

(3) Reduction of instrument thermal interaction

(4) Improvement in the ease of alignment with the sample transport system

(5) Allowance for removal of the soil analysis group as a cluster

Studies to determine materials best suited for applications in the chromatograph have continued at Hughes. Most materials reviewed were considered acceptable; however, irradiated polyethylene and silicone rubber were considered unacceptable because of severe outgassing. A study is in progress to determine the elastomer that is best suited for use in seals. Tests of materials in static and dynamic sealing applications are being conducted at low pressure (10^{-9} mm Hg) and low temperature. The lowest temperature at which a dynamic seal is still effective will determine the minimum operating temperature for the instrument.

9. Geophysical Instruments

Considerable emphasis during this report period has been placed on items applicable to the A-21 spacecraft – the surface temperature instrument and the subsurface logging sonde. Difficulties in the development of the subsurface magnetic susceptibility sensor, located in the sonde, has led to a series of detailed investigations of this portion of the system.

During April, an error analysis of the data processing portion of the subsurface magnetic susceptibility experiment was completed. This study revealed that the proposed instrument auxiliary equipment could process instrument outputs over the range of 250×10^{-6} to $200{,}000 \times 10^{-6}$ cgs units to within the desired $\pm 10\%$ of the reading. In the range 10×10^{-6} to 250×10^{-6} cgs units, an accuracy of approximately ± 30 cgs units could be assured, as compared to the desired ± 25 cgs units.

Subsequent to these findings, an evaluation was made of the instrument sensor, which is located in the subsurface logging sonde. Data based on prototype units P-1 and P-2 indicated an extreme sensitivity of the sensor to changes in temperature. Preliminary laboratory tests and a review of this problem by JPL and Hughes at the instrument vendor (Texaco Experiment Incorporated) showed that the most probable cause was a change in coil resistance with a change of temperature. Minor dimensional changes in the coil forms of the sensor were

expected to have much less effect on the temperature sensitivity. Based on these findings, it was determined that a change in the instrument-spacecraft interface, allowing the vendor to incorporate the nulling coils as a part of the sensor design, would allow a potential partial solution to the problem (Fig. 21).

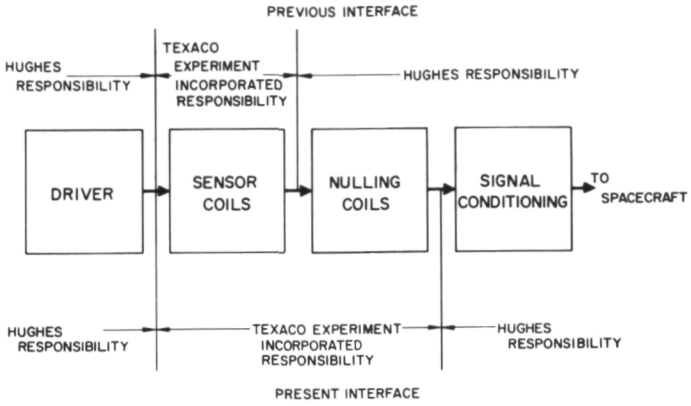

Fig. 21. Hughes/Texaco interface change for subsurface magnetic susceptibility experiment

Preliminary tests conducted at Hughes on KRS-5 indicate that this material is probably not suitable for use, as previously planned, in the interferometer spectrometer. Samples of the material subjected to vacuum and ultraviolet light levels expected on the Moon resulted in both excessive sublimation rates and reduction in IR transmissibility. A special test plan on suitable treatments or substitute materials has been negotiated with JPL, and work is progressing.

Recent meetings with Texaco Experiment Incorporated have produced nearly complete interconnections data for the surface temperature instrument and the subsurface logging sonde. It is expected that payload interconnections data and signal lists will be completed during the next report period.

Within the last month, the first power allocations document for the spacecraft and its payload has been prepared. This document, a summary of all unit power requirements, will serve as the basis for a second document listing power and thermal rates versus payload and/or spacecraft function being performed. It is intended that these two documents will serve as constraints on the ultimate determination of payload power management and its effect on such problems as night survival, operational sequences, etc.

Payload instrument auxiliaries are currently under review to assure that redesign required to accommodate payload modifications in the future will be minimized. In addition, interchangeability of auxiliaries and/or instruments is being reviewed. This review has revealed that the present design of the interferometer spectrometer, either in the sonde or surface temperature instrument, does not allow sensors or their associated electronics to be interchanged. Similarly it is expected that a change of the subsurface logging sonde would require a change of the electronics auxiliary associated with the subsurface density experiment. In addition, it is suspected that the magnetic susceptibility sensor and electronics auxiliary are mated. Work will continue in all of these areas and their effect on systems testing, mission operations, and spares requirements will be reviewed.

In April, Hughes received JPL authorization for the type approval testing and subsequent procurement of the geophysical instruments. Units that will be subjected to type approval tests are those which were developed and procured through JPL contracts. Negotiations to definitize the test program and associated specifications are currently in progress with JPL, Texaco, and General Motors. It is anticipated that Hughes will let subcontracts for T-21 prototype instruments during August.

10. Seismograph

Hughes has recently assisted in the completion of functional tests on the first operational prototype seismograph (Fig. 22). Further evaluation tests at Lamont Geological Observatory are continuing.

Future prototypes, though functionally similar, will be redesigned to reduce weight and increase reliability. Assistance to JPL and the vendor in planning and executing this modification program has already begun.

11. Radiation Detection Experiment

The radiation detection experiment has been redefined to include a Geiger-Mueller counter assembly in addition to the previously existing ionization chamber. As anticipated, thermal control and data processing are the principal problems in integrating this new device into the spacecraft. Presently, the G-M tube requires approximately 1 w of heater power to maintain it in an operating temperature range (above −50°C) throughout the lunar night. This energy represents the equivalent of approximately 7 lb of storage battery capacity. In order to minimize the disturbance to the remainder of the data processing system, it is desirable that the G-M counter time share the same subcarrier oscillator as the ionization chamber. Doing so results in a requirement for a 22-stage register, read out once per minute, along with a coded time signal.

A contract for the design and development of the ionization chamber, the other half of the radiation detection experiment, has been awarded to Electro-Optical Systems of Pasadena, scheduled to produce a total of five prototype chambers. The preliminary design of the unit is essentially complete including the development of the thermal control design, which was of particular concern in minimizing the nighttime heating power requirements. The first of the prototypes is scheduled for delivery on July 27, 1962.

12. Lunar Atmosphere Gauge

The lunar atmosphere gauge, which is designed to measure the total atmospheric pressure near the surface of the Moon, consists essentially of a modified Redhead gauge, power supply, and automatic scale switching electrometer. The equipment is currently being developed at the University of Michigan under the direction of Goddard Space Flight Center. Preliminary interface specifications have been completed and it is expected that final interface negotiations, including interconnections and outline and mounting drawings, will be completed during the next report period.

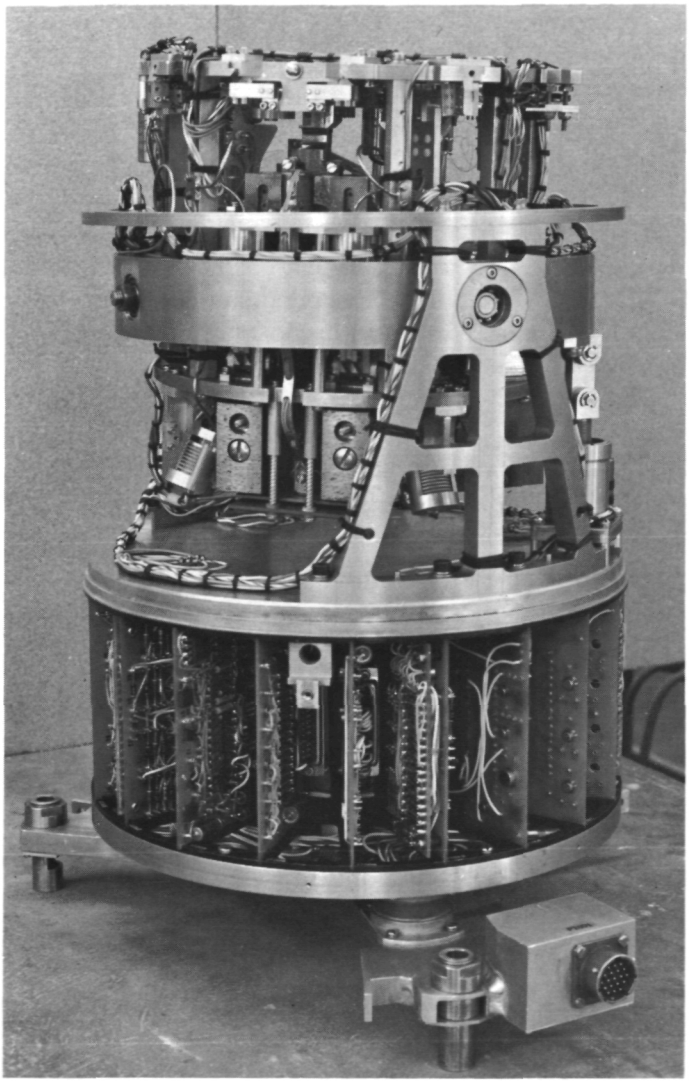

Fig. 22. Prototype seismograph with cover removed

13. Alpha Scattering Experiment

As part of the continuing effort to anticipate the introduction of advanced experiments into the *Surveyor* program, a study has been made of possible means for integrating an alpha scattering device into the existing system. A study which included an evaluation of the effects on mechanical, thermal, and signal processing design has shown that such an instrument can logically be introduced in one of three ways:

(1) Replacement of either the X-ray spectrometer or the X-ray diffractometer by the alpha scattering instrument

(2) Modification of the X-ray diffractometer, permitting the sample for the alpha scattering instrument to pass through the X-ray instrument

(3) Lengthening of the sample transport system, permitting the alpha scattering instrument to be interposed between the two X-ray machines

Preliminary studies reveal that processing of the data would require additional electronic auxiliary equipment in the spacecraft. Specifically, equipment would be necessary to scale down the expected 2200 bits/second to a rate more nearly compatible with the system design. Final results of these studies will be available near the end of this report period.

14. Mechanisms for Scientific Payload

a. TV mirror assemblies. The television mirror assemblies provide azimuth and elevation scanning capability for the television cameras. The time required for the mirror to move from its position during one picture exposure to its new position for taking the next picture becomes important in establishing the high speed, automatic TV survey. For that reason laboratory tests are being conducted to assure that the mechanical time constants of the system are satisfactorily short. Settling time tests have been completed on the TV mirror assemblies at ambient temperature and pressure. In the elevation axis, the time required for mirror vibrations to fall below an amplitude of ± 0.1 min arc is approximately

0.6 sec after initiation of a step command. This settling time is slightly less for a step in azimuth. An optical test fixture is being assembled for determining the mirror settling time in a vacuum environment.

During vibration testing of the developmental model, a structural failure occurred in one of the pivot support arms for the mirror (Fig. 23) with consequent failure of the azimuth drive gear (Fig. 24). The unit was being subjected to a 14.2 *g* lateral vibration in a direction parallel to the elevation pivot axis of the mirror. The failure occurred at an input frequency of approximately 100 cps and caused severe deformation of the dust cover hood. Prior to this failure, the unit had been subjected to the 14.2 *g* sinusoidal sweep vibration from 20 to 1500 cps in the thrust axis. The first sweep cycle had caused a dowel pin in the elevation drive unit to shear. The dowel pin arrangement was redesigned and the felt thickness at the mirror/hood interface was increased. After incorporation of these changes, the sweep vibration test was rerun and the unit performed satisfactorily.

The necessary design changes have been made to the support post structure arrangement and the unit is being repaired. The vibration and other mechanical environment tests will be repeated to assure reliability before proceeding with the thermal-vacuum tests.

A breadboard of the motor control logic circuitry has been built and tested for compatibility with the mirror drive motors. This logic circuitry will be used to drive the mirror assembly during thermal/vacuum testing.

A study has been made on the IR reflectivity from the lunar surface on the camera lens and vidicon through the mirror system. Two types of mirrors were compared; one made of beryllium with an aluminized front surface and the other made of quartz with a multilayer interference type coating. The temperature of the camera was calculated to be about 140° F assuming no additional heat reflected from the mirror assembly. The beryllium mirror with the vacuum-deposited aluminum surface increased the camera temperature approximately 20° F. The multilayer dichroic-coated quartz mirror contributed somewhat less to the temperature increase; however, weight tradeoffs, optical characteristics and state-of-the-art considerations favored the beryllium design. A mirror assembly temperature study was also conducted to determine if mounting of the interferometer spectrometer on the mirror assembly was still practical. As a result of the study, it was decided to retain the present installation of the instrument on the No. 3 TV mirror assembly.

b. Subsurface sampler. The subsurface sampler drills, a 1¼ in. hole in the lunar surface to a maximum depth

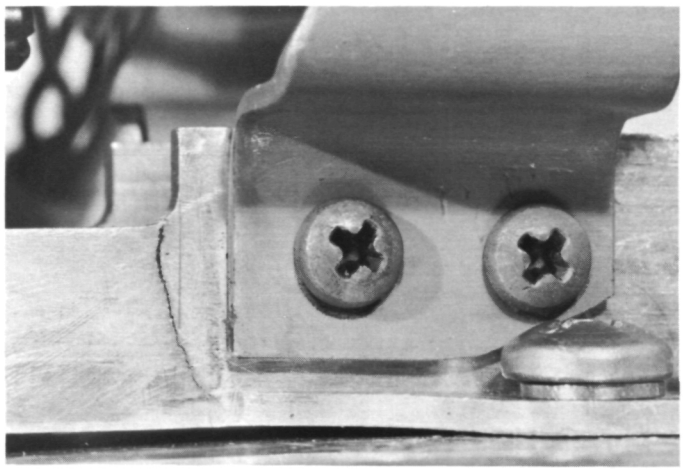

Fig. 23. Vibration-induced failure in mirror support arm

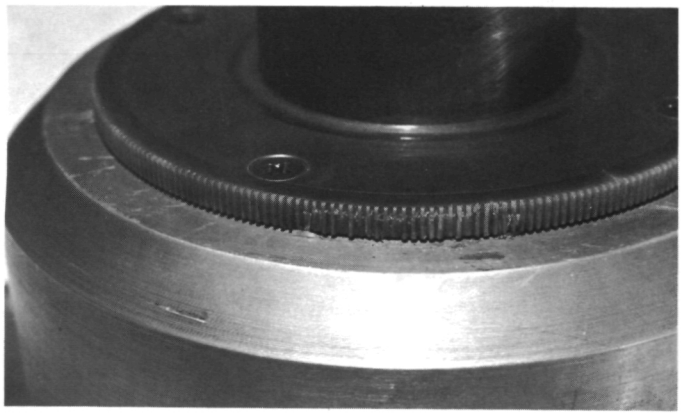

Fig. 24. Damage to azimuth drive gear from failure of mirror support arm

of 5 ft. It delivers selected samples to the sample analysis system and positions the subsurface geophysical probe in the drilled hole. The sampler comprises a drill head, drill shank, bit, sample dump mechanism, vertical drill feed, supporting structure, subsurface geophysical probe, lowering drive, and jettison device.

To reduce the weight of the subsurface sampler for the A-21 spacecraft, the general arrangement, supporting structure, and feed mechanisms have been redesigned (Fig. 25). The new weight, excluding wiring harness and subsurface geophysical probe, is 27.3 lb, compared to the previous design of 32.2 lb. The drill drive head and drill bit have not been changed. The center of gravity of the unit has been lowered 5 in. by locating the three feed motors with their associated gear boxes at the bottom of the drill assembly instead of at the top. The bottom guide plate bearing assembly has been combined

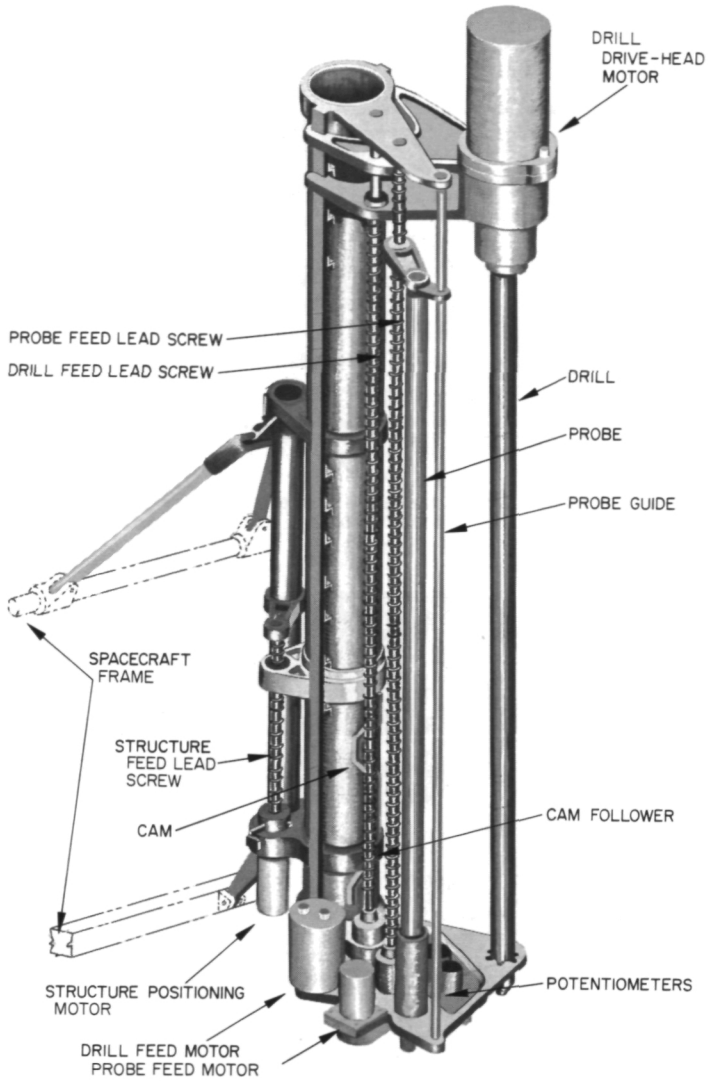

Fig. 25. Subsurface sampler for A-21 spacecraft

with a gear box housing common to both the drill and probe feed motors.

The split-movable guide track has been replaced by a continuous track. This change simplifies and permits safe operation of the subsurface sampler by reducing the number of operating commands from 29 to 9. The number of commands to drill from one subsurface level to the next has been decreased from 50 to 36. Figure 26 shows the interconnection of the motors, limit switches, and position potentiometers.

The drill feed screw and nut has been redesigned and has the following features: (1) the device is jam-proof by using teflon wool washers at both ends of the nut to wipe the threads free of dust ahead of the nut; (2) the nut is fabricated of a teflon-glass fiber material for low friction operation in a high vacuum; (3) the weight of the aluminum lead screw has been further decreased by matching the rectangular thread thickness and depth with the load characteristics of the nut; and (4) the screw is hard-anodized to prevent wear.

The previous breadboard drill drive head springs have averaged less than an hour of drilling life. The conical terminations tended to fracture near the attachment point at the end turn. The stress concentration at the end turn has been eliminated and the new spring assembly has been improved so that it is always under a compression load instead of the previous reversed load. The knowledge obtained from the breadboard drill drive head will be applied to the production drive head now being developed.

Tests to determine the optimum relation between drill rotation and impact hammer blows per minute have been completed. A second motor driving and controlling the drill bit rotation independently of the rate of impact hammer blows was installed on the breadboard drill head. Tests indicate that a drill speed of approximately 500 rpm for an impact rate of 2000 blows/min is optimum. This value is not critical, and the ratio of impact blows per minute to the drill rpm can be varied between 3 to 1 and 6 to 1 with less than a 15% variation in drilling rate.

The subsurface sampler drive head subcontract was awarded to Lear, Incorporated, Electro-Mechanical Division. Assembled within a single sealed case are the following: (1) 600-w, 16.8 to 22-v dc motor with integral radio interference filter; (2) dual gear box for driving the impact hammer crank and providing drill rotation; (3) 200 lb-in. torque limiting clutch in the drill rotation drive; and (4) free hammer resonant impact generating system with an anvil designed to couple to the drill shank.

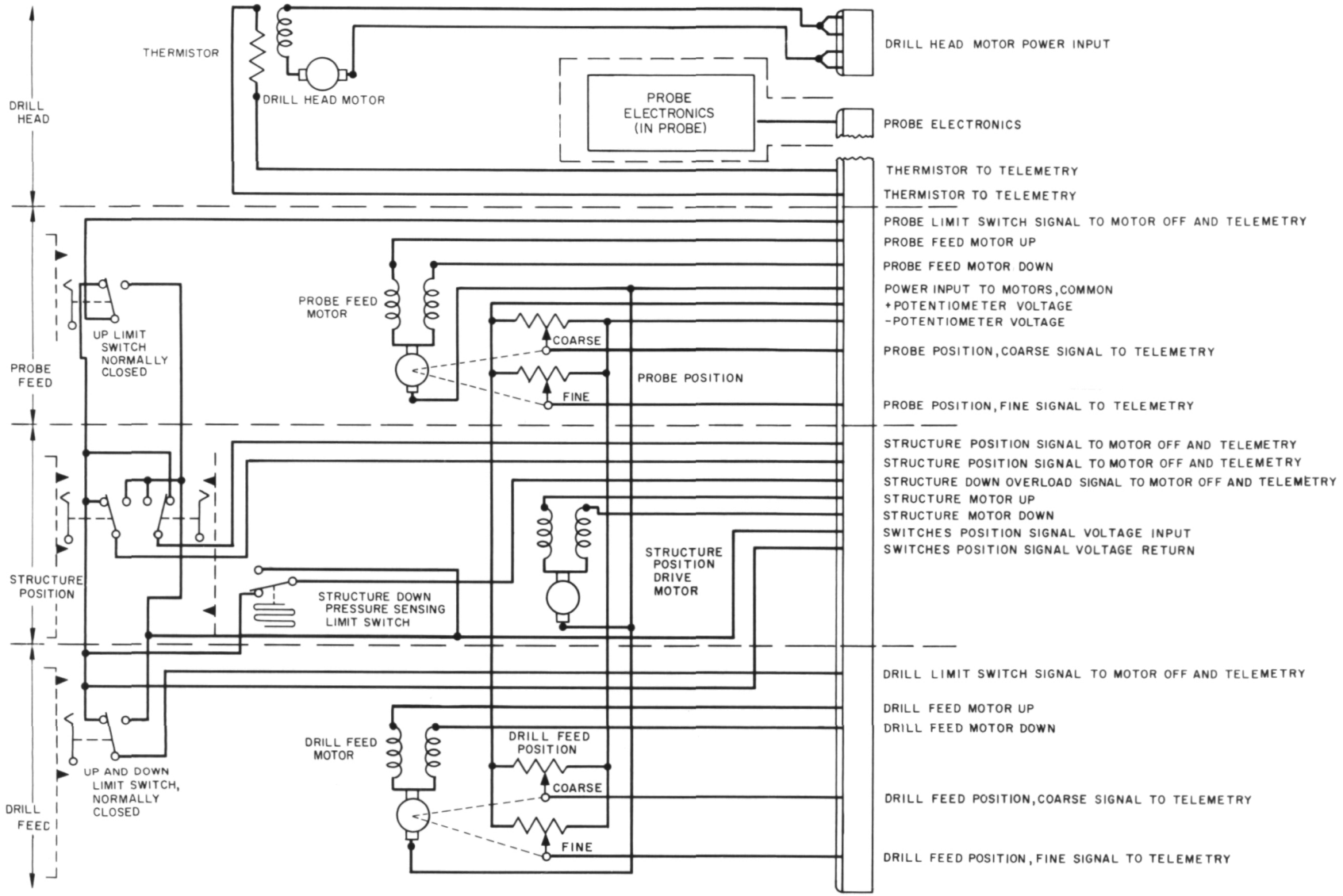

Fig. 26. Subsurface sampler interconnections

C. System Analysis

1. DSIF Acquisition Beamwidth Study

The beamwidth requirements for Deep Space Instrumentation Facility (DSIF) acquisition can be determined by dividing the injection-parameter dispersions into in-plane and crossrange components. The latter were discussed in Reference 1 with regard to acquisition at first visibility. Their effect at other points in the cone of visibility is of interest so that a suitable search policy may be initiated in those instances where acquisition is not achieved at the initial opportunity. The consequences of in-plane dispersions in the vicinity of the DSIF station can be determined from the dispersion in altitude.

Dispersions at the DSIF station are caused by two types of perturbations of the injection parameters. The first type results from injection errors not sensed by the vehicle guidance system. The second results from the fact that although the guidance system makes suitable velocity corrections to offset the effect at the Moon of recognized positional perturbations at injection, the displacement at the DSIF station will not, in general, be cancelled.

a. Altitude dispersions. The altitude dispersion in the vicinity of the DSIF station is obtained from the equation of the elliptic trajectory. The following notation is used:

r = radial distance from center of Earth

ν = true anomaly

E = eccentric anomaly

θ = central angle from injection to DSIF acquisition

V = vehicle velocity

h = vehicle altitude

a = semimajor axis of ellipse

e = eccentricity

μ = gravitational parameter = 3.9858×10^5 km^3/sec^2

It is assumed that injection occurs at perigee. Injection conditions are indicated by the subscript o, while non-subscripted variables refer to DSIF acquisition. The trajectory is described by:

$$r = a\,(1 - e\cos E)$$

Therefore,

$$\Delta h = \Delta r = (1 - e\cos E)\,\Delta a - a\cos E\,\Delta e + ae\sin E\,\Delta E \tag{1}$$

It can be shown that

$$\Delta a = 2a^2\left(\frac{\Delta r_o}{r_o^2} + \frac{V_o\,\Delta V_o}{\mu}\right) \tag{2}$$

and, for horizontal injection,

$$\Delta e = \frac{V_o}{\mu}\,(2r_o\,\Delta V_o + V_o\,\Delta r_o) \tag{3}$$

Also,

$$\Delta E = \sqrt{\frac{1-e}{1+e}}\;\frac{\cos^2\frac{E}{2}}{\cos^2\frac{\nu}{2}}\,\Delta\nu - \frac{\sin E}{1-e^2}\,\Delta e \tag{4}$$

$\Delta\nu$ has two components. The first results from perturbations of the radial velocity about its nominal value of 0. This component is given by:

$$\Delta\nu_1 = \Delta\nu_o = \sqrt{\frac{1+e}{1-e}}\,\Delta E_o \tag{5}$$

Since

$$\tan E = \sqrt{\mu/a}\,r\,\dot{r}\left(\frac{1}{rV^2 - \mu}\right)$$

$$\Delta E_o = E_o \cong \tan E_o = \sqrt{\frac{\mu}{a}}\,r_o\left(\frac{1}{r_o V_o^2 - \mu}\right)\dot{r}_o \tag{6}$$

The second component of $\Delta\nu$, corresponding to the change in θ resulting from an initial downrange displacement Δx_o, is given by

$$\Delta\nu_2 = \Delta\theta = -\frac{\Delta x_o}{r_o} \tag{7}$$

Combining Eq. 4 – 7,

$$\Delta E = \frac{\cos^2\frac{E}{2}}{\cos^2\frac{\nu}{2}}\left[\sqrt{\frac{\mu}{a}}\,r_o\left(\frac{1}{r_o V_o^2 - \mu}\right)\dot{r}_o - \sqrt{\frac{1-e}{1+e}}\,\frac{x_o}{r_o}\right] - \frac{\sin E}{1-e^2}\,\Delta e \tag{8}$$

Since $\nu = \theta$ for injection at perigee, Eq. 1, 2, 3, and 8 can be used to find the altitude displacement at any central angle from injection.

Detected perturbations. If the guidance system senses a displacement from the vehicle nominal position, the velocity will be adjusted in magnitude and/or direction so that the vehicle arrives at the orbital radius of the Moon at the correct central angle from injection. (Perturbations of the injection parameters have a negligible effect on the time of arrival.) Both magnitude and directional changes must be available since there is the added constraint that the energy remain constant.

Let H represent the energy and L the angular momentum. Let θ_m be the central angle from injection to the Moon at arrival. Then,

$$\Delta\theta_m = \left.\frac{\partial\theta_m}{\partial r_o}\right|_{H,\,\dot{r}_o} \Delta r_o + \left.\frac{\partial\theta_m}{\partial\dot{r}_o}\right|_{r_o,\,H} \Delta\dot{r}_o$$

For the nominal conditions $r_o = 6545$ km, $V_o = 10.975$ km/sec, and $\dot{r}_o = 0$,

$$\left.\frac{\partial\theta_m}{\partial r_o}\right|_{H,\,\dot{r}_o} = -1.17 \times 10^{-5}\ \text{rad/km}$$

$$\left.\frac{\partial\theta_m}{\partial\dot{r}_o}\right|_{r_o,\,H} = -1.74 \times 10^{-1}\ \frac{\text{rad}}{\text{km/sec}}$$

If $\Delta x_o = 0$, it is required that $\Delta\theta_m = 0$. For an assumed value of $\Delta r_o = 15.2$ km (50,000 ft), the required change in radial velocity is $\Delta\dot{r}_o = -1.02 \times 10^{-3}$ km/sec. The velocity must be reduced by $\Delta V_o = -0.0129$ km/sec.

On the other hand, if there is an initial downrange displacement $\Delta x_o = 15.2$ km with $\Delta r_o = 0$, θ_m must be reduced by $\Delta\theta_m = -\Delta x_o/r_o$. The required change in radial velocity is $\Delta\dot{r}_o = 13.4 \times 10^{-3}$ km/sec.

In this study it was assumed that Δr_o and Δx_o are uncorrelated and that the 3σ value of each is 15.2 km. The corresponding 3σ value of h, δh, is plotted as a function of θ in Figure 27.

Undetected perturbations. The effect of undetected injection dispersions are easily calculated if it is assumed that the detected and undetected perturbations are independent. The over-all injection-parameter covariance matrix is then the sum of the individual covariance matrices for the two types of perturbations. Under these conditions the values of δh for 3 days corresponding to maximum, zero, and minimum lunar declination are shown in Figure 27. The values for the first two cases are nearly coincident; consequently, they are represented by a single curve.

Each curve was generated using a single covariance matrix. However, the covariance matrix is a function of the required launch azimuth, which, together with the coast time, varies considerably during each day. (The range of coast times varies from about 7 deg at minimum lunar declination to 50 deg at maximum lunar declination.) In each case, the matrix used corresponds to a launch azimuth of 95 deg. The mark on each curve indicates the corresponding central angle from injection to Johannesburg. There is no mark for February 11, 1965 because a launch azimuth of 95 deg requires an injection beyond Johannesburg on that day. The close spacing of the curves over the entire range of coast times indicates that δh is primarily a function of the central angle from injection and that calculations based on a single covariance matrix can be expected to be reasonably accurate over a wide range of injection points. Since it is assumed that the contributions of the detected and the undetected errors to δh are independent, the square of the latter can be obtained as the difference between $(\delta h)^2$ and the square of the former.

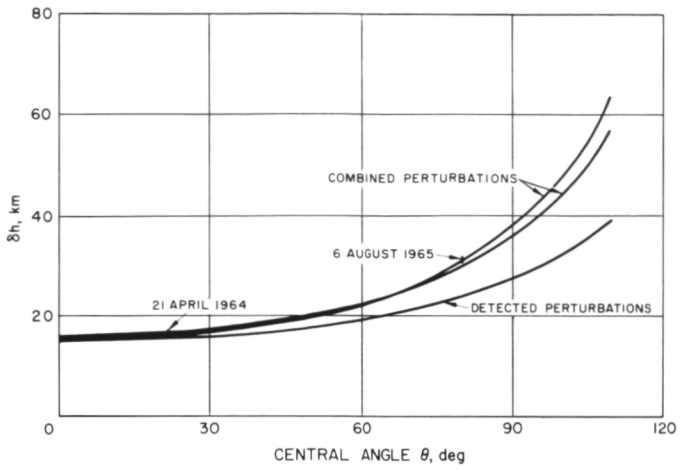

Fig. 27. Altitude dispersion

b. Beamwidth requirements. It is convenient to define the cone of visibility at the DSIF station to include all points that lie at least 10 deg above the horizon. Design of the acquisition antenna requires knowledge of the dispersions in spacecraft position within the acquisition cone. Since acquisition may not occur at the initial opportunity, knowledge of the dispersions throughout the cone, rather than just at the point when the cone is pierced by the nominal trajectory, is desirable.

At first visibility. The beamwidth required at the point of first visibility can be disposed of rather simply. Only detected (and compensated) perturbations in the injected crossrange position are considered first. It was shown in Reference 1 that for a trajectory which passes directly

over Johannesburg (and consequently maximizes the effect of a given crossrange displacement), the 3σ half-beamwidth at the initial acquisition opportunity has a maximum value of 3.1 deg for an initial displacement of 15.2 km. The maximum occurs for the largest value of θ_m under consideration – namely 175 deg and $\theta = 25$ deg.

The crossrange dispersion at DSIF acquisition results primarily from the initial crossrange velocity needed to offset the miss that would otherwise result at the Moon from the initial crossrange displacement. The undetected crossrange velocity dispersion is much smaller than the corresponding detected dispersion. Furthermore, it will be seen that the in-plane dispersions, which are essentially independent of the crossrange dispersion, occupy a beamwidth no greater than about 1.3 deg anywhere in the visibility cone. The maximum half-beamwidth required at first visibility may therefore be taken as 3.1 deg.

Maximum requirement within acquisition cone. An idea of the range of angular dispersions as measured by the DSIF station can be obtained by examining the case in which the horizontal component (at the trajectory plane) of the line of sight from the antenna to the vehicle is normal to the trajectory plane. The antenna-to-vehicle distance at this time is close to its minimum value, while the dominant dispersion, which is in the crossrange direction, is nearly perpendicular to the line of sight for a large fraction of the possible trajectories. Figure 28 shows the pertinent geometry.

A crossrange displacement Δy contributes $(\Delta y \sin \beta)/R$ radians to the elevation beamwidth. β and R are shown in Figure 29 as a function of θ and the angle α subtended at the center of the Earth by the line joining the antenna and the vehicle. α may be as large as 15 deg for the station at Johannesburg. It has been shown that

$$\Delta y = \frac{r}{r_o} \frac{\sin(\theta_m - \theta)}{\sin \theta_m} \Delta y_o$$

The 3σ value of Δy, δy, is plotted in Figure 30 for three different values of θ_m, with $\delta y_o = 15.2$ km. The corresponding elevation beamwidths are given in Figure 31. The beamwidth is of interest only when the angular rate of the vehicle does not exceed the tracking rate of the antenna. The latter is 0.7 deg/sec in both the hour angle and declination directions. The maximum trackable horizontal component of velocity therefore lies between 0.7 and 1 deg/sec, depending on the orientation of the velocity vector. This range of velocities is indicated by the dashed portions of the curves in Figure 31. The vehicle is above the station horizon except where θ and α are near 0 and 15 deg, respectively.

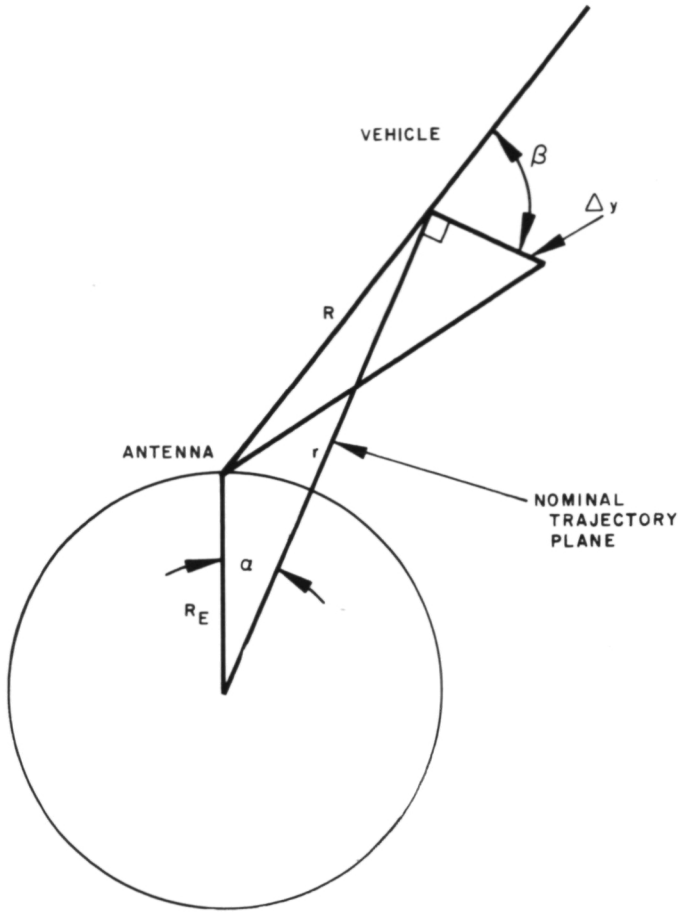

Fig. 28. Acquisition geometry

The in-plane dispersions contribute to both the elevation and the azimuth beamwidths. If the flight path angle is ϕ (Fig. 32) and if equal linear contributions in the elevation and azimuth directions are assumed, the dispersion in each direction is

$$\delta z = \frac{\delta h}{1 + \tan \phi} \cong \frac{\delta h}{1 + \tan \frac{\theta}{2}}$$

The contributions to the elevation and azimuth beamwidths are $(\delta z \cos \beta)/R$ and $(\delta z)/R$, respectively. These quantities are plotted in Figure 33.

A comparison of Figures 31 and 33, together with the fact that the in-plane and crossrange dispersions are independent, leads to the conclusion that the acquisition beamwidth at a given point is primarily a function of the crossrange dispersion and α. The former, in turn, is a strong function of both θ and θ_m. The beamwidth requirements are greatest for trajectories which pass directly over the station (i.e., $\alpha = 0$). The maximum half-beamwidth

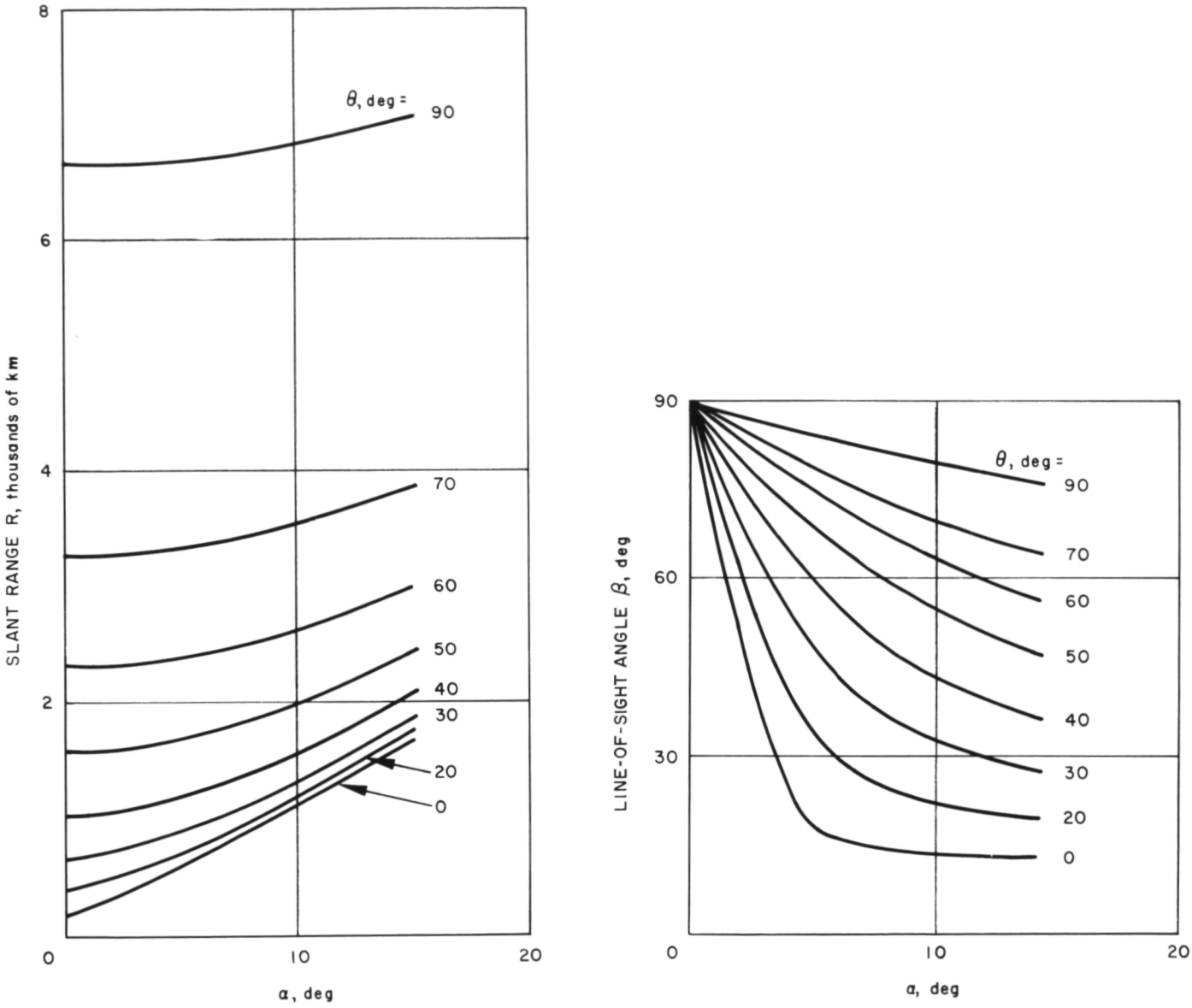

Fig. 29. Acquisition parameters

occurs at about $\theta = 35$ deg. Its value varies from about 3.5 to 9 deg as θ_m varies from 165 to 175 deg. Therefore, if acquisition is not accomplished at first visibility and no information is available on the crossrange dispersion, a search pattern would have to be employed to sweep the 6.2 deg acquisition cone over the required 18 deg field.

2. *Computer Program for Generation of Star Maps*

To determine the spacecraft attitude precisely during the transit to the Moon, two sensor systems are employed: the Sun and Canopus sensors. The vertical axis of the spacecraft (roll or z-axis) is held pointed toward the Sun by the primary Sun sensor. The boresight axis of the Canopus sensor lies in the x, z plane of the spacecraft. Hence, after acquiring Canopus, the spacecraft attitude is precisely defined.

To acquire Canopus, the spacecraft will be rotated about the roll axis at a constant speed with the roll axis pointed toward the Sun. The star sensor will be sighted at a preset angle from the x-axis and will sweep a 5 deg band. When the star intensity signal falls within the

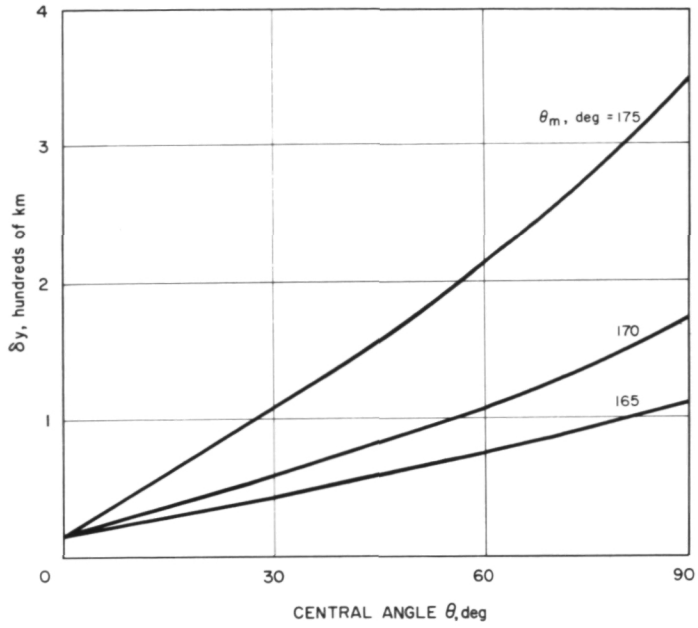

Fig. 30. Crossrange dispersion

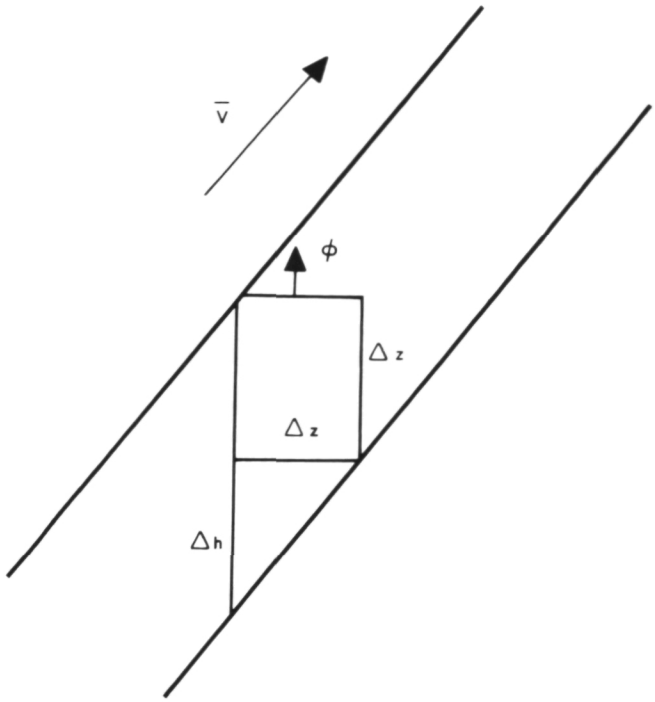

Fig. 32. In-plane dispersion

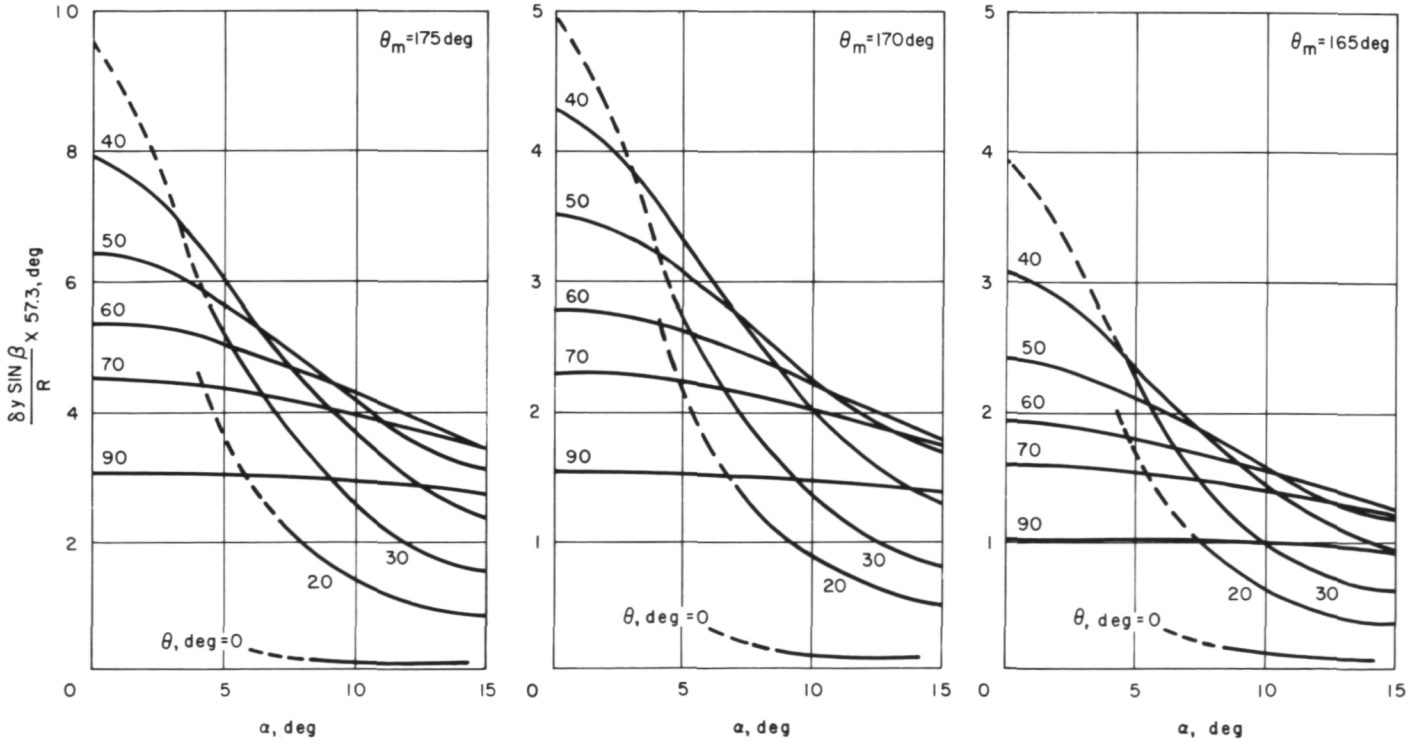

Fig. 31. Acquisition beamwidth due to crossrange dispersion

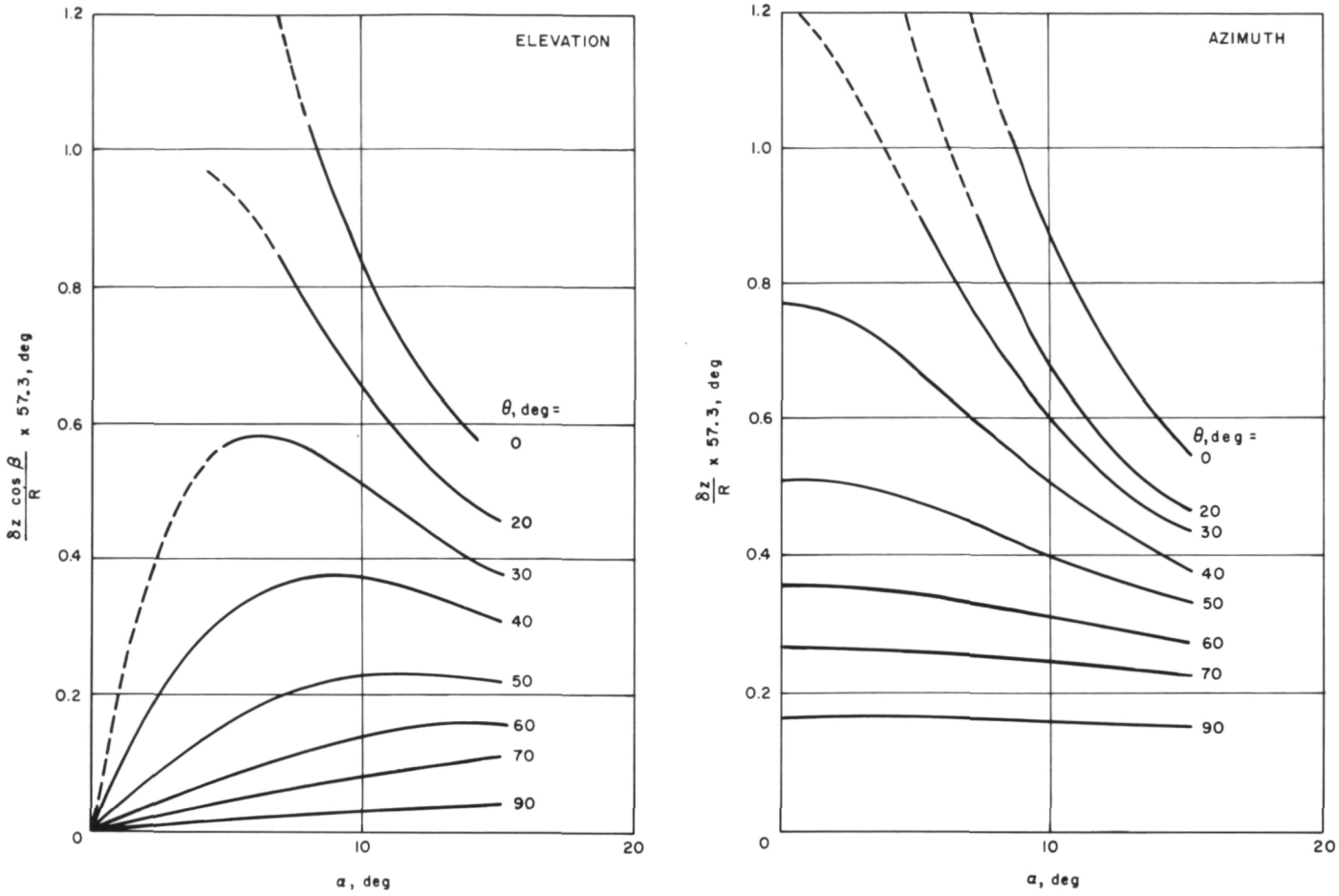

Fig. 33. Acquisition beamwidth due to altitude dispersion

proper threshold levels, the spacecraft will lock on by producing an error signal to control the vehicle roll attitude. The threshold levels will normally be set to exclude all stars except Canopus, and hence the spacecraft should lock on Canopus automatically.

As a second check of correct star lockon, a star verification procedure can be performed. During the star verification procedure, the spacecraft will be commanded to rotate at a constant speed about the roll axis as in star acquisition. The light intensity signal from the sensor will be telemetered to Earth. This will provide a map of star brightness vs roll angle, indicating the presence and brightness of all stars and planets within the particular band swept out. From this map, it should be possible to identify Canopus and determine whether or not the sensor is locked on this star. To check the star map obtained in the star verification, it is essential to know the position of each star and planet that can be seen by the sensor. A computer program is proposed which will generate reference maps from accurately known astronomical information, for use as standards against which the actual star maps obtained during verification maneuvers may be compared. These maps could be generated well in advance of the launch date.

The steps outlined for programming such calculations are as follows:

(1) Store in the computer the coordinates and brightness of the Sun, the brightest stars, and the planets.

(2) Define a set of spacecraft coordinates oriented so that the primary Sun sensor (— z-axis) points toward the Sun and the star sensor points to Canopus.

(3) Transform the positions of all stars and planets to this spacecraft coordinate system.

(4) Search for stars and planets which lie in the band

surveyed by the Canopus sensor and tabulate these celestial objects giving roll angle and brightness.

a. Detailed procedure. The following outline describes in detail the steps to obtain the reference maps:

(1) Determine the S4 magnitude of all stars of Type B which have a visual magnitude of 4.3 or brighter and of all other types of stars of visual magnitude 4 or brighter (Ref. 3, 4, 5, and 6). The expression for S4 magnitude in terms of quantities tabulated in References 4 and 5 is

$$m(S4) = V + 0.75\ (B\text{-}V)$$

where V is the observed magnitude through a yellow filter, reduced to outside the Earth's atmosphere. This is approximately equivalent to the photovisual magnitude on the International System. B is the observed magnitude through a blue filter and U for an ultraviolet filter, reduced to outside the Earth's atmosphere and including a zero-point correction to satisfy the condition that

$$U = B = V$$

for main-sequence stars of class AO on the MK (Morgan and Keenan) system.

(2) Convert $m(S4)$ of all stars to brightness using the following equations:

$$B_{S4i} = B_o\, 10^{-\frac{m_i(S4)}{2.5}}$$

$$B_o \cong 3.1 \times 10^{-13}\ \text{watt/cm}^2{}^a$$

(3) Store the following information in the computer for stars of $S4$ magnitude and brighter:

(a) Henry Draper Catalogue Number

(b) Right ascension (α) and declination (δ) in the Mean Geocentric Equatorial Coordinate System of 1963, Jan., 1^{d}0072, universal time (Julian date, JD = 2438030.572), a space fixed system (Ref. 3)

(c) Visual magnitude, m_i

(d) $S4$ magnitude, $m_i(S4)$

(e) $S4$ brightness, B_{S4i}

(4) Convert the angles α and δ to radians: α is given in terms of hr, min, and sec; and δ is in deg, min, and sec.

(5) Determine a unit vector to each star:

$$\hat{r}_{Ei} = X_{Ei}\,\hat{i} + Y_{Ei}\,\hat{j} + Z_{Ei}\,\hat{k}$$

$$X_{Ei} = \cos\delta_i \cos\alpha_i$$

$$Y_{Ei} = \cos\delta_i \sin\alpha_i$$

$$Z_{Ei} = \sin\delta_i$$

$$i = 1 \ldots \text{total number of stars}$$

(6) Read into the computer the (X, Y, Z) components, in astronomical units, of the Sun and planets (Venus, Mars, Jupiter, Saturn, Uranus, Neptune, and Pluto) for the date interval chosen (input first and last JD and ΔJD) from a tape available. Transform these components to the coordinate system used in Step 3b.

(7) Compute the $S4$ magnitude of the planets using the expressions in Figure 34 (Ref. 7, pp. 158-159; 8 and 9, pp. 311-316). Let

$$R_j = |\, r_{Epj}\,|$$

$$r_j = |\, r_{Spj}\,| + r_{SE}$$

where

r_{Epj} = vector Earth to planet (j), in astronomical units

r_{SE} = vector Sun to Earth, in astronomical units

Then find the unit vectors from Earth to planet (j) and Sun to Earth.

$$\hat{r}_{Epj} = \frac{r_{Epj}}{|\, r_{Epj}\,|}$$

$$\hat{r}_{SE} = \frac{r_{SE}}{|\, r_{SE}\,|}$$

To find the phase angle, a_j, of each planet, compute

$$a_j = \cos^{-1} \frac{\hat{r}_{Epj} \cdot (\hat{r}_{Spj} + \hat{r}_{SE})}{|\, \hat{r}_{Spj} + \hat{r}_{SE}\,|}\ (\text{deg})$$

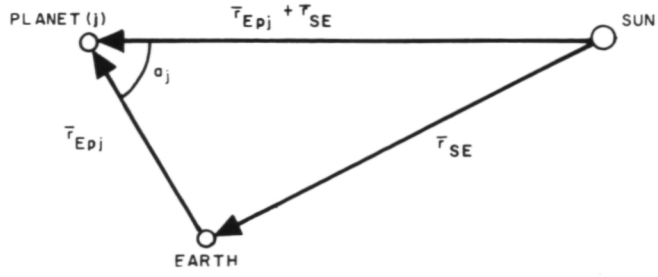

Fig. 34. Solar system geometry

[a]The value of B_o may vary with spectral type of star and hence requires further refinement.

Then the *S4* magnitudes of the planets are:

Venus

$$m_1(S4) = -3.14 + 5 \log_{10} r_1 R_1 + 0.09 \times 10^{-2} a_1 + 2.39 \times 10^{-4} a_1^2 - 0.65 \times 10^{-6} a_1^3$$

Mars

$$m_2(S4) = -1.95 + 5 \log_{10} r_2 R_2 + 0.0151 a_2$$

Jupiter

$$m_3(S4) = -8.4 + 5 \log_{10} r_3 R_3 + 0.015 a_3$$

Saturn

$$m_4(S4) = -8.19 + 5 \log_{10} r_4 R_4$$

Uranus

$$m_5(S4) = -6.2 + 5 \log_{10} r_5 R_5$$

Neptune

$$m_6(S4) = -6.4 + 5 \log_{10} r_6 R_6$$

Pluto

$$m_7(S4) = -0.2 + 5 \log_{10} r_7 R_7$$

Mercury is not included, since it will never be within the view field of the Canopus sensor. (The Sun-Earth-Mercury angle is always less than 28 deg while the Sun-Earth-Star sensor angle is always greater than 75 deg.)

The above equations were given by Allen in terms of visual magnitude. The color corrections listed in Table 9 convert visual to *S4* magnitude and have already been included in the equations as written (Ref. 7, pp. 159 and 183; 10, p. 6-82).

(8) Define the spacecraft coordinate system (Fig. 35) as follows:

$$\hat{z} = \hat{r}_{SE}$$

$$\hat{y} = \frac{\hat{r}_{EC} \times \hat{z}}{|\hat{r}_{EC} \times \hat{z}|}$$

$$\hat{x} = \hat{y} \times \hat{z}$$

where

r_{SE} = unit vector Sun to Earth

r_{EC} = unit vector Earth to Canopus

(assumes spacecraft located at center of Earth)

(9) Transform all star and planet positions from equatorial to spacecraft coordinates.

$$\hat{r}_{Si} = M \hat{r}_{Ei}$$

$$\hat{r}_{Spj} = M \hat{r}_{Epj}$$

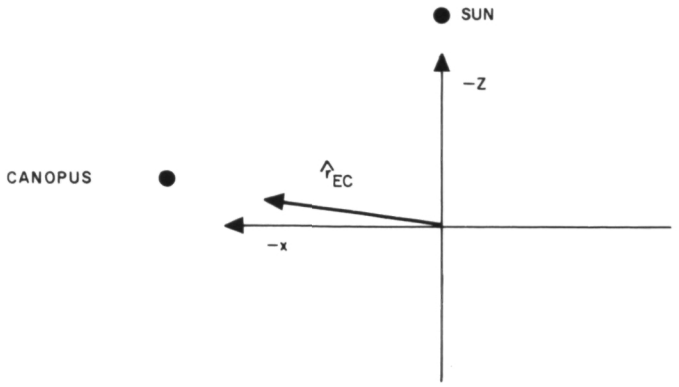

Fig. 35. Spacecraft coordinate system orientation

Table 9. Color corrections for planets

Planet	Color correction (C)	Spectral class	*m(S4) — m(V)*
Venus	0.8	K0	1
Mars	1.2	M0	1.1
Jupiter	0.4	G0	0.7
Saturn	0.7	K0	1
Uranus	0.4	G0	0.7
Neptune	0.6	G5	0.7
Pluto	0.7	K0	1

where the symbols are defined as follows:

$\hat{r}_{Ei}$ = unit vector, Earth-to-star *(i)* in Earth-centered equatorial coordinates

$\hat{r}_{Epj}$ = unit vector, Earth-to-planet *(j)* in Earth-centered equatorial coordinates

$\hat{r}_{Si}$ = unit vector, Earth-to-star *(i)* in Earth-centered spacecraft coordinates

$\hat{r}_{Spj}$ = unit vector, Earth-to-planet *(j)* in Earth-centered spacecraft coordinates

M = transformation matrix from Earth-centered equatorial to Earth-centered spacecraft coordinates

(10) Find θ_i and ϕ_i for each star, and θ_j and ϕ_j for each planet (Fig. 36).

$$\theta_i = \sin^{-1}\left(\frac{z_{Si}}{|\hat{r}_{Si}|}\right) \text{ (deg)}$$

$$\phi_i = \tan^{-1}\left(\frac{y_{Si}}{x_{Si}}\right) \text{ (deg)}$$

$$\theta_j = \sin^{-1}\left(\frac{z_{Spj}}{|\hat{r}_{Spj}|}\right) \text{ (deg)}$$

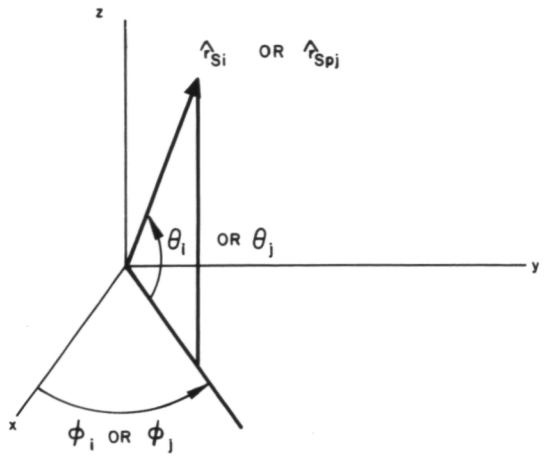

Fig. 36. Star or planet vector in spacecraft coordinates

$$\phi_j = \tan^{-1}\left(\frac{y_{Spj}}{x_{Spj}}\right) \text{ (deg)}$$

x_{Si}, y_{Si}, z_{Si} = components of $\hat{r}_{Si}$

$x_{Spj}, y_{Spj}, z_{Spj}$ = components of $\hat{r}_{Spj}$

(11) Use θ_C (θ_i for Canopus) from Step 10 to sort out all stars and planets (Fig. 37) such that:

$$|\theta_i - \theta_C - K_1| \leq K_2$$

$$|\theta_j - \theta_C - K_1| \leq K_2$$

K_1 = angular displacement of strip searched from θ_C

K_2 = angular width of strip searched

K_1 and K_2 constants will be chosen to feed into the computer for each date.

$$-90 \text{ deg} \leq K_1 \leq 90 \text{ deg}$$

$$0 \leq K_2 \leq 180 \text{ deg}$$

K_1 is included to provide the flexibility of making a star map strip with the Canopus field-of-view centerline shifted relative to the expected position to allow for certain failure modes.

(12) Compute the brightness of each planet selected in Step 11 from *m(S4)* determined in Step 7:

$$B_{S4j} = B_o\, 10^{-\frac{m_j(S4)}{2.5}}$$

(13) Print out all stars and planets selected in Step 11 in order of increasing ϕ giving:

Henry Draper Catalogue Number

ϕ_i or ϕ_j

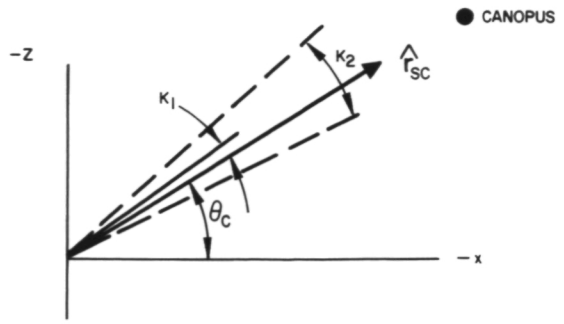

Fig. 37. Star sensor search band setting

S4 magnitude $m_i(S4)$ or $m_j(S4)$

Visual magnitude of all stars, m_i

S4 brightness, B_{S4i} or B_{S4j}

(14) Print out θ_C.

3. Postlanding Attitude Determination Program

While the attitude of the spacecraft is accurately known during descent, there is no reliable method of predicting its postlanding attitude. In addition to the scientific instrument requirements, the attitude of the spacecraft after landing is necessary to establish the following:

(1) Path of the planar array antenna to maintain Earth contact, as a function of time.

(2) Path of the solar panel to receive maximum energy, as a function of time.

(3) Position of the Sun with respect to the spacecraft for the thermal management program.

(4) Time of day-night terminator for sequence planning and the power management program.

The purpose of the postlanding attitude determination program is to facilitate pointing of the solar panel and planar array and, by providing an accurate computation of the spacecraft attitude, to determine the information itemized above. In order to determine the spacecraft attitude in a lunar system, two vectors, common to both lunar and spacecraft systems, must be established. If the landing site of the spacecraft is known in a lunar system and is taken to coincide with the origin of a spacecraft coordinate system, vectors from this point to any two heavenly bodies, whose coordinates are known in both the lunar and spacecraft systems, will be sufficient to determine the spacecraft attitude. The Earth and Sun are convenient bodies to fix two vectors since the spacecraft mission requires fixing these two bodies in the

spacecraft coordinate system through positioning of the solar panel and planar array antenna. After the planar array has been positioned, a more accurate determination of attitude may be made using the television system to fix the positions of known stars (or planets) in the spacecraft coordinate system. The general approach of the postlanding attitude determination program is as follows:

(1) Position solar panel on the Sun.

(2) Position planar array on the Earth.

(3) Calculate the spacecraft attitude determined by the landing coordinates of the spacecraft on the Moon, the Moon-Sun vector, and the Moon-Earth vector.

(4) Use the spacecraft attitude to search for stars and planets of known celestial coordinates with the spacecraft television.

(5) Determine a more precise spacecraft attitude from stars or planets.

(6) Calculate the desired output information using the best (highest confidence) attitude currently available.

a. Functional flow diagram. The functional flow diagram (Fig. 38) is a general outline of the sequence of operations necessary to satisfy the postlanding attitude determination program requirements. The operations are described in the order of occurrence.

Step 1 computes Sun and Earth coordinates in the selenographic coordinate system. Since these coordinates are functions of time, they are computed for the time of landing and for a sequence of specified time intervals after landing.

Steps 3 through 14[a] cover positioning the solar panel on the Sun by maximizing the Sun sensor output. To obtain a starting point for the search, the Sun position in spacecraft coordinates is computed for vertical landing and zero roll since retro engine firing. The roll gyro error indicates the initial direction of search in roll. The program computes the commands necessary to step the solar panel (and therefore the Sun sensor) ±180 deg from the initial position for roll search. The spacecraft physical constraints on the motion of the solar panel are considered in the computations of all commands. An operator[b] performs the search and monitors the Sun sensor output during the stepping procedure to find the maximum point. As long as the Sun sensor output is increasing, the search is continued in the same direction. If it is decreasing, the direction of search is reversed. When there is no Sun sensor output, the proper emergency procedure is adopted.

An identical search procedure is followed in elevation when a Sun sensor maximum output is obtained in roll, or when the roll search has covered 360 deg. If a Sun sensor maximum output was obtained in roll, the elevation search is performed along the roll angle where that maximum was obtained. If no maximum was obtained for the roll search, the Sun is directly over the spacecraft or the Sun sensor is malfunctioning. For the case of no Sun sensor maximum output, the roll angle for the elevation search is arbitrary. If no maximum is obtained in the elevation search, an analysis of the situation must be made by an operator before further operations are performed.

Steps 15 through 23[a] facilitate positioning of the planar array antenna on the Earth. The position of the solar panel for maximum Sun sensor output specifies the position of the Sun in spacecraft coordinates. Using the selenographic coordinates of the Sun and the position of the Sun in spacecraft coordinates, the spacecraft attitude can be determined within one Euler angle. By assuming that angle to be zero, a nominal position of the Earth in spacecraft coordinates is computed. The computer then calculates a set of commands to step the planar array in a search pattern about the nominal Earth direction, taking into consideration the physical constraints on the system motions, as mentioned previously. The search pattern commands are transmitted to the spacecraft by the operator, while a receiver is monitored for the planar array signal. If no planar array signal is received at the end of a defined search pattern sequence, an operator analysis will be required. When the planar array signal is received, the main lobe must be found and maximized by the command operator according to a preplanned sequence.

Step 24 computes the direction of the Earth in spacecraft coordinates using the planar array gimbal angles when its main lobe is being received by the Earth.

Step 24A computes an error or confidence number to be associated with the direction computed in Step 24.

[a]These steps are automatically omitted if the solar panel is already positioned on the Sun.

[b]These functions may be performed by machine.

[a]If the planar array is already positioned on the Earth, these steps are omitted.

Step 25 computes the spacecraft attitude using the selenographic coordinates of the Sun and Earth together with the spacecraft coordinates of the Sun and Earth.

Step 25A associates a confidence or error with the above attitude.

Step 26 finds the spacecraft coordinates and television coordinates of stars[a] whose brightness and celestial coordinates are an input to the program.

Step 27 computes TV step commands to obtain frames including stars whose spacecraft coordinates were computed in Step 26.

Step 28 is performed by an operator. TV pictures of stars are examined to determine the TV coordinates of the stars.

Step 29. Actual spacecraft coordinates of sighted stars are computed.

Step 30 computes confidence numbers for observed TV coordinates of sighted stars.

If there is more than one star visible, the computer performs Steps 32, 33, and 34. If only one star is visible, the computer performs Steps 32A, 32B, 33A, and 33B. If no stars are visible, the program proceeds directly to Step 35.

In steps 32, 33, and 34, attitude computations are performed based on pairs of sighted stars. First, the stars are paired so as to provide the most accurate attitude computations; the spacecraft attitude is then computed for each pair of stars. A confidence number or error is computed and associated with each attitude computed.

Steps 32A, 32B, 33A, and 33B are attitude computations using the positions of one star, the Earth, and the Sun. Confidence numbers or errors are computed for both attitude computations.

In Step 35, an operator must select one of the previously computed attitudes to be used in the remaining steps.

Step 36 computes the position of the Sun in spacecraft coordinates for selected times using the spacecraft attitude chosen in Step 35, and the selenographic coordinates of the Sun as a function of time from Step 1. This information is used with a television terrain survey to determine time to day-night terminator.

Step 36 computes optimum stepping commands to position the solar panel on the Sun and the planar array on the Earth for each time interval selected in Step 1. The program takes into consideration the spacecraft physical constraints on the motion of the solar panel and planar array antenna.

[a]Including planets other than Earth.

4. Design Mission Sequence for A-21, P-42

The design mission sequence shown in Fig. 39 and 40 illustrates the experiments which may be performed the first lunar day, the first lunar night, and the second lunar day within currently known constraints when touchdown occurs 157 hr before the day-night terminator (eighth day launch). The mission profile, assuming launch on the eighth day of the launch window, consists of the following operations:

(1) Drilling operation

(2) Subsurface geophysical experiment

(3) One wide angle and 14 narrow angle black and and white TV surveys

(4) Four color TV surveys

(5) Hourly scientific temperature and engineering data measurements

(6) 50-hr nighttime engineering thermal test

The total available energy provided by the solar panel during the first lunar day will be somewhat in excess of that required for the experiments, and the 157 hr remaining after touchdown far exceeds the number required for the scheduled experiments. The excess energy can thus be consumed during *controlled* discretionary reruns over points of interest as indicated by the reduction and analysis of the scheduled experiment data.

During the first lunar night, the amount of energy required by the scheduled experiments and thermal control equipment will exceed that provided by the battery. Under these conditions, the battery is expected to reach its cutoff potential at 217 to 242 hr after the day-night terminator, driving the spacecraft into an approximate 100 hr interval of inactive status during which all spacecraft functions cease and compartment temperatures decay to low subzero levels. The battery capacity available for night operations is based on empirical data which take into account the temperature profile and load schedule. There are currently in progress battery load tests which indicate that a greater amount of energy will be available than has been assumed in this sequence. The mission sequence will be revised to reflect this increase in available energy during the lunar night.

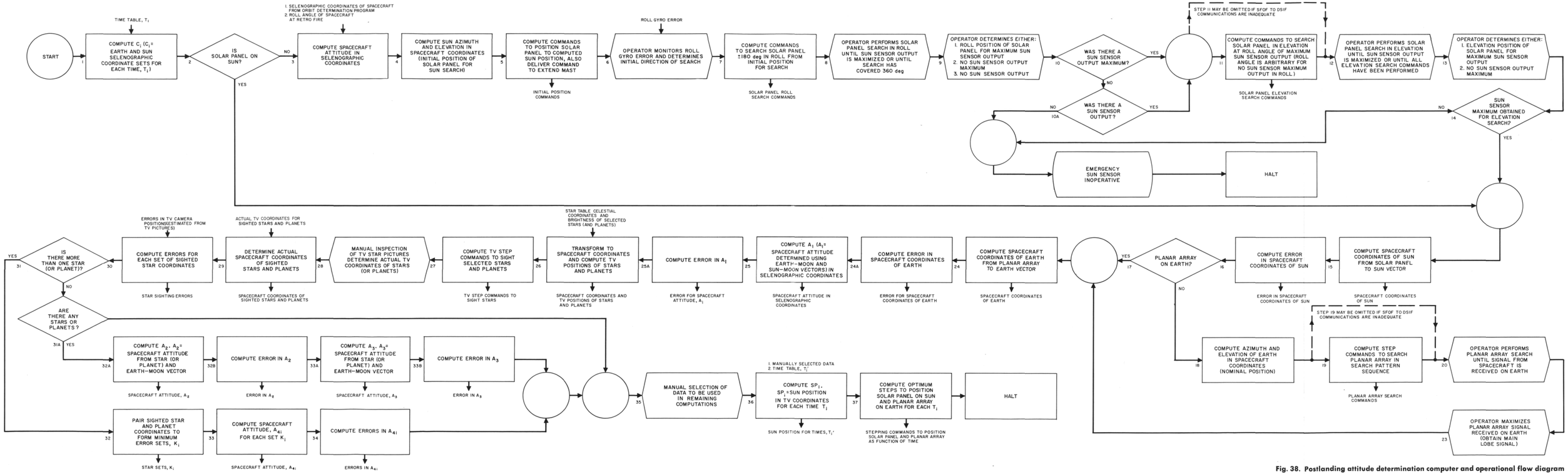

Fig. 38. Postlanding attitude determination computer and operational flow diagram

Page intentionally left blank

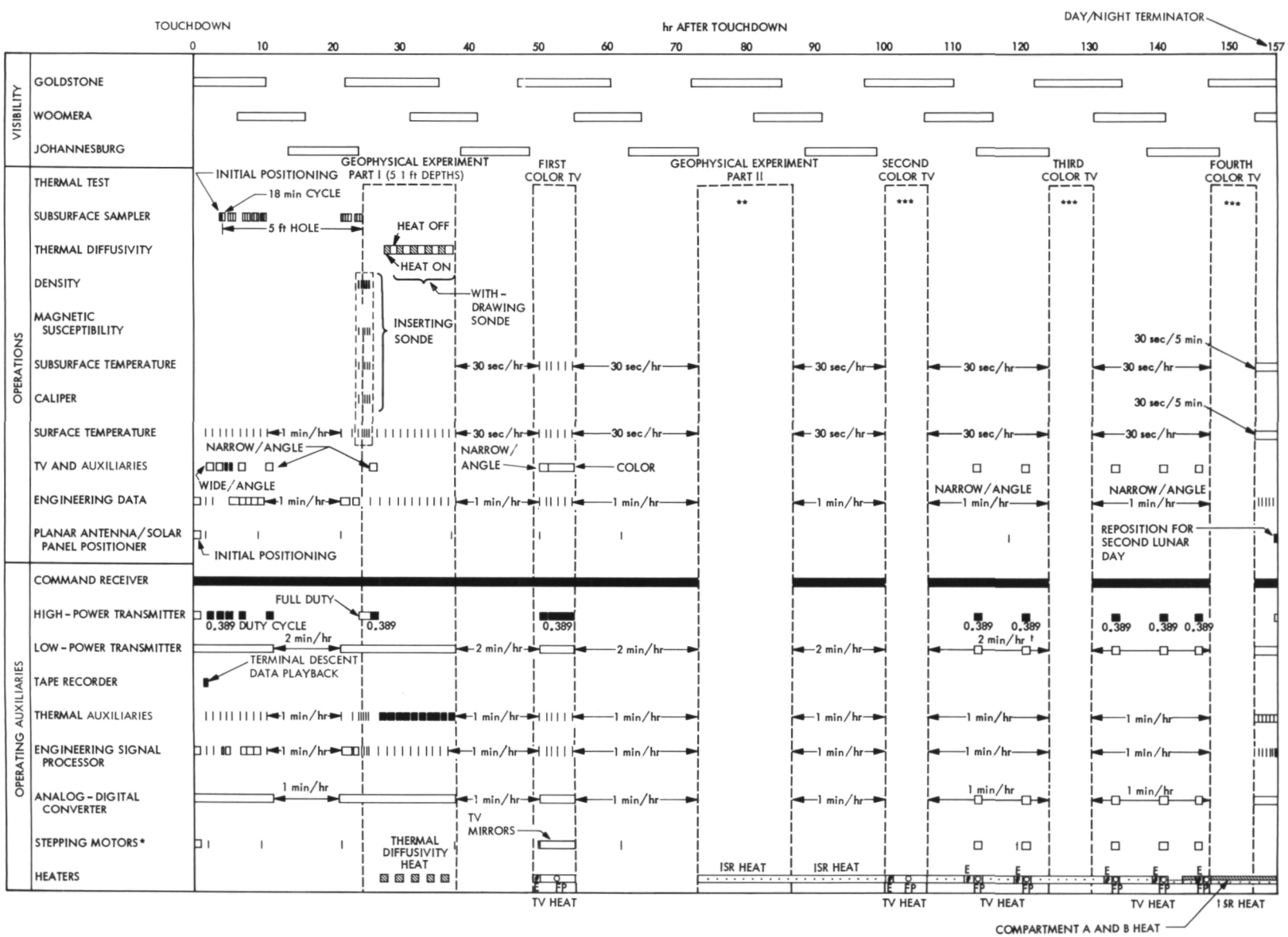

Fig. 39. Design mission sequence for first lunar day

CONFIDENTIAL

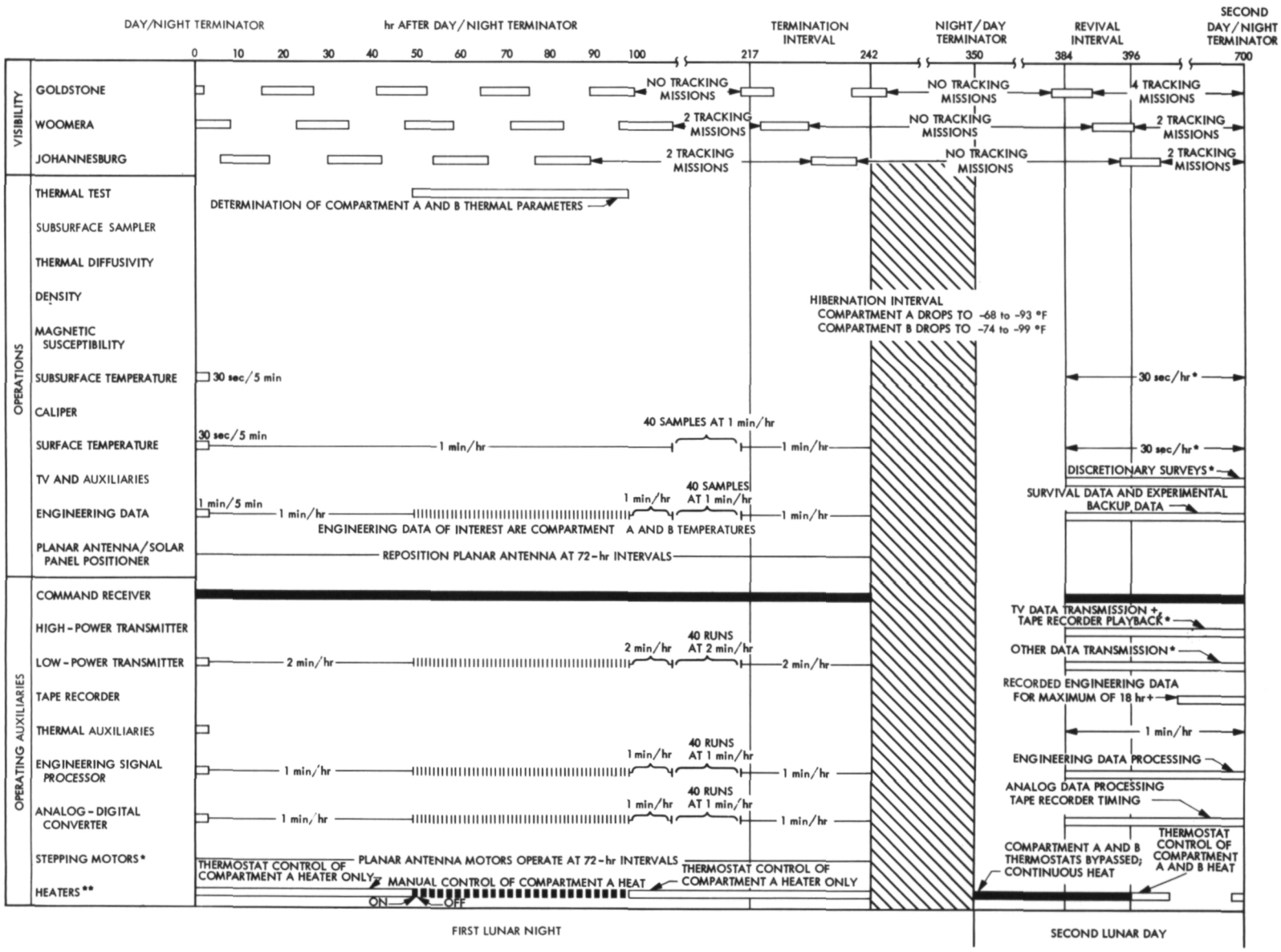

* ONLY DURING DSIF AVAILABILITY
\+ ONLY DURING DSIF DOWN PERIODS
** ISR HEATER NOT SHOWN

Fig. 40. Design mission sequence for first lunar night/second lunar day

CONFIDENTIAL

The program for the first lunar night will consist of hourly surface temperature and engineering data sampling and a 50-hr thermal test during the scheduled periods of DSIF availability. During the thermal test, an attempt will be made to determine the thermal parameters of Compartments A and B by manually controlling the duty cycle of the heater in A and monitoring the behavior of both compartment temperatures. No data will be recorded during DSIF down periods for the following reasons:

(1) The use of the tape recorder for the recording of data will result in excessive expenditure of energy, significantly shortening the period of active operation.

(2) The present requirement for processing the surface temperature through the analog-to-digital converter (high rate digital mode) exceeds the present capability of the tape recorder.

Spacecraft activity for the second lunar day is expected to be resumed at 34 to 47 hr after the night-day terminator since the solar panel will have provided power to the compartment heaters, bringing the compartments up to operating temperature. The program for the second lunar day will consist of real time discretionary TV and hourly sampling of engineering data and surface and subsurface temperature during the scheduled periods of DSIF visibility. During DSIF down periods, engineering data will be recorded for a maximum of 18 hr by means of the spacecraft tape recorder. The DSIF scheduling for the mission shown will consist of the following:

(1) Continuous tracking by all stations during the first lunar day.

(2) Continuous tracking by all stations for the first 100 hr of the first lunar night.

(3) Alternate Woomera and Johannesburg tracking (two tracking missions for each) between 112 and 215 hr after the day-night terminator.

(4) Two Goldstone, one Woomera, and one Johannesburg tracking mission between 215 and 242 hr after the day-night terminator.

(5) Continuous tracking between 381 and 404 hr after the day-night terminator (second lunar day).

(6) Four Goldstone, two Woomera, and two Johannesburg tracking missions for the remainder of the second day.

This schedule is a rearrangement of the schedule presently shown in the DSIF interface document and reflects the increased need for coverage during the first part of the lunar night. The total coverage required is approximately the same. It is felt that the preliminary nature of this sequence does not justify renegotiation of the DSIF requirements at this time.

The experiments, their associated operating auxiliaries, and DSIF tracking activity for the first lunar day are summarized in Figure 39. The program for the first lunar night and the second lunar day is given in Figure 40. The operational details of the thermal tests are presented from 50 to 100 hr after the day-night terminator. The three intervals associated with the survival of the spacecraft which are shown are defined as follows:

(1) During the termination interval which occurs between 217 and 242 hr after the day-night terminator, the spacecraft battery will reach cutoff potential and all power will be shut off automatically. The length of the interval has been determined from battery capacity and compartment thermal uncertainty considerations.

(2) During the hibernation interval which occurs between 242 to 350 hr after the day-night terminator, the spacecraft is completely without power and the compartment temperatures drop below zero F.

(3) During the revival interval which occurs between 384 to 396 hr after the day-night terminator (during the second lunar day), the spacecraft is expected to return to active status. The length of this interval is a function of the length of the termination interval and the rate at which compartment heating occurs after the night-day terminator.

D. Flight Control

1. Introduction

The flight control subsystem consists of those elements of the spacecraft which provide velocity and attitude control during the transit phase of the *Surveyor* mission. Functionally, the lunar radar and propulsion are included, although these items are covered in other sections. Elements of the flight control subsystem which are treated in this section include optical sensors, inertial instruments, attitude controls, and flight control electronics.

2. System Design

a. Summary. Significant design verification test results were obtained at both the subsystem and unit levels during this report period. At the subsystem level, coast phase attitude control system tests utilizing optical and inertial modes of operation resulted in a better understanding of the tolerances associated with closed-loop system operation, as well as the problems due to unit interactions. It was necessary to modify some circuit parameters in order to obtain system performance that meets the functional requirements. All modifications were accomplished by making component value changes. Successful demonstrations were made of the rate stabilization mode, inertial mode, and Sun mode operation. In addition, capture of a simulated star was achieved using the development model of the Canopus sensor. Subsystem electrical compatibility tests on portions of the attitude control systems are in progress. Development models of the inertial reference unit and roll actuator are being used in these tests.

At the unit level, three engineering models of the roll actuator were fabricated and are presently undergoing evaluation. Based on the results of initial tests, no major design changes are expected. Experience was gained in the use of the Sun-star simulator during acceptance testing of the engineering model of the Canopus sensor. Flight models of the gyros and accelerometer have successfully passed acceptance tests. All of these tests have provided a basis for establishing test criteria and procedures, as well as providing a better definition of test equipment requirements.

Modifications to the Sun acquisition sequence were incorporated into the coast phase logic circuits, and the primary Sun sensor field of view was enlarged to be compatible with the resulting change in Sun capture dynamics. The circuit changes resulted in minor revision to layout drawings while the enlarged sensor field of view was accomplished by rework of the primary Sun sensor shadow masks.

The programmed descent trajectory parameters for the lightweight spacecraft were established and implemented into the flight control circuits. The effects of tolerances and noise on the performance of the vernier descent control system is under investigation.

Initial tests of the roll actuator with no load indicated the presence of an undamped oscillation within the servo backlash region. This oscillation was eliminated by application of a spring load. Additional tests are planned using a simulation of the vernier engine load.

b. Coast phase attitude control system. The Sun acquisition sequence under study at the time of the previous bimonthly report has now been included as part of the coast phase attitude control system. This sequence may be understood in terms of Figure 41, where $\overline{P}\ \overline{Y}\ \overline{R}$ represents the coordinate system of the secondary Sun sensor and P Y R represents the coordinate system of the IRU. Prior to Sun acquisition, the attitude control system will be in the rate stabilize mode and the Sun position may be defined in terms of body coordinates as S. Following illumination of the secondary Sun sensor, a yaw command rate (about the Y-axis) is applied which causes the sunline to move on the $\widehat{SS_1}$ trajectory until the angle between the sunline and the $\overline{R}\ \overline{Y}$ plane (ϕ_s) is sufficiently small. At this point, S_1, a pitch command rate (about the P-axis) is applied which causes the sunline to move on the $\widehat{S_1S_2}$ trajectory. At S_2 the sunline trajectory enters the field of view of the primary Sun sensor. The system then automatically switches to primary Sun sensor control and nulls the angular error between the sunline and the roll (R) axis.

Results of an analog computer simulation of the operation of the attitude control system as the Sun enters the primary Sun sensor field of view are shown in Figure 42. The angles α and β are the direction cosine angles of the sunline with respect to the R Y and R P planes, respectively. The angular rates of the trajectories associated with the entry into the primary Sun sensor field of view, as shown in Figure 42, were chosen to be $|\dot{\alpha}| = 1$ deg/sec, $|\dot{\beta}| = 0$ deg/sec. The actual initial

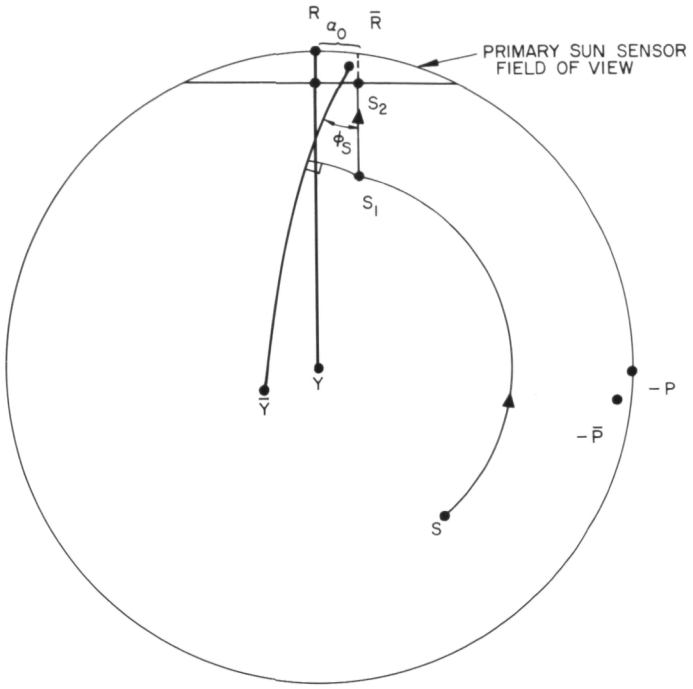

Fig. 41. Typical Sun acquisition geometry

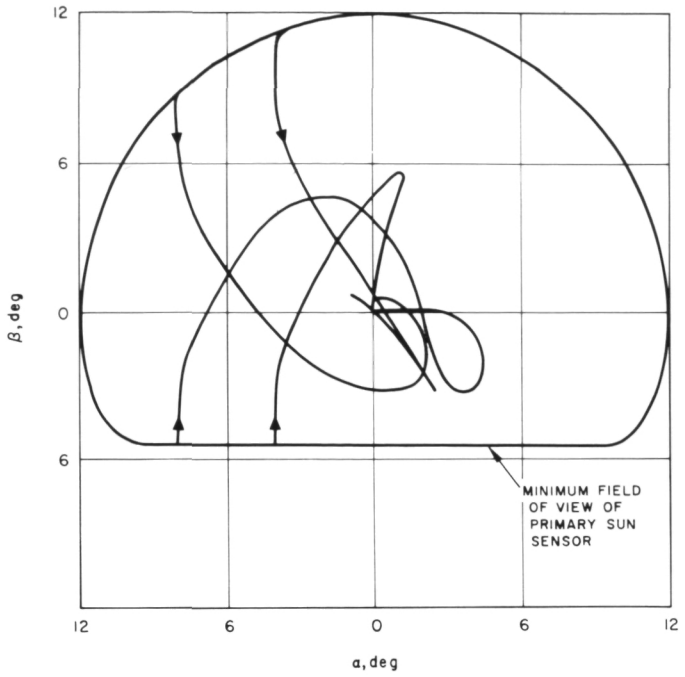

Fig. 42. Optical mode of Sun acquisition

angular rates are a function of the trajectory to the point of entry and the numbers chosen for the simulation are the expected maximum values.

Figure 42 shows that the initial value of α must be sufficiently small if successful Sun acquisition is to take place. Neglecting the dynamics of the problem, the inertial portion of Sun acquisition may be considered as a series of rotations about the inertial reference unit (IRU) axes. The misalignment between the IRU and the secondary Sun sensor is represented by a PYR Euler angle set ψ, θ, ϕ. Angle ϕ_s represents the bias error of the secondary Sun sensor and associated logic circuitry; ψ, θ, ϕ, and ϕ_s are random variables, statistically independent, and with zero mean. Thus, α_0, the static component of the initial value of α, has zero mean and its variance may be determined from the following equation:

$$\sigma^2_{\alpha_0} = \sigma^2_{\phi_s} + \frac{1}{2}\left(\sigma^2_{\phi} + \sigma^2_{\theta}\right)$$

The allowable misalignment and bias error must be restricted so that the 3σ value of α_0, plus a reasonable allowance for dynamic overshoots in α, is less than 8 deg.

c. Vernier descent phase. The parameters of the programmed descent trajectory have been established for the 2100-lb spacecraft (Fig. 43 and 44). The attitude and velocity control systems were modified as shown in Figures 45 and 46 to be compatible with the new trajectory requirements.

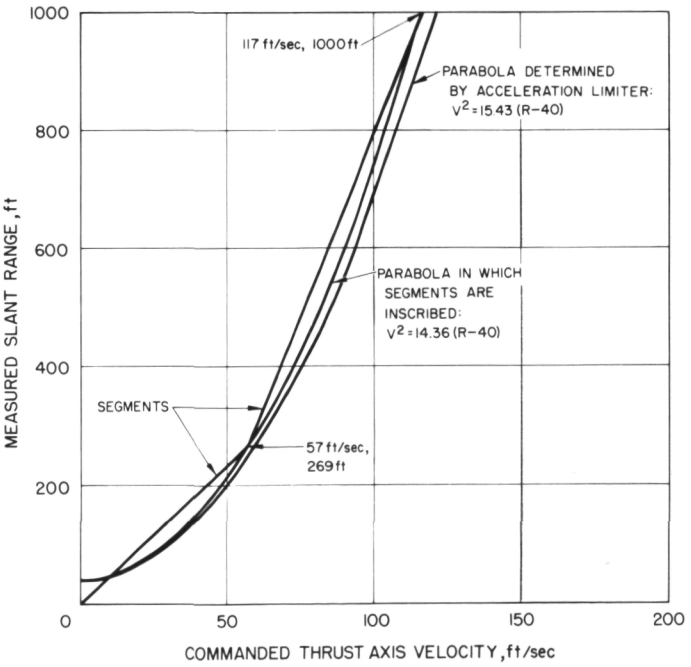

Fig. 43. Lower two command trajectory segments

A refinement of the computation of acceptable main retro burnout conditions of attitude, range, and velocity is in progress. Reference 1 contained a plot of acceptable

main retro burnout attitude contours in the range vs thrust axis velocity plane. This diagram was based on a model of the descent mode which was sufficiently simple to permit hand computation. The computation is now being refined through the use of an analog computer simulation based on a more accurate model. This study is being carried out by taking attitude vs thrust axis velocity traces from various initial conditions of range, velocity, and attitude. Traces are run for several initial attitudes at selected initial range and velocity points on the command trajectory. Typical traces are shown in Figure 47. The information contained in such traces will be used to construct an envelope of acceptable conditions of altitude, range, and velocity at main retro burnout.

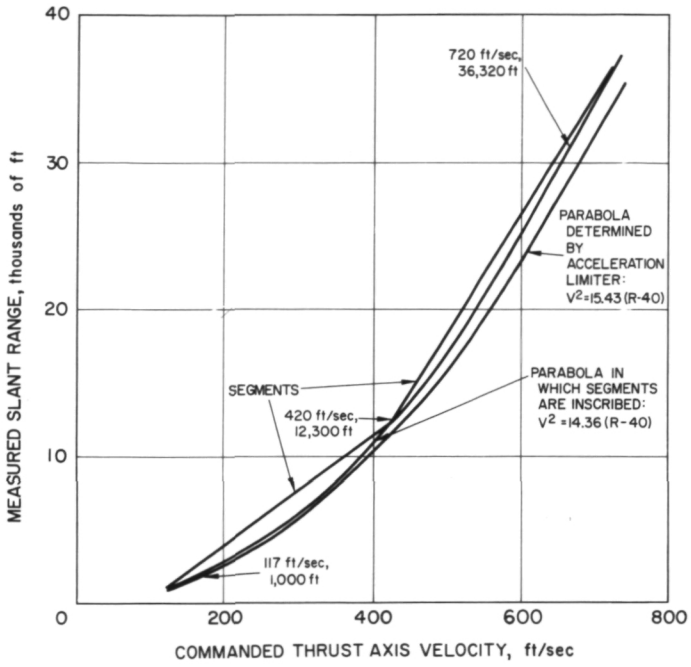

Fig. 44. Upper two command trajectory segments

An analog computer study of the attitude transient induced by vernier engine and main retro ignition was made using a two-engine, single-axis model of the spacecraft (Fig. 48). This model represents a worst case in the sense that two of the three vernier engines of the spacecraft were assumed to ignite simultaneously, followed by the third. Also, a main retro disturbance moment of 2250 in.-lb was assumed which is considerably in excess of 1800 in.-lb, for the predicted 3σ case. This delayed ignition sequence produces the greatest moment about the pitch axis. The following sequence of events was simulated:

(1) A timer signals the vernier engines to start.

(2) Engine 1 starts immediately.

(3) After a time delay, τ_1, due to random engine characteristics, Engine 2 starts.

(4) At a preset time, τ_2, after item (1) above, the timer signals the main retro to start.

The results of the study are shown in Figures 49, 50 and 51. Figure 49 shows the transient response of the vehicle during the foregoing sequence of events, while Figures 50 and 51 show peak vehicle rates and angles compiled from numerous computer runs typified by Figure 49. These results lead to several conclusions.

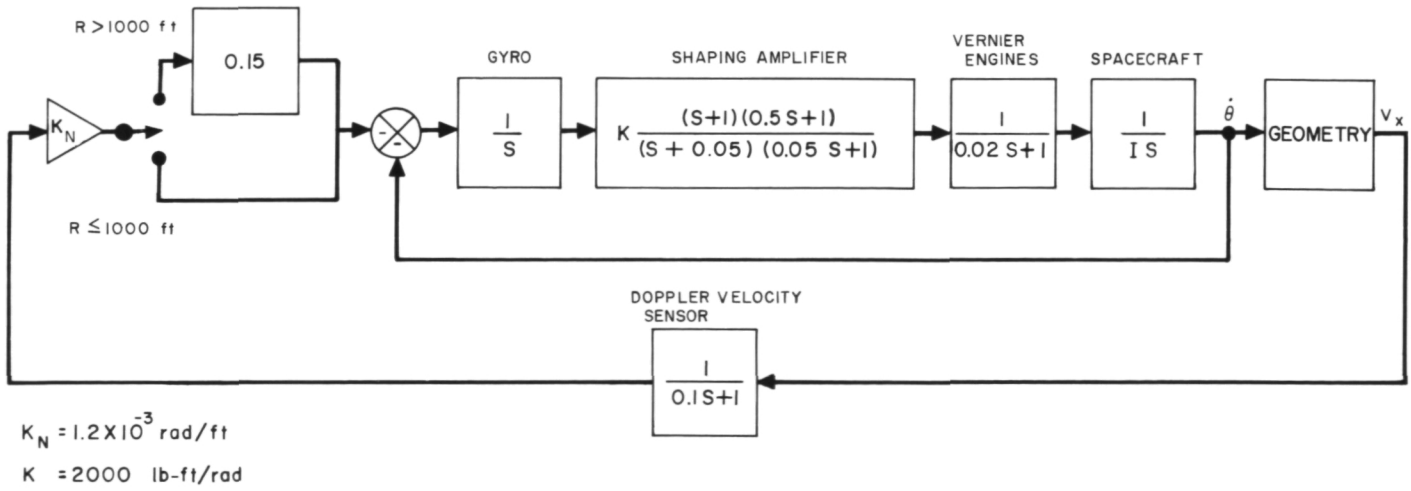

Fig. 45. Attitude control system for A-21 spacecraft

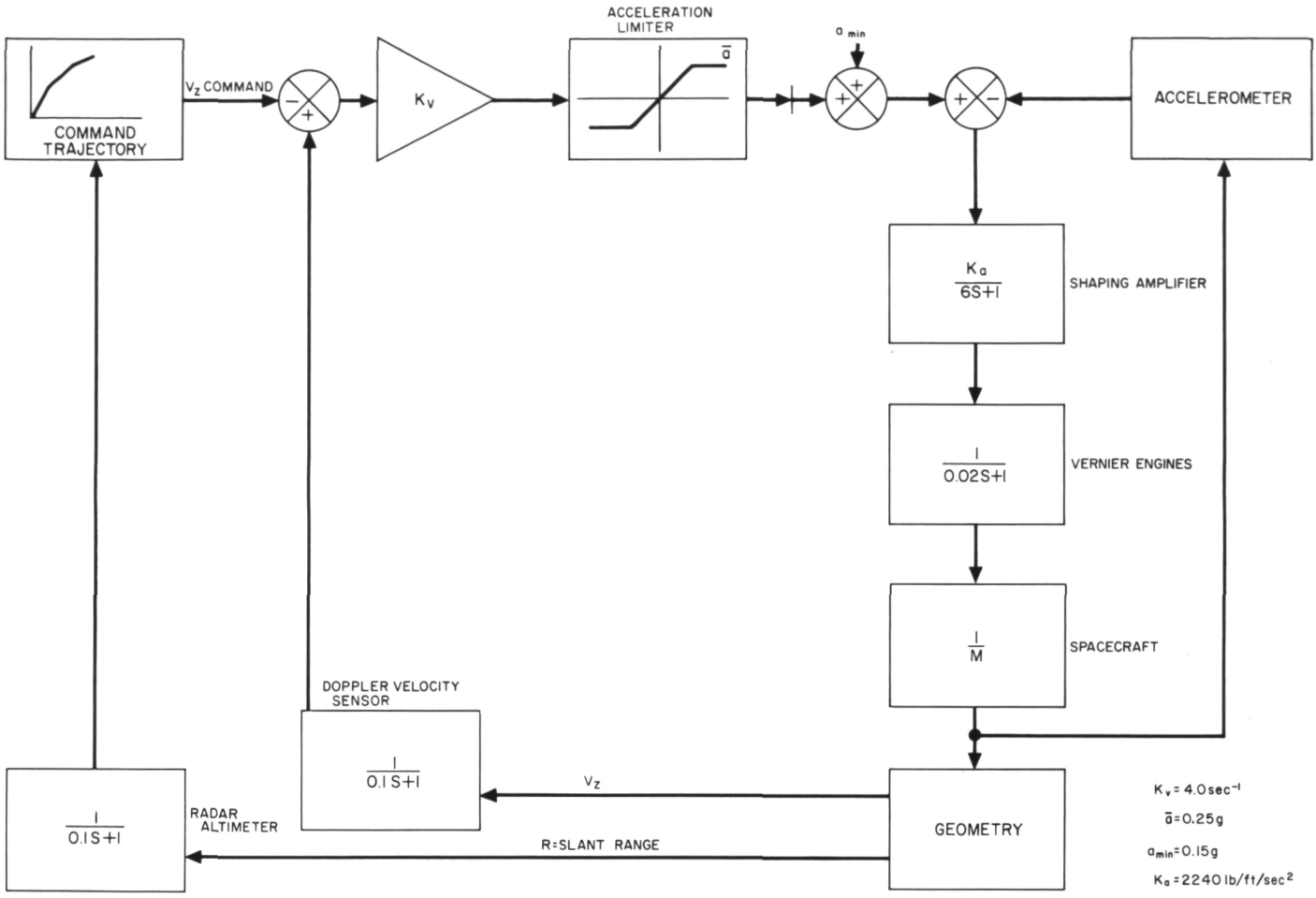

Fig. 46. Velocity control system for A-21 spacecraft

First, assuming present estimates of spacecraft moments of inertia are correct, the cross-coupling moments are less than 0.5 lb-ft in all cases. This establishes the validity of the single-axis model. Second, a time delay of 1 sec between vernier and main retro ignition signals is adequate to keep gyro excursions below 10 deg. Third, peak angles and rates are well-behaved functions of the parameters considered.

A study is in progress to verify that system performance is satisfactory in the presence of expected radar noise. System transfer functions will be utilized in conjunction with noise data in an effort to determine to what extent the spacecraft attitude and rate responses are affected by the presence of noise at various points within the control system. Saturation effects due to noise will also be investigated. Log-magnitude plots of the closed-loop transfer functions of interest are shown in Figures 52 and 53. These transfer function plots define the frequency response characteristics of the doppler attitude control system shown in block diagram form in Figure 54. The radar noise is expected to consist of both discrete or "ripple" frequency components and continuous spectra. The expected ripple frequencies are as follows:

Radar Output Signal	*Ripple Frequency*
V_x and V_y	4 to 22,000 cps
V_z	49 to 150,000 cps
Range	25 to 80,000 cps

Data on the amplitude of the ripple frequency noise and on the nature of continuous spectra noise are still being evaluated.

d. Thrust phase roll control. Preliminary tests on an engineering model of the roll actuator servo which comprises the inner position loop of the roll control system

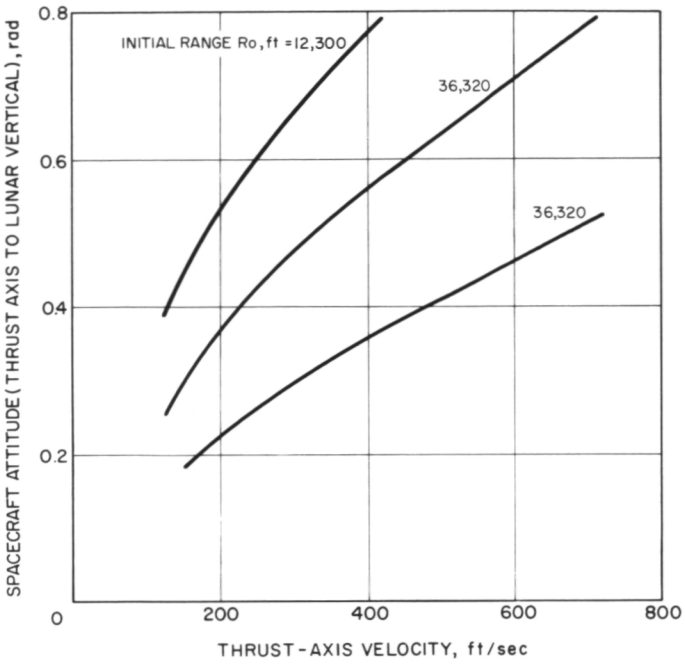

Fig. 47. Attitude versus thrust axes velocity as function of initial range

have been made. The engineering model consists of a breadboard modulator, servo amplifier, motor, gear train, and position pickoff connected as shown in Figure 55. For the initial tests, no inertial load was used on the gear train output shaft. As predicted from analog computer studies, the output shaft oscillated within the gear train backlash range about the desired output position in the absence of a bias torque on the output shaft. This oscillation can be removed by the addition of a very slight bias torque. Figure 56 shows the servo step response to a 12 deg command input with the nominal value of bias torque at its output. The maximum range of the output shaft is ±6 deg. The figure illustrates that the servo output is driven to the saturation velocity of the motor in a very short time and remains at that velocity for almost the entire transient period. The laboratory operation of the inner position loop is considered to be satisfactory.

Future plans call for a mixed simulation of the roll control system consisting of an engineering model of the roll actuator, breadboard circuits of the control circuitry external to the roll actuator, and an analog computer representation of the vehicle dynamics.

3. Subsystem Tests

a. Single-axis tests. Initial closed-loop tests were completed on the air-bearing table in the inertial, rate stabilization, and optical modes for the pitch, yaw, and roll-axes. The time to settle to a 0.3-deg pitch and yaw error was measured for various precession maneuvers both clockwise and counterclockwise with the pitch and yaw inertial deadband adjusted to ±0.2 deg and the gas jet amplifier damping parameter (K_ϵ) adjusted to a value of 6.35. The results are consistent with analog computer responses as indicated by Figures 57 and 58. Similar results were obtained in the Sun optical mode. Since the control system on the air-bearing table does not presently include a flight control programmer, the capture sequence was accomplished by manual commands through a radio link. This involved commanding the gyro to precess at the standard 0.5 deg/sec rate until the primary Sun sensor lockon signal was observed at approximately 8 deg of optical error at which time the Sun optical mode was initiated. The measured system settling times for various initial optical errors are shown in Figures 59 and 60. Measurements were also made of settling times in the pitch and yaw rate stabilization modes. Response to initial conditions of 1, 3, and 5 deg/sec resulted in corresponding settling times of 10.2, 30.6, and 48.6 sec in the pitch rate stabilization mode; and 21.2, 32.9, and 50 sec in the yaw rate stabilization mode.

The roll axis modes of operation on the air-bearing table exhibit an underdamped system behavior that is consistent neither with computer studies nor with measurements made in the pitch axis, although the control circuits are identical. Settling times measured in the roll axis were approximately twice as high as the equivalent times measured in the pitch axis. An investigation is being made to determine the cause of this behavior. Despite this discrepancy in system performance, star captures were successfully performed in the star optical mode using the development model Canopus sensor and a breadboard star simulator (Fig. 61) except for cases where the underdamped behavior of the roll channel caused excessively high angular rates (>0.8 deg/sec); the excessive angular rates prevented star capture for a small range of initial angle conditions. Under normal system operation, the angular capture rates will not exceed 0.8 deg/sec. Results of closed-loop tests performed in the star optical mode with the simulated star intensity set at the lower threshold of the Canopus gating channel were nearly identical to the data obtained with the simulated star at the proper intensity, except for a slight widening of the region in which star capture could not be achieved. In these tests, the star optical mode was initiated at the first indication of an error signal from the Canopus sensor.

The signal response of the development model Canopus sensor to the breadboard star simulator is shown in

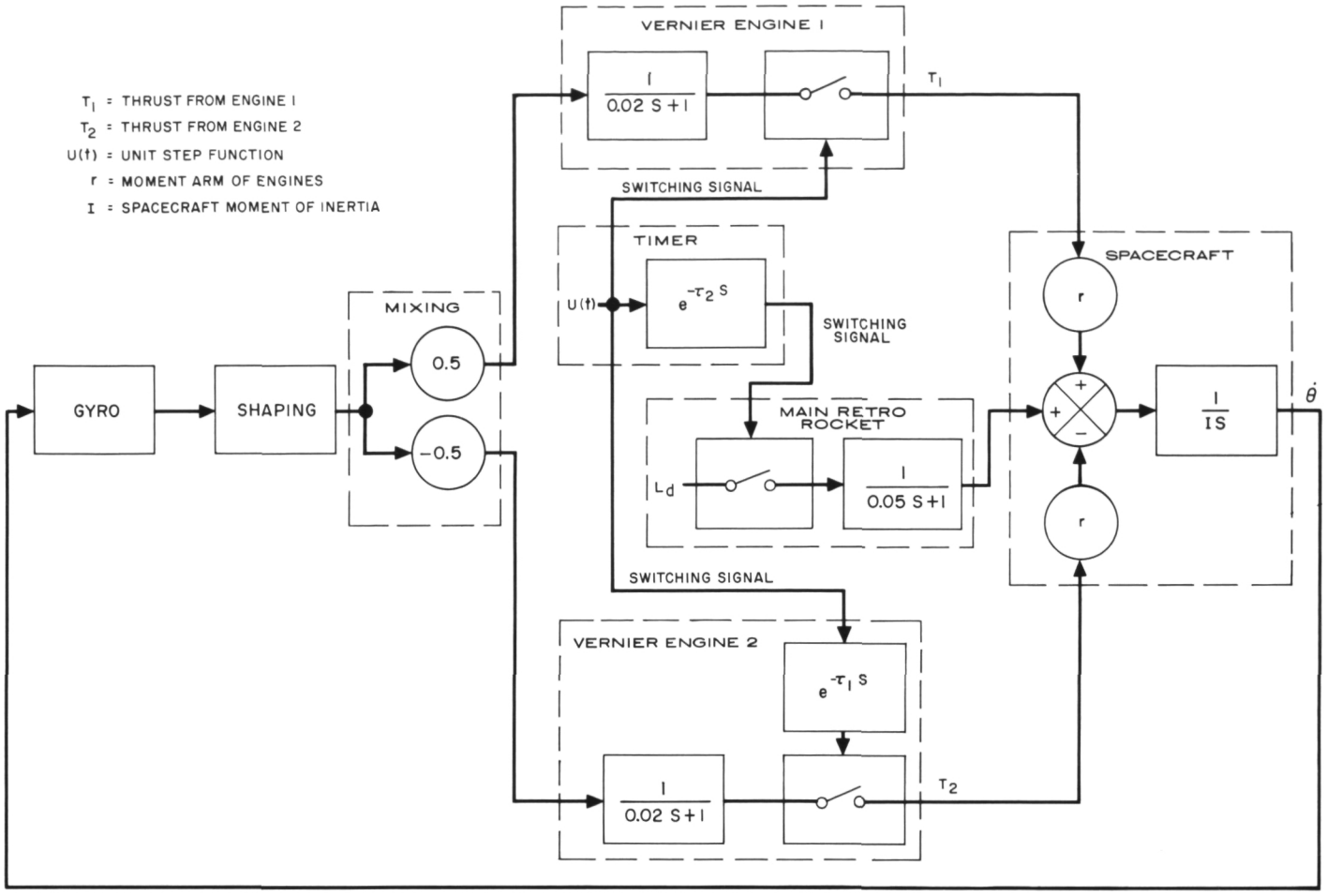

Fig. 48. Attitude transient from engine ignition

Figure 62. The response was identical when the breadboard star simulator was adjusted to provide an intensity two-thirds the intensity of Canopus.

The consignment gyro which failed during earlier closed-loop design verification tests was replaced with a prototype model gyro (Serial No. 3). The consignment gyro failure resulted from overheating due primarily to an improper warmup procedure and the non-fail-safe design of the gyro temperature controller. The controller has been modified to provide the necessary fail-safe features.

The linearity of the gyro output signal was determined as a function of angular displacement while installed on the air-bearing table; results were satisfactory, although this type of measurement is not sufficiently accurate to verify specification values. The gyro scale factor was found to be 2.82 mv/mrad compared to a specification value of 2.5 mv/mrad ±5%.

A linearity check of the phase detector and gyro ac amplifier was performed for position error signals between ±1 deg in the inertial mode. Results are shown in Figure 63.

Fabrication of the three-axis breadboard flight control circuits and the auxiliary test equipment which will be used in the electrical compatibility tests was completed. Delivery of the subsystem decoder-programmer breadboard for electrical compatibility tests will now take place on June 30 in order to permit incorporation of recent programmer changes. Development models of the roll actuator and inertial reference unit have been received and initial compatibility tests are in progress using these units in conjunction with the thrust phase control circuits.

b. T-2 test program. Preparation for subsystem testing of the flight control electronics and inertial reference

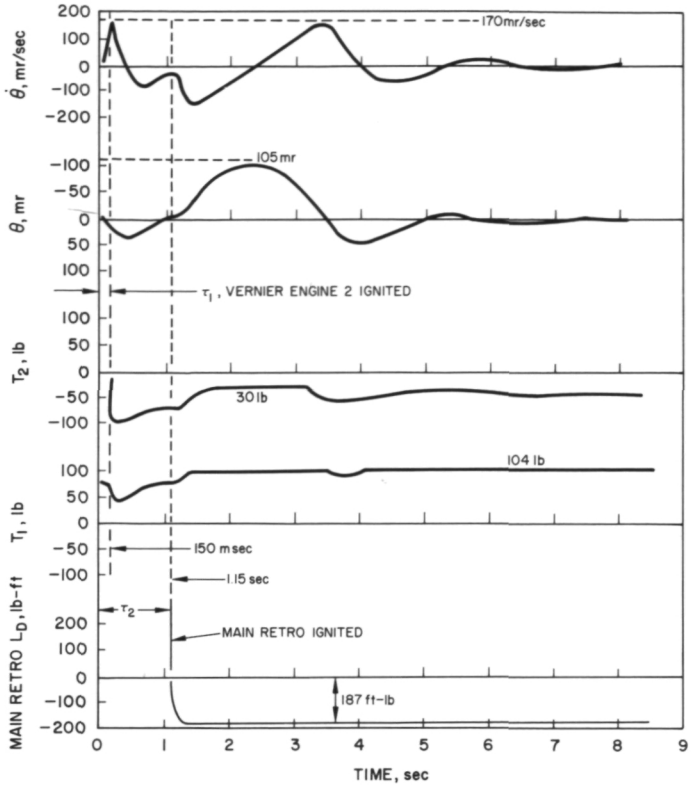

Fig. 49. Attitude control system transients at engine ignition

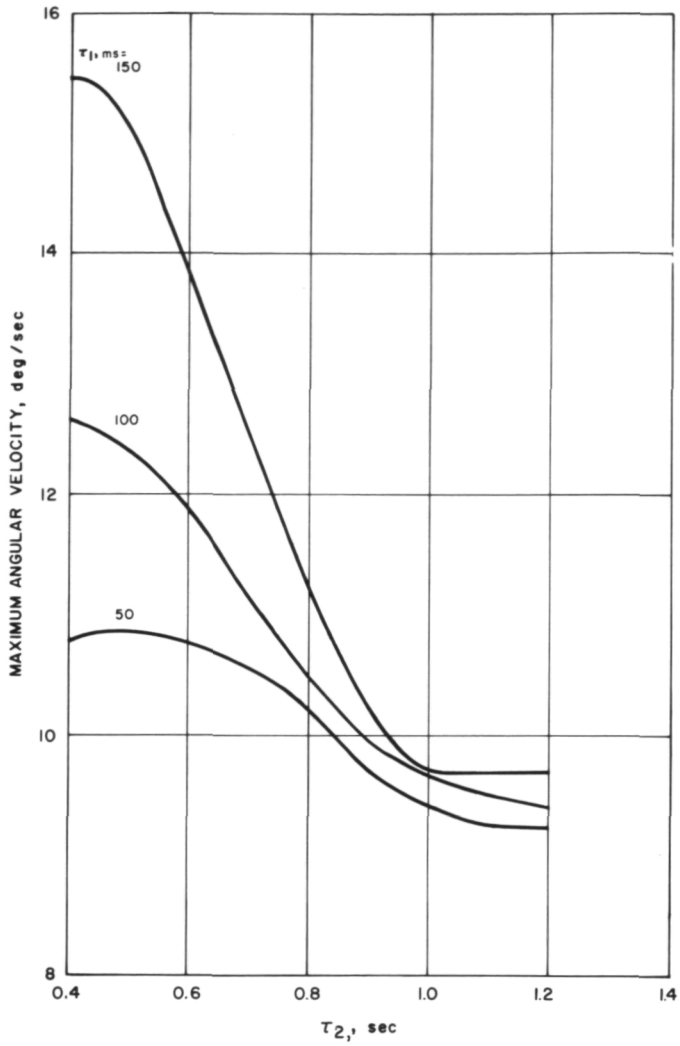

Fig. 50. Angular velocity vs retro-rocket ignition time

units is under way. A separate subsystem test interconnect wiring harness is being fabricated to facilitate the checkout of T-2 units. The wiring harness can also be used for system checkout following any rework required as a result of flight test.

Confirmation of the T-2 vehicle aerodynamic characteristics which have been used in all computer simulated studies to date will be attempted during drop tests of the T-2R recovery test vehicle. This vehicle will be aerodynamically similar to the T-2 vehicle. Results of present computer studies indicate that the T-2 vehicle dynamic response is very similar to the spacecraft response.

During this report period, an evaluation was made of the effect on the T-2 mission of vehicle weights 5 and 10 lb above the design objective. The results of this evaluation indicate that the 5 lb overweight condition does not cause serious problems, but the 10-lb overweight condition makes the final descent from 20 fps down to landing very critical. The present vehicle is computed to be less than 6 lb overweight.

Analysis of the vernier engine operation at sea level pressure disclosed that nozzle separation might occur at low thrust values. The low end of throttling is utilized on *Surveyor* primarily to minimize fuel requirements. Since T-2 is not primarily intended to show correlation of fuel usage, it is possible for T-2 to use higher minimum thrust levels in order to ensure that nozzle separation does not occur. A higher minimum thrust was used in an analog simulation with no undesirable effects on trajectory.

As the final vehicle weight, aerodynamics, and vernier engine thrust values become firm, the detailed test plans will be finalized.

4. Sensor Group Integration

a. Summary. A thermal study of the flight control sensor group (FCSG) has been completed. This study took into account the interaction of adjacent units on the spacecraft as well as thermal intercoupling in the FCSG.

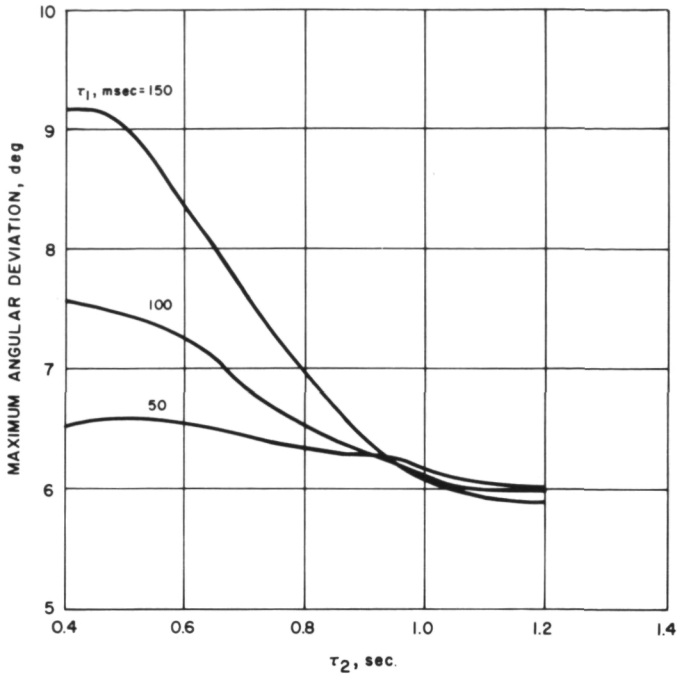

Fig. 51. Angular deviation vs retro-rocket ignition time

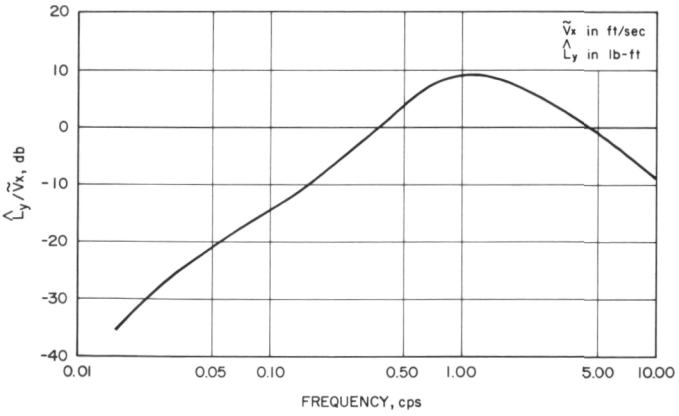

Fig. 52. Transfer function $\hat{L}_y / \tilde{V}_x$ vs frequency

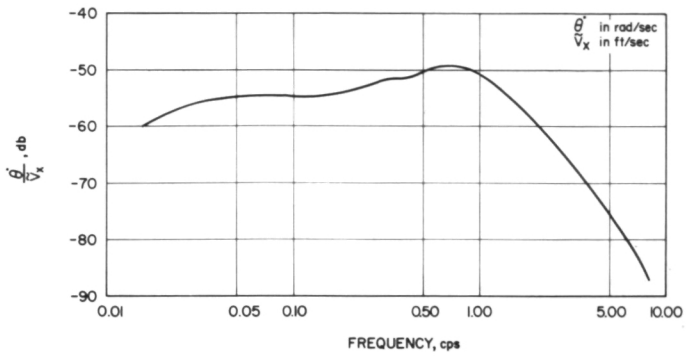

Fig. 53. Transfer function $\dot{\theta} / \tilde{V}_x$ vs frequency

A more detailed presentation of this study is given in Section G. As a result of this study, and information gained from previous vibration testing, a design freeze has been made, and prototype drawings are now in process of release.

Two test models, a thermal model and a structural model, using prototype quality hardware where necessary are being fabricated. The thermal model will use approximately 30 heaters to simulate heat dissipation throughout the unit, and 60 thermocouples will monitor temperatures during the simulated transit and descent phases of the mission.

The vibration model will use prototype mechanical hardware in the various units instead of the mechanical models used in previous testing. In this new series of structural and vibration tests, greater attention will be given to critical components within each unit. These tests are expected to uncover any dynamic interactions between units in the group which would not be evident in tests performed at a unit level.

b. Electronics unit. The flight control electronics unit has undergone several changes. Probably the most significant of these was the addition of another chassis board bringing the total to 11. Another change was the deletion

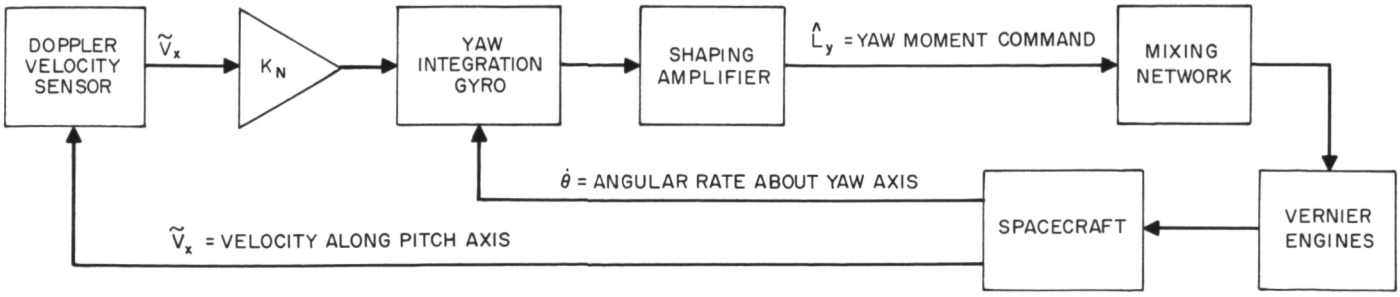

Fig. 54. Doppler attitude control, yaw axis

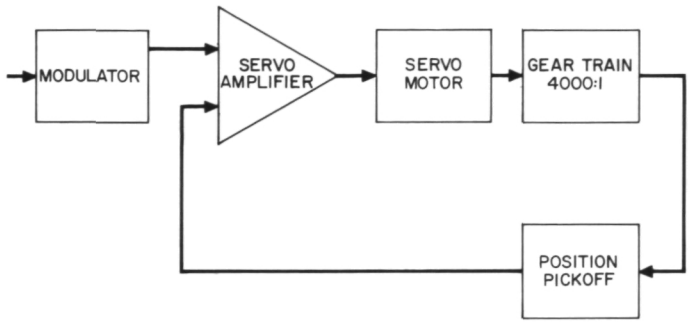

Fig. 55. Roll actuator servo

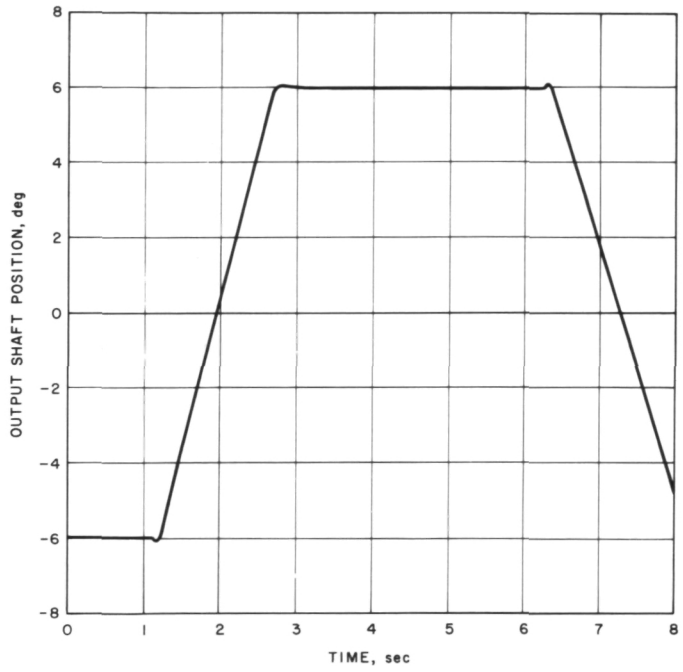

Fig. 56. Roll actuator servo response

of chassis connectors on Chassis 8 through 11. In addition, the teflon thermal insulators, which originally were to be placed under the mounting flanges, have been deleted for all chassis.

Originally, Chassis 8 through 10 were allotted for packaging the programmer and decoder circuitry. Due to circuit changes and the need for additional components, it became necessary to add another chassis. The large number of connections to each of these chassis made it necessary to eliminate chassis connectors because of weight and space considerations. Chassis connectors remain, however, on Chassis 1 through 7. Hard wiring directly to chassis board standoffs will be used on Chassis 8 through 11.

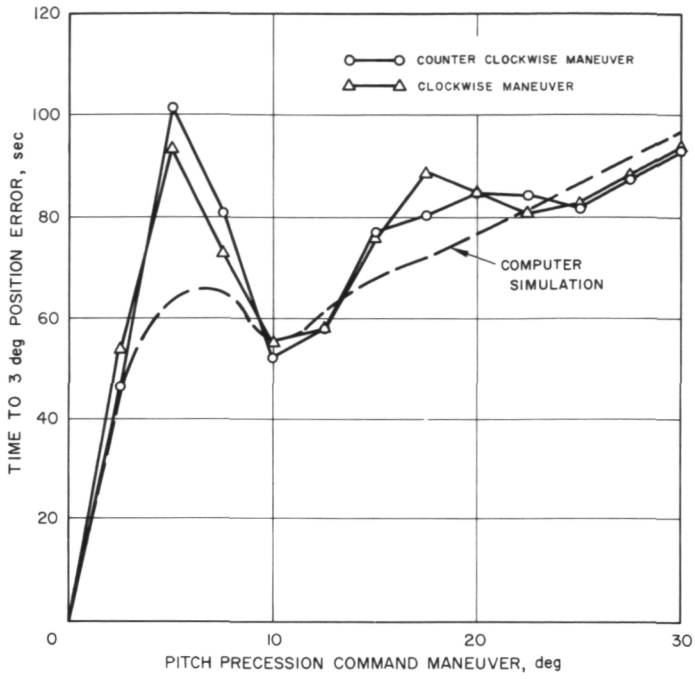

Fig. 57. Inertial-mode pitch response

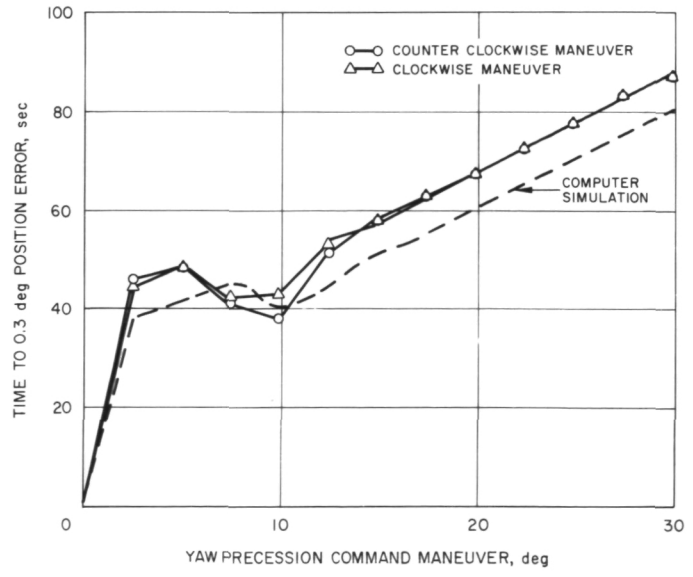

Fig. 58. Experimental inertial-mode yaw response

In order to accommodate the addition of one chassis board, the flight control unit dimensions had to be changed. Chassis are normally spaced approximately on 1-in. centers, which would imply an increase in the unit dimension of 1 in. It was determined, however, that Chassis 8, 9, and 10 could be spaced closer together. By

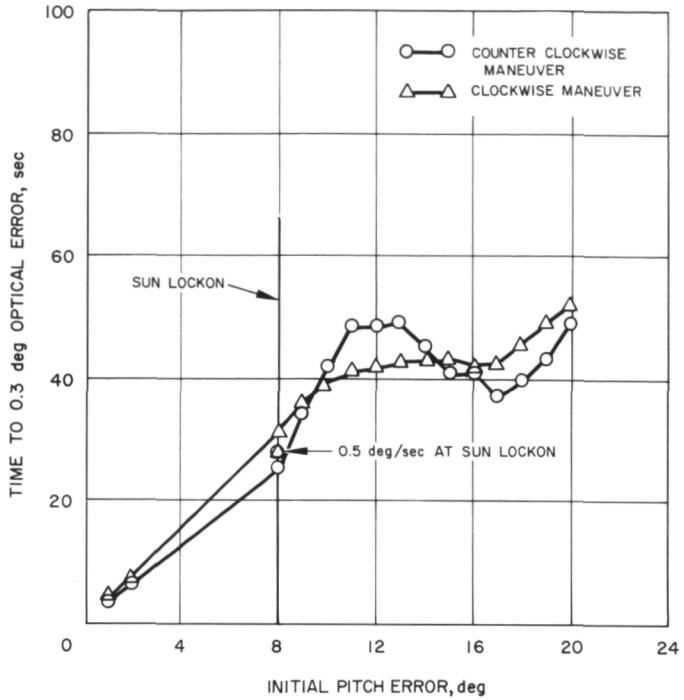

Fig. 59. Experimental optical-mode pitch response

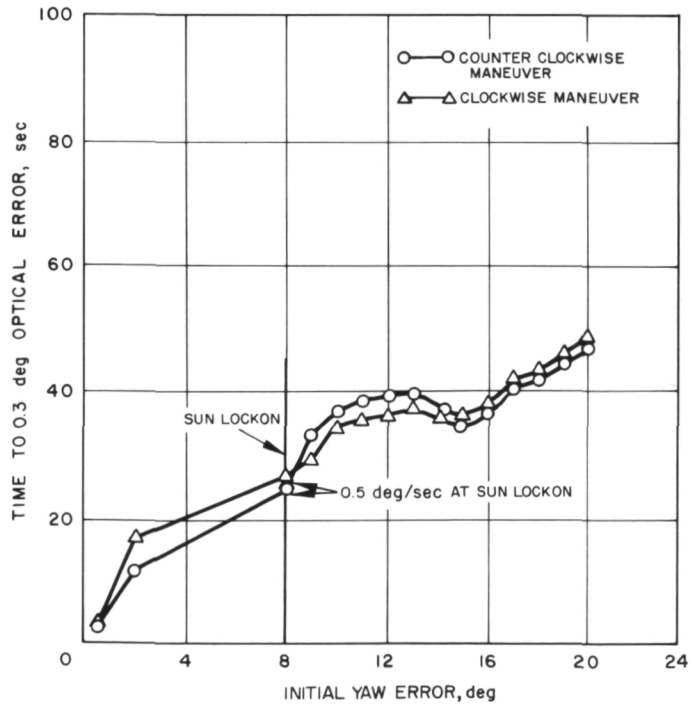

Fig. 60. Experimental optical-mode yaw response

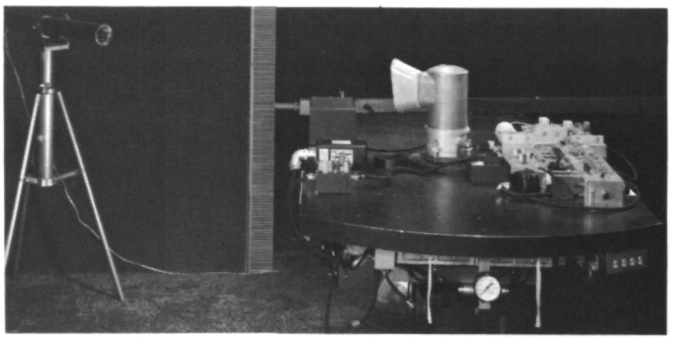

Fig. 61. Canopus sensor testing on air bearing table

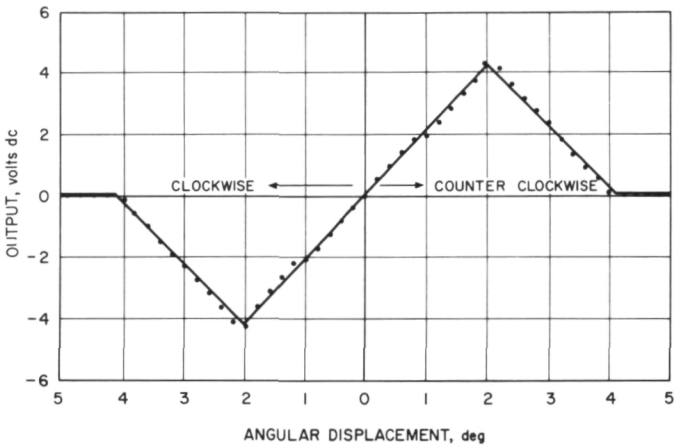

Fig. 62. Signal response on Canopus sensor

so doing, Chassis 11 was added with a resultant increase in the over-all unit dimension of only about 0.40 in. The present unit size is approximately 5.6 by 10 by 66 in., and the present weight estimate is 19.40 lb.

A new thermal analysis has been performed on the flight control unit, because of the unit structural changes and the relocation of certain circuits on the chassis boards. It was determined that the teflon thermal insulators could be deleted without significantly affecting the thermal characteristics of the unit. A weight saving of approximately 0.24 lb resulted. The bottom radiating surface will be utilized as follows: About 60% will be actual radiator and the remaining 40% will be polished to minimize heat energy absorption from the Moon. By relocating certain circuits and by utilizing a smaller portion of the bottom as radiator, the quiescent coast phase temperature has been raised closer to room temperature. In addition, the total temperature change encountered by certain sensitive circuits is expected to be only a few degrees Fahrenheit.

Some results of the latest thermal analysis are included in this report. A comparison may be made between these

temperature profiles and the corresponding profiles in the previous progress report. Figures 64 and 65 are temperature profiles of Chassis 5 and 6, which are expected to have the highest temperatures of all the chassis. Radiator temperature profiles are included in Figures 66 and 67. A minimum temperature of 49° F will occur on Chassis 4 during the coast phase, and the total coast-phase temperature change will probably not exceed 20° F. A maximum temperature of 140° F may be encountered on Chassis 5, if thrust phase power is on for 10 min prior to lunar landing. Chassis 6, which contains the ac electrical conversion unit (ECU) circuitry, will be at the next highest temperature of approximately 126° F.

All drafting and checking have been completed for the T-2 and T-21 electronics unit. Fabrication has started

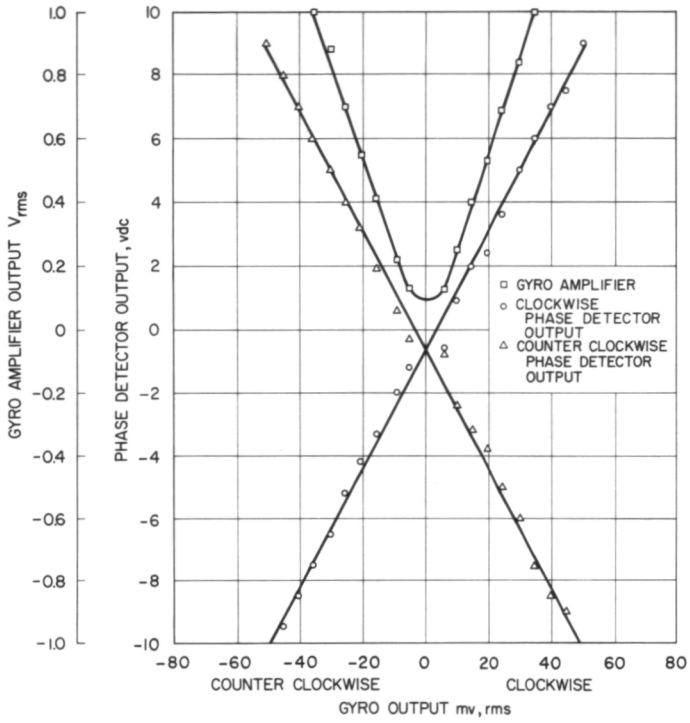

Fig. 63. Linearity check of phase detector and gyro amplifier

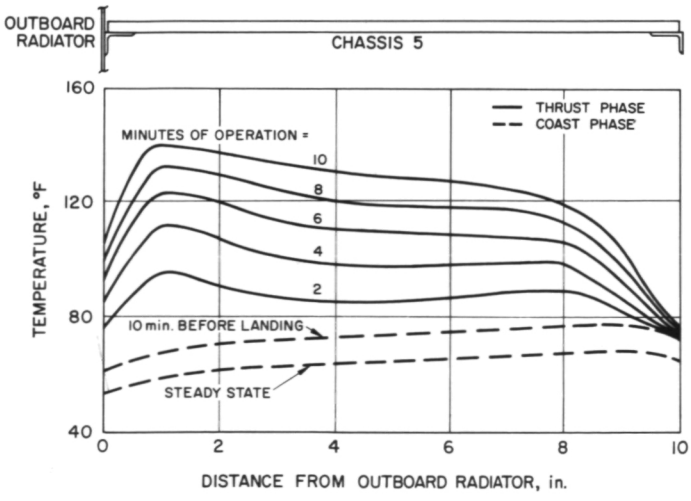

Fig. 64. Temperature profile for Chassis 5

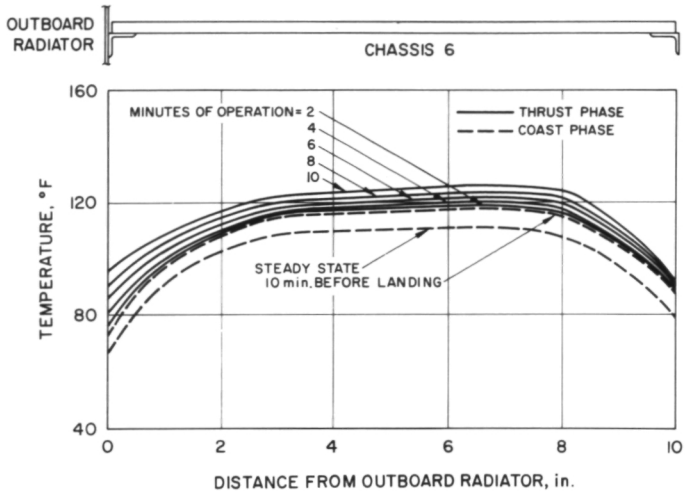

Fig. 65. Temperature profile for Chassis 6

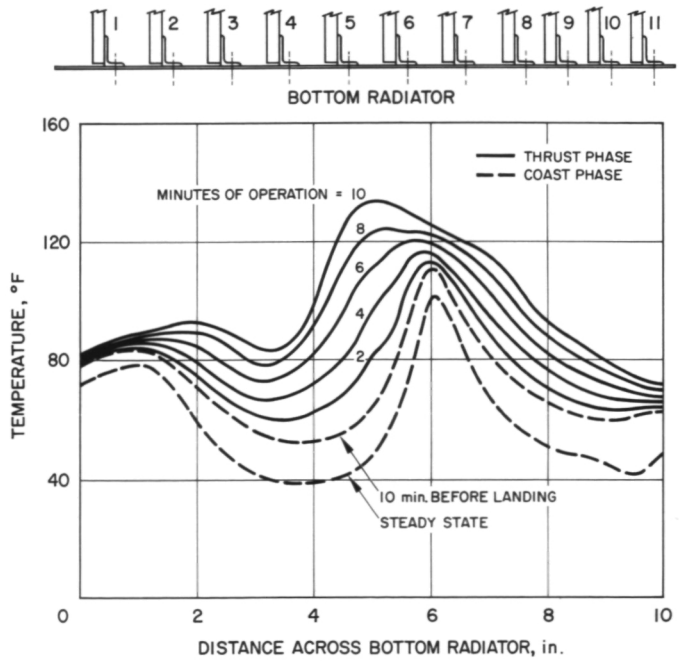

Fig. 66. Temperature profile across bottom radiator

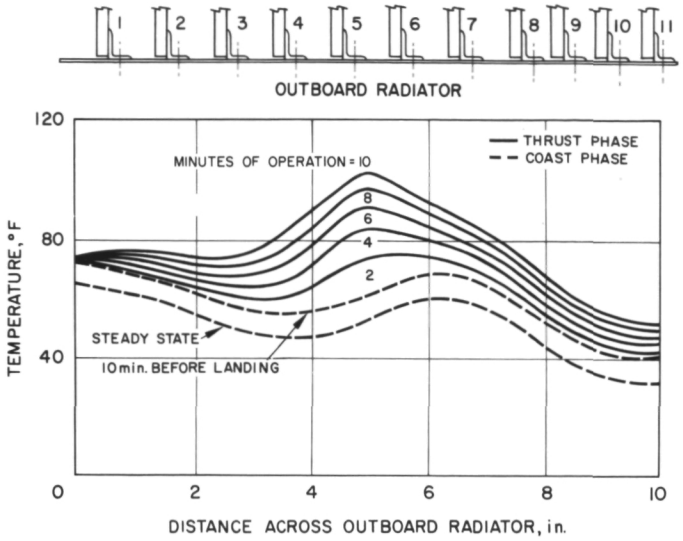

Fig. 67. Temperature profile across outboard radiator

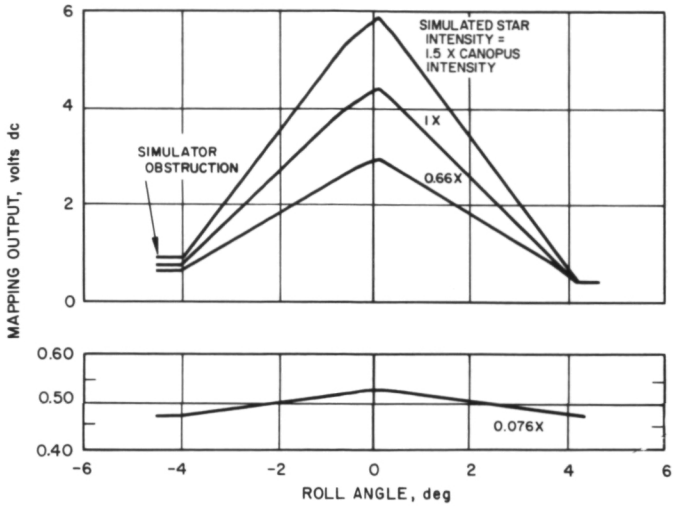

Fig. 68. Canopus sensor mapping output

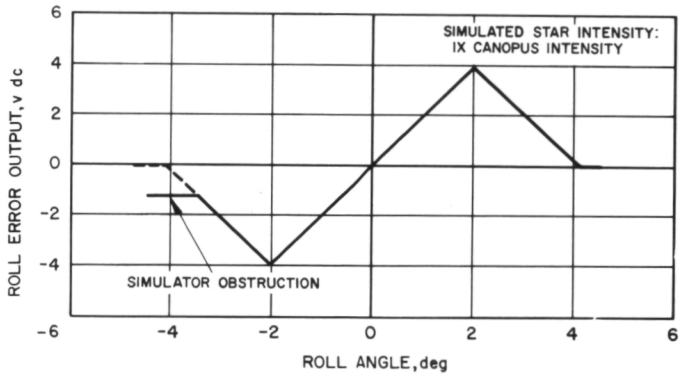

Fig. 69. Canopus sensor roll error output

on the T-21 chassis, and is approximately 75% completed on all T-2 chassis. Fabrication of test consoles is in process and checkout of the T-2 ECU chassis is under way. Checkout of the remaining T-2 chassis (Chassis 1 through 5) will begin shortly. The chassis for the T-2 unit are similar to T-21 except for certain component deletions.

5. Optical Sensors

a. Canopus sensor. The X-1 development model Canopus sensor and the Sun–star simulator were received, and initial unit checkout was completed with satisfactory results. This development unit had undergone extensive functional testing as well as environmental testing prior to delivery to Hughes Aircraft Company. Acceptance testing was limited to certain performance checks and did not include all specification requirements. Typical curves of the roll error signal and the mapping outputs are shown in Figures 68 and 69. The Canopus indicate signal was measured to be 10 v when the star is in the field of view. Noise levels were acceptable. The major portion of these tests were conducted in the Sun–star simulator, which provides both simulated sunlight and starlight. The simulated sunlight is of proper intensity with the filter removed from the sensor Sun channel. The star beam can be varied in intensity by inserting apertures of different sizes, and in direction (simulating different star positions) by means of two calibrated micrometer adjustments. The apertures furnished with the simulator provide star intensities of 1.5, 1.0, 0.66, and 0.076 times that of Canopus. The 1.5 and 0.66 intensities represent the threshold limits ($\pm$0.45 magnitude) for the Canopus indicate output signal, and 0.076 represents a star 2.8 magnitudes below Canopus (lower limit of detectability of the mapping channel). Operation was also checked with the sensor mounted on a rotating angular divided table. A small auxiliary lamp was used to illuminate the Sun channel and a breadboard model star simulator provided a fixed position star beam. Both the auxiliary lamp and the star simulator were adjusted in intensity to give the same sensor output levels as were obtained with the Sun-star simulator. Performance was essentially identical to that obtained with the Sun-star simulator. The Sun-star simulator appears limited for complete unit tests, in that the field of view cannot be checked when the sensor adjustable mirror is set for the extreme time-of-year excursions of the angle between

the sunline and starline (90 ±15 deg). This portion of the unit testing will have to be conducted with the auxiliary equipment.

During this report period the electronic assembly of the type approval test unit and the T-21 unit was completed.

Continued vibration testing with vibration isolators built into an engineering development model has eliminated the high frequencies as a problem area. However, low frequencies (approximately 200 cps) still pose a vibration problem resulting in undesirable motion of the adjustable mirror and possible malfunction of the photomultiplier tube. Minor design changes are being made in an attempt to overcome design weaknesses.

b. Sun sensors. In order to improve Sun acquisition performance, as discussed in Reference 1, the field of view of the primary Sun sensor has been enlarged and the secondary sensor acquisition cell response has been modified.

The field of view of the primary sensor is shown in Figure 70. The flattened shape is due to interference with Television Camera 2 in the lightweight vehicle configuration.

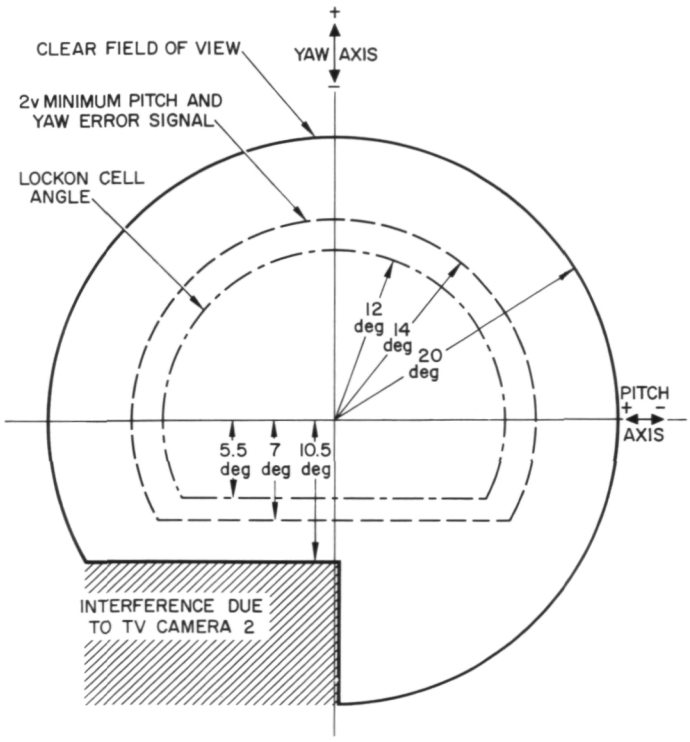

Fig. 70. Field of view of primary Sun sensor

The nominal lockon cell angle is shown by the dashed line in the figure. Usable pitch and yaw error signals will be supplied out to the angle indicated by the dotted line in the figure. Hardware to implement this change has been designed and is presently being fabricated. The major modifications involve changes in the shadow mask configuration and do not effect the basic design of the sensor.

The response of the secondary sensor acquisition cells has been modified as described later in this section. Accurate response is provided at the yaw–roll plane boundary where acquisition switching occurs, but somewhat less sharp response is required at the pitch–roll plane boundary. An improved developmental model of the secondary sensor has been constructed to give the desired resistance vs angle response. Tests on this model indicate that the required response can be obtained with the new design.

Tests on the developmental model of the primary sensor are continuing at the Sun sensor test facility. Some minor modifications are being made on the test equipment to ensure repeatability of the boresight axis to permit accurate sensor null stability checks.

The order of special photoconductive cells from Clairex Corporation has been received and cells are presently being inspected for mechanical and electrical adherence to the procurement specification. After the initial inspection, rigid qualification tests will be performed on a portion of the accepted cells.

6. Inertial Reference Unit (IRU)

a. Instruments. At the April coordination meeting at Kearfott, agreement was reached on all outstanding items of the procurement specification and the work statement. The Kearfott acceptance test procedure was revised, reviewed, and approved. The qualification test procedure was received and is being reviewed. This procedure will require minor upgrading to include additional testing requirements. The procurement specifications for both the gyro and the accelerometer were revised.

A total of 12 gyros have been delivered. Serial No. 1 was returned to the vendor because of an elastic restraint discrepancy and is being repaired. Serial No. 2 was returned to Kearfott for rework to the latest signal generator network configuration. Serial No. 6 and 7 were returned to Kearfott for analysis of intermittent torque-to-case short circuits. Of the remaining eight units, four have been tested and accepted and the remaining four are undergoing tests at Hughes. Table 10 presents a comparison of gyro drift rates as measured by the vendor

Table 10. Comparison of Kearfott and Hughes gyro drift measurements

Gyro serial number	Nonacceleration-Sensitive drift, deg/hr			Vector sum of acceleration-sensitive drift, deg/hr/g		
	Kearfott	Hughes	Variation	Kearfott	Hughes	Variation
3	+0.396	−0.120	0.516	0.282	0.450	0.168
4	−0.239	+0.150	0.389	0.410	0.450	0.040
5	−0.128	+0.250	0.378	0.302	0.532	0.230
6	+0.169	−0.138	0.307	0.212	0.560	0.348
8	−0.492	−0.550	0.058	0.875	1.320	0.445
9	−0.357	−1.970	[a]	0.681	0.820	0.139
10	−0.103	−1.950	[a]	0.610	1.150	0.540

[a] Excessive nonacceleration-sensitive drift rate.

and Hughes Aircraft Company, on a sample of seven gyros. Except for Serial No. 9 and 10, the variations indicated are within acceptable specification limits of ±1.0 deg/hr for non-acceleration-sensitive drift, and ±2.0 deg/hr/g for vector sum acceleration-sensitive drift. Serial No. 9 and 10 gyros are being used in the engineering development model of the IRU.

Two additional accelerometers were received, bringing the total to seven, which completes the initial procurement order. All of these instruments have been tested and accepted for use in the first inertial reference units. Table 11 depicts the measured output signal of six accelerometers in response to an acceleration of 0.11 g. The accelerometer has a sensitivity that varies with temperature approximately 0.01%/°F. In the initial design of the IRU, the entire instrument assembly, including the accelerometer, was to be temperature stabilized at 180° F. However, the existing design does not accurately control the accelerometer temperature; hence, there will be a change in the output voltage due to this temperature

Table 11. Accelerometer output voltage

Accelerometer number	Output voltage at 0.11 g, vdc[a]
6854A	3.325
6855A	3.331
6856A	3.312
6857A	3.316
6858A	3.324
6860A	3.337

[a] Specifications: 3.300 ±0.033 vdc. Above data have been corrected for axis alignment.

difference. Thermal vacuum tests of the IRU will ultimately fix the operating temperature of the accelerometer. If this temperature does not vary more than ±5° F from a known nominal value, there should be no degradation in performance.

Based on computer data, Table 12 shows the nominal accelerometer output voltage at 0.11 g vs temperature. These data were subsequently verified by test results over the temperature range from 140 to 180°. From Table 12, it can be seen that the shift of nominal output voltage will be small and the circuitry external to the IRU will be capable of change to accommodate a shift in the accelerometer nominal output voltage at 0.11 g of up to 0.3 v. This covers possible operating temperatures of the accelerometer. At the conclusion of IRU temperature tests, this nominal output voltage will be specifically defined, so that the proper control circuit bias resistors can be changed if required.

Table 12. Variation of accelerometer output with temperature

Accelerometer temperature, °F	Output voltage at 0.11 g, vdc
180[a]	3.300
160	3.293
140	3.287
120	3.280
100	3.274
80	3.267

[a] Specification control point.

b. Unit design. The engineering model inertial reference unit, which will be used for system compatibility tests, was assembled, checked out, and delivered for subsystem test. Figure 71 shows this unit mounted to the test fixture. This IRU contains three gyros, an accelerometer, and three temperature control modules that have been completely tested and accepted as components. The signal generator current source is included as a breadboard assembly at this time, but will be replaced by a module at a later date.

The detail specification for the inertial reference unit has been revised to reflect all changes and to incorporate additional data. The type approval test specification for this unit has been prepared and released. The flight acceptance test specification is being prepared and will be released after completion of the initial engineering unit evaluation tests.

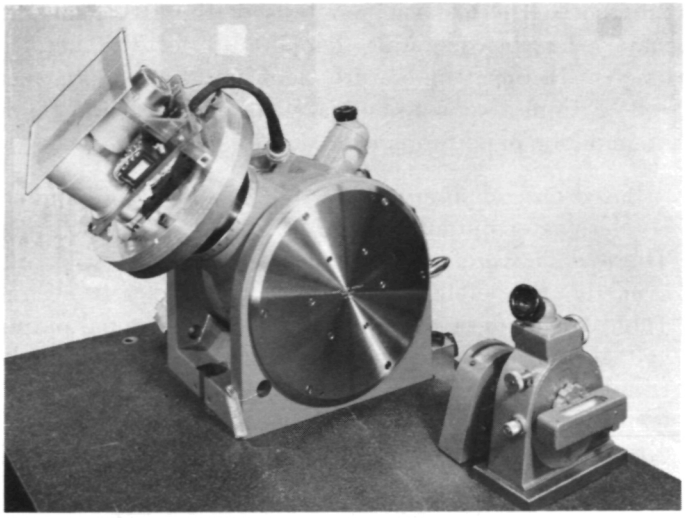

Fig. 71. Inertial reference unit on test fixture

Fabrication of a second engineering model and a thermal model have been completed. The T-2 unit is complete except for the installation of the accelerometer, which has not yet been received.

The design of the signal generator current source module has been completed and is now in fabrication. The first of these modules will be used in the electrical compatibility model IRU.

7. Attitude Control

a. Gas jet system. The changes in the gas tank charging connection required by the tank relocation have been coordinated with the vendor. No serious delay in delivery is anticipated.

Placement of the squib valve purchase order has been delayed by renegotiations with the vendor on the cost of a reliability program recently instituted. Possible schedule delays cannot be ascertained until the final delivery schedule is supplied.

The pressure transducer vendor, Bourns Laboratories, has delayed delivery of the engineering and qualification units because of their inability to meet the sterilization temperature requirements. This problem, according to the vendor, has now been overcome and deliveries are expected to start in June. Procurement of flight units has been delayed pending qualification. Because of the uncertainties associated with qualification and delivery, an attempt will be made to qualify a second source.

Prototype pressure controls are being fabricated and assembled for test. In-plant brazing of the pressure sensing bellows to the body is being developed to expedite delivery and minimize handling damage.

An investigation of the gas jet system manifold has disclosed that under steady-state operating conditions the temperature of the gas entering the jets may be low enough to seriously decrease the system total impulse. This condition exists even though the tank is thermally controlled. Consequently, modification of the tank thermal control is under consideration. In order to maintain a desirable gas jet inlet temperature, passive thermal control of approximately 2 ft of tubing on the top side of the legs is being investigated. Preliminary analysis indicates there are several possibilities of material and/or surface coatings that can be used to take advantage of solar radiation to maintain the desired temperature. Some coating of the tank surface may be necessary, however, to prevent possible excessive tank temperature during the injection period.

Six jet valves are in various stages of completion in addition to three which have been delivered for the electrical compatibility tests.

b. Roll actuator. Three engineering models of the roll actuator have been built and are undergoing evaluation. The decision to design the roll actuator at Hughes resulted in a general plan of approach directed toward outside procurement of position transducers and motors, with design and fabrication of the gear train taking place at Hughes. The engineering models incorporate gear trains which were obtained from an outside source so that evaluation of the complete basic design could take place as soon as possible. Tests will be made on the actuator both as an element in the subsystem control loop and as a functional unit in vernier engine tests to be conducted at the Reaction Motor Division of Thiokol Chemical Corporation.

The development model roll actuator is shown in Figure 72. Spur gears are used to accomplish the gear reduction of over 4000 to 1 as shown in Figure 73. The worm gear stage on the motor was introduced because space limitations prevented mounting the motor parallel to the axes of the spur gear shafts. The view of the actuator in Figure 74 shows the mounting face and the torque arm which drives the vernier engine. This torque arm embodies two basically conflicting design objectives which are: (1) to provide a driving link between the vernier engine and the roll actuator with negligible backlash in operation, and (2) to permit coupling of the actuator to the engine without requiring special assembly fixtures or instructions. These were accomplished by using that part of the output shaft

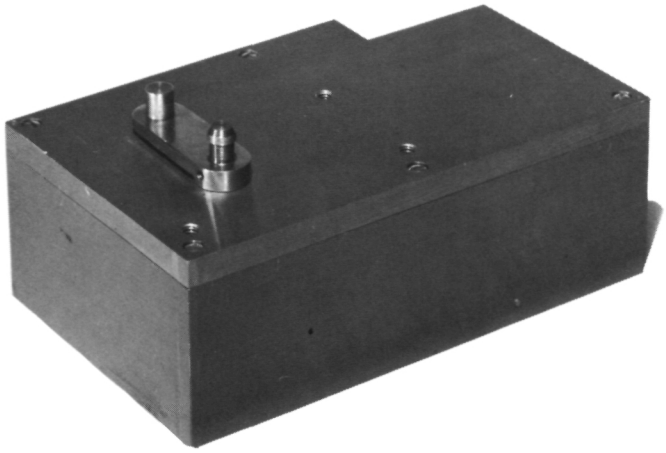

Fig. 72. Development model roll actuator

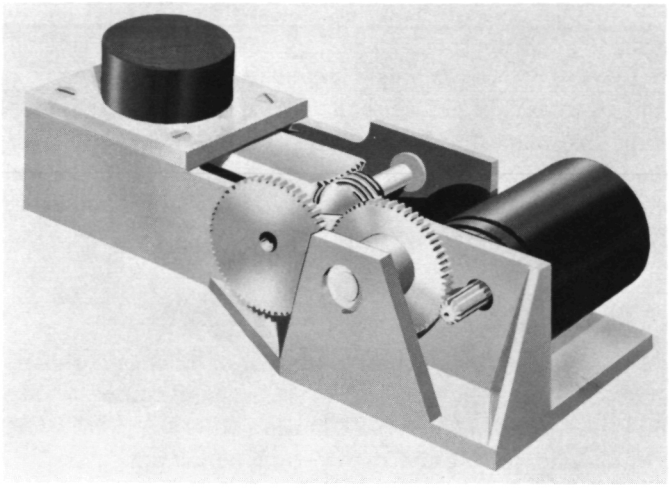

Fig. 74. Roll actuator mounting face and torque arm

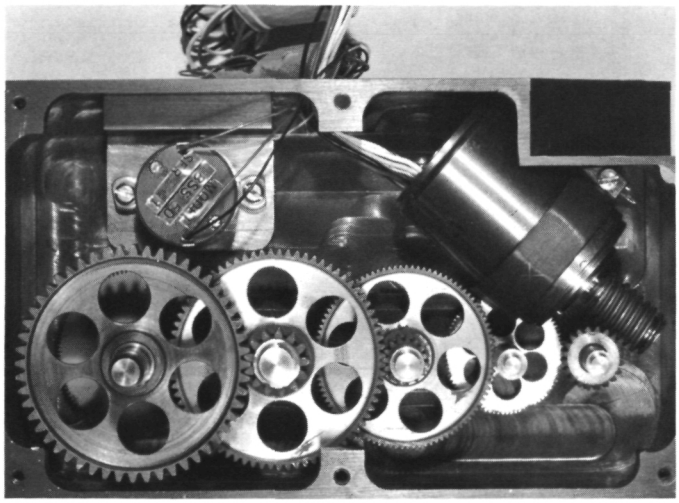

Fig. 73. Roll actuator gearing

which extends past the torque arm as a dowel pin to position the actuator accurately for concentricity. The drive pin at the end of the arm is 1.000 to 1.001 in. from the centerline of the dowel pin. It has a close tolerance diameter and mates with a close tolerance hole. This permits engagement of the pin in the driven part with a maximum clearance of less than 0.0015 in. and results in a backlash of $\frac{1}{10}$ deg with the maximum accumulation of adverse tolerances.

The motor and position transducer used in the development model actuator were procured to the requirements originally established for the roll actuator. The motor is a two-phase servomotor in a standard size 11 housing. Performance requirements are nominal for that size motor, 26 v rms input producing 0.60 in.-oz minimum stall torque and 6200 rpm minimum no-load speed. The position transducer is a special design induction potentiometer using a 10 v rms input and producing an output signal having a gain of 0.25 v/deg through an operating range of ± 6 deg. Development units of the motor and transducer have been tested and found to be well within Hughes requirements. Procurement specifications are in the final draft stage of completion.

The Hughes gear train design as illustrated in Figure 74 has been completed, and parts have been fabricated and are now in test. The basic decisions which resulted in the final design approach were: (1) to use the maximum pitch radius that could be accommodated for output gear, and (2) to use a worm gear on output stage. Use of a maximum pitch radius output gear has three advantages. It provides a minimum backlash at the output shaft without the use of excessively tight tolerances in the gear tooth form, bearing clearances, and gear center mounting distances. This permits greater reliability in achieving a backlash that does not exceed $\frac{1}{4}$ deg. The use of maximum pitch radius gears also reduces the gear tooth loading. Finally, it permits a design with a minimum number of gear stages with resulting weight and cost savings. This approach can be compared with the developmental model actuator which uses spur gears and for which five stages are required against the three stages of the Hughes design. Use of a worm gear permits mounting of the motor parallel to the face of the actuator to fit the space available, and putting the worm gear on the final stage reduces the tooth rubbing speeds for maximum wear life.

The roll actuator, in its final design, will be sealed in order to keep the functional elements from being exposed to a hard vacuum. It was decided that development of a seal was more practical than requiring induction potentiometers and standard motors to operate in a hard vacuum. One seal configuration has been fabricated and is ready for test, and a second design approach is in the fabrication stage.

8. Control Circuitry

Checkout of the three-axis control circuits breadboard chassis which will be used in subsystem compatability tests has been completed. During the checkout, test criteria and procedures for testing, adjusting, and calibrating the circuits were established. Much of this information will be used in preparing design specifications for each of the five flight control circuit chassis in the electronics unit.

The roll actuator control circuits are currently being tested in conjunction with a developmental model of the actuator.

Several changes were made to the coast phase control and the Sun acquisition logic circuits based upon closed-loop air-bearing table tests, additional system analyses, and a better understanding of system tolerances. In order to provide adequate system performance on the air-bearing table, it was necessary to reduce the gas jet switching amplifier deadband from 0.2 to 0.18 deg and increase the amplifier damping parameter $K\epsilon$ to provide a nominal value of 7.5. The latter change was made to ensure that the damping would never be less than the former value of 6.0 over the expected range of environmental conditions. In addition, the gyro circuit loop gain was reduced to 0.3 sec^{-1} from a value of 0.75 sec^{-1}. All changes were accomplished by changing component sizes and required no revisions to existing layouts.

The changes associated with the Sun acquisition logic circuits were more complex and did require layout changes. The mechanization of the automatic Sun acquisition logic was changed to improve system capture dynamics (as discussed previously in this section) and reduce the effects of design tolerances. Previously, the point at which the acquisition sequence "switched" from a yaw to a pitch maneuver depended on the width of the secondary Sun sensor cell sensitive overlap region. The width of this overlap was determined by electrical tolerances of individual sensor cells, mechanical tolerances of cells with respect to shadowing elements, and electrical tolerances associated with the cell readout flip-flops and their hysteresis bands. The limitations placed on these variables were caused by a practical limit on the effective area of the Sun lockon cell (the primary sensor center cell), and the capture mode dynamics. The difficulty arose when the approach path to the lockon area (approximately a cone about the roll axis) was too shallow; i.e., passed too far from the cone center.

The new mechanization involves an initial maneuver about the yaw axis until the Sun line of sight reaches the boundary between two cells. This boundary is nominally the yaw–roll plane which passes through the center of the lockon "cone." When a pitch maneuver is thus initiated, a memory flip-flop is set which causes that pitch maneuver to continue until the flip-flop is reset. No other maneuver is possible until the flip-flop is reset, regardless of secondary sensor cell illumination. The memory flip-flop is reset by removing the Sun command or by entering the Sun lockon cone.

Figure 75 illustrates the function of the secondary Sun sensor and the analog-to-digital conversion associated with it. The flip-flops have hysteresis as shown, such

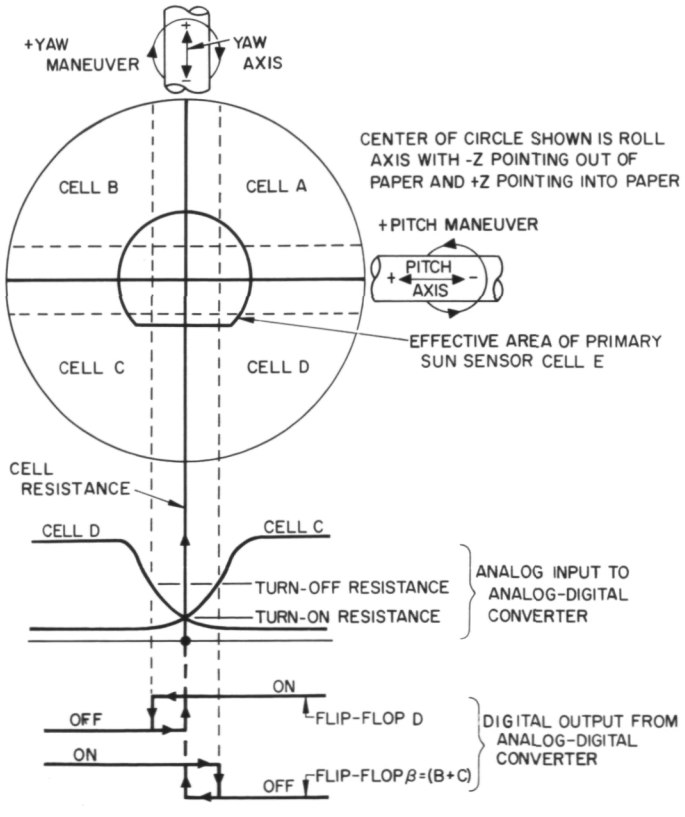

Fig. 75. Operation of secondary Sun sensor

that nominally a transition from yaw to pitch command occurs on the centerline, whether approached from the right or left. Figure 76 is a logic diagram that shows the generation of the desired logic expressions from the sensor inputs.

9. *Flight Control Programmer*

The product design for T-21 has been completed including module and printed-circuit-board layouts and final preparation of the etched circuit masters. The final

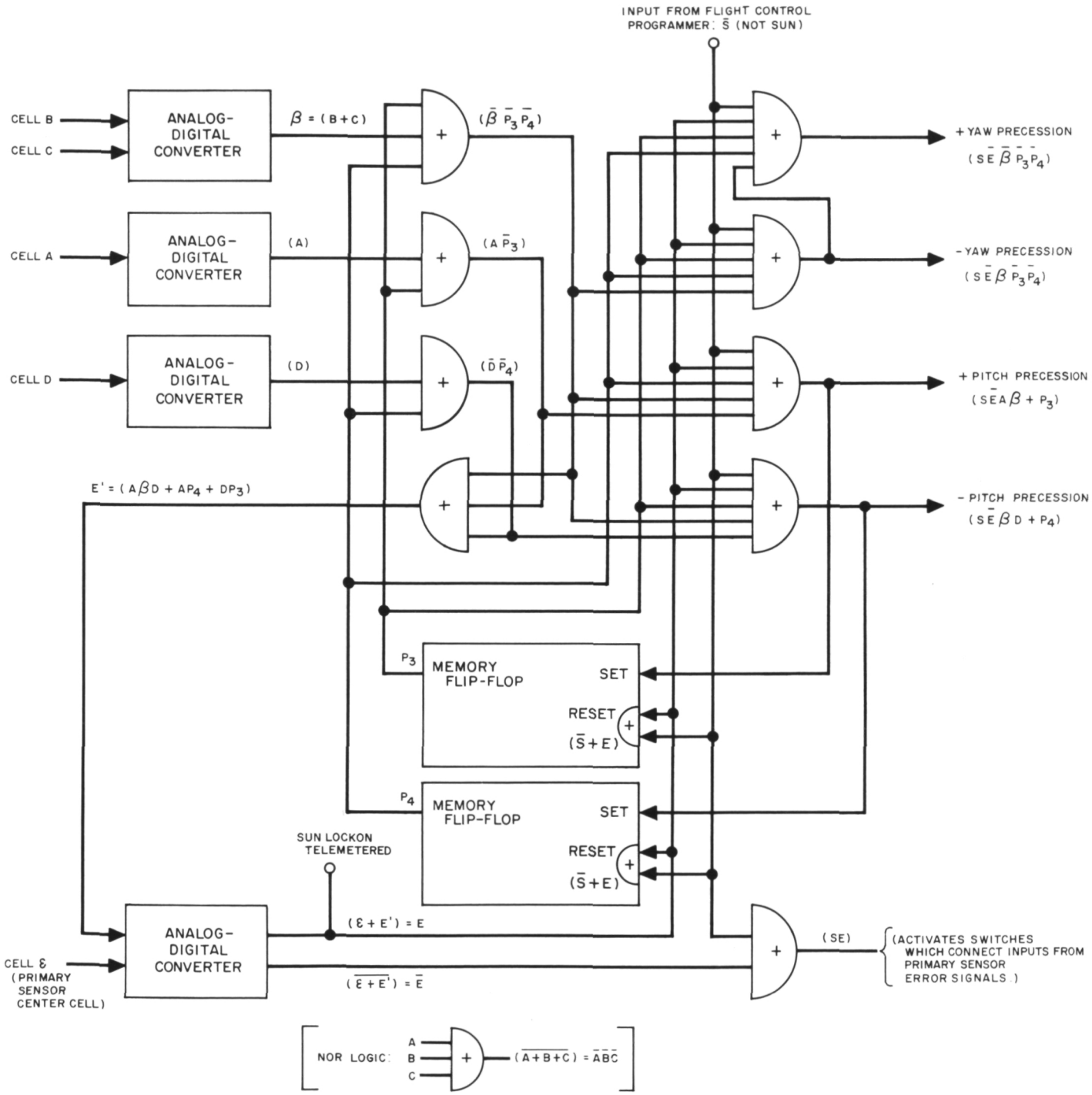

Fig. 76. Secondary Sun sensor logic

functional logic design was revised to include the following engineering changes:

(1) The fixed time delay between vernier engine ignition and main retro ignition was reduced from 8 to 1 sec in order to conserve vernier engine fuel.

(2) A signal was provided to change the bandwidth of the radar altimeter and doppler velocity sensor circuits at retro burnout or when the emergency retro eject command is received.

(3) Opening of the nitrogen dump valve was mechanized to take place by radio command rather than automatically at the time of main retro ignition. In addition, the command to close the nitrogen gate valve is now provided at retro-engine separation rather than at main retro ignition. These changes were made to permit the emergency firing of the main retro without the subsequent loss of a gas jet attitude control capability.

(4) A fifth commutator was added and the signal assignments in all five commutators were changed to provide a more logical arrangement.

The T-2 assembly which consists of five modules mounted on a single printed-circuit board was fabricated, tested, and delivered for inclusion in the flight controls electronic unit.

Investigation of the 12.8-kc crystal in a vibration environment revealed degraded performance at 15 g and higher. A ruggedized, higher-frequency crystal was substituted and the necessary circuit revisions incorporated. The new crystal provides adequate performance at vibration levels as high at 25 g and a shock mount is being designed to extend this range.

A design improvement study was initiated which has the following major objectives:

(1) Investigation of failure modes and reduction in circuit complexity.

(2) Redefinition of the logic design to provide simplification of internal circuits and eliminate any functional redundancies with interface circuits.

(3) Review packaging and fabrication techniques in order to achieve reductions in weight and volume.

E. Electronics

1. Introduction

This section covers the various systems of the spacecraft used for receiving and processing Earth-originated commands and transmitting data to Earth. Included are the following: (1) the radio frequency components consisting of two identical receivers and transmitters which assure reliability through redundancy, transponder interconnection circuits for operating the receivers and transmitters in the transponder mode, and the planar array (high-gain) and two omnidirectional antennas; (2) command decoding circuitry which receives Earth commands from the receiver and provides output signals to command all spacecraft functions; (3) signal processing circuitry for processing data for individual scientific experiments, processing basic spacecraft data through the engineering signal processor, and the final processing and multiplexing of data which modulates the transmitter. Also included are the radar systems associated with flight control functions of the spacecraft.

Spacecraft flight control electronics, power management, and the command and data handling console demodulator are discussed in Sections D, F, and L, respectively. The television system and the tape recorder are discussed in Section B.

2. Planar Array (High-Gain) Antenna

The primary function of the planar array antenna is to concentrate the energy of the wide-band television channel in the direction of the Earth. It is located high on the central mast of the spacecraft and will be used for transmitting some of the telemetry data.

This high-gain antenna is a slotted-waveguide planar array which is circularly polarized. This polarization is accomplished by utilizing crossed slots and pairs of complex slots in a manner that produces two orthogonal linearly polarized planar arrays in a given aperture. These two interlaced arrays are fed in time quadrature. Higher-order beams characteristic of large slot spacings are eliminated through the use of waveguides with wave-slowing corrugations which in turn allow a reduction of the slot spacings. This antenna has the following characteristics: A gain of 27 $\pm$0.5 db; a 3 db beamwidth of approximately 6½ deg; and a polarization which is elliptical with an axial ratio under 2 db.

The 0.4 db loss associated with use of the coaxial input reported in the last period has been investigated and no clear-cut reasons for this loss could be presented. The conclusion is that the transition has some loss and the remaining loss is due to a slight change in the feed slot excitations.

Preliminary measurements have been made utilizing an etched aluminum clad fiberglass panel for the aperture plate. Although the panel tested was only two linear arrays wide, the patterns obtained were satisfactory. However, contrary to what was expected, the 10 mil fiberglass covering changed the beamtilt from 6 to 4 deg. This is not serious since it can be brought back to 6 deg by a second-order correction in the slot spacing. Further measurements will be made on a full planar array panel.

Fabrication of the preprototype antenna has been completed. Figures 77 and 78 show partially and fully assembled views. It has been assembled by means of resistance welding and rivets. The aperture plate of this model is comprised of 0.002-in.-thick aluminum bonded to 0.010-in.-thick epoxy glass laminate. Slots are photochemically etched into the aluminum to form the antenna array. Because of the large size of the array, special equipment and processing techniques were developed to handle the etching. This array will be tested electrically and then fitted with a stiffening structure. It will then be installed on S-2 for exploratory vibration tests.

The release electrical design review has been written and presented, and the mechanical design has been finalized. Additional room may be required in the space envelope to allow for deeper stiffening brackets behind the array. This was deemed necessary to meet the vibration requirements without exceeding weight limitations. A structural model is being made for vibration tests to be conducted on June 16.

There has been no success in recovering the gain that was lost when the input terminal was changed from a waveguide input to a coaxial input. Preliminary measurements indicate that etching the slots in aluminum clad fiberglass will work satisfactorily. The new mechanical prototype is nearly complete. Redesign of the backup structure for greater mechanical strength within the weight allowance is proceeding.

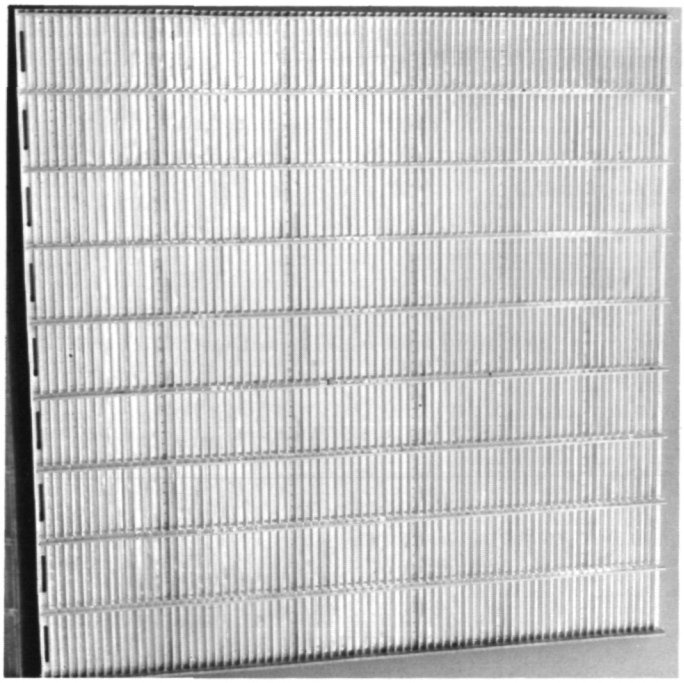

(a) Top view without aperture plate

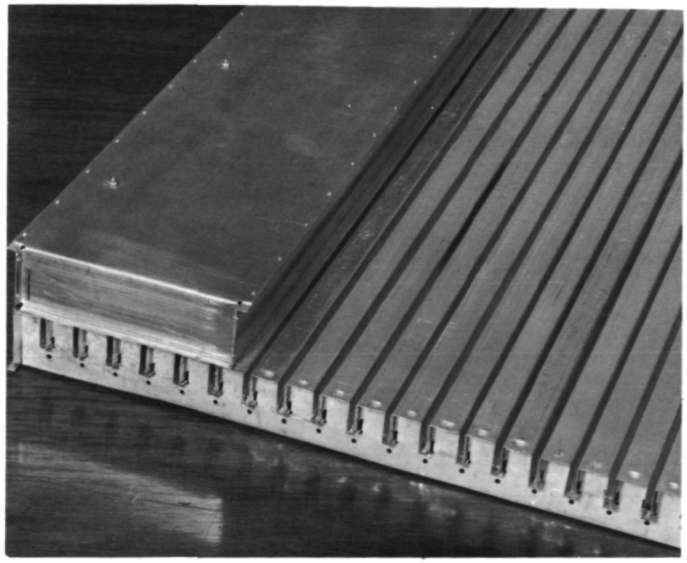

(b) Bottom view near feedguide end

Fig. 77. Mechanical prototype planar array antenna

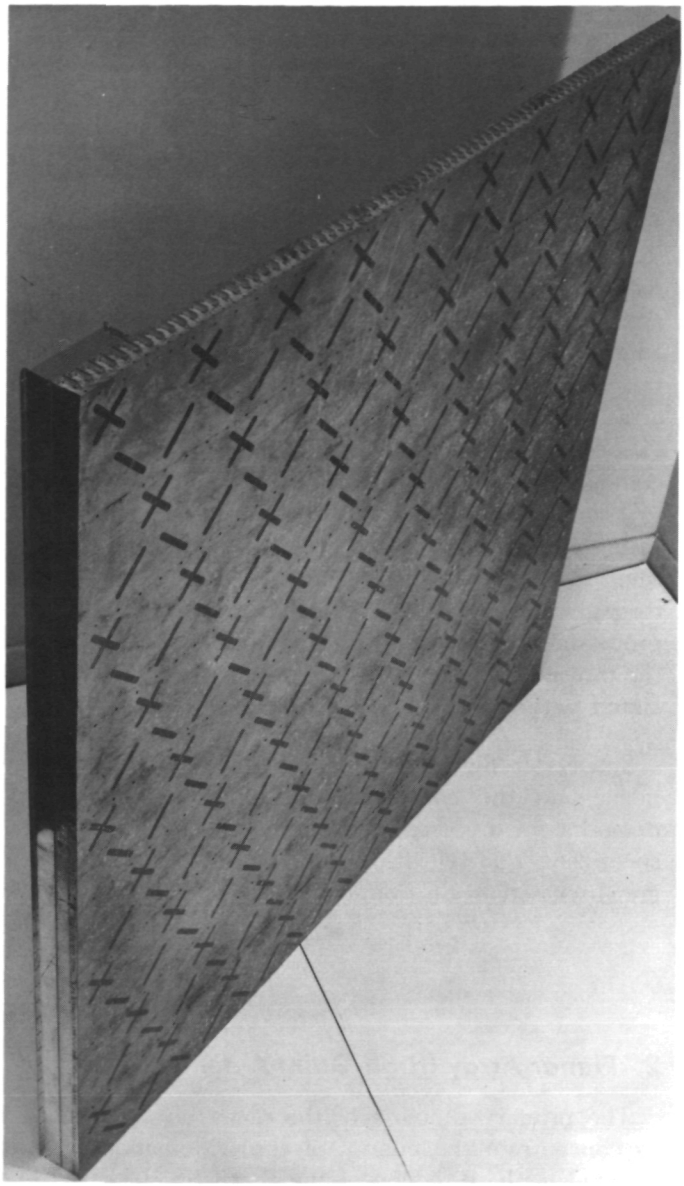

Fig. 78. Assembled mechanical prototype planar array antenna

3. *Omnidirectional Antenna*

The omnidirectional antenna system is designed to provide essentially spherical antenna pattern coverage about the *Surveyor* spacecraft. It is to be used in conjunction with the spacecraft command system, the doppler velocity tracking loop, the telemetry and television link, and the transmitter used for initial acquisition by the tracking station.

The antenna system consists of two circularly polarized low-gain antennas oriented with respect to each other and to the spacecraft in such a manner that optimum coverage is provided. Each of the two antennas is designed to provide broad pattern coverage (approximately 270 deg) in all directions except for a small cone behind the antenna within which the main bulk of the spacecraft lies.

Three approaches to the omnidirectional antenna design have been pursued. As discussed in Reference 1 the modified turnstile with the radiating elements perpendicular to the conical reflector was unsatisfactory in

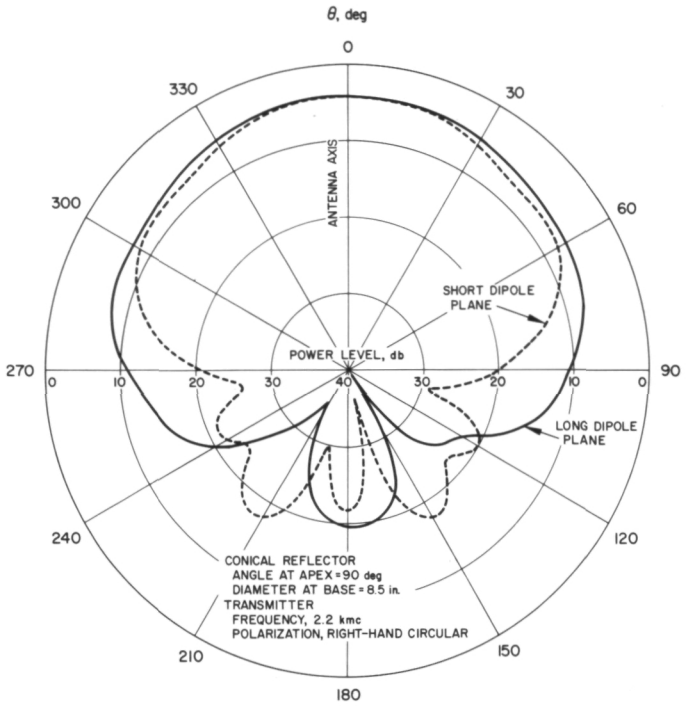

Fig. 79. Pattern of omnidirectional antenna with elements parallel to cone

pattern coverage performance, and development work was terminated. The remaining approaches consist of a modified turnstile with radiating elements parallel to the conical reflector and a backup design utilizing a slotted-cone configuration.

The best set of patterns obtained for the antenna with elements parallel to the cone are shown in Figures 79 and 80. Figure 79 shows the response of the antenna, in two orthogonal cuts, to a right-hand circularly polarized transmitting antenna. Figure 80 shows the vertical and horizontal components of these two cuts. The coverage of this antenna appears to be marginal; hence, most of the development work in this period has been concentrated on the slotted-cone type of antenna which has shown more promise.

Various feeding arrangements on the slotted antenna were tried: a loop feed with polarizing screws in the short section of circular waveguide behind the cone, a probe feed with polarizing screws, and a bisected turnstile feed. The turnstile feed proved to be the most compact and effective; therefore, it will be used in the final design of this antenna.

The patterns obtained with this antenna are shown in Figure 81. Figure 82 shows the breadboard slotted-cone antenna. An axial ratio of 2 db on axis has been obtained at the center frequency. It degrades to approximately 4 db at the two operating frequencies (2115 mc

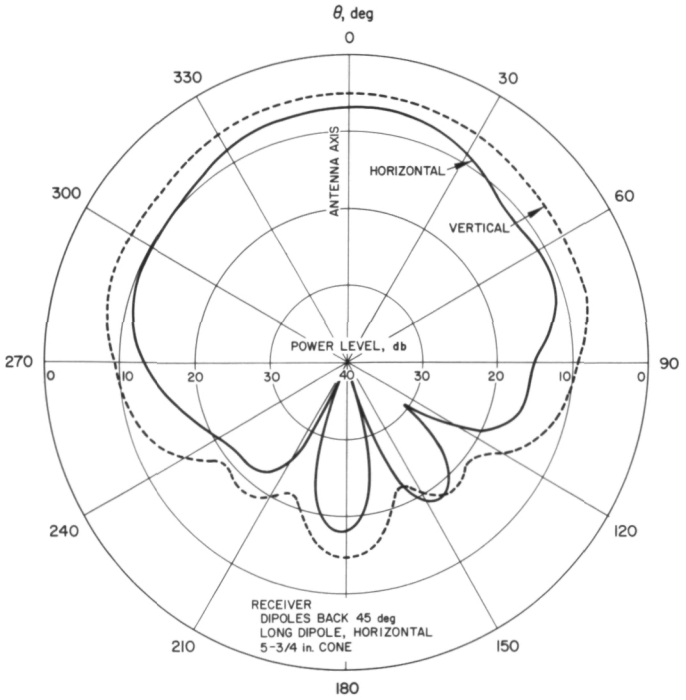

(a) Long dipole pattern

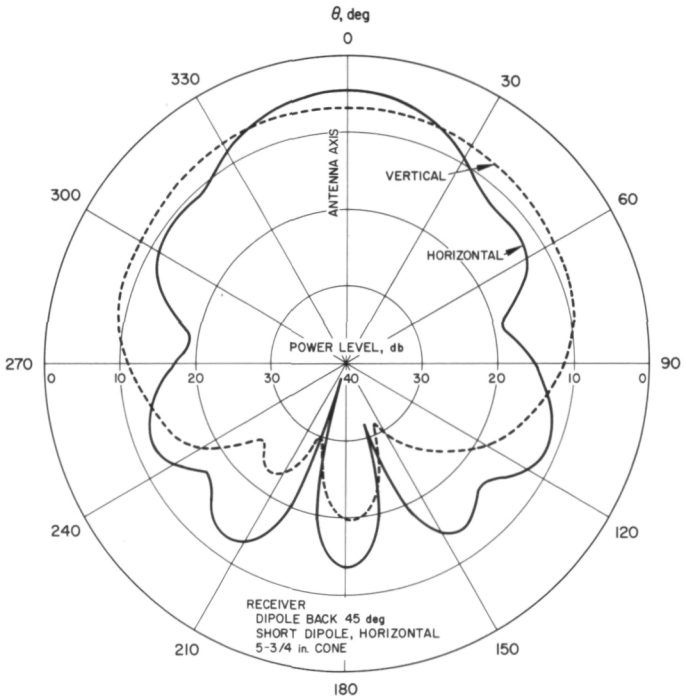

(b) Short dipole pattern

Fig. 80. Vertical and horizontal components of pattern of Figure 79 (2205 mc frequency)

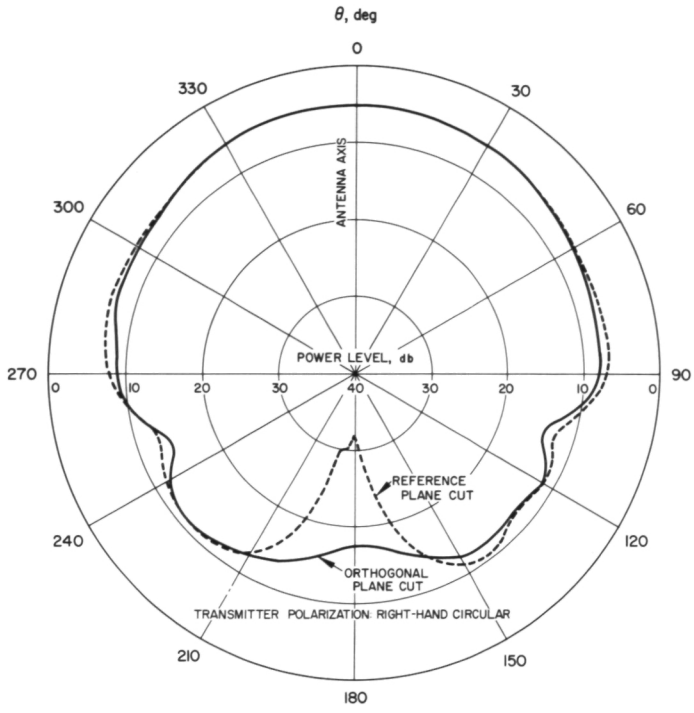

(a) Frequency: 2295 mc

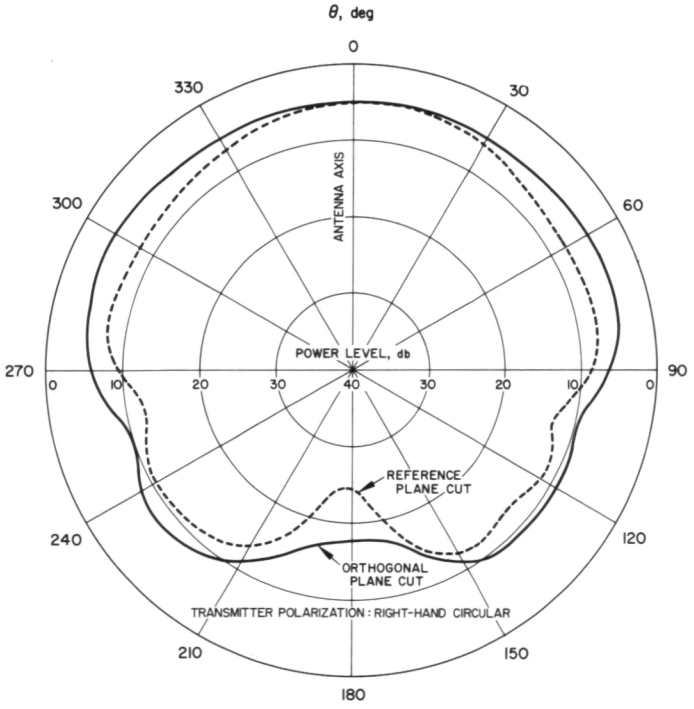

(b) Frequency: 2115 mc

Fig. 81. Slotted cone omnidirectional antenna patterns (transmitter antenna right hand circularly polarized helix)

and 2295 mc). Some additional effort will be directed toward reducing this ellipticity; however, the magnitude of the axial ratio on axis is of secondary importance and the final design will be determined by coverage patterns taken with the full-scale antenna test model of the spacecraft (MA-2).

The A-21 configuration of MA-2 has been received from Pacific Miniatures and is being fitted with struc-

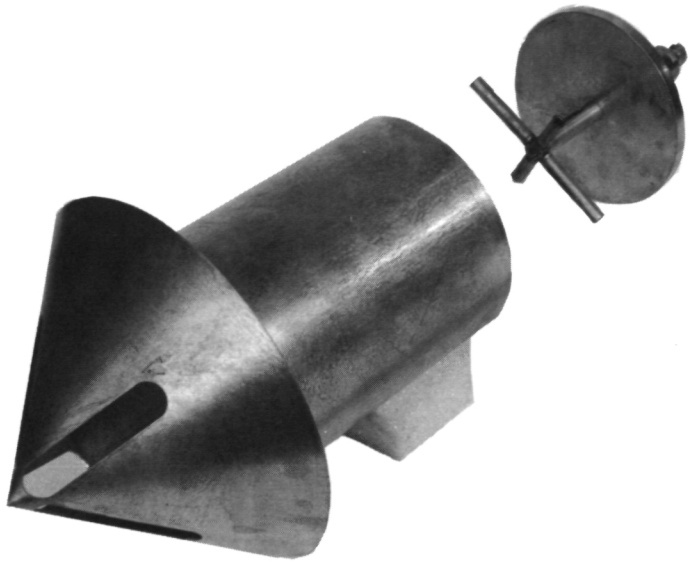

(a) Exploded view

(b) Assembled view

Fig. 82. Slotted cone omnidirectional antenna

tures for supporting it on the antenna test mount. Modifications to the receiver site of the 3000-ft range are complete, and radiation pattern measurement with MA-2 will start when the mounting arrangements are completed.

Studies of patterns taken on the quarter-scale model of the spacecraft to determine desirability of having polarization diversity capability at the DSIF stations have been completed. Two sets of full-coverage patterns were taken on the quarter-scale mode: one with a right-hand, and the other with a left-hand, circularly polarized transmitting antenna. These patterns were analyzed to determine what portion of the sphere showed an antenna pattern response lower than a chosen gain.

Curves were drawn of the response of single polarization and polarization diversity for two cases: (1) use of one antenna only and 2) use of both antennas with their composite patterns. Figure 83a shows the improvement in coverage obtained by using polarization diversity for Case 1 down to a gain of —30 db, and Figure 83b gives the same information for Case 2 down to a gain of —13 db.

It should be understood that these curves are only an indication of what may be obtained on full-scale antenna tests because many changes have been made in the spacecraft since the quarter-scale patterns were taken. Additional changes in response may result from modifications that have been made to the antenna design and from the fact that more nearly perfect circularity can be achieved in the transmitting antenna for the full-scale tests than was possible for the quarter-scale tests.

The slotted-cone antenna has progressed well along in development and should be completed shortly. Polarization diversity was demonstrated as being a desirable addition to DSIF capabilities. The new antenna positioner installation has been completed. Plans for the next period include completing the slotted-cone antenna development and beginning pattern studies using the MA-2. The pattern studies will indicate which antenna type provides the best pattern coverage. Additional studies of the advantages of using polarization diversity at the DSIF stations will be conducted.

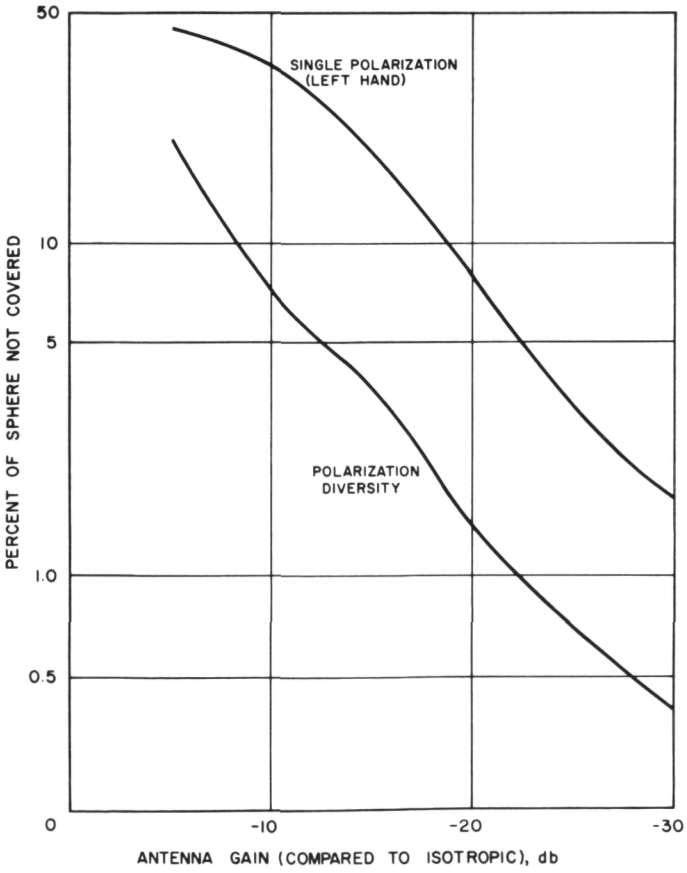

(a) Pattern of one antenna

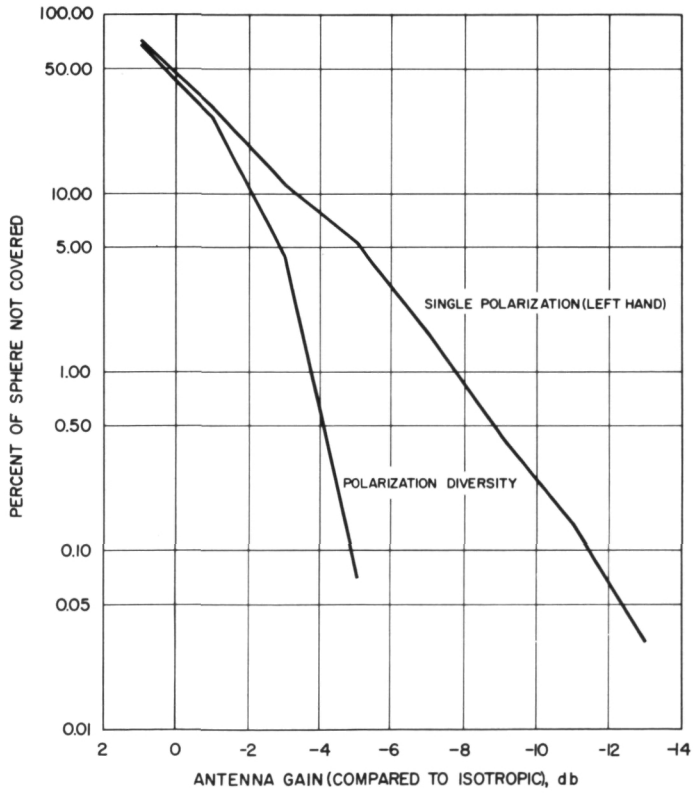

(b) Pattern of both antennas

Fig. 83. Omnidirectional antenna coverage on quarter scale model MA-1

4. Transmitter

Two identical transmitters are included in each spacecraft to assure reliability through redundancy. Each transmitter consists of exciter circuitry which receives video signals and generates a modulated voltage at 19.125 mc. The modulated power is then amplified and multiplied to 100 mw at 2295 mc by means of solid-state circuitry. This output can be radiated directly or a traveling-wave tube (TWT) amplifier may be switched into the path to provide 10 w of transmitter power. High or low power from either transmitter may be directed into any of the three antennas by means of RF latching switches.

The solid-state circuitry from the exciter up to 382.5 mc utilizes lumped constant circuit elements and is packaged in four modules. Multiplication from 382.5 to 2295 mc is accomplished with distributed constant circuitry, and the circuitry is housed in a separate package which is mounted adjacent to the four companion modules.

Development of transmitter circuitry is complete with the exception of the high-power mode RF power monitor, and the solid-state RF Module 2.

a. RF monitor. A stripline directional coupler with a diode for sensing RF power levels from the TWT is being designed. This device will be located in the circuit at a point beyond the diplexer and must be tailored to fit into an existing empty space.

The accuracy of the measurement will be dependent upon the accuracy with which the temperature at the measuring site can be deduced. It is planned to measure diode current and temperature with the TWT operating. By correlating this measurement with the transmitter telemetered temperature, measured simultaneously, it will be possible to calibrate the reading from a particular diode. Preliminary measurements of several diodes indicate that this elaborate measurement may be needed for calibration of each diode if meaningful data are to be obtained.

Once the power in the high-power mode is known, by exercising different power modes of the transmitter, it is possible to infer the level of power from the solid-state transmitter in the low-power mode.

b. Module 2. Development of a wide-band FM modulator for the *Surveyor* transmitter has resulted in a working breadboard. A block diagram of this modulator is shown in Figure 84.

A 25-kc low-pass filter attenuates the high-frequency video components applied to the voltage-controlled crystal oscillator (VCXO). This is necessary because at frequencies above 50 kc the VCXO output becomes distorted, and above 100 kc spurious crystal responses appear. The VCXO is necessary so that the modulator will have dc response and also have satisfactory long-term stability.

A 10-db attenuator isolates the VCXO from the phase modulator. The phase modulator gain is adjusted so that at a modulation frequency of 25 kc the frequency is equivalent to that caused by the VCXO. At modulation frequencies above 25 kc, the deviation increases at +6 db per octave, thus adding high-frequency pre-emphasis. High-frequency pre-emphasis further reduces the effects of spurious crystal responses mentioned above and also improves the system signal-to-noise ratio.

Following the phase modulator, a two-stage limiting amplifier is used to raise the power level of the RF signal and to eliminate any amplitude modulation occurring in the VCXO and phase modulator.

Tests of the VCXO show the long-term stability to be in excess of the required ±20 ppm. Development is continuing to see if this can be improved; however, the sensitivity, linearity, and environmental requirements seem to limit the long-term stability which can be achieved. Consequently, a relaxation of the required long-term stability is being requested (TV mode only).

System tests of the present breadboard are continuing in order to determine if the linearity is satisfactory at all frequencies. A second breadboard model is being built in the final T-module configuration.

c. RF attenuator design. A series of microwave attenuators has been devised so that any solid-state driver may be mated optimally with any TWT by simple selection

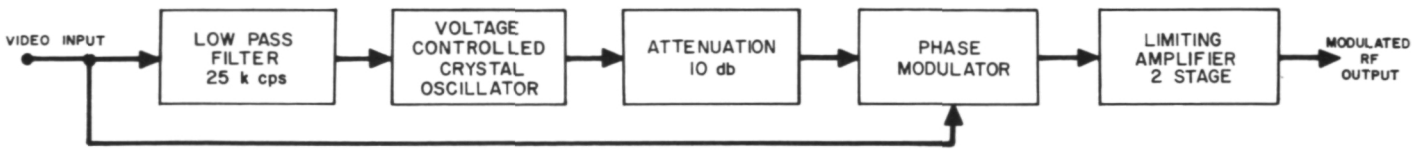

Fig. 84. Wide-band FM modulator block diagram

of a portion of the interconnecting RF line. The attenuators will be available in ½ db steps over a range from 4 to 10 db; however, it is presumed that the extreme values will be discontinued when the number of tubes available is large enough to assess the standard distribution in gain values.

d. Product design status. Detail drafting is complete on three of the four solid-state RF module assemblies, electrical conversion unit, and power switching circuits. Drawings of the stripline X6 multiplier are nearing completion.

Parts for prototype models are on order for all of the lumped constant circuitry including Module 2. Since this design was not firm, an anticipating list was written for qualification and ordering so that the few changed parts could be procured quickly at a later date without slipping schedules.

A detailed specification for the diplexer was released and parts were ordered. The RF latching switches for T-21 and type approval test units are scheuled for delivery by the manufacturer in June.

5. Command Receiver-Transponder Interconnections

The command link of the spacecraft telecommunications system contains two identical, independent command receivers. Both receivers operate continuously throughout the life of the spacecraft and provide continued operation of the command link in the event of a failure in one of the receivers. The command receiver normally operates as a crystal-controlled double-conversion FM receiver. Commands are frequency modulated on a subcarrier which in turn phase modulates the main carrier of the Earth-to-spacecraft transmissions. The digitized command signals are detected and fed to the central command decoder.

Transponder interconnection circuits are associated with each receiver such that each receiver may be connected to a transmitter for transponder operation, wherein the transmitted signal is in phase coherence with the received signal. When these circuits are activated by command signals, the receiver operates in a phase-lock mode. The receiver local oscillator signal, which is phase-coherent with the received signal, is fed to the transmitter exciter and transmitted back to Earth after the proper frequency multiplications have been applied to it.

a. Circuit development status. All circuitry has been released for product engineering. Initial tests of the second breadboard of the command receiver-transponder interconnections indicate satisfactory performance operating in transponder mode with the transmitter. Test specifications and procedures are about 90% complete.

b. Product design status. Detail and assembly drawings of the six RF modules are complete. The remaining drawings which include the electrical conversion unit circuitry and the main chassis details are in various stages of completion with final release expected to be no later than June 18, 1962. Prototypes of all RF modules have been fabricated and are in various stages of completion. Module A1 has been electrically tested and with minor circuit changes has performed satisfactorily.

6. Signal Processing

The signal processing system processes the variety of signals from the scientific instruments and the many channels of engineering information into a form suitable for modulating the transmitter. The spacecraft-to-Earth telemetry link, of which the signal processing circuits are a part, uses an FM-FM and FM-PM subcarrier system. FM-FM is used after landing and FM-PM is used during transit. Wide-band FM is used for television transmission.

The signal processing system may be divided into three main categories: engineering signal processor, central signal processor, and scientific signal processors.

Individual processing circuits are designed for each particular scientific instrument and are packaged with the instrument auxiliaries. The output of the individual circuits are either subcarrier signals or signals suitable for analog-to-digital conversion.

Most of the engineering information from the spacecraft is transmitted in a pulse-code-modulation format. The engineering signal processor contains circuits for commutating the data into a single channel such that it may be converted to a digital form. Circuitry also is included to handle a few signals that require special processing.

The central signal processor is the common link in the processing system. The various subcarrier signals from the scientific signal processor are combined and fed to the proper transmitter modulator. The analog-to-digital conversion process also is provided in the central signal processor.

The central signal processor circuit design was completed and released May 10. The advance bill of materials for this unit was released May 17. This unit is comprised of five printed-circuit boards and 52 modules. However, within these 52 modules, there are only 30 different types; 85% of the modules have completed final design. Fabrication of these modules will begin during the latter half of June.

The product design for this unit resulted in 19 different module types and a total of 80 modules per unit. Final module design is 80% completed. The six printed-circuit boards are 75% completed.

The final TV and geophysical thermal commutator circuit designs have been released. The advance bill of materials was released May 29. Final module design is complete for these modules and fabrication has begun on the subsystem decoders.

7. Command Decoding

The command decoding system of the *Surveyor* spacecraft decodes Earth-transmitted command messages from the spacecraft receivers and provides output signals to command the addressed subsystems. It can handle up to 960 ordinary commands, which control on-off operations, and magnitude commands, which control time-interval operations. The system consists of two redundant central command decoders (CCD), a receiver-decoder selector (RDS), and up to 30 subsystem command decoders (SD).

The RDS turns on an electrical conversion unit in one of the CCDs when a message is initially received from either or both receivers. The output of one of the two receivers is selected for decoding processing. The selected receiver and the selected central decoder are determined by the states of two RDS flip-flops that form a two-stage binary counter having four possible states which correspond to one combination of one receiver and one central decoder. The counter is indexed to its next state every time messages stop coming out of either receiver.

In order to synchronize the entire operation of the command decoding system, the central decoder unit derives synchronization and timing information from the incoming commands. The CCD compares the address and command bits of each message to their respective complements. If this comparison fails to check, the message is rejected. One additional command interlock is incorporated in the command structure. A two-command sequence is required to execute certain irreversible or otherwise critical commands. The address bits select and turn on one of the subsystem command decoders. The command bits are decoded in a diode decoding matrix in this decoder to select one of the outputs.

The major efforts on this unit are being expended in its product design. The circuit design was completed during the previous report period. Following the final circuit release the advance bill of material was prepared and issued for purchasing.

The unit consists of six printed-circuit boards on which are mounted 56 modules. However, by proper circuit and product design there are only 20 different types of modules.

The final module detail design has been completed. The printed-circuit boards for mounting these modules go through several stages in their design. First, the modules must be arranged on the boards in such a manner as to optimize interconnections. Having once solved the layout problem for all the boards – which implies solving the interboard interconnection problems, the design is frozen and the etch master stage is begun. In this step the master drawings from which the actual printed circuits are produced are accurately "drawn." The process used utilizes a tape method. The printed-circuit conductors are laid out on the master vellum using a special black tape and special black pads. This etch master is four times actual size. The next step in the process is a photographic reduction and preparation of a photomaster. This photomaster is used to produce the printed boards.

In the command decoder, the task of preparing the etch circuit master was subcontracted to a job shop, after the layout design had been completed. The printed cards will be fabricated during the latter half of June.

Final design of this unit dictated several changes in its outline and mounting dimensions. One connector was enlarged to provide for increased signal requirements; two mounting holes were relocated because of internal construction restraints. These changes were reflected in the June 1 outline and mounting release.

During module fabrication, the circuits contained within the modules are given several electrical performance checks. First, after the module has been welded it is checked for proper performance. This test is repeated after the module has been encapsulated and again after it has been heat-cycled. These tests ensure proper module operation and reduce unit checkout time. Test equipment for these tests is now being designed.

8. Electronic Packaging and Testing

The status of product design on individual electronic hardware items is covered elsewhere in this report along with the respective items. Progress in development of general packaging techniques and other activities of a general nature is given below.

a. Foam sandwich chassis. The foam sandwich chassis is an adhesively bonded structure. Tests of prototype chassis (to destruction) showed that failure modes were frequently adhesive; i. e., failure occurred at the inter-

face between the aluminum and adhesive. Because of this, surface preparation was studied in an attempt to improve adhesive bond reliability. Untreated, anodized, chemically etched, and liquid-honed aluminum specimens were bonded and then loaded in tension. The liquid-honed surfaces provided the greatest adhesion, which was essentially equal to the tensile strength of the adhesive itself. The anodized surface (originally used on the chassis tested) produced bonds having strength less than half those obtained with untreated surfaces.

Iridite-treated surfaces have yet to be investigated, and flight hardware will be either liquid honed or iridited according to the results obtained.

Because of the recent discovery of possible evaporation of the epoxy-polyamide adhesive originally used, a search is under way for an adhesive system which will not evaporate and yet will be otherwise equivalent to the epoxy-polyamide.

A method for machining the foam core accurately and economically has been developed. The foam drawing is made as an artboard (similar to etched-circuit artwork). The artwork pattern is then photochemically reproduced in an aluminum plate which serves as a template for milling the foam on a pantograph engraving machine.

Four methods of attaching mounting tabs to chassis were evaluated. Tensile loads were applied to the tabs in directions normal to the chassis. The attachment configuration with highest strength was one with rivets as close as possible to the tab flange and with the tab and chassis plate surfaces liquid honed prior to bonding. The tests showed that such a combined riveted-bonded joint was strong enough to withstand the peak loads which will occur during vibration. A few other methods of attaching tabs to chassis will be evaluated. The best method will be used to fabricate a chassis to be vibration tested to destruction.

b. Material and process standards. Development of the basic packaging technique (foam sandwich chassis, cordwood modules, and T-bar modules) included the selection of specific materials and processes.

New and revised Hughes Materials Specifications and Hughes Processes have been initiated to define essentially all of the approved materials for flight hardware. In addition, two production specifications were initiated which will define the series of processes necessary to fabricate a foam sandwich chassis and T-bar module.

All of the above-mentioned documents were mechanized in the form of drawing notes. These were grouped into several lists, each list being assigned to drawings of specific assemblies through the media of the Design Standards Book (described in Reference 1). This procedure will aid in producing uniform sets of drawings, and ultimately the hardware produced from the drawings will be of improved and uniform quality.

c. Test equipment. Test equipment for flight control electronics and TV camera breadboards is under fabrication. For the receiver, transmitter, altitude marking radar, and other electronic packages the test equipment design and fabrication will be started shortly. Plans at this time call for construction of only one of each unit and subsystem test equipment.

9. Subsystem Testing

An integration laboratory has been established for the purpose of testing *Surveyor* electronics components as a subsystem. The laboratory will operate through two phases: the first will be testing of breadboard hardware received from the circuit development areas, and the second will be testing of prototype hardware to be received after the hardware has passed type-approval testing.

The present status of the breadboard integration is shown in Figure 85. This figure indicates those items that have been delivered and the extent to which the interconnections have been completed. The receiver and command decoder have received and decoded commands which were modulated onto an RF signal. These commands have been used to turn the transponder interconnections on and off. When the transponder interconnections were turned on the receiver phase locked to the simulated ground station and provided the transmitter with a phase-coherent drive signal. Several interface problems have been found, and one has resulted in a minor circuit change in the receiver.

The subsystem breadboard integration will not contain a complete complement of the *Surveyor* electronics. Components not to be tested include the flight control electronics and the radars. Of the remaining electronic components, those which are redundant in the spacecraft (e.g., receiver, transmitter) will not be redundant in this breadboard subsystem test. In addition to these simplifications, the pulse code modulation in the engineering signal processing will be represented by two commutators which are identical in design to those which will be used but have fewer inputs.

10. Radars

a. Altitude marking radar. The purpose of the altitude marking radar (AMR) is to indicate the proper *Surveyor* spacecraft to lunar surface slant range to fire the retrorocket. The firing signal is generated at approximately

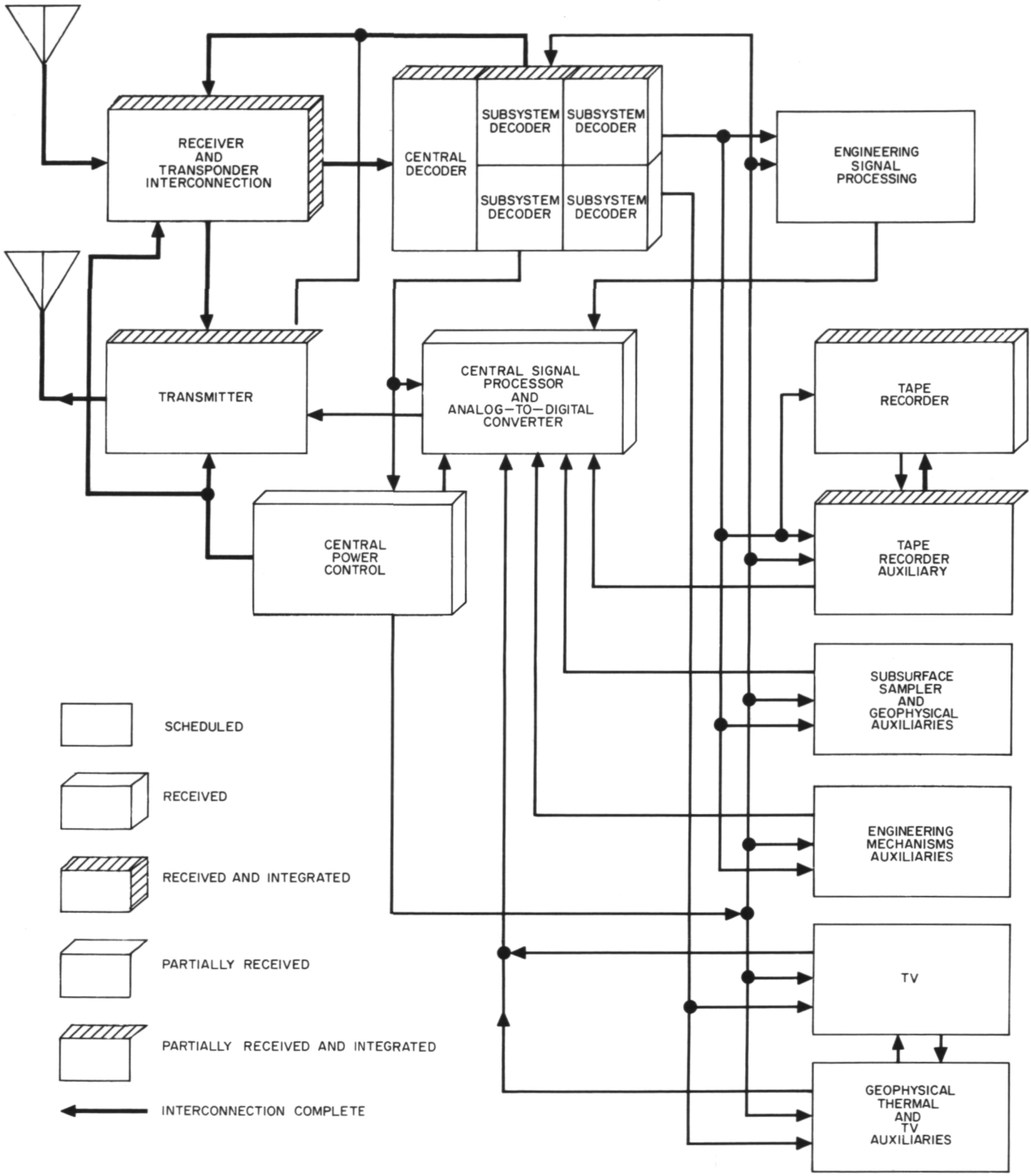

Fig. 85. Breadboard integration status for electronics subsystem testing

56 mi. The altitude marking radar employs pulse modulation of transmitted microwave energy in which the transit time of the return signal is compared to a predetermined delay (corresponding to slant range). At the appropriate range, the presence of microwave energy in the delayed gate is detected and integrated. If a preset threshold is exceeded in two channels, a marking signal is generated as required by the *Surveyor* system.

During this report period, effort was concentrated in three areas: fabrication of the breadboard for the altitude marking radar test equipment (AMRTE) which forms a portion of the system test equipment assembly (STEA) as well as serving as unit test equipment for flight acceptance testing product design of the AMR; and subcontracting the modulator and RF assembly of the AMR. Some preliminary vibration tests were also accomplished.

The AMRTE is designed to provide the minimum testing capability necessary to verify performance of the AMR for unit flight acceptance tests and to isolate faults to a field replaceable unit level when used as a part of the STEA. However, each test does not necessarily check one particular replaceable unit completely and individually; instead, in general, the test checks certain related functions of several related units simultaneously. To test each replaceable unit individually would require construction and/or purchase of additional test equipment to simulate inputs or loads which already exist in the AMR. This mode of testing has limitations in that if a unit which supplies the input to another is faulty, testing cannot proceed beyond the faulty unit until it is replaced. Acceptance of this limitation was considered reasonable for this equipment.

The AMRTE consists of a cabinet assembly, interconnection cables, and an AMR holding fixture which supports the AMR when it is not installed on the spacecraft. The interconnection cables are terminated at the rear lower part of the cabinet and at the holding fixture; a waveguide from the front of the cabinet couples RF energy into the AMR. Fabrication of the breadboard (shown in Fig. 86), which is electrically identical to the final STEA equipment, was completed during this period and system integration with the AMR was begun. A final design review of the AMRTE was conducted so that any required modification could be incorporated before the start of production, currently scheduled for July 1, 1962.

The product design of the AMR is continuing. The printed-circuit board layouts for the synchronizer and video processor have been completed; the layout of the regulator and electrical conversion unit is under way but has been delayed due to a circuit change which will increase the efficiency of the regulator. It was decided to accept the change since its incorporation will alleviate a thermal problem during testing. The short operating time of the AMR was included among the tradeoffs to achieve an optimum design; the thermal mass of the RF assembly is used as the heat-sink for the regulator. This solution is ideal for operation since it raises the magnetron temperature slightly, which is desirable and keeps the junction temperatures of the semiconductors in the electrical conversion unit (ECU) low enough for the time required to ensure reliable operation. With the previous design, the ECU would have required forced air cooling if test times greater than 10–15 min were required; with the new design, steady-state temperatures with only convection cooling will remain satisfactorily low.

Most of the drawings for the AMR were completed during this period, including schematics, the antenna feed, the top assembly, and the block diagram. Procurement of components is under way.

As reported previously, the newly designed feed that has a 10-in. waveguide taper from feed to dish did not meet specifications. Further tests were made on the old

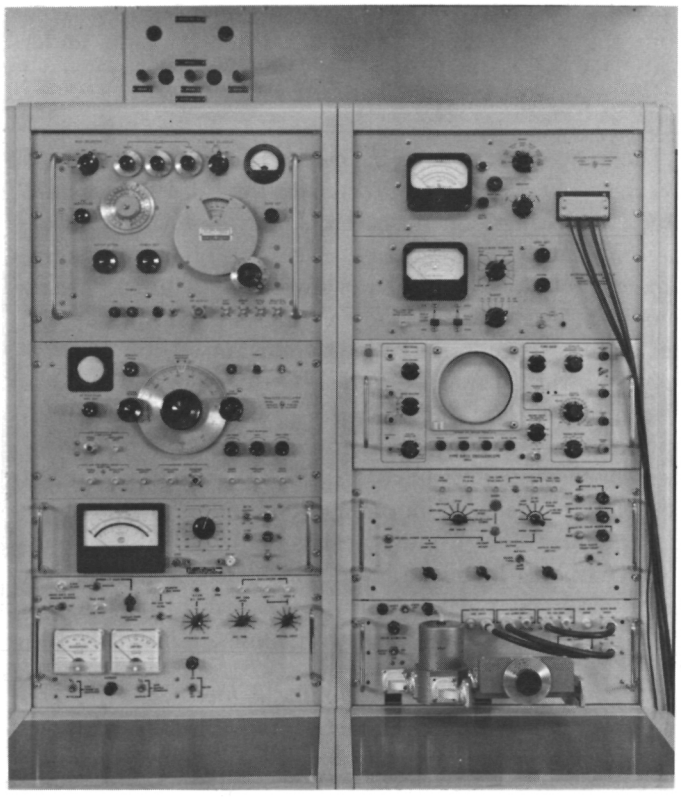

Fig. 86. Test equipment breadboard

feed which has a shorter taper section from half- to full-height waveguide. The original long fairing was cut down to a length of about 4 in. (along the half-height section of guide only). Results show that the fairing has most of its effect in the vicinity of the dipoles, and the excess length can be eliminated with a very small degradation of sidelobe level. The fabrication problem is then nearly eliminated. This feed with short fairings meets all previous specifications except the first sidelobe level in the H-plane which deviates by only 0.3 db. Circuit changes in the radar make these results satisfactory for the over-all system operation. Final impedance matching in a productized antenna is under way.

A vibration test fixture for testing the structural adequacy of the antenna dish has been fabricated. During this period preliminary vibration tests were initiated. A run was made at 2 g input and the dish behaved well; it displayed a fundamental resonance at 72 cps which correlates well with the calculated value of 70 cps. Its amplification at resonance was about 10 for this input level. When a repeat at a higher input level was attempted, an instrumentation failure in the test equipment caused the dish to be exposed to uncontrolled forces far in excess of design loads. This uncontrolled force caused the simulated electronics packages to break loose from the dish. Testing had to be interrupted for repair of the dish. The reworked dish has been received from the vendor and vibration testing is again under way. The results of the tests will be reported in the next issue of this summary.

The subcontracts have been let for the modulator and RF assembly. The subcontractor for the solid-state modulator is the Magnetic Research Corporation; the subcontractor for the RF assembly, consisting of a magnetron, four-port circulator, and transmit-receive tube, is Metcom, Inc. In each case, the subcontractor has agreed to meet the stringent operational and reliability requirements of the Hughes Aircraft Company specification. Precontract negotiations for the mixer are continuing; most of the problems have now been resolved. Both of the proposed vendors have agreed to the Hughes Aircraft Company outline and mounting dimensions for the mixer; consequently, the product design of the AMR can continue without being delayed. The PERT network is being modified to reflect this fact and to establish a required delivery date for the qualified mixer.

b. Radar altimeter and doppler velocity sensor. The purpose of the radar altimeter and doppler velocity sensor (RADVS), being developed by Ryan Electronics, is to provide spacecraft altitude, attitude, and velocity information to the spacecraft flight control system during the final portion of the lunar landing phase of the mission. The doppler velocity sensor utilizes three continuous-wave radar beams to obtain three orthogonal velocity components which are referenced to the spacecraft roll axis. The radar altimeter utilizes a single frequency-modulated beam directed along the spacecraft roll axis to obtain slant range to the lunar surface.

The RADVS consists of four major units. The klystron power supply modulator (KPSM) unit includes the altimeter klystron transmitter tube and the doppler velocity sensor tube, the high-voltage power supply for the klystrons, and the FM modulator. The velocity sensor receiver-transmitter consists of an antenna which produces two of the three doppler velocity beams and which also contains microwave filters and isolators, microwave-to-audio detectors, and gain-controlled preamplifiers. The altitude-velocity sensor receiver-transmitter is similar to the velocity sensor receiver-transmitter except that its function is to produce the third velocity sensor beam and the altitude beam.

The fourth unit is the signal data converter (SDC). This unit performs the search and tracking functions for all four channels and processes the signals to produce the velocity, altitude, altitude marks (1000 and 13 ft), and reliable operation signals.

The emphasis during this reporting period has been on fabrication of the development model system for the T-2 drop test. The status of the 205 modules required for this system as of May 1 (the latest date for which detailed information is available) is as follows:

Not realeased for manufacturing	8
Released, but not started (parts shortages)	4
In assembly	8
Assembly complete – held for final test procedure	3
In test	89
Completed – in bonded stores	93
Total modules/system	205

There are nine circuit boards required for the signal data converter. The status of these boards is as follows:

Not released for manufacturing	4
In assembly	1
Completed – in bonded stores	4
Total circuit boards/SDC	9

All metal parts for the signal data converter and the two preamplifiers have been fabricated and are undergoing a chem-etch (weight-reduction) process. The waveguide parts are being assembled into the two antenna assemblies prior to boresighting.

The klystron power supply modulator is in the final stages of product design and the waveguide design has been completed. It is anticipated that the system for T-2 will be delivered to Hughes on July 20. The test equipment is also progressing on schedule. The first model, to be used at Ryan for system test, is scheduled for completion early in June, and the second model will be delivered to Hughes with the system for T-2.

During this reporting period, the changes required to permit operation at extremes of velocity vector and spacecraft attitude angles have been incorporated into the specification (P.S. 232902, Revision D). These changes will result in a conditional reliable operational mode immediately following retro-rocket burnout if one or two of the velocity sensor beams are at angles which result in near-zero or negative velocity components along those beams. The addition of this mode will permit the limited information available under such conditions to be used to initiate corrective maneuvers.

Also, during this period, Revision E to P.S. 232902 was issued to add the capability to measure the microwave reflectivity of the lunar surface. The lunar reflectivity will be evaluated by telemetering signals corresponding to the strengths of the four received signals. These data, together with other telemetered data, will permit the calculation of reflectivity to be made.

Establishment of realistic thermal control for the various parts of the radar altimeter and doppler velocity sensor has been the subject of constant attention for several months. This is a particularly pressing problem in the case of the RADVS due to the extremely high power dissipated (430 w) and the short operating time (5½ min). In the interest of weight reduction, it is necessary to establish the lowest possible temperature at the time the system is energized to reduce the heat-sink mass requirements, while at the same time ensuring that the temperatures will not be so low that the accuracy will be degraded. This problem is so related both to the overall *Surveyor* spacecraft design (conducted heat, radiation view factors, solar radiation, spacecraft orientation, radiated lunar heat, etc.) and to the detail design of the RADVS components (internal thermal design, surface finishes, weight, etc.) that it has been treated as a joint engineering design problem by Hughes and Ryan.

During the reporting period, the solutions for temperature control of both the signal data converter and the klystron power supply modulator have been established. The turn-on temperatures for these units have been set at $+15 \pm 10°C$ and $-20 \pm 10°C$, respectively. This was accomplished by utilization of solar energy controlled by surface finish treatment.

A tentative solution for temperature control of the two antenna-preamplifier units is being investigated. These units are partially in shade and partially in sun during the transit phase of the mission. The dish structures were designed for low weight and are poor heat conductors. Also, several components in the preamplifier and microwave portions of the assemblies are temperature-sensitive. The use of solar heat to control the temperatures of these critical parts would require excessively high temperatures on the unshaded portions of the dishes and would also result in excessively high thermal gradients across the dish. It has been determined, as a result of a computer analysis, that a 0.002-in. aluminum cap bonded to the rear surface of the dish will reduce the thermal gradients and maximum temperatures to a reasonable level while still maintaining the required temperatures at the critical components. The problems involved in implementation of this solution are presently being investigated. In particular, tests are being conducted to determine whether the differences in thermal coefficients of expansion of the aluminum cap and the epoxy dish will cause boresight errors. Techniques for accomplishing the bonding are also under investigation.

At the second JPL/Hughes/Ryan design review, the question of antenna sidelobe effects was raised. An analysis of this problem has been completed and the results are reported in the following paragraphs:

Because of the wide range of vehicle attitudes and relative velocity vector orientations, a possibility exists in the velocity sensor for a frequency tracker to lock on to the doppler signal received by a sidelobe. The unwanted sidelobe signals can arise from the normal antenna sidelobes or from a cross-coupled lobe. This latter situation of lobe cross-coupling exists when the sidelobe of a receiving antenna beam coincides with the main transmitting lobe of a different transmitted beam. However, coincidence of a sidelobe and a mainlobe of two different beams may be expected only between velocity sensor beams 2 and 3 which share a common reflector. Present antenna measurements show the cross-coupled sidelobe gain will be down approximately 30 db from the mainlobe. Normal sidelobes are down by approximately the same amount (30 db) from the mainlobe.

In the case of the altimeter, it is less susceptible to sidelobe lockon than the velocity sensor, and cross-coupling lobe lock cannot occur at all.

Practical methods exist which will provide the necessary discrimination against tracker lockon to sidelobe return signals. For the case of the cross-coupled sidelobe lock (considered possible only between Beams 2 and 3 of the velocity sensor antenna), two conditions would

CONFIDENTIAL

exist simultaneously which will serve to identify this type of lock. First, the frequencies being tracked by Beam 2 and 3 trackers will be equal (giving $V_y=0$), and second, the amplitudes of the signals being tracked will differ by approximately 30 db. Relatively straightforward logic circuitry will detect these conditions and provide tracker lock rejection and initiate recycle of search.

For the case of a tracker locking on to any of its own beam's sidelobes, the tracker signal detection circuit can be utilized for discrimination purposes. This technique would use the present signal-to-noise comparison circuitry as it exists whenever the preamplifier gains are at maximum. However, for any preamplifier gain states less than maximum, a fixed threshold would be switched into the tracker acquisition circuitry. It then follows that when the preamplifiers have been switched to a gain state of 60 db or less, the signal-to-noise ratio must be 20 db or greater. Thus, if a mainlobe signal and sidelobe signal are both in the passband of the preamplifier, and each is scanned by the tracker during search, only that signal which exceeds the fixed threshold will be recognized. Since the mainlobe return will be at least 25 db above the sidelobe, appropriate sidelobe rejection may be accomplished. This latter method of sidelobe discrimination is applicable to both the velocity sensor and the altimeter.

It is planned to introduce essential sidelobe rejection capability into the RADVS simultaneously with the incorporation of the special logic circuitry required to handle the increased velocity vector angular orientation requirement. The first and all succeeding assured models will be so equipped.

Testing of the breadboard system has continued during this reporting period. The breadboard will be retained as an operating system until a system of more advanced design is available.

To assist in the evaluation of the breadboard altimeter system, a corner reflector has been erected on a vertical at a range of 1000 ft. The high and low deviation modes of operation of the altimeter will also be checked. The target will also be used in subsequent model test and evaluation.

Complete sets of new low-noise matched diodes were placed in the breadboard microwave system. Breadboard sensitivity is now representative of what the final RADVS will be.

The breadboard doppler simulator was reworked and readied for further tracker evaluation. The use of this simulator together with broad-band noise is essential to the evaluation of the signal data converter and the adjustment of the tracker signal detection circuits. The

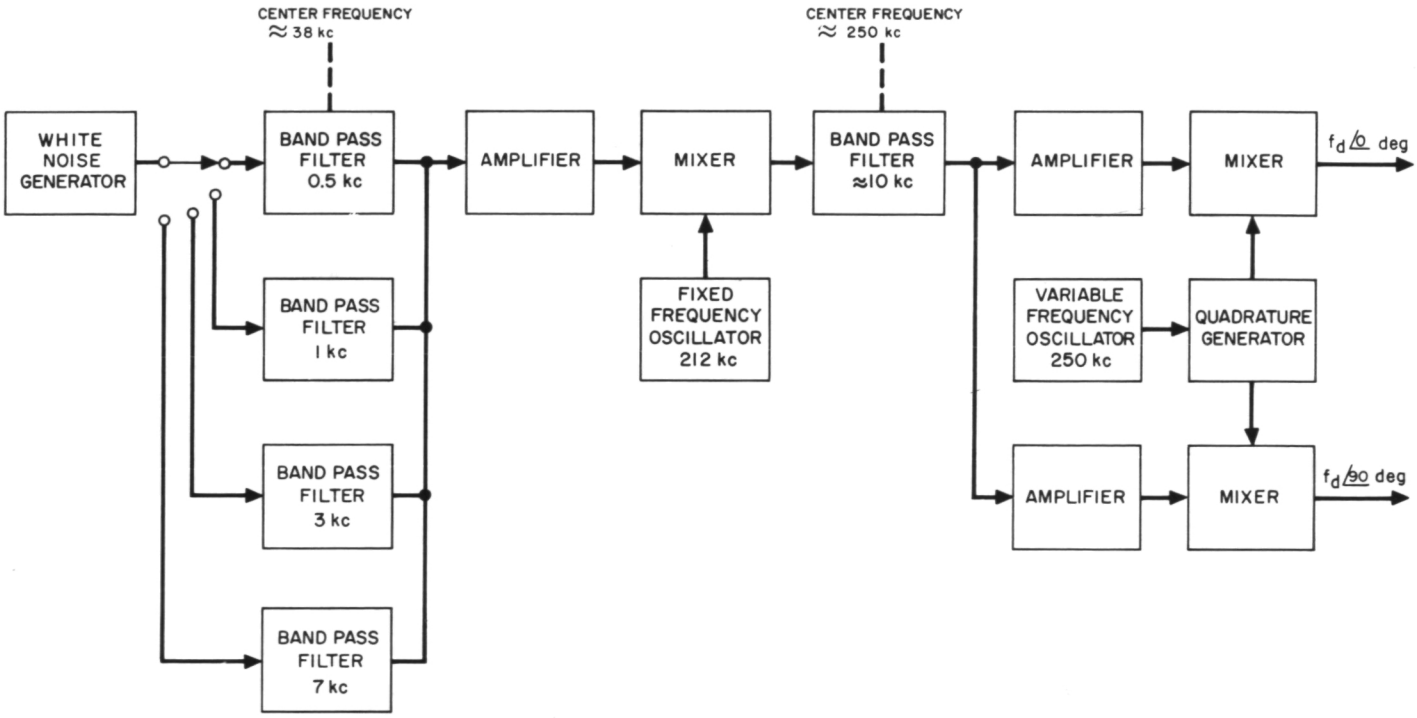

Fig. 87. Simplified block diagram of breadboard doppler simulator

CONFIDENTIAL

simulator provides doppler bandwidth of approximately 500 cps, 1000 cps, and 3000 cps and is adjustable over the range of approximately ±100 kc. The simplified block diagram of Figure 87 is descriptive of this doppler simulator. Correlation of tracker performance between signals derived from this simulator and the microwave signal simulation of RADVS test equipment will be made so that proper interpretation of results obtained using the actual test equipment may be made.

Joint Ryan/Hughes tests were conducted on the breadboard power supplies to determine the level of conducted RF interference that may be expected to be produced by the RADVS. Although the data resulting from these tests have not been completely reduced and analyzed, it appears that the conducted RF interference is approximately at the level to be expected from power supplies of the type used in the RADVS. Special attention will be paid to noise at those frequencies which may cause compatibility problems with other *Surveyor* systems during the period of RADVS operation.

Several questions concerning the theory of operation of the frequency-tracking loops in the RADVS were asked at the second design review. It was not possible to answer these questions adequately at the time of the meeting; however, an analysis was undertaken to determine the required information. A summary of this analysis follows.

The analysis of the frequency tracking loop is complicated by the fact that the output voltage of the frequency discriminator is not a regular function of instantaneous error frequency. Analysis is carried out in progressive steps treating the frequency discriminator as (1) a linear element, (2) a limited linear element, (3) a sampled data device with ideal frequency characteristics, and (4) a sampled data device with variable frequency response. Because of the uncertainties involved in the analysis of (4) above, detailed characteristics of the tracking loop can best be determined on the breadboard tracker. Some guidelines are established, however, by which the experimental data may be checked. The pertinent results are as follows:

(1) The tracker operates as a quasi-stable device with limit-cycle hunting existing in the loop.

(2) The static error with sine wave input is proportional to the amplitude of the hunting.

(3) The static error with spectrum input is equal to $\frac{(BW)f}{1.8\,V_{max}\,K_V}$ For a ramp input of rate R the error is $\frac{(BW)}{1.8\,V_{max}\,K_V}\,(f_o + Rt + R\tau)$

where

BW = spectrum bandwidth

f_o = initial frequency

V_{max} = maximum average voltage at discriminator output

K_V = variable frequency oscillator (VFO) sensitivity

τ = total open-loop system time constant

(4) The errors with spectrum inputs with bandwidths in excess of 100 cps are essentially independent of the loop gain in the narrow linear region of the discriminator. The governing factors are the spectral width, the VFO sensitivity, and the maximum voltage available at the integrator output.

F. Electrical Power Supply

Electrical power for the *Surveyor* spacecraft is supplied by a Sun-tracking planar solar panel and a sealed secondary silver-zinc battery. The solar panel is the prime source of power during transit and the lunar day, and the battery provides the electrical energy for operation during the lunar night.

The power management system is composed of a central power control unit and a variety of voltage converters, regulators, and power switches which are located in other units and which provide power management for the various instruments and subsystems. The central power control unit provides conversion of power from the solar panel, main bus regulation, overload sensing, battery charge control, and several switching functions. The optimum-charge regulator circuit provides the most efficient conversion of solar panel power to battery charging current. The battery output voltage from the unregulated bus is converted to the main regulated bus voltage by means of a boost regulator. A main overload trip circuit using tunnel-diode current sensing removes all nonessential spacecraft loads when an overload condition is detected. The battery charge logic system controls the charging current to the spacecraft batteries. Normally, the system operates in the automatic mode and the batteries are charged until their voltages reach a predeterminel level. A command mode is available whereby the battery may be commanded to be charged.

1. Progress Summary

Development model solar panel electrical and environmental type approval tests have been completed. A modified support arm and bracket structure assembly for the solar panel is presently undergoing environmental tests to establish vibration resonant points and to demonstrate the integrity of the redesigned secondary Sun sensor mounting. Fabrication of the MT-1 thermal model solar panel has been completed.

Solar panel power output analysis has been completed utilizing Phase I solar cell module test data and has shown higher power levels available during transit and the lunar day.

Testing of the eight experimental model batteries is 95% completed. Completion of the original test program has been hindered by the failure of four of the eight batteries at the extreme temperatures of 0°F and 125°F. Receipt of the ten development model batteries from Electric Storage Battery Company is expected in the near future. Electrical compatibility tests of the batteries and the breadboard central power control system have been initiated.

Final circuit releases have been made on the central power control system, both for the T-2 hardware, which contains only a boost regulator circuit, and for the prototype units for T-21. Drawings for the T-2 unit are being released for fabrication. Approximately 25% of the purchased components for the T-2 unit have been received. Procurement of parts for the T-21 prototype and type test unit has started, and product design layouts are proceeding. Circuits and product layouts have been modified such that the difference between T-25 and T-21 units consists only of components which can be deleted for T-21 if desired. The allocated volume for this unit has been increased to accommodate additional switching circuits and improve the thermal characteristics of the package.

The circuitry for the engineering mechanisms auxiliary has been redesigned to eliminate the need for several pyrotechnic switches. The squib firing circuitry associated with this auxiliary is now firm, and preliminary circuit release has been made.

Final circuit releases have been made on flight control electronics power conversion units, engineering and central signal processing power control circuits, transmitter high voltage and filament conversion units, TV auxiliary power circuits, and tape recorder switching and power conversion circuitry.

2. Solar Panel

a. Power output. An analysis of the solar panel performance on the lunar surface as a function of temperature and time was completed. The analysis utilized the results of the Phase I solar cell tests for determination of environmental degradation factors and for precise establishment of the solar cell electrical performance characteristics. Results of the analysis show considerably improved design power output values over those previously calculated. The peak power output near terminator conditions will vary from a maximum of 80 to 89 w after 175 hrs on the lunar surface to a minimum of 54

to 72 w at lunar noon after 725 hrs on the Moon. Several permanent degradation factors based on the Phase I type approval data were employed, as well as the normal nonpermanent variation due to temperature. Table 13 shows the significant degradation constants.

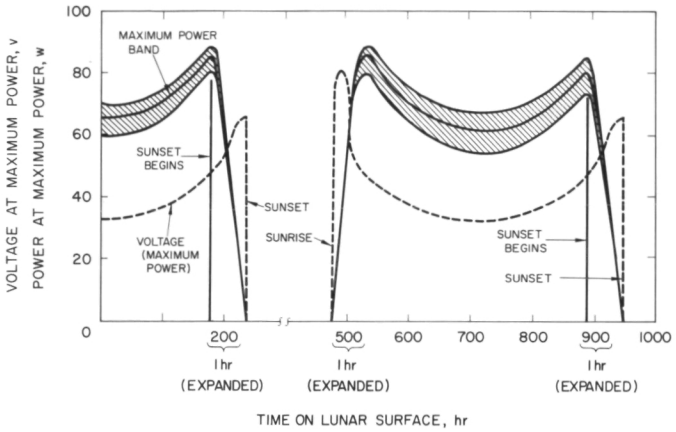

Fig. 88. Solar panel electrical performance on lunar surface

All degradations listed, excluding the cold soak, are assumed exponential with time; i.e., $P_t = P_o \exp(-\alpha t)$ where P_t is the power after t hours of the degradation environment, P_o is the power initially, and α is the degradation constant. The cold soak degradation is assumed to be a step function independent of the time spent at the cold extreme with $P = P_o[1 - \alpha]$, where α is the degradation constant and P the power after the cold environment.

Table 13. Permanent degradation contents

Type	α max, hr^{-1}	α mean, hr^{-1}	α min, hr^{-1}
Ethylene-oxide sterilization	0.00041	0.00021	0
High temperature — vacuum and high temperature sterilization	0.00028	0.00021	0.00015
Cold soak and/or temperature cycling	0.017 (dimensionless)	0.006 (dimensionless)	0

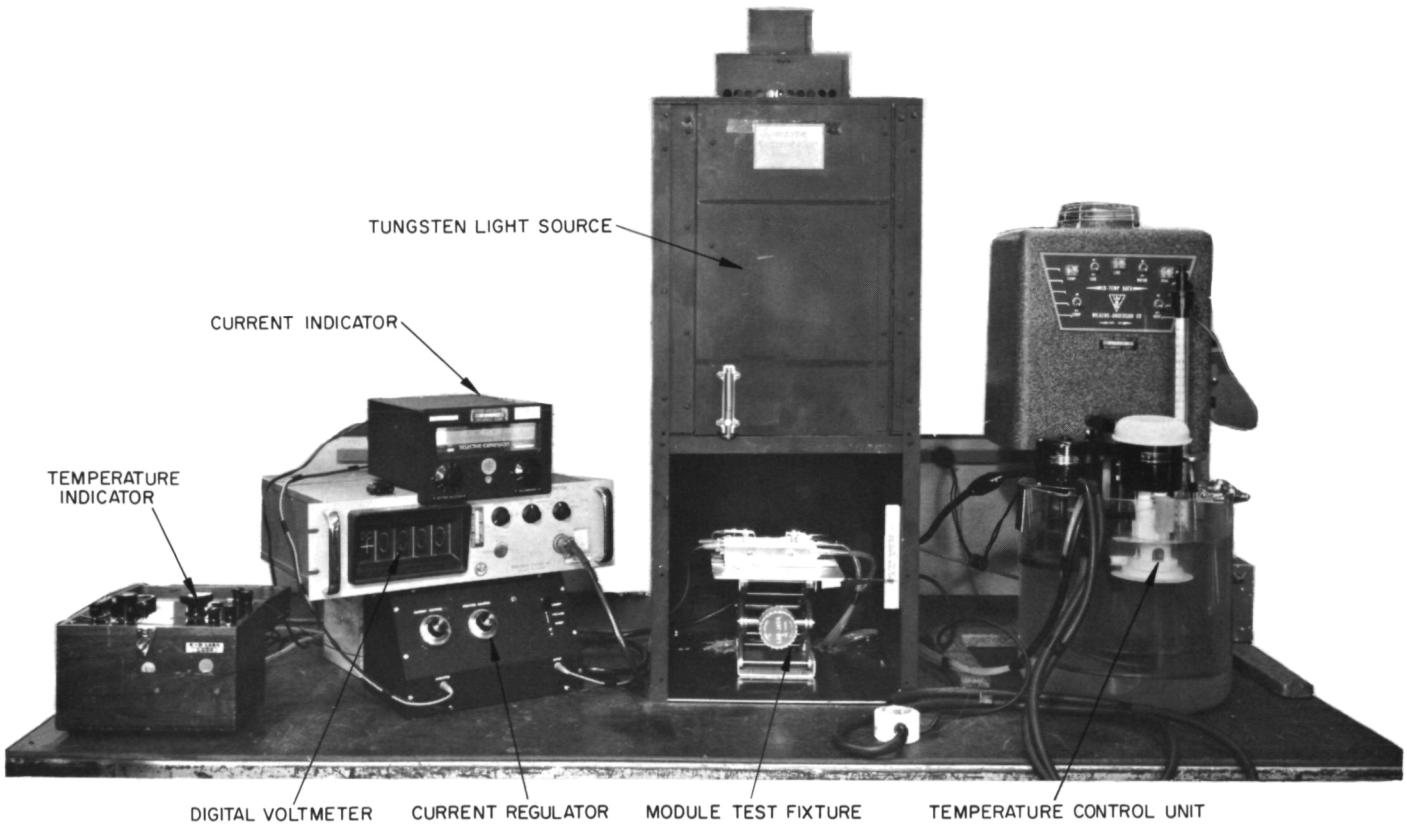

Fig. 89. Solar module electrical test setup

Figure 88 shows the variation with time of panel power and voltage on the lunar surface, assuming a landing at lunar noon on the equator.

b. Solar cell modules. The first two lots of Heliotek solar cell modules were delivered in accordance with the Phase II subcontract. Samples from both lots were taken to Table Mountain for sunlight performance measurements by both Heliotek and Hughes Aircraft Company. Using the sunlight data, correlation between the performances under the laboratory tungsten light source and Earth sunlight was established. This data aided in the formulation of an electrical performance test, which has been included in a solar cell module acceptance test procedure. The first two lots have been tested in accordance with this procedure, which calls for an electrical performance test on every module. The electrical performance test setup is shown in Figure 89. All 800 modules (400 per lot) exceeded the minimum and were found acceptable. Beginning with Lot 3, which will consist of modules to be used on the T-21 prototype panel, Hughes will maintain source inspection at Heliotek and will conduct 100% electrical performance tests at Hughes Aircraft Company.

c. Development panel tests. The first development panel was taken to Table Mountain for sunlight testing at the conclusion of the test program described in Reference 1. The purpose of the sunlight electrical tests was to compare the results with data obtained before the environmental test series began.

It was found that the short circuit current and maximum power of the partial panel (four series strings in parallel; 104 modules) were lower than the original values. This was due to the open failure of a five-cell module near the outboard corner of the panel. The open module resulted from the high deflections (approximately 6 in. double amplitude) incurred during vibration testing. E-I curves, taken before and after environmental testing, are given in Figures 90 and 91. It will be seen that the panel output is definitely current limited, indicating an open circuit in the series-parallel matrix. By successively shorting parallel subgroups, and observing the short circuit current, the subgroup having the open circuit was isolated. Subsequent shadowing of individual modules in each string located the open module.

After correcting the results to 25°C and 100 mw/cm² incident solar radiation, the panel output was found to be down by 13.2% (due to the open module) from the initial power. However, if the series strings had not been paralleled into a matrix, the open module would have caused a 25% decrease in power.

It might be pointed out that measurement of the true panel operating temperature is extremely difficult and great care must be taken to avoid serious errors. Further investigation is being carried out to firmly establish a reliable and accurate temperature measurement technique.

Testing of a modified support structure for the solar panel is under way in an effort to raise the natural frequencies of the panel-support arm assembly. The new secondary Sun sensor mount is also being tested. Both of these items are shown in Figure 92. Note that the design of the secondary Sun sensor itself has changed since the publication of Reference 1.

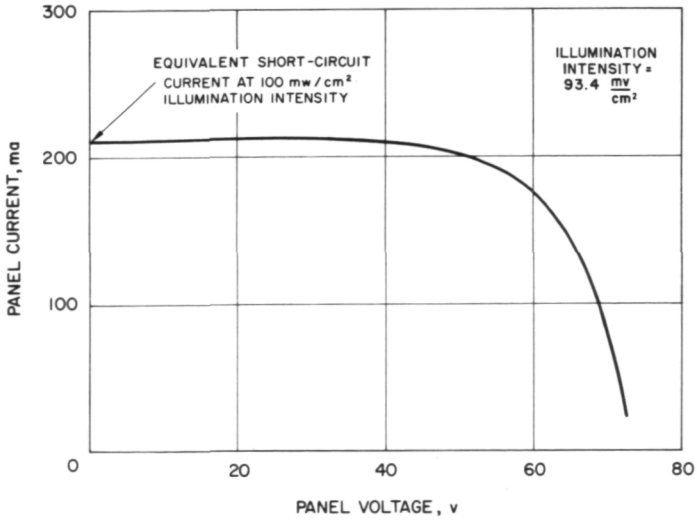

Fig. 90. Development panel E-1 curve before environmental test

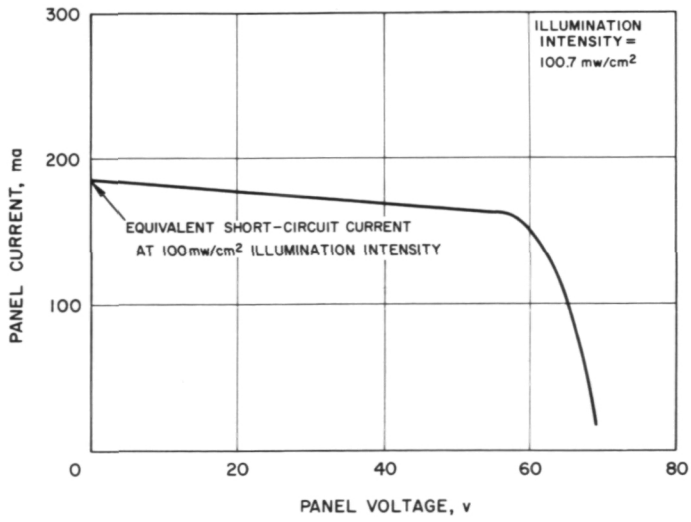

Fig. 91. Development panel E-1 curve after environmental test

A second developmental solar panel is in process for testing according to the revised Hughes type approval specification. The vibration levels have been considerably increased in the latest revision of this specification, particularly for the solar panel.

A thermal model mockup of the solar panel has been designed and is being fabricated for use in the MT-1 series of thermal-vacuum tests. This thermal model has the proper thermal control surfaces to simulate the flight panel design, including power dissipation.

d. Solar simulator. The spectral distribution of the Optical Coating Laboratory, Inc. (OCLI) solar simulator was determined by means of a calibrated Perkin-Elmer spectrophotometer. The energy spectrum of the simulator was substantially lower than the F. S. Johnson curve in the 0.55 to 0.70 μ range. Differences in the energy spectrum are shown in Figure 93. However, the uncertainty magnitudes involved in this type of measurement could be greater than 10%. Before shipment of the simulator to Hughes, OCLI performed the same measurement and found agreement with the F.S. Johnson curve to the tolerances set by the Hughes procurement specifications (see Figure 93). It will be noted that the OCLI measurement indicated a dip in the energy spectrum in the same spectral region but a deviation from the Johnson curve less than the Hughes measurement would indicate.

On the basis of analyses and experimental work in process, Hughes Aircraft Company will decide whether to utilize the simulator, as is, for acceptance testing solar cell modules, or to return the instrument to OCLI for further modification. Analysis indicated a typical solar cell would yield 5% less power when tested under the simulator than in space when the illumination intensity between 0.4 and 1.2 μ was kept equal to that of space.

A test program has been initiated to determine the probable error involved if the present simulator is employed in the acceptance tests. A large sample of modules with sunlight performance curves from Table Mountain will be employed. Short circuit currents under the simulator will be compared with the expected short circuit current values in space from the sunlight information. If there is a relatively constant difference in the two values, the present simulator will probably be utilized in future acceptance testing without modification. Figure 94 shows the solar simulator facing the solar module test fixture and Figure 95 illustrates details of the fixture.

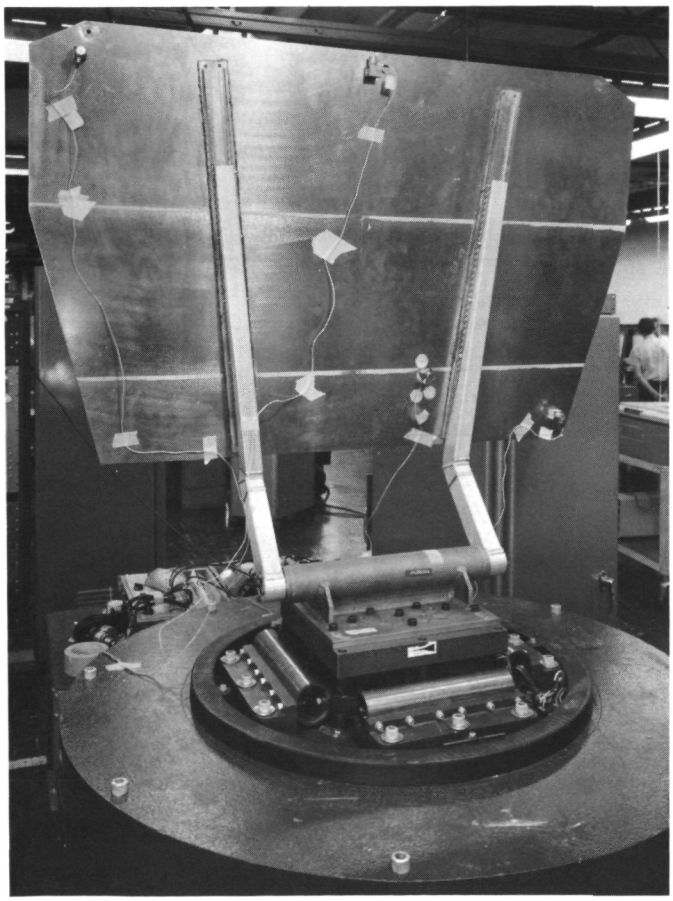

Fig. 92. Modified support structure panel

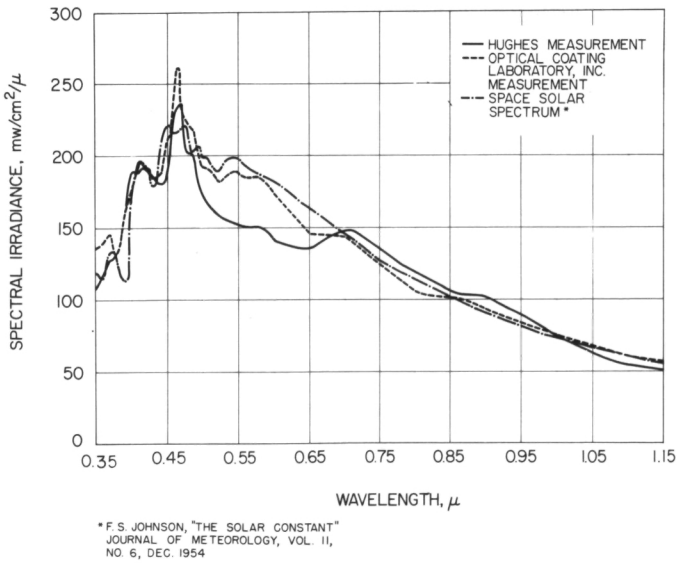

Fig. 93. Solar simulator spectral distribution

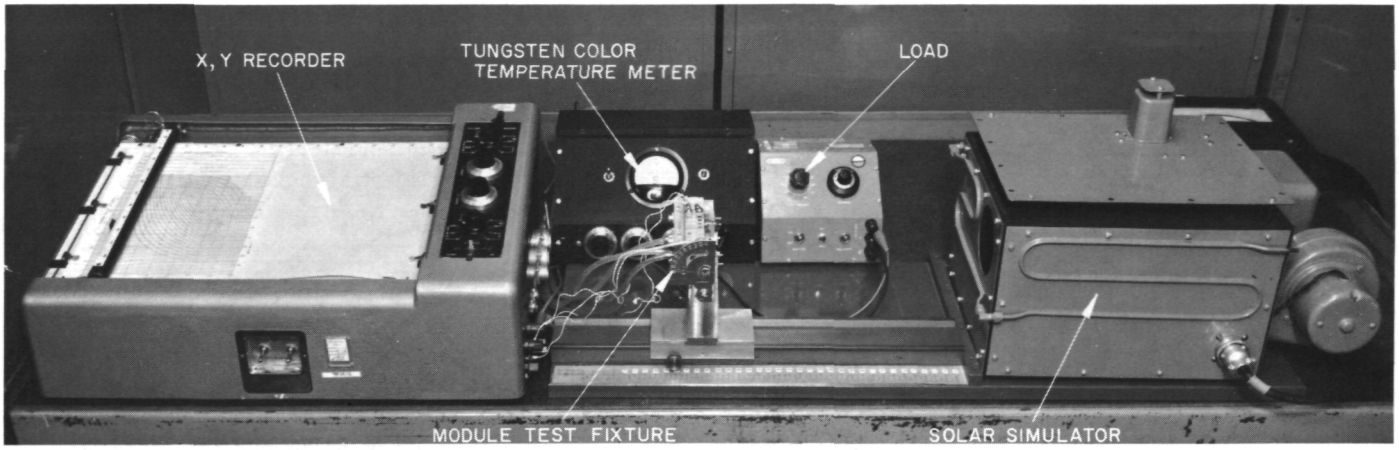

Fig. 94. Solar simulator electrical test setup

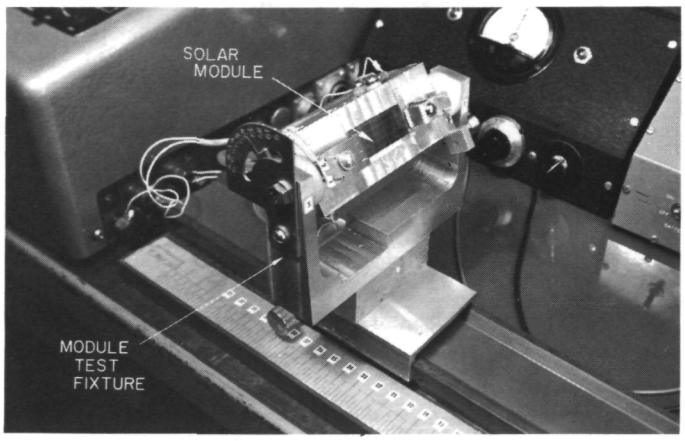

Fig. 95. Solar module test fixture

3. *Battery*

The *Surveyor* experimental battery test program is approximately 95% complete. Tests which are presently incomplete are the dynamic charge voltage surge test and the charge matrix test. The test program, as initially planned, was not completed due to the failure of four of the eight batteries. In all cases failures were experienced at the extreme environmental conditions of 0°F and 125°F. The symptoms of the failures were leaking cells accompanied by internal shorts. The problem appears to be one of thermal contraction and expansion between the battery magnesium case and the polystyrene cell cases. The ratio of thermal expansion of the polystyrene to magnesium is approximately 3:1. Therefore, battery operation at temperatures other than the manufacturing temperature of 75°F results in high compressive and tension loads between the cell cases and the battery case. This problem is expected to be resolved by providing a resilient bond between the cell cases and the battery case instead of the presently employed rigid epoxy bond. Also under investigation is the increase in cell pack tightness at low temperatures due to the thermal contraction of the polystyrene cell case.

Analysis of the experimental battery test data is approximately 60% complete and indicates that the battery problem statement will be met with some minor modification which has already been incorporated in the developmental model battery.

The capacity characteristics of the experimental model *Surveyor* battery are presented in Figures 96 and 97. Capacity vs. battery temperatures of 0°F to 130°F for constant current discharge rates of 2.0, 10.0, and 20.0 amp are shown in Figure 96. Examination of plotted data points also shows the temperature rise of the battery when discharged at the specified rates in controlled environmental chamber conditions of 0, 75, and 125°F. These temperature differences are summarized in Table 14.

Table 14. Battery test temperature variations

Test chamber temperature, °F	Discharge rate, amp	Battery temperature, °F	Rise in battery temperature, °F
0	20	40	40
0	10	29	29
0	2	14	14
75	20	127	52
75	10	100	25
75	2	80	5
125	2	130	5

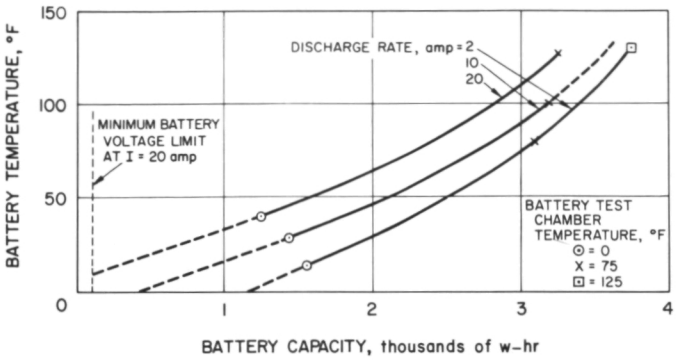

Fig. 96. Experimental battery capacity vs temperature

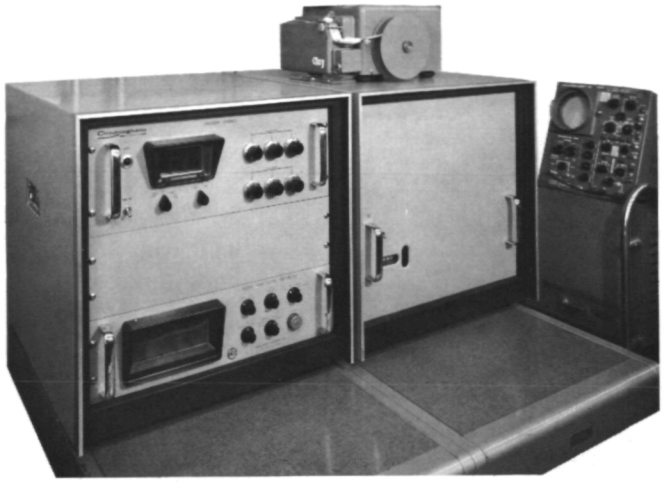

Fig. 98. Automatic data center

Figure 97 represents a cross-plot of the data presented in Figure 96 and defines battery capacity at constant temperatures and varying ampere rates.

The development model batteries X9 through X18 are expected to be received by July 1962. The required test equipment to implement testing of the development model batteries is 95% complete. The 300-channel automatic data center (Fig. 98) was set up and in operation by May 25, 1962. This data center will provide all battery data in the form of a punched tape which will in turn be tabulated and plotted by a Bendix G-15 computer.

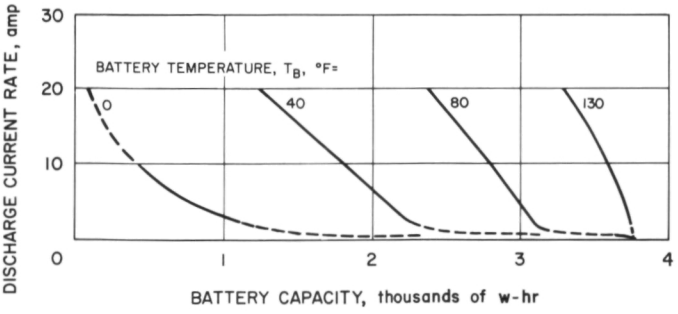

Fig. 97. Experimental battery capacity vs discharge rate

The test program for the development model batteries will include the following tests: Initial capacity, charge matrix, discharge matrix, dynamic charge surge and internal impedance, systems integration, vibration, shock, and acceleration, and thermal vacuum mission simulation. The completion of the development model battery tests is scheduled for September 2, 1962.

4. *Power Management System*

a. Central power control. The central power control system consists of the following circuits: optimum charge regulator circuit, boost regulator circuit, battery charge logic circuit, overload/under voltage-trip circuit, solar panel and planar array switch circuits, heater blanket switch circuit for TV Camera 4, and the gyro switch for flight control power.

Boost regulator. Final circuit release has been made on the boost regulator and layout design is well under way. Tests have been conducted with the boost regulator breadboard to check compatibility with subsystem loads. The estimated worst case load is during transit with the flight control system ac loads causing large current modulation on the output of the boost regulators. Tests were conducted with flight control breadboards connected to the boost regulator breadboard, and with full-level auxiliary loads on the boost regulator. The resulting modulation at the terminals of the boost regulator was less than 20 mv. With steady-state load, the total ripple on the output of the boost regulator is now less than 20 mv peak-to-peak. The change of output voltage with load is too small to measure for changes in load from 150 ma to 6 amp. From 150 ma to no-load, the load voltage change is 20 mv. Regulation takes place at 150 ma by switching, rather than by linear series regulation. The switching type of regulation is predicted to have zero output resistance. The losses at no-load are below 2.1 w; the initial goal was for no-load losses of less than 2.5 w. The efficiency under load is greater than 85% for loads above 1 amp. The maximum efficiency is about 90%, which

occurs at approximately 75% of full load, with the efficiency dropping slightly at full load due to I^2R losses in the transformer and filter inductor.

Overload trip circuit. Final circuits were released on the overload trip circuit. The circuitry has been modified to include an active regulator for nonessential loads. Thus, the boost regulator will hold the essential load voltage at 29.0 vdc while the overload trip circuit regulator will deliver 29.0 vdc to the nonessential loads. The efficiency of the overload trip circuit is maintained high by having only 0.7 v across the main pass-transistor and providing bias voltages by a 32-v output from the boost regulator.

Battery charge logic. Final circuit release has been made on the battery charge logic. Only very minor modifications have been made in this circuit since the preliminary release.

Optimum charge regulator. Final circuit release has been made and layout is under way. Compatibility tests between this regulator and the boost regulator indicate that under "full battery" conditions the optimum charge regulator can power the boost regulator directly.

b. Engineering mechanisms auxiliary. The squib firing circuitry in the engineering mechanisms auxiliary has been modified as described in Reference 1. This modification allows elimination of several pyrotechnic switches by using transistor switches to "arm" the squib firing bus. Separate silicon-controlled rectifiers for each squib allow

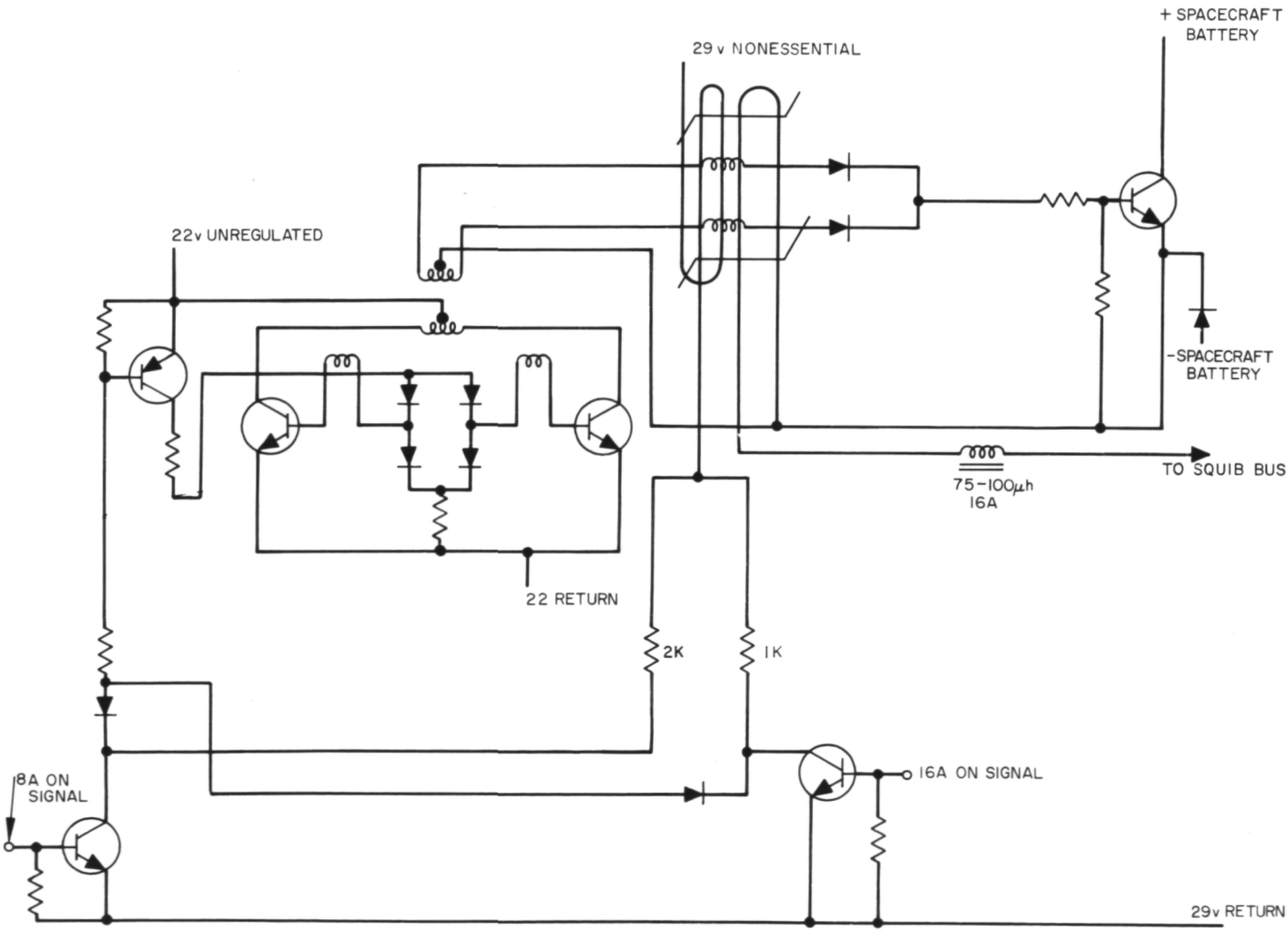

Fig. 99. *Constant-current switch schematic (8 and 16 amp)*

selection of the squibs to be fired each time the bus is armed. Since the last report there has been a change in the configuration of the transistor switch. It is now designed as a constant-current source which will provide either 8 or 16 amp depending on the turn-on signal supplied to the switch. With this change, all the current-limiting resistors can be eliminated and the problem of variable cable drop is eliminated. The diagram of the constant-current switch is shown in Figure 99. The wave shapes of the 8 and 16 amp current pulses are shown in Figure 100.

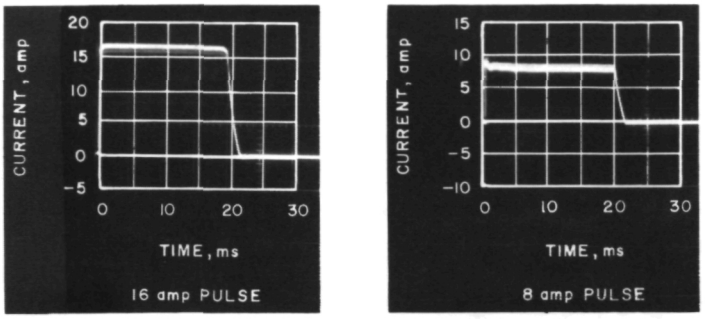

Fig. 100. Constant-current pulses

G. Thermal Control

1. Compartment Group

Compartment thermal development has expanded to include experimentally derived radiation view factors from critical radiating surfaces to the spacecraft, an estimate of the effects of the change to the A-21 configuration on transient and steady-state thermal performance of Compartments A and B and appropriate modification to the detailed analysis of Compartment A to reflect the equipment rearrangement of the A-21 compartments.

In a continuing effort to obtain both accurate and current design parameters the Form Factometer has been used in conjunction with the M-12 mockup (A-25 configuration) to obtain experimental view factors from specific equipment on the spacecraft to the collective spacecraft surfaces in view. A permanent record of these view factors has been established by photographing the experimental setups. The objective has been twofold: 1) to gather accurate view factor data for use in continuing analyses, and 2) to confirm the view factor values used in previous analyses and subsequent performance predictions.

View factors were obtained for the following locations: Compartment A radiators, 9 points; Compartment B radiators, 12 points, TV Camera 2 vidicon radiator, 3 points, and the inertial reference unit radiator, 5 points.

Table 17 presents typical area-averaged values of radiation view factors from the entire radiator to the collective spacecraft surfaces excepting the solar panel/planar antenna assembly.

The view factors to the solar panel/antenna assembly were omitted since accurate view factor information to the panels had been obtained previously using a smaller mockup. View factors are also being gathered for remote subsystems; since these subsystems have irregular surfaces, however, more data are necessary before total area-average values can be assigned to each item.

The view factors obtained for Compartments A and B and the inertial reference unit (IRU) radiators to the spacecraft are equal to or less than design values used in previous performance calculations. Verification of these basic thermal parameters offers considerable confidence to the thermal performance predictions made for the compartment group.

Although the view factor information compiled reflects the A-25 configuration, the view factor photographs can be easily interpreted to compensate for the removal or relocation of TV cameras, which are the only A-21 items that have changed from a compartment radiator view factor standpoint.

Present estimates of compartment power dissipation and weight indicate that the change to the A-21 configuration will not alter previous transient and steady-state compartment performance curves. The detailed thermal analysis of Compartment A is in the process of being modified to reflect the equipment arrangement in the A-21 version.

The lunar night heat losses from Compartments A and B have been reexamined. The individual heat losses are presented in Figures 101 and 102 as a function of compartment temperature for Compartments A and B, respectively. As indicated in the figures, the largest heat

Table 17. Radiation view factors from spacecraft radiators to spacecraft (A-25 configuration)

Radiator location	Average view factor to spacecraft[a]
Compartment A	0.13
Compartment B	0.13
Inertial reference unit	0.40
TV camera vidicon radiator	0.30

[a]Solar panel and antenna assembly not included.

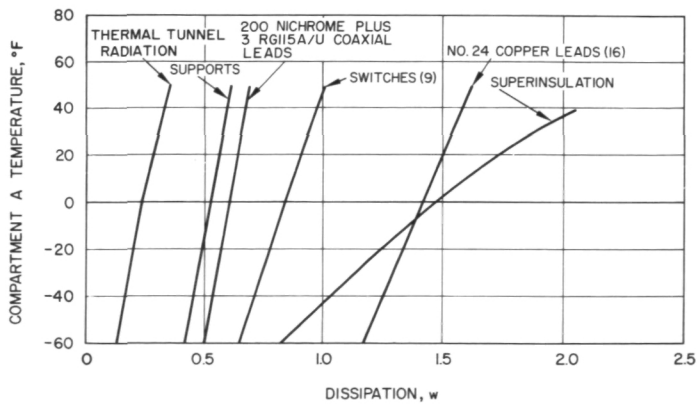

Fig. 101. Lunar night heat loss from Compartment A

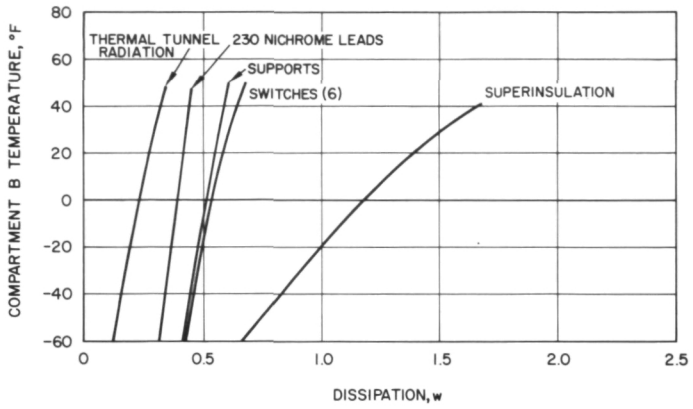

Fig. 102. Lunar night heat loss from Compartment B

losses are now associated with the superinsulation and the 16 24-gage copper wires which exit Compartment A. Attempts being made to reduce the superinsulation losses are discussed in detail under "5 Superinsulation" below.

The 16 24-gage copper wires which exit Compartment A are used to power the subsurface sampler and the radar altimeter and doppler velocity sensor (RADVS). At present, all other leads are utilizing nichrome inserts. Studies are under way to determine if the number of copper wires can be reduced.

An optimization study relating battery capacity characteristics and Compartment A heat loss as a function of temperature has indicated that increased system lunar night capability may exist if the battery is maintained at 40°F rather than 0°F as originally planned. With the present system (i.e., 16 24-gage copper wires exiting Compartment A) it is anticipated that battery capacity can be increased at a rate higher than the increase in thermal losses, resulting in an appreciable net saving.

Figure 103 presents the minimum compartment energy dissipation requirements as a function of Compartment A (battery) temperature and number of 24-gage copper leads. Also shown are the dissipation requirements for a revised configuration where the critical leads exit from Compartment B. Implicit in Figure 103 is a mandatory 2.64 w plus 10% of the Compartment A heater dissipation in the power control system (Compartment B).

Figure 104 gives the Compartment B temperatures which correspond with the internal dissipations of the previous figure. In the case where Compartment A is at 40°F, the strong coupling influence of the thermal tunnel is observed (i.e., Compartment B is at approximately 30°F).

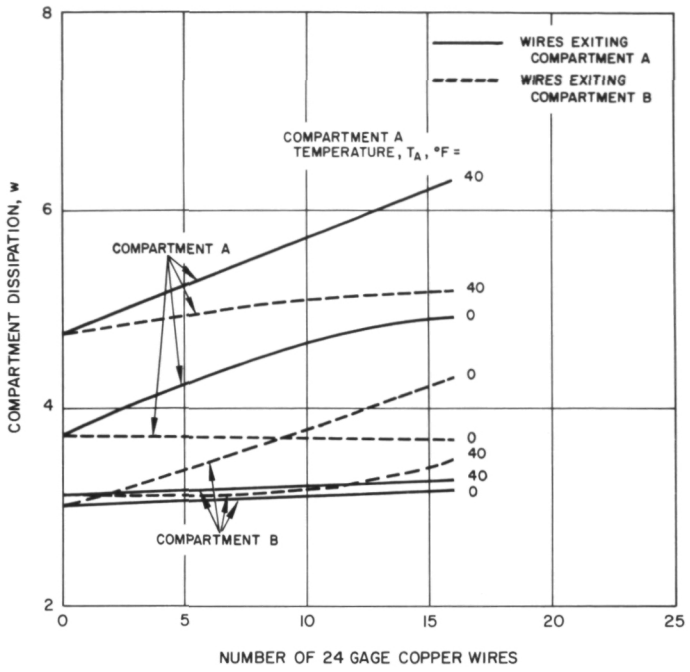

Fig. 103. Minimum compartment dissipation requirements

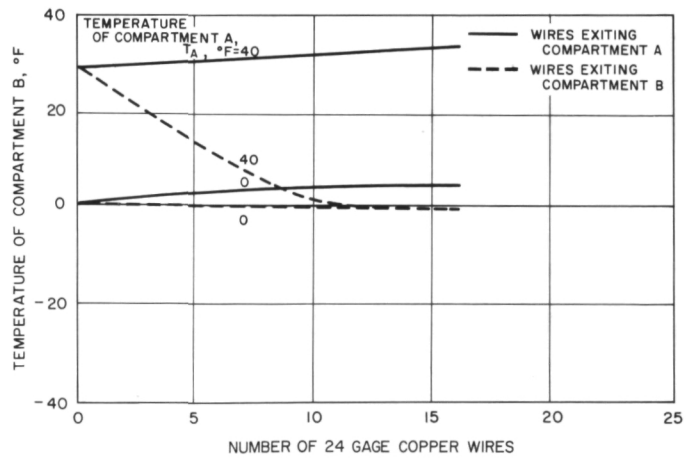

Fig. 104. Compartment B temperature corresponding to requirements of figure 103

Figure 105 indicates the minimum 350-hr lunar night survival energy requirements. As indicated above, the increased energy required to maintain Compartment A at 40°F is more than offset by the increase in battery capacity at the higher temperature.

2. Remote Subsystem Group

a. Radar altimeter and doppler velocity sensor. The detailed thermal analysis of the radar altimeter and

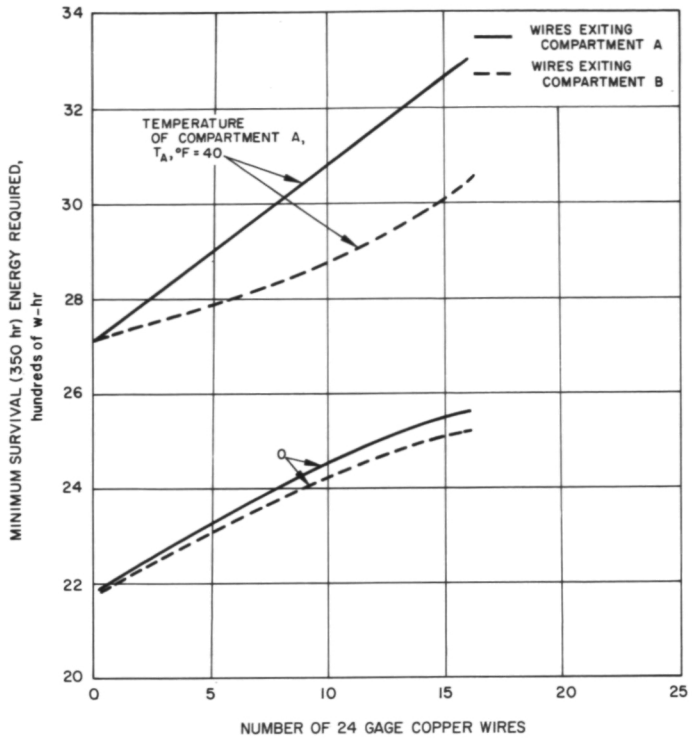

Fig. 105. Minimum energy requirement for lunar night survival

doppler velocity sensor (RADVS) has been completed. In general, the thermal design goals were achieved.

Initially, the over-all design of the RADVS equipment was overweight; a large portion of the excess weight was attributable to the thermal requirements of the equipment. Additionally, first thermal analyses of the antennas indicated that temperatures were excessively low and temperature gradients too high. The purposes of the analysis were therefore to:

(1) Determine the passive thermal control required during transit to achieve the predetermined optimum start temperature for the high-power dissipating equipment.

(2) Provide assurance that the equipment mounted on the antenna dishes will not exceed temperature tolerances during transit.

(3) Minimize the temperature differentials that might exist within the antennas during transit.

Based on the klystron power supply module (KPSM) package location, shape, and orientation on the spaceframe with respect to the Sun during transit, the package outer surface steady-state temperature was determined for several surface coating combinations of the Hughes Aircraft Company inorganic white paint and polished aluminum. The results are based on property values of $\alpha = 0.24$, $\epsilon = 0.955$ for the white paint, and $\alpha = 0.35$, $\epsilon = 0.05$ for the polished aluminum. Results are shown in Figure 106. The coating configuration corresponding to −5°F (the desired start temperature for this package) is equivalent to 20% white and 80% polished aluminum. Included in the analysis were (1) heat loss by conduction through the mounting bracket, (2) heat loss by conduction out of the two waveguides, (3) heat loss by radiation to space, and (4) heat loss by radiation coupling to the spacecraft.

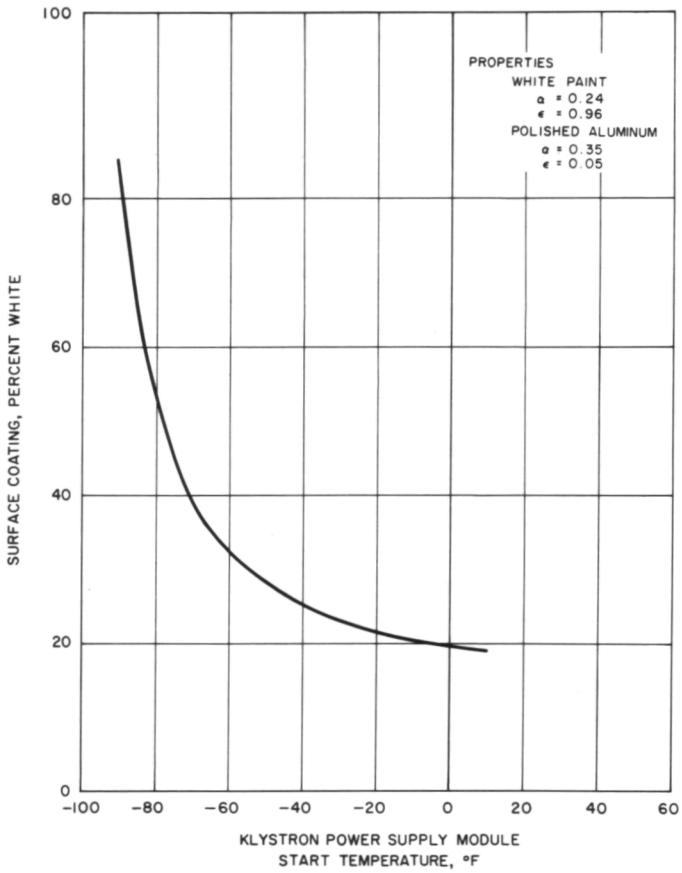

Fig. 106. Effect of surface coating on klystron power supply module

The start temperature of the equipment must stay within the allowable temperature tolerance (−5°F ±18°F) when the terminal phase maneuver changes the spacecraft orientation with respect to the Sun; two extreme possibilities which could exist were examined:

(1) Spacecraft oriented so that the KPSM package is out of direct sunlight during the terminal phase.

(2) Spacecraft oriented so that the KPSM package receives maximum possible sunlight and heat load from the lunar surface during the terminal phase.

For the first case, all heat inputs to the KPSM package are assumed to be equal to zero and the heat loss is by conduction through the mounting bracketry and the waveguides and by radiation to the surroundings. In 25-min, the terminal phase period, the KPSM package temperature drops approximately 10°F. For the other case where the package receives maximum solar illumination, the temperature will rise approximately 2°F in the same time. A uniform distribution of white paint over 20% of the package surface with bare polished aluminum as the remaining surface will assure that the equipment start temperature will be within the specified limits.

The thermal analysis of the signal data converter (SDC) was similar to the KPSM analysis except that the desired operating start temperature was set at 59 ±18°F. With the package mounted at a 20-deg tilt with respect to the spacecraft roll axis and receiving an unobstructed view of the Sun during transit, the final coating configuration that corresponds to a steady-state transit temperature of 59°F is 19% white paint and 81% polished aluminum over the complete package.

If the terminal phase of the *Surveyor* mission causes the SDC to become completely shaded for 25 min, the temperature will drop approximately 18°F. If the spacecraft is oriented during the terminal maneuver so that the maximum solar flux is received, the temperatures will rise approximately 6°F. Therefore, the SDC can be maintained within the specified limits.

Extensive thermal study of the RADVS antennas has been made. These studies have shown that during transit the antenna temperature will drop in some areas to less than −100°F. This extreme drop poses two problems: (1) the minimum allowable temperature of some of the equipment mounted on the antennas is −50°F, and (2) temperature gradients and differential expansions in the antennas could lead to undesirable distortions causing intolerable reflected signal errors and possible structural damage.

In the early thermal analysis of the antennas, a thermal network consisting of 40 nodes representing various portions of the antennas was utilized. For the recent detailed analysis an extensive thermal network of 140 nodes was developed in which the antennas and equipment mounted on the antenna were represented. Many different antenna configurations were analyzed in an effort to raise the temperatures of critical components to tolerable levels and to reduce temperature differentials as much as possible. A listing of some of the more informative computer runs is given in Table 18.

Both active and passive means of thermal control were analyzed. The active systems considered relied on uniform electrical heating on the top surface of the antenna; the passive systems consisted of utilization and distribution of solar heat which is incident on limited portions of each antenna. For the altimeter velocity sensor antenna, which appeared to be the most critical from a thermal standpoint, the position of the solar panel in the transit phase is significant. It was determined that if the solar panel could be moved to another location in transit, the problem of maintaining the AVS antenna at satisfactory temperatures was simplified. However, since a change in the position of the solar panel would involve a significant amount of change in the over-all system, a thermal control system that would perform satisfactorily with the solar panel in any position will be required.

The first five cases in Table 18 were based on the preliminary computer model, while the later cases were calculated on the more comprehensive and detailed network model. Only Cases 6, 9, 10, 11, 13, and 14 meet the minimum temperature requirement of −50°F. Case 6, however, requires that the solar panel be moved to another location where it will not shade either antenna during transit.

Cases 9, 10, and 11 offer solutions to the thermal problems regardless of the solar panel position. They assume uniform heating and 1 in. of superinsulation over the top surface of the antenna. In these cases it was assumed that only the septum of the antenna was a low-emittance surface since it was at first felt that a vapor deposit of aluminum on the reflecting bottom side of the antenna might produce undesirable microphonics in the system. With this configuration, uniform heating of 0.1 Btu/hr in.^{2} is ample to maintain the antenna within thermal tolerances. However, a vapor deposit of aluminum on the bottom side may be possible; if this were incorporated into the above configuration, 0.075 Btu/hr in.^{2} of heating during transit would be sufficient. This corresponds to approximately 9 w per antenna. This configuration also involves the use of approximately 0.4 lb of superinsulation on the top surface.

Cases 12 and 13 approximate the temperature requirements of the antenna by utilizing a heat conducting foil on the top surface of the antenna and vapor-deposited aluminum over the complete assembly. This system is satisfactory regardless of solar panel position; in fact, if the solar panel is moved to another location, the antenna

Table 18. RADVS antenna thermal analysis results

Case	Configuration	Temperature, °F				Comments
		Sunny edge	Shaded edge	Critical parts, top	Waveguide filters	
1	0.007 in. all-aluminum construction	50	3	—	—	No solar panel $\epsilon = 0.05$ all over
2	0.0007 aluminum honeycomb core, 0.005 fiberglass cover sheets	327	−116	—	—	Same
3	Same as Case 2 with 0.007 foil cover over top	281	−70	—	—	Same
4	Same as Case 2 with 0.0015 foil cover	245	−39	—	—	Same
5	Same as Case 2 with 0.0033 foil cover	174	15	—	—	Same
6	Same as Case 2	450	−71	−10	−13	Improved analytical model — no solar panel
7	Same as Case 2 except $\epsilon = 0.3$ all over	154	−93	−46	−80	Same
8	Same as Case 7 but include solar panel	143	−90	−108	−106	Includes solar panel
9	Add uniform heat and insulate top, $\epsilon = 0.05$ on septum, $Q = 0.1$ Btu/in.^{2} hr	28	−18	~0	~−20	Same
10	Same as Case 9 except $Q = 0.3$ Btu/in.^{2} hr	161	160	9	1	Same
11	Same as Case 9 except $Q = 0.5$ Btu/in.^{2} hr	246	246	~80	~50	Same
12	Same as Case 2 except add 0.002 aluminum foil on top	79	−98	−58	−69	Same
13	Same as Case 2 with 0.0025 foil on top	109	−95	−53	−64	Same
14	Same as Case 13 with black strip on top over septum (sunny area only)	221	−84	−31	−41	Same

maximum temperature can be lowered while the minimum temperature can be raised by proper application of coating patterns on the illuminated portions of the antennas. Thus, the temperature gradients and total temperature excursions of the antennas can be reduced.

Case 14 represents an attempt to raise the critical antenna temperatures from the marginal values of Case 13. The configuration is identical to Case 13 except that on the top of the antenna directly over the septum, a 2-in. wide stripe of black paint ($\alpha = 0.97$, $\epsilon = 0.93$) is assumed to extend from the outboard edge of the antenna to the shadowline. This results in raising the critical temperatures by about 20°F. At first glance, this appears to be a contradiction to theory since the α/ϵ ratio for the aluminum foil is about 4 while the α/ϵ for black paint is only about 1. However, it can be shown that in the presence of a large thermal conduction term, the equilibrium temperature for the black paint surface can actually be significantly higher than for the polished aluminum surface. By comparison of Cases 13 and 14, however, it can be seen that to raise the critical temperature 20°F by this method, it is necessary to raise the antenna maximum temperature by about 100°F.

The thermal problems associated with the velocity sensor antenna do not appear to be as serious as with the altimeter velocity sensor antenna because of the increased area receiving solar illumination during transit. In fact, the critical components, preamplifiers, crystals, etc., are mounted on an illuminated portion of the antenna, and, therefore, require that a portion of the package be painted white to keep the temperatures sufficiently low. It has been recommended that the critical components packaged on the velocity sensor antenna be of polished aluminum with a white stripe pattern covering 80% of the top and outboard side. This will result in a steady-state transit temperature of about 30°F for this package.

The problem of differential temperatures on the antenna has not been completely solved. The subcontractor has not been able to determine the allowable thermal excursions or temperature gradients within the antenna. This problem is currently under both experimental and analytical investigation by the vendor. An approximate temperature map of the AVS antenna for the configuration of Case 14 is shown in Figure 107.

b. Vernier propulsion system. The study of the vernier system thermal protection problem which occurs during flight acceptance tests is nearly complete. The original scope of the study concerned protection of the vernier system hardware during the lunar night flight acceptance tests; however, it has been expanded to include protection of the hardware during the lunar day tests. The technique of covering vernier hardware with aluminum foil heater blankets provides effective protection for transit and lunar night; however, the high α/ϵ ratio of

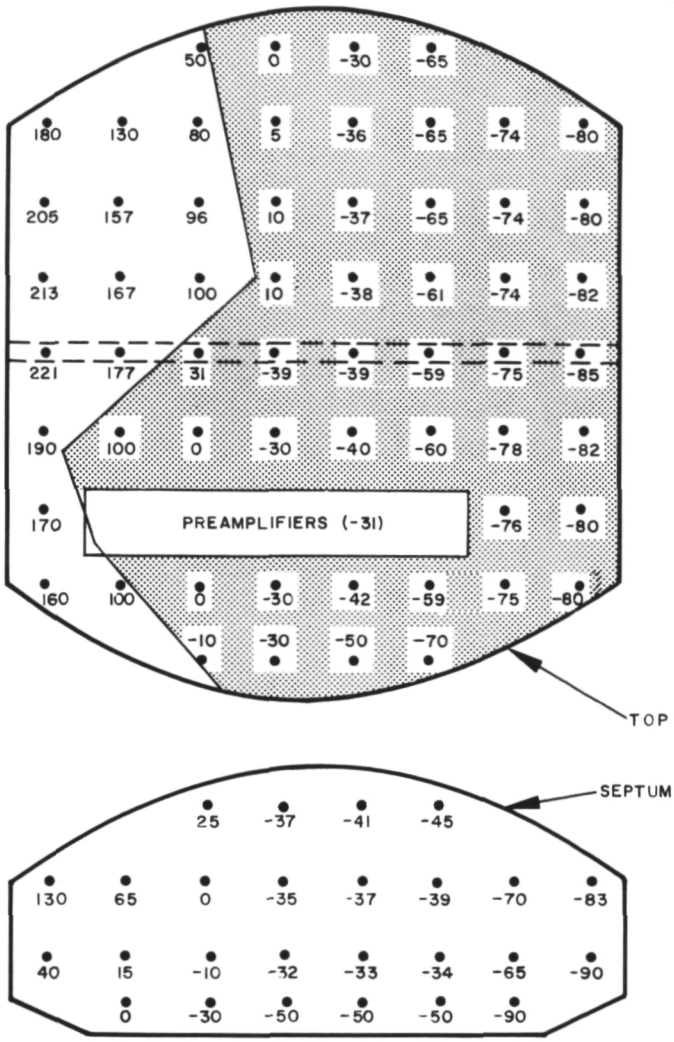

Fig. 107. Altitude velocity sensor antenna during transit (°F)

the aluminum foil would cause vernier system hardware temperatures at lunar noon to be in excess of 300°F. The maximum allowable temperature of this hardware is 257°F; therefore, appropriate α/ϵ ratio adjustments are required. One solution is to make blankets of approximately ten sheets of ¼ mil aluminized mylar and an outer sheet of aluminized teflon. This type of blanket possesses a low emittance factor from the heater interface to lunar night or transit environment and will require a minimum amount of auxiliary heating (approximately 48 w) to maintain all vernier hardware at 0°F. A minimum heater power is desirable since large power sources would raise the temperature of both the spaceframe and local equipment making evaluation of test data complex.

A detailed thermal analysis of the spaceframe assuming auxiliary heating levels of 48 w and a simulated —320°F liquid nitrogen cold wall resulted in spaceframe temperatures ranging from —200°F on lower tubes to —245°F on upper tubes. It is expected that these spaceframe temperatures can be compensated by proper scaling of test data.

Effective temperature control during lunar day is expected by minimizing the radiation equilibrium temperatures on the outer surface of the heater blanket through the use of low α/ϵ ratio aluminized teflon surfaces to reradiate the lunar and solar energy inputs. The problem is complicated by the conductive heat load imposed on the vernier hardware by spaceframe lower tube temperatures estimated to be 250 to 350°F. (The lower tubes are polished for temperature control during transit.) In this instance, the attractive radiation barrier offered by the blanket for lunar night tests is a hindrance to effective re-radiation of spaceframe heat conducted to the tanks and engines through the attach bracketry. The goal of performing an uninterrupted lunar day and night test to observe the spacecraft reaction to the day/night terminator phase justifies the continuing search for a solution.

The vernier system has been the subject of study to explore fully the ability of passive thermal control techniques to provide satisfactory thermal control for the vernier engines, pressurization and propellant tanks, and lines under the environmental conditions existing during the transit phase of the mission. Careful consideration has been given because of the limitations encountered in maintaining all vernier subsystem temperatures between 0 and 100°F. The technique requires selective surface treatments and extreme thermal isolation. The selective surface treatment method is sensitive to the diverse radiation environments existing during the transit portion of the mission. For example, one environmental requirement is: up to 1 hr of no sunlight and random orientation to the Sun followed by the normal transit attitude. In this example, direct solar irradiation for extended periods dictates the radiative surface property requirements.

Collectively the subsystem functional requirements and varying transit environmental conditions have imposed limitations on the number of practical thermal control solutions that exist. Practicality is measured in terms of the probability of providing satisfactory thermal protection by any given method, together with demands for additional weight and auxiliary heating. A detailed analysis of the vernier engine was performed to determine the temperature distribution in the engine for several

combinations of engine body and valve surface properties. The results presented in Figure 108 indicate a temperature gradient 45°F from the engine body section to the midsection on the diffuser cone. The steady-state temperatures corresponding to a normal transit attitude indicate that surface property values of $\alpha \simeq 0.2$ and $\epsilon \simeq 0.05$ are required to maintain the critical body and valve portions of the engine between the desired 30 to 40°F range during transit. Conduction into a —70°F spaceframe (even with thermal isolation) and radiation losses from the high emittance ($\epsilon = 0.72$) radiation-cooled diffuser cone constitute significant sources of heat loss from the engine. Vapor-deposited aluminum on the engine body and polished aluminum valves and lines is the surface treatment being considered for this application. Samples of the engine body substrate with various surface treatments are being tested to determine compatibility with the design requirements.

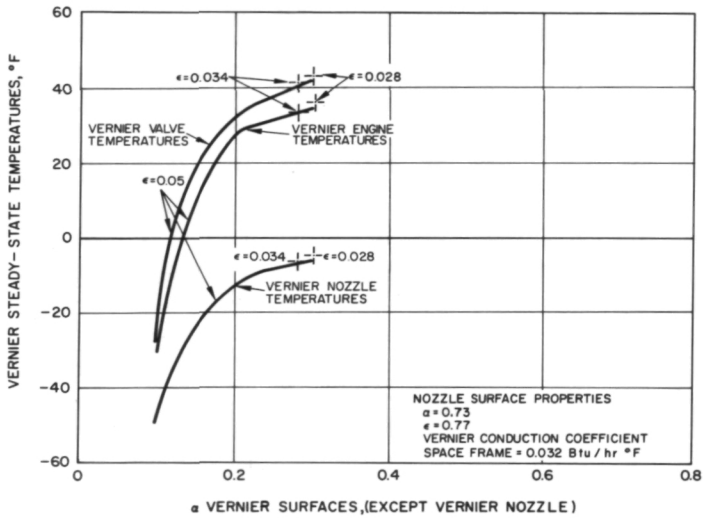

Fig. 108. Vernier propulsion system steady-state temperature during transit

The surface properties producing acceptable vernier engine temperatures during the normal transit attitude phase must also be compatible with the allowable vernier engine cooling rates and minimum temperatures that can be tolerated during nonilluminated periods. To design for a cooling period of 1 hr, the solar absorptance and infrared emittance are the controlling variables in achieving an adequate equilibrium temperature of about 35°F. Figure 109 shows the transient response at various sections of the engine and indicates that a solar absorptance of $\alpha \simeq 0.3$ on the engine body is desirable to provide up to 1 hr of cooling capability above 0°F. Additional study to arrive at a solution compatible with all aspects of the problem is continuing.

A study is under way to determine the thermal control requirements of the helium and nitrogen lines. Proper temperature control of the enclosed gas and a proper match of boundary conditions where gaslines enter the tanks are the objectives. Passive techniques are being studied; however, initial considerations suggest that auxiliary heating for the helium lines may be required. Power requirements are estimated at 5.5 w; this corresponds to a gasline-to-spaceframe total attachment conductance of 0.04 Btu/hr °F and a gasline surface emittance of $\epsilon = 0.05$.

c. Retro-rocket engine. Continuing studies into the effects of vernier engine exhaust impingement on the

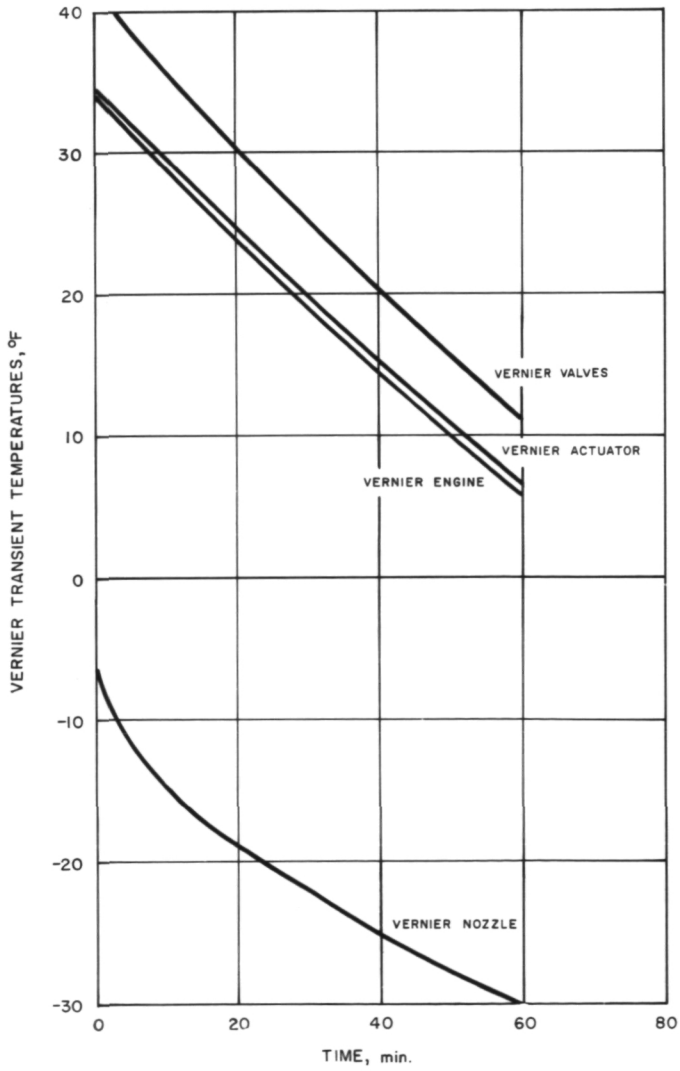

Fig. 109. Vernier propulsion system cooling from steady-state conditions ($\alpha = 0.3$; $\epsilon = 0.05$)

retro nozzle and altitude marking radar (AMR) dish prompted a reexamination of the effectiveness of the main retro nozzle aluminized mylar superinsulation blanket. The twofold question considered was (1) could the nozzle withstand direct vernier exhaust impingement if no insulation were present, and (2) what effect would removal of the radiation barrier blanket have on propellant temperature at ignition.

The existing two-dimensional thermal analysis of the main retro was expanded to include the heating effect attributed to vernier exhaust impingement on a bare nozzle. The critical heating period from vernier heat inputs occurs during the midcourse maneuver. After 40 sec of simulated vernier exhaust impingement the nozzle reached 320°F. At retro ignition, however, the predicted minimum propellant temperature decreased 5° from the previous low of 22°F. Based on these values, it appears desirable that the superinsulation blanket be retained to eliminate this source of heat loss. If the aluminized mylar remains on the nozzle, the original suggestion of applying an insulating batt of Refrasil over the superinsulation remains the preferred method of protection.

d. Shock absorber. The thermal model of the shock/leg assembly has been expanded to include the telescoping portion of the leg structure which has significant influence on the problem. The preferred surface properties for the shock assembly are an $\alpha = 0.3$ and $\epsilon = 0.24$ to provide shock fluid temperatures of 40 to 100°F during the entire launch-to-lunar touchdown phase, including a maximum 1 hr cooling (no Sun) period. The search for a surface treatment which will satisfy the requirements has focused on aluminized silicone paints which display values in that range. Factors such as acceptable tolerances and stability during the transit period are presently being assessed for the magnitude and predictability.

e. Flight control sensor group. The flight control sensor group (FCSG) thermal study is complete. As previously reported, the objective was to study the internal FCSG coupling effects and the radiant interaction of the package with the various spacecraft surfaces. A detailed thermal model simulating the package and its environment was fabricated. Figure 110 shows the model subdivisions used. The FCSG units were previously analyzed on an individual basis and a basic thermal design adopted. In the current analysis, the units comprising the FCSG were subdivided to permit emphasis on the thermal conductive and radiative coupling parameters and their ultimate influence on the thermal behavior of each unit.

0 SPACE
1 FLIGHT CONTROL ELECTRONICS
2 ---- NOT USED
3 MOUNTING PLATE
4 GYROS
5 GYRO RADIATOR
6 CANOPUS SENSOR (INTERNAL)
7 CANOPUS SENSOR RADIATION SHIELD SECTOR 1 COVERING CAN SECTOR 1
8 CANOPUS SENSOR RADIATION SHIELD SECTOR 2 COVERING CAN SECTOR 2
9 CANOPUS SENSOR RADIATION SHIELD SECTOR 3 COVERING CAN SECTOR 3
10 CANOPUS SENSOR RADIATION SHIELD SECTOR 4 COVERING CAN SECTOR 4
11 COMPARTMENT B
12 WIRE HARNESS FROM ELECTRONICS TO INERTIAL REFERENCE UNIT (IRU)
13 SPACEFRAME
14 IRU DUST COVER
15 CANOPUS SENSOR RADIATOR
16 WIRE HARNESS FROM CANOPUS SENSOR TO ELECTRONICS
17 WIRE HARNESS FROM ELECTRONICS TO ACCELEROMETER, INERTIA SWITCH AND SUN SENSOR
18 CANOPUS SENSOR SUN SHADE
19 GYRO GLASS EPOXY MOUNT
20 CANOPUS SENSOR CAN SECTOR 1
21 CANOPUS SENSOR CAN SECTOR 2
22 CANOPUS SENSOR CAN SECTOR 3
23 CANOPUS SENSOR CAN SECTOR 4
24 RADIATION SHIELD AROUND LOWER SECTION OF CANOPUS SENSOR
25 SUPPORT TUBES FROM SPACEFRAME

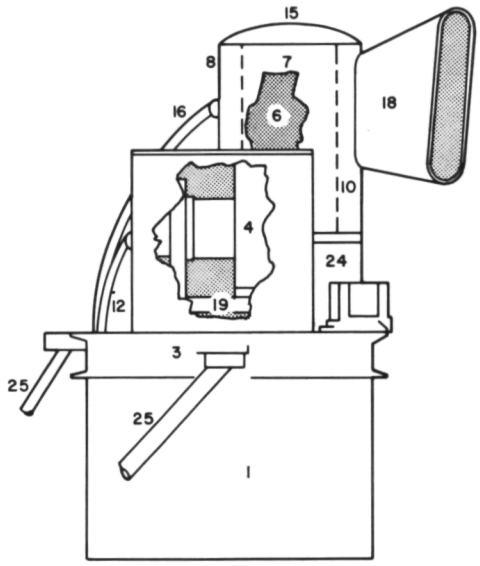

Fig. 110. Thermal analysis modes for flight control sensor group

Operational uncertainties required that the flight control electronics (FCE) unit power dissipation and surface treatment be used as boundary conditions. A typical mission profile was chosen to provide a maximum of data with a reasonable consumption of computer time. The profile consisted of 17 hr of overhead solar input with the spacecraft in the normal transit attitude (designated Phase I in Fig. 111) followed by a maneuver resulting in solar input directly into the Canopus sensor star window for a period of 1 hr (Phase II). This was followed by a return to normal transit attitude for 1 hr and concluded with 1 hr of complete shade (Phase IV). The temperature response of the units to the assumed mission profile is presented in Figure 111. The thermal behavior described in Figure 111 considers the following assumed

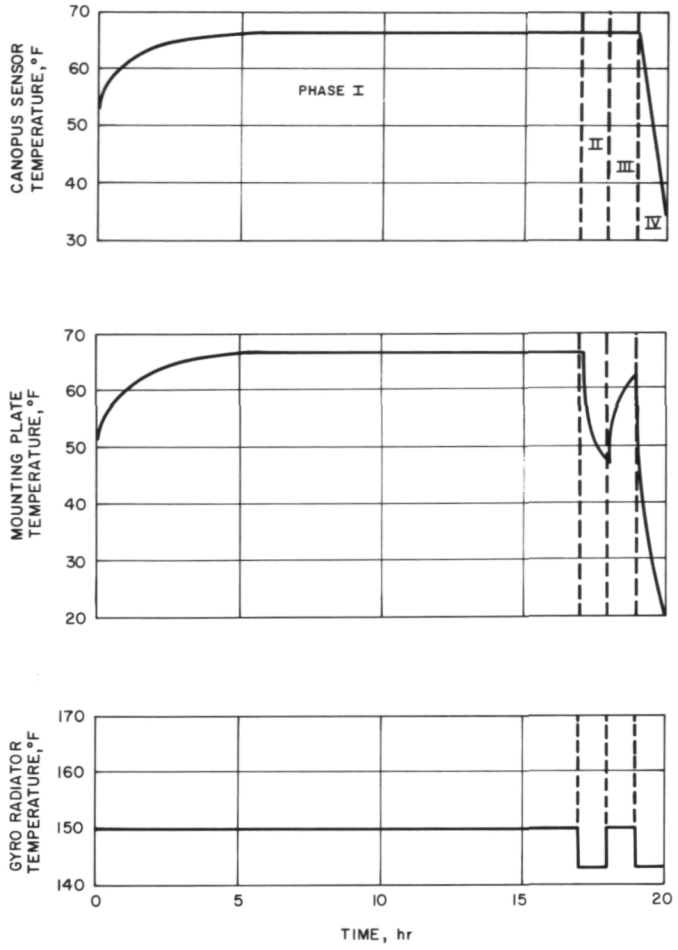

Fig. 111. Typical temperature transients in flight control sensor group

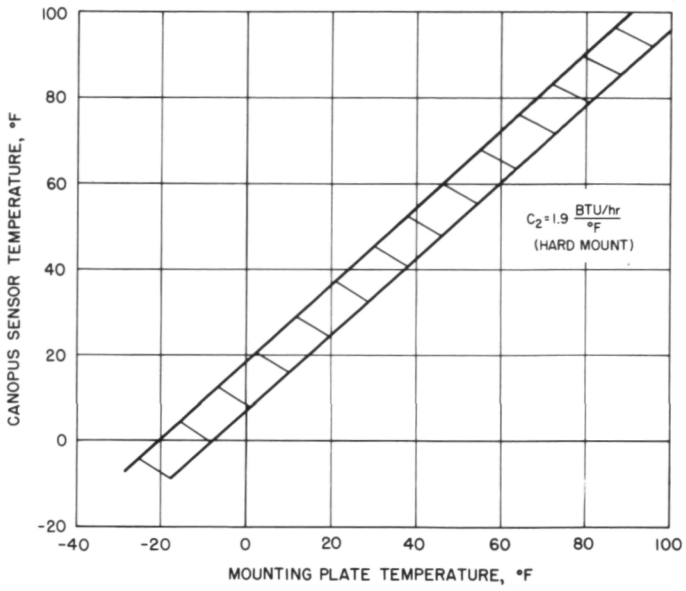

Fig. 112. Canopus sensor temperature

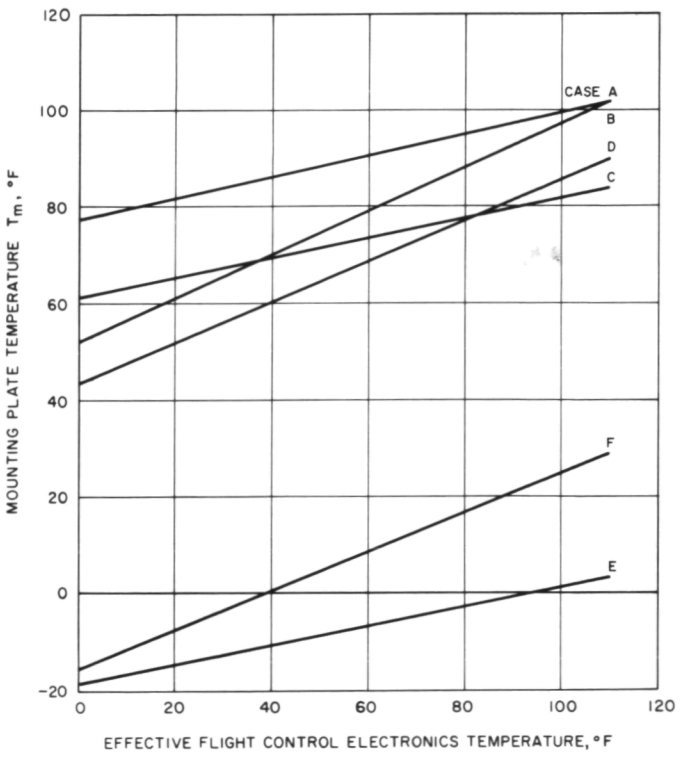

Fig. 113. Flight control electronics temperature

conduction and radiative variables: (1) hard mounting all sensor group units to the mounting plate, (2) isolating the mounting plate from the spaceframe, (3) mounting plate surface property values of $\alpha = 0.5$ and $\epsilon = 0.5$, and (4) an effective FCE temperature of 30°F.

The temperature variations of the IRU gyro radiator, (Fig. 111) are indicative of the gyro auxiliary heating required during maneuvers. The analysis determined the magnitude of collective heat losses by conduction and radiation from the gyros at a boundary temperature of 180°F. These heat losses are balanced by normal gyro dissipation and the gyro auxiliary heaters. The assessment of magnitude of the individual heat losses relative to the total available power assures optimization of the gyro temperature control system.

The temperature variations of the Canopus sensor and flight control electronics units are presented in Figures 112 and 113 as a function of the sensor group mounting plate temperature. Each case corresponds to the parametric values presented in Table 19. Acceptable Canopus sensor temperatures exist (Fig. 112) for a

wide range of mounting plate temperatures. The hard-mounted design was recommended to aid alignment and reduce vibration. Using data from Figure 113 and anticipated FCE temperatures, the operational conditions of the FCSG may be established. This information is available and is presently being implemented into the study. The study indicates that the FCSG recommended design should have satisfactory thermal performance. The radiative surface treatment and property values are presented in Table 20.

Table 19. Mounting conductances and surface properties

Case	C_1 Btu/hr/°F	C_2 Btu/hr/°F	C_3 Btu/hr/°F	ϵ_m	α_m
A	0.25	0.18	0.1	0.5	0.5
B	0.75	1.9	0.1	0.5	0.5
C	0.25	0.18	0.23	0.5	0.5
D	0.75	1.9	0.23	0.5	0.5
E	0.25	0.18	0.23	0.96	0.24
F	0.75	1.9	0.23	0.96	0.24

Nomenclature:

C_1	Conductance between mounting plate and flight control electronics.
C_2	Conductance between mounting plate and Canopus sensor.
C_3	Conductance between mounting plate and spaceframe.
ϵ_m	Infrared emittance of mounting plate
α_m	Solar absorptance of mounting plate.

f. Solar panel–planar antenna. A detailed study of the solar panel–antenna assembly, including the associated drive motors, has been initiated to predict both transit and lunar phase temperatures for various launch windows and lunar landing sites. At present little is known about the temperature history of the mechanisms which drive the panels. Investigation will focus on determining transient behavior near the lunar terminators. The panel and antenna positioning drive motors are located throughout the panel assembly and mast; therefore, considerable emphasis has been placed on formulating an accurate thermal model which accounts for conduction coupling and radiant interchange between the item under study and the collective thermal environment.

Preliminary calculations indicate that solar cell temperatures are approximately 105°F during transit with the spacecraft being in its normal transit attitude. Further study of the lunar phase is awaiting completion of the calculation of the radiation view factors needed to perform the analysis.

Table 20. Assumed flight control sensor group surface treatment and property values

Canopus sensor	
Casting	Polished aluminum, $\epsilon = 0.05$
Radiation shield	Aluminum foil, $\epsilon = 0.05$
Can	Polished aluminum, $\epsilon = 0.05$
Radiator	White paint, $\alpha = 0.24$, $\epsilon = 0.96$
Sun shade	White paint, $\alpha = 0.24$, $\epsilon = 0.96$ outside Black paint, $\alpha = 0.93$, $\epsilon = 0.96$ inside
Inertial reference unit	
Radiator	Second surface mirror, $\alpha = 0.12$, $\epsilon = 0.85$ outside Gold plate, $\epsilon = 0.03$ inside
Glass epoxy	Single sheet of aluminized mylar, $\epsilon = 0.06$ inside Aluminum foil, $\epsilon = 0.06$ outside
Heat conductors	Polished aluminum, $\epsilon = 0.06$
Spaceframe supports	Polished aluminum, $\alpha = 0.30$, $\epsilon = 0.06$
Side of compartment B	White paint, $\alpha = 0.24$, $\epsilon = 0.96$
Spaceframe	(Effectively), $\epsilon = 0.85$
Mounting plate	Variable

3. Scientific Payload

The geiger counter experiment vendor has supplied Hughes Aircraft Company with a thermal analysis of the instrument which has been evaluated in detail. Three design conditions shown below have been considered.

(1) *Lunar night – no insulation on electronics:* For this case, rough calculations have been made to determine heat input requirements at various temperatures. Results are almost identical to the results given in the vendor's analysis.

(2) *Lunar night – foam insulation surrounding electronics:* For this case, rough heat balances were set up for the package with a polyurethane foam around the electronics. Based on the thermal properties of the foam and package, the calculated total night heat loss was about one-third that calculated by the vendor. From this rough analysis and based on the selected properties, the vendor's results are probably on the conservative side. However, the extremely low value assumed for thermal conductivity (0.013 Btu/hr ft °F) of the foam material is questionable. Until definite confirmation of the thermal properties of this material is obtained, the computed results will not be considered conservative.

(3) *Lunar day operation:* For this case, the correct lunar properties and conditions were used by the vendor in the analysis. The maximum operating temperature of the geiger counter has, however, been underestimated by the vendor. The lunar

heat load at lunar noon was calculated at 13 Btu/hr but should be 34 Btu/hr. (The vendor used projected area instead of the true surface area.) The solar load was calculated at 17 Btu/hr but should be 25 Btu/hr for maximum solar illumination. The calculated operating temperature was 113°F, but should be about 230°F based on the assumed surface and material properties. The actual maximum operating temperature can probably be lowered significantly by a proper adjustment of surface coating with no loss of lunar night capability. This problem will be coordinated further by Hughes.

A preliminary thermal analysis of the surface temperature instrument (STI) sensor has been completed. Results indicate that with proper external surface treatment, the maximum operating temperature of the instrument as designed can be maintained below the allowable limit of 170°F. With the addition of cyclic heating during lunar night, the minimum operating temperature —10°F can be maintained.

For the lunar mission, the instrument is mounted to the mirror shaft of TV Camera 3. Its function is to measure the temperature of the lunar surface at a point that is never shaded by the spacecraft during lunar day. The STI sensor, therefore, views the same general area as TV Camera 3. For thermal analysis purposes, the sensor position is assumed bounded by the two extremes:

(1) STI sensor in horizontal position pointing at any horizon.

(2) STI sensor in vertical position pointing directly downward, normal to lunar surface.

Investigation determined that the outer surface treatment for daytime operation and optimum night operation required that the upper half of the horizontal cylinder be painted inorganic white of properties $\alpha = 0.24$, $\epsilon = 0.955$, and the bottom half of the horizontal cylinder be a polished aluminum finish with an emittance, $\epsilon = 0.05$. The STI sensor was analyzed for operation during lunar noon, terminator, and lunar night. It is possible at terminator under certain conditions for the temperature of TV Camera 3 to be 340°F.

At lunar noon operation, three sensor positions relative to the lunar surface were analyzed: (1) sensor pointing at any horizon, (2) sensor pointing at lunar surface at 45-deg angle, and (3) sensor pointing directly downward, normal to lunar surface. The STI sensor steady-state temperatures resulting from the analysis are shown in Figure 114. For the vertical position, it is possible for the sensor temperature to be at the maximum allowable value of 170°F.

Although the temperature of the lunar surface drops to about —150°F at terminator, the STI sensor temperature under certain conditions could be much higher. When the sensor is pointing directly or nearly directly down toward the lunar surface and the solar radiation is directly incident on the polished aluminum side of the vertical instrument, the temperature of the sensor will be 140°F. When the Sun is on the opposite horizon and its radiation is incident on the white side of the cylinder and also on the TV Camera 3 mirror, the temperature of the sensor will be 155°F.

The STI sensor is required to operate during the lunar night for 5 min every hour. It is necessary that the temperature of the instrument be maintained above —10°F during the periods of operation. This can be accomplished either by applying continuous or periodic heating to the instrument. If continuous heating is used, 2.25 w will be required to maintain instrument temperature at —10°F. If cyclic heating is employed with a 5-min preheat before

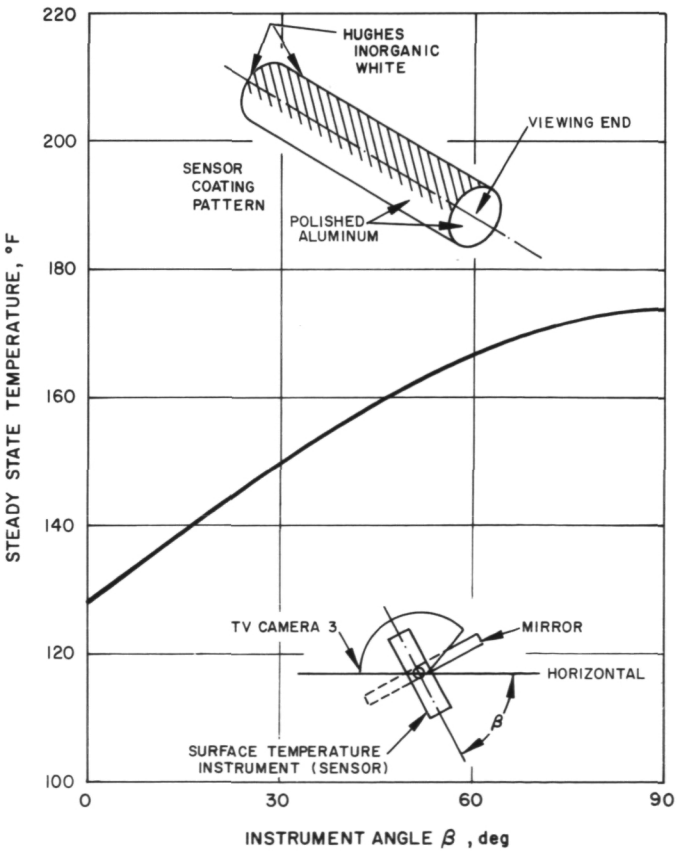

Fig. 114. Lunar noon operation temperature of surface temperature instrument

operation each hour, 20 w will be required. Since the cost in total energy for night operation is 35% greater for the continuous heating case than for the cyclic heating case, periodic heating during night operation has been recommended. Both cases have assumed wiring having nichrome isolation. The surface treatment recommended is shown in Figure 114, i.e., white on top half of horizontal cylinder and on nonviewing end of instrument, and polished aluminum on bottom half of cylinder and viewing end of instrument.

It was suggested that temperature differentials during the 5-min operating period may cause inaccuracies in the telemetered data from the instrument. This must be defined more completely before a valid internal thermal analysis can be performed. Direct thermal coordination with the vendor will be required.

The lunar night power penalty for this instrument may be excessive when compared to other *Surveyor* packages. Therefore, the thermal analysis of an insulated package concept to eliminate a large portion of the current night power requirement while maintaining satisfactory lunar noon operation is continuing.

A new mounting concept has been discussed in joint meetings between the suppliers of the gas chromatograph, the X-ray diffractometer, X-ray spectrometer, and Hughes Aircraft Company, for the soil analysis group of instruments and the soil transport mechanism. It was agreed that thermal isolation of instruments from each other and from the spacecraft must be examined. This is especially important for the X-ray diffractometer radiator, which may reach 325°F.

The latest design concept for the gas chromatograph includes lunar night survival capability without auxiliary heating. This reduces the lunar night heating requirements by 2 w (700 w/hr). In addition, the package insulation has been eliminated resulting in a weight saving of approximately ¼ lb.

The location of the high-voltage power supplies (HVPS) is still considered as nonoptimum. Relocation will improve the thermal control and mechanical mounting of the soil analysis group. Until a new location is found the HVPS will be assumed mounted in the present location.

4. Thermal Switches

Several of the MT-1 prototype switches have been assembled. These first units are undergoing thermal vacuum tests to verify closure temperature and fully closed conductance. The balance of the 15 units to be used in the MT-1 transit and lunar day tests are being assembled. Performance will be tested in the near future.

Switch cases are now being fabricated from a glass laminate material which is capable of withstanding the sterilization temperature. The thermal conductivity of this material is roughly two and one-half times that of the materials previously considered (polystyrene, rexolite, and ablatalite). However, the low value of case conductance has been retained by reducing the wall thickness to 0.003 to 0.004 in. The switch mockups and all of the MT-1 prototype models to be used in the MT-1 lunar night tests have been assembled with new glass cases.

Flatness and finish of the switch contact surfaces is being obtained by a combination of mechanical and hand lapping. The aluminum contacts are copper plated and then mechanically lapped flat. A mirror finish is obtained on the copper by careful hand lapping. The final step is a 0.001-in.-thick gold flash over the copper. The finished gold surfaces are flat within one light band.

An investigation of materials has suggested three "antiseizure" (subliming) substances. Table 21 shows the pertinent properties of these materials.

Table 21. Properties of antiseizure materials

Property	Phenanthrene	Anthracene	Phenanthrene anthracene (equal parts by weight)
Melting point, °F	213	421	284
Weight required per switch	Less than 2 grams	Less than 1 gram	Less than 2 grams
Vapor pressures, mm Hg			
at 68°F	5.7×10^{-5}	2.0×10^{-6}	To be determined
at 50°F	1.7×10^{-5}	4.3×10^{-7}	
at 32°F	4.0×10^{-6}	1.2×10^{-7}	

Although phenanthrene has a desirable range of vapor pressure, its low melting point would preclude its presence during heat sterilization. Anthracene has a sufficiently high melting point, but its vapor pressure might not provide an adequate margin over the pressures at which cold welding may occur (10^{-8} mm Hg and below). A mixture of these two materials may offer the best solution, since the melting point can be adjusted to an adequate level and the vapor pressure of the combination will tend toward that of phenanthrene.

Preparations are being made to subject at least three spare switches from the MT-1 prototype group to a series

of reliability/type approval tests. These tests will include applicable portions of the type approval environmental specification and a vacuum check of thermal performance following exposure to each of the several environments.

5. Superinsulation

Recent information indicates that the aluminized mylar currently being used may have more than an optimum thickness of aluminum deposition. Since test data indicate heat losses six or seven times the theoretical radiation loss, lateral conduction through the aluminum layer may be "shorting" out the sheets between the points of physical contact. If so, a reduction in aluminum thickness can greatly reduce the conduction-type losses while not drastically affecting the emittance.

Experience gained during the actual assembly of the MT-1 Compartment A indicates that several modifications are required in the mylar patterns. In general, complete interweaving in the corners results in a high packing density that may reduce the insulation effectiveness. Modifications are planned for the MT-1 Compartment B assembly.

6. Thermal Coatings

During the past 2 mo paint studies have continued. Although designs are based on a solar absorptance, $\alpha = 0.24$, for the white inorganic paint, specimens have been obtained with $\alpha = 0.17$ over a wavelength region of 0.3 to 2.7 μ. This particularly low value was obtained on a specimen baked at 482°F (250°C) for 2 hr. As this is an intolerable temperature for the 7075 aluminum used as the major spacecraft material, studies are now under way to determine the value spread and ultraviolet stability of paint baked at only 260°F. (127°C). The two paints being studied for their stability are Hughes Aircraft Company inorganic white, and Lockheed Missile and Space Division inorganic white.

A visit was made to Lockheed Missile and Space Division (LMSD), Palo Alto, to obtain data concerning their inorganic white paint. A sample of the white paint and complete preparation and application details were obtained.

A study is also in progress to evaluate 357X Johns-Mansville tape for masking during painting. Although Lockheed indicated complete satisfaction with the tape, application per their recommendation was disappointing. At the moment, minimum use of masking tape is recommended.

A number of metal specimens have been prepared for substrate preparation tests. These tests will evaluate: (1) both LMSD and Hughes Aircraft Company cleaning sequences prior to painting, (2) the applicability of Hughes Aircraft Company and LMSD inorganic paint to two-coat application, (3) bending tests to check relative adhesion between the paints, and (4) the effect of 260°F baking on both paints.

The new surface preparation (cleaning) techniques being evaluated are: (1) the Hughes process of vapor degreasing, cleaning with an alkaline non-etch cleaner, washing with water, and drying; and (2) the LMSD process of vapor degreasing, scrubbing the unmasked portion with household Ajax cleaner, then unmasking and dipping in 150°F Alkalume 13 aluminum brightener and cleaner. After washing with water, drying and re-masking, the surface is ready to be painted. The LMSD process appears to give a somewhat better chance for adhesion since the surface is mechanically roughened. However, no major adhesion problems have been noted with the Hughes process.

The possibility of using LMSD white inorganic paint in preference to Hughes paint was examined. Typical of the problems which arise are initial bake temperature and final α after ultraviolet irradiation. A sample of the LMSD paint obtained from other sources and measured in the Gier-Dunkle equipment gave a value of $\alpha = 0.19$.

The LMSD data were for paint baked at 250°C. Before a final decision can be made, the LMSD paint must be evaluated when baked at 260°F. The sample must then be submitted to ultraviolet irradiation along with a similarly treated specimen of Hughes paint. This comparison test is now in process and specimens will be in irradiation testing in June.

Samples of aluminized teflon FEP type A (to be used as a wing harness wrapping) were examined for α and ϵ values as a function of teflon thickness. The values reflect the change in infrared emittance as a function of teflon thickness. The values obtained are:

1-mil teflon $\alpha = 0.21$	$\epsilon = 0.57$
2-mil teflon $\alpha = 0.15$	$\epsilon = 0.58$
5-mil teflon $\alpha = 0.16$	$\epsilon = 0.89$

Second-surface vycor mirrors for the MT-1 thermal switches were ordered. Mosaics of four mirror panels were made and appear satisfactory. Mirrors obtained to date indicate that quality control may be a major factor.

7. MT-1 Tests

All subsystems not included in the A-21 spacecraft were removed from the MT-1. In addition, redistribution of power dissipations within the compartments was effected to simulate the repackaging required for the A-21. Plans for a lunar night test of Sector 3 were postponed since the A-21 sector dissipates no power during the night.

The Sector 1 lunar night test began on June 11, 1962, and is in progress in the Lockheed 9½ ft cold-wall chamber located near Saugus, Calif. Figure 115 shows the sector during assembly. Figure 116 shows the completed assembly just prior to shipment to Saugus. A total of 144 temperatures are being monitored automatically at regular intervals for the duration of the test. The data are being recorded on IBM punched cards which will be automatically processed in both tabular and graphical form. These temperature data will be used to evaluate the adequacy of the thermal isolation design of Compartment A. Information will also be obtained on the spaceframe cooling rates and on the adequacy of the vernier system thermal insulation techniques. Although the latter system is not required to survive the lunar night, the night test environment can be used to obtain an approximation of the heat loss rate to be expected in transit. Sector 1 is being tested on a 24-hr basis because of the long thermal time constants involved and the test is expected to require from 2 to 3 wk. Test results to date indicate generally satisfactory performance.

Sector 2 is to be ready for test in late-July. All instrumentation modifications to the Sector 2 harness have been defined and the harness is being fabricated. Plans are to perform the initial lunar night test of this sector in the Hughes Aircraft Company environmental facility.

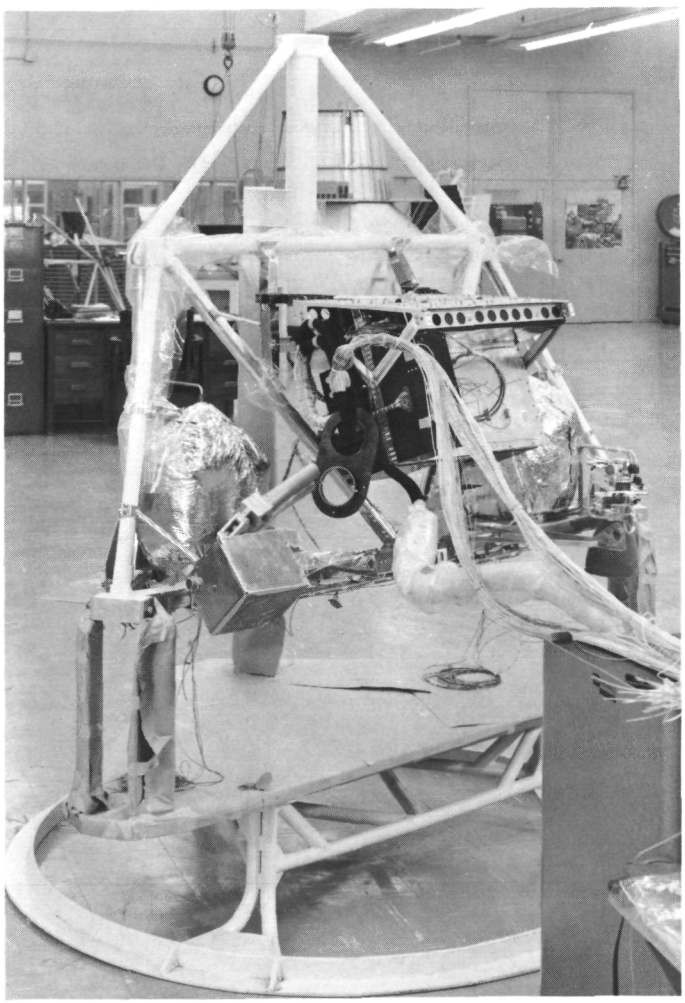

Fig. 115. MT-1 Sector during assembly

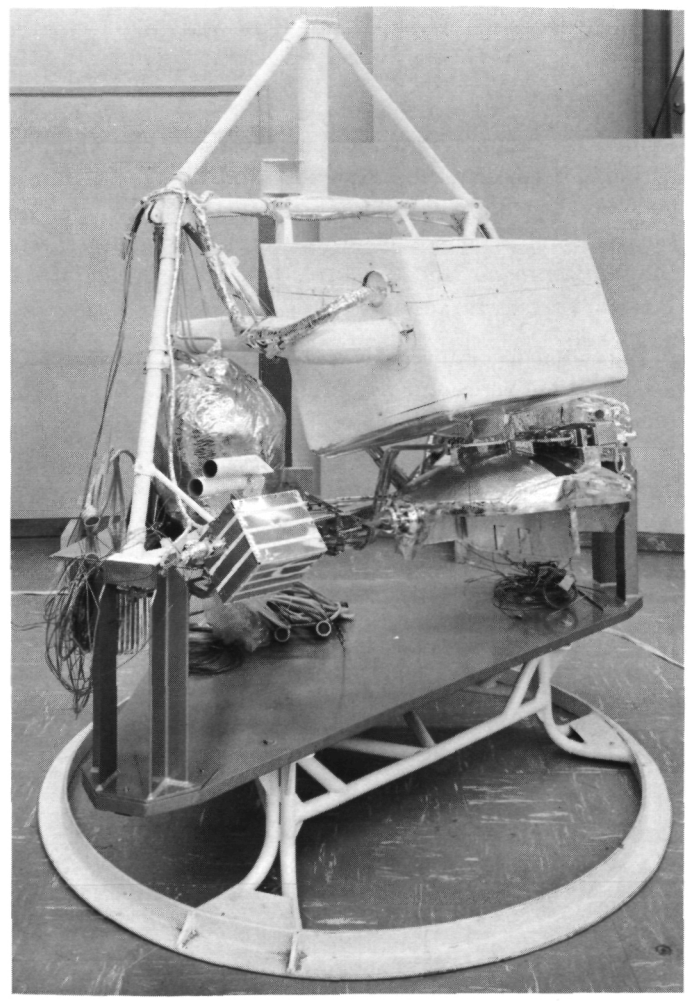

Fig. 116. MT-1 Thermal test sector

8. Radioisotope Thermoelectric Generator (RTG) Integration

The recent discussion concerning the location of the RTG on later spacecraft has prompted considerable study of the thermal interaction between the RTG and the spacecraft. A decision has been made not utilize the waste thermal energy for thermal control, but rather to keep the present system unchanged and utilize electrical heating. The aspects under study by Hughes Aircraft Company are the temperature rise of local spacecraft equipment due to radiant interaction effects, the location of the dc-to-dc converter including internal dissipation levels and wire lead thermal conduction effects, and pre-launch conditioning of the RTG.

The RTG as a heat source dissipates approximately 900 w of net thermal energy and will have an effective surface temperature of 320°F during lunar night and 420°F during lunar day. Roughly 500 w of the load will be dissipated by radiation from an actively controlled "dump" door; the remainder will be radiated from the external radiating area of 3 ft^2.

Possible locations of the RTG on the spacecraft were limited by center-of-gravity considerations. Optimum location is between Compartment A and Leg 2, previously occupied by the bevameter. In this location the effect of the RTG on local spacecraft surfaces was analyzed for the maximum radiant flux levels from the surface of the RTG in specific directions.

Flux density limitations (in a preliminary interface specification) represent the initial attempt to describe the thermal constraints associated with using an RTG on the spacecraft. Table 22 presents these limitations of allowable thermal radiation flux densities leaving the RTG in the specified direction. The remaining questions will be dealt with as the interface studies progress.

Table 22. Allowable thermal radiation

Direction of radiation	Maximum flux density at surface of RTG, watts/ft^2	Mission phase
To Compartment A		
Top surface	0	All
End adjacent to RTG	100	Lunar day
To solar panel/antenna assembly	800	Lunar day & Transit
To retro-engine	100	Transit
To vernier engine tanks	155	Transit
To vernier thrust chamber no. 2	1000	Transit
To spaceframe	75	Lunar day
Outboard from spacecraft	No requirement	—

9. Air-Conditioning Test

The GDA shroud air-conditioning conceptual design has been frozen. The design will utilize an upper and lower shroud ring for directing the coolant onto the critical spacecraft surfaces. Plans have been formulated to evaluate the proposed coolant distribution system. The test, to be conducted at Hughes Aircraft Company, will utilize the M-12 mockup fitted with electrical heaters to simulate the actual energy dissipation during the pre-launch checkout. Adequate instrumentation will be attached to provide verification of successful air-conditioning. The tests are scheduled for early 1963.

H. Engineering Mechanics

1. Touchdown Dynamics

Design parameters for the A-21 shock absorbers have been determined to achieve the necessary load and stability requirements. Figure 117 shows the lateral g loading on the planar array antenna-solar panel group which corresponds to the most pessimistic (minimum) touchdown weight. On the basis of the 3σ flight control dispersion ellipse, the g loading for the A-21 spacecraft is slightly better than that for the A-25. Package vertical g loading is similarly improved (Fig. 118). Stability of the A-21, compared with that for the A-25 (Fig. 119), is slightly improved at negative touchdown lateral velocities; no instability was found for the lightweight spacecraft at positive lateral velocities.

The IBM computer program for soft surface landings, though not yet complete, has yielded useful results. With a 772-lb (A-25) touchdown weight and a landing on a soft level surface at a vertical velocity of 20 ft/sec, the foot pads are predicted to penetrate the surface to a depth of 7.5 in. The bottom of the spaceframe will penetrate approximately 5.9 in. Upon extension of the shock absorber, the bottom of the spaceframe would be approximately 10 in. above the surface. It is expected that soft surface landings will not result in appreciably different maximum shock absorber loads from those experienced with hard surface landings. Package g loading, however,

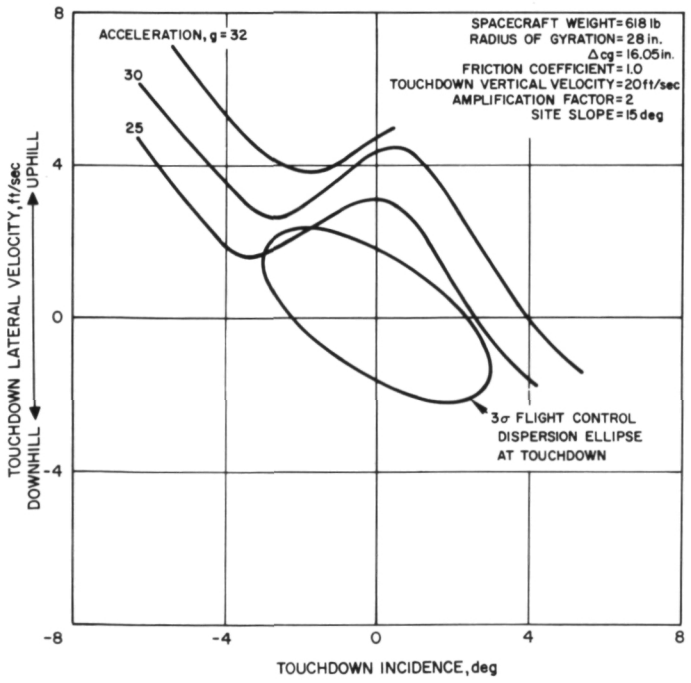

Fig. 117. Touchdown lateral acceleration of A-21 planar antenna-solar panel

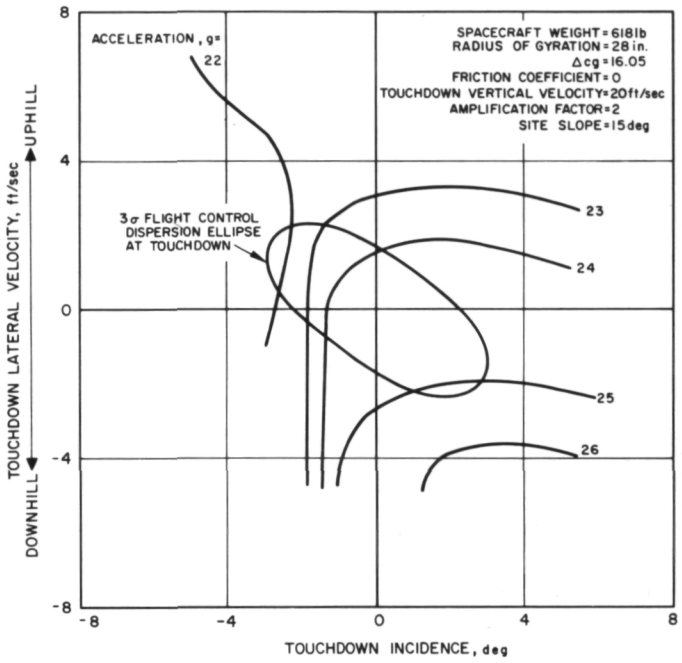

Fig. 118. Touchdown vertical acceleration of A-21 package

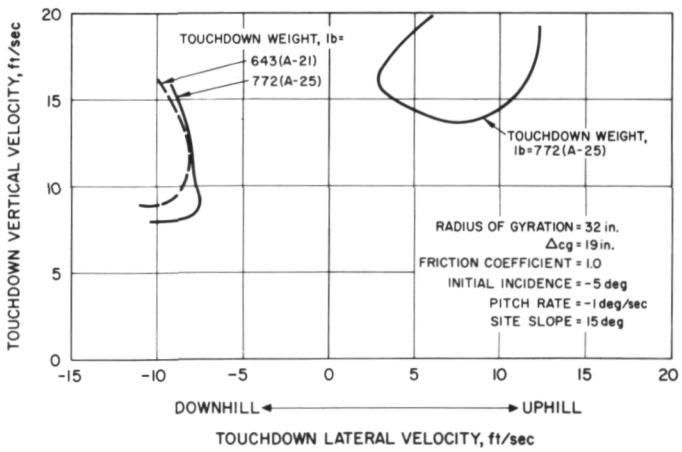

Fig. 119. Comparison of stability limits in A-21 and A-25 spacecraft

is expected to decrease considerably, and spacecraft stability will also improve.

2. Full-Scale Drop Test (T-1)

The accidental damage to the T-1 test vehicle was repaired and on April 25, 1962, the drop test program was resumed. The first of the series of drops was to determine the toppling stability on a 15 deg slope. This series of stability drops has now been completed for both the downhill and uphill instability regions. The site slope is being increased to 25 deg to investigate the slope capability of the vehicle. Drops are also planned to investigate crosshill stability, landings on the soft surface, and landings at maximum load.

During the stability investigation for a 15 deg slope, a total of 16 different velocity conditions were checked, nine to determine the downhill instability region and the rest to investigate the recently discovered uphill instability. Table 23 lists all the points investigated so far during the test program; of primary interest are the stability drops (4 through 19) and the maximum angle to which each spaceframe tilted. Preliminary angles were determined from the film coverage and from a potentiometer connected between the "anti-gravity" cable and vehicle spaceframe.

Figure 120 is a reproduction of Figure 125 from Reference 1 with the test points superimposed. The curves represent the IBM computer prediction of the stability boundaries showing the effect of friction coefficient. The test results are being investigated in detail for correlation with the IBM results.

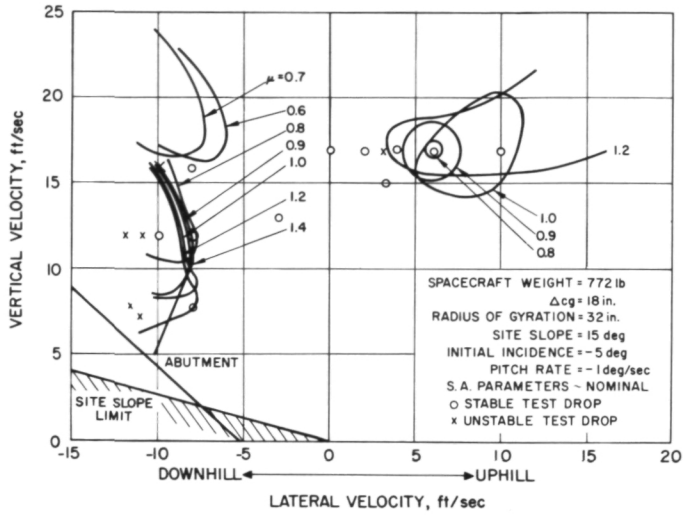

Fig. 120. T-1 drop test results compared with computed stability boundaries

Table 23. T-1 drop test data

T = spacecraft topple

Condition	Velocity, ft/sec		Surface slope, deg	Tilt angle, deg		
	Vertical	Lateral		Computed[a]	Potentiometer	Film
(1) Smooth surface	15	0	0	0		
(2) Single leg uphill	13	3[b]	15	19.2		
(3) Single leg downhill	13	3[b]	15	19.9		
(4) Single leg uphill on simulated rocky surface	12	12[b]	15	T	T	T
(5)	12	8[b]	15	41.5	21.9	22
(6)	12	10[b]	15	T	33.1	38
(7)	12	11[b]	15	T	T	T
(8)	8	12[b]	15	23.9	T	T
(9)	7	11[b]	15	23.3	T	T
(10)	8	8[b]	15	31.0		35
(11)	16	10[b]	15	41.2	T	T
(12)	16	8[b]	15	23.3		40
(13)	17	6[c]	15	T		30
(14)	17	10[c]	15	T		15
(15)	17	3[c]	15	31.5	T	T
(16)	17	0[c]	15	25.2		30
(17)	17	2[c]	15	24.9		32
(18)	17	4[c]	15	35.9		30
(19)	15	3[c]	15	29.2		30

[a] IBM calculations used friction coefficient = 1.0.
[b] Downhill.
[c] Uphill.

In all the stability drops, the vehicle was oriented with the single leg pointed uphill with an initial incidence of 5 deg. The direction of the incidence was such as to increase the angle between the vehicle and the slope. A simulated rocky surface was used in all cases. For the first few drops, rocks were simulated by 4-in. cubes of hardwood rigidly attached to the surface (see Fig. 132 of Ref. 1). The "rock" height was reduced to 2 in. after the sixth test. It is felt that the ability to land on 10 cm proturbances has been demonstrated. Any further testing on such a harsh surface with the possibility of damaging the T-1 test vehicle is thought to be an unnecessary risk. For test purposes, the high friction is still apparent with the 2-in. simulated rocks. Figure 121 shows the test platform and T-1 in a drop position; the "rocks" in the foreground are the original 4-in. cubes; farther up the slope are the 2 in. high "rocks."

During the tests, several modifications were made in the footpads to improve performance. The effects of using a lower dentisy material, of drilling hole patterns in the bottom and sides of the pad, of embedding a ½ in. wire mesh in the pad, and of tightly enclosing the pad in different types of fiberglass bags were investigated separately. The desired shear and crushing characteristics were attained by a combination of the first and second methods. The fiberglass bag also prevents pieces of footpad from being scattered over the landing area.

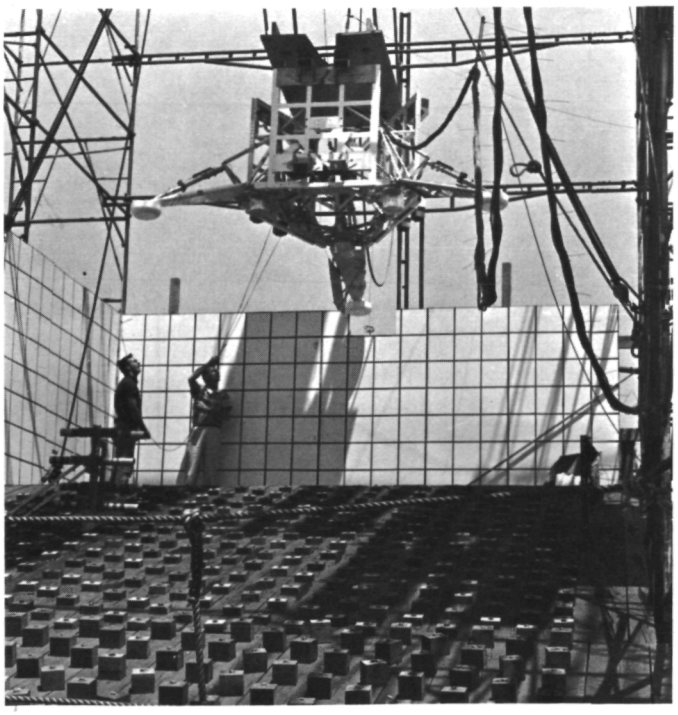

Fig. 121. T-1 drop test facility showing different sizes of simulated rocks

The crushable honeycomb blocks are continuing to perform their function satisfactorily. Figure 122 illustrates the manner in which the blocks act as energy absorbers. The whole block, initially 7 in. high, was crushed from impact on the platform; there was in addition local crushing from the "rocks."

3. Shock Absorber Development

The second group of three development shock absorbers, to be used on the S-2 vehicle, were received on April 24, 1962. Additional testing by the National Water Lift Company after delivery of the original T-1 shock absorbers resulted in minor modifications to the second three units resulting in better definition of parameters. The improved shock absorbers were installed on T-1 after the second stability drop onto the 15 deg slope. The original shock absorbers will be used on the S-2 vehicle for the vibration tests where mass simulation, rather than operating parameters, is of major importance. Prototype low damping units will be available for the drop test of S-2.

The report of the spring and damper development tests was received from the National Water Lift Company and indicates satisfactory determination of fluid volume and metering pin configuration. The method of testing the units was improved to give satisfactory results. The test stand used for the T-1 and S-2 shock absorbers (Fig. 123) will be used for all tests of prototype and flight units.

A new developmental shock absorber will be used to determine the orifice size for the A-21 spacecraft. This developmental model will also permit testing of a more

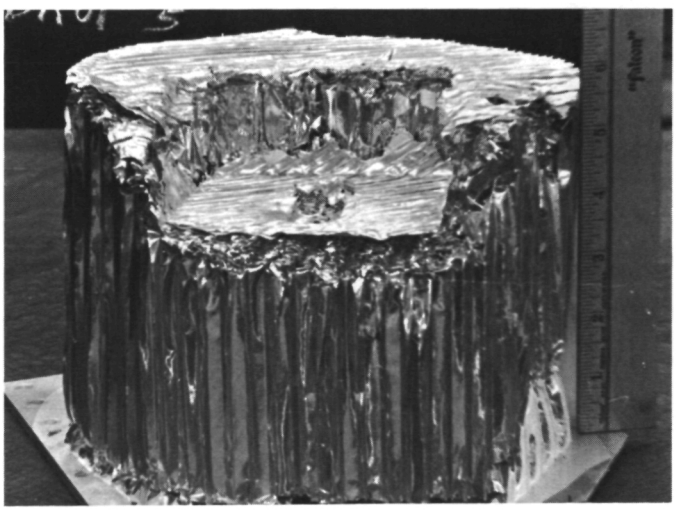

Fig. 122. Crushable block after T-1 drop test

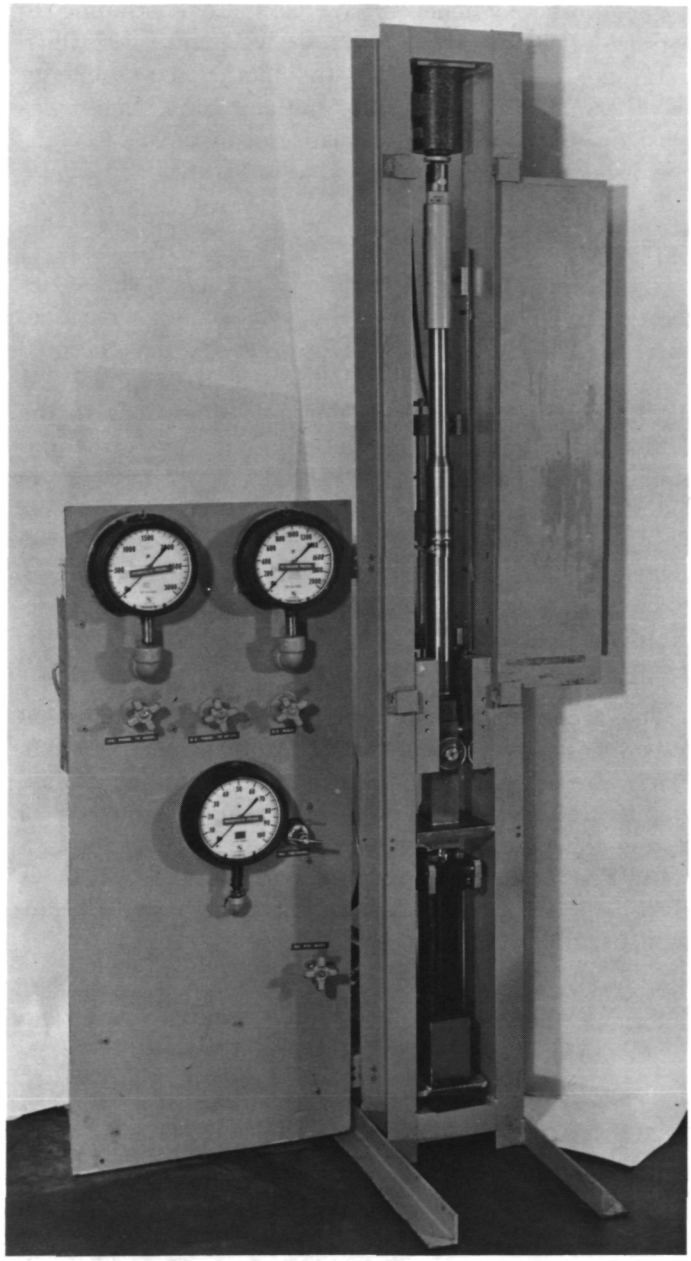

Fig. 123. Shock absorber test stand

representative unit prior to completion of the prototype shock absorbers to verify operating parameters for the final configuration.

Special tooling for use in manufacture of the flight shock absorbers has been completed. This tooling will be used in manufacturing prototype units for T-21 and type approval units so that the tooling can be checked out and the type approval units manufactured under production conditions. Machining of a few of the long-lead-time parts for prototype models has been started.

Detail drawings for the production model shock absorbers have been released by the National Water Lift Company and are being examined in detail at Hughes.

4. Structural Dynamics and Loads

A revised structural design criteria and loads report has been written and is now being reviewed for publication. This report upgrades the boost phase and landing loads of the report issued November 13, 1961. The revisions reflect loads information from Computer Engineering Associates (CEA) analytical studies and S-1 vibration tests.

Typical revised boost phase loads are shown in Table 24. Each column represents a set of maximum vibratory loads, applied to the spaceframe simultaneously, and resulting from response of the spacecraft in a resonant vibration condition. Thirty-two loading conditions apply: those specified by the 16 columns of Table 24 and 16 additional cases obtained by reversing the signs of all load factor terms in the table. The number of cycles of fully reversed loading for each resonant condition is given in Table 25. Additional loading conditions, similar in form to those in Table 25, will be included in a revised loads report. The revised boost phase loads, except for the solar panel and antenna, are less severe than those specified previously. In addition, the total number of cycles of fatigue loading has been reduced.

The revised landing loads are shown in Table 26. Nine sets of simultaneous loads apply: the loads resulting from a three-point landing listed in Column 1, and the loads resulting from downhill landings listed in Columns 2 through 9. The revised landing loads show larger lateral accelerations of Compartments A and B, subsurface sampler, and flight control sensor group and larger longitudinal accelerations of the antenna mast than specified in the original document. All other lateral and longitudinal load factors are either unchanged or less than stated previously.

In response to a request from General Dynamics, Astronautics Division (GDA), a 7 deg-of-freedom model of the spacecraft was synthesized, taking into account results of the S-1 vibration tests. The model was transmitted to GDA in the latter part of March for use in examining the interaction between the spacecraft and the *Centaur* flight control system. In addition, the model was analyzed at Hughes to establish the validity of the model and determine the loads that would be imposed on the *Centaur* if the vibration levels of JPL Specifica-

Table 24. Boost flight design limit load factors for SC-1 spaceframe

Unit	Load factor[a]	Mode 1	2	3	4	5	6	7	8	9	10	11	12	13	14	15	16
Compartment A	M_X	0.2	1.0	0.6	−2.1	1.9	11.7	−0.3	−9.0	−1.2	−0.3	−1.2	3.4	5.4	0	0	0
	M_Y	−0.4	3.3	−0.6	−8.8	2.4	−0.4	0.5	−0.2	1.9	−3.7	−0.5	−0.1	2.6	0	0	0
	M_Z	−0.8	1.3	−2.5	−8.0	−5.6	5.8	−0.5	3.9	−1.6	−0.7	1.7	−2.3	−8.2	0	0	0
TV Cameras 3 and 4	M_X	0.4	−1.7	0.6	7.3	3.7	3.5	−1.0	−0.5	19.4	−6.5	1.0	2.5	−20.0	0	0	0
	M_Y	0	3.4	1.7	−5.7	5.1	−2.4	0.5	−3.4	4.7	1.0	−0.7	−2.3	2.2	0	0	0
	M_Z	0	1.3	2.8	−0.4	1.9	−3.0	0	−7.5	−10.5	−8.6	0.4	0	−16.6	0	0	0
Subsurface sampler	M_X	1.0	0.8	9.0	0.6	−6.2	7.0	−0.3	6.3	5.6	7.8	−2.3	1.5	−16.2	0	0	0
	M_Y	−0.6	−3.6	−15.7	5.9	15.9	1.3	0	−4.1	2.5	1.4	−2.3	0.2	−9.6	0	0	0
	M_Z	0	3.4	5.0	−5.4	0	5.5	0.8	−7.8	−3.5	−8.3	2.1	−2.6	11.0	0	0	0
Compartment B	M_X	0.2	−1.2	−0.2	2.9	−2.9	4.0	0.8	−13.0	−1.2	4.5	3.3	−9.0	−1.4	0	0	0
	M_Y	0.4	3.1	2.0	−2.9	9.2	−0.3	−0.5	0.1	−1.6	5.4	11.5	0.8	−1.4	0	0	0
	M_Z	0.6	1.2	2.8	1.2	10.3	3.9	−1.3	8.2	1.8	−1.4	−1.5	−2.0	−3.4	0	0	0
Flight control sensor	M_X	0	−1.9	−1.7	1.9	−7.6	0.4	0.8	−3.7	−1.0	−0.3	−3.8	0.3	1.2	0	0	0
	M_Y	0	0.2	0.3	0	1.4	0.7	−0.5	−0.6	−0.2	−0.7	2.5	−0.5	5.2	0	0	0
	M_Z	0.6	−0.8	1.4	3.1	3.5	4.4	0.8	3.4	2.3	−3.4	−3.2	−2.7	3.4	0	0	0
Antenna solar panel mast	M_X	16.0	1.8	−2.7	−3.5	−2.5	−1.9	−2.4	0.2	−0.3	−0.1	0.2	0.1	0	0	0	0
	M_Y	−0.4	19.1	−5.7	19.1	−5.6	1.6	0	0.8	0.7	−0.4	−0.1	0	0.1	0	0	0
	M_Z	1.0	0.2	−0.3	−0.4	0	0.9	1.8	2.5	−0.6	0.5	−0.2	−0.7	2.9	0	0	30.0
Oxidizer Tank	M_X	1.3	0	1.3	0	0	1.3	0	0	0	0	0	0	0	−5.0	0	0
	M_Y	0	1.3	0	−1.3	1.3	0	0	0	0	0	0	0	0	−8.7	0	0
	M_Z	0	1.3	0	−2.9	0.8	0.7	0	2.1	−6.2	2.2	−4.6	−1.9	3.2	0	0	0
Oxidizer Tank 2	M_X	1.3	0	1.3	0	0	1.3	0	0	0	0	0	0	0	−5.0	0	0
	M_Y	0	1.3	0	−1.3	1.3	0	0	0	0	0	0	0	0	8.7	0	0
	M_Z	0	−1.0	−1.7	0.6	−1.8	1.7	0	4.2	5.4	4.6	−0.1	0.3	8.4	0	0	0
Oxidizer Tank 3	M_X	1.3	0	1.3	0	0	1.3	0	0	0	0	0	0	0	10.0	0	0
	M_Y	0	1.3	0	−1.3	1.3	0	0	0	0	0	0	0	0	0	0	0
	M_Z	0.2	−0.2	0.8	1.5	3.0	2.8	−0.8	1.5	1.0	−2.5	0.7	−1.8	7.2	0	0	0
Fuel Tank 1	M_X	1.3	0	1.3	0	0	1.3	0	0	0	0	0	0	0	0	5.0	0
	M_Y	0	1.3	0	−1.3	1.3	0	0	0	0	0	0	0	0	0	−8.7	0
	M_Z	−0.2	0	−1.6	−2.1	−2.1	1.5	0	3.1	5.8	3.8	0	−0.6	7.2	0	0	0
Fuel Tank 2	M_X	1.3	0	1.3	0	0	1.3	0	0	0	0	0	0	0	0	−10.0	0
	M_Y	0	1.3	0	−1.3	1.3	0	0	0	0	0	0	0	0	0	0	0
	M_Z	0	−1.2	0	2.7	0.6	3.2	−0.8	1.4	−0.6	−1.5	0.7	−0.7	6.6	0	0	0
Fuel Tank 3	M_X	1.3	0	1.3	0	0	1.3	0	0	0	0	0	0	0	0	5.0	0
	M_Y	0	1.3	0	−1.3	1.3	0	0	0	0	0	0	0	0	0	8.7	0
	M_Z	0	1.2	0.8	−1.2	3.7	0.3	−0.3	3.2	−4.7	2.0	−4.5	−1.9	3.2	0	0	0
TV Camera 2	M_X	0.4	0	1.3	1.9	2.9	2.8	0	2.7	0.8	−0.2	−0.7	−1.4	−2.4	0	0	0
	M_Y	0	1.5	0.3	−2.5	2.7	−1.1	0	−1.0	−0.6	1.6	1.7	−0.2	0	0	0	0
	M_Z	0.6	1.0	3.0	1.5	10.2	4.3	−1.5	7.0	3.3	−3.5	0.9	−3.5	3.2	0	0	0
Helium Tank	M_X	0.6	0	2.0	3.1	4.6	4.3	0	−4.2	1.2	−0.3	−1.2	−2.2	−3.8	0	0	0
	M_Y	0	2.5	0.5	−3.8	4.1	−1.8	0	−1.6	−1.0	2.4	2.7	−0.3	0.2	0	0	0
	M_Z	0.2	−3.1	−1.9	6.3	−0.6	6.4	−1.3	6.0	−3.3	0.6	1.2	1.1	5.4	0	0	0
Nitrogen Tank	M_X	0.2	0	0.3	0.4	0.6	0.6	0	0.6	0.2	0	−0.1	−0.3	−0.6	0	0	0
	M_Y	0	0.4	0	−0.6	0.6	−0.2	0	−0.2	−0.2	0.3	0.4	0	0	0	0	0
	M_Z	0	0	0	0	0.2	0.4	0	0.7	0	0.3	−0.2	−0.4	0.8	0	0	0

[a] M_X, M_Y, M_Z are load factors in x, y, z directions, respectively, in g. Z axis is in direction of thrust, positive upward. X and Y axes are lateral axes, with Y positive toward Leg 1. Origin of coordinate system is cg of spacecraft. X, Y, Z axes form left-hand coordinate system.

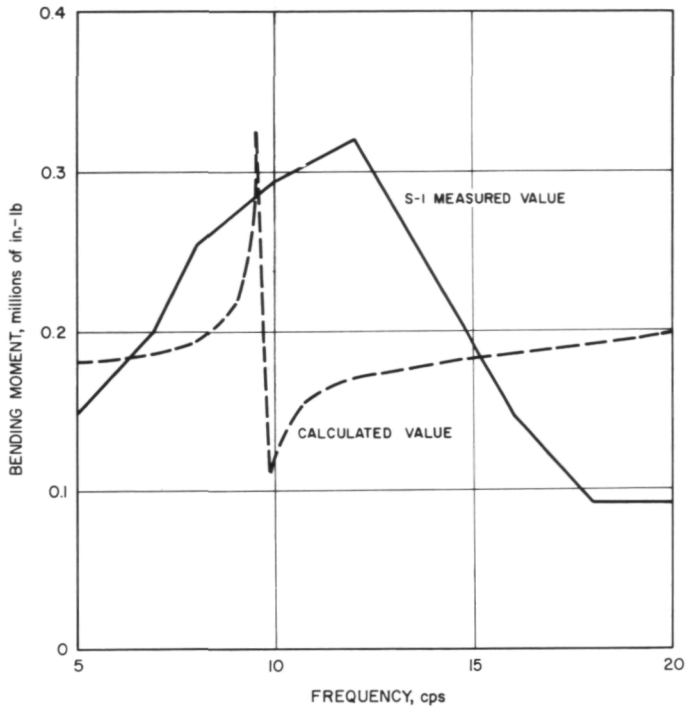

Fig. 124. Bending moment at adapter base from lateral vibration

Table 25. Cycles of fully reversed boost phase fatigue loads

Mode[a]	Number of cycles
1	330
2	330
3	330
4	330
5	330
6	330
7	348
8	370
9	455
10	510
11	560
12	625
13	678
14	696
15	812
16	1160

[a]As defined in Table 24.

tion 30240A were to occur at the *Centaur-Surveyor* separation plane. In Figure 124, the model is compared with results from the S-1 vibration test in terms of bending moment at the adapter base with lateral vibration levels of JPL Specification 30240A at the separation plane.

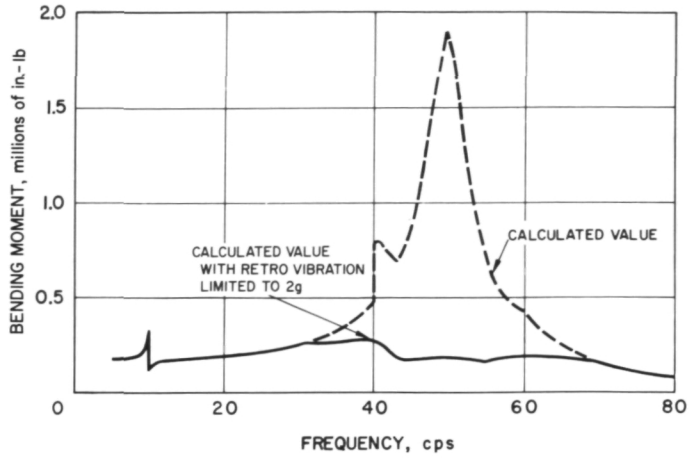

Fig. 125. Effect on bending moment of limiting retro-rocket vibration to 2 *g*

In the low frequency range, the model adequately represents the spacecraft with respect to the magnitude of the loads imposed on the *Centaur*. Similar correspondence exists in the high frequency range except that the frequency of maximum load is different in the two cases, because the S-1 was mounted on the Hughes adapter while the mathematical model included the GDA adapter. Figure 125 again shows the bending moment imposed on the *Centaur* nose when the vibration levels specified by JPL exist at the *Surveyor* separation plane and compares the effect of limiting the response of the retro-rocket to 2 *g*, as permitted in JPL Specification 30240A. To accomplish this, the vibration levels at the separation plane were reduced in the frequency band between 30 and 70 cps.

On May 17, 1962, Hughes representatives visited Thiokol-Elkton Division for discussions concerning the details of measuring the vibration of four retro-engines during static firings. The test chamber where the firings will be conducted and the instrumentation laboratory where the data will be recorded were inspected. Some accelerometer data from previous heavy weight retro-engine firings were also inspected. There should be no major technical problems for either Thiokol or Hughes in implementing these vibration measurements.

The participation of Thiokol in this program will consist of supplying detailed installation data, modifying their test stand for nine accelerometers, insulating cables and accelerometers, and installing instrumentation lines from the chamber to an outside weatherproof amplifier box and from there to a tape recorder within the instrumentation laboratory. The tape recorder will be an Ampex Model FR-100, 14-channel wideband recorder

Table 26. Design limit landing load factors for SC-1 spaceframe

Site slope, deg		0	15	15	15	15	15	15	15	15
Vertical velocity, ft/sec		20	20	20	20	20	20	20	20	20
Lateral velocity (downhill), ft/sec		0	5	5	5	4	4	4	0	0
Leg orientation		——	Leg 1 Uphill	Leg 2 Uphill	Leg 3 Uphill	Leg 1 Downhill	Leg 2 Downhill	Leg 3 Downhill	Leg 1 Uphill	Leg 1 Downhill
Spacecraft attitude[a], deg		0	0	0	0	1	1	1	0	0
Compartment A	m_X[b]	6.9	−2.4	−6.1	6.1	3.6	3.5	−3.5	−2.4	3.2
	m_Y	4.0	−5.7	3.5	3.5	7.9	−2.0	−2.0	−3.7	6.5
	m_Z	−20.	−13.	−13.	−25.	−18.	−25.	1.0	−13.	−18.
TV Cameras 3 and 4	m_X	0	0	−6.1	6.1	0	3.5	−3.5	0.	0.
	m_Y	0	−7.0	3.5	3.5	4.0	−2.0	−2.0	0.	0.
	m_Z	−25.	−25.	−13.	−20.	1.0	−25.	−13.	−25.	−20.
Subsurface sampler	m_X	−15.	−10.	−6.1	6.1	15.0	3.5	−3.5	−10.0	15.0
	m_Y	−15.	−15.	3.5	3.5	−11.0	−2.0	−2.0	−14.0	−10.0
	m_Z	−25.	−25.	−13.	−13.	−22.	−25.	−25.	−25.	−22.
Compartment B	m_X	−6.9	4.3	−6.1	6.1	−4.8	3.5	−3.5	4.3	−4.5
	m_Y	4.0	−12.6	3.5	3.5	9.7	−2.0	−2.0	−10.6	8.4
	m_Z	−20.	−18.	−25.	−13.	−25.	1.	−25.	−18.	−25.
Flight control sensor	m_X	−8.7	6.7	−6.1	6.1	−5.1	3.5	−3.5	6.7	−4.6
	m_Y	5.0	−10.5	3.5	3.5	13.3	−2.0	−2.0	−8.5	12.0
	m_Z	−25.	−16.	−25.	−13.	−23.	1.	−25.	−16.	−23.
Antenna-solar panel mast	m_X	6.0	−6.0	−14.8	14.8	−4.0	14.8	−14.8	−6.0	−4.0
	m_Y	4.0	−22.	8.5	8.5	32.	−8.5	−8.5	−10.0	15.0
	m_Z	−25.	−25.	−25.	−25.	−25.	−25.	−25.	−25.	−25.
Oxidizer Tank 1	m_X	0	0	−6.1	6.1	0	3.5	−3.5	0.	0.
	m_Y	0	−7.0	3.5	3.5	4.0	−2.0	−2.0	0.	0.
	m_Z	−25.	−13.	−25.	−25.	−25.	1.0	1.0	−13.	−25.
Oxidizer Tank 2	m_X	0	0	−6.1	6.1	0	3.5	−3.5	0.	0.
	m_Y	0	−7.0	3.5	3.5	4.0	−2.0	−2.0	0.	0.
	m_Z	−25.	−25.	−13.0	−25.	1.0	−25.	1.0	−25.	1.0
Oxidizer Tank 3	m_X	0	0	−6.1	6.1	0	3.5	−3.5	0.	0.
	m_Y	0	−7.0	3.5	3.5	4.0	−2.0	−2.0	0.	0.
	m_Z	−25.	−25.	−25.	−13.	1.0	1.0	−25.	−25.	1.0
Fuel Tank 1	m_X	0	0	−6.1	6.1	0	3.5	−3.5	0.	0.
	m_Y	0	−7.0	3.5	3.5	4.0	−2.0	−2.0	0.	0.
	m_Z	−25.	−13.	−25.	−25.	−25.	1.0	1.0	−13.	−25.
Fuel Tank 2	m_X	0	0	−6.1	6.1	0	3.5	−3.5	0.	0.
	m_Y	0	−7.0	3.5	3.5	4.0	−2.0	−2.0	0.	0.
	m_Z	−25.	−25.	−13.0	−25.	1.0	−25.	1.0	−25.	1.0
Fuel Tank 3	m_X	0	0	−6.1	6.1	0	3.5	−3.5	0.	0.
	m_Y	0	−7.0	3.5	3.5	4.0	−2.0	−2.0	0.	0.
	m_Z	−25.	−25.	−25.	−13.	1.0	1.0	−25.	−25.	1.0
TV Camera 2	m_X	0	0	−6.1	6.1	0	3.5	−3.5	0.	0.
	m_Y	0	−7.0	3.5	3.5	4.0	−2.0	−2.0	0.	0.
	m_Z	−25.	−20.	−25.	−13.	1.0	1.0	−25.	−20.	−25.
Hellium tank	m_X	0	0	−6.1	6.1	0	3.5	−3.5	0.	0.
	m_Y	0	−7.0	3.5	3.5	4.0	−2.0	−2.0	0.	0.
	m_Z	−25.	−25.	−20.0	−13.	1.0	−13.0	−25.	−25.	1.0
Nitrogen tank	m_X	0	0	−6.1	6.1	0	3.5	−3.5	0.	0.
	m_Y	0	−7.0	3.5	3.5	4.0	−2.0	−2.0	0.	0.
	m_Z	−25.	−25.	−13.0	−20.	1.0	−25.	−13.0	−25.	1.0

[a] Roll axis inclination toward hill from lunar perpendicular.

[b] M_X, M_Y, M_Z are load factors in X, Y, Z directions in g.

which is compatible with Hughes data reduction equipment. Thiokol will operate the instrumentation and supply assistance during instrumentation installation and calibration. The first firing in which Hughes will be involved will be in early July.

5. Vibration Tests

Present efforts on the S-2 test program are to develop a data acquisition system and the modal excitation system. Parts of the data acquisition system will have to be transported between laboratories several times. As a result, it may have to be assembled in an easily transportable trailer. The connections to the S-2 vehicles will probably be ganged at a suitable terminal arrangement to accelerate the decoupling and reattachment of the connectors, which may exceed 120 in number.

A multiplexing system is being prepared for tape recording all instrumentation outputs simultaneously. The oscillograph recorded signals from the tests of S-1 indicated a need for signal conditioning before final data reduction. The amount of usable data will be markedly increased when the tape recorded signal can be filtered to separate the frequencies of interest from the total complex trace superimposed.

A modal excitation system to be procured by Hughes will not be available in time for the S-2 program. Efforts are under way to assemble an interim system utilizing Air Force equipment obtained from General Dynamics.

The test program has been modified to incorporate the change in the A-21 spacecraft. This change has delayed the selection of strain gage locations but will not cause additional change in the test schedule. The test program is presently planned for the period from August to October with data reduction and report completion tentatively scheduled for March, 1963. The vibration tests have been rescheduled to permit early deformation measurements under simulated retro-rocket thrust to verify conformance with the Hughes Functional Requirements Specification.

6. Flight Vehicle Instrumentation

The procurement specification for the flight vehicle accelerometer-amplifier system has been modified to meet the current instrumentation requirements of the A-21 spacecraft, and will be released for proposals during June, 1962. The number of accelerometers has been reduced from nine, as reported in Reference 1, to four on the spacecraft and three on the adapter, pending JPL and GDA approval of the adapter accelerometers. In addition, a strain gage transducer has been located on each of the three shock absorbers. The locations of the sensors are shown in Figure 126. If the adapter accelerometers are accepted, the data transmitting and recording scheme will be as shown in Table 27; if they are not, it will be as shown in Table 28.

In the scheme shown in Table 27, the vibrations during boost detected by the radially placed accelerometers on the adapter would be transmitted directly by the *Centaur telemetry*. The gains of these accelerometer amplifier systems would be chosen for boost vibration levels. The accelerometers on the spacecraft, however, must measure low separation-plane acceleration levels during boost and descent and high response levels during landing. Therefore, the vertically oriented spacecraft accelerometer amplifier systems were changed to have two outputs: a high gain output corresponding to the expected boost and descent vibration and a low gain output corresponding to the landing response. The accelerometer amplifier low gain outputs are always connected to the tape recorder. To record high gain vibration data during boost would require switching. Switching was rejected on the basis of added weight and changes to electronic circuitry. Therefore high gain vibration can be obtained only during descent through *Surveyor* telemetry. If adapter accelerometer-amplifiers are not adopted, the *Centaur* channels would be used for the high gain outputs during boost. This redundancy of data acquisition would increase reliability.

Two semiconductor strain gage vendors have indicated that installation of strain gages on the shock absorbers is feasible. The constant current power supplies required will be installed with the accelerometer amplifiers. Potentiometers are being installed in the landing gear pivot shafts to measure the landing gear arm angular positions after landing. This is a simple installation which requires only a sleeve over the potentiometer and an arm from the potentiometer shaft to the landing gear arm.

7. Spaceframe Stress Analysis (T-21, SC-1)

The drawings from which T-21 and SC-1 will be fabricated were released in mid-May 1962. As noted earlier in this section, the boost design loads have been revised. The T-21, SC-1 spaceframe has been analyzed for the first 14 boost conditions appearing in Table 24.

In the fatigue analysis, the oscillatory loads of Table 24 were superimposed on a steady-state load corresponding to the average thrust acceleration imposed during the entire boost phase. Miner's theory was used to calculate the cumulative fatigue damage incurred by the various spaceframe members. A factor of safety in

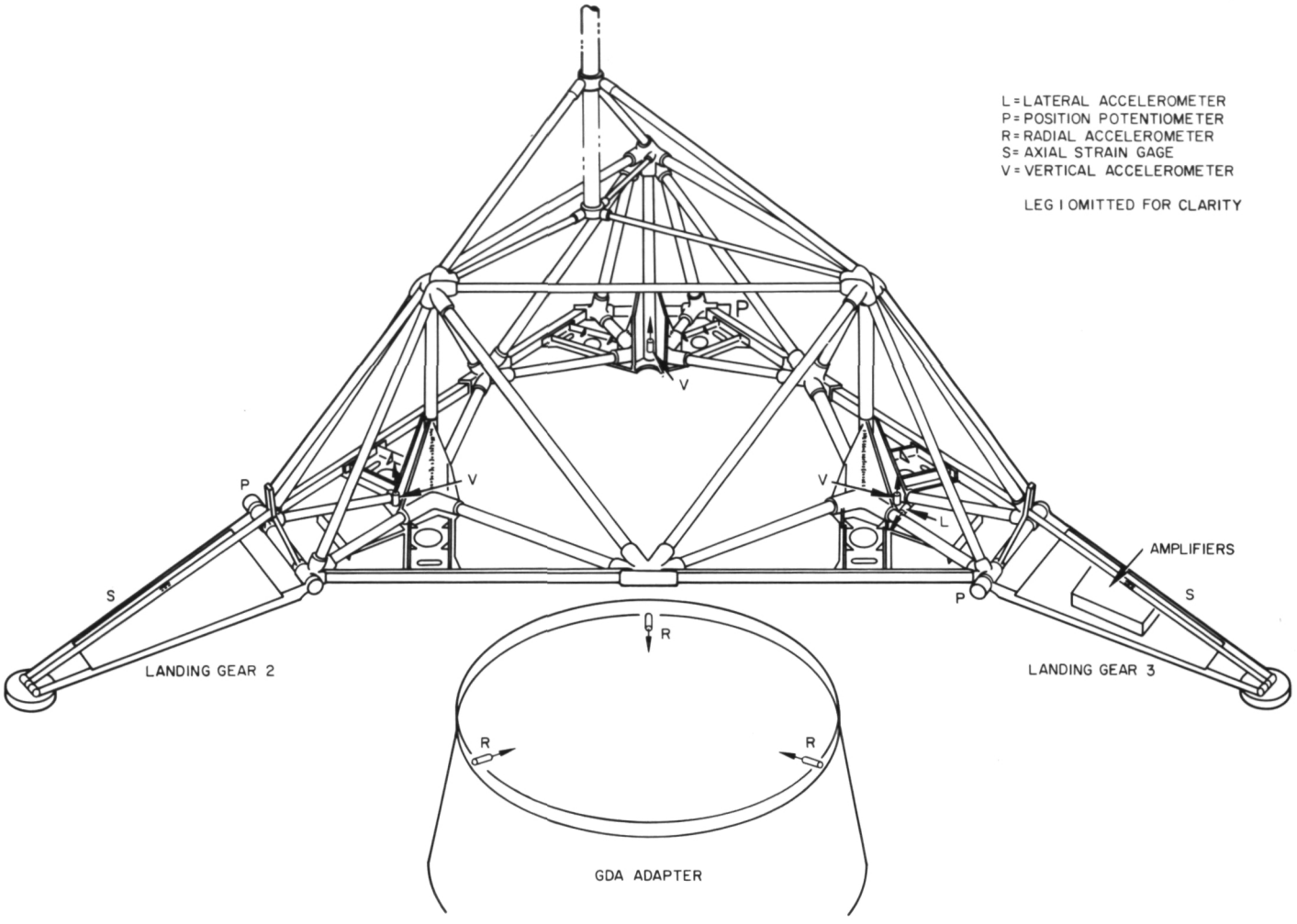

Fig. 126. Flight vehicle instrumentation

fatigue was maintained by using the lower edge of the S-N curve scatterband or by using a reduction factor of four on the allowable number of cycles where only mean S-N curves were available.

The reduction of boost design loads and unloading of the spaceframe caused by the change from a 2500- to a 2100-lb vehicle have resulted in a net decrease in spaceframe tube weight of approximately 3 lb. Another reduction of ½ lb resulted from detailed analysis of the vernier fuel tank supports. Matrix analyses of the latest landing load conditions (Tab. 26) were initiated in the period immediately following the T-21, SC-1 drawing release to determine if further weight reductions are possible.

A list of typical spaceframe tubes and the corresponding load conditions and failure modes which determined their size is presented in Figure 127. The majority of the attachments used to join spaceframe tubes to the clusters will be blind aluminum rivets; steel fasteners may be required in some locations.

Deflection studies and static tests of S-2 have disclosed that static deflections of the vernier engines and of the flight control sensor group exceed functional requirements during vernier engine firing and retrorocket maximum thrust. Since in both cases a large part of the deflection is caused by local spaceframe deformation, local stiffening of a few spaceframe members as well as the support bracketry should correct both deficiencies. Analysis which will lead to design recommendations is currently in progress. A separate deflection study performed by means of the spaceframe matrix analysis has indicated that the lateral shift of the spacecraft center of gravity during peak retro deceleration is marginally high. To verify the magnitude of this center

Table 27. Flight vehicle instrumentation if adapter accelerometers are used

TRANSDUCER				TRANSMISSION CHANNEL					
				Launch and boost		Retro descent		Touchdown	Lunar
Location	Type	Axis	Gain	Direct transmission from *Centaur*	*Surveyor* tape recorder	Direct transmission from *Surveyor*	*Surveyor* tape recorder	*Surveyor* tape recorder	Direct transmission from *Surveyor*
Centaur adapter									
Near Leg 1	Accelerometer	Radial	Low High	1					
Near Leg 2	Accelerometer	Radial	Low High	2					
Near Leg 3	Accelerometer	Radial	Low High	3					
Spacecraft									
Leg 1	Accelerometer	Z	Low High		1	1	1	1	
Leg 2	Accelerometer	Z	Low High		2	2	2	2	
Leg 3	Accelerometer	Z	Low High		3	3	3	3	
Leg 3	Accelerometer	Tangential	Low High		4	4	4	4	
Damper 1	Strain gauge				5		5	5	
Damper 2	Strain gauge				6		6	6	
Damper 3	Strain gauge				7		7	7	
Leg 1	Angular position potentiometer								Commutated
Leg 2	Angular position potentiometer								Commutated
Leg 3	Angular position potentiometer								Commutated

of gravity shift, the test schedule for S-2 has been modified to allow a static load deflection test, which will simulate the retro firing condition, prior to the S-2 vibration tests.

Stress analysis is currently in progress for the T-21 and SC-1 substructure, comprising the bracketry and tubes required to attach the external components and instruments to the basic spaceframe. A decision has been made to attach the substructure to the basic frame with saddle type fittings riveted to the spaceframe tubes. To compensate for the stress concentrations created by the addition of rivet holes, it may be necessary to reinforce locally some of the primary spaceframe members with bonded doublers where the tubes are critical in fatigue. Despite the addition of doublers to the basic frame, it is anticipated that a weight reduction will result since a saddle fitting encircles only 180 deg of a tube circumference instead of the 360 deg contact required for bolted clamp fittings such as those used on S-1 and S-2.

8. *Spaceframe Stress Analysis (T-2)*

The internal loads for the descent dynamics test spaceframe T-2 have been determined for the limit design loads described in Table 17 of Reference 1 by means of a matrix analysis. On the basis of these loads, a weight saving of 2.44 lb could be effected in the vehicle frame. The particular tubes and the load and failure conditions that determine their size are shown in Figure 128. It may be observed that only two conditions design the major portion of the spaceframe. The other conditions are useful in analyzing spaceframe joints and attachments of components to the spaceframe. Since the loads may act in any direction, the tubes are symmetrical with respect to the spaceframe centerline with the exception of the area where the aerodynamic disc is attached; the arrangement of this item requires somewhat heavier spaceframe members.

Several other design changes resulting from a stress analysis of the T-2 substructure resulted in a slight additional reduction in total vehicle weight.

9. *Landing Gear Stress Analysis and Tests*

Several improvements have been made in the landing gear for T-21 and SC-1, resulting in a 40% weight reduction. By using resistance spot welds instead of rivets to attach the upper and lower skins to the tubes and ribs comprising the leg frame, the upper skin thickness was reduced from 0.025 to 0.016 in. and the lower from 0.025

Table 28. Flight vehicle instrumentation if adapter accelerometers are not used

TRANSDUCER				TRANSMISSION CHANNEL					
				Launch and boost		Retro-vernier		Touchdown	Lunar
Location	Type	Axis	Gain	Direct transmission from *Centaur*	*Surveyor* tape recorder	Direct transmission from *Surveyor*	*Surveyor* tape recorder	*Surveyor* tape recorder	Direct transmission from *Surveyor*
Spacecraft									
Leg 1	Accelerometer	Z	Low		1		1	1	
			High	1		1			
Leg 2	Accelerometer	Z	Low		2		2	2	
			High	2		2			
Leg 3	Accelerometer	Z	Low		3		3	3	
			High			3			
Leg 3	Accelerometer	Tangential	Low		4		4	4	
			High	3		4			
Damper 1	Strain gauge				5		5	5	
Damper 2	Strain gauge				6		6	6	
Damper 3	Strain gauge				7		7	7	
Leg 1	Angular position potentiometer								Commutated
Leg 2	Angular position potentiometer								Commutated
Leg 3	Angular position potentiometer								Commutated

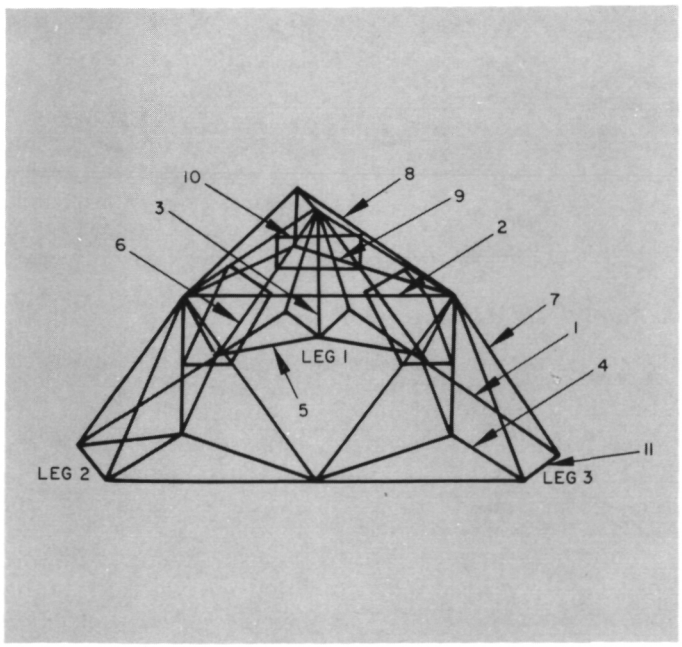

ESTIMATED CRITICAL CONDITIONS AT LOCATIONS SHOWN		
NUMBER	CRITICAL CONDITION	MODE OF FAILURE
1	30g LANDING	ULTIMATE STRESS
2	30g LANDING	ULTIMATE STRESS
3	TRANSVERSE LANDING	ULTIMATE STRESS
4	TRANSVERSE LANDING	ULTIMATE STRESS
5	BOOST	FATIGUE
6	BOOST	FATIGUE
7	LANDING	BUCKLING
8	LANDING	BUCKLING
9	BOOST	FATIGUE
10	BOOST	FATIGUE
11	TRANSVERSE LANDING	ULTIMATE STRESS

Fig. 127. Critical design conditions for T-21, SC-1 spaceframe members

TUBE	CONDITION	MODE OF FAILURE
1	PARACHUTE DEPLOYMENT	ULTIMATE COMBINED STRESS
2	PARACHUTE DEPLOYMENT	ULTIMATE COMBINED STRESS
3	PARACHUTE DEPLOYMENT	ULTIMATE COMBINED STRESS
4	PARACHUTE DEPLOYMENT	ULTIMATE COMBINED STRESS
5	LANDING	BEAM COLUMN
5a	LANDING	BEAM COLUMN
6	PARACHUTE DEPLOYMENT	ULTIMATE COMBINED STRESS
7	PARACHUTE DEPLOYMENT	ULTIMATE COMBINED STRESS
8	PARACHUTE DEPLOYMENT	ULTIMATE COMBINED STRESS
9	PARACHUTE DEPLOYMENT	BEAM COLUMN
10	PARACHUTE DEPLOYMENT	ULTIMATE COMBINED STRESS
11	PARACHUTE DEPLOYMENT	ULTIMATE COMBINED STRESS
12	PARACHUTE DEPLOYMENT	ULTIMATE COMBINED STRESS
13	PARACHUTE DEPLOYMENT	ULTIMATE COMBINED STRESS

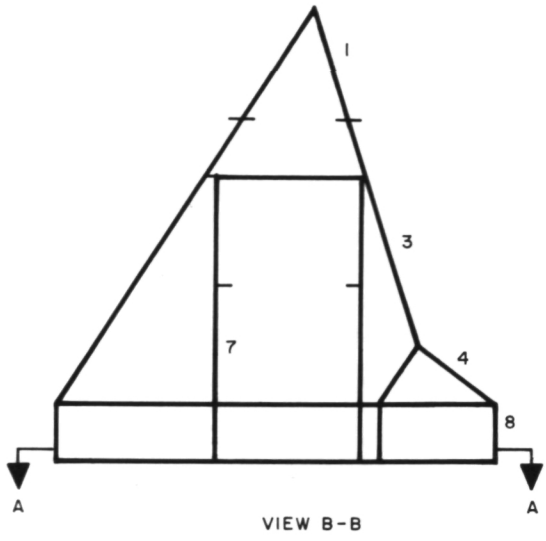

VIEW B-B

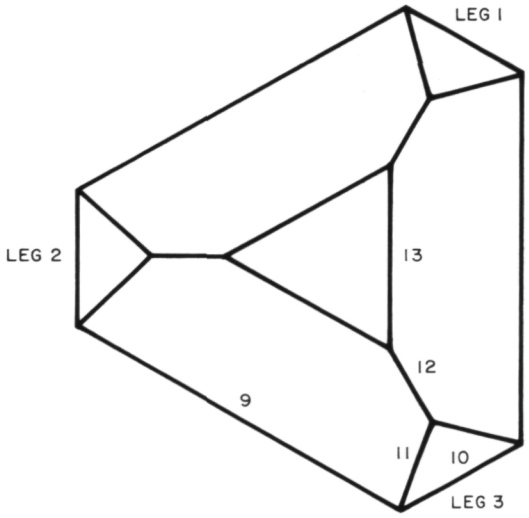

VIEW A-A
ONLY MEMBERS IN PLANE ARE SHOWN

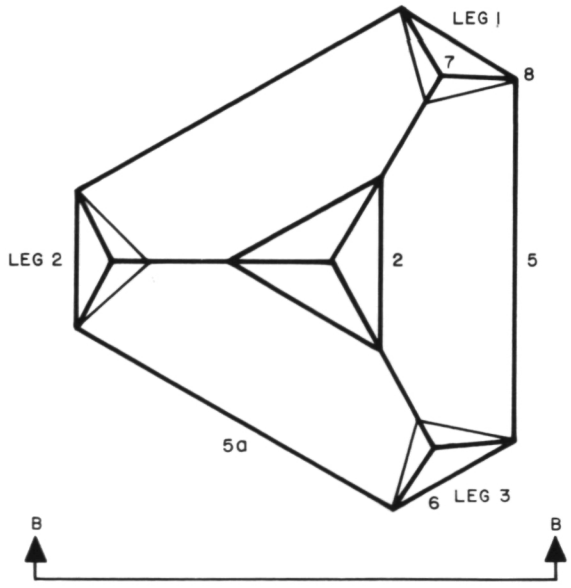

Fig. 128. Critical design conditions for T-2 spaceframe members

to 0.012 in. An additional modification was incorporation of tubes of variable wall thickness, resulting in improved distribution of material.

Since only limited information is available concerning spot welding of 7075-T6 aluminum, tests are planned to determine the static and fatigue strength of these particular spot welded joints. Specimens simulating the type of spot welded joints used on the landing gear leg are being fabricated and will be tested when available. In the absence of specific spot weld test data, the allowable loads for spot welded aluminum sheet given in MIL-HDBK-5 were used in the stress analysis of the T-21 and SC-1 landing gear drawings which were released on June 1, 1962.

Static tests were performed on a landing gear locking strut for the critical load condition encountered during touchdown (Fig. 129). This member acts as a column which, in normal operation, transfers the entire compression load through two pivoted pawls located 180 deg

apart on the outer circumference of the main tube to a lug engaged during deployment of the landing gear. During the first test, no damage resulted from 100% design load applied to the strut in compression with both pawls engaged. In the second test, only one pawl was engaged, simulating abnormal operation of the pawls during gear deployment. A compressive load of 90% of design load resulted in a small amount of permanent set in the region of the pin and lug caused by high bearing stresses. As a result of the second test, minor redesign will be carried out to improve structural characteristics.

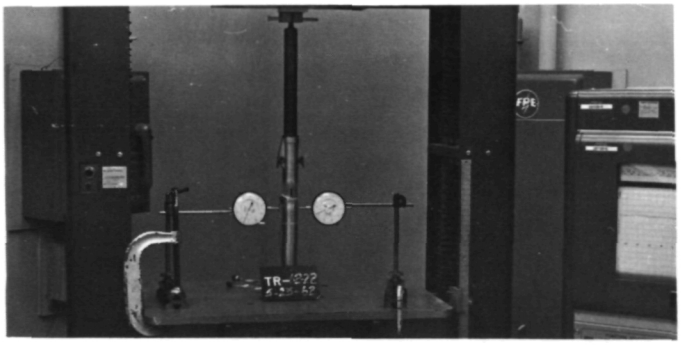

Fig. 129. Load testing of landing gear lock strut

I. Propulsion

1. Introduction

The spacecraft has two propulsion systems, a spherical solid propellant retro-rocket engine and a vernier propulsion system. The retro-rocket engine decelerates the spacecraft preparatory to landing; development of this engine has been subcontracted to the Elkton Division of Thiokol Chemical Corporation. The vernier propulsion system uses liquid propellant and has three thrust chambers; it performs incremental velocity corrections for the midcourse maneuver and terminal descent and controls attitude during operation of the retro-rocket engine. One vernier chamber is swiveled to supply a roll-control thrust component. Development of the vernier system has been subcontracted to the Reaction Motors Division (RMD) of Thiokol.

2. Progress Summary

Contract negotiations have been completed with the Elkton Division of Thiokol Chemical Corporation for a combined main retro-rocket engine program to meet the requirements of both the A-21 and A-25 spacecraft. Specifications, work statements, and detail program plans for development, test, and delivery of the two engine configurations have been established. One heavy-wall A-25 retro-rocket engine has been successfully tested under simulated altitude conditions (approximately 100,000 ft). The flight-weight engine case procurement problem associated with the termination of manufacturing at Kaiser Fleetwings and transferring tooling and materials to the Lycoming Division of AVCO has been resolved with no delay in schedules.

Design of vernier propulsion systems for the T-2 and T-21 vehicles has been frozen, and hardware is being fabricated for these units. Complete vernier system tests have been successfully completed under acceleration conditions expected during retro-engine firing and under environmental temperature conditions expected during transit. The performance levels have been determined and, while somewhat lower than specified, are acceptable for the missions currently planned.

3. Retro-Rocket Engine

The A-21 and A-25 retro-rocket engine configurations are identical except for propellant weight, propellant configuration, and minor differences in nozzle throat diameter. The 36-in.-diameter spherical case is formed by welding two premachined hemispheres of D6AC Ladish tool steel. Asbestos filled buna-N rubber is used for case insulation. The igniter is a pyrogen type.

Table 29 compares the predicted performance of the A-21 and A-25 retro-rocket engines at vacuum conditions and 50° F.

Table 29. Predicted performance of A-21 and A-25 retro-rocket engines at vacuum and 50°F

Characteristic	A-21	A-25
Total impulse, lb-sec	349,000	420,100
Propellant specific impulse, lb-sec/lb	294	294
Average thrust, lb	8309	9400
Action time, sec	42.0	44.6
Nozzle expansion ratio	47/1	46/1
Propellant mass ratio ($W_{PROPELLANT}/W_{TOTAL}$)	0.894	0.911

a. Retro-rocket tests

(1) A-21 retro-rocket engine: Two A-21 retro-rocket engines have been fabricated using flight-type components. The first test, at sea level, of the A-21 retro-rocket engine is scheduled for June 22, 1962. The second engine is scheduled for test in the altitude test facility on July 5, 1962.

(2) A-25 retro-rocket engine: Testing to date of the A-25 retro-rocket engine has demonstrated the structural integrity of the flight system, compatibility with environmental requirements, and performance. Eight heavy-wall engines have been tested prior to the very successful test of a flight-weight A-25 retro-rocket engine. An additional four engines have been cast.

The first firing in the vacuum facility at Arnold Engineering Development Center was made. The desired 100,000-ft altitude simulation was achieved. Preliminary data indicated that the rocket engine performed satisfactorily except that the total impulse was about 4½% less than predicted. Test data are being reduced to accurately determine rocket engine ballistic parameters.

b. Flight-weight cases. Prior to termination of operations, the Kaiser Fleetwings Division completed fabri-

cation and test of 12 case assemblies. Lycoming Division of AVCO has been selected to fabricate the additional cases necessary for completion of the program. All tooling has been transferred, and initial machining was started on May 23, 1962. Only minor modifications are required for some tools to adapt to Lycoming equipment. The manufacturing processes developed by Kaiser Fleetwings will remain the same. Delivery of cases by Lycoming is scheduled to begin on July 21, 1962.

c. Antenna separation tests. Ejection characteristics of the altitude marking radar antenna were determined by a retro-engine antenna separation test. The antenna was mated to an inert engine, and a pyrogen igniter was used for pressurization. Clean separation was achieved. Separation occurred 0.012 sec after application of the firing current and prior to typical complete ignition of the engine propellant (Fig. 130).

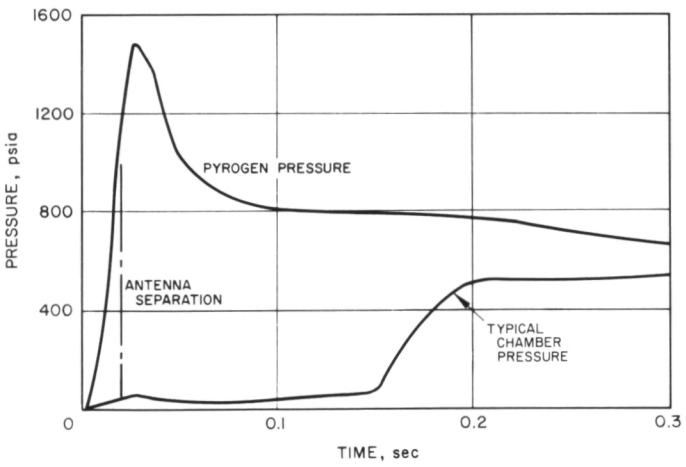

Fig. 130. Antenna separation from retro engine

d. Altitude test facility. The redesigned diffuser for the altitude test facility has been fabricated. This diffuser was modified to achieve altitude conditions throughout a run and will permit resumption of A-25 retro-rocket engine testing at Thiokol Elkton. A heavy-wall engine will be fired in this facility to verify diffuser performance prior to test of flight-weight engines. Analysis of diffuser design and engine performance indicates that one stage of exhaust augmentation may be required for testing of A-21 engines in the altitude test facility.

e. Tooling. Fabrication of all items of special tooling has been completed. The multicomponent test stand is ready for installation, and the center-of-gravity measurement and thrust alignment tooling are in operation.

f. Retro-engine—Thermal control. Analysis indicated that vernier propulsion operation for the midcourse correction will induce temperatures up to 1500° F in the vicinity of the retro-engine nozzle expansion cone. Exposure to this thermal environment would drastically degrade the effectiveness of the nozzle thermal radiation shielding. Several methods of protecting the thermal shielding were investigated. The results of thermal analyses indicate that a blanket of silica glass fiber of graduated thickness will provide adequate protection with minimum additional weight. Fabrication of prototype insulation blanket hardware is currently in progress.

4. Vernier Engine System

The vernier propulsion system consists of a cold helium propellant pressurization system, a liquid propellant tankage system, and three thrust chamber assemblies, each of which can supply any thrust level between 30 and 104 lb on command. Monomethyl hydrazine is used as the fuel, as well as for regenerative cooling of the thrust chamber. Nitrogen tetroxide with 10% nitric oxide (a freezing point depressant) is used as the oxidizer. The system is capable of providing approximately 50,000 lb-sec total impulse. Coordination between the Hughes Aircraft Company and Thiokol, RMD, has culminated in a detailed definition of the vernier propulsion system installation on T-2, T-21, and propulsion quality assurance vehicles. Vernier propulsion deliveries for T-2 and T-21 are scheduled for August and September 1962, respectively.

a. Complete system development. During this report period, all altitude firing tests in the development phase of the program and the ambient temperature tests were completed with the exception of thermal gradient testing, minimum temperature (0° F) testing, and maximum temperature (100° F) testing under pressure conditions simulating approximately 100,000 ft of altitude. Analysis of the data obtained from this series of systems tests is currently in progress. However, preliminary investigation indicates satisfactory system operation.

Sea level firings of a complete system under acceleration conditions of 10 g were conducted to evaluate system operation at the g level expected during main retro burning. Preliminary data indicate satisfactory durability and performance. Further sea level testing to be accomplished prior to completion of the development phase of the program are tests to determine propellant unbalance forces. All systems testing is expected to be completed early in the next report period, which will

conclude the development phase for the vernier propulsion system.

b. Component development. Approval (prequality assurance) testing of all components has been completed. Table 30 summarizes the conditions to which each component was subjected during the approval tests. A component-by-component summary is presented below to indicate the configuration which will enter the quality assurance phase of testing.

(1) Helium tank – this tank is fabricated of 7-4 titanium alloy and is spherical in shape.

(2) Helium fill-release-dump valve assembly – this assembly is composed of a squib activated valve which releases helium to the propellant feed system, a squib activated valve which dumps helium from the storage tank in case of emergency, a quick disconnect fill valve for introducing helium into the storage tank, and a pressure transducer for sensing storage tank pressure.

(3) Helium regulator – relief valve-check valve assembly – this assembly is composed of a two-stage regulator which reduces helium storage pressure to 690 psi for the propellant feed system, a check valve, and a relief valve for each leg of the propellant feed system (fuel and oxidizer).

(4) Propellant tanks – these tanks (three oxidizer and three fuel tanks for each system) are fabricated of 7178 aluminum. They are cylindrical with a low length-to-diameter ratio with hemispherical ends.

Table 30. Vernier propulsion component tests

Test	Helium tank	Fill-release dump (squib) valve	Regulator-check-relief valve assembly	Quick disconnect		Quick disconnect (helium)	Shutoff valve	Throttle valve	Propellant tank	Thrust chamber	Bladders (3 bladders, 1 from each of 3 lots[a]
				Fuel	Oxidizer						
Examination of product	X	X	X	X	X	X	X	X	X	X	X
Proof pressure	X	X	X	X	X	X	X		X	X	
Leakage	X	X	X	X	X	X	X	X	X	X	X
Capacity	X								X		
Functional			X	X	X	X	X	X			
Endurance	X		X	X	X	X	X	X	X	X	
Sterilization (internal)		X	X	X	X	X	X	X			
Vibration	X	X	X				X	X			
Burst	X	X	X	X	X	X	X	X	X		
Compatibility (test conditions check)				X	X						
Altitude			X				X		X	X	
High temperature		X	X					X	X	X	
Low temperature		X	X				X	X	X	X	
Humidity		X									
Continuity		X									
Electrical characteristics								X			
No fire		X									
Explosion-proof							X	X			
Actuation		X									
Flow and lockup		X									
Pressure drop		X									
Acceleration[b]											
Dry cycle							X				
Response time							X				

[a]Ten cycles of expulsion to 90-95% under ambient temperature conditions. One cycle of expulsion to 100% under 0°F temperature conditions.

[b]All components will be subjected to acceleration testing on a system basis.

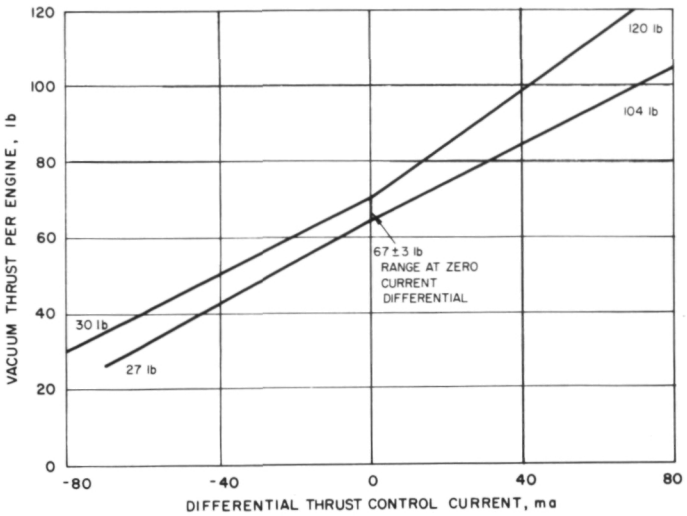

Fig. 131. Vernier engine thrust control envelope

(5) Propellant bladders — fuel bladders and oxidizer bladders are fabricated from laminated TFE-FEP teflon.

(6) Throttle valve — this valve is comprised of a single torque-motor-driven flow controller with one flow control reed and one pressure balancing piston for each propellant constituent. The throttle valve characteristics lie in the envelope presented in Figure 131.

(7) On-off valve — this valve is solenoid piloted and helium operated with a helium purged chamber between the fuel and oxidizer poppets.

(8) Thrust chamber — this chamber is regeneratively cooled with fuel and utilizes a radiation-cooled nozzle extension to increase the expansion ratio to 86:1. The chamber is internally coated with Rokide Z to reduce heat transfer to the fuel to an acceptable level.

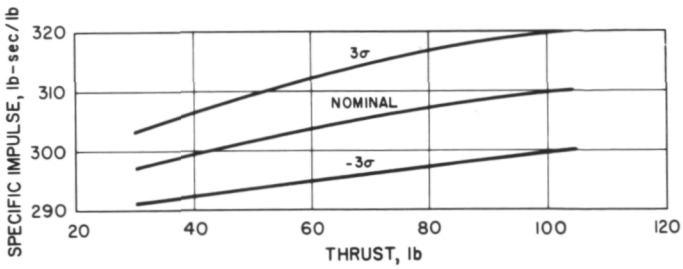

Fig. 132. Thrust chamber performance at vacuum conditions

The thrust chamber assembly is comprised of a throttle valve, an on-off valve, and a thrust chamber. The performance of this unit has been determined and is shown in Figure 132. Although this performance is lower than specified, it is adequate for the *Surveyor* mission, and no further development to upgrade performance is planned.

c. Thermal control. A specification covering all thermal control hardware and coating application, inspection, and protection procedures has been released. Thermal control hardware for prototype and qualification spaceframes is currently being fabricated.

Developmental vernier hardware was coated in accordance with thermal control requirements and will be tested on a developmental spaceframe to determine the adequacy of the thermal control materials recommended for use on the vernier propulsion system.

J. Spacecraft Vehicle and Mechanisms for Basic Bus

1. Spacecraft Vehicle

a. General arrangement. The configuration for the A-21 spacecraft has been defined as shown in the general arrangement drawing (Fig. 1). A one-fifth scale model of this configuration has been fabricated (Fig. 133). Detail design of this configuration is now proceeding.

b. Wiring harness. Thermal analysis indicates that the wiring harness requires a wrapping material with low solar absorptivity and high emissivity, as well as a light weight and durability in direct sunlight. Tests show that Type A FEP teflon tape of one to a few thousandths inch thick and aluminized on one side meets the requirements. An additional benefit would be increased electrical shielding of the harness, if the aluminized surface can be grounded.

c. Landing gear tests. Landing gear deployment occurs prior to separation of the spacecraft from the *Centaur* booster. At that time the equipment is weightless. To simulate this condition, tests are being carried out (Fig. 134). Elements of the grear are supported by wires to reduce the effects of gravity. The radial load imposed on the bearings by these wires is small enough to be neglected. The changing mechanical advantage of the lock strut causes the frictional torque to vary through the 122 deg swing of the leg. This frictional torque, not including the drag of the pawls on the locking strut, varies between 2 and 8 in-lb. The tests confirmed the adequacy of dry molybdenum-disulphide lubricant, isolated the friction effect of the locking pawls at various pawl spring loads, and set the lower limit of actuator spring torque.

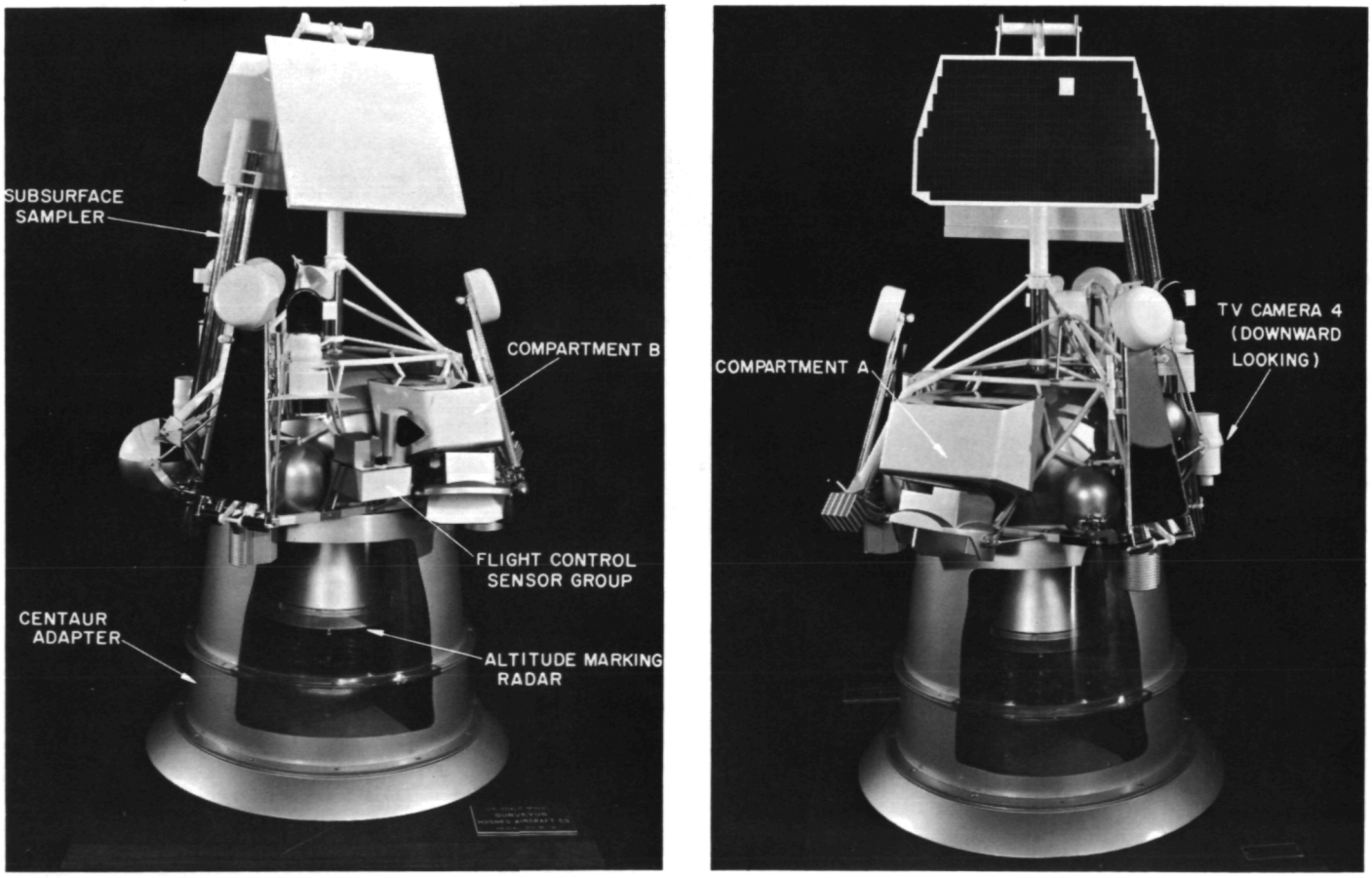

Fig. 133. One-fifth scale model of A-21 spacecraft configuration On Centaur

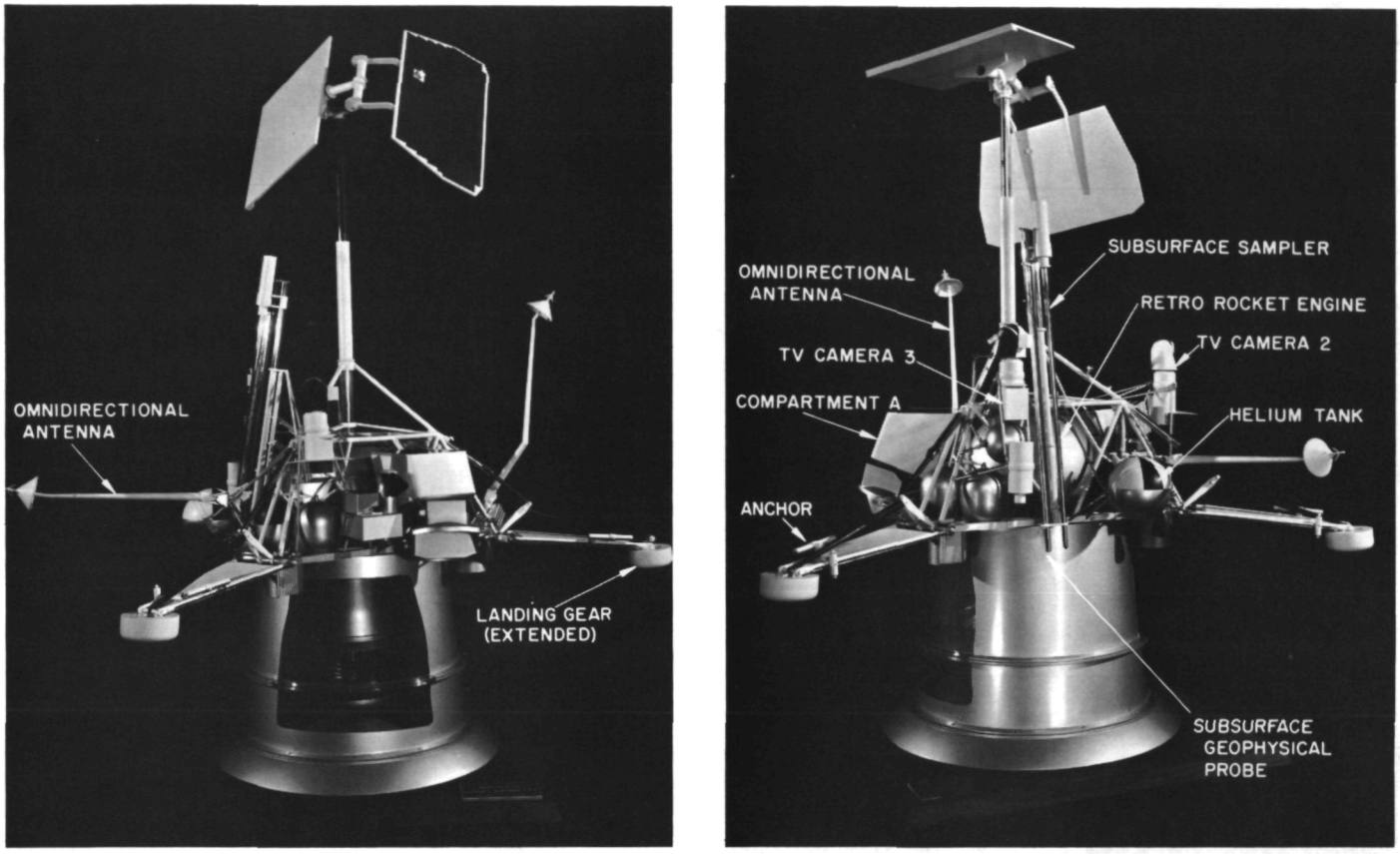

Fig. 133. continued. One-fifth scale model of A-21 spacecraft configuration Legs and antennas extended

Preliminary tests with the present deployment actuating springs show the leg is extended in approximately 2 sec. The impact load at the end of extension is close to the predicted loads, indicating that the cushion at the shock absorber telescoping interface operates satisfactorily. Decelerations of 29 to 37 *g* were measured 36 in. from pivot. The instrumentation of this system is shown in Figure 135.

d. Special test vehicle design and fabrication

Thermal test mockup MT-1. Sector 1 of the three sectors of the thermal test mockup (MT-1) has been completed and prepared for tests. The tests are described in Section G.

Sector 2 of MT-1 is being assembled. It is scheduled for lunar night tests at the Hughes facility upon completion of the Sector 1 tests. Arrangement of units on Sector 3 is being modified to represent the A-21 spacecraft configuration.

T-2. The T-2 vehicle for testing the soft landing system is comprised of a special lightweight frame to which is mounted the doppler radar system, flight control sensor group, vernier propulsion system, and several special recovery elements. It will be dropped from a tethered balloon to demonstrate the final approach and landing capability of the spacecraft. The parachute and air bags of the recovery system will be tested on a special test vehicle designated T-2R.

The air bags are carried in a collapsed condition to protect them from the vernier engine jets. At the end of rocket burning the bags are inflated by CO_2 gas. The bags inflate fully within ½ sec. Upon impact, a diaphragm ruptures from the increased pressure within the bag, breaking an aluminum foil electrical conductor to actuate a relay that jettisons the parachute and isolates the battery, so that damage due to shorts will be avoided. A calibrated orifice permits controlled escape of the gas within the bag to absorb the kinetic energy of touchdown. The air-bag operation has been tested as described in Section K.

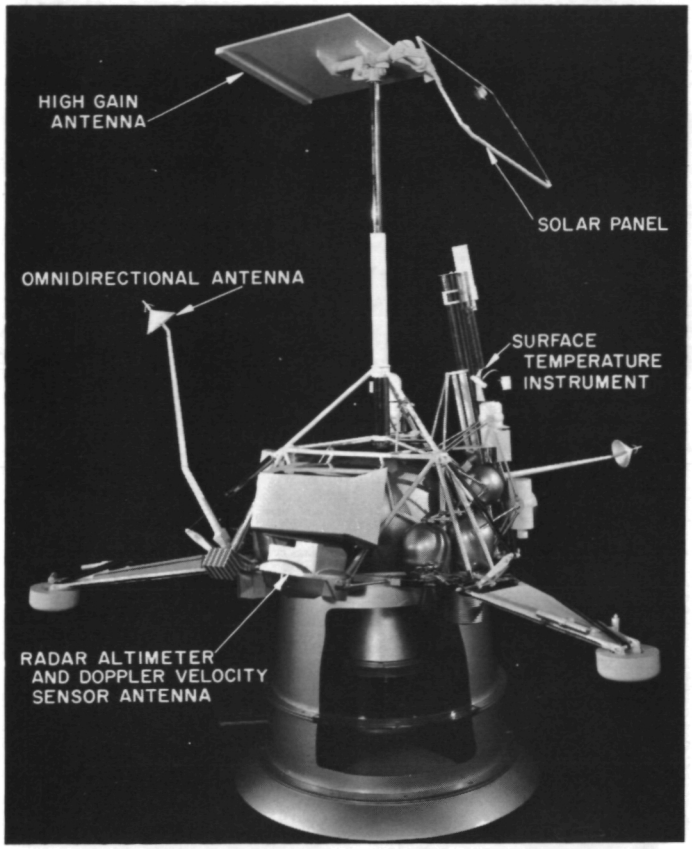

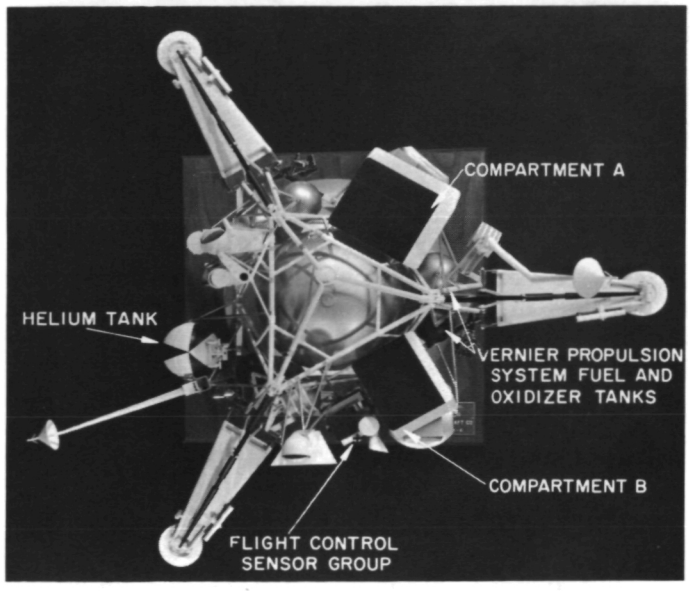

Fig. 133 continued. One-fifth scale model of A-21 spacecraft configuration. View from top with planar antenna solar panel removed

S-2. The S-2 will be used for vibration testing. It is nearing completion preparatory to instrumentation. S-2 is shown without instrumentation in Figure 136.

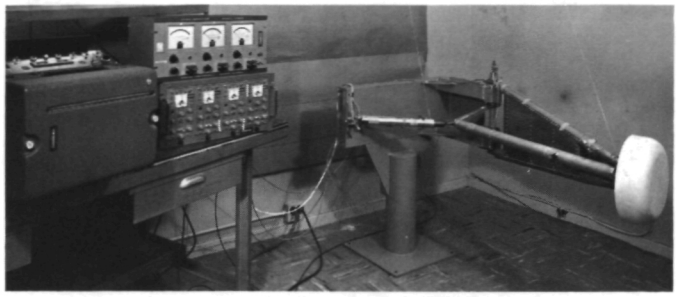

Fig. 134. Testing of landing gear deployment

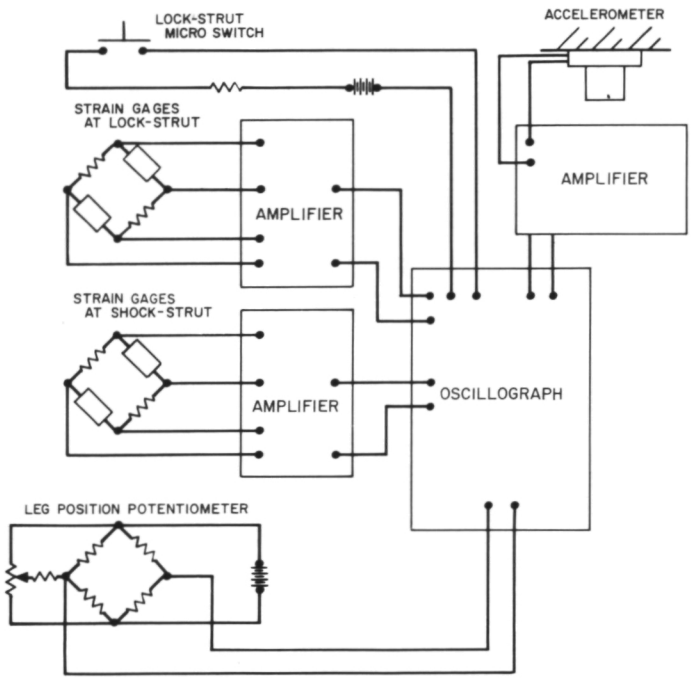

Fig. 135. Landing gear test instrumentation

S-6 and S-7. S-6 (Fig. 137) and S-7 will be used for type approval and flight control testing of the vernier propulsion system. These vehicles are nearing completion.

M-12-21. An engineering mockup of the spacecraft is being modified to represent the A-21 configuration. This vehicle will be used to fit the wiring harness for the T-21 type-approval test spacecraft.

2. Basic Bus Mechanisms

a. Omnidirectional antenna mechanism. The omnidirectional antenna mechanisms extend the omnidirectional antennas to the operating position after shroud separation. The decision has been made to fabricate the tapered

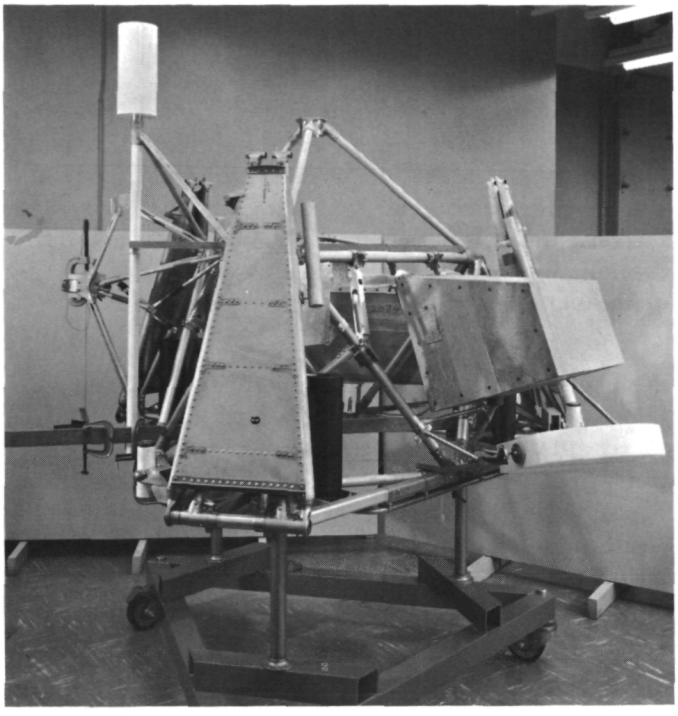

Fig. 136. S-2 vibration test vehicle

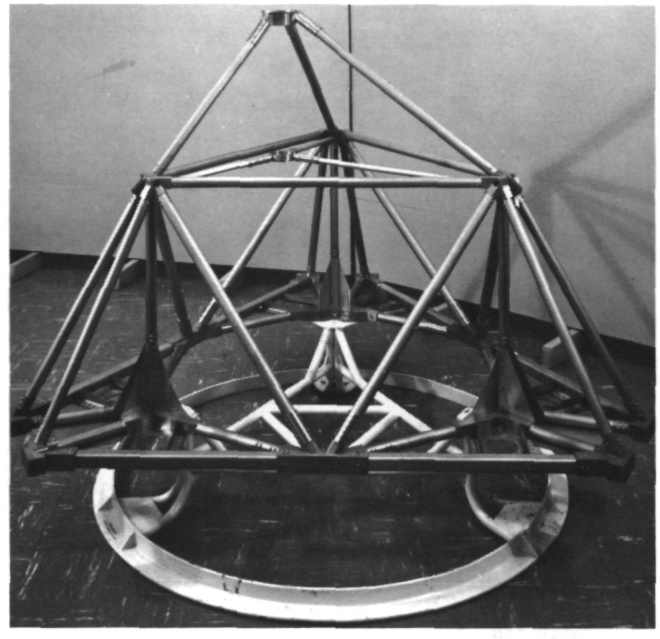

Fig. 137. S-6 vernier propulsion test vehicle

tubes for the antenna deployment mechanism from filament-wound fiberglass. The stress analysis has been completed and the tubes have been ordered. Vendor delivery is expected in late June. In the meantime, fabrication of aluminum tube sections of representative mass and inertia has been completed for vacuum chamber testing of the spring drive mechanism. A mockup of Omnidirectional Antenna No. 2, fabricated from stepped sections of aluminum, is shown in Figure 138. The actuating spring has been redesigned to a mousetrap type configuration, resulting in elimination of separate end fittings and simplification of the design.

b. Antenna-solar panel positioner. The antenna-solar panel positioner positions the planar antenna and solar panel during transit and lunar operations. The engineering test model of the four-axis design is being assembled for functional testing. A development model of the earlier five-axis design (Fig. 139) will be subjected to thermal-vacuum tests starting in June. Vibration and shock testing will follow the thermal-vacuum tests.

Because of the complexity of the positioning requirements, a parallel design effort is continuing on the polar axis drive. A breadboard model of a torque feedback limiter is being tested, and a spring-loaded multi-disc brake is in the final design stage. Either of these designs may replace the present worm gear drive, if such a course is indicated by test program results.

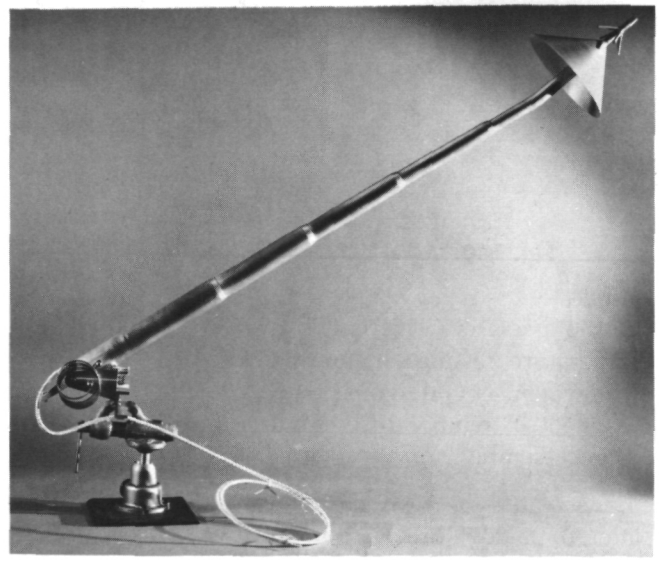

Fig. 138. Omnidirectional antenna mechanism no. 2 stowed

Tests are in progress to determine low temperature operating capability of individual subassemblies. The polar axis drive worm gear and bushings for the five-axis design have been tested at temperatures as low as —100° F. Operating capability was lost at this temperature due to differential thermal expansion of dissimilar metals. The four-axis design, operating at lower stress levels, permits the use of similar materials through-

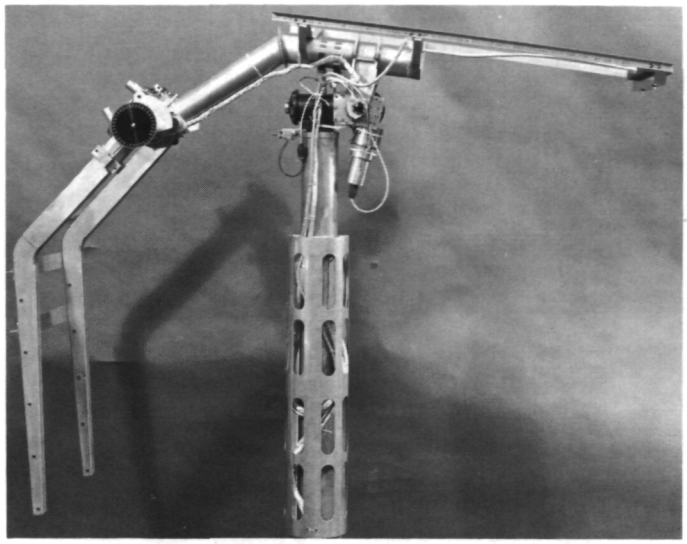

Fig. 139. Five-axis developmental positioner

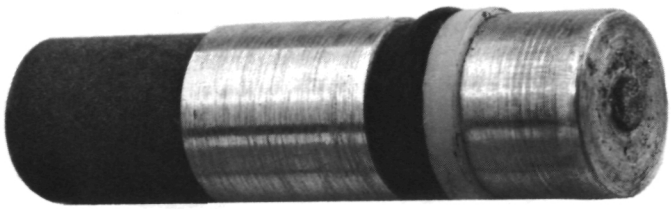

Fig. 140. Mast extension filter/restrictor

out the assembly. This unit is presently undergoing low temperature testing. In addition, the roll axis bearing arrangement is undergoing thermal cycling to determine the effect of temperature variation on the friction level of the assembly.

Mast extension tests have been conducted using the sintered metal filter-restrictor (Fig. 140), in place of an adjustable orifice, for the cold gas supply. Extension rates and pressure regulation are shown in Figure 141. This type of gas regulation will be incorporated in the prototype design.

Structural testing to destruction has been performed on many of the typical welded joints of the mechanism. No failures have occurred below 142% of design load.

c. Motors and mechanisms drive units

Rotary solenoid and pulsed phase motors. Testing of bidirectional stepping motors in a high temperature-vacuum environment has continued. As a result of a series of modifications to these motors, they are now capable of continuous operation for periods up to 3 hr in an environment of 275° F and vacuum of 10^{-6} mm Hg. Modifications have included teflon insulation, larger diameter coil wire, detent mechanism and armature bushing modifications, teflon coil wrapping, and lubrication with "Micro-seal" glass-graphite dry film. Motor response times have remained practically constant during the environmental tests when operated at the low end of the voltage supply (15 v dc).

Drive mechanisms. The three-stage planetary drive mechanism designed for the antenna-solar panel positioner, when coupled to a modified motor, has been successfully tested against a maximum unbalance load of 96 lb-in with an inertia load of 5 slug-ft-sec^2 at temperatures of ±275° F in a vacuum of 10^{-6} mm Hg (Tab. 31). The single cluster planetary drive has also been successfully driven against a full stall load without damage at temperatures of ±275° F in a vacuum of 10^{-6} mm Hg.

Drive mechanism lip seal. The drive mechanism lip seal was statically pressure tested for a period of 6 wk. With the pressure external to the seal maintained at less than 10^{-6} mm Hg, the pressure within the drive mechanism cover remained above 8.8×10^{-2} mm Hg. In a dynamic test conducted over a 16-day period operation of the motor reduced the pressure within the drive mechanism to 3.2×10^{-2} mm Hg. The dynamic test setup is shown in Figure 142.

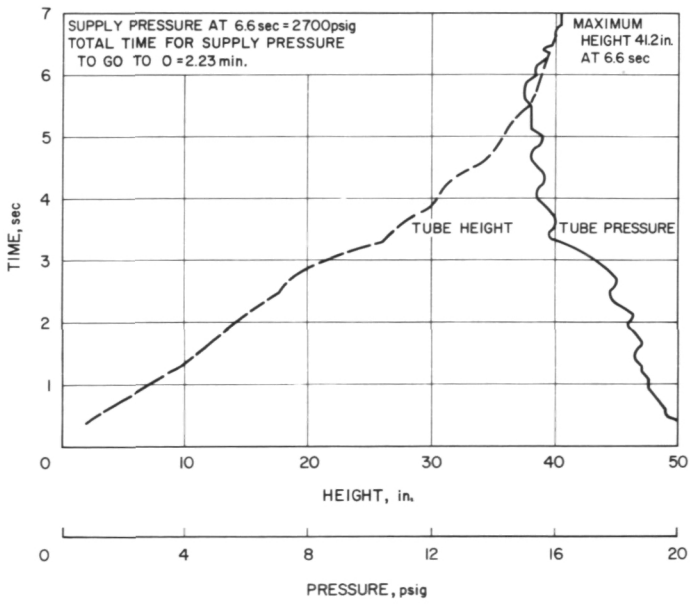

Fig. 141. Mast extension test performance

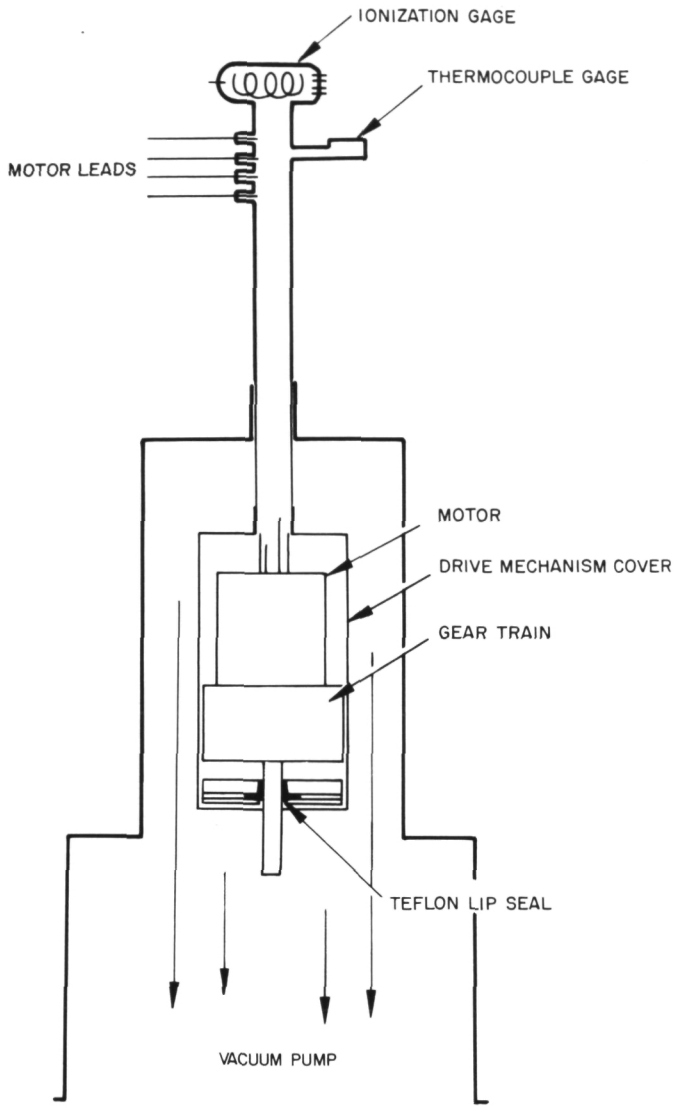

Fig. 142. Test setup for drive mechanism lip seal

The preliminary test results have indicated a strong possibility that operation with conventional lubricants can be attained in vacuum within the normal temperature range of such lubricants. Further testing is planned at anticipated lunar temperature extremes.

Table 31. Temperature-vacuum tests of planetary drive with 15v supplied to motor

Temperature	Response rate, ms		Current, amp
	With load	Against load	
70° F	12.0	19	9.6
275° F	12.5	25	8.0
−275° F	13.0	19	10.0

Fig. 143. Hole produced by shaped charge for anchor (S-20)

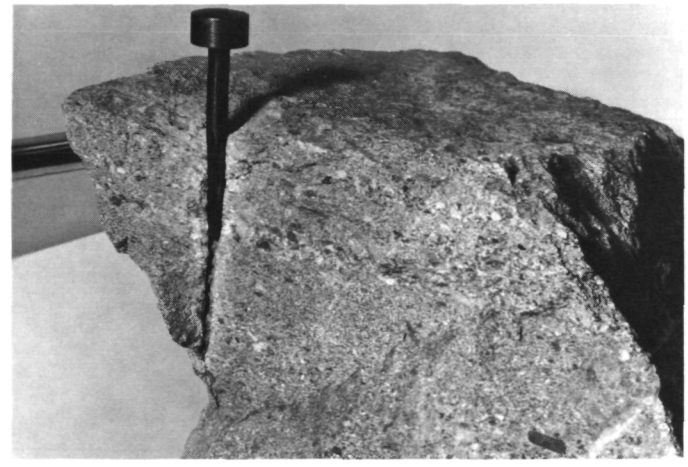

Fig. 144. Anchor spike in hole (S-21)

d. Separation sensing and arming device. The separation sensing and arming device senses *Centaur* spacecraft separation and provides an interruption of certain of the spacecraft explosive circuitry. Development tests have been successfully completed on the double-pole double-throw switch and actuating mechanism. The tests were conducted under full environmental requirements and at full peak current values anticipated in the circuit.

The preseparation arming circuit has been removed from this device, requiring a redesign of the separation sensing and arming circuitry. The enclosing case of the separation sensing and arming device has also been redesigned to allow the addition of thermal insulation to the retro-rocket.

The prototype drawing package has been released for production, and procurement of prototype purchased parts has been initiated.

e. Anchoring device. The anchoring device provides a shear pin from the spacecraft to the lunar surface to minimize spacecraft movement after landing. A preliminary vendor design review was conducted on May 18, including examination of material compatibility and safety and compliance with the *Surveyor* requirements. Considerable design effort has been expended by the subcontractor to provide reliability of operation and incorporate safety features within the limits of size and weight allowed for this device.

Developmental test firings of shaped charges by the subcontractor have been made in hard granite to determine penetration and hole size characteristics (Fig. 143). A tapered, serrated titanium spike was driven into one of the shaped holes with a gravity load equivalent to the explosive force which will propel the actual spike (Fig. 144). A vertical pull of 1200 lb was required to remove the spike from the granite. Tests are continuing to obtain the optimum shaped charge size for maximum penetration and hole control.

The developmental anchor mechanism has been successfully subjected to vacuum, temperature, shock, vibration, and acceleration environments.

K. Reliability and System Test

1. Reliability

a. Reliability estimate for A-21 spacecraft. Updated reliability estimates for the A-21 spacecraft indicate an increase in probability of success for all major mission phases. The results, compared with those in Reference 1, are as follows:

Mission phase	*Previous report*	*Current Report*	*80% confidence interval*
Transit and landing	0.74	0.78	0.55 to 0.95
First lunar day	0.38	0.75	0.50 to 0.94

The increases in reliability are largely attributable to clearer delineation of mission times up to the day-night terminator, which resulted in operating periods shorter than previously planned for many subsystems; updating of component failure rates was also a factor. In particular, the flight control electronics subsystem was substantially improved by updating of the electronic parts failure rate. The retro-rocket engine reliability has also improved significantly from an upgrading of the insulation reliability (from 0.923 to 0.981) on the basis of data from recent firings.

Some of the major changes resulting from clearer definition of required operating periods are shown in Table 32. The receiving decoder selector and central command decoder functions are now based on a mission on-time less than 10% of the previous time. The present mission profile includes additional consideration for the effect of equipment cycling.

Previously, for lack of better definition, it was assumed that the decoders would operate continuously for the entire lunar day (i.e., 163 hr). As a result of redefinition of the mission times for these two items, a net reliability gain of approximately 5% has been realized.

Revised failure rates for electrical components are generally lower than those used earlier. They reflect state-of-the-art improvements from vendor development programs, and also as the result of increased knowledge of space environment. Examples of reduction in failure rates are as follows:

Table 32. Changes in reliability estimates for A-21 spacecraft

Item	Present mission time,including on-off cycle, hr	Previous mission time, assuming continuous operation, hr	Reliability gain, %
Receiver decoder selector	13	163	1
Central command decoder	6.5	163	4
Spacecraft structure	157	446	3
Wiring harness and electrical connections	157	446	13

Component	*Failure rate per 1000 hr, % Previous*	*Current*
Switching diodes	0.250	0.009
Carbon resistors	0.010	0.005
General-purpose transistors	0.070	0.020

Some component failure rates, such as those for zener diodes and electric motors, were increased, but the overall effect of revised failure rates was to increase the system reliability estimate by about 4%.

b. Subsystem reliability estimates. Reliability estimates are upgraded continuously. Current estimates of mean reliability according to functional subsystem are compared to previous estimates in Table 33. The lunar phase estimates are for the period between landing and start of the day-night terminator. The 80% confidence interval for each phase, including consideration of anticipated test time prior to launch (about 150 hr), is given in Figure 145.

2. Quality Assurance

Acceptance criteria for *Surveyor* flight materials and processes have been defined in a series of Materials and Processes Acceptance Requirement Specifications. They define the requirements for chemical and metallurgical acceptance testing and give supplemental information on such matters as sampling requirements, procurement, and handling and storage requirements.

To assure compliance with the applicable Quality Control System Specification, MIL-Q-9858, surveillance

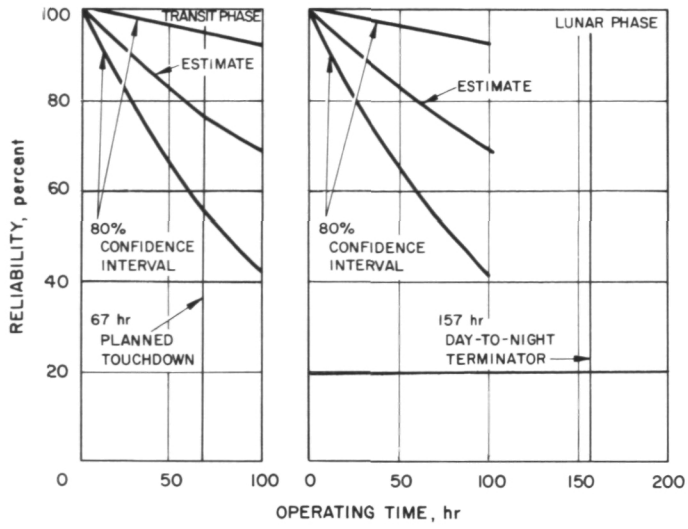

Fig. 145. Current spacecraft reliability estimate

Table 33. Mean reliability estimates for A-21 spacecraft

Identification	Flight and landing phase		Lunar phase	
	Previous	Current	Previous	Current
System	0.74	0.78	0.38	0.75
Command data and decoding	0.99	0.98	0.55	0.99
Data processing	0.99	0.99	0.99	0.87
Structures	0.97	0.97	0.80	0.94
Thermal controls	0.99	0.99	0.99	0.99
Telecommunications	0.99	0.98	0.99	0.99
Flight controls	0.90	0.94	—	—
Propulsion	0.89	0.94	—	—
Electrical power	0.96	0.96	0.89	0.92
Mechanisms	0.99	0.99	—	—

has been conducted with favorable conclusions at the following major subcontractors:

- Kearfott Division, General Precision Incorporated (gyros)
- The Electric Storage Battery Company (battery)
- Thiokol Chemical Corporation, Reaction Motors Division (vernier propulsion system)
- Thiokol Chemical Corporation, Elkton Division (retro-rocket engine)
- Heliotek Corporation (solar cell modules)
- Vector Manufacturing Corporation (subcarrier oscillator)
- Ryan Electronics Division of Ryan Aeronautical Corporation (radar altimeter and doppler velocity sensor)
- Consolidated Electrodynamics Corporation (tape recorder)
- National Waterlift Company (shock absorbers)
- Conax Corporation (boom pressure source)
- Santa Barbara Research Center (Canopus sensor)
- Menasco Manufacturing Company (gas tank)

Quality control plans have been received and approved from Electric Storage Battery, Kearfott, and Ryan Aeronautical. Receipt of a plan from Thiokol, Elkton, is imminent. Further detail has been requested from Thiokol, RMD, and National Waterlift.

A high-reliability component receiving inspection facility has been established for acceptance testing of *Surveyor* flight and T-21 components. Acceptance consists in 100% testing of selected characteristics, and comparison of Hughes to supplier data and statistical significance tests where appropriate. Components are individually packaged and identified with serial and lot numbers. This identification remains with the components until completion of module assembly and test, and thus provides for tracing of failures to lot origin.

3. System Test

a. T-2 recovery system. The T-2 recovery system design has been completed and purchase orders have been issued for all components.

Preliminary testing has been conducted on the air-bag portion of the recovery system. A total of 20 drops have been made, utilizing a single air-bag mounted on a test frame. (On T-2, the air-bag system will consist of three bags mounted to the spaceframe.) The test fixture to which the air-bag is attached is weighted with 60 lb of lead, which is roughly equivalent of one-third the total weight of the T-2 vehicle. The test fixture is attached to three guide wires and is dropped from a height of 6 ft 4 in. (Fig. 146). The requirements of the air-bag are that the landing shock of the vehicle be limited to 8 g or less at a landing velocity of 20 ft/sec and that the bag be reusable and easily repaired in the field. The air-bag tested measured 14×14 in.^{2} and 15 in. high and was fabricated from rubber-coated nylon.

A circular cutout of 4 in. in diameter on one side of the bag is fitted with a variable 4-in. orifice and a 4-in. pressure diaphragm. The diaphragm is fabricated from 0.005-in.-thick latex rubber. The air-bag was inflated to a pressure of 14.7 psia with CO_2 gas.

Fig. 146. Air-bag drop test

It was found that the pressure diaphragm contributed little to the over-all performance of the bag; however, it was of importance in bag inflation. The size of the variable orifice did contribute greatly to bag performance. The initial orifice tested was fabricated of the same material as the air-bag and in the shape of a truncated cone 6 in. long, 4 in. in diameter at the base and 2½ in. in diameter at the top. The 2½-in. top was further restricted by rubber bands sewn into the material. It was found that this orifice gave accelerations of 15 to 18 g and pressures of the order of 3 psia with considerable bounce of the test fixture. The orifice was then modified to a 4-in-diameter cylinder with one end restricted with rubber bands sewn into the material. This configuration gave accelerations of 7.7 to 8.2 g and pressures of 1.95 psia to 2.1 psia with negligible bounce.

An additional series of drops will be made with a single bag to test a 5-in.-diameter cylindrical orifice restricted at one end. It is expected that the accelerations and pressures will be further reduced.

Complete recovery system tests are scheduled to commence on August 1, 1962, with the T-2R test vehicle. This vehicle, consisting of a T-2 frame suitably ballasted and equipped with a stabilization chute, camera tracking aids, and complete recovery hardware, will go through a series of tests both at Hughes Aircraft Company and at AFMDC. These tests are planned to verify design and operation of the balloon system, the stabilization system, the recovery chute, and air-bag system. In addition, information concerning optical tracking accuracy will be obtained.

The T-2 command receiver, which will be utilized as an override for the event programmer in case of a required early recovery, has been received and unit evaluation has been initiated.

b. System test equipment assembly (STEA). Approximately 88% of the drawings for the basic bus portion of the STEA have been released for manufacturing. Fabrication is proceeding as planned with final checkout of racks scheduled to start on September 15, 1962. Vendor proposals for the *Surveyor* Launch Operations Trailer (SLOT) are presently being evaluated. The major elements of the STEA are discussed below.

STEA transmitter and receiver. Fabrication and testing of breadboard assemblies for the STEA transmitter and receiver has been completed.

Prototype assemblies have been fabricated and are presently undergoing tests before final assembly into the complete units. Prototype assemblies of the 60-mc IF amplifier, the 2.4-mc IF amplifier, the 2.4-mc phase detector chassis, and the 260- to 780-mc stripline multiplexer are shown in Figures 147, 148, 149, and 150. The breadboard model of the 5.2- to 260-mc multiplier is shown in Figure 151.

Changes made to allow greater flexibility of design include the following:

(1) Two 12½-in. panel assemblies will be used instead of four 7-in. assemblies.

(2) Only one voltage-controlled crystal oscillator will be contained in each receiver and the frequency will be changed by the use of crystal plug-in units rather than by switching.

(3) The 10, 20, and 30 kc IF filters will be of the lumped constant rather than the crystal lattice type.

Figures 152 and 153 are block diagrams of the present configuration of the receiver and transmitter (the previous designs were shown in Reference 11). A discus-

sion of the significant elements used in the transmitter and receiver modules follows.

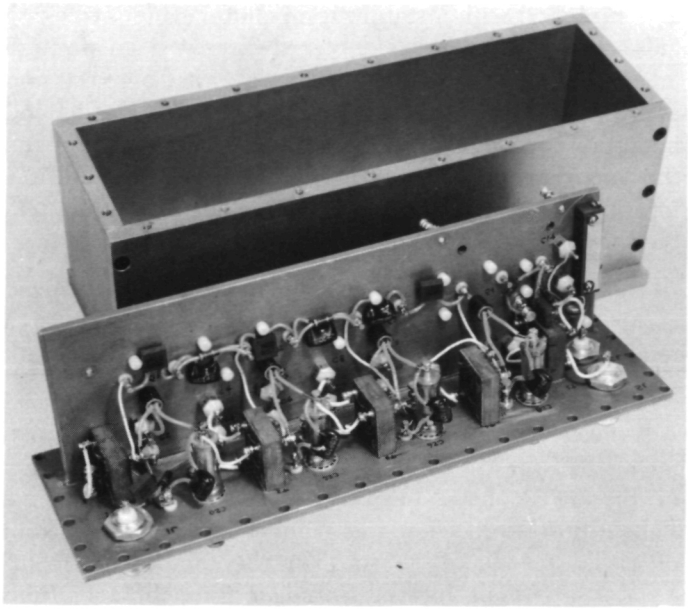

Fig. 147. 60-mc IF amplifier

Receiver: The measured noise figure of the mixer preamplifier is about 10 db maximum. The bandwidth is greater than 8 mc and the RF-to-IF gain is 25 db.

The 60-mc IF amplifier consists of four stages, synchronously tuned, with fixed broad band neutralization.

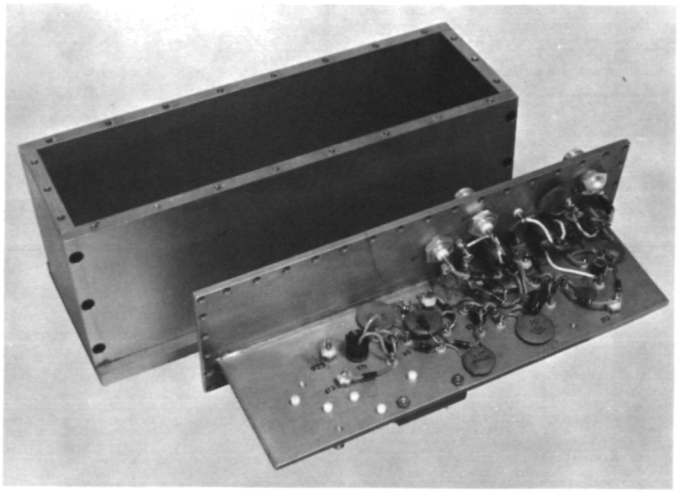

Fig. 148. 2.4-mc IF amplifier

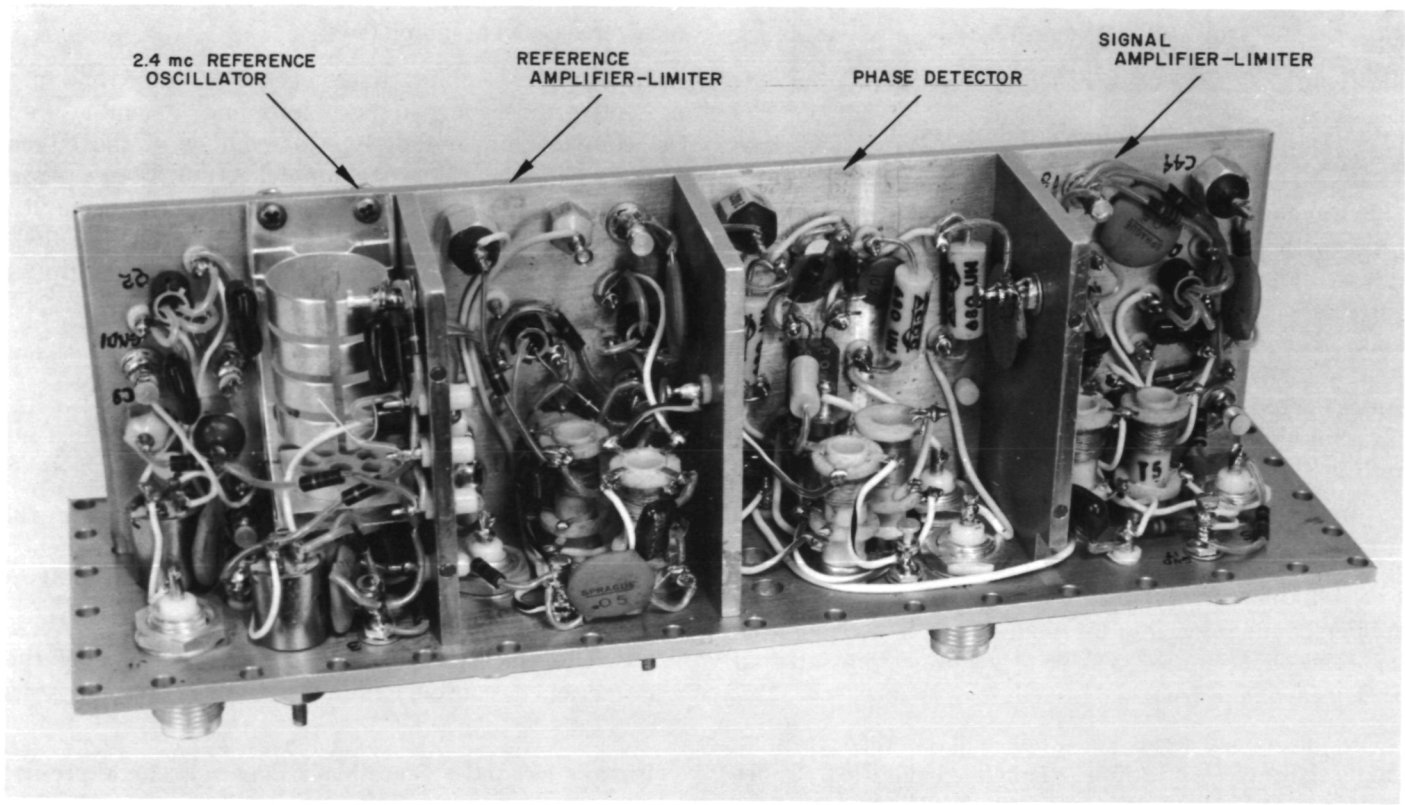

Fig. 149. 2.4-mc phase detector chassis

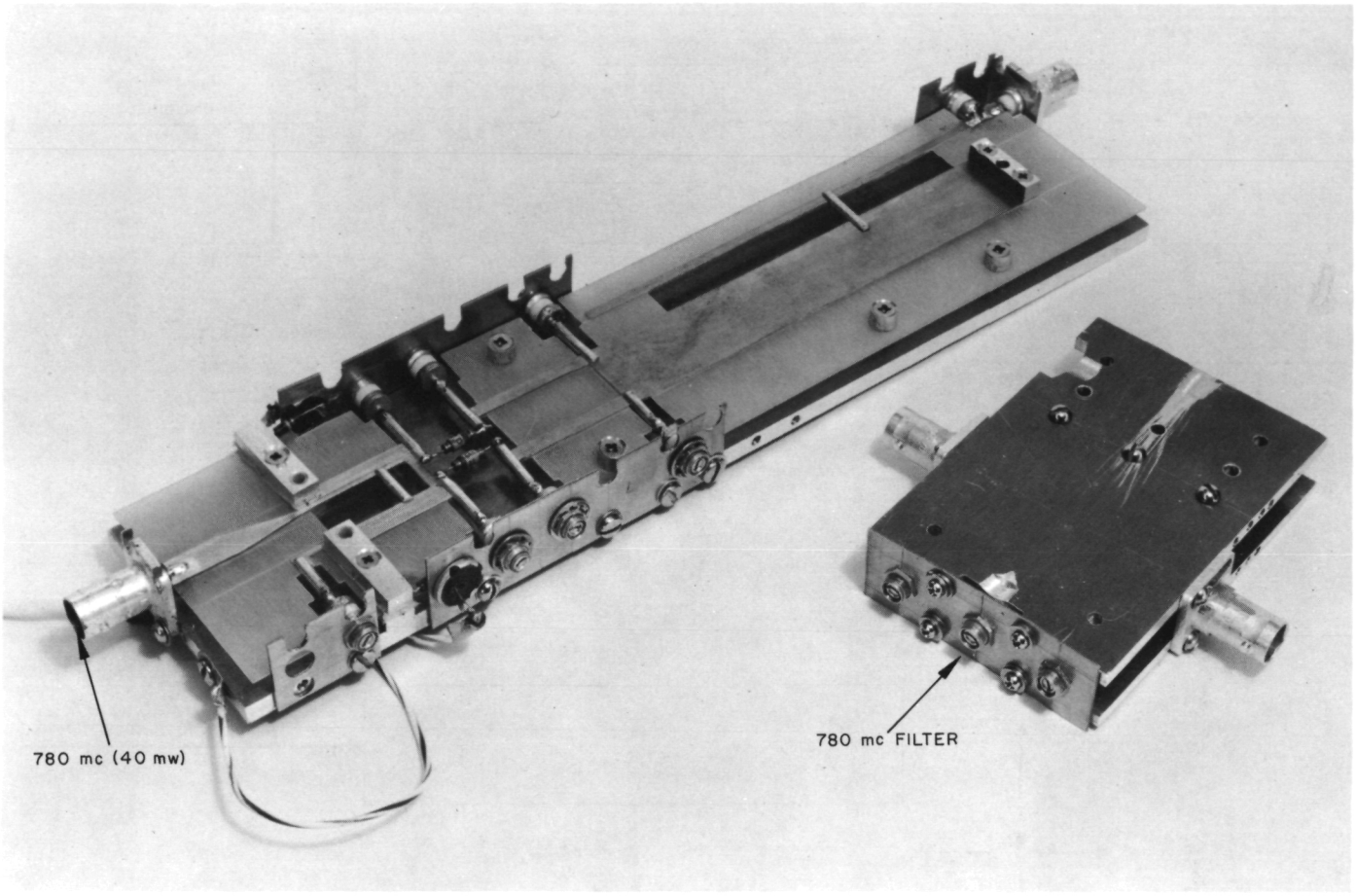

Fig. 150. Stripline multiplier and three-section filter

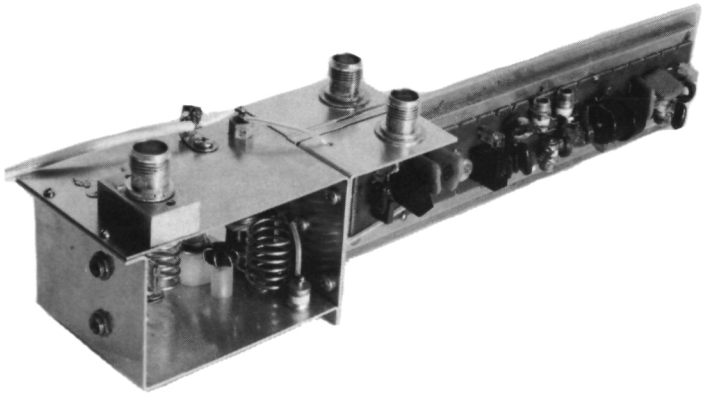

Fig. 151. 5.2- to 260-mc multiplier

The amplifier is designed to minimize the effects of individual transistors and the variation of their parameters on the passband and also to minimize the effect of AGC on the passband. AGC compensation is achieved by the use of diodes located to compensate for the change in the output admittances of the transistors with change in operating current. The first stage is operated at fixed bias to ensure minimum noise figure over the total operating range. The interstage winding ratio is 1:1.85 and the interstage Q is 5.6. This results in an over-all bandwidth of 10 mc and a maximum gain of about 50 db. The AGC circuit consists of a diode detector and a dc amplifier. The second and third stages are gain controlled. At the option of the operator, the amplifier can be operated in MANUAL gain mode.

The circuitry for the second mixer and local oscillator module includes a 20.8-mc crystal oscillator. The crystal is mounted in a "change-of-state" oven for temperature control. The second stage is an X3 multiplier which drives a buffer amplifier and filter. The spur levels at the output of the filter are down by at least 60 db from the 8 mw 62.4-mc local oscillator signal. The mixer consists of a pair of matched diodes in a balanced circuit. Conversion efficiency is about —12 db.

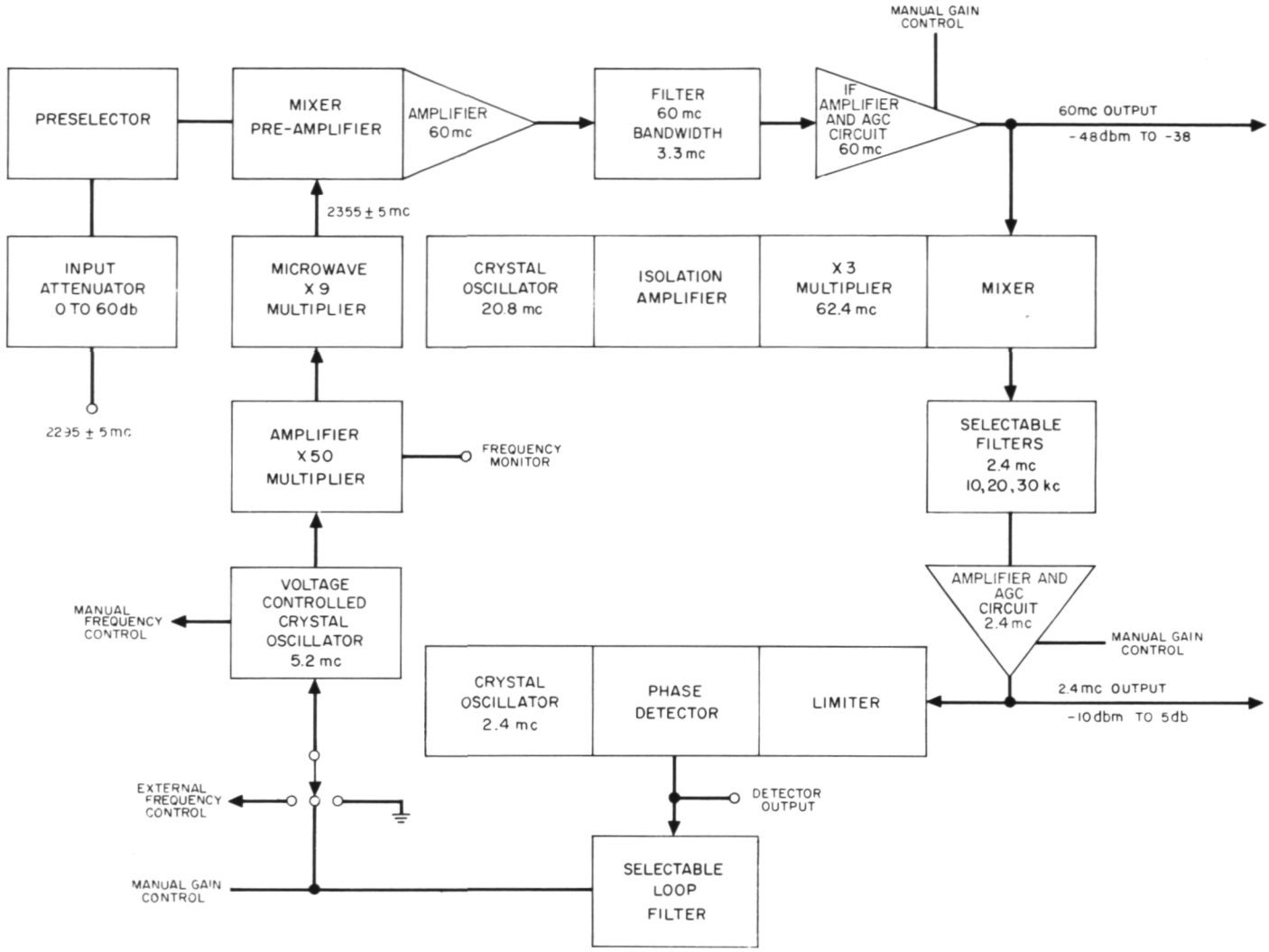

Fig. 152. UHF receiver for STEA

The 2.4-mc IF amplifier consists of two stages of gain and an AGC amplifier, diode detector, and dc amplifier stage (for AGC level). The total IF gain is 40 db with a 150-kc bandpass.

The phase detector module consists of the 2.4-mc reference oscillator, the phase detector, and the limiters. The 2.4-mc reference oscillator uses the same basic oscillator circuit that is used for the 20.8-mc oscillator in the second mixer module. The 2.4-mc signal from the IF amplifier is applied to the signal channel isolation amplifier and limiter. This circuit provides at least 10 db of gain margin to ensure limiting at the threshold sensitivity level. The phase detector produces an output that is proportional to the phase difference between the reference and signal channels.

The loop filter is designed to switch time constants and control the response of the locked loop to either 1000, 200, or 20 cps noise bandwidth. The output of the filter is used to drive the voltage-controlled oscillator and the input is derived from the phase detector.

In the voltage-controlled crystal oscillator (VCXO), the 5.2-mc signal is generated in the first stage. The amplifier section is a common base, parallel-tuned circuit, designed to operate Class A. The gain of this amplifier is 10 db. This amplifier also functions as a limiter to help maintain a constant output over a temperature range. A change in frequency is accomplished by changing the bias to the Varicaps. This will detune the loop from resonance, creating a phase shift which causes the crystal to be "pulled" from its resonant frequency.

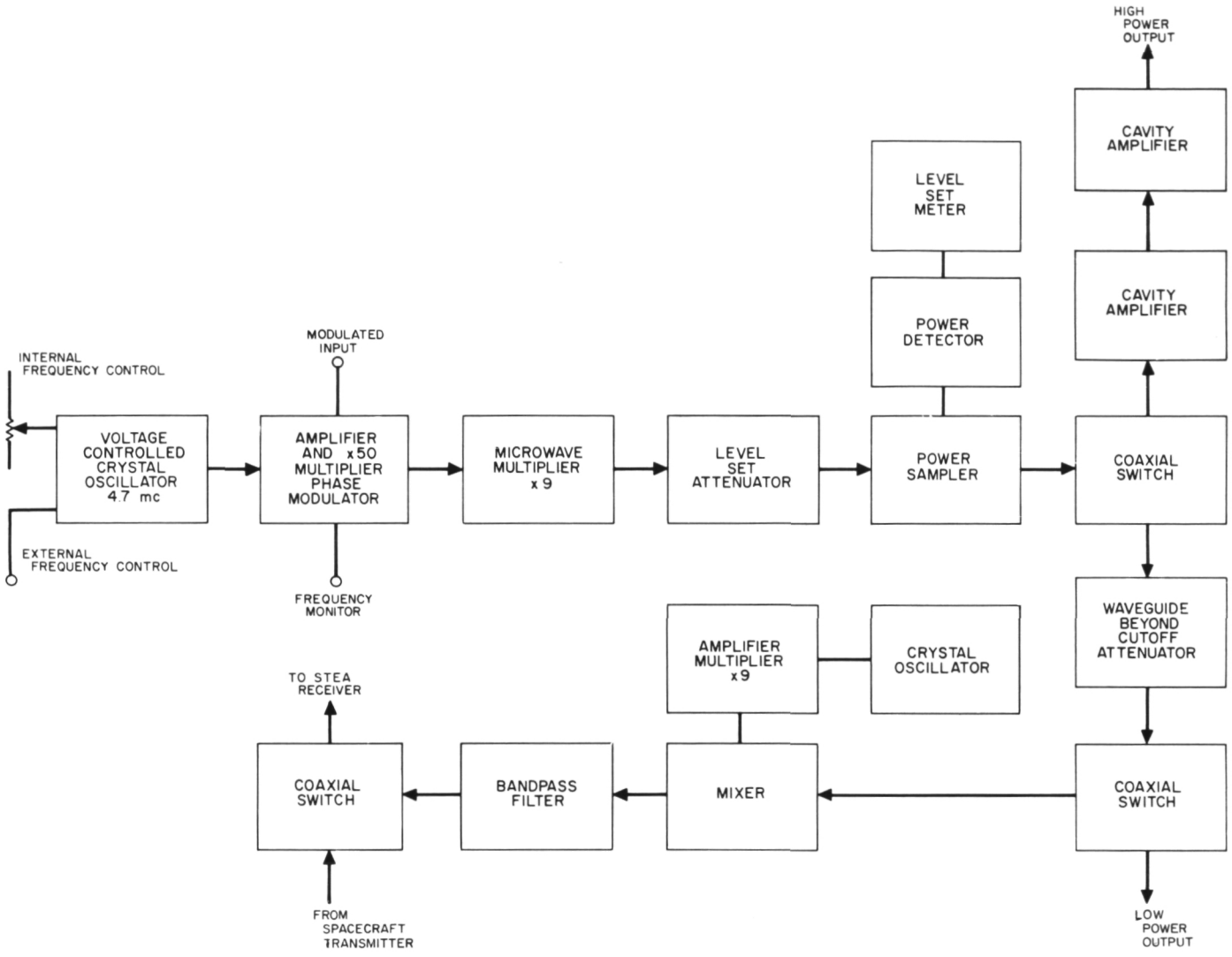

Fig. 153. UHF transmitter for STEA

The crystal used in this VCXO is a Midland unit inclosed in a glass envelope. The frequency stability is improved by inclosing the crystal in a "change-of-state" oven.

The 5.2-to-260-mc multiplier consists of two quintupler stages and one doubler. The first quintupler consists of a 5.2-mc amplifier, a varactor diode multiplier, and a filter section. The second stage is a 26-mc buffer amplifier. Together with the filter section, this amplifier and associated filter contribute to a flattening of the bandpass curve as well as providing additional attenuation of the 5.2-mc harmonics, bringing the spurious rejection to well over 90 db. The second quintupler consists of a buffer amplifier, a varactor diode, and filter section. This provides an output of 130 mc with a 6% bandpass. At this point, there is an output to drive a 130-mc frequency monitor amplifier to provide an output power of 100 mw at a frequency of 260 mc.

The 260-mc-to-780-mc multiplier is used to drive the final multiplier. This circuit utilizes two varactor diodes in a balanced strip-line circuit and, with 100 mw input, provides an output of 35 mw at 780 mc.

The 780-mc-to-2340-mc multiplier is a sealed version of the 260-to-780-mc multiplier using the same basic configuration, but with an additional output filter to reduce harmonic content. With 35 mw of drive available, the efficiency of 30% will result in a 10.5-mw output.

Transmitter: The basic VCXO and multiplier chain is the same in the transmitter as in the receiver, except that the crystal frequency is 4.7 mc and the subsequent

multiplier frequencies are changed accordingly. In addition, there is a high-power amplifier in the transmitter consisting of a pair of triode cavity amplifiers that increase the power output by 20 db.

An internal conversion capability has been incorporated into the transmitter, which will allow the phase jitter characteristics to be checked out without the need of an external receiver. This circuitry utilizes an extra mixer, a bandpass filter, oscillator and multiplier chain, and coaxial switching. The transmitter frequency is converted to match that of the STEA receiver to permit direct reception of the transmitted signal.

4. Telecommunications RF Test Rack

The telecommunications RF test rack design was completed and released for fabrication during the preceding report period. It consists of a three-bay test rack and the associated portable and auxiliary test equipment. This equipment is utilized for system tests on the spacecraft transmitters, receivers, transponders, antenna, and related items. The triple rack contains a test transmitter, test receiver, several items of commercial equipment, and assorted control and monitoring panels. A set of auxiliary RF test equipment to provide supplemental backup for the RF test rack includes RF attenuators, power loads, cables, antennas, and portable test equipment which can be moved up close to the spacecraft for troubleshooting purposes. The triple rack contains the following panel assemblies:

(1) Meter and control panel, to provide for control of power to the spacecraft RF subsystem and to provide indicators for telemetry outputs.

(2) UHF transmitter, to simulate the DSIF transmitter functions during spacecraft testing and mission simulation. Commands originated in the command and data handling console (CDC) will modulate the transmitter for the purpose of testing each spacecraft subsystem via the telemetry link and to command the spacecraft simulated mission sequence. The transmitter will also become the command link for launch checkout operations. Power output will be 1 w.

(3) UHF receiver, to simulate the DSIF receiver functions during spacecraft testing. This unit will receive signals from the spacecraft transmitter and provide frequency conversion and selectivity such that output IF signals of 60 mc at bandwidths of 3.3 mc (3 db), and 2.4 mc at bandwidths of 10, 20, and 30 kc, will be available at the CDC input for demodulation, decommutation, and analysis of transmitted data from the spacecraft. The receiver will also provide phase coherent detection of the spacecraft transmitter signal. This will facilitate frequency stability measurements and transponder evaluation.

(4) Subsystem decoder output simulator, to simulate the output of the RF subsystem decoder and thus provide direct hardline command capability to the RF subsystems on the spacecraft. This will allow parallel testing of the RF and command functions.

(5) RF load panel, contains directional couplers, RF loads, attenuators, coaxial switching, and an RF power meter to provide proper signal distribution and loading of the spacecraft and STEA receiver inputs and transmitter outputs.

(6) RF power meter, HP Type 431A and thermistor mount, to measure RF output power of the spacecraft transmitters and the transmitter VCXO. The thermistor mount is the detector for the power meter. This item is also used to calibrate the STEA transmitter output.

(7) Function generator, HP Type 202A, to sweep the STEA transmitter frequency for transponder tests and to be used as a modulation source for spacecraft transmitter tests such as modulation index, bandwidth, linearity, and phase shift.

(8) Audio oscillator, HP Type 200CD, to provide extended range tests of the spacecraft transmitter modulation capabilities up to 220 kc.

(9) Electronic counter, CMC Type 727, to permit measurement of the spacecraft transmitter and receiver frequencies as well as frequencies of the STEA transmitter and receiver. In addition, it will be used when accurate measurement of modulation frequencies and external interfering RF signals is required.

(10) Signal access panel, to serve as a patchboard for connections between spacecraft circuitry and STEA equipment and between CDC outputs and STEA equipment during system tests.

(11) Oscilloscope, Tektronix Type RM 503, to provide visual observation of spacecraft transmitter and receiver signal waveforms. Frequency response, phase shift, and signal characteristics can be determined.

(12) VTVM panel, contains HP Type 412A dc and HP Type 400H ac vacuum tube voltmeters to

assist in verifying signal levels, power levels, and telemetry calibrations.

(13) Intercom panel, to provide for communication between the RF test rack and the test director or any other test position required during system checkout.

(14) Writing shelf, for use in tabulating test data during test activities.

(15) Digital recorder, HP Type 562 AR, to produce a printed record of frequency measurements during frequency and stability checks. This is particularly useful during short-term drift tests where the interval of measurement is only 1 sec. During prelaunch and postlaunch operations, the spacecraft transmitter frequency is to be provided to JPL with a time lag of 5 min maximum. This information will be taken from the printed output of the frequency counter and converted to actual spacecraft frequency by calculation. The last six significant figures of frequency will be recorded, plus a six-column time code.

(16) Blower, McLean Type 2EB412E, to provide forced air circulation at room temperature and thus prevent overheating of the equipment in the rack. Air pressure interlock is provided to prevent equipment operation in the absence of blower power.

(17) Timer panel, contains the running time indicators, on-off cycle counters, and associated circuitry required to maintain a running log of spacecraft equipment operating time and on-off cycles.

(18) UHF signal generator, HP Type 616B, to be used as a signal source for VSWR and attenuation and bandwidth measurements on the antennas, diplexers, and transmission system, in addition to providing bandwidth and spurious response measurements of the spacecraft and STEA receivers and identification of spurious responses in the La Voie spectrum analyzer.

(19) Spectrum analyzer, La Voie Type LA-18M, required to measure the spectrum purity of the spacecraft transmitter by observing the level of harmonic and other spurious signal outputs. The spectrum analyzer will also be used to evaluate and measure FM and PM characteristics of the spacecraft transmitter and for gross comparative tests of antenna gains and pattern.

The telecommunications portable RF test set will be used to supplement the measurement capability of the telecommunications RF test rack. Certain tests will be performed with greater accuracy and ease when the portable equipment is tied more closely to the spacecraft electronics. In particular, microwave measurements are subject to less error if long coaxial lines are avoided. Generally, this equipment will be used for microwave measurements on RF power, receiver noise figure, VSWR, isolation, attenuation, and insertion loss. Functional descriptions for each item are as follows:

(1) Directional coupler, Narda Type 3003-10, for sampling the RF signal when measurements of modulation bandwidth, phase shift, and sensitivity are desired. Also, used in spectrum analysis, power output, and carrier noise tests. In general, the coupler will be used whenever RF energy is sampled by any item of equipment for test purposes.

(2) Dummy load, Sierra 160-20MN, to properly terminate the output of the spacecraft transmitter in either low- or high-power mode of operation with spacecraft antennas disconnected.

(3) Coaxial attenuators, Empire AT-50 series, to provide 3, 6, 10, and 20 db of attenuation as well as circuit isolation for such items of equipment as the power meter and the UHF signal generator, HP-616BR, when performing microwave measurements of power, VSWR, and insertion loss.

(4) VHF signal generator, HP-606A, required for investigation of spurious responses in spacecraft receivers, spectrum analyzer, and STEA receivers and for measurement of receiver IF characteristics and calibration of the FM discriminators.

(5) Noise figure meter, HP-340B and UHF Noise Source, HP-349A, to measure the input noise figure of the spacecraft receivers, a basic test of receiver performance. It will operate at an IF input frequency of 9.6 mc for measurement of spacecraft receiver noise figure and at 60 mc for measurement of STEA receiver noise figure.

(6) Coaxial termination, HP-908A, to accurately load and match the item under test when VSWR measurements are made on coaxial switches, diplexers, and transmission lines.

(7) Clip-on ammeter, HP Type 428B, used for monitoring direct currents whenever desirable to do so without interrupting the circuit.

(8) Low-pass filter, Microlab LA-30N, inserted between the signal source and the item under test, when performing VSWR measurements, error due to harmonics and spurious signals will be minimized. Attenuation at the second harmonic of the spacecraft transmitting frequency is > 20 db.

(9) Standing-wave indicator, HP-415B, used for slotted line techniques in performing VSWR and insertion loss measurements. It provides a highly sensitive tuned voltmeter having square low calibration over a wide operating level. This device is connected to the output of the probe detector of the slotted line.

(10) Slotted line, HP-805C, used to sample the standing-wave pattern of portions of the subsystem during VSWR and insertion loss measurements, an activity of "unit" analysis.

(11) Double stub tuner, Don-Lan Electronics, S-100, to improve the accuracy of the slotted line technique when performing insertion loss measurements by tuning out residual reactance on the line.

(12) Bolometer mount, Narda 561 NF and Element, Narda N603, a final detector of the square-wave modulation introduced on the "flattened" line during insertion loss measurements. The sensing device for the detector is the standing-wave indicator, HP-415B.

(13) Standard gain horn, Scientific Atlanta Type SGH-1.7, has a polarized feed with a 12-in. reflector. It is used in making relative gain tests between the spacecraft omnidirectional and planar array antennas and in providing an over-the-air link to the spacecraft during tests.

(14) Multimeter, ac/dc volt-ohm-milliammeter, Triplett Type 630A, used as a general-purpose portable test instrument around the spacecraft and STEA.

5. STEA Vernier Engine Checkout Cart

All vernier propulsion systems will undergo one acceptance test firing at Thiokol, RMD, after installation on the spaceframe. From this time until the actual midcourse correction maneuver, no live firings will be conducted. It has become necessary to devise qualitative and quasi-quantitative methods for verifying proper operation of the vernier engine system during the various phases of system test.

In the vernier propulsion system, the propellants are expelled from collapsible bladders surrounded by helium gas at a constant pressure. Thrust is regulated by controlling fluid flow through throttle valves and is initiated and terminated by solenoid-actuated propellant valves. It is apparent that a high degree of confidence in vernier engine operation can be obtained by monitoring the fluid flow characteristics of the system under known commands. This will be accomplished in system test using dry nitrogen gas as the flow medium. Leakage checks will be performed by introducing helium gas into the system in accordance with certain isolation schedules and using a helium-sensitive apparatus for leak detection. This method corresponds with RMD procedures and will facilitate the correlation of known leakage rates with design specifications.

Propellant tankage has been designed with very low margins of safety to minimize weight. Operating pressures will be maintained well below one-half design pressures to keep the system safe and preclude the use of special barricades in system test areas.

Figure 154 shows the vernier propulsion system with the test equipment connected. It is important that the bladders in the fuel and oxidizer tanks remain distended during all test routines since it has been found that collapsing them about their standpipes causes perforations and subsequent leaks. A special check valve assembly will be used as a "fuse" to permit reverse flow as the collapsing pressure approaches the bladder internal pressure.

Commercially procured bottles of nitrogen and helium will be used as the gas source. Gas flow meters in the main propellant supply lines will monitor oxidizer-to-fuel ratio. Flow meters are also installed in the exhaust line from each engine. Using RMD calibration data, a correlation can be obtained between exhaust gas flow and throttle valve opening. This, in turn, may be interpreted as a thrust level. Maximum flow with the fully open throttle valve is presently estimated at 12 standard ft^3/min per valve with 200 lb/$in.^2$ supply pressure. Special test access adapters will permit the introduction of control signals to the throttle and propellant valves from a portable checkout console as well as from flight control electronics.

Throttle valve actuations are very limited by reliability considerations. Accordingly, dummy loads (variable resistors) are used for all preliminary operations such as calibration and gross error checks. These may be set to the measured resistance of the throttle valve coils. The electrical design will also permit group testing of the flight control electronics and the vernier propulsion

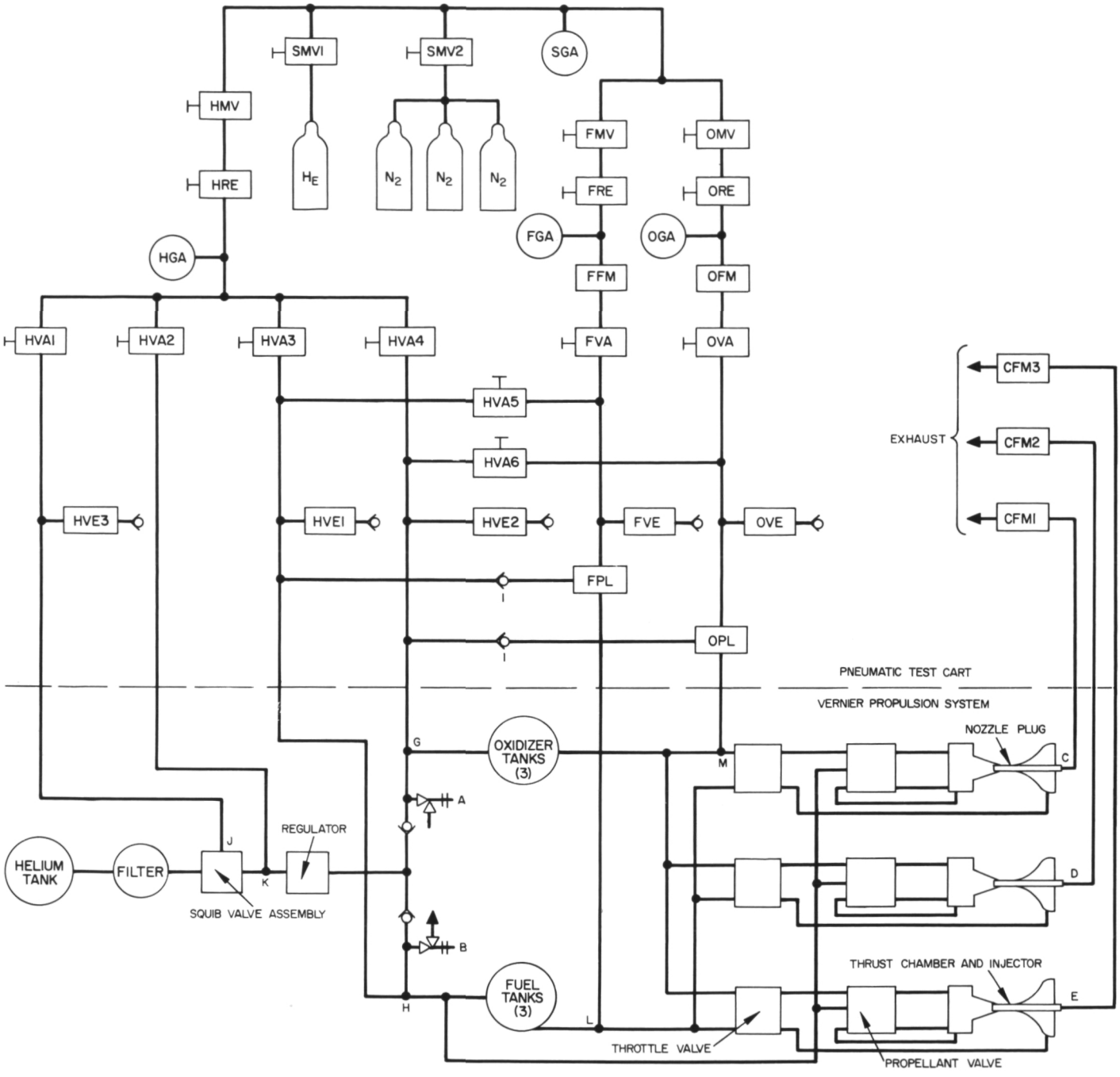

VALVE AND FITTING CODE

FIRST LETTER: SYSTEM		SECOND TWO LETTERS: COMPONENT	
F	FUEL	MV	MAIN VALVE, ON-OFF
H	HELIUM	VA	VALVE, ON-OFF
N	NITROGEN	VE	VALVE, VENT WITH 2 psi CHECK VALVE
O	OXIDIZER	RE	REGULATOR
C	COMBINATION FUEL-OXIDIZER	GA	GAGE, PRESSURE
S	SUPPLY (HE OR N_2)	FL	FILTER
		FM	FLOW METER
		PL	PLENUM CHAMBER

NUMBER SUFFIX COMPLETES CODE WHEN MORE THAN ONE COMPONENT OF PARTICULAR TYPE IS USED IN SAME SYSTEM.

Fig. 154. Vernier propulsion test system

system to progress simultaneously and independently. Vernier engine group testing will involve the checking of the throttle valves at their extremes (full, open or full, closed) and at any intermediate position. Control circuitry is identical to that of the flight control system and includes an oscillator for introducing 400-cycle dither for smoother valve operation.

Propellant valve actuations are not as severely limited as throttle valve cycling. Dummy loads are also used in this circuitry to permit the segregation of group testing, as described above. The electrical design will permit valve checkout in either of its extreme positions.

All electrical and pneumatic components of the vernier engine checkout equipment will be mounted on a cart. The cart will consist of a rigid frame, towing bar, brakes, four wheels with pneumatic tires, and a suspension system, the latter being an ICC requirement for transporting high-pressure gas bottles. The use of a cart will facilitate the sharing of checkout equipment among the various system test areas.

CONFIDENTIAL

L. Mission Operations

1. Command and Data Handling Console

The prototype command and data handling console (CDC) has been assembled and preliminary systems tests are in progress. The television monitor and photo recorder, after being subjected to the preliminary system tests, was returned to the subcontractor temporarily for completion of subystem tests. As system tests are completed on the major CDC systems, they are being subjected to RF interference tests in the environmental laboratories to determine the radiated and conducted noise spectrums generated and the noise susceptibility. The complete CDC (equipment racks and operating console) is shown in Figure 155.

a. Command generator. The command generator is shown in Figure 156 in a position extended from the console and tilted up 90 deg. The unit is of modular construction and is divided into two major portions. The upper portion is the main encoder and its associated circuits and the lower portion, which pivots downward, contains the auxiliary encoder and associated circuits. The encoders are independent in their operation. Access to the circuit cards can be obtained from either end (card or connector) for ease of maintenance. Adequate space has been provided for further expansion.

b. Time and digital data processing. All binary coded decimal and binary data are brought to the system display patch board from both decommutators. By using

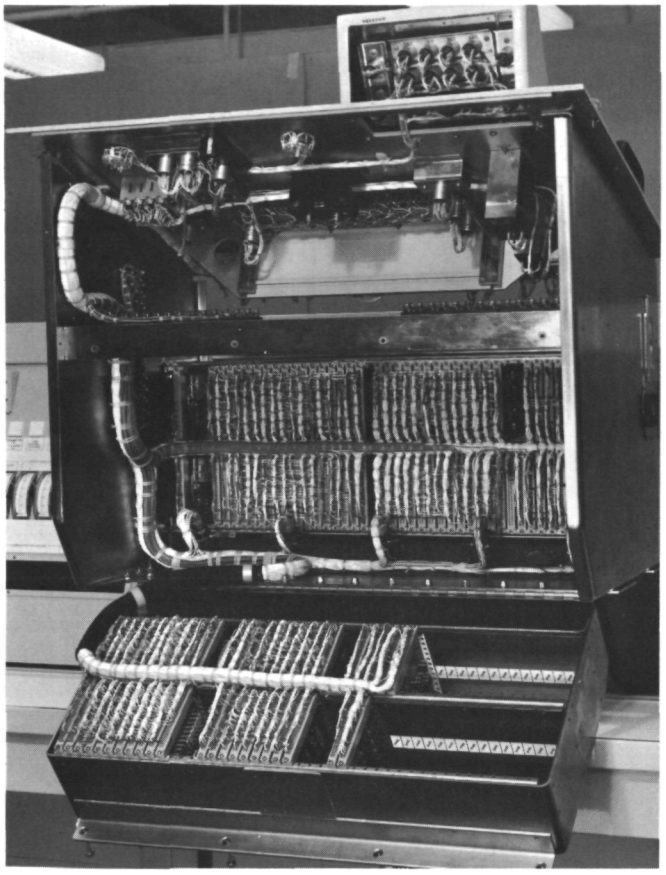

Fig. 156. CDC command generator (bottom view)

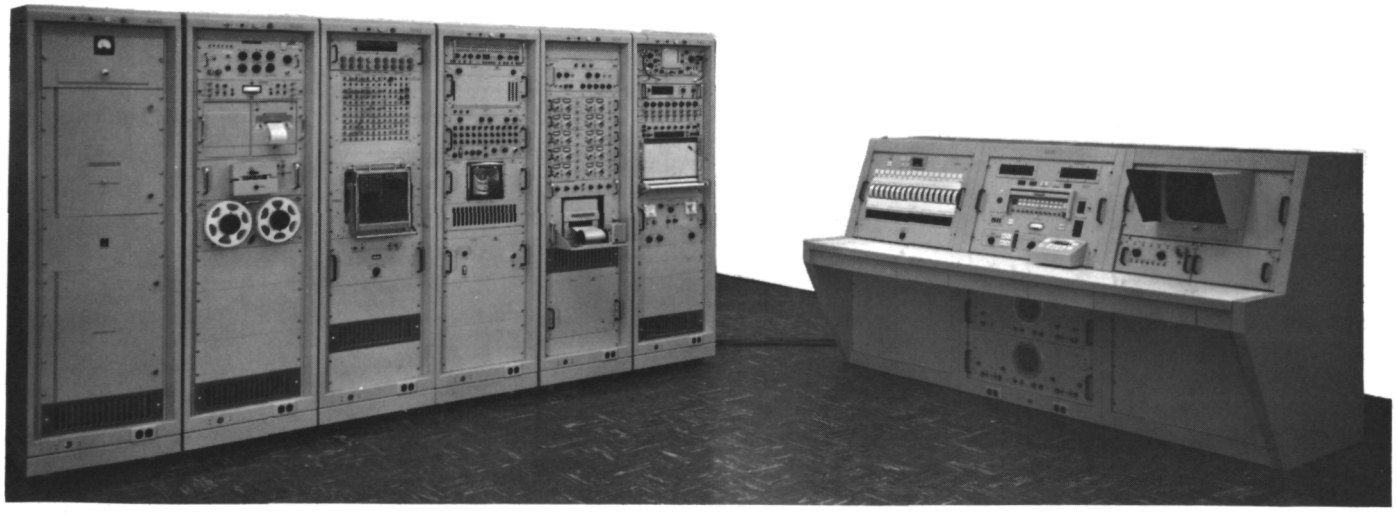

Fig. 155. Prototype command and data handling console

CONFIDENTIAL

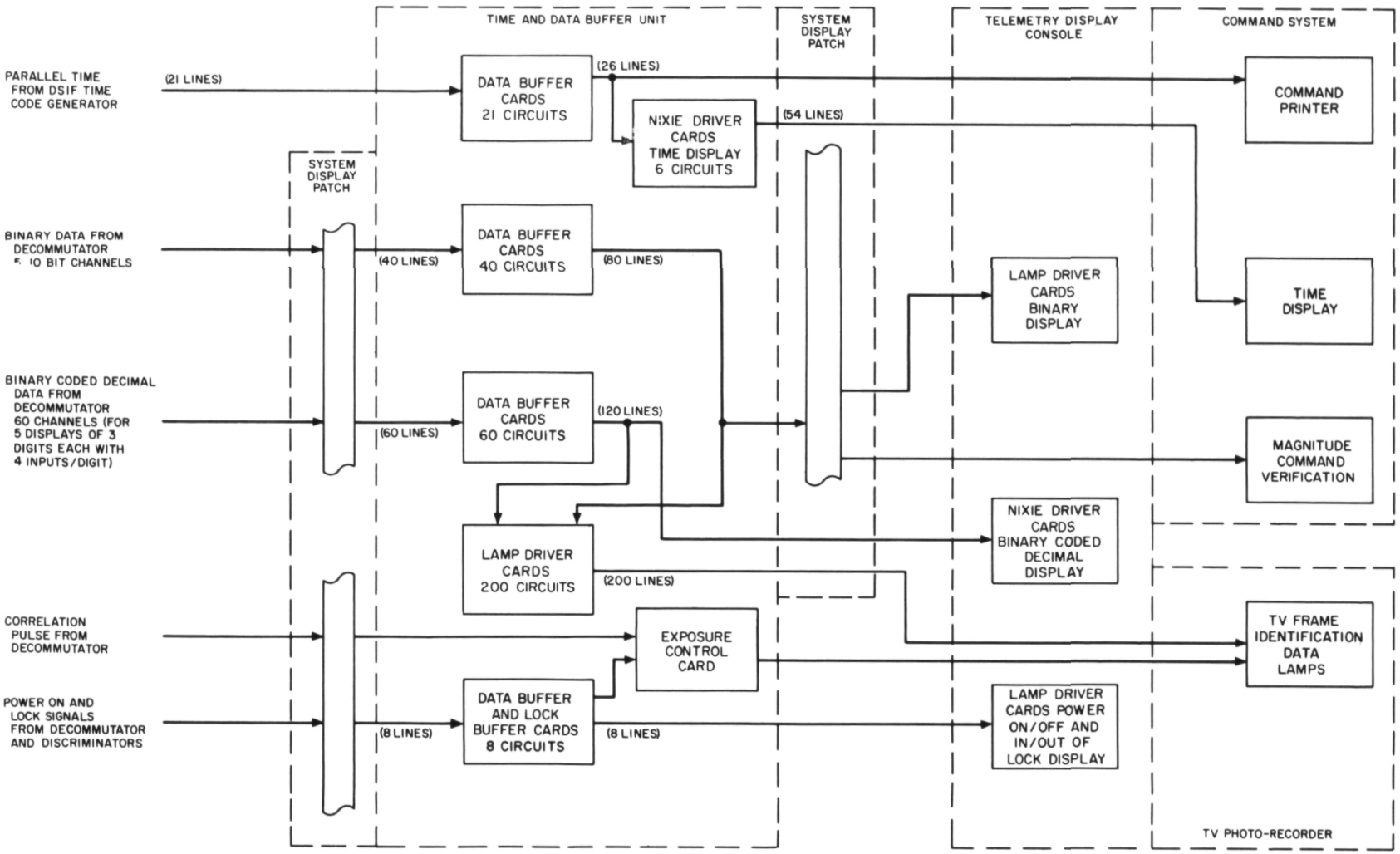

Fig. 157. CDC time and data processing

CONFIDENTIAL

CONFIDENTIAL

the appropriate preprogrammed patch board, the outputs of the desired on-line decommutators are connected to the time and data buffer unit for further processing. This unit processes the decommutated and station time digital data to produce low-impedance data complements suitable for driving the associated displays and matrices. The unit also controls the TV frame identification data lamp recording function. The processing of time codes and digital data is described in the paragraphs below and is shown in Figure 157.

Three basic circuits are used in the time and data buffer unit and telemetry display console. The first circuit is a data buffer amplifier/inverter used in the data buffer cards to lower the impedance and create the complement of the digital data. The second circuit is an "AND" gate, lamp driver circuit used in the lamp driver cards to allow the decoding of data and the turning on of incandescent lamps. The third circuit is a binary coded decimal (BCD) to decimal converting matrix and a driver for the various Nixie readouts.

The station time in the form of single-ended BCD logic is brought to the time and data buffer unit from the DSIF time code generator. Here the complement is created and the impedance is lowered. The BCD code is converted to decimal and is used to drive visual readouts on the front of the time and data buffer unit and command console. The buffered BCD is also connected to the command printer where a record is made of commands transmitted and the exact time when they were transmitted. The time is displayed and recorded in hours, minutes, and seconds.

Both the BCD and binary data outputs of the decommutator are brought through the system display patch board to the buffer unit where the complement is created and the impedance is lowered. The buffered BCD and complement are then used to drive a BCD to decimal conversion matrix and Nixie driver circuit for data display on the telemetry display console.

The buffered binary data and complement are returned to the system display patch board where by use of preprogrammed patch boards the binary data are appropriately routed to lamp drivers for decoding. The lamp drivers in the time and data buffer unit decode the BCD and binary data to create an appropriate lamp pattern for recording as part of the TV frame identification data on the TV photorecorder film. The lamp drivers in the telemetry display console decode the binary data into appropriate lamp patterns for display on the 16 telemetry console binary lamps.

One other noteworthy feature concerning the time and data buffer unit is that each separate function is individually fused. For instance, if there is a failure in the TV lamp driver area, all other functions will continue to operate.

Consolidation of so much of the digital processing circuitry into a single unit resulted in approximately 740 input and output connections to be brought to the rear of a unit only 7 in. high. To enable the unit to be withdrawn for maintenance and troubleshooting there was the problem of either using jumper cable or having long multiple-wire twisted cables which are bulky and only semiflexible. An alternate approach has been adopted using contour cables which enable the unit to be withdrawn and rotated while operating. As shown in Figure 158, the time and buffer unit is completely withdrawn from the rack and is tilted for access to the bottom of the unit. The cables are flexible and retract easily into the rack when the unit is inserted. Tension springs will be applied to retract the cables and hold them toward the rear of the rack out of the way.

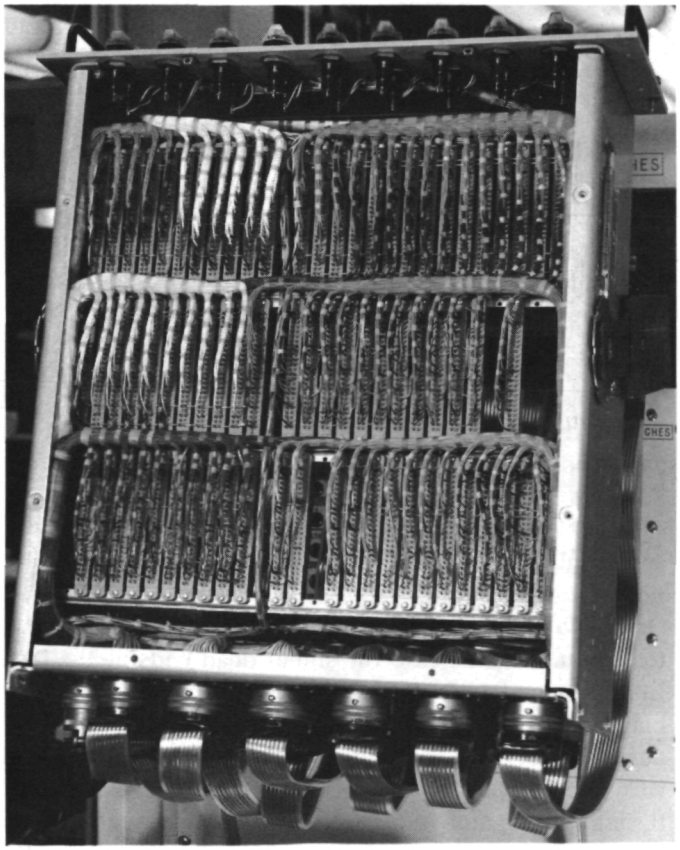

Fig. 158. CDC time and buffer unit (bottom view)

c. System patching and interconnections. The primary design objectives for the CDC patching and interconnection arrangements are:

(1) Flexibility of system configuration.

(2) Reliability of interconnections.

(3) Ease of switching to on-line spares.

(4) Ease of system test.

In large measure these objectives have been achieved in the design. There are three patch panels utilized in the CDC. The first is the decommutator patch board described in a previous bi-monthly summary. The second is the system display patch board, and the third is the telemetry data patch panel. The latter two, which are pictured in Figure 159, will be functionally described here.

The system display patch board is a high-density board containing 1280 contacts of which approximately 750 are used. Its main purpose is to switch between the 180 output lines of each of the two on-line decommutators. Switching from the active decommutator to the spare is easily done by removing one prewired patch board and inserting another. This method of switching results in higher reliability than using a multipole switch or relays and allows greater system flexibility. An example of the flexibility of the patch is that part of the telemetry displays can be driven from one decommutator and the rest from the No. 2 decommutator in the event that two pulse-code-modulated telemetry signals are being received simultaneously. The secondary function is to allow the changing of telemetry displays on the console during television data reception without altering the format of frame identification data being recorded on the photographic film.

The telemetry display patch panel is a low-density panel containing a field of 126 telephone-type jacks. The two main functions of this panel are to provide most of the telemetry system test points at a centralized point and to allow rerouting of certain telemetry signals, particularly during station routine checkout and calibration. One type of jack on the panel is used strictly for monitoring, and in this case the signal dead-ends at the jack. In the second type of jack, the signal passes through a pair of normally closed contacts on the jack to its normal destination. When a plug is inserted into this type of jack, the contacts are opened and the signal is rerouted through the patch cord as desired. Two switches are provided on the panel for selecting the inputs to the discriminators and to the television monitoring and photographic recording unit. When these switches are in positions other than "operate," a red "no data" lamp is lighted as a warning to the operator.

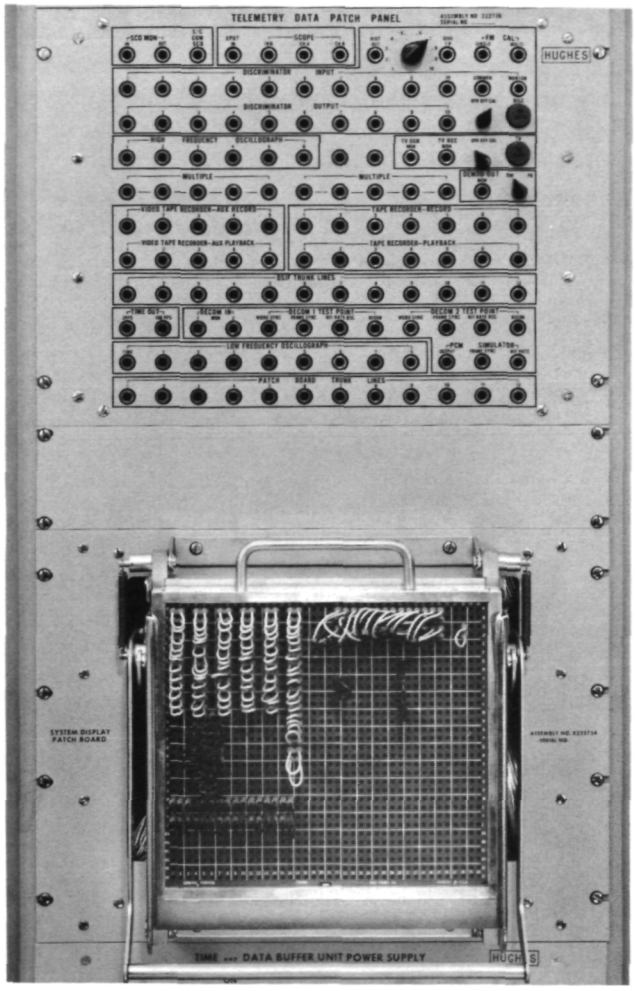

Fig. 159. CDC telemetry data patch panel and system display patchboard

The bulk of the system interconnections pass through Rack 7 of the CDC. (This rack contains the patch panels described above and the time and data buffer unit.) Interconnecting cables therefore proceed from Rack 7 to the other racks of the system directly and are so laid out that no branches are necessary. This simplifies routing and replacement and results in higher reliability. Within the racks, the same philosophy (no branches in cables) is used to the maximum extent practicable.

d. Radio frequency interference. CDC equipment must be capable of meeting two separate radio frequency interference (RFI) requirements in order to fulfill its operational requirements as a part of the DSIF network

and as a part of the system test equipment assembly (STEA) installation.

JPL Specification No. 8907 was established as the RFI guide for the CDC equipment as installed at the DSIF in order to ensure that no interference with existing DSIF S-band equipment resulted. A level of 3 mv at critical DSIF receiver frequencies was established as the goal. Hughes Aircraft Company Specification No. 226100 has been established as the guide for the CDC in a STEA configuration to ensure no interference with the STEA equipment or the spacecraft being tested. In either of the above installations, the CDC must not be susceptible to the ambient RFI environment.

The CDC has been examined for areas of possible RFI improvement and a plan developed for RFI compatibility with either a DSIF or STEA installation. The two main areas of expected improvement will be due to modification of equipment racks and the addition of ac power line filtering. Some of the more important rack modifications being performed are as follows:

(1) All rack panels and the mating surface of the rack will be spot faced to bare metal at point of attachment.

(2) Threaded holes for mounting hardware will be cleaned of paint to bare metal.

(3) The amount of mounting hardware will be increased where necessary to ensure minimum mating gaps.

(4) Grounding straps will be installed over all rack door hinges.

(5) Knife edges and mating hardware will be installed in three places on latch side of rack door.

(6) Ground studs will be installed in racks to ensure equipment chassis grounds.

(7) All equipment ground studs will be tied together at one common system ground point. This point is to be grounded to DSIF ground plane or STEA system ground point.

(8) Front panels of units will be grounded to the racks by methods compatible with the construction of the units.

(9) AC power line filtering will be installed in all equipment racks as close as possible to point of entry, using solid conduit.

In addition to the above, optimum techniques are being adhered to in wiring the CDC system as follows:

(1) AC neutral wires will be twisted and routed with all ac prime power leads. The ac neutral will be common with the other ground points at the system ground point only.

(2) All wire shields will be connected to ground at the sending end only, to minimize ground loops. All wire shields will be carried through all connectors to ensure shield continuity.

(3) Coaxial shields at panel feed-throughs will be insulated from ground to prevent unwanted ground loops and fed through for continuity.

Preliminary RFI test results have been obtained on Rack 6 which contains the pulse-code-modulation (PCM) simulator and the decommutator units (i.e., PCM input drawer, programmer, power supply and analog outputs, and the rack blower). The high-frequency oscillograph (Visicorder) was tested separately as a unit. In each of the above cases, RFI test results for both radiated and conducted noise indicate levels well below minimums for DSIF requirements. STEA requirements were exceeded in the 1 to 15 mc broad-band radiated noise test and this will be investigated further. The remaining racks of equipment are to be tested upon completion of functional tests and upon availability of the test facilities.

e. CDC demodulator. The CDC demodulator accepts IF signals from the DSIF receiver and recovers the video signals generated in the spacecraft. The demodulator operates in one of four modes: (1) normal television and wide-band telemetry, (2) phase modulation, (3) narrow-band telemetry, and (4) emergency television. In the first mode, a wide-band frequency discriminator demodulates the first signal. The second mode is used during transponder operation when the DSIF receiver is tracking the received signal. In this mode, a phase tracking loop in the demodulator also tracks the received carrier and the video is obtained from the output of the phase detector. The other two modes differ only in bandwidth. The IF signal is obtained from the narrow-band output of the DSIF receiver and is demodulated with a frequency discriminator. For emergency television, a crystal filter is inserted in the circuit to provide further narrowing of the predetection bandwidth.

Unit test of the prototype unit has been completed except for RFI tests which will be run in the near future. Components have been ordered for four more units, and when the drawings are completed in June, shop fabrication of these units will begin.

CONFIDENTIAL

2. *Surveyor Spacecraft Simulator*

A system design study for the *Surveyor* spacecraft simulator (SSS) has resulted in a configuration requiring a simpler equipment complement than previously specified while retaining all of the important operational features.

Figure 160 is the block diagram of the equipment. A number of actual spacecraft units will be used where simulation would be difficult and where a large portion of the capability of each unit can be utilized. Some of these units are employed in incomplete form where part of the unit is performing functions which are not necessary to the system operation and can be conveniently deleted.

Other portions of the simulator perform functions which can be effectively implemented with purchased components. Notable among these are several microwave components, built-in test instruments, and power supplies. These components have been carefully selected from product lines of proved capability and quality.

The final group of items in Figure 160 comprise the general-purpose subsystem simulator (GPSS), command readout and entry, and the patch panel. Comparison with the previous specification indicates that the actual-to-simulated spacecraft equipment interface has been moved in the latest configuration to a point which generally divides the system between the auxiliaries and the central command decoding and signal-processing units. This change produces a number of significant advantages:

1) In closed-loop operation, signals supplied to the CDC via the DSIF are identical in all salient respects to those which would be supplied by the spacecraft. This essentially unreduced capability can be effected with a radically reduced equipment complement. For example, subsystem command decoding need be accomplished only once, instead of once for each of the numerous subsystems. This same decoding logic can be used fairly simply to implement a number of functions, such as gating the various subcarrier oscillators (SCOs) to produce signals typical of those carrying engineering or scientific data, driving the indicating devices of the command readout, and handling magnitude commands in a manner typical of the spacecraft.

2) Additional useful features, such as the facility for entering commands at the simulator, can be provided inexpensively.

3) In addition to the cost savings resulting from the reduction of sheer equipment bulk, an opportunity for realizing further savings is evident. Since the special simulation equipment need not be identical to that of the spacecraft, it can be composed of elements which will operate effectively in the simulator environment, but which could not survive the severe environment of the spacecraft.

4) Spares provisioning for the simulator in the field can provide backup capability for a much greater functional portion of the system and at lower cost.

5) Late availability of some items of spacecraft hardware (experimental auxiliaries) would have required that a simulator of the previous configuration include simulated individual spacecraft units (at a prohibitive cost) or sacrifice some of the required functional capability. The new configuration ensures the complete capability, regardless of the availability of spacecraft auxiliaries.

6) The much simpler system of this simulator will improve reliability and simplify troubleshooting in the field.

7) The new simulator configuration is more flexible and can thus be used with minor modifications to simulate additional spacecraft functions.

a. RF components. The RF chain of the *Surveyor* spacecraft simulator will consist of basic bus transmitter and diplexer and a basic bus command receiver with transponder interconnections which are identical to those incorporated in the spacecraft. The transmitter output will be limited to 0.1 w, thereby eliminating a need for the traveling-wave tube power amplifier.

In conjunction with the basic bus items mentioned, additional RF components will be provided. A 10-db directional coupler will be provided on the output of the transmitter so that an RF wattmeter may be connected to monitor continually the power output of the transmitter. A variable attenuator (0 – 70 db) in series with the output will simulate transmission at lunar ranges to the DSIF. The output is then coupled through the diplexer for simultaneous transmission and reception from the DSIF CDC system.

The received signal is coupled through the diplexer and then attenuated before being coupled to the input of the receiver. Two attenuators will be used, one fixed (60 db) and one variable (0 – 90 db), to simulate reception of signals at lunar ranges. An S-band signal generator will be provided to supply a calibrated signal to the receiver. A coaxial switch will be provided to switch the receiver input from the diplexer to the signal generator for calibration.

CONFIDENTIAL

CONFIDENTIAL

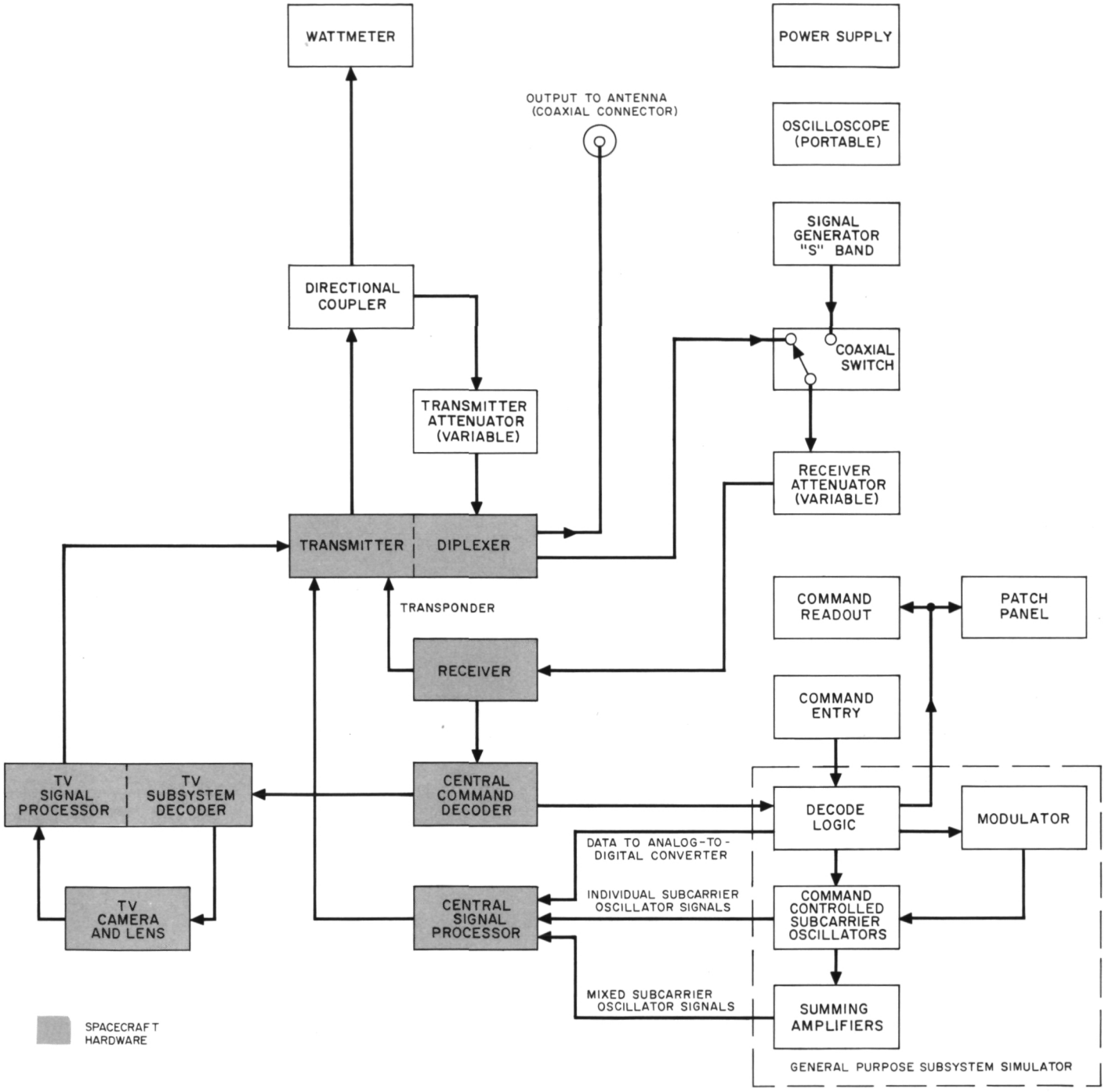

Fig. 160. *Surveyor* spacecraft simulator

The receiver will process the RF signal and provide the proper information to the central command decoder (CCD) in a digital code and also provide a phase-locking output to the transmitter.

The transmitter will have the identical capabilities of a spacecraft transmitter in that any one of three oscillators may be used to provide the carrier frequency. A transmitter local oscillator is used for transmission of simulated scientific data and normal television data or a transmitter crystal-controlled, voltage-controlled oscillator may be used for emergency TV transmission. During phase-locked transponder operation, the receiver local oscillator will provide the carrier frequency.

CONFIDENTIAL

CONFIDENTIAL

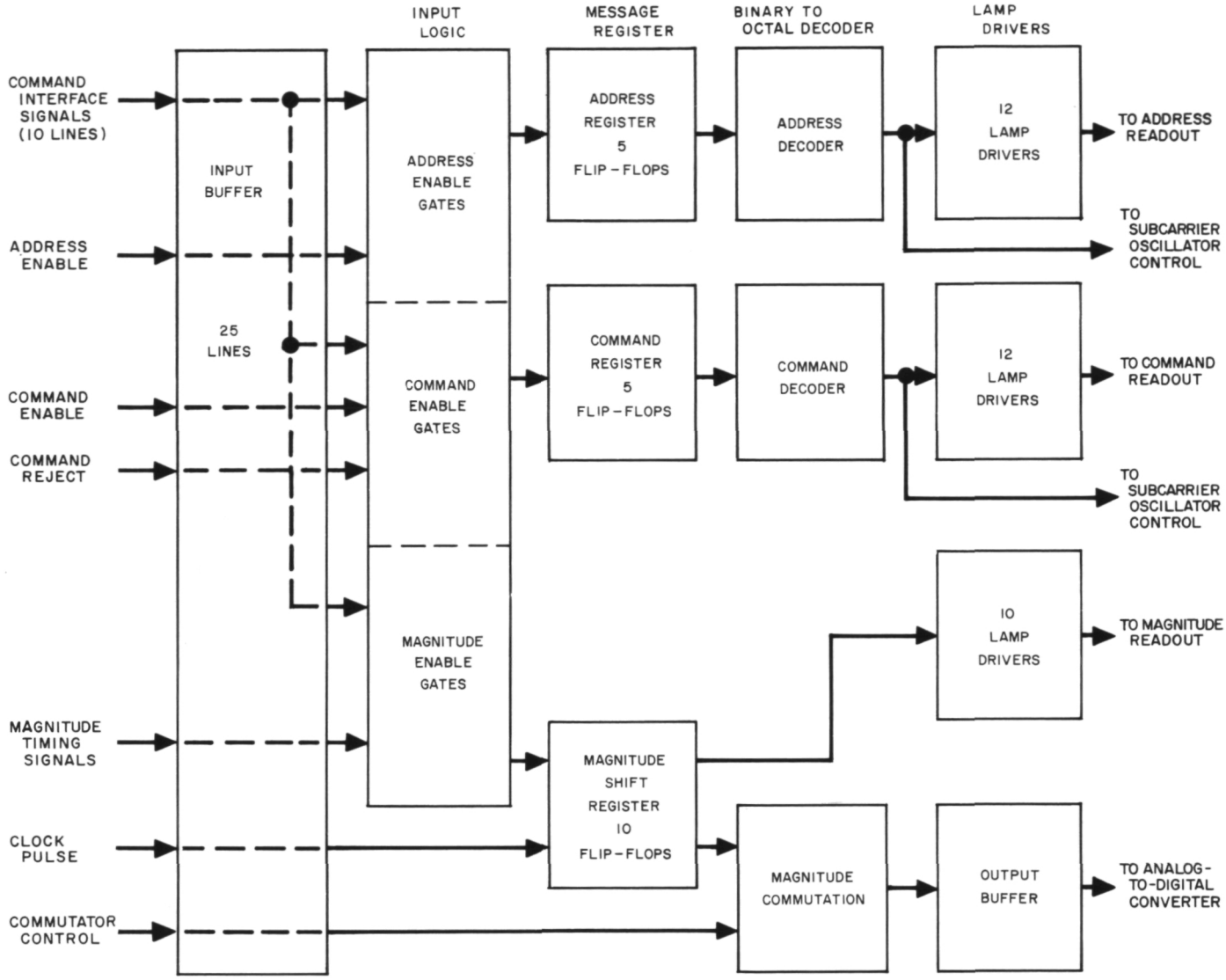

Fig. 161. Decode logic

Spare units for the basic bus items (transmitter diplexer and receiver transponder) are to be supplied. Other RF components (attenuators, coaxial switch, directional coupler, and wattmeter) are highly reliable and need not have spares.

b. TV subsystem. The television system of the SSS will consist of modified basic bus *Surveyor* spacecraft hardware. It will include a TV signal processor, a No. 2 camera unit, a subsystem decoder, and standard RETMA test patterns.

The subsystem decoder will accept TV commands from the central command decoder as 5-bit words. It will decode the commands and send them on to the camera and lens system. The camera will accept and execute the commands, then transfer video, mirror, and line position information to the TV signal processor. Mirror and line position information leaving the camera will be analog. This information will be converted in the TV signal processor to binary form.

The output of the TV signal processor, which consists of video and binary position information, is fed to the transmitter. Positioning information will be transmitted continuously for each frame, except when video information is being transmited. The TV system will operate in both the normal and emergency modes.

A special lens will be specified to optimize the mechanical packaging configuration.

CONFIDENTIAL

c. Central command decoder. Command decoding in the SSS will utilize a central command decoder identical to the basic bus unit in the *Surveyor* spacecraft. The fully redundant unit will be used, allowing closed-loop operation of the central decoder select unit and obviating the necessity for a spare unit.

Inputs to the central command decoder are in the form of standard-length serial binary words. These words will be sent to the general-purpose subsystem simulator (GPSS) where they produce responses typical of those which would result in the spacecraft. Failure of the complement check or loss of word synchronization during transmission causes the central command decoder to initiate a command reject signal in the GPSS which is transmitted back to the DSIF.

d. Central signal processor. The signal-processing system of the SSS will contain a central signal processor which is basic bus *Surveyor* spacecraft hardware. This unit will be identical to that used on the spacecraft with the following exception: since redundancy is not necessary for this portion of the SSS, one analog-to-digital converter and two weighted summing amplifiers (those for modulation of Transmitter B) will not be included.

The central signal processor will gather all pertinent data and verification signals and prepare them for subsequent transmission.

The central signal processor will include the following circuits: one analog-to-digital converter, three subcarrier oscillators with associated bandpass filters, and four summing amplifiers.

e. General-purpose subsystem simulator. The general-purpose subsystem simulator (GPSS) performs the functions of command decoding and signal processing on the subsystem level. Command decoding is performed only once and results in control signals for the address and command readouts as well as to the subcarrier oscillators (SCOs), modulators, and signal generator. The unit performs functions which are virtually identical to those performed by the spacecraft engineering signal processor, the flight control electronics, the various scientific auxiliaries, and special signal generation equipment which drives the auxiliaries.

The logic (see Figure 161) will simulate the scientific and engineering subsystem decoders, drive the readouts, and control the SCO modulators and signal generators.

Input buffering is provided to translate the input signals from the central command decoder and the analog-to-digital converter in the central signal processor into levels that are compatible with the standard digital elements proposed for the GPSS.

Input logic directs the command interface signals to the address, command, and magnitude registers. Direction is accomplished by use of the control signals developed in the central command decoder. All logic is accomplished by standard "nor" elements.

The address and command registers are parallel entry flip-flop registers storing the information in binary form. Each address and command is stored until the next message is received.

The magnitude shift register is used to provide storage for command magnitudes in a manner similar to that used by the flight control subsystems of the spacecraft. This register provides input to the magnitude readouts and to a commutator logic block which performs a function of the engineering signal processor. Commutating control signals are received from the analog-to-digital converter and the commutated magnitude outputs return to the digital input of the analog-to-digital converter for telemetering back to the CDC. Decode logic is provided to translate the address and command binary codes into octal form for direct numerical readout.

Octal information from the binary-to-octal decode logic is fed through the SCO, modulator, and signal generator (see Figure 162) for feedback through the central signal processor and the microwave link to the CDC. A switch is provided to disconnect transmitter power to allow the SSS to perform as an on-line monitor.

In response to an on-off command, the control logic sums addresses and commands to select and control operation of the proper SCO or signal generator. Memory is provided so that multiple channel operations can be accomplished.

Each subcarrier oscillator is a purchased item. Twelve such units provide the complement of frequencies necessary for simulation of the required functions. Six of the SCOs are for standard center frequencies; the other six represent some redesign of existing circuits by the manufacturer.

Some of the subcarriers must be modulated to simulate the telemetered data in a meaningful manner. A modulator will be designed for this purpose. Preliminary system study indicates that four modulating signals (two rectangular and two sinusoidal) will be sufficient to provide this meaningful simulation of all specified data. The modulation sources will be controlled independently of the SCOs by the control logic.

CONFIDENTIAL

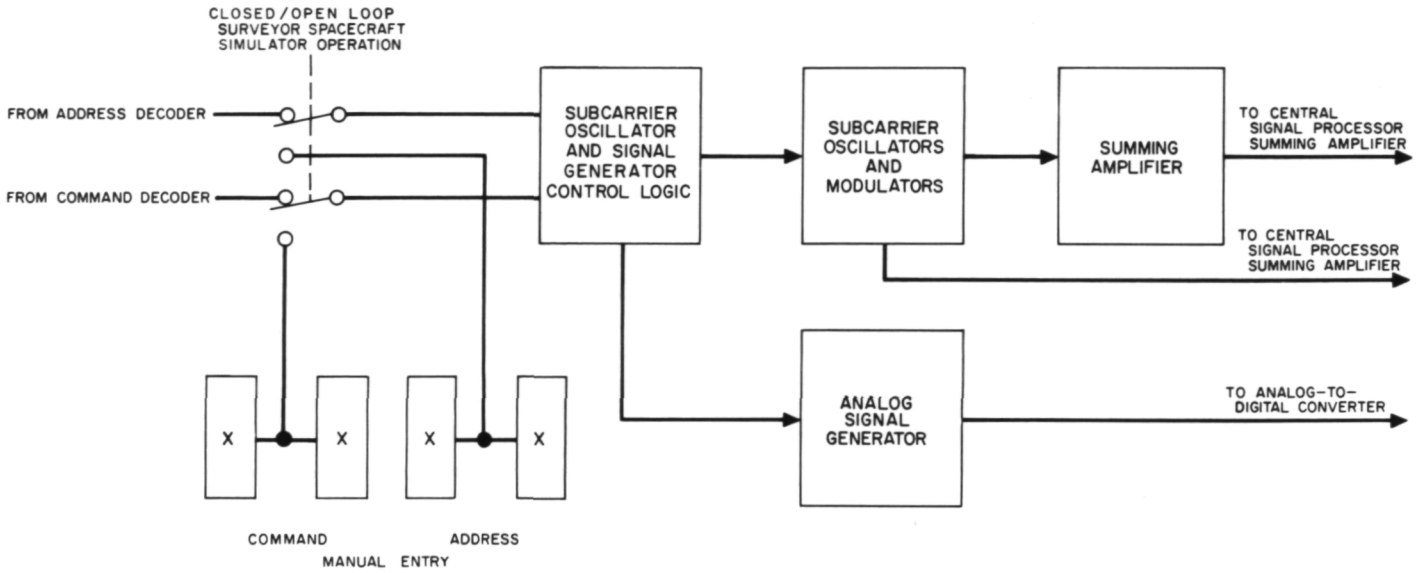

Fig. 162. Subcarrier oscillators and summing amplifiers block diagram

Weighted summing amplifiers will be provided to mix SCO outputs in simulations of tape recorder playback, accelerometer data processing, and the acoustic velocity experiment. These amplifiers will be of an existing design but repackaged on standard cards for equipment capability. This design has bandwidth, dynamic range, and stability, which are more than adequate for this application.

This highly flexible arrangement allows use of a minimum number of components. Most units perform at least two functions. For example, the 70-kc SCO is (1) pulse-modulated and mixed with six other SCOs for "tape recorder playback," (2) sinusoidally modulated and mixed with three other oscillators for acoustic velocity experiment simulation, (3) used unmodulated in combination with three other SCOs for engineering data, and (4) used by itself as the "density" SCO.

The signal generator responds in a manner to simulate most of the engineering signal processor functions. It switches standard analog signals into the analog-to-digital converter. These signals are interrupted by the commutator control signals to simulate commutator operation.

f. Command readouts. The projection readout devices for ordinary command readout are used extensively throughout the display systems. Light from a standard 28-v bulb is projected through a photographic negative containing the legend to be read out. The lamps may be changed from the front panel without special tools. Standard lamps are used to drive the readouts.

g. Command entry. The "closed/open loop" switch will allow addresses and commands to be entered at the SSS for CDC receiver exercise without requiring the CDC transmit cycle to function. In addition to the use of GPSS equipment, manual entry of ordinary commands on the four numbered dials can be used to control the TV subsystem.

h. Patch panel. A patch panel will be provided to enable the operator to monitor, test, and control various functions of the simulator. Typical signals monitored will be command enable and reject signals, input/output signals of all subunits, and outputs of the central signal processor. Other features shall include scope synchronizing signals, a central command decoder control switch, and provision for utilizing the gray bar generator.

Examples of functions which will be possible by use of the patch panel are troubleshooting, direct interconnection of the SSS and the CDC in a closed loop which excludes the DSIF, and monitoring of the modulating signals to the transmitter.

i. Power supplies. Dc power is required at five different voltage levels within the SSS. The spacecraft units require +29 and +22 v, while the SSS equipment will operate from +29, +15, −15, and −28 v. Higher voltages are required by some spacecraft circuits, but these are produced within the unit requiring them by electrical conversion units (ECUs). The ECUs operate from one of the primary voltages.

CONFIDENTIAL

Four primary power supplies will provide the power necessary for operation of the SSS. One of these, the +29-v supply, will provide both of the basic spacecraft voltages. Plus 22-v power will be derived from this supply through use of a Zener diode. The other supplies will provide +15, −15, and −28 v.

The functions of all four of these supplies are well within the specified capability of a single lambda power supply. Thus, a single unit in the spares complement will provide the necessary backup for any of the primary power supplies.

3. Air-Conditioning Test

The retro-rocket and other sensitive items in the encapsulated spacecraft must be maintained within prescribed temperature limits. Various heat dissipating packages within the nose fairing plus solar impingement on the nose fairing create a heat problem. Air-conditioning ducts within the nose fairing are provided after enshroudment, and the temperature under the nose fairing is maintained at 85 ± 5°F after spacecraft/*Centaur* mating until lift-off.

In order to designate proper air distribution ducting locations and to determine the quantity of air required to maintain specified temperatures, joint air-conditioning tests will be performed by General Dynamics, Astronautics Division, and Hughes Aircraft Company in Culver City.

The air-conditioning tests will be performed as described in the following test plan outline:

I. *Test Objectives* – The major air-conditioning test plan objectives shall consist of the following:

(a) Demonstrate that the air distributed within the sealed nose fairing cavity will maintain the spacecraft retro-rocket at the required temperature of 85 ± 5°F.

(b) Verify that the ductings within the nose fairing are located properly to permit the air flowing from the holes within the ducting to the required heat dissipating packages at the required quantity and temperature to maintain the package at the specified temperature (see Hughes Aircraft Company Specification No. 239500).

(c) Determine and reorient, as necessary, the location of the air holes on the ductings to provide proper air distribution around the encapsulated spacecraft.

(d) Define and determine the best location for the temperature sensor within the spacecraft for use during the on-stand air-conditioning operation at AMR.

(e) Determine the effect of the peak spacecraft power dissipation on the temperature environment.

II. *Equipment*

Hughes-Supplied Equipment – Hughes Aircraft Company will supply the following for the GDA air-conditioning test:

(a) A modified spacecraft mockup with simulated heaters on the heat dissipating packages.

(b) Manual heater control instrumentation such as thermocouples, pressure transducers, flowmeters, and the required recorders.

(c) A small cooling unit to simulate the lower *Centaur* dissipating temperature. The unit shall be capable of maintaining temperatures within limits to be determined jointly by GDA and Hughes.

(d) Handling equipment for all Hughes supplied items.

(e) In addition to the above, Hughes Aircraft Company, in conjunction with GDA, will supply the necessary personnel to perform the tests.

GDA-Supplied Equipment – GDA will supply the following:

(a) A nose fairing with the associated air ducting and the required lower bulkhead, or seal.

(b) An air-conditioning unit capable of performing similarly to the GDA-AMR on-stand air-conditioning unit.

(c) Handling equipment for GDA-supplied items.

(d) In addition to the above, GDA, in conjunction with Hughes Aircraft Company, will supply sufficient personnel to perform the tests.

III. *Test Support Requirements* – The spacecraft mockup will be provided with heaters within the heat dissipating packages. The heaters will be wired to a separate control panel where they can be turned on independently, or as required, during the actual countdown checkout performance at AMR.

Heat Lamps – Heat lamps shall be provided with the capability of dissipating or radiating temperatures from 100 to 140°F on the outside nose fairing skin to simulate solar impingement.

Thermocouples – Thermocouples shall be provided in the following quantities for the following locations:

(a) Three on the retro-rocket casing near the attachment point.

(b) Three around the thrust chamber nozzle.

(c) Three around the upper portion and three (3) around the middle of the retro-rocket casing.

(d) Two at each propellant tank.

(e) Two at the lower section of the nose fairing.

(f) Two at the upper nose fairing.

Pressure Transducers – Pressure transducers shall be provided in the following quantities for the following locations:

(a) One will be located at the air intake ducting in front of the biological filter and one behind the filter.

(b) One at the outlet ducting.

(c) Three on the retro-rocket casing.

(d) One at the upper section of the nose fairing cavity.

(e) Two at the lower section of the nose fairing cavity.

Flow Meters – Flow meters shall be supplied in the following quantities and at the following locations:

(a) One will be located at the intake.

(b) One at the outlet ducting.

(c) One in front of the biological filter.

(d) One behind the biological filter.

(e) Two at the required air shower section of the inside ducting.

(f) Two at the lower section of the ducting.

(g) In addition to the above, two 16-channel Brown recorders for temperature measurement and one 18-channel Brush recorder will be required.

Cooling and Air-Conditioning Equipment – A cooling unit (as specified in Part II, Hughes-Supplied Equipment) will be used to simulate the temperature between the *Centaur* and the *Surveyor* transition area. GDA will supply a mobile air-conditioning unit (as specified in Part II, GDA-Supplied Equipment) together with the interconnecting ducting, nose fairing and required seal. Biological filters shall be supplied to define the pressure drop across the filter. A cover with openings for the required air ducting will be required around the *Surveyor/Centaur* transition area to simulate the cylindrical sections of the nose fairing.

IV. *Test Methods*

Procedures – The procedures for evaluating the air distribution of the air-conditioning unit and the air distribution ducting within the nose fairing will be basically as follows:

(a) The spacecraft mockup will be instrumented and encapsulated in the nose fairing.

(b) The transition area between the spacecraft and the *Centaur* will be covered with a tent-like covering and the ducting of the smaller cooler will be inserted.

(c) Subsequent to encapsulation and connection of air-conditioning, each heat dissipating package will be turned on in the same sequential order as required during countdown procedure.

(d) The air-conditioning and lower cooling unit will be turned on and the temperature airflow and pressure measured continuously during the test run.

Data Evaluation – At the end of the first test run (running time: approximately 5 to 8 hr) the data will be evaluated to define the pressure and temperature within the nose fairing.

Ducting Reorientation – If required, the air distribution ducting will be oriented after the first run to gain better temperature control during the second test run.

Criteria of Success – The criteria of success shall consist of achieving the specified test objective (see Part I, Test Objectives). The test runs will be repeated as required to achieve the criteria of success.

4. Surveyor Spacecraft Handling Equipment and Procedures

The *Surveyor* spacecraft requires specially designed equipment for shipping and handling because of the complex configuration of the spacecraft. Requirements imposed by temperature control criteria also necessitate the use of special handling equipment. The following describes the handling equipment for the *Surevyor*, the method of transportation, assembly, and handling from Culver City to the Cape Canaveral Missile Test Annex launch complex. Any portion of these procedures may be reversed for recycle preparation.

Major handling equipment for the program is listed in Table 34. Spacecraft handling procedures and the use

of associated handling equipment will be as shown in Figures 163 through 168.

a. Spacecraft shipment. During assembly and test procedures at Hughes Aircraft Company, Culver City, the spacecraft will be mounted on the handling stand which is bolted to the spacecraft at the interface. The stand height will permit placement of the landing gear in the extended position above the ground. The stand will also be used when the spacecraft is transported on ground transport vehicle No. 1 (GTV No. 1). GTV No. 1 is used in handling the unencapsulated spacecraft. GTV No. 2 will be used in handling the completely assembled spacecraft, nose fairing, and adapters.

After completion of spacecraft assembly and heat sterilization processes at Culver City, the spacecraft will be packaged for shipment in a clean condition. The clean spacecraft will then be mounted on the GTV No. 1 and the protective cover installed. GTV No. 1, with the spacecraft mounted, will be loaded aboard a moving van for transport to General Dynamics, Astronautics Division for combined system tests.

b. Retro-rocket handling. The retro-rocket engine will be packed in a special container and shipped separately to Cape Canaveral from the Thiokol Chemical Corporation.

Upon arrival at the explosive safe area, the retro-rocket will be removed from its shipping container by means of a special lifting tool. The retro-rocket motor will be fitted with a special mounting ring and then mounted on the rocket engine stand. After the retro-rocket has been fitted with the rocket engine roll-over tool, the retro-rocket will be lifted from the engine stand by the sling hoist.

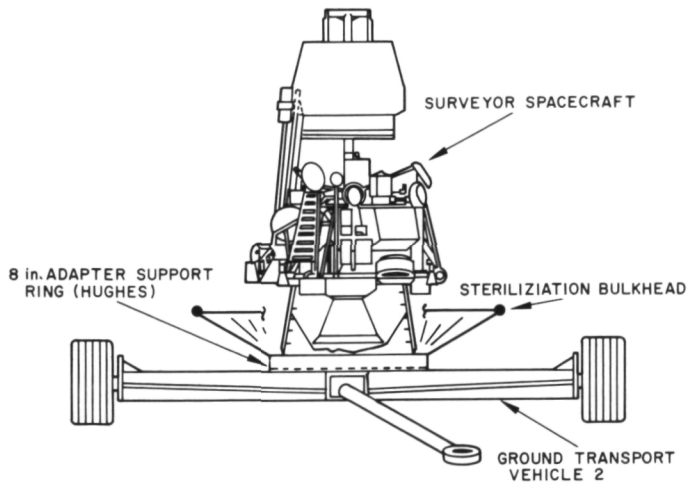

Fig. 163. *Surveyor* spacecraft and Ground Transport Vehicle No. 2

Table 34. Spacecraft handling equipment

Hughes-supplied equipment	Use
Handling stand	To support spacecraft prior to upper payload adapter (GDA) installation.
Ground transport vehicle No. 1 (small)	To transport spacecraft prior to spacecraft mating to GDA nose fairing and torus assembly.
Ground transport vehicle No. 2 (large)	To transport assembled spacecraft and nose fairing.
Hoisting slings	To handle spacecraft during checkout and installation of the retro-rocket.
Rocket engine roll-over tool	To rotate rocket engine 180 deg in preparation for spacecraft installation.
Rocket engine stand	To support rocket engine prior to spacecraft installation.
Adapter support ring	An 8-in. support ring used at the interface of the aft portion of the forward payload adapter. This will protect the altitude marking radar while transporting on ground transport vehicle No. 2.
Weight, balance and optical dock equipment	The retro installation cart will be used to install the retro-rocket (or dummy) into the spacecraft.
Mobile temperature control unit (MTCU)	To maintain proper temperature of the spacecraft after encapsulation within the nose fairing. The unit is mobile and will be towed in a trail position with the spacecraft during transport to launch area and will be disconnected when spacecraft/*Centaur* mating procedures are conducted.
Special lifting tool for retro-rocket	To lift the retro-rocket from the shipping case.
Special mounting ring for retro-rocket	The special mounting ring will be required before the retro-rocket can be mounted on the retro-rocket installation cart.
Work platforms provided and designed by Hughes as required to perform spacecraft tasks that cannot be reached from the ground.	

GDA-supplied equipment	Use
Nose fairing support ring	A platform for holding the nose fairing halves above the floor prior to assembly.
Nose fairing slings	Overhead cables used in assembling the nose fairing halves.
Nose fairing torus halves	Two half-rings which will be assembled around the nose fairing for lifting the nose fairing/spacecraft during *Centaur* mating operations.
Torus handling slings	Cables used to lift and assemble the two torus half-rings.
Torus assembly handling carts	Two torus-nose fairing carts will be used to encapsulate the spacecraft within the nose fairing.
Spacecraft support arms	Support arms used to attach the nose fairing to the spacecraft during the spacecraft/nose fairing/*Centaur* mating procedures. Support arms will be installed just prior to lifting the assembled spacecraft/nose fairing from ground transport vehicle No. 2 at the launch pad and removed *after mating procedures are completed.*
Centaur stretch sling cables	To support the *Atlas/Centaur* during the period of time the launch vehicles are not fully pressurized.
Stretch adapter sections	Used to support *Atlas/Centaur* (on stand) and as attach points for the stretch slings.
Cylindrical nose fairing sections	The nose fairing sections are installed last in the nose fairing/*Centaur* securing operation.
Work platforms	Designed and provided by GDA as required to perform nose fairing tasks in the final assembly area.
Environmental shroud	Maintains temperature control during test.
Fore and aft payload adapters	Used in mating the spacecraft to *Centaur*.

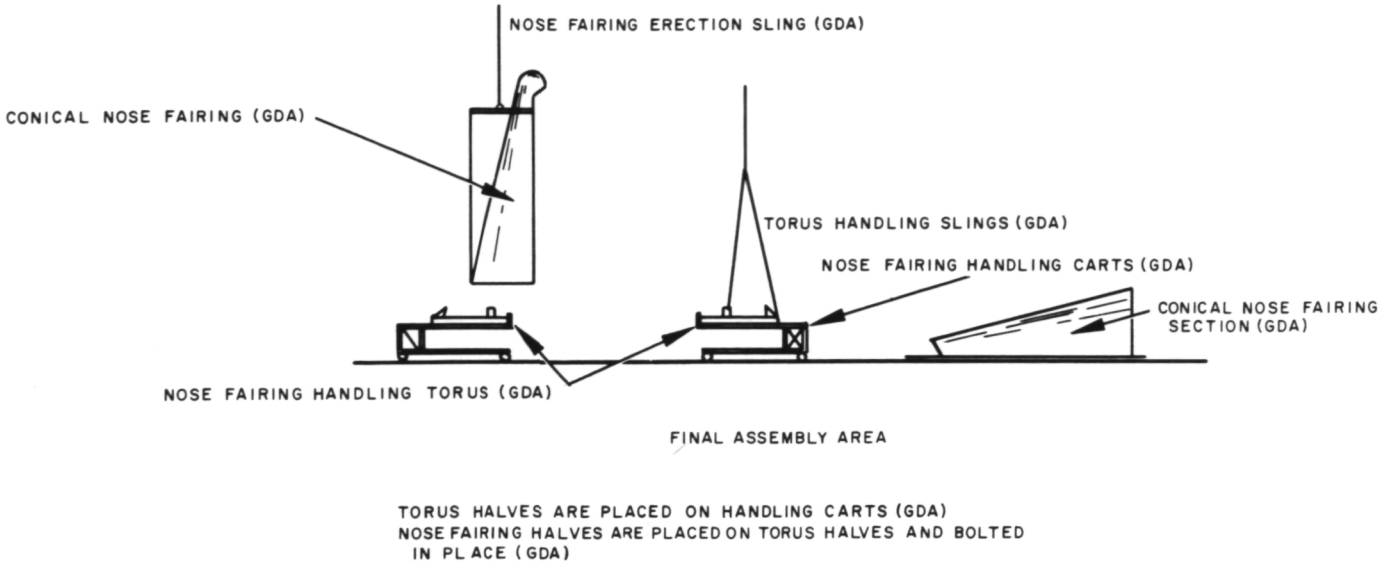

Fig. 164. Mating of nose fairing and encapsulated spacecraft

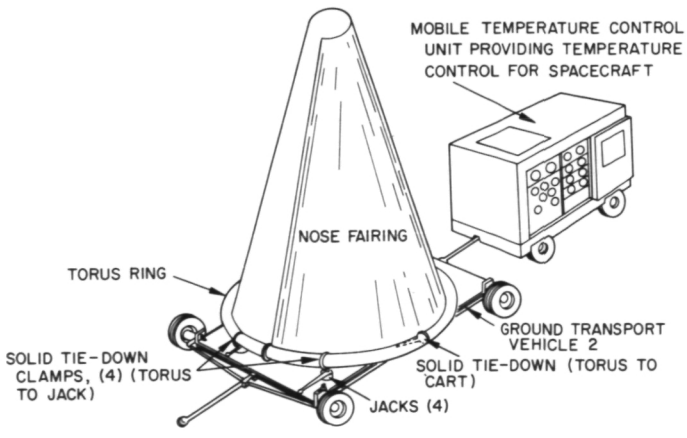

Fig. 165. Spacecraft inside nose fairing in *towing configuration*

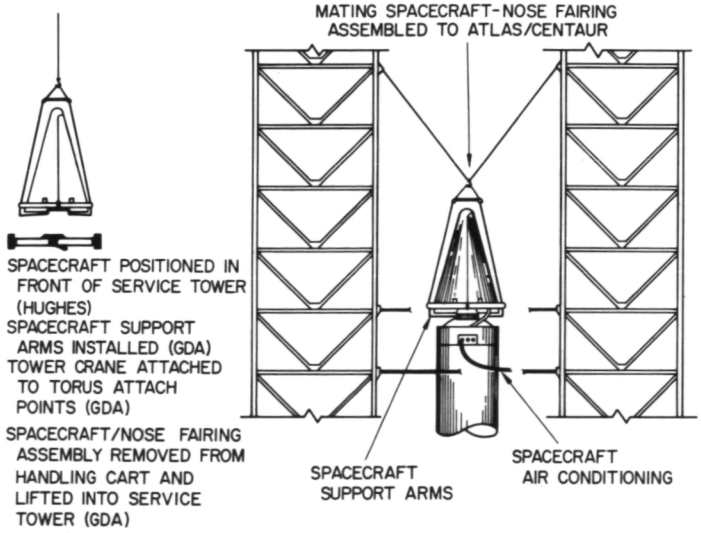

Fig. 166. Payload-launch vehicle mating operation

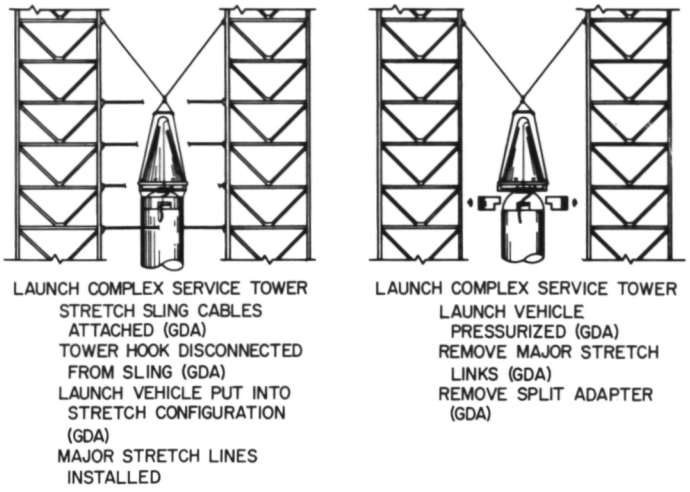

Fig. 167. Spacecraft installed on *Centaur* in system test configuration

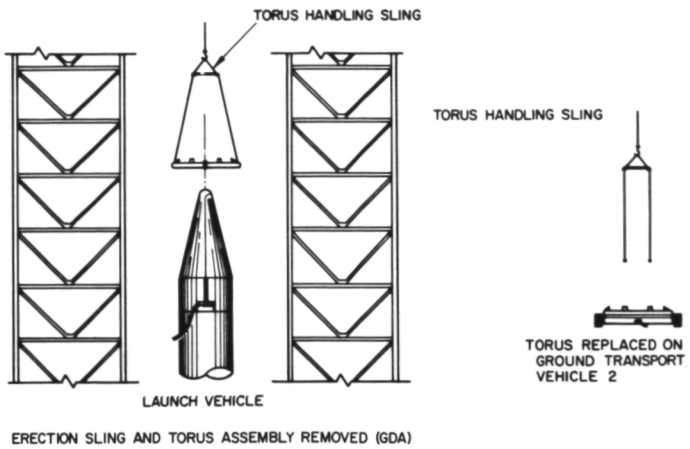

Fig. 168. Removal of torus (spacecraft-launch vehicle ready for launch)

The roll-over tool will be used to rotate the retro-rocket 180 deg to position the thrust chamber down prior to lowering the rocket assembly to the installation cart.

c. Retro-rocket installation. After spacecraft assembly at the spacecraft checkout facility and field acceptance tests have been completed, the spacecraft will be transported to the explosive safe area for assembly of all flight equipment. The spacecraft will be loaded with the required propellant and high-pressure gas in the propellant loading area and the retro-rocket installation sequence will proceed as follows:

(1) The spacecraft is returned to the final assembly test area.
(2) The retro-rocket is mounted on the weight, balance, and optical dock equipment.
(3) The spacecraft is hoisted and lowered over the positioned retro-rocket and secured.

d. Mounting spacecraft on ground transport vehicle No. 2. Weight, balance, and optical check procedures are performed. The assembled spacecraft is lifted from the weight and balance dock and the forward payload adapter installed. The adapter support ring is fitted to the forward payload adapter. The spacecraft is installed on the locater ring of GTV No. 2. The nose fairing is assembled upon the torus ring and torus-nose fairing handling carts.

e. Mating spacecraft and nose fairing. The two torus and nose fairing handling carts are brought to the spacecraft test area together with both halves of the nose fairing, both halves of the torus ring, and the required handling slings. Each half of the torus ring is installed on a torus and nose fairing handling cart. The two handling carts are positioned opposite each other and the halves of the torus ring bolted together. The nose fairing halves are fastened together on the support ring. The assembled nose fairing is then positioned on the assembled torus ring and attached. The assembled nose fairing and torus ring are then separated on the carts with the torus ring halves still attached to the nose fairing halves in preparation for encapsulating the spacecraft.

During the nose fairing/torus ring mating operation, the sterilization bulkhead is attached to the upper payload adapter which has been mounted on a support ring to prevent damage to the membrane seal. The spacecraft is then mounted on the forward payload adapter and the entire assembly is placed on GTV No. 2.

The nose fairing-torus ring halves are in a separated configuration and each half is mounted on a torus nose fairing handling cart. The two assemblies are positioned on opposite sides of the GTV No. 2. The torus nose fairing carts are fitted with a guide rail that will be mated to a receiving fixture previously installed under the bed of the GTV No. 2.

The guide rail and fixture provide the alignment necessary to prevent membrane seal damage and facilitate final mating of the nose fairing. After removal of the torus handling carts, the spacecraft is sealed in the nose fairing and is ready for terminal surface sterilization utilizing the mobile sterilization and temperature control unit.

f. Transporting the encapsulated and sealed spacecraft to launch complex. After terminal surface sterilization, the spacecraft, connected to the mobile temperature control unit, is transported to the launch complex.

The mobile temperature control unit, attached to the spacecraft in the trail position, will maintain temperature control of the spacecraft throughout transportation and up to mating operation.

g. Spacecraft/Centaur mating operation at launch complex. The normal condition of the *Atlas/Centaur* at the launch pad is with stretch slings installed and pressure in both the *Atlas* and the *Centaur*.

Upon arrival at the pad the encapsulated spacecraft is located where attachments can be made with the overhead *Atlas/Centaur* gantry crane.

Before the spacecraft is removed from the GTV No. 2, the three support arms must be installed to tie the spacecraft to the torus nose fairing assembly.

The gantry crane and slings are connected to the torus ring. The torus ring now supports both the nose fairing and the spacecraft through the support arms. The adapter ring is removed along with all tiedown and jacks supporting the torus-nose fairing assembly. The mobile temperature control unit is disconnected and the stretch slings supporting the *Atlas/Centaur* are removed. The spacecraft is then hoisted above the *Centaur* where the upper payload adapter (attached to the spacecraft) is bolted to the lower payload adapter (attached to the *Centaur*). The *Atlas/Centaur* stretch cables are then attached. At this time the torus-nose fairing is supported with the *Atlas/Centaur* stretch cable. The environmental shroud is installed and the air-conditioning line and all umbilical connections are installed. The stretch links between the torus and the *Centaur* are connected and combined system tests are ready to be started.

h. Launch preparations. After all testing is completed, the final mating of the spacecraft and *Centaur* is completed in the following sequence:

(1) Pressurize launch vehicle.

(2) Remove stretch links between torus and *Centaur*.

(3) Remove environmental shroud.

(4) Install permanent cylindrical section.

(5) Remove spacecraft support arms.

The *Atlas/Centaur/Surveyor* is ready for launch countdown.

References

1. *Surveyor Spacecraft System Bimonthly Progress Summary,* Hughes Aircraft Company, SS 106, mid-February 1962 through mid-April 1962.

2. *Lunar Night Survivability and Alternate Payload Capability for Surveyor Spacecraft for Launches 4 and 5,* Hughes Aircraft Company, SSD 2323R, 25 June 1962.

3. *American Ephemeris and Nautical Almanac,* 1963, pp. 282-292.

4. Johnson, H. L. and Morgan, W. W., "Fundamental Stellar Photometry for Standards of Spectral Type on the Revised System of the Yerkes Spectral Atlas," *The Astrophysical Journal,* Vol. 117, No. 3, May, 1953.

5. Hogg, A. R., "Photometric Observations of 244 Bright Stars," Mt. Stromlo Observatory, The Australian National University, Canberra, A.C.T., Memograph, November, 1958.

6. Hyde, Gerald R. and Blount, George H., "Relative Detector Response to the Irradiance from the Stars," Santa Barbara Research Center, Goleta, California.

7. Allen, C. W., "Astrophysical Quantities," Athlone Press, London, 1955.

8. *Design Review Inventory for Canopus Sensor Surveyor,* Santa Barbara Research Center, Goleta, California, December 5, 1961.

9. *Explanatory Supplement to the Astronomical Ephemeris,* 1961, pp. 311-316.

10. *American Institute of Physics Handbook,* McGraw-Hill, New York, 1957.

11. *Surveyor Spacecraft System Bimonthly Progress Summary,* Hughes Aircraft Company SS 104, mid-October 1961 through mid-December 1961.

CONFIDENTIAL

This document contains information affecting the national defense of the United States, within the meaning of the Espionage Laws, Title 18, U.S.C., Sections 793 and 794, the transmission or revelation of which in any manner to an unauthorized person is prohibited by law.

CONFIDENTIAL